Yu Sun and Xinyu Liu (Eds.)

Micro- and Nanomanipulation Tools

AMN
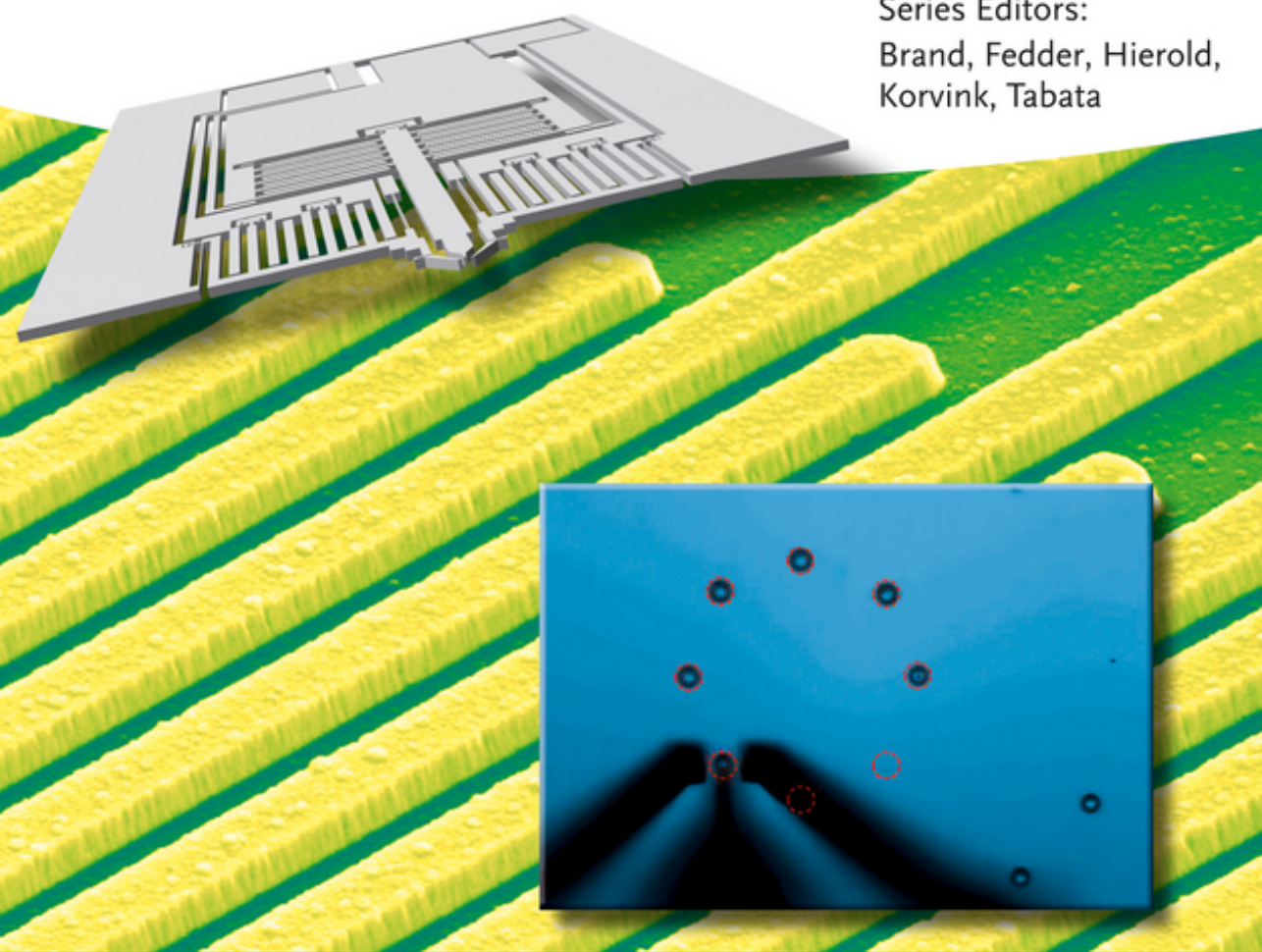
Edited by
Yu Sun and Xinyu Liu

Micro- and Nanomanipulation Tools

Related Titles

Briand, D., Yeatman, E., Roundy, S. (eds.)

Micro Energy Harvesting

2015
Print ISBN: 978-3-527-31902-2; also available in electronic formats

Brand, O., Dufour, I., Heinrich, S.M., Josse, F. (eds.)

Resonant MEMS
Fundamentals, Implementation, and Application

2015
Print ISBN: 978-3-527-33545-9; also available in electronic formats

Grossard, M., Chaillet, N., Régnier, S. (eds.)

Flexible Robotics / Applications to Multiscale Manipulations

2013
Print ISBN: 978-1-848-21520-7; also available in electronic formats

Bechtold, T., Schrag, G., Feng, L. (eds.)

System-level Modeling of MEMS

2013
Print ISBN: 978-3-527-31903-9; also available in electronic formats

Someya, T. (ed.)

Stretchable Electronics

2013
Print ISBN: 978-3-527-32978-6; also available in electronic formats

Troccaz, J. (ed.)

Medical Robotics

2012
Print ISBN: 978-1-848-21334-0; also available in electronic formats

Korvink, J.G., Smith, P.J., Shin, D. (eds.)

Inkjet-based Micromanufacturing

2012
Print ISBN: 978-3-527-31904-6; also available in electronic formats

Koc, M., Ozel, T. (eds.)

Micro-Manufacturing
Design and Manufacturing of Micro-Products

2011
Print ISBN: 978-0-470-55644-3; also available in electronic formats

Gauthier, M., Régnier, S. (eds.)

Robotic Microassembly

2010
Print ISBN: 978-0-470-48417-3; also available in electronic formats

Chaillet, N., Regnier, S.

Microrobotics for Micromanipulation

2010
Print ISBN: 978-1-848-21186-5; also available in electronic formats

Edited by Yu Sun and Xinyu Liu

Micro- and Nanomanipulation Tools

WILEY-VCH

Verlag GmbH & Co. KGaA

The Editors

Prof. Yu Sun
University of Toronto
Mechanical and Industrial Engineering
5 King's College Road
Toronto
ON M5S 3G8
Canada

Prof. Xinyu Liu
McGill University
Mechanical Engineering
817 Sherbrooke Street West
Montreal
QC H3A 0C3
Canada

Contents

About the Editors

Yu Sun is a Professor at the University of Toronto with cross appointments to Department of Mechanical and Industrial Engineering, Institute of Biomaterials and Biomedical Engineering, and Department of Electrical and Computer Engineering. He is the Canada Research Chair in Micro and Nanoengineering Systems. He was inducted Fellow of ASME, IEEE, and CAE for his work on micro–nano devices and robotic systems. His awards include the 2010 IEEE Robotics and Automation Society Early Career Award and an NSERC E.W.R. Steacie Memorial Fellowship in 2013.

Xinyu Liu is an Assistant Professor in the Department of Mechanical Engineering at McGill University, Canada, and also holds the positions of Canada Research Chair in Microfluidics and BioMEMS and Chwang-Seto Faculty Scholar. He received the Grand Challenge Canada Star in Global Health Award, the CMC Douglas R. Colton Medal for Research Excellence, and several best paper awards at major engineering and biomedical conferences. His current research interests include microfluidics, MEMS, and robotic micro and nanomanipulation.

Series Editors Preface

Since the advent of nanotechnology in the 1980s and 1990s and the award-winning developments of instruments to explore the domain of atoms and molecules by scanning tunneling and atomic force microscopes, the manipulation of individual atoms and molecules by applying forces even at room temperature was on the agenda of scientists. Stimulated by these early experiments, researchers and engineers started to develop and commercialize instruments for surface characterization and pattern transfer with nanometer resolution, which are as easy to operate at environmental conditions as optical microscopes. These developments became possible by the unprecedented progress in microsystems technology, integrating new functional materials beyond silicon and offering a technology platform for new applications in other scientific disciplines, such as the life sciences and its biomedical applications. In addition to the application of mechanical forces on small scales, researchers learned to apply electric, magnetic, and electrodynamic forces up to the frequency of light to manipulate objects from micron scales down to nanometers.

We present the 13th volume of Advanced Micro & Nanosystems (AMN), entitled Micro and Nano Manipulation Tools.

Prof. Yu Sun, University of Toronto, and Prof. Xinyu Liu, McGill University, are both renowned experts in this domain. They were very successful in coordinating a number of leading researchers and authors to present a book on micro and nanomanipulation. This book will be of great benefit for not only scientists and graduate students, entering the field or looking for specific information, but also industry researchers, technology strategists, and deciders in companies, who want to get a quick, but comprehensive access to the exciting and emerging field of micro and nanomanipulation in instruments, new processes, and fabrication technology.

June 2015   *Zürich, Christofer Hierold*

Preface

The capability of manipulating micrometer and nanometer-sized objects, such as cells and nanomaterials, enables new discoveries in biology, medicine, and materials science as well as industrial applications. Emerging robotics and microdevice technologies are proven to be effective in achieving high accuracy, precision, and throughput in micro and nanomanipulation tasks.

This book introduces recently developed tools for micro and nanomanipulation and presents example applications such as biomolecule screening, clinical diagnostics, surgery, and semiconductor packaging. These tools manipulate micro and nano objects using a multitude of physical means, including mechanical field, magnetic field, thermal field, fluidic field, acoustic field, optical field, surface tension, dielectrophoresis, electrostatics, and piezoelectricity. Some of these tools perform manipulation directly on microdevices while others manipulate objects using off-chip approaches. Microdevices are often integrated into robotic systems to combine their unique on-chip and off-chip manipulation capacities to tackle challenging tasks that cannot be fulfilled using a single method.

The topics in this book fall into two themes: "On-Chip and Device-Based Micro and Nano Manipulation" and "Robotic Tools and Techniques for Micro and Nano Manipulation."

- Chapter 1 reviews microfluidic techniques for performing high-speed cell manipulation tasks such as separation, sorting, characterization, weighing, lysis, and stimulation.
- Chapter 2 summarizes optical-induced electrokinetic techniques for on-chip manipulation and assembly of micro/nano objects.
- Chapter 3 discusses the physical behavior of DNA molecules in nanoslit confinement and slitlike nanofluidic devices for DNA manipulation.
- Chapter 4 summarizes microfluidic approaches for the manipulation and assembly of one-dimensional nanomaterials with applications in device construction.
- Chapter 5 reviews microfluidic platforms utilizing optically induced dielectrophoresis for cell and molecule manipulation.
- Chapter 6 reviews the design, fabrication, characterization, and biomedical applications of magnetically driven microrobots operated inside microfluidic channels.

- Chapter 7 discusses MEMS-based nanotweezers for the manipulation and characterization of molecules and cells.
- Chapter 8 summarizes untethered surgical devices at small scales and the corresponding localization, actuation, powering, and control techniques.
- Chapter 9 describes a new single-chip scanning probe microscopy technique and its image performance.
- Chapter 10 provides an overview of untethered magnetically driven micro-robotic devices for manipulating micro objects.
- Chapter 11 presents a robotic micro-compression system for measuring and mapping stiffness and topography of plant cell walls.
- Chapter 12 discusses a micromanipulation technique employing magnetotactic bacteria as microactuator swarms for the manipulation and transport of micro/nano objects.
- Chapter 13 reports the stiffness and kinematic analysis of a compliant parallel micromanipulator for biomedical manipulation.
- Chapter 14 reviews robotic systems and techniques for the manipulation of cells and small organisms.
- Chapter 15 summarizes commercially available tools for micromanipulation and highlights opportunities and market barriers.
- Chapter 16 presents a robot-aided micromanipulation system integrating optical tweezers and microfluidic devices for cell sorting and transportation.
- Chapter 17 describes the application of atomic force microscopy (AFM) to investigating molecular interactions involved in rituximab targeted therapy of lymphoma.
- Chapter 18 discusses an AFM-based dual-probe robotic system for the manipulation and characterization of cells and nanostructures.
- Chapter 19 reviews nanorobotic manipulation tools and techniques for the manipulation and characterization of helical nanostructures.
- Chapter 20 summarizes automated micro and nano handling techniques inside scanning electron microscopes (SEMs).
- Chapter 21 reviews robotic cell manipulation with microfluidic devices and under environmental SEM imaging.

Thanks to advances in tool and technique development, manipulation tasks that were not possible to achieve a couple of decades ago now have become routines; manipulation tasks that were manually done previously are now automated and executed faster, more accurately, and more precisely. As the micro-nanotechnology sector strides forward rapidly, the demand for advanced micro and nanomanipulation tools and techniques is becoming ever stronger. The strong demand virtually guarantees that more powerful micro-nanomanipulation tools will continue to emerge.

We thank all of the chapter authors and reviewers, and hope this book contributes to the education of next-generation micro-nanotechnologists and becomes a useful reference for students and researchers who develop new tools

and who use micro-nanomanipulation tools to study science or solve industry challenges.

June 2015   *Yu Sun and Xinyu Liu*
                                                   Toronto and Montréal, Canada

List of Contributors

Alex Abramson
Johns Hopkins University
Department of Chemical and
Biomolecular Engineering
3400 N Charles Street
Baltimore
MD 21218
USA

Mohd Ridzuan Ahmad
Universiti Teknologi Malaysia
Department of Control and
Mechatronics Engineering
Faculty of Electrical Engineering
Malaysia

Fumihito Arai
Nagoya University
Department of Micro-Nano
Systems Engineering
Furo-cho, Chikusa-ku
Nagoya
Aichi 464-8603
Japan

Malte Bartenwerfer
University of Oldenburg
Division Microrobotics and
Control Engineering
AMiR, Department of
Computing Science
Ammerländer Heerstraße
114-118
26129 Oldenburg
Lower Saxony
Germany

Shuxun Chen
City University of Hong Kong
Department of Mechanical and
Biomedical Engineering
83 Tat Chee Avenue
Kowloon Tong
Hong Kong
China

Andrew Choi
Johns Hopkins University
Department of Chemical and
Biomolecular Engineering
3400 N Charles Street
Baltimore
MD 21218
USA

Aram J. Chung
Rensselaer Polytechnic Institute
Department of Mechanical
Aerospace and Nuclear
Engineering
110 8th Street
Troy
NY 12180
USA

Cédric Clévy
Université Bourgogne
Franche-Comté / CNRS
Institute FEMTO-ST
Département AS2M
24 rue Savary
25000 besançon
France

Dominique Collard
The University of Tokyo
Institute of Industrial Science
LIMMS/CNRS-IIS (UMI 2820)
4-6-1 Komaba
Meguro Ku
Tokyo 153-8505
Japan

and

The University of Tokyo
Institute of Industrial Science
Center for International
Research on Micronano
Mechatronics (CIRMM)
4-6-1 Komaba
Meguro-ku
Tokyo 153-8505
Japan

Eric Diller
University of Toronto
Department of Mechanical and
Industrial Engineering
5 King's College Road
Toronto
ON M5S 3G8
Canada

Lixin Dong
Michigan State University
College of Engineering
Department of Electrical and
Computer Engineering
428 S. Shaw Lane
East Lansing
MI 48824-1226
USA

Xianke Dong
McGill University
Department of Mechanical
Engineering
Sherbrooke Street West 817
Montreal
QC H3A 0C3
Canada

Sergej Fatikow
University of Oldenburg
Division Microrobotics and
Control Engineering
AMiR
Department of Computing
Science
Ammerländer Heerstraße
114-118
26129 Oldenburg
Lower Saxony
Germany

Dimitrios Felekis
ETH Zurich
Institute of Robotics and
Intelligent Systems
Tannenstrasse 3
CH-8092 Zurich
Switzerland

Hiroyuki Fujita
The University of Tokyo
Institute of Industrial Science
Center for International
Research on Micronano
Mechatronics (CIRMM)
4-6-1 Komaba
Meguro-ku
Tokyo 153-8505
Japan

Toshio Fukuda
Nagoya University
Institute for Advanced Research
Furo-cho
Chikusa-ku
Nagoya 464-8601
Aichi
Japan

and

Meijo University
Department of Mechatronics
Engineering
Shiogamaguchi
Tempaku-ku
Nagoya 468-8502
Aichi
Japan

Michaël Gauthier
Université Bourgogne
Franche-Comté / CNRS
Institute FEMTO-ST
Département AS2M
24 rue Savary
25000 besançon
France

David H. Gracias
Johns Hopkins University
Department of Chemical and
Biomolecular Engineering
3400 N Charles Street
Baltimore
MD 21218
USA

and

Johns Hopkins University
Department of Materials Science
and Engineering
3400 N Charles Street
Baltimore
MD 21218
USA

Ueli Grossniklaus
University of Zurich
Institute of Plant Biology
Zollikerstrasse 107
CH-8008 Zurich
Switzerland

Hervé Guillou
The University of Tokyo
Institute of Industrial Science
LIMMS/CNRS-IIS (UMI 2820)
4-6-1 Komaba
Meguro Ku
Tokyo 153-8505
Japan

and

Université Grenoble Alpes
Institut NEEL
F-38000 Grenoble
France

and

CNRS
Institut NEEL
F-38042 Grenoble
France

Evin Gultepe
Johns Hopkins University
Department of Chemical and
Biomolecular Engineering
3400 N Charles Street
Baltimore
MD 21218
USA

Qiuquan Guo
South China University of
Technology
School of Electronic and
Information Engineering
380 Wushan Road
Guangzhou
Guangdong 510640
China

Masaya Hagiwara
Osaka Prefecture University
Nanoscience and
Nanotechnology Research
Center
1-2 Gakuen-cho
Naka-ku
Osaka 599-8570
Japan

David Hériban
Percipio Robotics SA
18 rue Savary
25000 Besançon
France

Soojung Claire Hur
The Rowland Institute at Harvard
University
100 Edwin H. Land Boulevard
Cambridge
MA 02142
USA

Laurent Jalabert
The University of Tokyo
Institute of Industrial Science
LIMMS/CNRS-IIS (UMI 2820)
4-6-1 Komaba
Meguro Ku
Tokyo 153-8505
Japan

Qianru Jin
Johns Hopkins University
Department of Chemical and
Biomolecular Engineering
3400 N Charles Street
Baltimore
MD 21218
USA

Wes Johnson
University of Toronto
Department of Mechanical and
Industrial Engineering
5 King's College Road
Ontario
ON M5S 3G8
Canada

Pasi Kallio
Institute of Automation and
Control
Tampere University of
Technology
P.O. Box 692
33101 Tampere
Finland

Tomohiro Kawahara
Kyushu Institute of Technology
Department of Biological
Functions Engineering
2-4 Hibikino
Wakamatsu-ku
Kitakyushu
Fukuoka 808-0196
Japan

Momoko Kumemura
The University of Tokyo
Institute of Industrial Science
LIMMS/CNRS-IIS (UMI 2820)
4-6-1 Komaba
Meguro Ku
Tokyo 153-8505
Japan

and

The University of Tokyo
Institute of Industrial Science
Center for International
Research on Micronano
Mechatronics (CIRMM)
4-6-1 Komaba
Meguro-ku
Tokyo 153-8505
Japan

Nicolas Lafitte
The University of Tokyo
Institute of Industrial Science
LIMMS/CNRS-IIS (UMI 2820)
4-6-1 Komaba
Meguro Ku
Tokyo 153-8505
Japan

and

The University of Tokyo
Institute of Industrial Science
Center for International
Research on Micronano
Mechatronics (CIRMM)
4-6-1 Komaba
Meguro-ku
Tokyo 153-8505
Japan

Sam Lai
City University of Hong Kong,
College of Science and
Engineering
Department of Mechanical and
Biomedical Engineering
83 Tat Chee Avenue
Kowloon Tong
Hong Kong 999077
China

Gwo-Bin Lee
National Tsing Hua University
Institute of Biomedical
Engineering
Institute of NanoEngineering and
Microsystems
Department of Power
Mechanical Engineering
101, Section 2, Kuang-Fu Road
Hsinchu 30013
Taiwan

Mi Li
State Key Laboratory of Robotics
Shenyang Institute of
Automation
Chinese Academy of Sciences
No. 114 Nanta Street
Shenyang 110016
Liaoning Province
China

and

University of Chinese Academy
of Sciences
No. 19A Yuquan Road
Shijingshan District
Beijing 100049
China

Wen Jung Li
Chinese Academy of Sciences
Shenyang Institute of
Automation
114 Nanta street
Shenhe District, Shenyang City
Liaoning Province
P. R. China

and

City University of Hong Kong
College of Science and
Engineering
Department of Mechanical and
Biomedical Engineering
83 Tat Chee Avenue
Kowloon Tong
Hong Kong 999077
China

Yangmin Li
University of Macau
Department of
Electromechanical Engineering
Faculty of Science and
Technology
Avenida da Universidade E11
Taipa
Macao 999078
China

and

Tianjin University of Technology
Tianjin Key Laboratory for
Advanced Mechatronic System
Design and Intelligent Control
School of Mechanical
Engineering
Binshui West Road
Xiqing District
Tianjin 300384
China

Yen-Heng Lin
Chang Gung University
Department of Electronic
Engineering
Graduate Institute of Medical
Mechatronics
259 Wen-Hwa 1st Road
Kwei-Shan
Tao-Yuan 333
Taiwan

Lianqing Liu
State Key Laboratory of Robotics
Shenyang Institute of
Automation
Chinese Academy of Sciences
No. 114 Nanta Street
Shenyang 110016
Liaoning Province
China

Xinyu Liu
McGill University
Department of Mechanical
Engineering
Sherbrooke Street West
Montreal
QC H3A 0C3
Canada

Raafat R. Mansour
University of Waterloo
Electrical and Computer
Engineering Department
200 University Avenue West
Waterloo
ON, N2L 3G1
Canada

and

Integrated Circuit Scanning
Probe Instruments (ICSPI Corp)
248 Corrie Crescent
Waterloo
ON, N2L 6E1
Canada

Sylvain Martel
École Polytechnique de Montréal
(EPM)
NanoRobotics Laboratory
Department of Computer and
Software Engineering
Institute of Biomedical
Engineering
2500
Chemin de Polytechnique
Montréal
QC H3T 1J4
Canada

Manuel Mikczinski
University of Oldenburg
Division Microrobotics and
Control Engineering
AMiR
Department of Computing
Science
Ammerländer Heerstraße
114-118
26129 Oldenburg
Lower Saxony
Germany

Masahiro Nakajima
Nagoya University
Department of Micro-Nano
Systems Engineering
Furo-cho
Chikusa-ku
Nagoya 464-8601
Aichi
Japan

Bradley J. Nelson
ETH Zurich
Institute of Robotics and
Intelligent Systems
Tannenstrasse 3
8092 Zurich
Switzerland

Stéphane Régnier
Institut des Systèmes Intelligents
et de Robotique (ISIR)
UPMC/CNRS UMR 7222
4 Place Jussieu
Boite Courrier 173
75252 Paris Cedex 05
75005 Paris
France

Neil Sarkar
University of Waterloo
Electrical and Computer
Engineering Department
200 University Avenue West
Waterloo
ON, N2L 3G1
Canada

and

Integrated Circuit Scanning
Probe Instruments (ICSPI Corp)
248 Corrie Crescent
Waterloo
ON, N2L 6E1
Canada

Metin Sitti
Carnegie Mellon University
Department of Mechanical
Engineering
5000 Forbes Avenue
Scaife Hall 423
Pittsburgh
PA 15213
USA

and

Max Planck Institute for
Intelligent Systems
Heisenbergstr. 3
70569 Stuttgart
Germany

Samuel M. Stavis
National Institute of Standards
and Technology
Center for Nanoscale Science
and Technology
100 Bureau Drive MS 6203
Gaithersburg
MD 20899
USA

Elizabeth A. Strychalski
National Institute of Standards
and Technology
Material Measurement
Laboratory
100 Bureau Drive MS 8312
Gaithersburg
MD 20899
USA

Dong Sun
City University of Hong Kong
Department of Mechanical and
Biomedical Engineering
83 Tat Chee Avenue
Kowloon Tong
Hong Kong
China

Yu Sun
University of Toronto
Department of Mechanical and
Industrial Engineering
5 King's College Road
ON M5S 3G8
Canada

Masaru Takeuchi
Nagoya University
Department of Micro-Nano
Systems Engineering
Furo-cho, Chikusa-ku
Nagoya 464-8601
Aichi
Japan

Tobias Tiemerding
University of Oldenburg
Division Microrobotics and
Control Engineering
AMiR
Department of Computing
Science
Ammerländer Heerstraße
114-118
26129 Oldenburg
Lower Saxony
Germany

Hannes Vogler
University of Zurich
Institute of Plant Biology
Zollikerstrasse 107
CH-8008 Zurich
Switzerland

Fei Fei Wang
Chinese Academy of Sciences
Shenyang Institute of
Automation
114 Nanta street
Shenhe District, Shenyang City
Liaoning Province
P. R. China

and

University of Chinese Academy
of Sciences
No. 19A Yuquan Road
Beijing 100049
P. R. China

Xiaolin Wang
City University of Hong Kong
Department of Mechanical and
Biomedical Engineering
83 Tat Chee Avenue
Kowloon Tong
Hong Kong
China

and

University of California
Department of Biomedical
Engineering
3120 Natural Sciences II
Irvine
CA 92697
USA

Yuechao Wang
State Key Laboratory of Robotics
Shenyang Institute of
Automation
Chinese Academy of Sciences
No. 114 Nanta Street
Shenyang 110016
Liaoning Province
China

Ning Xi
State Key Laboratory of Robotics
Shenyang Institute of
Automation
Chinese Academy of Sciences
No. 114 Nanta Street
Shenyang 110016
Liaoning Province
China

and

Department of Electrical and
Computer Engineering
College of Engineering
Michigan State University
No. 220 Trowbridge Road
East Lansing
MI 48824
USA

Xiao Xiao
University of Macau
Department of
Electromechanical Engineering
Faculty of Science and
Technology
Avenida da Universidade E11
Taipa
Macao 999078
China

Hui Xie
Harbin Institute of Technology
The State Key Laboratory of
Robotics and Systems
2 Yikuang
Harbin 150080
P.R. China

Jun Yang
South China University of
Technology
School of Electronic and
Information Engineering
380 Wushan Road
Guangzhou
Guangdong 510640
China

Miao Yu
Michigan State University
College of Engineering
Department of Electrical and
Computer Engineering
428 S. Shaw Lane
East Lansing
MI 48824-1226
USA

Li Zhang
The Chinese University of Hong
Kong
Faculty of Engineering
Department of Mechanical and
Automation Engineering
Shatin NT
Hong Kong
China

and

The Chinese University of Hong
Kong
Chow Yuk Ho Technology
Centre for Innovative Medicine
Shatin NT
Hong Kong
China

Shaolin Zhou
Western University (The
University of Western Ontario)
Department of Mechanical and
Materials Engineering
1151 Richmond Street
London
ON N6A 3K7
Canada

and

South China University of
Technology
School of Electronic and
Information Engineering
380 Wushan Road
Guangzhou
Guangdong 510640
China

Sören Zimmermann
University of Oldenburg
Division Microrobotics and
Control Engineering
AMiR
Department of Computing
Science
Ammerländer Heerstraße
114-118
26129 Oldenburg
Lower Saxony
Germany

1
High-Speed Microfluidic Manipulation of Cells

Aram J. Chung and Soojung Claire Hur

1.1
Introduction

The ability to manipulate biological cells is extremely useful for various biomedical and industrial applications. The grand challenge is determining how to manipulate cells (i) precisely (i.e., in a controlled manner), (ii) noninvasively (i.e., mimicking biological environment), and (iii) rapidly (i.e., high processing rate). In order to realize ideal cell manipulation, a microfluidics-based technique has been employed and explored extensively as a prime approach [1, 2]. This is largely because microfluidics-based cell manipulations provide unique opportunities for sophisticated and advanced biological assays. For example, an intrinsic laminar flow phenomenon allows for localized subcellular spatial and temporal flow control [3, 4]. In addition, the possibility of handling large numbers of cells via massive parallelization enables high-throughput single-cell processes [5–7], and the potential integration with other modalities permits fully integrated and automated systems [8, 9].

In this chapter, we will mainly discuss recent advancements in microfluidic cell manipulation techniques, which operate in a "high-speed" manner. General cell manipulation techniques using microchannels have been thoroughly reviewed and can be found elsewhere [10–15]. A high-speed process is extremely crucial for cell manipulation because the process speed directly correlates with biological sample volumes (i.e., throughput) that the technique is capable of analyzing. In fact, the demand is increasing for cell manipulation techniques that can process large volumes of biofluids (on the order from milliliters to liters), such as blood, pleural fluid, and urine [16–18]. High-speed cell manipulation is especially required to minimize residence times of cellular samples in microfluidic devices when off-chip analyses are necessary. Furthermore, there still remain many challenges to resolve cytotoxicity associated with extended cell residence times in microfluidic platforms [19].

We will interchangeably use cell processing rate (e.g., cells min^{-1}) and volumetric flow rate (e.g., μl min^{-1}) when we describe "high-speed" microfluidic cell manipulation techniques. The threshold values for "high speed" will vary with cellular manipulation purposes. This is a proper way to conduct meaningful comparisons among various techniques because analysis methods are contingent upon their biological research questions. For example, throughputs of individual cell interrogation and separation are incommensurable not only due to the types of biological samples, but also the desired measurements to be taken. It should be noted that the process time can be interpreted as time required for (i) sample preparations, (ii) processing a given volume, (iii) data analysis, and/or (iv) combinations of all mentioned. We mainly limit our discussion to the time that cells are residing in microfluidic devices, but we will discuss other time considerations as well. Finally, we exclude static cell manipulations from discussions, despite their massively parallel cell manipulation capabilities [5, 20], because of their predetermined and inflexible throughput.

As shown in Figure 1.1, cell manipulation in microfluidic devices can be categorized into *direct* (Section 1.2) and *indirect* (Section 1.3) methods. Individual cellular physical morphology can be modulated "directly" by applying forces, or cells' flowing path can be "indirectly" altered by external stimuli while the cell morphology remains intact within microfluidic platforms. First, we will introduce each cell manipulation technique, classify further based on its working principle, and discuss the advantages and disadvantages of the technology. We tabulated all techniques and summarized the cell processing rate based on the individual technique to easily compare all different approaches. In the last section, we briefly summarized the main ideas of this chapter and provided our outlook on microfluidics-based cell manipulation and insights on where the technology should head.
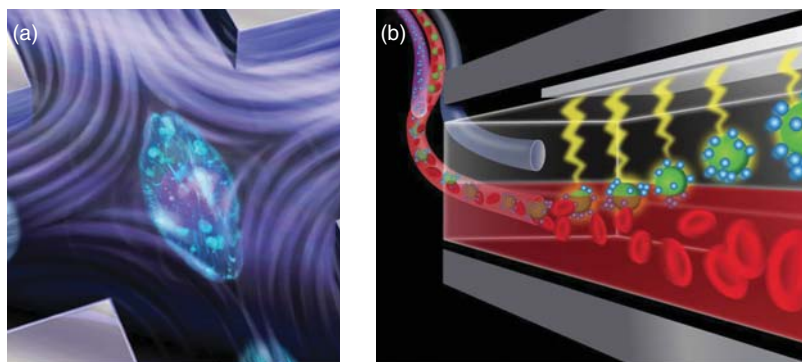
Figure 1.1 Two major examples of cell manipulation approaches in microfluidic channels, namely (a) direct cell [5] and (b) indirect cell manipulation [21].

1.2
Direct Cell Manipulation

Direct cellular manipulation involves processes that induce cell morphological changes under applied forces. The morphology of tested cells can be changed electrically, magnetically, optically, or mechanically [10–15]. We start by introducing each cell manipulation mechanism and discussing its advantages and limitations with respect to cell processing rate. Also, all direct cell manipulation techniques are tabulated in Table 1.1, comparing their characteristics.

1.2.1
Electrical Cell Manipulation

Electrical approaches, including patch clamp [22], impedance spectroscopy [23, 24], electroporation [25], and cell lysis [26], have been used to characterize and/or manipulate cells directly. Even though it is not possible to process a large number of cells rapidly due to challenging cell positioning tasks before cell manipulation, electrical cell manipulation techniques have elucidated many biologically meaningful cellular properties (e.g., size, membrane capacitance, and conductivity) and offered precise and relatively noninvasive cell manipulations [15].

One high-speed method from electrical techniques that should be highlighted is the impedance-based cell manipulation. The method monitors impedance changes in real time, allowing high-speed cellular property measurements. Typically, a current is generated by a conductive cell solution via metal electrodes with a small gap that are patterned on the substrate. The impedance changes are made when the cells pass over the electrodes (i.e., when the cells perturb the current path). For AC (alternating current) manipulation, most techniques are based on either low or intermediate frequencies. At low frequencies, the impedance amplitude indicates the cell size information since the cell membrane acts as a dielectric barrier, and at intermediate frequencies, membrane polarization is suppressed so that membrane properties can be obtained. Therefore, cell size, membrane, or cytoplasmic property information can be extracted based on impedance signatures [27, 28].

Because of its information richness, the technique was popularly used as an *impedance-based cytometer.* Reported sample processing rates based on impedance measurements can reach as high as $50\,000$ cells s^{-1} depending upon the operational electrical parameters and tested cellular characteristics [29]. Through this technology, distinct cellular properties from various cell types, including fibroblasts [30], leukocytes [31], adipocytes [30], cancer cell lines [32], and red blood cells (RBCs) [33, 34], were investigated. It should be noted that high-frequency-based impedance cytometers were also recently developed. At high frequencies, intracellular structures and cytosolic properties can be collected because of the negligibly polarized membranes [28]. Haandbæk *et al.* [35] reported an impedance cytometer discriminating wild-type yeast cells from

mutants at a high-frequency operating mode (up to 500 MHz) by characterizing subcellular components such as vacuoles. Since the calculated correlations are strongly influenced by cellular size and dielectric properties, often discrimination of cells with similar size/dielectric properties becomes a challenge. Despite this drawback, the impedance measuring technique is one of high-speed cell property measurement processes.

1.2.2
Magnetic Cell Manipulation

Magnetic cell manipulation approaches provide noninvasive, high-throughput, and efficient cell control [36, 37]. Conventional protocols to manipulate cells via magnetic forces require functionalizing cells with magnetic elements before cell interrogation; therefore, additional time should be considered for sample preparation. Most direct magnetic techniques, magnetic tweezers for example, operate under static flow conditions and are not in the scope of this chapter; however, detailed descriptions and their recent advances can be found elsewhere [38, 39]. Note that high-speed magnetic cell positioning and separation approaches as indirect cell manipulation methods are discussed separately in section "Magnetic Cell Separation".

1.2.3
Optical Cell Manipulation

An optical stretcher is a representative example of optical cell interrogation. Two laterally aligned optical fibers are used to create a spatially well-defined optical trap, stretching cells in microfluidic channels. As a powerful cell biophysical property measurement tool, optical cell stretchers have been mainly used for evaluating viscoelastic properties and deformability of various cell types such as RBCs, leukemia, and cancer cells [40–42]. This technique was applied as a cancer diagnostic tool as well [43]. As another prime optical cell manipulation method, optical tweezers have been used to manipulate cells for single-cell level biophysical studies [44, 45]. Optical tweezers utilize a tightly focused laser beam to trap cells by a momentum transfer, attracting cells into the center of the beam [46]. Optical tweezers are a versatile cell manipulation technique since the trapped cell can be manipulated directly by modulating the beam conditions and/or indirectly by translating the beam position. Even though optical cell manipulation techniques are not suited for performing high-throughput cell analysis ($N < 100$), it should be noted that their noninvasive nature allows for precise single-cell examination [47–49]. Extended use of the technique is anticipated if real-time data analysis capabilities and higher processing rates become possible [50].

1.2.4
Mechanical Cell Manipulation

In recent years, mechanical biomarkers (e.g., cell deformability) have gained much attention as an alternative to conventional molecular biomarkers (e.g., antibody conjugated with fluorescence) because measuring cell deformability simplifies complex detection schemes and can eliminate costly and lengthy cellular labeling and sample preparation processes [51, 52]. In order to induce cellular mechanical deformation, there are two major procedures that have been utilized in microfluidics, namely constriction-based (Section 1.2.4.1) and shear-induced (Section 1.2.4.2) cell manipulation.

1.2.4.1 **Constriction-Based Cell Manipulation**
Cell deformability is characterized by flowing cells through a narrow bottleneck region with a gap smaller than the cell diameter. Channels with a sudden narrowing or arrays of local constrictions (e.g., slits) are widely adopted designs (see Figure 1.2). In short, as suspended cells are injected into the microchannels, cells are forced to pass through a constriction(s), experiencing significant deformation. Depending on its purpose, constriction-based mechanical cell manipulation can be further classified into cell interrogation (see section "Constriction-Based Cell Interrogation") and cell separation (see section "Constriction-Based Cell Separation").

Constriction-Based Cell Interrogation
One of the major research focuses using constriction-based cell interrogation is investigating RBC biophysics, rheology, and associated diseases, including malaria, sickle cell disease, and sepsis [12, 52]. For instance, artesunate (ART) is a widely used drug for the treatment of malaria, and ART selectively induces stiffness changes in *Plasmodium falciparum*-infected RBCs, enabling identification of infected cells by monitoring cell transit velocity through a series of constrictions [59]. In addition, the deformability of RBCs from *Plasmodium yoelii*-infected mice was characterized to elucidate the correlation between splenic clearance and RBC deformability [60]. While great advancements were made understanding single-cell level biomechanical properties, most reported techniques operated at low processing rates ($1 - 2$ cells s^{-1}). Low-speed operation could be preferred for single-cell studies; however, higher processing rates should be addressed for cell state identification applications (i.e., diagnosis) to provide a statistical significance. Since constriction-based cell manipulation itself is often limited to high-speed cell processing, hybrid systems combining constriction-based cell deformation with other technologies, such as optics and electronics, were investigated. Another merit by integration with other modalities is multiparameter measurements, allowing precise cell characterizations. As shown in Figure 1.2a, Zheng *et al.* [53] reported a microfluidic platform combining electrical and mechanical modalities, obtaining signatures of each RBC, such as transit time, impedance amplitude ratio, and impedance phase increase with a

(a)

(b)

(c)

(d)

(e)

(f)
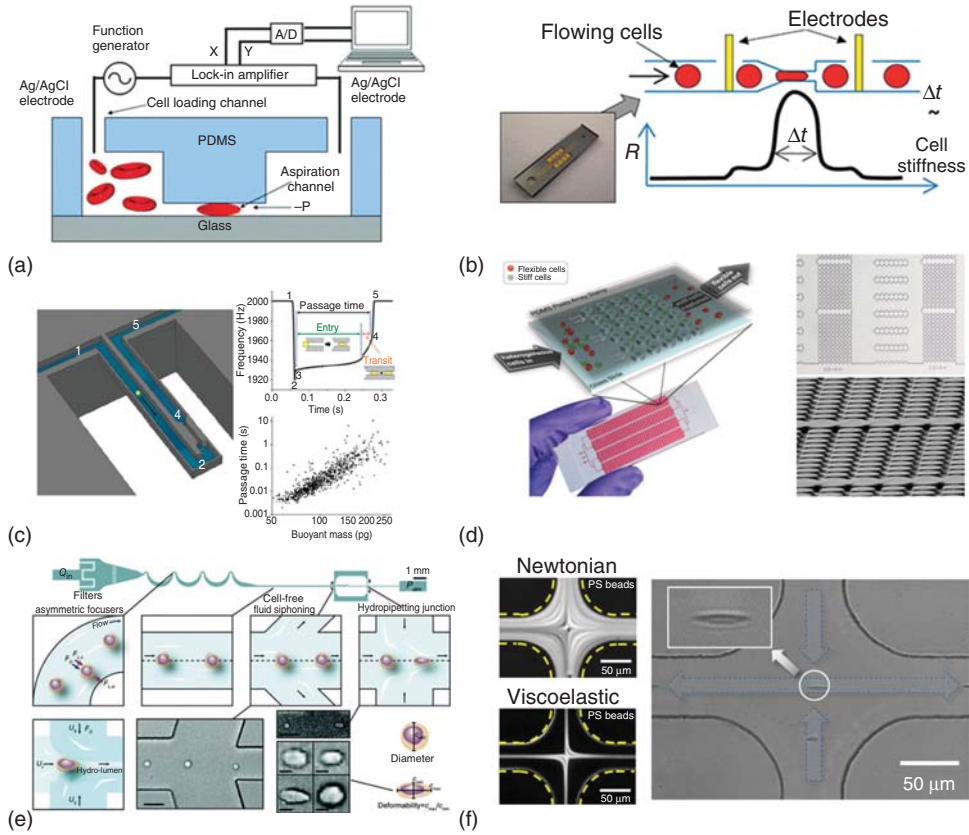
Figure 1.2 Direct cell manipulation techniques. Cell morphology can be manipulated (a,b) mechanically and electrically [53, 54], (c) mechanically and optically [55], (d) through cell and wall interactions [56], or (e,f) by pure hydrodynamic forces [57, 58].

throughput of $100-150$ cells s^{-1}. Two Ag/AgCl electrodes were used to measure electrical impedance signals. By concentrating all electrical field lines to pass through the RBCs' membrane, higher cell responses were shown. In a similar manner, impedance measurements can be applied to cancer cells. Adamo *et al.* [54] reported a simple straight microchannel with a constriction where electrodes were patterned on the substrate (see Figure 1.2b). High-throughput (800 cells min^{-1}) HeLa cell interrogation was demonstrated and the correlations between transition time, cell stiffness, and size were reported. It should be noted that impedance-based platforms do not require a costly high-speed camera (more discussion can be found in Section 1.2.4.2), and real-time data acquisition is possible.

An optical approach was also combined with constriction-based cell deformation. A platform using a suspended microchannel resonator (SMR) was proposed (see Figure 1.2c) [55]. SMR consisted of a hollow microfluidic channel embedded in a silicon cantilever [61]. The resonance frequency is measured by the deflection

of a laser beam, and its changes were recorded as a cell enters the SMR and passes the local constriction. The frequency signatures were later translated into cell transit time and velocity information. Various cell types including mouse and human lung cancer cell lines, mouse embryonic fibroblasts, as well as a mouse lymphoblastic leukemia cell line were tested with high-speed processing rates of 10^5 and $\sim 10^3$ cells h^{-1}. While the SMR setup relies on highly complex, costly, and nontrivial fabrication and measurement techniques, higher throughput was shown and additional cell information (e.g., friction information) was able to be collected.

Constriction-Based Cell Separation

Cell separation was also demonstrated via channel geometry-induced cell deformation. Note that this section focuses on cell deformability-based sorting via channel constrictions, but general deformability-based cell separation is discussed in section "Deformability-Based Cell Separation" separately. Commonly, cells pass through an array of local constrictions whose gap dimension gradually decreases. Cell stiffness dictates the passage time, and separation is accomplished by the time difference. Zhang *et al.* [56] separated two distinct cell populations from a mixture of breast cancer cell lines (MDA-ME-436 and SUM 1479) using an array of microbarriers (see Figure 1.2d). Soft cells passed constrictions easily whereas stiff cells lagged or remained trapped so that resident time-dependent cell separation was attained with a throughput of 3.3×10^4 cells min^{-1} (2 ml h^{-1}). Similarly, Preira *et al.* [62] separated leukocytes from whole blood based on their stiffness using a flow rate as high as 100 ml h^{-1}, demonstrating a possibility for circulating tumor cell (CTC) detection.

The constriction-based mechanical cell manipulation technique (both interrogation and separation) provides label-free cellular property measurements and relatively simple cell processing procedures. However, there are a few fundamental drawbacks that should be mentioned from constriction-based cell manipulation techniques: (i) Cell–wall interaction: Interactions between the cell and channel wall play a critical role in affecting the cell passage phenomena. Each contribution from adhesion and friction should be decoupled and investigated separately, revealing pure deformability attributes. (ii) Clogging: Constriction-based platforms can hardly be free from clogging issues. Once the channel is clogged, a new chip must be used, and hence a robust operation for a long duration is hard to expect. One promising solution for clog-free cell filtration was recently reported [63] where the cross section of a microfluidic channel can be adjusted not only to de-clog but also to capture cells based on a combination of size and deformability with a throughput of 900 000 cells h^{-1}.

1.2.4.2 Shear-Induced Cell Manipulation

Cells can be directly manipulated with fluid flow as another mechanical cell manipulation method. Typically, a microchannel with a constriction whose cross-sectional dimension is larger than the cell diameter is used. Instead of cells that experience direct contact with channel walls, their shapes are modulated by flow

shear stress. This is an excellent approach to study cells because this phenomenon mimics biophysical environment. For example, when RBCs travel in blood capillaries, they experience significant shear stresses inducing deformation [64]. By monitoring dynamic cell shape changes under shear flow, RBC biophysics, such as deformation (e.g., elongation) [65], traveling motions/patterns [66], and adenosine triphosphate (ATP) release [67], were investigated. Despite its simple experimental approach, this method did not expand much because it suffers from at least one of the following drawbacks: (i) Nonuniform shear stress: Since cells were randomly distributed throughout the channel cross section, individual cells experience nonuniform shear stress. Cells traveling near the channel center or the wall experience different magnitudes of shear stresses, producing inconsistent data. (ii) Poor imaging: Without a proper cell positioning step, imaging becomes a great challenge because cells are traveling in all different imaging planes. (iii) Low throughput: Shear-induced cell manipulation techniques rely on relatively low flow speed and concentration for analysis, making the approach not ideal for high-speed cell processing.

For both constriction-based and shear-induced cell controls, cells should be transported by the flow to induce cell deformation; therefore, the flow rate simply determines the throughput of the system. In order to increase throughput, naively increasing the flow rate would seem like an easy solution; however, when the Reynolds number ($Re = \rho U L_c / \mu$: a dimensionless parameter describing the ratio of inertial and viscous forces, where ρ is the fluid density, U is the mean flow velocity, L_c is the characteristic length of the channel, and μ is the fluid viscosity) becomes nonzero, flow behavior significantly deviates from Stokes flow. For example, the cross-sectional profile of the hydrodynamic flow focusing distorts as Reynolds number increases [68, 69]. It is important to note that at finite Reynolds number ($Re \approx 10-100$), two inertial effects: *Inertial particle migration* and *secondary flows* can be found [70–72], and by taking advantage of these two effects, extremely high-speed cell manipulations are possible. The reader is directed to other reviews [70–72] to seek a complete background and underlying physics of inertial focusing.

Gossett *et al.* [73] demonstrated an inertial cell stretcher with a high-throughput cell processing rate (2000 cell s^{-1}). Cells were first inertially focused in the middle of the channel and hit the fluidic wall at the cross junction where extension flow stretches cells. The platform provides higher throughput, precise cell positioning, and higher strain rates. The device was used for identification of leukocytes and malignant pleural cells, and characterization of pluripotent stem cells. Later, Tse *et al.* [74] reported that the identical platform can be used as a clinical diagnostic tool. They created deformability maps by testing patient samples, which could potentially help reduce cytology-based laboratory workloads and assist clinical decision-making. As an alternative inertial cell stretching approach, recently Dudani *et al.* [57] reported a pinched-flow hydrodynamic stretcher (see Figure 1.2e). The platform utilizes a self-sheathing flow from a single input solution, and an order of magnitude higher throughput (65 000 cells s^{-1}) compared to the previous design [73, 74] was achieved.

Inertial cell stretchers [57, 73, 74] are based on two-position cell focusing with respect to a vertical axis [70–72]; thus, one of the imaging planes should be out of focus, resulting in blurry image collection. Considering cell flow velocity (as high as a few meters per second), blurriness of the recorded images is a critical issue. Focusing cells upstream in a single-stream (i.e., single focal plane) manner can be an effective solution (discussed in Section 1.3.2.1), although recently exploiting non-Newtonian fluids to focus cells in a microchannel was reported [58]. Cells flowing in non-Newtonian fluids experience an elastic force in addition to the inertial lift forces, migrating cells into the center of the channel [70]. Since all cells were positioned in the center of the channel [75, 76], the imaging quality was improved significantly and a uniform shear stress was applied. As shown in Figure 1.2f, RBCs were stretched in a cross junction [58], analogous to a hydrodynamic cell stretcher [73, 74] with a throughput of $110\,\text{cells}\,\text{s}^{-1}$. Non-Newtonian cell manipulation offers better imaging and uniform shearing, although lower strain rates and relatively slow processing rates compared to inertial focusing should be addressed in the future.

For inertia-based microfluidic platforms, the cell travels extremely fast; therefore, normally high-speed microscopy is employed to examine cell deformation events. High-speed microscopy records a large number of image stacks as a data-rich approach, revealing direct cell information; however, real-time processing remains a great challenge due to slow data transfer and computationally demanding image analysis. Moreover, a high-speed camera mounted to a microscope makes the system costly and limits potential for miniaturization. As a promising imaging solution, recently Goda *et al.* [77] reported an ultrafast optical imaging technology for automated, real-time, and high-throughput cell analysis [78]. The technique could be operated with a high cell processing rate ($100\,000\,\text{cells}\,\text{s}^{-1}$), but its requirement of a cell labeling process is a drawback. Therefore, more efforts to avoid high-speed microscopy or developments on faster image analysis strategies [79] should be made to further advance inertia-based cell manipulations (Table 1.1).

1.3
Indirect Cell Manipulation

This section discusses techniques that shift flowing paths of cells as indirect cell manipulation with a focus on high-speed processing. Cell path manipulation processes are normally conducted for two main objectives: cell separation (Section 1.3.1) and cell alignment (Section 1.3.2).

1.3.1
Cell Separation

We set two thresholds defining high-speed cell separation: volumetric processing rate (Q) and cell processing rate (measured in $\text{cells}\,\text{min}^{-1}$). This is because

Table 1.1 Direct cell manipulations.

Mechanisms	Techniques	Sample types	Applications	Reported throughput[a]	Converted throughput Cell counts (cells min^{-1})	References
Electrical	Patch clamp	RAW 264.7, CHO-K1, HIT-T15, and RIN m5F	Recording macroscopic ion channel protein activities	$N = 17$	N/A	[22]
	Impedance spectroscopy	HeLa	Cell impedance measurements	N/A	N/A	[23]
	Impedance spectroscopy	HeLa	Cell impedance response to external chemical perturbations	N/A	N/A	[24]
	Electroporation	K562	Molecule delivery	20 cells per run	N/A	[25]
	Cell lysis	RBC	Lysis	$N = 2 \times 10^3 - 3 \times 10^3$	N/A	[26]
	Impedance-based cytometer	3T3	Cell discrimination	1×10^3 cells min^{-1}	1×10^3	[30]
	Impedance-based cytometer	Leukocytes	Cell discrimination	$5\,\mu l\,min^{-1}$	5×10^3	[31]
	Impedance-based cytometer	MCF7	Cell discrimination	N/A	N/A	[32]
	Impedance-based cytometer	RBC	Cell discrimination	1×10^3 cells min^{-1}	1×10^3	[33]
	Impedance-based cytometer	RBC	Cell discrimination	N/A	N/A	[34]
	Impedance-based cytometer	Yeast	Subcellular morphology characterization	$2\,\mu l\,min^{-1}$	$1 \times 10^4 - 2 \times 10^4$	[35]

Category	Technique	Cell type	Application	Throughput		Ref.
Optical	Optical stretcher	Myeloid cells	Migration of cells	$N = 44$	N/A	[40]
	Optical stretcher	MCF-7, MCF-10, and modMCF-7	Measuring cell deformability	$N = 83$	N/A	[41]
	Optical stretcher	3T3	Measure the viscoelastic properties of dielectric materials	$N = 20$	N/A	[42]
	Optical stretcher	OKF-4TERT1, OKF-6TERT1, HN, BHY, CAL-27, and CAL-33	Cancer screening	$N = 71$	N/A	[43]
Mechanical	Constriction	RBC	Deformability measurement	$2 \times 10^1 - 2 \times 10^2 \ \mu m \ s^{-1}$	N/A	[59]
	Constriction	RBC	Deformability measurement	N/A	N/A	[60]
Mechanical + electrical	Constriction + electrical	RBC	Deformability measurement	$1 \times 10^2 - 1.5 \times 10^2$ cells s^{-1}	$6 \times 10^3 - 9 \times 10^3$	[53]
	Constriction + electrical	HeLa	Deformability measurement	8×10^2 cells min^{-1}	8×10^2	[54]
Mechanical + optical	Constriction + optical	RBC, H1650, H1975, HCC827, and L1210	Deformability measurement and surface friction of cancer cells	RBC: 1×10^5 cells h^{-1} Others: $\sim 10^3$ cells h^{-1}	N/A	[55]
Mechanical	Constriction	MDA-MB-436 and SUM 1479	Deformability-based separation	$1 - 2$ ml h^{-1}	$1.7 \times 10^4 - 3.3 \times 10^4$	[56]
	Constriction	Leukocytes from whole blood	Deformability-based separation	$1.27 \times 10^1 - 1 \times 10^2$ ml h^{-1}	N/A	[62]
	Constriction	UC13 from leukocytes	Deformability-based separation	9×10^5 cells h^{-1}	1.5×10^4	[63]

(continued overleaf)

Table 1.1 (*Continued*)

Mechanisms	Techniques	Sample types	Applications	Reported throughput[a]	Converted throughput Cell counts (cells min^{-1})	References
	Shear-induced	RBC	Deformability measurement	$10\,\mu l\,min^{-1}$	1×10^3	[65]
	Shear-induced	RBC	Characterizing RBC traveling motion	$3\,\mu l\,min^{-1}$	N/A	[66]
	Shear-induced	RBC	RBC biophysical property characterization under shear flow	$N = 65$	N/A	[67]
	Shear-induced (inertia)	Leukocytes, malignant pleural cells, and pluripotent stem cells	Deformability-based cytometer	$2 \times 10^3\,cells\,s^{-1}$	1.2×10^5	[73]
	Shear-induced (inertia)	Malignant pleural effusions (patients' sample)	Deformability-based cell identification	$1 \times 10^3\,cells\,s^{-1}$	6×10^4	[74]
	Shear-induced (inertia)	HeLa and Jurkat	Deformability-based cytometer	$6.5 \times 10^4\,cells\,s^{-1}$	3.9×10^6	[57]
	Shear-induced (inertia using non-Newtonian fluid)	RBC and Human Mesenchymal Stem Cells (hMSC)	Deformability measurement	$12\,\mu l\,h^{-1}$	6.6×10^3	[58]

a) *N* stands for maximum number of cells for particular measurements.

limiting the definition of "high speed" to solely one or the other could potentially mislead the figure of merit of an approach. For techniques dealing with blood samples, the throughput will be converted into whole blood processing rate. High speed is defined for techniques with a whole blood processing rate greater than $1\,\mu l\,min^{-1}$. Regarding cultured cells or RBC-free samples, devices capable of processing greater than 10^6 cells min^{-1} are considered high-speed techniques. In the following sections, we discuss two major microfluidic techniques that can separate various cellular types based on hydrodynamic (Section 1.3.1.1) and nonhydrodynamic methods (Section 1.3.1.2). Note that other general cell separation approaches can be found elsewhere [80–87].

1.3.1.1 Hydrodynamic (Passive) Cell Separation

Current state-of-the-art cell manipulation systems can be categorized into passive and active methods depending upon the presence of an external force. Regarding passive systems, the ability to manipulate cells without the aids of external forces allows for simple and cost-effective detection. Various intrinsic biophysical properties, such as cellular size, deformability, and shape, have been exploited to classify different subpopulations of cells via hydrodynamic approaches. In the following sections, we describe recent advances in high-speed microfluidic devices that are capable of purifying cells based on the interactions between cellular biophysical properties and fluid as one of the indirect cell manipulation methods.

Size-Based Cell Separation

Blood is the most complex and information-rich media revealing general patient health and various disease progressions [64]. Thus, the ability to analyze "large" blood volumes (on the order of milliliters) precisely in a "high-speed" manner is a critical task. Surprisingly, there are not so many microfluidic platforms capable of processing whole blood (i.e., undiluted blood) or samples with a very high hematocrit level [21, 88–95]. Among them, one successful cell separation method that should be highlighted is deterministic lateral displacement (DLD)-based platforms [96, 97]. Briefly, when cells (or particles) travel through an array of microposts in DLD systems, cells with a diameter greater than the critical dimension collide more with microposts, laterally deflecting their path perpendicular to the primary flow. On the other hand, cells below the critical dimension stay within their initial streamlines. Cell migration motions are not random and can be tuned precisely based on the critical dimension determined by micropost geometry, channel and cell dimensions, and other arrangements [98]. DLD has been widely used for blood cell fractionation, rare cell detection, and RBC removal before performing additional downstream biological assays [97]. For example, Inglis *et al.* [92] demonstrated a buffer-free DLD platform for leukocyte enrichment from whole blood. Significantly high whole blood processing rates of $115\,\mu l\,min^{-1}$ (9.5×10^6 cells s^{-1}) were reported. Later, Loutherback *et al.* [99] purified rare cancer cells from diluted bloods with an increased throughput of 2.5×10^9 cells min^{-1}. As shown in Figure 1.3a, the platform uses triangular posts over conventional circular microposts, providing a more efficient and clog-free operation. Liu

(a)

(b)

(c)

(d)
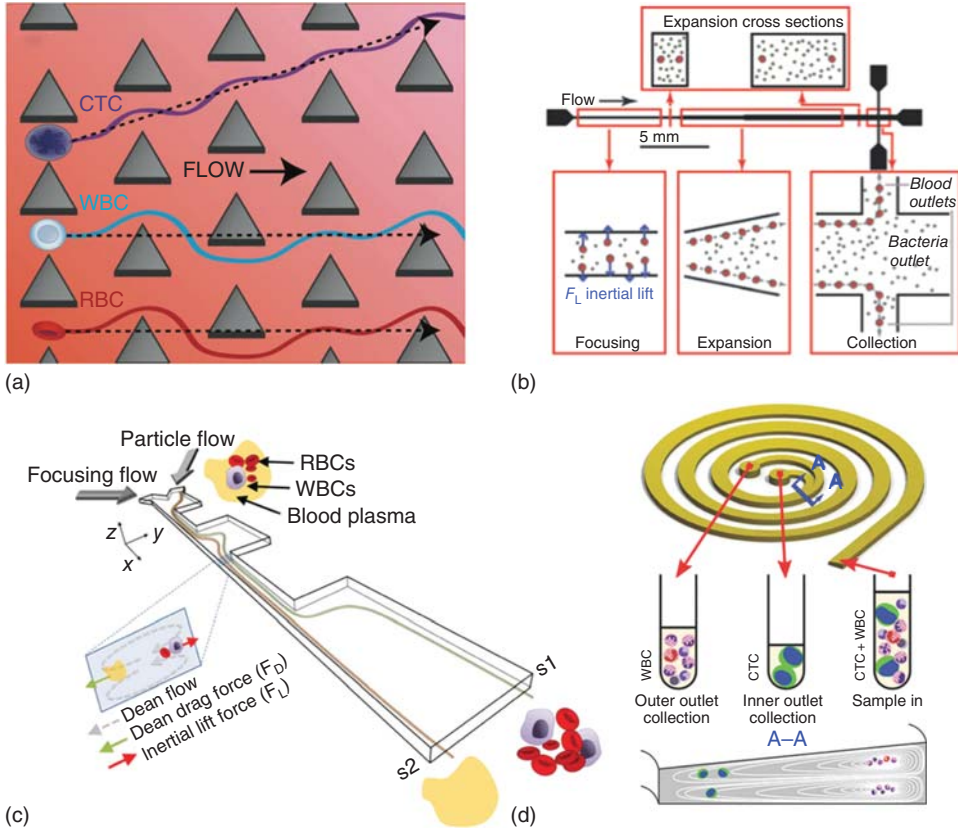
Figure 1.3 Indirect hydrodynamic size-dependent cell separation systems. Cells with various sizes experience different magnitudes of hydrodynamic forces, inducing lateral migrations, when they are flown through (a) arrays of microposts [99], (b) a straight microchannel [100], (c) a microfluidic channel with series of contracting and expanding geometries [91], or (d) spiral microchannels [89]. As the modification degree of lateral migrations is strongly influenced by cellular sizes, various cell types can be separated downstream.

et al. [101] also used a triangular micropost array enriching various cancer cell lines from diluted peripheral whole blood with a maximum throughput of $2 \, ml \, min^{-1}$.

Even though DLD-based techniques hold great promise for high-speed blood purification, fluid inertia-based microfluidic devices have been investigated to reach higher throughputs. Inertial effects in microfluidic systems have recently been recognized as a robust way of manipulating microscale particles because they fundamentally offer high-speed sample processing, simple operation, precise cell manipulation, and a great potential for automation and miniaturization [70, 71]. As we briefly mentioned in Section 1.2.4.2, there are two types of inertial

effects: inertial particle migration and secondary flow, which can be exploited for cell separations as well. At finite Reynolds numbers, the flowing cells/particles experience two directional lift forces: shear-gradient lift forces and wall-effect lift forces. Broadly speaking, a balance of these two counteracting lift forces results in cell migrations across streamlines [70–72]. For a square channel, due to the channel's fourfold symmetry, particles or cells migrate toward midpoints of the four channel walls, forming four particle/cell chains. Research findings showed that these lift forces vary with cell diameter, deformability, channel geometry, and flow conditions [70–72]. The magnitudes of the lift forces strongly correlate with cell sizes ($F_L \propto \rho U^2 a^4/H^2$) [102]; therefore, cells with large size differences will have distinctive lateral positions. For example, larger cells focus close to the channel center whereas smaller ones focus closer to the wall. As shown in Figure 1.3b, Mach and Di Carlo [100] separated bacterial cells from blood with a throughput of 4×10^8 cells min^{-1} based on cell size difference. It should be noted that the equilibrium positions of two distinct cell sizes are relatively close; therefore, additional efforts on modifying channel designs, such as gradually expanding channel widths [100] or inverting channel aspect ratios [103], have been implemented to enhance separation efficiency.

Periodic channel geometry variations also have been used to develop size-based cell separation devices. As shown in Figure 1.3c, microchannels with a series of contractions and expansions are implemented to separate cells based on their sizes. As cells flow through the device, they periodically experience inconsistent lift forces depending upon the presence of the wall, and the net force directs cells with larger diameter closer to the channel wall. Using this mechanism, greater than 10^7 cells min^{-1}, equivalent to processing whole blood at $2 \, \mu l \, min^{-1}$ or more, were processed for CTC purification [91, 104–106]. A similar channel layout can be used to trap cells in microvortices created in the expansion regions [107–110]. With an absence of channel wall in the vicinity of cellular flow paths at expansion regions, cells are exposed to a dominant shear-gradient lift force. Since bigger cells experience a larger shear-gradient lift force, they were more prone to be pushed and trapped inside the microvortices formed in expansion chambers. Using this vortex cell trapping mechanism, CTC purification has been demonstrated with throughputs ranging from 5×10^8 to 4×10^9 cells min^{-1}, equivalent to processing whole blood from 114 to 490 $\mu l \, min^{-1}$ [107–110].

The other major inertial effect found in microchannels utilizes a secondary flow. In a curved channel, fluid elements in the center travel faster than those near the channel walls due to momentum mismatch, creating a pair of secondary flow known as *Dean flow* [111]. Dean flow exerts an additional hydrodynamic force, namely Dean drag force, and cells with varying sizes experience different net forces (a sum of Dean drag, Stokes drag, wall-effect, and shear-gradient lift forces), resulting in size-based lateral equilibrium positions. Dean flow-based cell manipulation is a powerful method offering extremely high throughputs for CTC purification, blood cell fractionation, and cell cycle synchronizations with throughputs ranging from 2.5×10^5 to 2.5×10^8 cells min^{-1} [90, 94, 112–119]. As shown in Figure 1.3d, trapezoidal cross-sectional shapes of spiral channels are reported

[89, 120, 121], allowing higher separation efficiency for enriching CTCs with a throughput from 7.5 ml of patients' blood samples (lysed blood) within 8 min, equivalent to 6.6×10^5 cells min^{-1} [89, 90].

Inertial focusing, in general, operates with diluted samples to minimize inter-particle interactions [122] while maximizing purity and efficiency. However, their inherently fast operating flow speeds allow superior throughputs (greater than a few million cells per minute, equivalent to a few microliters of whole blood per minute). Furthermore, the simple microchannel design of inertial focusing devices allows further enhancement of throughput by parallelizing [100] or stacking [118] the single channels.

Deformability-Based Cell Separation

Cells can be purified using their intrinsic stiffness, and much effort has been made on investigating RBC deformability. Regarding RBC deformability-based separation, a hydrodynamic lift, scaling with deformability of the RBCs, induces migration of soft RBCs toward the center of the channel, creating a cell-free layer near the wall, and the phenomenon is known as *Fåhraeus – Lindqvist effect* (*a.k.a. Sigma effect*) [123]. As shown in Figure 1.4a, Faivre *et al.* [88] explored the variations of RBC rheology affecting cell-free layer widths based on hematocrit counts, flow speeds, and constriction geometries. They were able to purify a plasma-rich solution from threefold diluted blood at the processing rate of 17 μl min^{-1}. Sollier *et al.* [127] exploited the recovery time in which RBCs return to their initial positions after passing a contraction to extract plasma with a processing rate of 5 μl min^{-1} using 20-fold diluted blood. Jain *et al.* [128] has utilized a straight microfluidic channel with sudden expansion geometry to extract stiffer white blood cells (WBCs) from twofold diluted whole blood with a processing rate of 14 μl min^{-1}. Using a similar phenomenon, Hou *et al.* [95] demonstrated that more stiff malaria-infected erythrocytes can be filtered from the normal blood cells using a straight microfluidic channel. The device can be operated using whole blood and was capable of processing at 5 μl min^{-1}.

In order to achieve higher throughputs, deformability-based cell separation was demonstrated via inertial microfluidics. Deformable particles have modified lateral equilibrium positions compared to their rigid counterparts with similar sizes because they experience an additional lift force, ascribed to nonlinear mismatch of velocities and stresses at the interface [129]. As the magnitude of deformability-induced lateral force scales with cellular softness, cells with a different deformability value can be used for separation. For example, softer cells can be found closer to the channel center where the shear stress is at the minimum whereas stiff cells remain close to the channel wall. As illustrated in Figure 1.4b, separating cancer cells spiked in lysed blood has been demonstrated using combined effects of the inertial focusing and the deformability-induced cell migration [124]. The inherently high flow rates allowed purification of more deformable and larger cancer cells from the lysed blood with a throughput of 22 000 cells min^{-1}, equivalent to processing 3 μl of whole blood per minute [124]. This value is more than a 40-fold improvement over that of previous cell
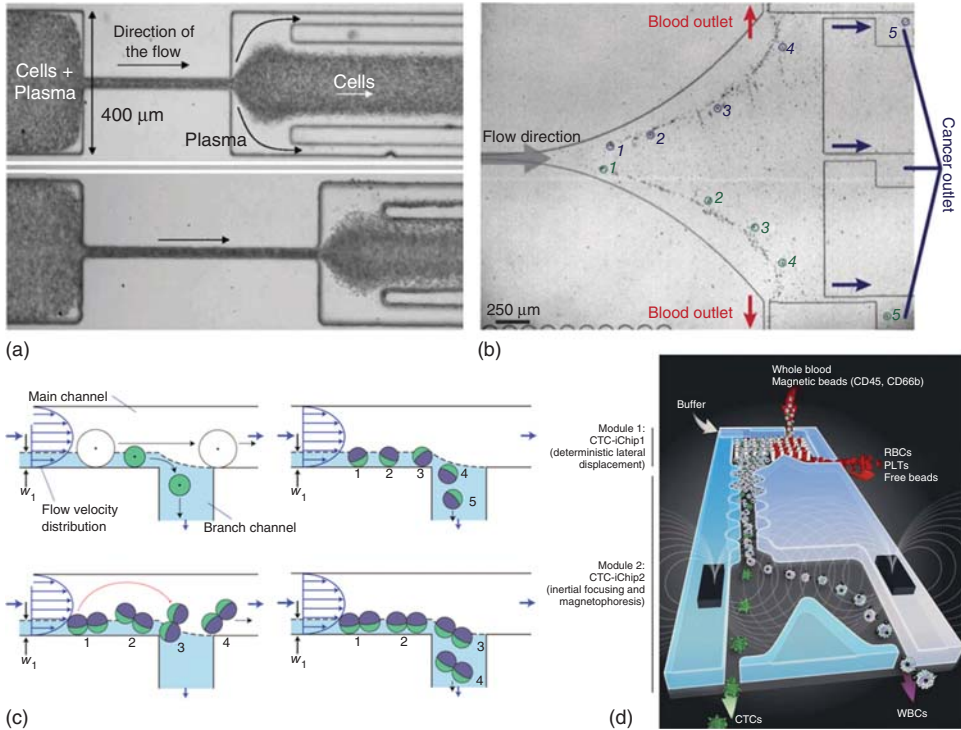
Figure 1.4 Separation of various cell types based on (a,b) cellular deformability, (c) shape, and (d) combination of multiple distinguishing markers. Lateral positions of cells with various deformability can be differentially manipulated by using (a) geometrical constrictions [88] as well as (b) deformability-induced lift forces [124]. (c) Effective diameters of tumbling nonspherical cells tend to be larger than their actual length, allowing shape-based cell separations [125]. (d) Systems capable of processing large volumes of cellular samples can be integrated upstream of conventional affinity-based cell sorting techniques [126].

purification techniques utilizing the hydrodynamic lift force alone [130]. These deformability-based cell separation techniques hold great promise for simple and cost-effective target cell purification systems for cells with little-to-no known surface biomarkers.

Shape-Based Cell Purification

Similar to size and deformability, the shape can serve as a unique cell separation parameter for various biological particles and organisms. The use of the aforementioned DLD techniques was expanded for shape-based cell sorting [131]. In particular, parasites were purified from the infected blood since the long parasites' morphology result in a larger effective size, causing them to deflect across streamlines, while smaller RBCs faithfully remain in their initial streamlines [93]. They processed twofold diluted blood with a flow rate of 60 µl min^{-1}.

The shape-based separation was also implemented to purify subpopulations from yeasts and tissue digests. Inertial focusing of nonspherical particles has been examined, and it was found that, for nonspherical but symmetric particles, the rotational diameter that the particles create as they tumble determines their lateral location in the channel [132]. Utilizing this characteristic, budding yeasts were purified based on their elongated lengths, synchronized with their cell cycle [133]. They processed the sample at the rate of $60\,\mu l\,min^{-1}$ equivalent to $90\,000\,cells\,min^{-1}$. Moreover, differences in lateral equilibrium positions of nonspherical multicellular clusters of mature somatic cells and smaller spherical progenitor cells were utilized for adrenal cortical progenitor cell enrichment [134].

Similar to inertial focusing of nonspherical particles [132], elongated budding yeasts create a larger rotational trajectory as they tumble through the hydrodynamic filtration systems, making them behave like spherical particles with a larger diameter (see Figure 1.4c). Utilizing the enlarged effective diameter of budding yeast, Sugaya *et al.* [125] separated nonspherical budding yeasts from their smaller counterparts with a throughput of $1.5 \times 10^6\,cells\,min^{-1}$. Shape-based cell separation techniques suggest a new paradigm for target cell enrichment strategies in various biological applications (Table 1.2).

1.3.1.2 Nonhydrodynamic (Active) Particle Separation

Nonhydrodynamic bioparticle separation utilizes external forces. In general, separation is achieved by deflecting cells' lateral position in response to external stimuli, such as acoustic, electric, optic, and magnetic forces, whose magnitudes vary with cellular properties. We describe individual cell separation mechanisms for various nonhydrodynamic methods and mainly highlight high-speed methods in this section. We also tabulate each nonhydrodynamic particle separation in Table 1.3. More general indirect cell separation approaches can be found elsewhere [81, 84, 135–137].

Acoustic Cell Separation

Acoustic cell manipulation utilizes acoustic waves transduced by applied electric fields on piezoelectric materials [138]. Typical layouts consist of piezoelectrics patterned on the substrate and a microfluidic channel. The radial acoustic force acting on a particle is given by

$$F_r = -\left(\frac{\pi p_0^2 V_p \beta_m}{2\lambda} \right) \left(\frac{5\rho_p - 2\rho_m}{2\rho_p + \rho_m} - \frac{\beta_p}{\beta_m} \right) \sin(2kx), \qquad (1.1)$$

where p_0 is the pressure amplitude, V is the particle volume, β is the compressibility, λ is the ultrasound wavelength, ρ is the density, and k is the wave number. Subscripts "p" and "m" denote the particle and the fluid medium, respectively [139, 140]. Normally, particles or cells are transported in either pressure nodes or antinodes depending upon their properties, allowing various cell patterning. For example, both point and linear cell alignments can be

Table 1.2 Indirect cell manipulations: hydrodynamic separation.

Mechanisms	Techniques	Sample types	Applications	Reported throughput	Converted throughput			References
					Whole blood (μl min^{-1})	Flow rate (μl min^{-1})	Cell counts (cells min^{-1})	
Hydrodynamic: Size	Slanted spiral inertial focusing	Lysed blood + cancer cells, lysed patient's samples	CTC purification	7.5 ml/8 min	938	1700	6.6×10^5	[89]
	Slanted spiral inertial focusing	Lysed blood + cancer cells, lysed patient's samples	CTC purification	7.5 ml/8 min	938	1700	6.6×10^5	[90]
	CEA	Whole blood + cancer cells	CTC purification	1.1×10^8 cells min^{-1}	5	6000	1.1×10^8	[91]
	DLD	Whole blood cells	Blood fractionation	115 μl min^{-1} atm^{-1}	115	115	5.9×10^8	[92]
	DLD	Diluted blood + cancer cells	CTC purification	5 ml min^{-1}	500	5000	2.5×10^9	[99]
	DLD	Diluted blood + cancer cells	CTC purification	2 ml min^{-1}	200	2000	1×10^9	[101]
	Inertial focusing	Diluted blood + bacterial cells	Sepsis filtration	4×10^8 cells min^{-1}	2.2	200	4×10^8	[100]
	Inertial focusing	Diluted blood + cancer cells	CTC purification	100 μl min^{-1}	1.8	100	8.9×10^6	[103]
	CEA + Steric filters	Diluted blood + cancer cells	CTC purification	130 μl min^{-1}	2.9	130	1.4×10^7	[104]
	Pinched Flow	Diluted blood + cancer cells	CTC purification	400 μl min^{-1}	18	400	8.9×10^7	[105]
	Multi-orifice	Diluted blood + cancer cells	CTC purification	126 μl min^{-1}	1.3	126	6.3×10^6	[106]
	Vortex trapping	Diluted/lysed blood + cancer cells	CTC purification	7.5×10^6 cells s^{-1}	114	4000	4.5×10^8	[107]

(continued overleaf)

Table 1.2 *(Continued)*

Mechanisms	Techniques	Sample types	Applications	Reported throughput	Converted throughput			References
					Whole blood (μl min^{-1})	Flow rate (μl min^{-1})	Cell counts (cells min^{-1})	
	Vortex trapping	Diluted blood + cancer cells	CTC purification	4.4 ml min^{-1}	489	4400	2.4×10^9	[108]
	Vortex trapping	RBC-lysed pleural samples (patient's samples)	CTC purification	50 ml/10 min	NA	6000	NA	[109]
	Vortex trapping	Diluted patient's samples	CTC purification	7.5 ml/20 min	375	4000	3.6×10^9	[110]
	Asymmetric curve inertial focusing	Diluted blood	Blood fractionation	1 ml min^{-1}	22	1000	1.1×10^8	[112]
	Symmetric curve inertial focusing	Diluted blood + murine cancer cells	Cell separation/CTC purification	600 μl min^{-1}	6	600	3×10^7	[113]
	Multistage inertial focusing + Dean force	Diluted blood + cancer cells	CTC purification	565 μl min^{-1}	13	565	6.3×10^7	[114]
	Spiral inertial focusing with sheath fluid	Diluted/lysed blood + cancer cells or patient's samples	CTC purification	100 μl min^{-1}	50	100	2.5×10^8	[94]
	Spiral inertial focusing	Diluted blood	Blood fractionation	1×10^6 cells min^{-1}	2.2	1000	1×10^6	[115]
	Spiral inertial focusing	Cancer cells	Cell separation	1×10^6 cells min^{-1}	NA	3000	1×10^6	[116]
	Spiral Inertial Focusing	Mesenchymal stem cells	Cell cycle synchronization	2.5×10^5 cells min^{-1}	NA	2500	2.5×10^5	[117]

Category	Method	Sample	Application	Throughput				Ref
	Stacked spiral inertial focusing	Lysed patient's samples	CTC purification	7.5 ml/5 min	1500	NA	1.1×10^7	[118]
	Double spiral inertial focusing	Diluted blood + cancer cells	CTC purification	3.3×10^7 cells min^{-1}	20	333	3.3×10^7	[119]
	Slanted spiral inertial focusing	Diluted blood	Blood fractionation	0.8 ml min^{-1}	10	800	5×10^7	[121]
Hydrodynamic: Deformability	Expansion/ contraction	Diluted blood	Blood fractionation	1 ml h^{-1}	5.9	17	3×10^7	[88]
	Lateral migration	Diluted blood	Blood fractionation	100 µl min^{-1}	5	100.00	4.7×10^7	[127]
	Expansion	Diluted blood	Blood fractionation	1×10^4 cells µl^{-1} at $\gamma = 400$ s^{-1}	6.8	13.5	1.4×10^5	[128]
	Lateral migration	Healthy + infected RBC	Malaria-infected RBC purification	5 µl min^{-1}	5	5	2×10^7	[95]
	Inertial focusing	Lysed blood + cancer cells	CTC purification	2.2×10^4 cells min^{-1}	3.14	60	2.2×10^4	[124]
	Hydrodynamic lift	Dilute blood + cancer cells	CTC purification	20 ml h^{-1}	0.07	0.33	6.3×10^5	[130]
Hydrodynamic: Shape	DLD	Whole blood + parasites	Infection detection	600 µm s^{-1}	1	60	3×10^8	[93]
	Inertial focusing	Budding yeast	Cell cycle synchronization	60 µl min^{-1}	NA	60	9×10^4	[133]
	Inertial focusing	Tissue digest	Stem cell purification	60 µl min^{-1}	NA	60	2.4×10^4	[134]
	Hydrodynamic filtration	Budding yeast	Cell cycle synchronization	15 µl min^{-1}	NA	15	1.5×10^6	[125]

achieved by modulating system parameters, such as acoustic wavelength and the cells' density, deformability, and size. Point or linear cell alignment is a powerful technology to manipulate multiple cells, and recently Ding *et al.* [141] developed acoustic tweezers using surface acoustic waves, demonstrating active cell and organism transport. However, since cells were trapped in spatially defined nodes, the technique has limited throughput. For high-throughput applications, acoustic waves have been used for cell sorting. As can be seen in Eq. (1.1), the radial acoustic force varies with different or cell-specific parameters. For example, RBCs, platelets, and leukocytes were successfully discriminated depending on their size [142] or size with density [143]. Yang *et al.* [144] also demonstrated separation of viable breast cancer cells (MCF7) from nonviable counterparts based on their volumetric differences. Toward higher throughput, Adams *et al.* reported separation of RBCs from whole blood by applying an acoustic wave in the vertical direction without the use of a burdensome sheath fluid (see Figure 1.5a). The sample processing rate reached as high as $21\,\mathrm{h}^{-1}$ as one of the fastest processing methods [145]. Acoustophoretic cell manipulation techniques provide many advantages including high-speed, label-free, simple, noninvasive, precise, and tunable cell manipulations.

Electrical Cell Separation

Dielectrophoresis (DEP) is a representative electrical cell manipulation technique that relies on the Coulomb response of polarized cells or particles exposed to a nonuniform electrical field [149]. The time average force acting on a dielectric micro-object can be expressed as follows:

$$F_{\mathrm{DEP}} = 2\pi\varepsilon_{\mathrm{m}}r^3 f_{\mathrm{CM}}(\nabla E^2), \tag{1.2}$$

where ε_{m} is the absolute permittivity of the medium, r is the radius of the micro-object, f_{CM} is the Clausius–Mossotti (CM) factor, and E is the root mean square (RMS) amplitude of the electrical field. The derivation of Eq. (1.2) and the theoretical background can be found elsewhere [149, 150]. By modifying various parameters listed in Eq. (1.2), one can precisely predict and control overall cell behavior and motions in the solution. Depending on the relative permittivity values between cells and the medium, the direction that cells migrate can be reversed. Cells can be transported toward a region of either stronger (positive DEP; higher polarization of micro-objective compared to medium) or lower electrical field (negative DEP; smaller polarization of micro-objective than medium) regions. Note that the DEP force is directly proportional to the square of the applied electrical field; therefore, both AC and DC fields can be used for cell manipulations [151].

The general approach is that cells flow in microchannels with electrodes patterned on the substrate. Once cells approach to the electric field region, they are laterally deflected. The degree of cell migration varies with electrical properties and other parameters (see Eq. (1.2)). Mammalian [152–156] and bacterial cells [157] were successfully classified based on cell volume ($F_{\mathrm{DEP}} \propto r^3$). It should be noted that DEP-based cell manipulation methods have not been well
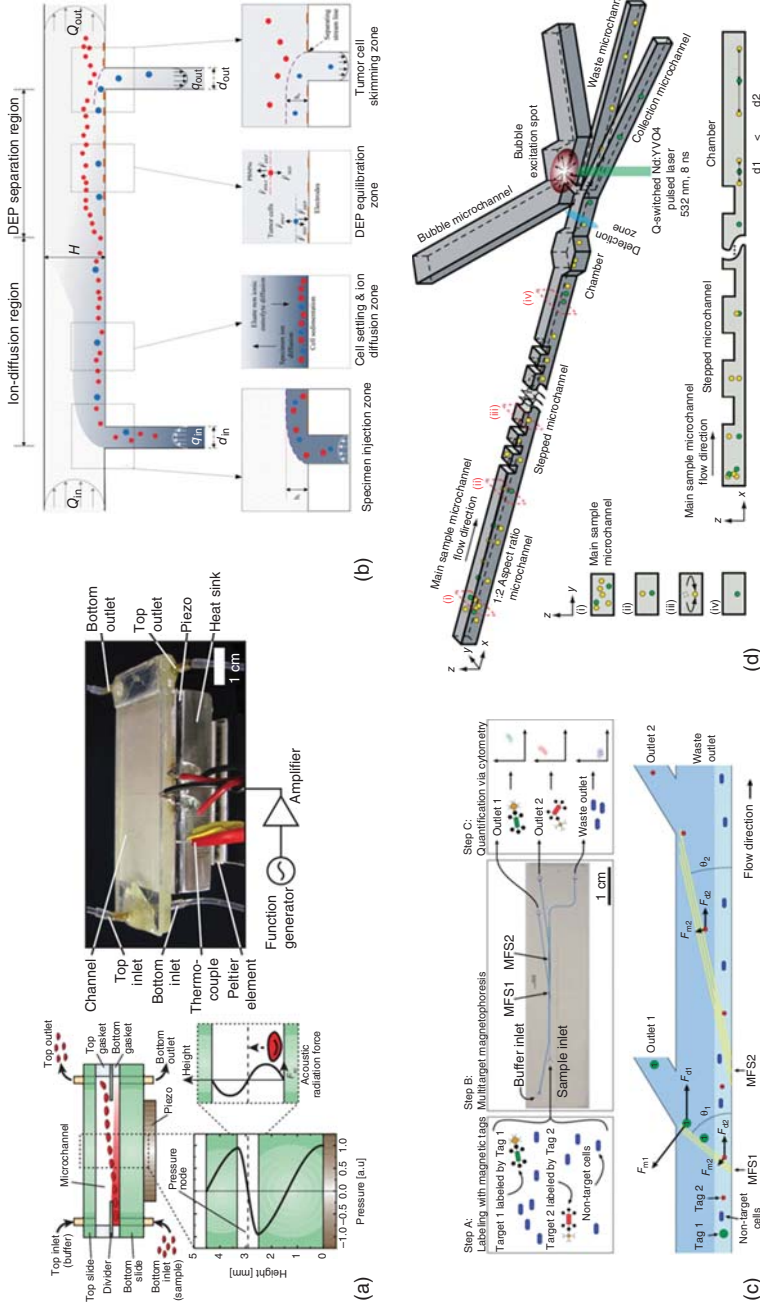
Figure 1.5 Nonhydrodynamic cell manipulation techniques (a–c) and cell alignment (d). (a) Acoustic force deflected RBCs selectively for RBC separation [145]. (b) Circulating tumor cells are displaced vertically by dielectrophoretic force from peripheral blood mononuclear cell (PBMN) [146]. (c) Magnetically tagged cells are sorted in response to the degree of magnetic forces [147]. (d) AB3955 cells are inertially focused and classified upon their fluorescence signals [148].

favored for high-speed cell separation because of the relatively low-throughput cell ($<10^6$ cells min^{-1}) processing limit. However, recently, Shim *et al.* [146] reported a promising DEP chip with a high processing rate of 10 ml h^{-1} (equivalent to 4×10^7 cells min^{-1}) as shown in Figure 1.5b. Even though pure whole blood was not processed and device fabrication was not trivial, it showed precise, continuous, and label-free cell manipulation with a high processing rate.

Magnetic Cell Separation

The ability to sort cells using magnetic forces has been extensively utilized for cell separation. Magnetophoresis can be achieved by utilizing intrinsic cell magnetization or cell functionalization with magnetic elements. For instance, deoxyhemoglobin RBCs can be naturally magnetized under applied magnetic fields, and label-free separation of RBCs from whole blood was demonstrated [158]. However, due to their weak response to magnetic fields, impractically high magnetic fields should be applied to improve separation efficiency. Therefore, magnetic element labeling is more preferred rather than exploiting natural magnetism. The magnetic force acting on a particle can be written as

$$\overrightarrow{F}_{\mathrm{M}} = \frac{V\chi}{\mu_{\mathrm{o}}}(\overrightarrow{B}.\nabla)\overrightarrow{B}, \tag{1.3}$$

where V is the volume of the magnetic particle, χ is the magnetic susceptibility, μ_{o} is the magnetic permeability in vacuum, and $\overrightarrow{B}$ is the magnetic field [37]. In general, magnetically labeled cells are injected into microfluidic channels, and an external magnetic source is used to deflect cell lateral positions based on their magnetic responses [36]. The magnetic-activated cell sorter (MACS) is a prime example of a high-speed cell separation technique ($>10^7$ cells min^{-1}) [159]. Normally, cells are conjugated with magnetic nanoparticles whose surfaces are coated with antibodies binding to antigens expressed on target cells. As shown in Figure 1.5c, Adams *et al.* [147] used MACS-based multimagnetic tagging methods differentiating different bacterial cell types with a throughput of 10^9 cells h^{-1}. The MACS mechanism was also used to purify living fungal pathogens bound to magnetic particles covered with opsonins from whole blood at a processing rate of 20 ml h^{-1} [21] (see Figure 1.1b). Even though the time to process cells in microfluidic devices is short, a nontrivial and lengthy sample preparation step is required for magnetic cell manipulations.

Instead of tagging magnetic elements on cell surface, endocytosis of magnetic nanoparticles can be used to indirectly manipulate cellular positions in flow [160]. Depending on endocytotic capacity of magnetic nanoparticles, cells showed a different degree of magnetic responses. Robert *et al.* [161] recently demonstrated separation of monocytes and macrophages based on amounts of internalized magnetic nanoparticles. Even though the use of internalization-based approach is limited because of its relatively low cell processing rate ($10-100$ cells s^{-1}) and high cytotoxicity of nanoparticles [162], this approach opened a door for integrated cell manipulations as a future direction. For example, internalized

nanoparticles can be used for enhanced imaging, hyperthermia, and controlling local cell motions and mitoses [163].

Optical Cell Separation

Cell sorting exerted by optical forces has also been employed for cell separation. Optics-based cell separation was shown using cellular optical characteristics, such as refractive index [164] or light patterns [165]; however, similar to direct cell manipulations, most techniques still exhibit extremely limited processing rates. Regarding high-throughput cell separation applications, microfluidic fluorescence-activated cell sorter (FACS) is one of the major optical cell sorting examples [166]. Briefly, a stream of cells exiting a capillary tube breaks into individual droplets, and droplet trajectories are deflected laterally upon their fluorescence (i.e., charge) responses to the applied external field. FACS throughput reaches as high as $50\,000$ cells s^{-1}, analyzing cells rapidly; however, it should be noted that fluorescent labeling should be done before cell interrogation, and the processing rate is still not high enough for rare cell detections [167]. Note that flow cytometry is discussed in Section 1.3.2.1 separately.

Hybrid Cell Purification Systems

There have been innovative attempts to develop a new cell manipulation method by combining multiple cell manipulation techniques together to enhance their performance. The most commonly integrated technique with other modalities is magnetophoresis because it allows to selectively deflect labeled cells attained upstream by other indirect cell manipulation methods. DLD and magnetophoresis were combined to purify CTCs from patients' blood samples [126, 168]. DLD-based platforms were used to exhaust overly populated RBCs from the whole blood, and magnetophoresis were subsequently used to deflect the flowing path of magnetically labeled WBCs (see Figure 1.4d). This hybrid system was able to process $150\,\mu l$ of whole blood per minute, showing great potential for practical CTC detections. Magnetophoresis was also incorporated with the hydrodynamic filtration technique [169]. They first guided HeLa and Jurkat cells based on their sizes toward outlets, and those separated cells' streams were further branched out based on the expression level of CD4 with a throughput of 6000 cells min^{-1}. There exist other innovative hybrid cell separation techniques that are not discussed here due to their low operational speeds, but more details can be found elsewhere [170−172] (Table 1.3).

1.3.2
Cell Alignment (Focusing)

Along with cell separation, another key cell path manipulation method is cell alignment (focusing). In this section, cell alignment/focusing is defined as the phenomena forming a cell train/chain(s) as they travel downstream. Cell focusing also can be achieved by exposing flowing cells to either hydrodynamic forces (active) or nonhydrodynamic forces (passive). Cell focusing is an extremely

Table 1.3 Indirect cell manipulations: nonhydrodynamic separation.

Mechanisms	Techniques	Sample types	Applications	Reported throughput	Converted throughput Cell counts (cells min^{-1})	References
Acoustic: size	Acoustophoresis	Whole blood	Cell separation	2.7×10^4 cells s^{-1}	1.6×10^6	[142]
Acoustic: size/density	Acoustophoresis	Diluted blood	Cell separation	0.76 ml min^{-1}	4.9×10^9	[143]
Acoustic: size	Acoustophoresis	Cancer cells	Cell separation	12 ml h^{-1}	2×10^5	[144]
	Acoustophoresis	Whole blood + microparticles	Cell separation	21 h^{-1} (whole blood)	N/A	[145]
Electrical: density and dielectric properties	Dielectrophoresis	Lysed blood	Cell separation (leukocytes subpopulation)	0.2 ml min^{-1}	4×10^5	[152]
Electrical: size and dielectric properties	Dielectrophoresis	Diluted blood + cancer cells	CTC detection	1.5–12 ml min^{-1}	$3 \times 10^2 - 6 \times 10^4$	[153]
Electrical: size	Dielectrophoresis	Diluted blood	Cell separation	1 mm s^{-1}	$1 - 2 \times 10^4$	[154]
Electrical: size (volume)	Dielectrophoresis	Cancer cells	Cell separation (cell cycle based)	2×10^5 cells h^{-1}	3.3×10^3	[155]
Electrical: size	Dielectrophoresis	Diluted blood + cancer cells	Cell separation	0.1–0.5 ml h^{-1}	N/A	[156]
	Dielectrophoresis	Bacterial cells + diluted blood or cerebrospinal fluid	Cell separation	330 µl h^{-1}	1.7×10^3	[157]
	Dielectrophoresis	Diluted blood + cancer cells	CTC detection	1×10^6 cells min^{-1}	1×10^6	[146]
Magnetic: natural magnetism	Magnetophoresis	Whole blood	Cell separation	N/A	N/A	[158]

	Method	Sample	Application	Throughput		Reference
Magnetic labeling	Magnetophoresis	Spleen + myeloma cells	Cell separation	10^9 cells/15 min	6.7×10^7	[159]
	Magnetophoresis	Bacterial cells	Cell separation	10^9 cells h^{-1}	1.7×10^7	[147]
	Magnetophoresis	Fungal cells + whole blood	Pathogen clearance from blood	20 ml h^{-1} (whole blood)	NA	[21]
Magnetic: endocytotic capacity	Magnetophoresis	White blood cells	Cell separation	$1\times10^1 - 1\times10^2$ cells s^{-1}	$6\times10^2 - 6\times10^3$	[161]
Optical	Reflective index	N/A	Cell (RBC) separation	N/A	N/A	[164]
	Light pattern	Diluted blood	Cell separation	N/A	N/A	[165]
	Fluorescence	Cancer cells	Cell separation (FACS)	1.06×10^2 cells s^{-1}	6.4×10^3	[166]
Hybrid	DLD + magneto-phoresis	Whole blood + cancer cells or patients' sample	CTC purification	1×10^4 cells s^{-1}	6×10^5	[168]
	DLD + magneto-phoresis + asymmetric inertial focusing	Whole blood + cancer cells or patients' sample	CTC purification	1×10^7 cells s^{-1}	6×10^8	[126]
	Hydrodynamic filtration + magnetophoresis	Cancer + lymphocyte cells	Cell separation	100 cells s^{-1}	6×10^3	[169]

useful technique preceding additional biological assays [173] because, by accurately positioning the locations of flowing cells in microchannels, sophisticated cell manipulation and higher cell sorting efficiencies can be achieved. Cell alignment has several specific purposes, and we discuss some of their main objectives.

1.3.2.1 Cell Alignment (Focusing) for Flow Cytometry

The most widely explored cell focusing application is flow cytometry. Flow cytometry is a powerful and high-speed analytical tool because it is capable of performing single molecule detection, imaging, counting, analysis, sorting (e.g., FACS), immunophenotyping, and classification of various cellular types [167]. Conventional flow cytometers deliver cells through a thin capillary called a *flow cell* where cells are focused and optically interrogated. Since the sensitivity and specificity of the fluorescent signal detections strongly depend on the proximity of the fluorescent label and laser beam spot, focusing cells upstream is a crucial task. Cells and particles are normally focused hydrodynamically via sheath fluid. As the sheath is delivered with a higher flow rate compared to the core flow speed, the diameter of the cell stream becomes compatible to the size of the interrogation beam spot. Sheath fluid-based cell focusing offers simple and precise three-dimensional cell focusing; however, extremely large volumes of sheath fluid are required to narrow down the cell stream and to process large-volume samples [167]. In order to address this shortcoming, various sheathless cell focusing [173] methods are reported for next-generation flow cytometers. Among those, we discuss here high-speed and simple sheathless cell focusing techniques, particularly inertial focusing and acoustophoresis.

As discussed in Section 1.2.4.2, at finite Reynolds numbers, inertial lift forces can be utilized to position cells and particles precisely in a predictable manner [70–72]. Since inertial focusing creates multiple cell/particle chains across the channel cross section (e.g., two, four, or more depending on channel shape, flow speed, and aspect ratio) [70–72], Dean flow has been implemented to create a single-cell stream [174, 175]. Solely utilizing fluid inertia to focus particles, flow cytometer applications were successfully demonstrated [176, 177]. Recently, single-stream cell focusing was also achieved in straight microchannels containing columns. The platform exploited inertial flows induced by interactions between fluid and channel structure [178, 179], and its applicability as FACS was demonstrated with a throughput of 6×10^5 cells min^{-1} processing lymphoma cells [148] (see Figure 1.5d). As another inertial approach, Hur *et al.* [180] used a high-aspect ratio channel, creating two cell chains and positioning all cells in a single focal plane. By massively parallelizing microchannels, an ultrahigh throughput (10^6 cells s^{-1}) image cytometer was reported. Inertial particle focusing mechanism strongly depends on particle sizes so that it still remains a challenge to design a universal microfluidic channel that focuses various cell sizes; nevertheless, because of its simple and passive mechanism and rapid processing rate, inertial focusing holds a great promise.

Another cell focusing approach is through acoustophoresis. Standing surface acoustic wave (SSAW)-based microfluidic cytometers [181–183] and acoustic actuated fluorescence-activated sorting of microparticles were demonstrated [184] by utilizing the interactions between acoustic waves and cells. Moreover, there are several commercially available flow cytometers adopting acoustophoresis in combination with hydrodynamic focusing [167, 185]. Compared to passive cell focusing methods, the acoustic wave-based cell focusing technique relies on an external apparatus; therefore, the approach requires relatively more complicated fabrication procedures. However, as discussed in section "Acoustic Cell Separation", acoustophoresis offers label-free, rapid, simple, noninvasive, precise, and tunable cell manipulations, posing itself as one of the most promising candidates for flow cytometry.

1.3.2.2 Cell Solution Exchange

High-speed cell alignment can be used for rapid solution exchange by manipulating cell flow paths. Solution exchange steps are frequently conducted to label and wash cells for downstream imaging and analysis [186]. Centrifugation is the easiest and most common approach to isolate cells from complex backgrounds; however, it is slow and labor-intensive, and sample loss during the recovery step is inevitable [18]. In order to address these shortcomings, Gossett *et al.* [187] reported a novel microfluidic platform named Rapid Inertial Solution Exchange (RInSE), exploiting inertial cell migration. Through a modulation of channel aspect ratio, cell lateral positions were manipulated, extracting cells from one stream to the other. In short, leukocytes were inertially transferred into a solution of phosphate buffered saline (PBS) from a lysed whole blood sample with a throughput of $1000\,\mathrm{cell\,s^{-1}}$ and 96% efficiency. This approach was expanded later for automated continuous cytomorphological staining [188] and time-controlled transient chemical treatment of cells (on the order of $1\,\mathrm{ms}$) [189]. It is true that large output volumes were induced, requiring a further concentration step; nonetheless, the method offers high-speed cell process with very high efficiency. As another cell solution exchange, platforms utilizing microvortices were reported. The typical channel geometry consists of a straight microchannel with a series of expansion–contraction chambers (see section "Size-Based Cell Separation" for the detailed mechanism). While cells were trapped in recirculating microvortices in the expansion chambers, new solutions were injected for solution exchange. Mach *et al.* [108] demonstrated various cell labeling with antibodies to intracellular components (cytokeratin), cell surface proteins epithelial cell adhesion molecule (EpCAM), fluorogenic enzyme substrates (Calcein AM), and direct labeling of DNA 4′,6-diamidino-2-phenylindole (DAPI). It should be noted that microvortices-based solution exchange does not require any postconcentration step as compared to RInSE, but the number of cells that can be processed simultaneously is predetermined and inflexible (Table 1.4).

Table 1.4 Indirect cell manipulations: cell alignment.

Mechanisms	Techniques	Sample types	Applications	Reported throughput (cells s^{-1})	Converted throughput Cell counts (cells min^{-1})	References
Hydrodynamic	Inertial particle focusing + geometry-induced secondary flow	Cancer and leukemia cells	Focusing/flow cytometer	3.4×10^4	2×10^6	[178]
	Inertial particle focusing + geometry-induced secondary flow	Cancer and leukemia cells	Focusing/flow cytometer	1.3×10^4	7.8×10^5	[179]
	Inertial particle focusing + geometry-induced secondary flow	Lymphoma cells	Focusing/FACS	1×10^4	6×10^5	[148]
	Inertial particle focusing	Diluted blood	Cell counting	1×10^6	6×10^7	[180]
Acoustic	Acoustophoresis	Cancer cells	Cell counting	1×10^3	6×10^4	[181]
Hydrodynamic	Inertial particle focusing	Lysed blood	Solution exchange	1×10^3	6×10^4	[187]
	Inertial particle focusing	Cancer cells	Cytomorphological staining	N/A	N/A	[188]
	Inertial particle focusing	Cancer cells	Transient chemical treatments	N/A	N/A	[189]

1.4
Summary

We have discussed various microfluidic techniques for cell manipulation, and "high-speed" cell manipulations are successfully achieved with various approaches. Each technique has its own advantages and disadvantages, and sometimes hybrid approaches provide more cellular information. Depending on biological questions, one should decide which technique would be the most adequate to characterize and analyze cell biological properties precisely and rapidly. Along with the processing speed of the microfluidic platform for the chosen approaches, one should take into account the following two time considerations: (i) Sample preparation time and (ii) data analysis. In reality, it is true that a fairly large amount of time is spent for sample preparation before microfluidic tests to deal with large and heterogeneous cell samples. In addition, we cannot ignore the time to analyze readouts from the microfluidic platforms to extract meaningful data as post processing. For example, an image stack from a high-speed camera should be processed, and electrical signals should be translated into useful cell biophysical properties later. Therefore, true high-speed cell manipulation processing can be attained considering all time requirements, and a holistic effort to reduce time for sample preparation, sample processing, and data analysis should be pursued simultaneously.

Acknowledgments

References

1. Kovarik, M.L., Gach, P.C., Ornoff, D.M., Wang, Y., Balowski, J., Farrag, L., and Allbritton, N.L. (2011) Micro total analysis systems for cell biology and biochemical assays. *Anal. Chem.*, **84** (2), 516–540.
2. Haeberle, S. and Zengerle, R. (2007) Microfluidic platforms for lab-on-a-chip applications. *Lab Chip*, **7** (9), 1094–1110.
3. Takayama, S., Ostuni, E., LeDuc, P., Naruse, K., Ingber, D.E., and Whitesides, G.M. (2001) Subcellular positioning of small molecules. *Nature*, **411** (6841), 1016.
4. Takayama, S., Ostuni, E., LeDuc, P., Naruse, K., Ingber, D.E., and Whitesides, G.M. (2003) Selective chemical treatment of cellular microdomains using multiple laminar streams. *Chem. Biol.*, **10** (2), 123–130.
5. Weaver, W.M., Tseng, P., Kunze, A., Masaeli, M., Chung, A.J., Dudani, J.S., Kittur, H., Kulkarni, R.P., and Di Carlo, D. (2014) Advances in high-throughput single-cell microtechnologies. *Curr. Opin. Biotechnol.*, **25**, 114–123.
6. El-Ali, J., Sorger, P.K., and Jensen, K.F. (2006) Cells on chips. *Nature*, **442** (7101), 403–411.
7. Stone, H.A., Stroock, A.D., and Ajdari, A. (2004) Engineering flows in small devices: microfluidics toward a lab-on-a-chip. *Annu. Rev. Fluid Mech.*, **36** (1), 381–411.

8. Erickson, D. and Li, D. (2004) Integrated microfluidic devices. *Anal. Chim. Acta*, **507** (1), 11–26.

9. Melin, J. and Quake, S.R. (2007) Microfluidic large-scale integration: the evolution of design rules for biological automation. *Annu. Rev. Biophys. Biomol. Struct.*, **36** (1), 213–231.

10. Kim, S.M., Lee, S.H., and Suh, K.Y. (2008) Cell research with physically modified microfluidic channels: a review. *Lab Chip*, **8** (7), 1015–1023.

11. Mu, X., Zheng, W., Sun, J., Zhang, W., and Jiang, X. (2013) Microfluidics for manipulating cells. *Small*, **9** (1), 9–21.

12. Zheng, Y., Nguyen, J., Wei, Y., and Sun, Y. (2013) Recent advances in microfluidic techniques for single-cell biophysical characterization. *Lab Chip*, **13** (13), 2464–2483.

13. Yi, C., Li, C.-W., Ji, S., and Yang, M. (2006) Microfluidics technology for manipulation and analysis of biological cells. *Anal. Chim. Acta*, **560** (1), 1–23.

14. Andersson, H. and van den Berg, A. (2003) Microfluidic devices for cellomics: a review. *Sens. Actuators B*, **92** (3), 315–325.

15. Yun, H., Kim, K., and Lee, W.G. (2013) Cell manipulation in microfluidics. *Biofabrication*, **5** (2), 022001.

16. Jin, C., McFaul, S.M., Duffy, S.P., Deng, X., Tavassoli, P., Black, P.C., and Ma, H. (2014) Technologies for label-free separation of circulating tumor cells: from historical foundations to recent developments. *Lab Chip*, **14** (1), 32–44.

17. Hyun, K.-A. and Jung, H.-I. (2014) Advances and critical concerns with the microfluidic enrichments of circulating tumor cells. *Lab Chip*, **14** (1), 45–56.

18. Mach, A.J., Adeyiga, O.B., and Di Carlo, D. (2013) Microfluidic sample preparation for diagnostic cytopathology. *Lab Chip*, **13** (6), 1011–1026.

19. Young, E.W.K. and Beebe, D.J. (2010) Fundamentals of microfluidic cell culture in controlled microenvironments. *Chem. Soc. Rev.*, **39** (3), 1036–1048.

20. Carlo, D.D. and Lee, L.P. (2006) Dynamic single-cell analysis for quantitative biology. *Anal. Chem.*, **78** (23), 7918–7925.

21. Yung, C.W., Fiering, J., Mueller, A.J., and Ingber, D.E. (2009) Micromagnetic-microfluidic blood cleansing device. *Lab Chip*, **9** (9), 1171–1177.

22. Pantoja, R., Nagarah, J.M., Starace, D.M., Melosh, N.A., Blunck, R., Bezanilla, F., and Heath, J.R. (2004) Silicon chip-based patch-clamp electrodes integrated with PDMS microfluidics. *Biosens. Bioelectron.*, **20** (3), 509–517.

23. Jang, L.-S. and Wang, M.-H. (2007) Microfluidic device for cell capture and impedance measurement. *Biomed. Microdevices*, **9** (5), 737–743.

24. Malleo, D., Nevill, J.T., Lee, L.P., and Morgan, H. (2010) Continuous differential impedance spectroscopy of single cells. *Microfluid. Nanofluid.*, **9** (2-3), 191–198.

25. Yun, H. and Hur, S.C. (2013) Sequential multi-molecule delivery using vortex-assisted electroporation. *Lab Chip*, **13** (14), 2764–2772.

26. Bao, N., Kodippili, G.C., Giger, K.M., Fowler, V.M., Low, P.S., and Lu, C. (2011) Single-cell electrical lysis of erythrocytes detects deficiencies in the cytoskeletal protein network. *Lab Chip*, **11** (18), 3053–3056.

27. Sun, T. and Morgan, H. (2010) Single-cell microfluidic impedance cytometry: a review. *Microfluid. Nanofluid.*, **8** (4), 423–443.

28. Cheung, K.C., Di Berardino, M., Schade-Kampmann, G., Hebeisen, M., Pierzchalski, A., Bocsi, J., Mittag, A., and Tárnok, A. (2010) Microfluidic impedance-based flow cytometry. *Cytometry A*, **77A** (7), 648–666.

29. Heikali, D. and Di Carlo, D. (2010) A niche for microfluidics in portable hematology analyzers. *J. Assoc. Lab. Autom.*, **15** (4), 319–328.

30. Schade-Kampmann, G., Huwiler, A., Hebeisen, M., Hessler, T., and Di Berardino, M. (2008) On-chip non-invasive and label-free cell discrimination by impedance spectroscopy. *Cell Prolif.*, **41** (5), 830–840.

31. Holmes, D., Pettigrew, D., Reccius, C.H., Gwyer, J.D., van Berkel, C., Holloway, J., Davies, D.E., and Morgan, H. (2009) Leukocyte analysis and differentiation using high speed microfluidic

single cell impedance cytometry. *Lab Chip*, **9** (20), 2881–2889.

32. Pierzchalski, A., Hebeisen, M., Mittag, A., Di Berardino, M., and Tarnok, A. (2010) Label-free single cell analysis with a chip-based impedance flow cytometer. BiOS. 2010: International Society for Optics and Photonics.

33. Cheung, K., Gawad, S., and Renaud, P. (2005) Impedance spectroscopy flow cytometry: on-chip label-free cell differentiation. *Cytometry A*, **65A** (2), 124–132.

34. Du, E., Ha, S., Diez-Silva, M., Dao, M., Suresh, S., and Chandrakasan, A.P. (2013) Electric impedance microflow cytometry for characterization of cell disease states. *Lab Chip*, **13** (19), 3903–3909.

35. Haandbæk, N., Burgel, S.C., Heer, F., and Hierlemann, A. (2014) Characterization of subcellular morphology of single yeast cells using high frequency microfluidic impedance cytometer. *Lab Chip*, **14** (2), 369–377.

36. Pamme, N. (2006) Magnetism and microfluidics. *Lab Chip*, **6** (1), 24–38.

37. Gijs, M.A. (2004) Magnetic bead handling on-chip: new opportunities for analytical applications. *Microfluid. Nanofluid.*, **1** (1), 22–40.

38. Kilinc, D. and Lee, G.U. (2014) Advances in magnetic tweezers for single molecule and cell biophysics. *Integr. Biol.*, **6** (1), 27–34.

39. De Vlaminck, I. and Dekker, C. (2012) Recent advances in magnetic tweezers. *Annu. Rev. Biophys.*, **41** (1), 453–472.

40. Lautenschläger, F., Paschke, S., Schinkinger, S., Bruel, A., Beil, M., and Guck, J. (2009) The regulatory role of cell mechanics for migration of differentiating myeloid cells. *Proc. Natl. Acad. Sci. U.S.A.*, **106** (37), 15696–15701.

41. Lincoln, B., Erickson, H.M., Schinkinger, S., Wottawah, F., Mitchell, D., Ulvick, S., Bilby, C., and Guck, J. (2004) Deformability-based flow cytometry. *Cytometry A*, **59A** (2), 203–209.

42. Guck, J., Ananthakrishnan, R., Mahmood, H., Moon, T.J., Cunningham, C.C., and Käs, J. (2001) The optical stretcher: a novel laser tool to micromanipulate cells. *Biophys. J.*, **81** (2), 767–784.

43. Remmerbach, T.W., Wottawah, F., Dietrich, J., Lincoln, B., Wittekind, C., and Guck, J. (2009) Oral cancer diagnosis by mechanical phenotyping. *Cancer Res.*, **69** (5), 1728–1732.

44. Ashkin, A., Dziedzic, J., and Yamane, T. (1987) Optical trapping and manipulation of single cells using infrared laser beams. *Nature*, **330** (6150), 769–771.

45. Piggee, C. (2008) Optical tweezers: not just for physicists anymore. *Anal. Chem.*, **81** (1), 16–19.

46. Neuman, K.C. and Block, S.M. (2004) Optical trapping. *Rev. Sci. Instrum.*, **75** (9), 2787–2809.

47. Grier, D.G. (2003) A revolution in optical manipulation. *Nature*, **424** (6950), 810–816.

48. Zhang, H. and Liu, K.-K. (2008) Optical tweezers for single cells. *J. R. Soc. Interface*, **5** (24), 671–690.

49. Dholakia, K., Reece, P., and Gu, M. (2008) Optical micromanipulation. *Chem. Soc. Rev.*, **37** (1), 42–55.

50. Padgett, M. and Di Leonardo, R. (2011) Holographic optical tweezers and their relevance to lab on chip devices. *Lab Chip*, **11** (7), 1196–1205.

51. Di Carlo, D. (2012) A mechanical biomarker of cell state in medicine. *Jala*, **17** (1), 32–42.

52. Mao, X. and Huang, T.J. (2012) Exploiting mechanical biomarkers in microfluidics. *Lab Chip*, **12** (20), 4006–4009.

53. Zheng, Y., Shojaei-Baghini, E., Azad, A., Wang, C., and Sun, Y. (2012) High-throughput biophysical measurement of human red blood cells. *Lab Chip*, **12** (14), 2560–2567.

54. Adamo, A., Sharei, A., Adamo, L., Lee, B., Mao, S., and Jensen, K.F. (2012) Microfluidics-based assessment of cell deformability. *Anal. Chem.*, **84** (15), 6438–6443.

55. Byun, S., Son, S., Amodei, D., Cermak, N., Shaw, J., Kang, J.H., Hecht, V.C., Winslow, M.M., Jacks, T., Mallick, P., and Manalis, S.R. (2013) Characterizing deformability and surface friction

of cancer cells. *Proc. Natl. Acad. Sci. U.S.A.*, **110** (19), 7580–7585.

56. Zhang, W., Kai, K., Choi, D.S., Iwamoto, T., Nguyen, Y.H., Wong, H., Landis, M.D., Ueno, N.T., Chang, J., and Qin, L. (2012) Microfluidics separation reveals the stem-cell–like deformability of tumor-initiating cells. *Proc. Natl. Acad. Sci. U.S.A.*

57. Dudani, J.S., Gossett, D.R., Tse, H.T.K., and Di Carlo, D. (2013) Pinched-flow hydrodynamic stretching of single-cells. *Lab Chip*, **13** (18), 3728–3734.

58. Cha, S., Shin, T., Lee, S.S., Shim, W., Lee, G., Lee, S.J., Kim, Y., and Kim, J.M. (2012) Cell stretching measurement utilizing viscoelastic particle focusing. *Anal. Chem.*, **84** (23), 10471–10477.

59. Huang, S., Undisz, A., Diez-Silva, M., Bow, H., Dao, M., and Han, J. (2013) Dynamic deformability of Plasmodium falciparum-infected erythrocytes exposed to artesunate in vitro. *Integr. Biol.*, **5** (2), 414–422.

60. Huang, S., Amaladoss, A., Liu, M., Chen, H., Zhang, R., Preiser, P.R., Dao, M., and Han, J. (2014) In vivo splenic clearance correlates with in vitro deformability of red blood cells from plasmodium yoelii-infected mice. *Infect. Immun.*, **82** (6), 2532–2541.

61. Burg, T.P., Godin, M., Knudsen, S.M., Shen, W., Carlson, G., Foster, J.S., Babcock, K., and Manalis, S.R. (2007) Weighing of biomolecules, single cells and single nanoparticles in fluid. *Nature*, **446** (7139), 1066–1069.

62. Preira, P., Grandne, V., Forel, J.M., Gabriele, S., Camara, M., and Theodoly, O. (2013) Passive circulating cell sorting by deformability using a microfluidic gradual filter. *Lab Chip*, **13** (1), 161–170.

63. Beattie, W., Qin, X., Wang, L., and Ma, H. (2014) Clog-free cell filtration using resettable cell traps. *Lab Chip*, **14** (15), 2657–2665.

64. Toner, M. and Irimia, D. (2005) Blood-on-a-chip. *Ann. Rev. Biomed. Eng.*, **7** (1), 77–103.

65. Lee, S., Yim, Y., Ahn, K., and Lee, S. (2009) Extensional flow-based assessment of red blood cell deformability using hyperbolic converging

microchannel. *Biomed. Microdevices*, **11** (5), 1021–1027.

66. Forsyth, A.M., Wan, J., Ristenpart, W.D., and Stone, H.A. (2010) The dynamic behavior of chemically "stiffened" red blood cells in microchannel flows. *Microvasc. Res.*, **80** (1), 37–43.

67. Forsyth, A.M., Wan, J., Owrutsky, P.D., Abkarian, M., and Stone, H.A. (2011) Multiscale approach to link red blood cell dynamics, shear viscosity, and ATP release. *Proc. Natl. Acad. Sci. U.S.A.*, **108** (27), 10986–10991.

68. Park, H.Y., Qiu, X.Y., Rhoades, E., Korlach, J., Kwok, L.W., Zipfel, W.R., Webb, W.W., and Pollack, L. (2006) Achieving uniform mixing in a microfluidic device: hydrodynamic focusing prior to mixing. *Anal. Chem.*, **78** (13), 4465–4473.

69. Lee, G.-B., Chang, C.-C., Huang, S.-B., and Yang, R.-J. (2006) The hydrodynamic focusing effect inside rectangular microchannels. *J. Micromech. Microeng.*, **16** (5), 1024.

70. Amini, H., Lee, W., and Di Carlo, D. (2014) Inertial microfluidic physics. *Lab Chip*, **14** (15), 2739–2761.

71. Di Carlo, D. (2009) Inertial microfluidics. *Lab Chip*, **9** (21), 3038–3046.

72. Martel, J.M. and Toner, M. (2014) Inertial focusing in microfluidics. *Annu. Rev. Biomed. Eng.*, **16** (1), 371–396.

73. Gossett, D.R., Tse, H.T.K., Lee, S.A., Ying, Y., Lindgren, A.G., Yang, O.O., Rao, J., Clark, A.T., and Di Carlo, D. (2012) Hydrodynamic stretching of single cells for large population mechanical phenotyping. *Proc. Natl. Acad. Sci. U.S.A.*, **109** (20), 7630–7635.

74. Tse, H.T.K., Gossett, D.R., Moon, Y.S., Masaeli, M., Sohsman, M., Ying, Y., Mislick, K., Adams, R.P., Rao, J., and Di Carlo, D. (2013) Quantitative diagnosis of malignant pleural effusions by single-cell mechanophenotyping. *Sci. Transl. Med.*, **5** (212), 212ra163.

75. Yang, S., Kim, J.Y., Lee, S.J., Lee, S.S., and Kim, J.M. (2011) Sheathless elasto-inertial particle focusing and continuous separation in a straight rectangular microchannel. *Lab Chip*, **11** (2), 266–273.

76. Nam, J., Lim, H., Kim, D., Jung, H., and Shin, S. (2012) Continuous separation of microparticles in a microfluidic channel via the elasto-inertial effect of non-Newtonian fluid. *Lab Chip*, **12** (7), 1347–1354.

77. Goda, K., Tsia, K., and Jalali, B. (2009) Serial time-encoded amplified imaging for real-time observation of fast dynamic phenomena. *Nature*, **458** (7242), 1145–1149.

78. Goda, K., Ayazi, A., Gossett, D.R., Sadasivam, J., Lonappan, C.K., Sollier, E., Fard, A.M., Hur, S.C., Adam, J., Murray, C., Wang, C., Brackbill, N., Di Carlo, D., and Jalali, B. (2012) High-throughput single-microparticle imaging flow analyzer. *Proc. Natl. Acad. Sci. U.S.A.*, **109** (29), 11630–11635.

79. Tse, H.T.K., Meng, P., Gossett, D.R., Irturk, A., Kastner, R., and Di Carlo, D. (2011) Strategies for implementing hardware-assisted high-throughput cellular image analysis. *J. Assoc. Lab. Automat.*, **16** (6), 422–430.

80. Gao, Y., Li, W., and Pappas, D. (2013) Recent advances in microfluidic cell separations. *Analyst*, **138** (17), 4714–4721.

81. Gossett, D.R., Weaver, W.M., Mach, A.J., Hur, S.C., Tse, H.T.K., Lee, W., Amini, H., and Di Carlo, D. (2010) Label-free cell separation and sorting in microfluidic systems. *Anal. Bioanal.Chem.*, **397** (8), 3249–3267.

82. Jackson, E.L. and Lu, H. (2013) Advances in microfluidic cell separation and manipulation. *Curr. Opin. Chem. Eng.*, **2** (4), 398–404.

83. Geislinger, T.M. and Franke, T. (2014) Hydrodynamic lift of vesicles and red blood cells in flow—from Fåhræus & Lindqvist to microfluidic cell sorting. *Adv. Colloid Interface Sci.*, **208**, 161–176.

84. Bhagat, A.A.S., Bow, H., Hou, H.W., Tan, S.J., Han, J., and Lim, C.T. (2010) Microfluidics for cell separation. *Med. Biol. Eng. Comput.*, **48** (10), 999–1014.

85. Hou, H.W., Lee, W.C., Leong, M.C., Sonam, S., Vedula, S.R.K., and Lim, C.T. (2011) Microfluidics for applications in cell mechanics and mechanobiology. *Cell. Mol. Bioeng.*, **4** (4), 591–602.

86. Çetin, B., Özer, M.B., and Solmaz, M.E. (2014) Microfluidic bio-particle manipulation for biotechnology. *Biochem. Eng. J.*

87. Pratt, E.D., Huang, C., Hawkins, B.G., Gleghorn, J.P., and Kirby, B.J. (2011) Rare cell capture in microfluidic devices. *Chem. Eng. Sci.*, **66** (7), 1508–1522.

88. Faivre, M., Abkarian, M., Bickraj, K., and Stone, H.A. (2006) Geometrical focusing of cells in a microfluidic device: an approach to separate blood plasma. *Biorheology*, **43** (2), 147–159.

89. Warkiani, M.E., Guan, G., Luan, K.B., Lee, W.C., Bhagat, A.A.S., Kant Chaudhuri, P., Tan, D.S.-W., Lim, W.T., Lee, S.C., Chen, P.C.Y., Lim, C.T., and Han, J. (2014) Slanted spiral microfluidics for the ultra-fast, label-free isolation of circulating tumor cells. *Lab Chip*, **14** (1), 128–137.

90. Warkiani, M.E., Khoo, B.L., Tan, D.S.-W., Bhagat, A.A.S., Lim, W.-T., Yap, Y.S., Lee, S.C., Soo, R.A., Han, J., and Lim, C.T. (2014) An ultra-high-throughput spiral microfluidic biochip for the enrichment of circulating tumor cells. *Analyst*, **139** (13), 3245–3255.

91. Lee, M.G., Shin, J.H., Bae, C.Y., Choi, S., and Park, J.-K. (2013) Label-free cancer cell separation from human whole blood using inertial microfluidics at low shear stress. *Anal. Chem.*, **85** (13), 6213–6218.

92. Inglis, D.W., Lord, M., and Nordon, R.E. (2011) Scaling deterministic lateral displacement arrays for high throughput and dilution-free enrichment of leukocytes. *J. Micromech. Microeng.*, **21** (5), 054024.

93. Holm, S.H., Beech, J.P., Barrett, M.P., and Tegenfeldt, J.O. (2011) Separation of parasites from human blood using deterministic lateral displacement. *Lab Chip*, **11** (7), 1326–1332.

94. Hou, H.W., Warkiani, M.E., Khoo, B.L., Li, Z.R., Soo, R.A., Tan, D.S.-W., Lim, W.-T., Han, J., Bhagat, A.A.S., and Lim, C.T. (2013) Isolation and retrieval of circulating tumor cells using centrifugal forces. *Sci. Rep.*, **3**, 1259.

95. Hou, H.W., Bhagat, A.A.S., Chong, A.G.L., Mao, P., Tan, K.S.W., Han, J., and Lim, C.T. (2010) Deformability based cell margination—a simple microfluidic design for malaria-infected erythrocyte separation. *Lab Chip*, **10** (19), 2605–2613.

96. Huang, L.R., Cox, E.C., Austin, R.H., and Sturm, J.C. (2004) Continuous particle separation through deterministic lateral displacement. *Science*, **304** (5673), 987–990.

97. McGrath, J.S., Jimenez, M., and Bridle, H.L. (2014) Deterministic lateral displacement for particle separation: a review. *Lab Chip*, **14** (21), 4139–4158.

98. Inglis, D.W., Davis, J.A., Austin, R.H., and Sturm, J.C. (2006) Critical particle size for fractionation by deterministic lateral displacement. *Lab Chip*, **6** (5), 655–658.

99. Loutherback, K., D'Silva, J., Liu, L., Wu, A., Austin, R.H., and Sturm, J.C. (2012) Deterministic separation of cancer cells from blood at 10 mL/min. *AIP Adv.*, **2** (4), 042107.

100. Mach, A.J. and Di Carlo, D. (2010) Continuous scalable blood filtration device using inertial microfluidics. *Biotechnol. Bioeng.*, **107** (2), 302–311.

101. Liu, Z., Huang, F., Du, J., Shu, W., Feng, H., Xu, X., and Chen, Y. (2013) Rapid isolation of cancer cells using microfluidic deterministic lateral displacement structure. *Biomicrofluidics*, **7** (1), 011801.

102. Ho, B.P. and Leal, L.G. (1974) Inertial migration of rigid spheres in two-dimensional unidirectional flows. *J. Fluid Mech.*, **65** (02), 365–400.

103. Zhou, J., Giridhar, P.V., Kasper, S., and Papautsky, I. (2013) Modulation of aspect ratio for complete separation in an inertial microfluidic channel. *Lab Chip*, **13** (10), 1919–1929.

104. Shen, S., Ma, C., Zhao, L., Wang, Y., Wang, J.-C., Xu, J., Li, T., Pang, L., and Wang, J. (2014) High-throughput rare cell separation from blood samples using steric hindrance and inertial microfluidics. *Lab Chip*, **14**, 2525–2538.

105. Bhagat, A.A.S., Hou, H.W., Li, L.D., Lim, C.T., and Han, J. (2011) Pinched flow coupled shear-modulated inertial microfluidics for high-throughput rare blood cell separation. *Lab Chip*, **11** (11), 1870–1878.

106. Moon, H.-S., Kwon, K., Hyun, K.-A., Sim, T.S., Park, J.C., Lee, J.-G., and Jung, H.-I. (2013) Continual collection and re-separation of circulating tumor cells from blood using multi-stage multi-orifice flow fractionation. *Biomicrofluidics*, **7** (1), 014105.

107. Hur, S.C., Mach, A.J., and Di Carlo, D. (2011) High-throughput size-based rare cell enrichment using microscale vortices. *Biomicrofluidics*, **5** (2), 022206.

108. Mach, A.J., Kim, J.H., Arshi, A., Hur, S.C., and Di Carlo, D. (2011) Automated cellular sample preparation using a Centrifuge-on-a-Chip. *Lab Chip*, **11** (17), 2827–2834.

109. Che, J., Mach, A.J., Go, D.E., Talati, I., Ying, Y., Rao, J.Y., Kulkarni, R.P., and Di Carlo, D. (2013) Microfluidic purification and concentration of malignant pleural effusions for improved molecular and cytomorphological diagnostics. *PLoS One*, **8** (10), e78194.

110. Sollier, E., Go, D.E., Che, J., Gossett, D.R., O'Byrne, S., Weaver, W.M., Kummer, N., Rettig, M., Goldman, J., and Nickols, N. (2014) Size-selective collection of circulating tumor cells using vortex technology. *Lab Chip*, **14** (1), 63–77.

111. Berger, S.A., Talbot, L., and Yao, L.S. (1983) Flow in curved pipes. *Annu. Rev. Fluid Mech.*, **15**, 461–512.

112. Di Carlo, D., Edd, J.F., Irimia, D., Tompkins, R.G., and Toner, M. (2008) Equilibrium separation and filtration of particles using differential inertial focusing. *Anal. Chem.*, **80** (6), 2204–2211.

113. Zhang, J., Yan, S., Sluyter, R., Li, W., Alici, G., and Nguyen, N.-T. (2014) Inertial particle separation by differential equilibrium positions in a symmetrical serpentine micro-channel. *Sci. Rep.*, **4**.

114. Tanaka, T., Ishikawa, T., Numayama-Tsuruta, K., Imai, Y., Ueno, H., Matsuki, N., and Yamaguchi, T. (2012) Separation of cancer cells from a

red blood cell suspension using inertial force. *Lab Chip*, **12** (21), 4336–4343.

115. Nivedita, N. and Papautsky, I. (2013) Continuous separation of blood cells in spiral microfluidic devices. *Biomicrofluidics*, **7** (5), 054101.

116. Kuntaegowdanahalli, S.S., Bhagat, A.A.S., Kumar, G., and Papautsky, I. (2009) Inertial microfluidics for continuous particle separation in spiral microchannels. *Lab Chip*, **9** (20), 2973–2980.

117. Lee, W.C., Bhagat, A.A.S., Huang, S., Van Vliet, K.J., Han, J., and Lim, C.T. (2011) High-throughput cell cycle synchronization using inertial forces in spiral microchannels. *Lab Chip*, **11** (7), 1359–1367.

118. Khoo, B.L., Warkiani, M.E., Tan, D.S.-W., Bhagat, A.A.S., Irwin, D., Lau, D.P., Lim, A.S., Lim, K.H., Krisna, S.S., and Lim, W.-T. (2014) Clinical validation of an ultra high-throughput spiral microfluidics for the detection and enrichment of viable circulating tumor cells. *PLoS One*, **9** (7), e99409.

119. Sun, J., Li, M., Liu, C., Zhang, Y., Liu, D., Liu, W., Hu, G., and Jiang, X. (2012) Double spiral microchannel for label-free tumor cell separation and enrichment. *Lab Chip*, **12** (20), 3952–3960.

120. Guan, G., Wu, L., Bhagat, A.A., Li, Z., Chen, P.C., Chao, S., Ong, C.J., and Han, J. (2013) Spiral microchannel with rectangular and trapezoidal cross-sections for size based particle separation. *Sci. Rep.*, **3**.

121. Wu, L.D., Guan, G.F., Hou, H.W., Bhagat, A.A.S., and Han, J. (2012) Separation of leukocytes from blood using spiral channel with trapezoid cross-section. *Anal. Chem.*, **84** (21), 9324–9331.

122. Lee, W., Amini, H., Stone, H.A., and Di Carlo, D. (2010) Dynamic self-assembly and control of microfluidic particle crystals. *Proc. Natl. Acad. Sci. U.S.A.*, **107** (52), 22413–22418.

123. Fahraus, R. and Lindqvist, T. (1931) The viscosity of the blood in narrow capillary tubes. *Am. J. Physiol.*, **96** (3), 562–568.

124. Hur, S.C., Henderson-MacLennan, N.K., McCabe, E.R., and Di Carlo, D. (2011) Deformability-based cell classification and enrichment using inertial microfluidics. *Lab Chip*, **11** (5), 912–920.

125. Sugaya, S., Yamada, M., and Seki, M. (2011) Observation of nonspherical particle behaviors for continuous shape-based separation using hydrodynamic filtration. *Biomicrofluidics*, **5** (2), 024103.

126. Ozkumur, E., Shah, A.M., Ciciliano, J.C., Emmink, B.L., Miyamoto, D.T., Brachtel, E., Yu, M., Chen, P.-i., Morgan, B., and Trautwein, J. (2013) Inertial focusing for tumor antigen–dependent and–independent sorting of rare circulating tumor cells. *Sci. Transl. Med.*, **5** (179), 179ra147.

127. Sollier, E., Rostaing, H., Pouteau, P., Fouillet, Y., and Achard, J.-L. (2009) Passive microfluidic devices for plasma extraction from whole human blood. *Sens. Actuators B*, **141** (2), 617–624.

128. Jain, A. and Munn, L.L. (2009) Determinants of leukocyte margination in rectangular microchannels. *PLoS One*, **4** (9), e7104.

129. Magnaudet, J., Takagi, S., and Legendre, D. (2003) Drag, deformation and lateral migration of a buoyant drop moving near a wall. *J. Fluid Mech.*, **476**, 115–157.

130. Geislinger, T.M. and Franke, T. (2013) Sorting of circulating tumor cells (MV3-melanoma) and red blood cells using non-inertial lift. *Biomicrofluidics*, **7** (4), 044120.

131. Beech, J.P., Holm, S.H., Adolfsson, K., and Tegenfeldt, J.O. (2012) Sorting cells by size, shape and deformability. *Lab Chip*, **12** (6), 1048–1051.

132. Hur, S.C., Choi, S.-E., Kwon, S., and Di Carlo, D. (2011) Inertial focusing of non-spherical microparticles. *Appl. Phys. Lett.*, **99** (4), 044101.

133. Masaeli, M., Sollier, E., Amini, H., Mao, W., Camacho, K., Doshi, N., Mitragotri, S., Alexeev, A., and Di Carlo, D. (2012) Continuous inertial focusing and separation of particles by shape. *Phys. Rev. X*, **2** (3), 031017.

134. Hur, S.C., Brinckerhoff, T.Z., Walthers, C.M., Dunn, J.C., and Di Carlo, D. (2012) Label-free enrichment of adrenal cortical progenitor cells using inertial microfluidics. *PLoS One*, **7** (10), e46550.

135. Sajeesh, P. and Sen, A. (2014) Particle separation and sorting in microfluidic devices: a review. *Microfluid. Nanofluid.*, **17** (1), 1–52.

136. Watarai, H. (2013) Continuous separation principles using external microaction forces. *Annu. Rev. Anal. Chem.*, **6** (1), 353–378.

137. Lenshof, A. and Laurell, T. (2010) Continuous separation of cells and particles in microfluidic systems. *Chem. Soc. Rev.*, **39** (3), 1203–1217.

138. Yeo, L.Y. and Friend, J.R. (2014) Surface acoustic wave microfluidics. *Annu. Rev. Fluid Mech.*, **46** (1), 379–406.

139. Laurell, T., Petersson, F., and Nilsson, A. (2007) Chip integrated strategies for acoustic separation and manipulation of cells and particles. *Chem. Soc. Rev.*, **36** (3), 492–506.

140. Lenshof, A., Magnusson, C., and Laurell, T. (2012) Acoustofluidics 8: Applications of acoustophoresis in continuous flow microsystems. *Lab Chip*, **12** (7), 1210–1223.

141. Ding, X., Lin, S.-C.S., Kiraly, B., Yue, H., Li, S., Chiang, I.-K., Shi, J., Benkovic, S.J., and Huang, T.J. (2012) On-chip manipulation of single microparticles, cells, and organisms using surface acoustic waves. *Proc. Natl. Acad. Sci. U.S.A.*, **109** (28), 11105–11109.

142. Nam, J., Lim, H., Kim, D., and Shin, S. (2011) Separation of platelets from whole blood using standing surface acoustic waves in a microchannel. *Lab Chip*, **11** (19), 3361–3364.

143. Petersson, F., Åberg, L., Swärd-Nilsson, A.-M., and Laurell, T. (2007) Free flow acoustophoresis: microfluidic-based mode of particle and cell separation. *Anal. Chem.*, **79** (14), 5117–5123.

144. Yang, A.H.J. and Soh, H.T. (2012) Acoustophoretic sorting of viable mammalian cells in a microfluidic device. *Anal. Chem.*, **84** (24), 10756–10762.

145. Adams, J.D., Ebbesen, C.L., Barnkob, R., Yang, A.H.J., Soh, H.T., and Bruus, H. (2012) High-throughput, temperature-controlled microchannel acoustophoresis device made with rapid prototyping. *J. Micromech. Microeng.*, **22** (7), 075017.

146. Shim, S., Stemke-Hale, K., Tsimberidou, A.M., Noshari, J., Anderson, T.E., and Gascoyne, P.R. (2013) Antibody-independent isolation of circulating tumor cells by continuous-flow dielectrophoresis. *Biomicrofluidics*, **7** (1), 011807.

147. Adams, J.D., Kim, U., and Soh, H.T. (2008) Multitarget magnetic activated cell sorter. *Proc. Natl. Acad. Sci. U.S.A.*, **105** (47), 18165–18170.

148. Chen, Y., Chung, A.J., Wu, T.-H., Teitell, M.A., Di Carlo, D., and Chiou, P.Y. (2014) Pulsed laser activated cell sorting with three dimensional sheathless inertial focusing. *Small*, **10** (9), 1746–1751.

149. Kirby, B.J. (2010) *Micro-and Nanoscale Fluid Mechanics: Transport in Microfluidic Devices*, Cambridge University Press.

150. Pethig, R. (2010) Review Article—Dielectrophoresis: Status of the theory, technology, and applications. *Biomicrofluidics*, **4** (2), 022811.

151. Kang, Y., Li, D., Kalams, S.A., and Eid, J.E. (2008) DC-Dielectrophoretic separation of biological cells by size. *Biomed. Microdevices*, **10** (2), 243–249.

152. Yang, J., Huang, Y., Wang, X.-B., Becker, F.F., and Gascoyne, P.R.C. (2000) Differential analysis of human leukocytes by dielectrophoretic field-flow-fractionation. *Biophys. J.*, **78** (5), 2680–2689.

153. Gascoyne, P.R.C., Noshari, J., Anderson, T.J., and Becker, F.F. (2009) Isolation of rare cells from cell mixtures by dielectrophoresis. *Electrophoresis*, **30** (8), 1388–1398.

154. Piacentini, N., Mernier, G., Tornay, R., and Renaud, P. (2011) Separation of platelets from other blood cells in continuous-flow by dielectrophoresis field-flow-fractionation. *Biomicrofluidics*, **5** (3), 34122–341228.

155. Kim, U., Shu, C.-W., Dane, K.Y., Daugherty, P.S., Wang, J.Y., and Soh, H. (2007) Selection of mammalian cells based on their cell-cycle phase using dielectrophoresis. *Proc. Natl. Acad. Sci. U.S.A.*, **104** (52), 20708–20712.

156. Alazzam, A., Stiharu, I., Bhat, R., and Meguerditchian, A.-N. (2011) Inter-digitated comb-like electrodes for continuous separation of malignant cells from blood using dielectrophoresis. *Electrophoresis*, **32** (11), 1327–1336.

157. Park, S., Zhang, Y., Wang, T.-H., and Yang, S. (2011) Continuous dielectrophoretic bacterial separation and concentration from physiological media of high conductivity. *Lab Chip*, **11** (17), 2893–2900.

158. Melville, D., Paul, F., and Roath, S. (1975) Direct magnetic separation of red cells from whole blood. *Nature*, **255** (5511), 706–706.

159. Miltenyi, S., Muller, W., Weichel, W., and Radbruch, A. (1990) High gradient magnetic cell separation with MACS. *Cytometry*, **11** (2), 231–238.

160. Iversen, T.-G., Skotland, T., and Sandvig, K. (2011) Endocytosis and intracellular transport of nanoparticles: Present knowledge and need for future studies. *Nano Today*, **6** (2), 176–185.

161. Robert, D., Pamme, N., Conjeaud, H., Gazeau, F., Iles, A., and Wilhelm, C. (2011) Cell sorting by endocytotic capacity in a microfluidic magnetophoresis device. *Lab Chip*, **11** (11), 1902–1910.

162. Jones, C.F. and Grainger, D.W. (2009) In vitro assessments of nanomaterial toxicity. *Adv. Drug Delivery Rev.*, **61** (6), 438–456.

163. Tseng, P., Judy, J.W., and Di Carlo, D. (2012) Magnetic nanoparticle-mediated massively parallel mechanical modulation of single-cell behavior. *Nat. Methods*, **9** (11), 1113–1119.

164. MacDonald, M., Spalding, G., and Dholakia, K. (2003) Microfluidic sorting in an optical lattice. *Nature*, **426** (6965), 421–424.

165. Baumgartl, J., Hannappel, G.M., Stevenson, D.J., Day, D., Gu, M., and Dholakia, K. (2009) Optical redistribution of microparticles and cells between microwells. *Lab Chip*, **9** (10), 1334–1336.

166. Wang, M.M., Tu, E., Raymond, D.E., Yang, J.M., Zhang, H.C., Hagen, N., Dees, B., Mercer, E.M., Forster, A.H., Kariv, I., Marchand, P.J., and Butler, W.F. (2005) Microfluidic sorting of mammalian cells by optical force switching. *Nat. Biotechnol.*, **23** (1), 83–87.

167. Piyasena, M.E. and Graves, S.W. (2014) The intersection of flow cytometry with microfluidics and microfabrication. *Lab Chip*, **14** (6), 1044–1059.

168. Karabacak, N.M., Spuhler, P.S., Fachin, F., Lim, E.J., Pai, V., Ozkumur, E., Martel, J.M., Kojic, N., Smith, K., and Chen, P.-I. (2014) Microfluidic, marker-free isolation of circulating tumor cells from blood samples. *Nat. Protoc.*, **9** (3), 694–710.

169. Mizuno, M., Yamada, M., Mitamura, R., Ike, K., Toyama, K., and Seki, M. (2013) Magnetophoresis-integrated hydrodynamic filtration system for size-and surface marker-based two-dimensional cell sorting. *Anal. Chem.*, **85** (16), 7666–7673.

170. Parichehreh, V., Medepallai, K., Babbarwal, K., and Sethu, P. (2013) Microfluidic inertia enhanced phase partitioning for enriching nucleated cell populations in blood. *Lab Chip*, **13** (5), 892–900.

171. Seo, H.-K., Kim, Y.-H., Kim, H.-O., and Kim, Y.-J. (2010) Hybrid cell sorters for on-chip cell separation by hydrodynamics and magnetophoresis. *J. Micromech. Microeng.*, **20** (9), 095019.

172. Choi, S., Levy, O., Coelho, M.B., Cabral, J.M., Karp, J.M., and Karnik, R. (2014) A cell rolling cytometer reveals the correlation between mesenchymal stem cell dynamic adhesion and differentiation state. *Lab Chip*, **14** (1), 161–166.

173. Xuan, X.C., Zhu, J.J., and Church, C. (2010) Particle focusing in microfluidic devices. *Microfluid. Nanofluid.*, **9** (1), 1–16.

174. Martel, J.M. and Toner, M. (2012) Inertial focusing dynamics in spiral microchannels. *Phys. Fluids*, **24** (3), 032001.

175. Martel, J.M. and Toner, M. (2013) Particle focusing in curved microfluidic channels. *Sci. Rep.*, **3** (3340), 1–8.

176. Oakey, J., Applegate, R.W., Arellano, E., Di Carlo, D., Graves, S.W., and Toner, M. (2010) Particle focusing in staged inertial microfluidic devices for flow cytometry. *Anal. Chem.*, **82** (9), 3862–3867.

177. Bhagat, A.A.S., Kuntaegowdanahalli, S.S., Kaval, N., Seliskar, C.J., and Papautsky, I. (2010) Inertial microfluidics for sheath-less high-throughput flow cytometry. *Biomed. Microdevices*, **12** (2), 187–195.

178. Chung, A.J., Gossett, D.R., and Di Carlo, D. (2013) Three dimensional, sheathless, and high-throughput microparticle inertial focusing through geometry-induced secondary flows. *Small*, **9** (5), 685–690.

179. Chung, A.J., Pulido, D., Oka, J.C., Amini, H., Masaeli, M., and Di Carlo, D. (2013) Microstructure-induced helical vortices allow single-stream and long-term inertial focusing. *Lab Chip*, **13** (15), 2942–2949.

180. Hur, S.C., Tse, H.T.K., and Di Carlo, D. (2010) Sheathless inertial cell ordering for extreme throughput flow cytometry. *Lab Chip*, **10** (3), 274–280.

181. Chen, Y., Nawaz, A.A., Zhao, Y., Huang, P.-H., McCoy, J.P., Levine, S.J., Wang, L., and Huang, T.J. (2014) Standing surface acoustic wave (SSAW)-based microfluidic cytometer. *Lab Chip*, **14** (5), 916–923.

182. Shi, J., Yazdi, S., Steven Lin, S.-C., Ding, X., Chiang, I.K., Sharp, K., and Huang, T.J. (2011) Three-dimensional continuous particle focusing in a microfluidic channel via standing surface acoustic waves (SSAW). *Lab Chip*, **11** (14), 2319–2324.

183. Shi, J., Huang, H., Stratton, Z., Huang, Y., and Huang, T.J. (2009) Continuous particle separation in a microfluidic channel via standing surface acoustic waves (SSAW). *Lab Chip*, **9** (23), 3354–3359.

184. Jakobsson, O., Grenvall, C., Nordin, M., Evander, M., and Laurell, T. (2014) Acoustic actuated fluorescence activated sorting of microparticles. *Lab Chip*, **14** (11), 1943–1950.

185. Zucker, R.M. and Fisher, N.C.,. (2001) *Evaluation and Purchase of an Analytical Flow Cytometer: Some of the Numerous Factors to Consider*, Current Protocols in Cytometry, John Wiley & Sons, Inc., New York.

186. Duda, D.G., Cohen, K.S., Scadden, D.T., and Jain, R.K. (2007) A protocol for phenotypic detection and enumeration of circulating endothelial cells and circulating progenitor cells in human blood. *Nat. Protoc.*, **2** (4), 805–810.

187. Gossett, D.R., Tse, H.T.K., Dudani, J.S., Goda, K., Woods, T.A., Graves, S.W., and Di Carlo, D. (2012) Inertial manipulation and transfer of microparticles across laminar fluid streams. *Small*, **8** (17), 2757–2764.

188. Tan, A.P., Dudani, J.S., Arshi, A., Lee, R.J., Tse, H.T.K., Gossett, D.R., and Di Carlo, D. (2014) Continuous-flow cytomorphological staining and analysis. *Lab Chip*, **14** (3), 522–531.

189. Dudani, J.S., Go, D.E., Gossett, D.R., Tan, A.P., and Di Carlo, D. (2014) Mediating millisecond reaction time around particles and cells. *Anal. Chem.*, **86** (3), 1502–1510.

2
Micro and Nano Manipulation and Assembly by Optically Induced Electrokinetics

Fei Fei Wang, Sam Lai, Lianqing Liu, Gwo-Bin Lee, and Wen Jung Li

2.1
Introduction

In the past 25 years, integrated circuit (IC) and microelectromechanical systems (MEMSs) technologies have moved much beyond the microdomain, and into the submicro-, nanoscopic, and, even, the molecular scales. Today, we have the capability to fabricate, manipulate, and assemble matters at the micro-, nano-, or molecular scales. This progress into "seeing" and manipulating matters that are smaller than visible light wavelength scale is impacting a range of fields including semiconductor physics, biological studies, pharmaceutical development, and many other scientific and technological applications. A range of new methods to generate physical forces have been developed in the process. For example, mechanical forces can now be applied to micro-, nano-, and biological entities using atomic force microscope probes [1], microgrippers [2], or pipettes [3]. However, disadvantages of these approaches, including inflection of mechanical damages on objects being manipulated and their relatively low manipulation speed, make manipulation of large quantities of objects difficult. In order to address these disadvantages, noncontact or noninvasive methods for micro-, nano-, and biological manipulation have also been explored in the past two decades.

Manipulation devices based on magnetic forces [4], acoustic waves [5, 6], hydrodynamic flows [7], light waves [8], or electrokinetic forces [9] are among the major noninvasive technologies available today. Each of them has its own advantages and disadvantages. Methods based on magnetic fields need premodification on objects with magnetic beads which constrains their application domain. In addition, movement controlled by permanent magnets is not precise enough for many proposed applications. Also, the high resistance of the magnetic coil generates significant heat during manipulation [10]. Acoustic traps show good selectivity but cannot achieve parallel manipulation of single entities. Microfluidic devices exploiting hydrodynamic flows are suitable for cell population sorting, but have difficulties in trapping or controlling specific single objects.

Electrokinetic forces generated from patterned electrodes capable of inducing the desired spatial distribution of electric field have been exploited to control

objects spanning from millimeter droplets to nanometer beads and, even, thin polymer films [11–14]. Among the many electrokinetic forces, dielectrophoretic (DEP) forces, in particular, have led to several object manipulation applications, and at the same time exhibiting a range of attractive features: (i) the fabrication of microelectrodes is compatible with conventional photolithography; (ii) the magnitude and direction of DEP force are related to the object's properties, which is useful in sorting systems [11]; and (iii) the ability to operate on particles with or without net charge. Initially, the DEP were generated by a static pattern of metal electrodes, which confines the method's flexibility as it is not dynamically reconfigurable. Dynamic individual or parallel manipulation through DEP was achieved later through the introduction of a two-dimensional programmable electrode arrays. However, such devices were limited by the fabrication accuracy of IC and higher chip cost [15, 16].

On the other hand, optical tweezers, a widely used pure light manipulation method, has now evolved into a powerful tool in the study of physics, chemistry, and biology phenomena, since they were introduced by Ashkin in 1986 [8]. By exploiting the radiation pressure and gradient force generated at the brightest point in a tightly focused laser beam [8], optical tweezers can manipulate microscale to molecular scale entities with a spatial resolution of $0.1-2$ nm [17]. However, notwithstanding such a high resolution, there continue to be drawbacks such as limited manipulation area, photodamage, and sample heating due to high optical intensities used to form stable traps; they also fall short in terms of selectivity and exclusivity [16, 17].

With regard to the requirement for achieving high-resolution and high-throughput manipulation at the same time, all of these aforementioned technologies have failed [18]. Fortunately, as discussed in the remaining sections of this chapter, a more recently developed technology that uses *light* to induce controllable *electrokinetic* forces for manipulating micro-, nano-, and biological entities has been found to be extremely versatile, and could satisfy the requirement for achieving high-resolution and high-throughput manipulation tasks. As light illuminates the world, it has also lit up many human industries and research areas. A particularly noteworthy example is the photolithography-based IC manufacturing industry, where light is used as the medium for transporting patterns from predefined masks to the photoresist. Apart from this spatial light modulation through a predefined mask, researchers and engineers have also proposed various devices for flexible modulation purposes, such as programmable digital micro-mirror devices (DMDs), MEMS mirror arrays, and liquid-crystal-based spatial light modulators. In the areas of micro- and nanoscale manipulation, a major question concerns how one could introduce light waves into conventional methods to endow them with flexibility, noninvasive properties, dynamic capabilities, a higher degree of freedom [19], and achieve high resolution and high throughput at the same time. In this chapter, we introduce a manipulation technology that is based on combining *optical* and *electrokinetic* principles – more specifically, *optically induced electrokinetics* (OEK) and its applications in manipulation and assembly of micro- and nanoscale entities.

One of the first combinations of optics and electrokinetics was reported by Mizuno *et al.* in 1993 [20]. Electrothermal vortex, which was generated when the focused infrared laser beam was illuminated perpendicular to both the liquid film and the direction of an AC electric field, was explored to translate and stretch DNAs [20, 21]. In 2000, Hayward *et al.* [22] developed another integration mechanism based on adjusting local conductivity of one substrate by light illumination. The apparatus used by Hayward *et al.* consisted of two parallel electrodes of a brass cathode and a transparent indium tin oxide (ITO) anode. When UV light illuminated on the heavily doped n-type semiconductor ITO electrode, a higher current appears [22]. Colloidal particles with diameters of submicrometers and 2 µm could be assembled when the UV light pattern modulated by a prefabricated mask illuminated the ITO film and a DC field was applied [22]. After 4 years, Gong *et al.* [23] achieved colloidal assembly and crystallization through a combination of DEP and electroosmotic mechanisms by applying an AC signal and a scanning laser (532 nm) on two parallel ITO electrodes.

Following the pioneering work by Hayward *et al.* [22], researchers have explored materials with highly efficient photoconductive layers and biocompatibilities [24–29]. By replacing the laser spot with a programmable illumination system and introducing a highly efficient photosensitive material, Chiou *et al.*
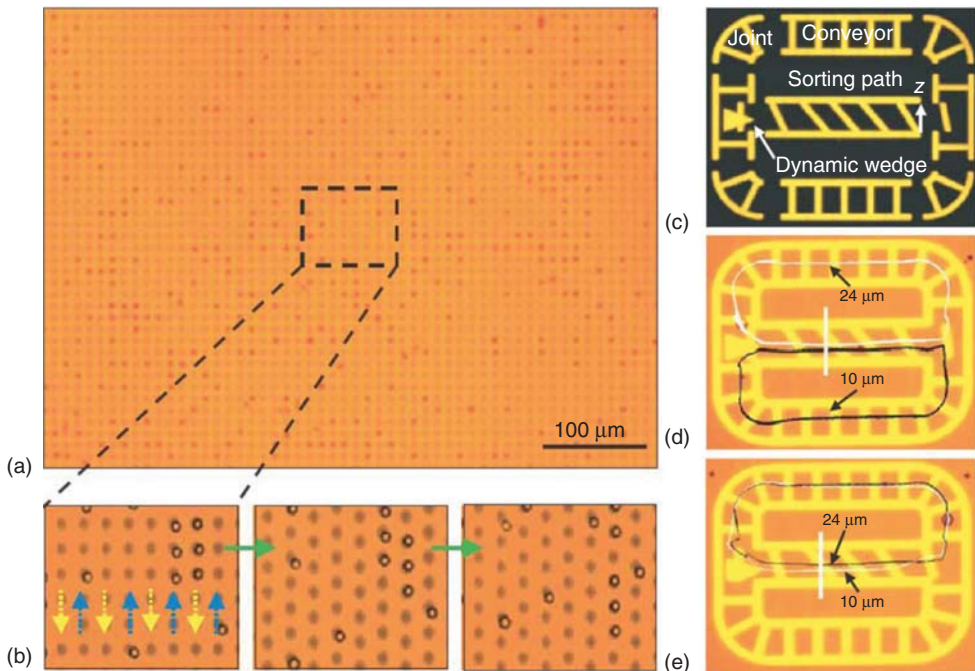
Figure 2.1 (a) Massively parallel manipulation of single polystyrene particles by ODEP force. (b) Parallel transportation of single particles by ODEP. (c–e) Examples of integrated virtual "optical machines." [18]

[18] demonstrated an optical image-driven high-resolution dielectrophoresis technique for the parallel manipulation of single cells and microparticles (see Figure 2.1). This technology, which is generally referred to as *optoelectronic tweezers* (*OET*s) or *optically induced dielectrophoresis* (*ODEP*), retains the advantages of two well-established manipulation methods: operational flexibility of optical tweezers and high throughput and material selectivity of electrode-based DEP [16, 18]. However, since the optical energy is not used directly for trapping but just to trigger the nonuniform electric field, it is found to require five orders lower optical intensity than optical tweezers [18]. As a result, by choosing an appropriate objective lens, the manipulation area can be 500 times larger than that of optical tweezers; the manipulation of 15 000 particle traps on a $1.3 \times 1.0\,\text{mm}^2$ area has been demonstrated [18]. Further, the trap stiffness of ODEP is found to be $1.6 \times 10^{-6}\text{N m}^{-1}$ mW, which is 2 orders of magnitude larger than that possible with optical tweezers [30].

The basic chip structure used in a typical ODEP experiment consists of two parallel electrodes: a transparent ITO electrode and a photosensitive electrode containing a hydrogenated amorphous silicon (a-Si:H) layer (thickness of ∼1 μm) deposited onto an ITO-coated glass using a plasma-enhanced chemical vapor deposition (PECVD) process (Figure 2.2b,c). A chamber is formed by separating the two electrodes with approximately 60–100-μm spacers (usually a double-sided tape), into which the solution containing objects to be operated is injected. Usually, the electric field is generated in the chip by an AC bias with
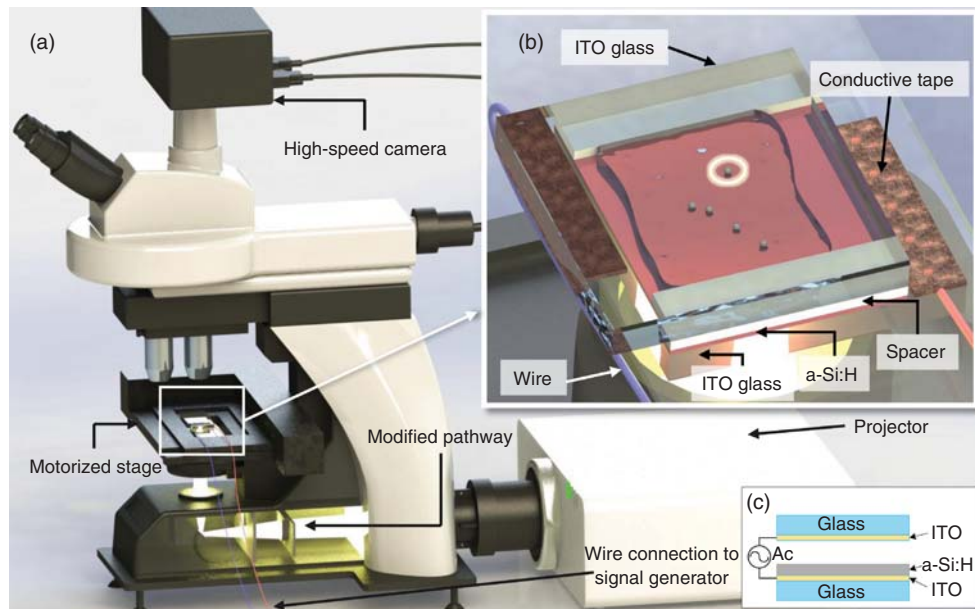
Figure 2.2 (a) Components of the ODEP system. (b) An illustration of the ODEP chip. (c) Cross-sectional illustration of an OEK chip.

adjustable amplitude and frequency. Collectively, the two substrates with the spacer are referred to as the *OEK chip*, as heterogeneous electrokinetic forces can be generated in the fluidic medium inside the chip when light images are projected on to the a-Si:H layer.

After assembly, this OEK chip is placed under an optical microscope to enable observation of the objects to be operated (Figure 2.2a). Static light patterns used to trigger the ODEP force can be generated through a photomask [22], a diaphragm [31], or a single focused laser spot [25, 32]. Dynamic or programmable manipulation can be achieved by a DMD [18, 33, 34], a projector [35, 36], or a liquid-crystal-based spatial light modulator [37, 38]. Additional optical components, including an objective lens, are usually needed to focus light patterns on to the photosensitive layer to obtain a resolution of $1 – 20\,\mu m$ [19].

Since its inception in 2005, a range of OEK-based applications have been demonstrated, including manipulation of single cells [18], concentration and transport of multiple *Escherichia coli* cells [32], cell counting and lysis [39], microparticle counting and sorting [40], manipulation of single DNA molecules [41], parallel trapping of single- and multiwall carbon nanotubes (CNTs) [42], manipulation and patterning of single-wall CNTs [43], dynamic manipulation and separation of individual semiconducting and metallic nanowires [30], dynamic patterning of nanoparticles [44], control of local chemical concentration in [31] or the pH [34] of a fluid, selective electroporation [45], and manipulation oil-in-water emulsion droplets [46].

2.2
Optically Induced Electrokinetic (OEK) Forces

2.2.1
Classical Electrokinetic Forces

2.2.1.1 Dielectrophoresis (DEP)

Earlier research work indicated that a particle in a nonuniform AC electric field experiences DEP forces that are derived from interactions between the spatial heterogeneity of the magnitude and the phase of the field with the in-phase and out-of-phase components of the induced dipole moment [47]. The time-averaged DEP force $\langle F(t) \rangle$ exerted on a dielectric particle due to an imposed electric field, E, can be approximated in terms of dipole effects as [9, 47, 48]

$$\langle f_{\mathrm{DEP}} \rangle = 2\pi\varepsilon_{\mathrm{m}} r^3 \left\{ \mathrm{Re}\,(K^*)\,\nabla(E_{\mathrm{rms}})^2 + \mathrm{Im}(K^*)(E_{x0}^2 \nabla\varphi_{\mathrm{x}} + E_{y0}^2 \nabla\varphi_{\mathrm{y}} + E_{z0}^2 \nabla\varphi_{\mathrm{z}}) \right\},$$

$$(2.1)$$

where ε_{m} denotes the permittivity of the liquid medium, r is the particle radius, and E_{rms} is the root-mean-square value of the electric field strength. E_{i0} and φ_i $(i = x,\ y,\ z)$ are the magnitudes and phases of the electric field components in the principal axis directions, respectively. K^* is the Clausius–Mossotti (CM)

factor, which measures the strength of effective polarization of a spherical particle, and can be estimated as

$$K^* = \frac{\varepsilon_p^* - \varepsilon_m^*}{\varepsilon_p^* + 2\varepsilon_m^*}, \; \varepsilon_p^* = \varepsilon_p^* - j\frac{\sigma_p}{\omega}, \; \varepsilon_m^* = \varepsilon_m - j\frac{\sigma_m}{\omega}, \tag{2.2}$$

where ε_p^* and ε_m^* are the frequency-dependent complex permittivities of the particle and medium, respectively, ε is the permittivity of the particle or medium (denoted by a subscript p or m, respectively), σ is the conductivity of the particle or medium, and ω is the angular frequency of the electric field [49]. If the particles are nonhomogeneous, for example, biological cells, the CM factor requires a modification during manipulation [36, 49, 50].

With regard to conventional DEP, the force is dependent on the in-phase component of the induced dipole moment and on the magnitude of the heterogeneous electric field, that is, the first component of Eq. (2.1) [46, 49]. Depending on whether CM factor is positive or negative, this force pushes the particle toward either strong or weak field regions, respectively [9, 48]. By contrast, traveling-wave dielectrophoresis relies on the out-of-phase component of the induced dipole moment and on phase nonuniformity, that is, the secondary component of Eq. (2.1) [47]. Unlike DEP, the electrophoretic phenomena vanish in the absence of a net charge on the particle or in an alternating field [9].

2.2.1.2 AC Electroosmosis (ACEO)

When subjected to an electrical potential, an electrical double layer (EDL) is generated near a wall exposed to an ionic fluid. The motion of the fluidic medium relative to the substrate driven by Coulombic force arising from the interaction of electric field with the net mobile electric charge in the EDL is termed *electroosmosis*. The velocity of this motion is linearly proportional to the electric field and is influenced by the substrate material and liquid properties. The slip velocity or Helmholtz−Smoluchowski velocity of the liquid at the interface is [51, 52]

$$u_{\text{slip}} = -\frac{\varepsilon\varsigma E_t}{\eta}, \tag{2.3}$$

where ε is the permittivity of the liquid, ς is the zeta potential, E_t is the tangential electric field, and η is the dynamic viscosity.

A similar steady fluid motion has been observed and was termed AC electroosmosis (ACEO) when the DC voltage is replaced with an AC voltage, except for the electric field and the double-layer charge, which are time-varying [53]. Unlike DC electroosmosis, ACEO shows frequency dependence arising out of the fact that the EDL acts as a parallel plate capacitor, whose capacitance varies with the layer's thickness which is related to liquid conductivity [54]. The thickness of EDL can then be described by Gouy−Chapman theory [33, 54, 55]:

$$d_{\text{DEL}} = \left(\frac{2\sigma_m z^2 e}{\mu_m \varepsilon_m k_B T}\right)^{-1/2}, \tag{2.4}$$

where z is the valence of the ion, e is the charge on an electron, μ_m is the bulk ion mobility, and k_B is the Boltzmann constant.

2.2.1.3 Electrothermal Effects (ET)

Joule heating could be induced in a liquid in response to the applied electric field that induces gradients in electrical conductivity and permittivity. The fluid motion resulting from the interaction between these gradients and electric field is termed *electrothermal flow*. The power per unit volume induced by the applied electric field (E) is given as [56]

$$W = \sigma_m |E|^2 \tag{2.5}$$

The time-averaged electrical force density, which drives the electrothermal (ET) flow, is [56, 57]

$$\langle f_{ET} \rangle = \frac{1}{2} \text{Re} \left[\frac{\sigma_m \varepsilon_m (\alpha - \beta)}{\sigma_m + i\omega\varepsilon_m} (\nabla T \cdot E)E^* - \frac{1}{2}\varepsilon_m \alpha |E|^2 \nabla T \right],$$

$$\alpha = \frac{1}{\varepsilon_m} \left(\frac{\partial \varepsilon_m}{\partial T} \right) \text{ and } \beta = \frac{1}{\sigma_m} \left(\frac{\partial \sigma_m}{\partial T} \right). \tag{2.6}$$

where $*$ indicates the complex conjugate and T is the temperature. For electrolytes, $\alpha \approx -0.004 \text{ K}^{-1}$ and $\beta \approx 0.02 \text{ K}^{-1}$ [53].

2.2.1.4 Buoyancy Effects

Another parasitic effect resulting from Joule heating or temperature gradient is the change of fluid density and therefore potential natural convection [58]. This influence can be estimated by the buoyancy force, f_g, as follows [58]:

$$f_g = \Delta\rho_m g = \frac{\partial\rho_m}{\partial T} \Delta T g \tag{2.7}$$

where g is the acceleration due to gravity and ρ_m is the density of the medium.

The buoyancy effects can be compensated by a pure pressure gradient, so there may be no fluid flow appearance. However, this balance can be disturbed by Rayleigh–Bénard convection at high enough temperature gradients. When the Rayleigh number reaches a critical value ($\sim$1500), natural convection appears. The Rayleigh number is given by [57]

$$Ra = \frac{g|\partial\rho_m/\partial T|\Delta T h^3}{\eta\alpha} \tag{2.8}$$

where α is the thermal diffusivity coefficient, α is the thermal diffusivity coefficient, and h is a system characteristic height.

2.2.1.5 Brownian Motion

The random motion of particles suspended in a fluid is called *Brownian* motion. Statistically, the average value of the forces and velocity resulting from the collision of particles with the atoms or molecules in the fluid in Brownian motion is zero. On the other hand, the root-mean-square displacement of a particle under Brownian motion is [59]

$$\lambda_x = \sqrt{2Dt} = \sqrt{\frac{k_B T}{3\pi r\eta}t} \tag{2.9}$$

where D is the diffusion constant, t is the observation period, k_B is the Boltzmann constant, and T is the absolute temperature. The function of Brownian motion on particles can be treated as an effective random force with a maximum value approximately given by [60]

$$F_{Brownian} = \frac{k_B T}{v^{1/3}} \tag{2.10}$$

where v is the volume of the particle.

2.2.2
Optically Induced Electrokinetic Forces

2.2.2.1 OEK Chip: Operational Principle and Design
The introduction of optics to generate electrokinetics provides a flexible approach to modulate the physical and chemical fields (including electrical, force, temperature, and chemical gradients) appearing in a microfluidic chip by simply adjusting the electrical properties of the photosensitive (a-Si:H) layer. Without illumination, the majority of applied AC voltage drops across the a-Si:H layer. However, in the presence of light, the partial voltage on liquid layer is significantly increased due to approximately $3-4$ orders of magnitude increase of the conductivity of a-Si:H when illuminated, which arises from the creation of electron-hole pairs [54, 61]. A spatial electric field gradient without phase nonuniformity is created near the illuminated area when an AC bias is applied between the two electrodes (Figure 2.3a). In this case, the time-averaged DEP force for spherical particles can be expressed as

$$\langle f_{ODEP} \rangle = 2\pi\varepsilon_m r^3 \text{Re}(K^*)\nabla(E_{rms})^2 \tag{2.11}$$

(a)   (b)
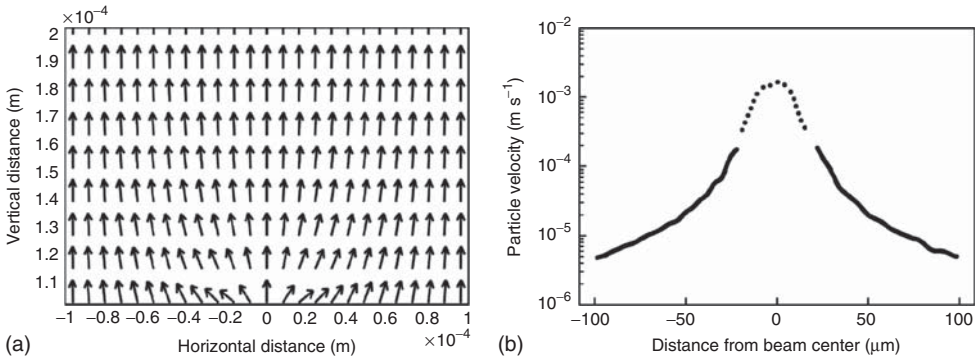
Figure 2.3 (a) Simulation results for the electric field distribution. (b) Simulation results showing the relationship between the maximum velocity of a 10-μm particle and the distance for optical power of 1 mW and an illumination spot size of 20 μm at 5 μm above the a-Si:H surface. The dotted region corresponds to the points within 18 μm of the light; they are not valid because of the effects of vertical DEP force acting on the particle. 10 Vpp and 100 kHz AC voltage was used in this simulation. The light center is at position zero [54].

The velocity arising from ODEP for a spherical particle, which can be calculated from Stokes' equation, is

$$u_{\text{ODEP}} = \frac{\langle f_{\text{ODEP}} \rangle}{6\pi\eta r} \tag{2.12}$$

The simulated maximum velocity arising from ODEP is shown in Figure 2.3b [54]. Note that the velocity decreases as particle moves away from the beam's center since the lateral component of ODEP force decreases. This horizontal component of the ODEP force also suffers a dramatic drop along the vertical direction [54].

In the regions surrounding the light pattern, a tangential electric field component is generated at the EDL when an AC voltage is applied, which causes the optically induced ACEO. During this process, the ionic charges at the surface of the EDL are driven toward the center of the illuminated area by the optically induced tangential field near the surface, which will cause microvortices in the OEK chip as shown in Figure 2.4a,c [33].

In the OEK chip, phonon generation due to the absorbance of incident photons in the a-Si:H can induce local temperature increase besides the influence from Joule heating [54]. By exploring the temperature gradients resulting from the interaction between amorphous silicon and the light pattern projected from a projector focused by an objective lens with an intensity of 5.3 W cm^{-2}, Hu *et al.* [62] studied the use of optically controlled bubble microrobots to manipulate glass microbeads and assemble microblocks and cell-encapsulating hydrogel beads based on the thermocapillary flow effect. Thus, the local temperature of the medium in OEK chip needs to be controlled properly to ensure cellular viability for the biological applications [63, 64], especially in a parallel manipulation system [16, 18, 33, 38, 65], where a complex light image covering a large area is used. In other words,
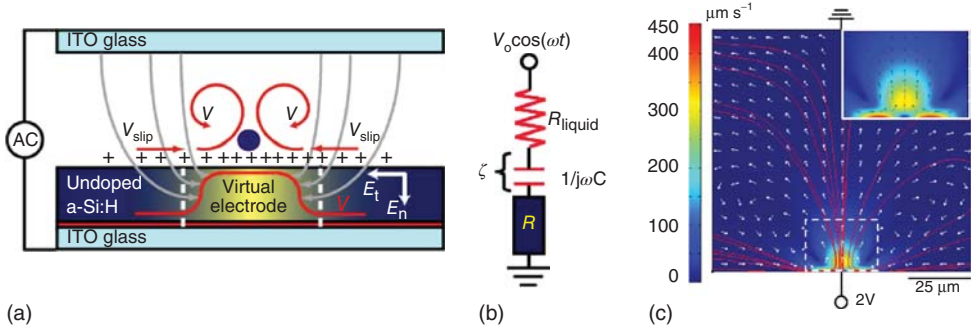
Figure 2.4 An illustration of optically induced ACEO. (a) A microvortex generated by the interactions of light-induced tangential component of electric field with the charges in EDL, which represents the situation in a half AC cycle. (b) The equivalent circuit model along an electric field line, which was used to calculate the zeta potential. (c) Optically induced ACEO flow near a virtual electrode. The highest velocity appeared on the surface at the edge of a light-induced virtual electrode [33].
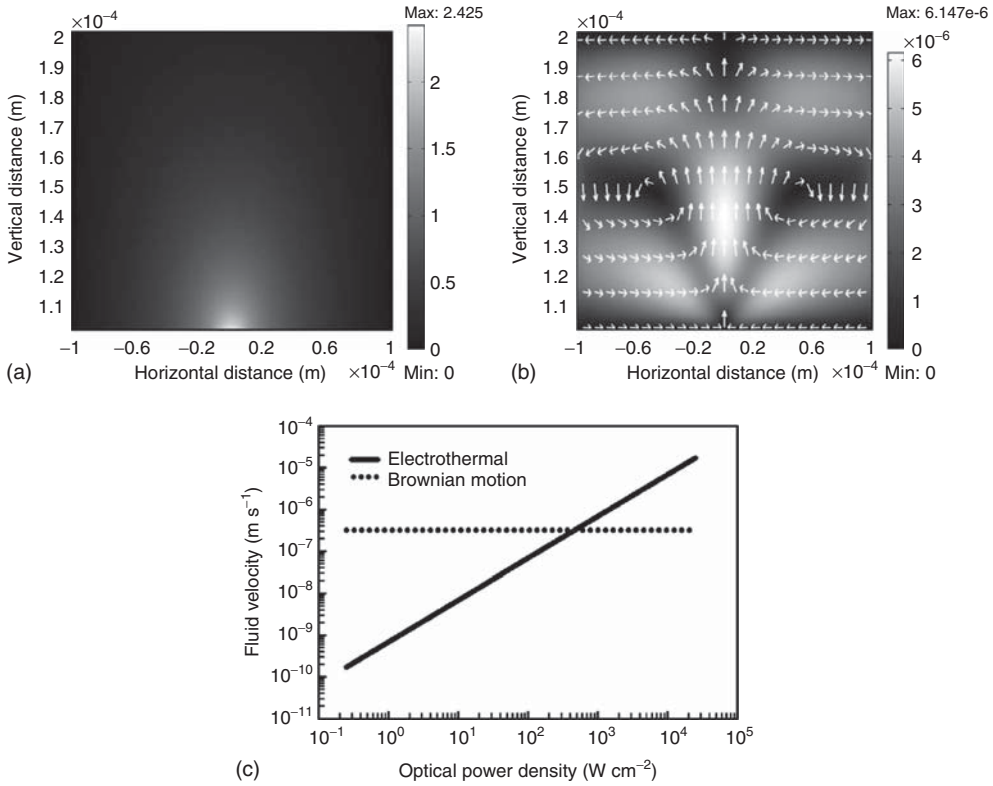
Figure 2.5 (a) Temperature increase distribution due to a 1-mW laser with a Gaussian distribution focused on a 20-µm spot size. (b) A simulation result for fluid flow due to ET effects at 20 Vpp and 100 kHz, with a light intensity of 250 W cm^{-2}. (c) The simulated dependence of ET fluid velocity on incident optical power density at 20 Vpp and 100 kHz [54].

the temperature increase in the OEK chip could set a limit for more complex biological manipulation in a large control region. In a reflective system, where the projected light for manipulation is illuminated through the objective lens of the optical microscope, a stage temperature controller can be used to control the temperature of OEK chip since it is easier to install a heat sink [63, 66]. Figure 2.5a shows the simulated temperature increase distribution in an OEK chip illuminated by a 20-µm laser beam with an intensity of 250 W cm^{-2} at 20 Vpp [54]. This simulated temperature increase is similar to the experimentally achieved results, although different chip structures, boundary conditions, light intensities, and light patterns were used [63, 66]. The simulated distribution of flow due to the ET effect and the relationship between the maximum flow velocity and light intensity are shown in Figure 2.5b,c [54]. The optically induced ET effect is dominant when light with a high intensity and large electric field is applied [54].

The most common phenomenon in OEK devices is the buoyancy effect, which arises when light pattern is projected on the photosensitive layer giving rise to
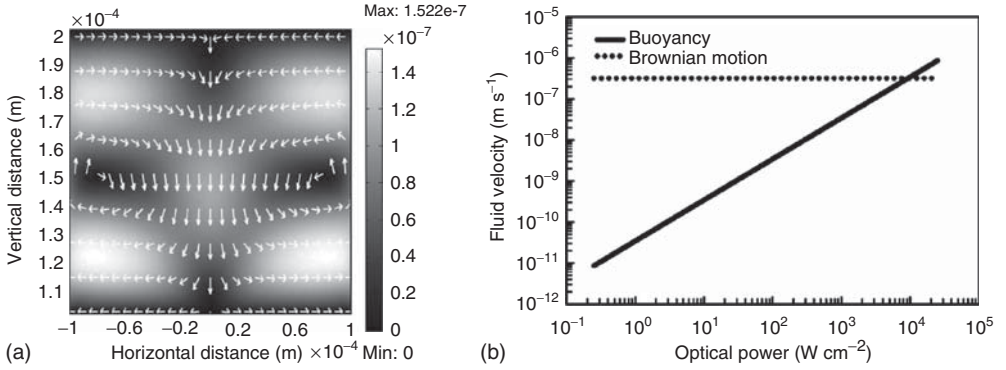
Figure 2.6 (a) A simulation result of fluid flow due to buoyancy effects at 20 Vpp and 100 kHz, with a light intensity of 250 W cm^{-2}. (b) The simulated dependence of buoyancy fluid velocity on incident optical power density at 20 Vpp and 100 kHz [54].

natural convection even in the absence of electric field. The fluid motion induced by the buoyancy effect is in a direction opposite to the ACEO and ET effect (Figure 2.6a) and is weaker than other effects (Figure 2.6b) [54].

The principle of OEK-based manipulation is shown in Figure 2.7a, which represents a modification of the mechanism of OET/ODEP [32] but is more general. All of these electrokinetic forces appear in an OEK chip, and the total force induces a movement of particles in a fluidic medium inside the chip. According to researchers, each of these electrokinetic forces can be made the dominant factor in an OEK chip by adjusting parameters of optics (wavelength and intensity), electric field (amplitude and frequency of AC voltage), and the conductivity of the medium or the chip structures.

The general operational principle as a function of optical power and frequency is shown in Figure 2.7b [67]. In operating regimes with relatively higher frequencies and lower optical powers, DEP turns out to be the dominant factor in moving particles. As the frequency decreases or optical power increases, the optically induced
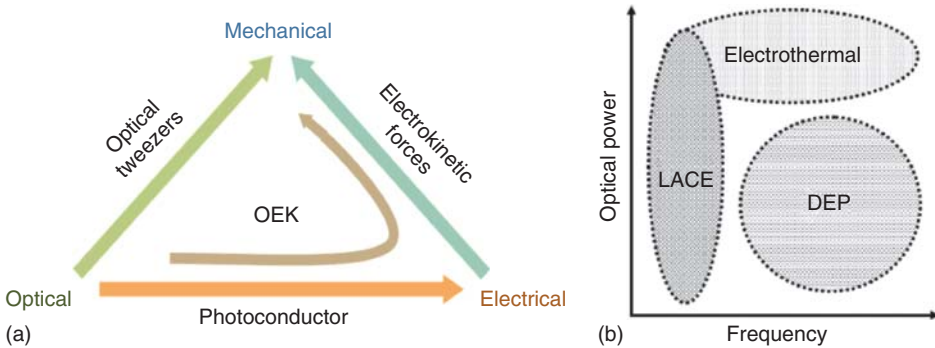
Figure 2.7 (a) Energy conversion in an OEK chip. (b) OEK operational regimes as a function of frequency and optical power [67].

ACEO or ET effect will become noticeable. In order to effectively trigger the optically induced ACEO, the optimal applied AC frequency can be estimated by [33]

$$f_{\text{opt}} = \frac{1}{2\pi} \frac{\sigma_{\text{m}}}{\varepsilon_{\text{m}}} \frac{d_{\text{DEL}}}{H} \tag{2.13}$$

where H is the liquid layer thickness and d_{DEL} can be calculated from Eq. (2.4).

Besides these externally controllable parameters, the particle size also influences the operational principle. As the size of the object decreases, the ODEP force will dramatically reduce since it scales as the cube of the radius. On the other hand, Brownian motion becomes more intense. Hence, in order to effectively control submicron particles, the electric field needs to be increased by increasing the AC amplitude or shrinking the characteristic dimensions of the device, which will enhance the ACEO effect. Owing to the enlarged electric field, the interaction of the altered properties of the medium induced by Joule heating gives rise to enhanced ET effects and even buoyancy forces. The Brownian motion will also become more intense due to the temperature increase. In addition, a strong electric field could cause electrolysis, which changes the local chemical composition and therefore imposes limitations on manipulations [33].

Another important parameter is fluid conductivity. The difference between fluid conductivity and the photo- and dark-conductivity values of a-Si:H decides the strength and distribution of the electric field in an OEK chip. Because of the limited photoconductivity of a-Si:H, this kind of OEK device can only operate in the medium with conductivity smaller than $0.1\,\text{S}\,\text{m}^{-1}$ [28]. For biological applications, however, cells need to be captured in biological media exhibiting conductivity of $1-2\,\text{S}\,\text{m}^{-1}$ to ensure cellular viability, which need to be replaced by isotonic solution with low conductivity in a-Si:H-based OEK device. To overcome this limitation, a phototransistor with photoconductivity 500 times higher than a-Si:H was introduced into OEK devices, which enabled the cell manipulation in culture media [28, 68]. The relationship between the impedances in this phototransistor-based OET is $Z_{\text{Dark}} > Z_{\text{Media}} > Z_{\text{Light}}$, where Z_{Dark} and Z_{Light} are the dark- and photo-impedance of phototransistor and Z_{Media} is the impedance of the medium [28].

This variation in device structure also provides an approach to modulate the physical fields appearing in an OEK chip. The trapping of nanoparticles was achieved by directly decreasing the distance between the two electrodes to enhance the electric field strength [69]. As shown in Figure 2.3a, the existence of a nonuniform vertical component of the electric field gives rise to an unbalanced ODEP force. This vertical force will drag objects closer to the electrode, thus inducing damage of biological samples. In order to solve this problem, a three-dimensional (3D) OEK chip consisting of two parallel photosensitive layers was designed to set up a symmetrical spatial electric field and focus the object in the middle of the liquid layer [70]. A single-sided ODEP device was also developed to enable manipulation based on a modulation of lateral electric field generated by the interdigitated electrodes patterned on a single-side substrate [61] or a floating electrode [65, 71].

2.2.2.2 Spectrum-Dependent ODEP Force

The absorption coefficient of the a-Si:H film in an OEK chip is proportional to illumination intensity [72] and increases nonlinearly with increasing incident optical frequency [73–75]. When illuminated by a different optical spectrum, the a-Si:H exhibits a different response in exciting the generated electron-hole pairs, that is, the conductivity of the a-Si:H film changes as a function of incident optical spectrum. The dependence of the a-Si:H film's photoconductivity on incident light can be expressed as [76]

$$\Delta\sigma = e\beta\alpha\mu_n\tau_n S/hf_l \qquad (2.14)$$

where e is the electron charge ($e = 1.6 \times 10^{-19}$C), β is the number of pairs of the excited electron-hole per absorbed photon ($\beta = 1$), α is the absorption coefficient of the a-Si:H, μ_n is the mobility of the electron, τ_n is the life of the electron ($\mu_n\tau_n = 10^{-7}$cm^2 V^{-1} from Ref. [77]), S is the optical power, h is the Planck's constant ($h = 6.63 \times 10^{-34}$ J·s), and f_l is the frequency of light projected onto the a-Si:H film. Hence, the ratio, α/f_l, governs the change of conductivity of the a-Si:H film with all other factors in Eq. (2.14) held constant. Substituting averaged experimental data for the absorption coefficient published by others [73–75] into Equation (2.14), the calculated results show a negative correlation between photoconductivity and wavelength (Figure 2.8) [76]. Simulation results have also shown that the relationship between ODEP force and wavelength follows the Fermi–Dirac Function, which validates the observation that the ODEP
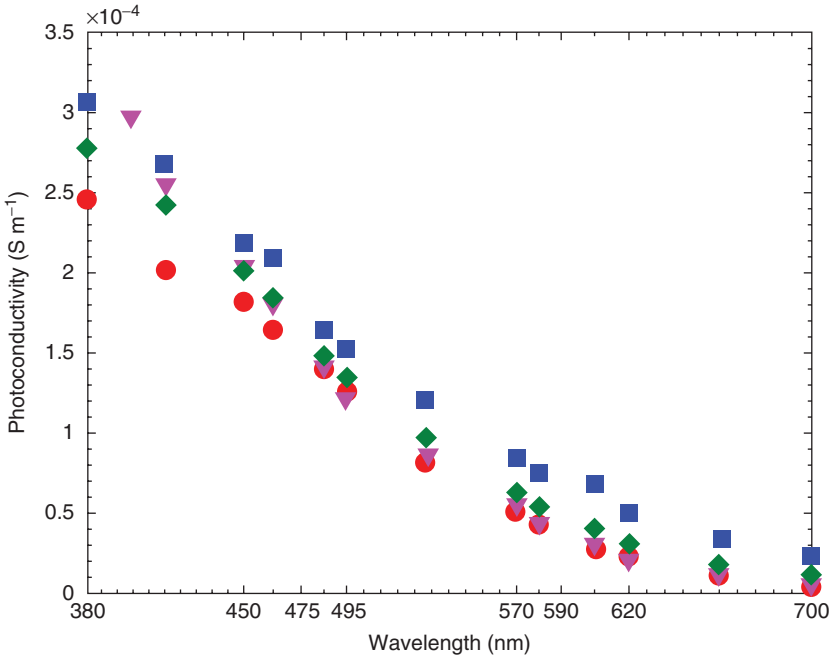
Figure 2.8 The relationship between photoconductivity of the a-Si:H and the projected light wavelength [76].

(a)

(b)

(c)
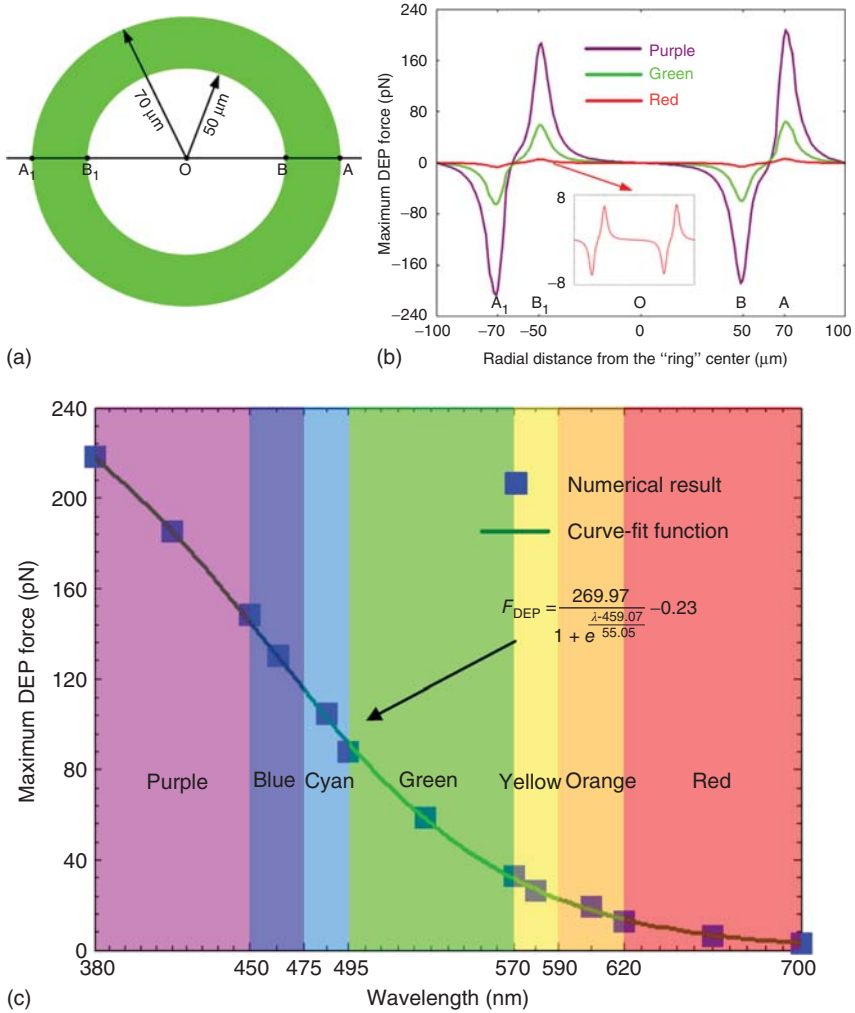
Figure 2.9 (a) The projected light pattern used in simulation. (b) The simulated maximum DEP force for a 10-μm polystyrene bead with respect to different light colors at 20 Vpp and 30 kHz, with liquid conductivity of 9×10^{-3} S m^{-1} and dark-conductivity of the a-Si:H film of 1×10^{-11} S m^{-1}. (c) The maximum DEP force acting on a 10-μm polystyrene bead at different optical wavelengths [76].

force depends strongly on the electron-hole carrier generation phenomenon in optoelectronic materials (Figure 2.9) [76]. The experimental results also confirm the spectrum dependence of ODEP force (Figure 2.10).

2.2.2.3 Waveform-Dependent ODEP Force

As reported by many research groups, an AC source with a sine function waveform is typically used to power OEK devices. Simulation and experimental results
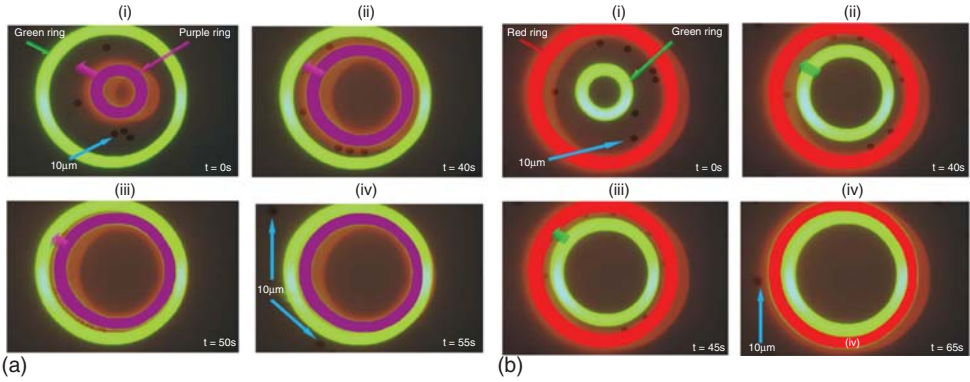
Figure 2.10 (a) Experimental results showing that the magnitude of the ODEP force induced by a purple ring is higher than that induced by a green ring. (i) A purple ring (as an inner and moving ring) and a green ring (outer and stationary ring) were projected onto the ODEP chip and no bias voltage was applied. (ii) Bias voltage was switched on (20 Vpp, 30 kHz, square wave) and the purple ring was continuously enlarged. Then, the 10-μm polystyrene beads were pushed toward the inner edge of the green ring. (iii) The beads stayed between the gap of the two rings when the gap was equal to or greater than the diameter of the beads. (a) The purple ring continues to expand and pushes the bead through the green ring. (b) Experimental results for green and red rings using the process described in (a) [76].

revealed that the waveform of applied voltage has influence on the ODEP force as shown in Figure 2.11. The square waveform can actually increase the optically induced DEP force in OEK chips. It is evident from the figure that the maximum velocities for manipulating a 10-μm bead utilizing the square wave, sine wave, and triangular wave are 260, 140, and 85 $\mu m\,s^{-1}$, respectively [76].

2.3
OEK-Based Manipulation and Assembly

2.3.1
Manipulation and Assembly of Nonbiological Materials

Two of the most attractive characteristics of OEK-based manipulation and assembly are (i) operational flexibility and (ii) the operational mechanisms are not restricted by the objects' electrical properties. Hence, OEK-based manipulation technology enables assembling dielectric, semiconducting, and metallic objects scaling from micrometer to nanometer levels in a fluidic medium using dominant electrokinetic forces such as ODEP, optically induced ACEO, or ET flow.

Ever since the first reported work on using ODEP to manipulate microscale objects in early 2000s, ODEP-based manipulation gradually extended from micro- to nanoscales. The trapping and assembly of dielectric polystyrene beads with
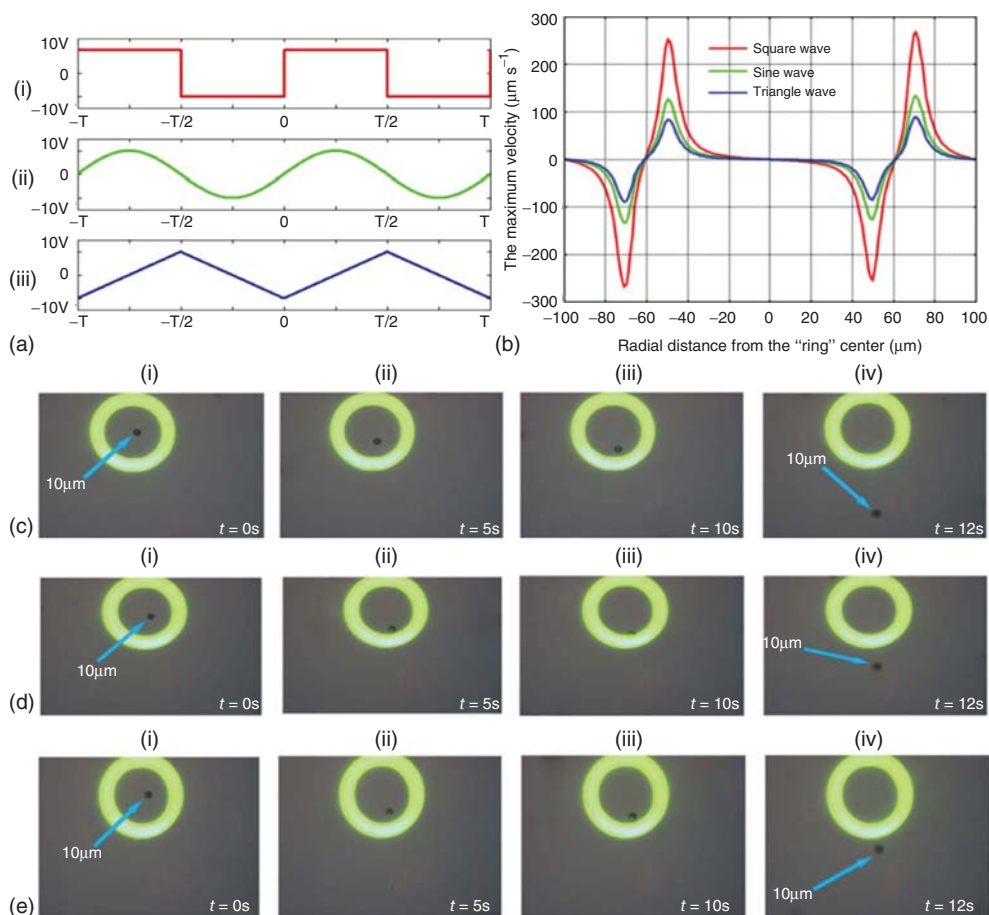
Figure 2.11 (a) Waveforms of the (i) square wave, (ii) sine wave, and (iii) triangular wave with the same Vpp of 20 V and frequency of 30 kHz. (b) The simulated maximum velocity induced by the ODEP force acting on a 10-μm polystyrene bead for different waveforms when illuminated by the green ring with size shown in Figure 2.9a. The photo- and dark-conductivity of a-Si:H is 4×10^{-5} and 1×10^{-11} S m^{-1}, respectively. The liquid conductivity is 9×10^{-3} S m^{-1} [76]. Experimental process of the ODEP manipulation of a 10-μm polystyrene bead using the square wave (c), sine wave (d), and triangular wave (e). (c) (i) No bias voltage was applied across the liquid medium. (ii) A bias voltage was applied and the stage on which the ODEP chip is placed moves at a velocity of 50 μm s^{-1}; the bead was trapped in the "ring" as it moves. (iii) The velocity of the stage increased to 250 μm s^{-1}, and the bead remains trapped. (iv) The bead lagged behind when the velocity of the stage exceeds 260 μm s^{-1}. (d) Steps (i) and (ii) are the same as those explained in (c). (iii) The velocity of the stage was increased to 135 μm s^{-1}. (iv) The bead lagged behind when the stage velocity exceeded 140 μm s^{-1}. (e) Steps (i) and (ii) are the same as those explained in (c). (iii) The stage velocity increased to 80 μm s^{-1}. (iv) The bead lagged behind when the stage velocity exceeds 85 μm s^{-1} [76].

diameters ranging from hundreds of micrometers down to submicrometers have been reported [18, 25, 27, 37, 78].

Tien *et al.* [79] reported that the assembly of anisotropic particles in an InGaAs/InGaAsP multiquantum well (MQW) microdisk laser with thickness of 200 nm and diameter of 5 or 10 μm on a Si platform by a single-side ODEP device to ensure the movement of microdisks is parallel to the device surface. The alignment accuracy estimated from the scanning electron microscopic (SEM) images taken after a-Si:H removal by XeF$_2$ etching at 40 °C is better than 0.25 μm (Figure 2.12a,b) [79].

Electrokinetic forces have also proved to be effective in manipulating nanostructures, for example, nanotubes and nanowires. Besides the ODEP force, one-dimensional nanomaterials also experience a torque aligning them with the electric field (see electric field vectors in Figure 2.3a [30, 42]). With 20 Vpp applied voltage, the maximum trapping velocity of an individual silicon nanowire with diameter of 100 nm and length of 5 μm approaches 135 μm s^{-1} [30]. Jamshidi *et al.* [30] demonstrated the possibility of separating metallic (silver) nanowires from semiconducting (silicon) nanowires based on the different polarizabilities and real-time assembly of large-scale nanowires as shown in Figure 2.12c,d. The trapping and assembly of CNTs using ODEP mechanism have also been explored [42, 80].

A common problem that arises in manipulations of zero-dimensional nanostructures is that the ODEP force is proportional to the volume of the entities and therefore drops dramatically as the size decreases (shown in Figure 2.13a). However, benefitting from the small volume, these nanoscale particles can be immersed in regions with the highest $\nabla(E_{rms})^2$, and therefore, the limitation can be overcome [69, 81]. For example, trapped by the ODEP force, 100-nm-diameter gold nanoparticles can be transported with a velocity of ∼68 μm s^{-1} at 20 Vpp and 100 kHz [69].

For manipulations based on optically induced ACEO or ET flow, the particles can be concentrated in long range by the light-patterned vortices. The velocity induced by ET flow varies with voltage to the fourth power ($u_{ET} \propto E^4 \propto V^4$), which provides an effective approach for particle collection [58, 82, 83]. In this process, the DEP force and optically induced ACEO or ET flow are responsible for collecting particles over the short and long range, respectively [84]. At the same time, the DEP forces, particle-induced ACEO, electrophoresis, and electrostatic force between particles function as immobilization factors attracting particles to substrate surface [33, 84, 85]. Real-time assembly of 15−20-nm-diameter quantum dots, 50-nm- to 6-μm-diameter polystyrene particles, 90-nm-diameter gold nanoparticles, CNTs, and silicon nanowires in large scale have been demonstrated (Figure 2.14) [33, 84, 85]. Experimental results also showed that the optimal applied AC frequency for crystalline patterning of micro- or nanobeads decreases as the bead diameter increases. The phenomenon is not influenced by the AC magnitude, which only affects the concentration time [85].

5 μm microdisk assembly
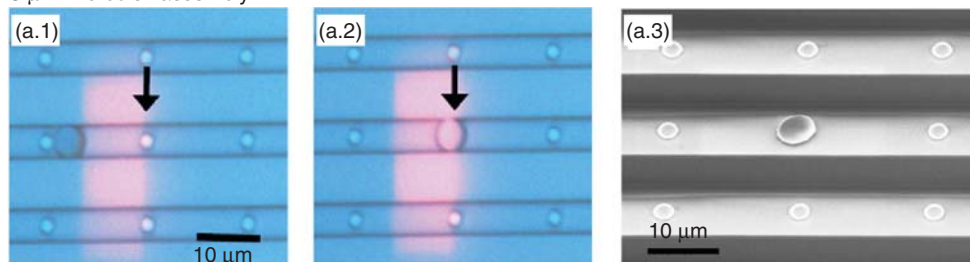
10 μm microdisk assembly
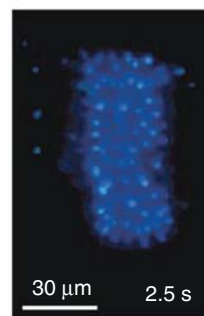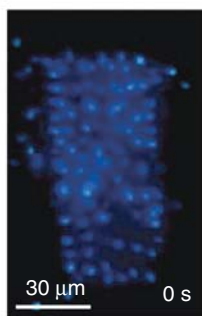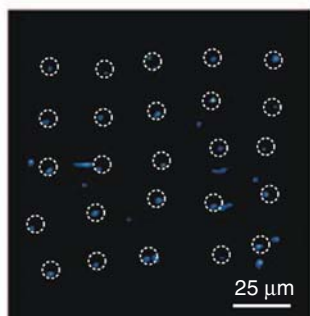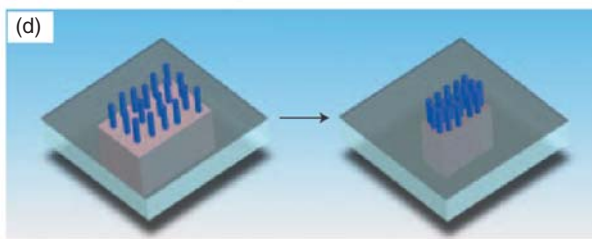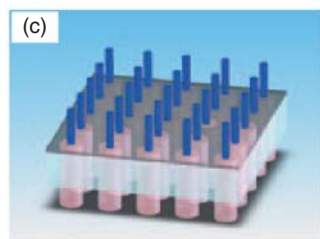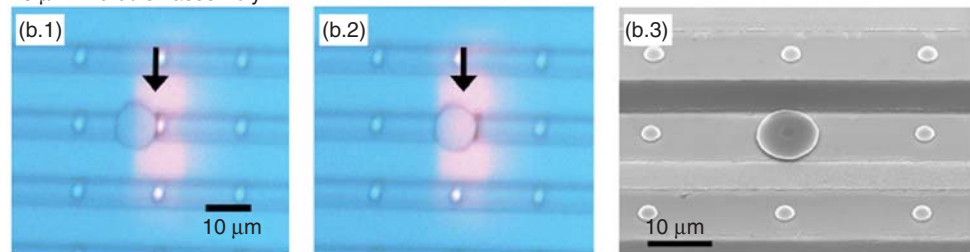
Figure 2.12 Assembly of a 5-μm-diameter III–V microdisk (a) and a 10-μm-diameter microdisk (b) onto 3-μm-diameter silicon pedestals using single-side ODEP force [79]. (c) Assembly of a 5 × 5 single silver nanowire array. (d) Control of nanowire density by adjusting the size of the trapping pattern in large area. More than 80 silver nanowires are concentrated from an area of ∼3000 to 2000 μm² [30].

(a)
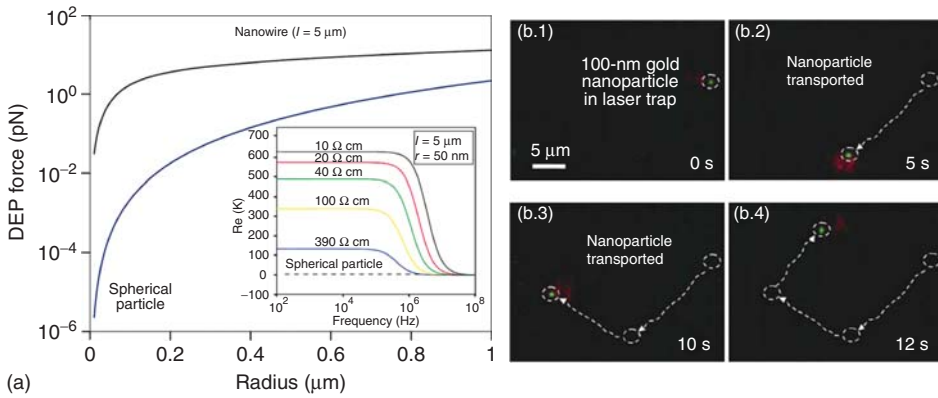
Figure 2.13 (a) Comparison of the DEP force for a 5-µm-long nanowire and a spherical bead as a function of radius. The inset shows the simulated results of Re(K^*) over a range of frequencies for different nanowire resistivities with 5-µm length and 50-nm radius [30]. (b) Trapping and transport of a single 100-nm gold nanoparticle using ODEP-based mechanism [69].
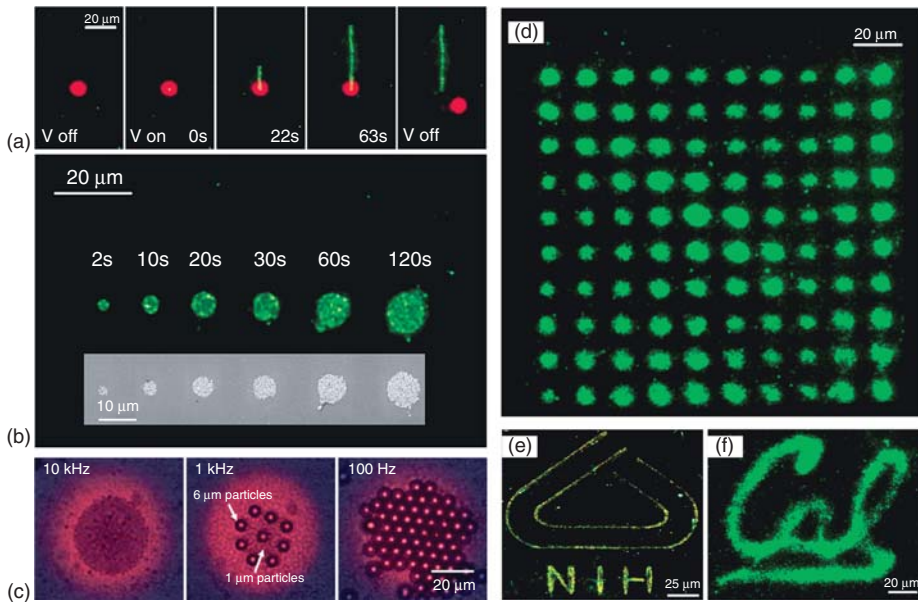
Figure 2.14 (a) Real-time patterning of gold nanoparticles with 90-nm diameter. The red spot is the light pattern and the green areas represent the patterned nanoparticles. (b) Increasing the exposure time expands the patterned area and density of particles within the illuminated region. The inset shows the SEM images associated with finally patterned structures. (c) Experimental results for the 1- and 6-µm particles concentrated in the illuminated area (red zone) at the frequency conditions of 10 kHz, 1 kHz, and 100 Hz. (d–f) Large-area patterning of 90-nm diameter gold nanoparticles in the form of a 10×10 array, over $150 \times 140 \, \mu m^2$, "NIH" logo and "CAL" logo. (Panels (a,b) and (d–f) from Ref. [84]. Panel (c) from Ref. [85].)

2.3.2
Biological Entities: Cells and Molecules

Single-cell manipulation plays an important role in stem cell studies [86], single-cell behavior investigations [87], gene therapy [88], intracytoplasmic sperm injection, and other similar biomedical science and engineering areas [10]. As discussed earlier, by combining the advantages of optical tweezers and electrode-based DEP, ODEP ensures the massively parallel manipulation of single cells [16, 18]. ODEP-based trapping and manipulation of many cell types such as HeLa cells [28, 44, 45, 89–91], red and white blood cells [38, 92–94], Jurkat cells [61], delicate human liver cells (HepG2) [29], yeast cells [95], porcine oocytes [96], protozoa [97], oral and prostate cancer cells [39, 98], fibrosarcoma cells [99], Burkitt's lymphoma cells [36], Melan-a cells [100], human sperm cells [101], *E. coli* bacteria [32], and human B cells have been demonstrated [18].

Since the magnitude and direction of DEP force are related to the objects' properties, for example, geometric shape, size, and electric properties, ODEP-based manipulation provides a flexible way for cell sorting. By using the dielectric differences between live and dead cells, which are induced by selective loss of the permeability of dead cells' membranes, Chiou *et al*. [18] demonstrated the feasibility of separating live human B cells from dead cells (Figure 2.15a). Hwang *et al*. [96] managed to differentiate normal oocytes from nutrient-starved abnormal oocytes on the basis of positive ODEP force and the reduction in friction force caused by the balance of gravity and the pulling-up component of the ODEP force (Figure 2.15b). Liang *et al*. [36] reported a rapid negative ODEP force-based method for purifying Raji cell from red blood cells using a label-free process (Figure 2.15c).

On the other hand, the optically induced torque in OEK chips has been exploited to adjust highly motile protozoan cells' moving direction [97] and induce cell self-rotation [93]. The latter method (i.e., cell self-rotation in an OEK chip) has the potential to be used to identify cell types and elucidate the electrical and physical properties of cells.

In an OEK device, the spatial distribution of the electric field can be modulated by a projected light image. In the presence of light, the partial voltage drop on liquid layer is significantly increased suggesting a relatively strong electric field, which enables selective electroporation of cells while having little influence on cells in dark areas. Valley *et al*. [45] reported the injection of propidium iodide into a HeLa cell by optically induced electroporation at an electric field strength of $1.5 \, \text{kV} \, \text{cm}^{-1}$ (Figure 2.15f). By adjusting the applied voltage and illumination power density, Lin *et al*. [39, 98] demonstrated selective cell lysis of fibroblasts and oral cancer cells.

Recently, certain cell properties studied in an OEK chip have been attracting much research attention. Neale *et al*. [92] reported on the measurement of the relative stiffness of murine erythrocytes by subjecting these cells into illuminated regions with uniform electric field and therefore no net electrical force is experienced by the cells. However, the partial electrical forces on each side of the
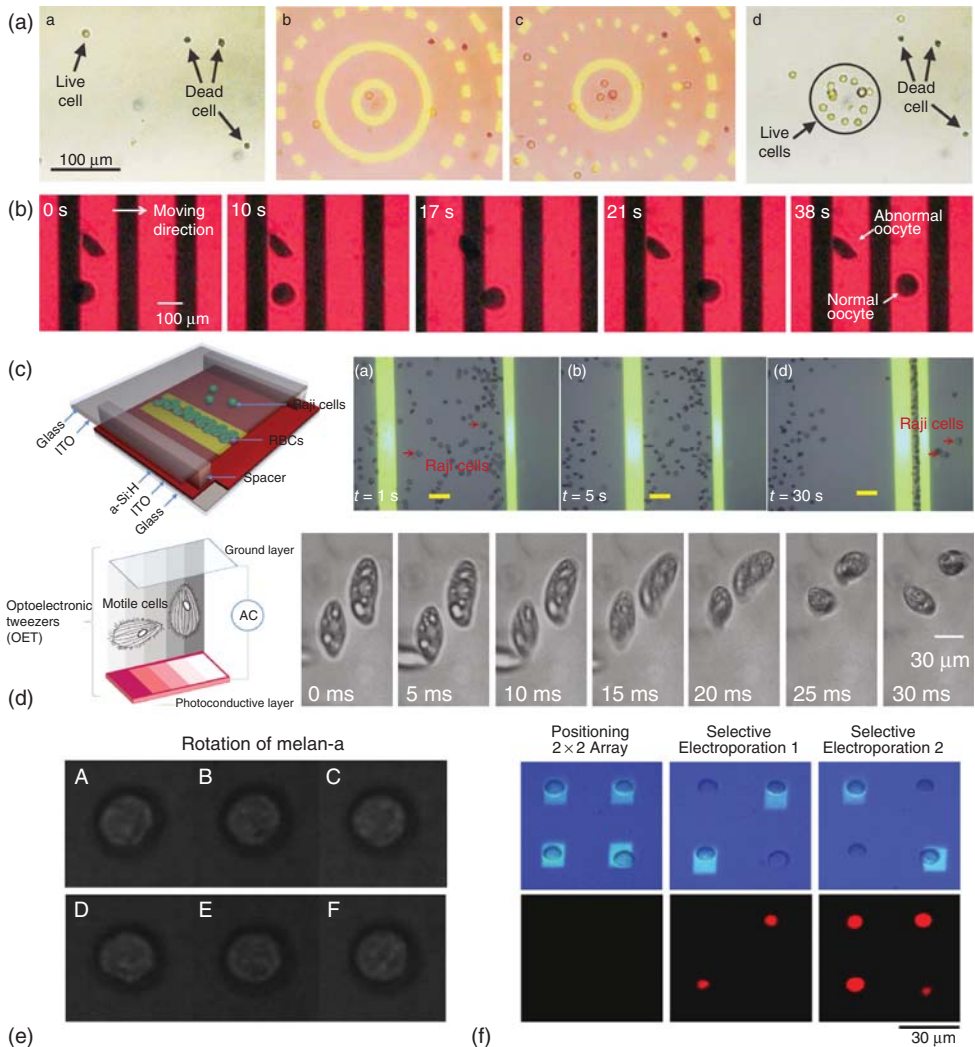
Figure 2.15 (a) Selective collection of live human B cells from a mixture of live and dead cells [18]. (b) Discrimination of normal and nutrient-starved abnormal oocytes using an optical line scanning from left to right [96]. (c) The real-time separation of Raji cells from red blood cells (RBCs) with a concentration ratio of 1 : 40. All scale bars are 25 μm [36]. (d) A typical alignment behavior of *Tetrahymena pyriformis* induced by optically induced electroorientation [97]. (e) Rotation of melan-a. Time lapse for a melan-a cell completing one revolution. Images were taken 0.155 s apart. The rotational speed was 65 rpm [93]. (f) Parallel single-cell optically induced electroporation of HeLa cells for propidium iodide injection [45].

induced dipole stretched the cells [92]. Zhao *et al.* [102] reported a technique combining sedimentation theory, computer vision, and microparticle manipulation techniques in an OEK device to selectively measure the volume, density, and mass of a single cell or the values for multiple cells with an accuracy comparable to existing methods.

Manipulations of λ-phage DNA by a positive ODEP force overcoming thermo-induced convection induced by laser illumination on a-Si:H layer have been demonstrated by Hoeb *et al.* (Figure 2.16a) [103]. By exploiting the flexibility of ODEP, Lin *et al.* [104] reported the elongation and rotation of λ-phage DNA by negative ODEP force controlling microbeads bounded indirectly at one end of DNA (Figure 2.16b,c). The stretching of a DNA molecule can also be achieved
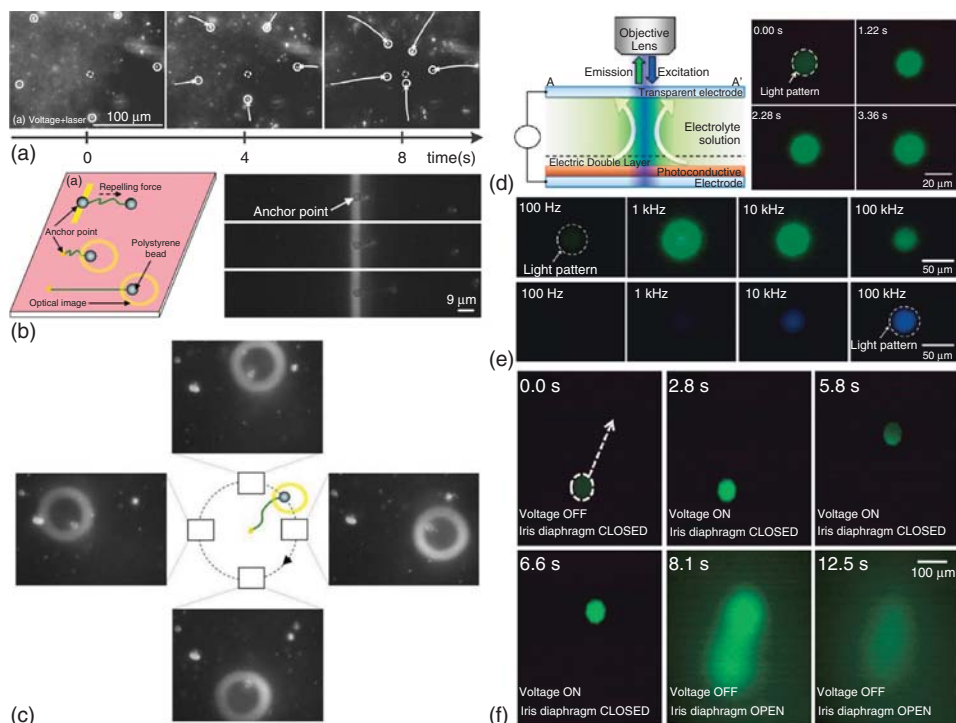
Figure 2.16 (a) Concentration of DNA toward a laser spot by ODEP force at 10 Vpp, 100 kHz, and 1.4 mW light power [103]. (b) A single DNA molecule is stretched by gradually increasing the amplitude of the applied voltage and therefore increasing the negative ODEP force [104]. (c) A bead-tethered single DNA molecule can be rotated by ODEP force [104]. (d) Time lapse images showing variations in the concentration of FITC-dextran in the illuminated region at a voltage of 10 Vpp with 1 kHz by OET mechanisms. (e) Collection of (upper) FITC-dextran and (lower) bisbenzimide against the applied AC frequencies from 100 Hz to 100 kHz. All these pictures were taken at the steady state about 3 s after the voltage was applied. (f) Spatial control of the local concentration of FITC-dextran at 10 Vpp and 1 kHz by OET mechanisms. (Panels (d–f) from Ref. [31].)

by laser-induced ET microvortex. [105] In addition, Chiou *et al*. [33] presented the concentration of λ-phage DNA based on optically induced ACEO in a large area (circle with diameter about 100 μm). Experimental results also proved that the concentration of biomolecules, such as dextran and serum albumin, can be selectively modulated by OEK mechanisms including optically induced ACEO, positive ODEP force, and electrostatic interactions through adjustments of the operational time, amplitude, and frequency of AC voltage and initial concentration (Figure 2.16d–f) [31].

During the process of manipulation by OEK principles, particles have a large possibility to suffer nonspecific adhesion on the device surface, which induces cell damage, contamination, or even loss of manipulation control. Several methods have been reported to solve this problem; two of which have been mentioned earlier, that is, using two photoconductive layers to achieve 3D focusing [70] and balancing the gravity with pulling-up ODEP force [96]. Another approach consists of modifying the OEK device with an antifouling coating. By binding bovine serum albumin to the Teflon-coated a-Si:H surface or grafting poly(ethylene glycol) to SiO_2-covered a-Si:H surface, which serve as antifouling layers, Lau *et al*. [44] demonstrated the reduction of nonspecific adherence by a factor of 30.

2.3.3
Manipulation of Fluidic Thin Films

A thin liquid film becomes unstable when destabilizing forces overcome the inherently stabilizing equilibrium forces acting on it. This leads to the growth of surface capillary waves engendered by thermal fluctuations [14, 44, 106, 107]. As instabilities propagate through film surface, structures with spatial correlation are generated to minimize system energy. In 2000, Schäffer *et al*. [14] demonstrated that an external electric field can be used to induce electrohydrodynamic (EHD) instability at the interface of polymer film and air layer, and successfully patterned the polymer film.

The polymer structures induced by homogeneous and unpatterned electrodes used in electrohydrodynamic instability (EHDI) experiments self-organize into hexagonal arrays (Figure 2.17d) [14, 108, 109] or grow randomly [110] (Figure 2.17c). The randomly generated nucleation sites limit the applicability of this process for patterning polymers over large areas [111, 112]. A common strategy for the alignment of final structures is to use topographically patterned electrodes, for example, arrays of rings [113], squares [114], rectangles, triangles [108, 110, 115], arbitrary structures [108], or large-scale alignment. However, the fabrication of topographically patterned electrodes requires a complex process that cannot be changed once started [116].

By introducing the modulation ability of light on physical fields, a method called *optically induced electrohydrodynamic instability* (OEHI) was developed by Wang *et al*. [116, 117] to control the nucleation sites appeared in the EHD instability. The basic device structure is similar to the OEK chip; however, the liquid layer is
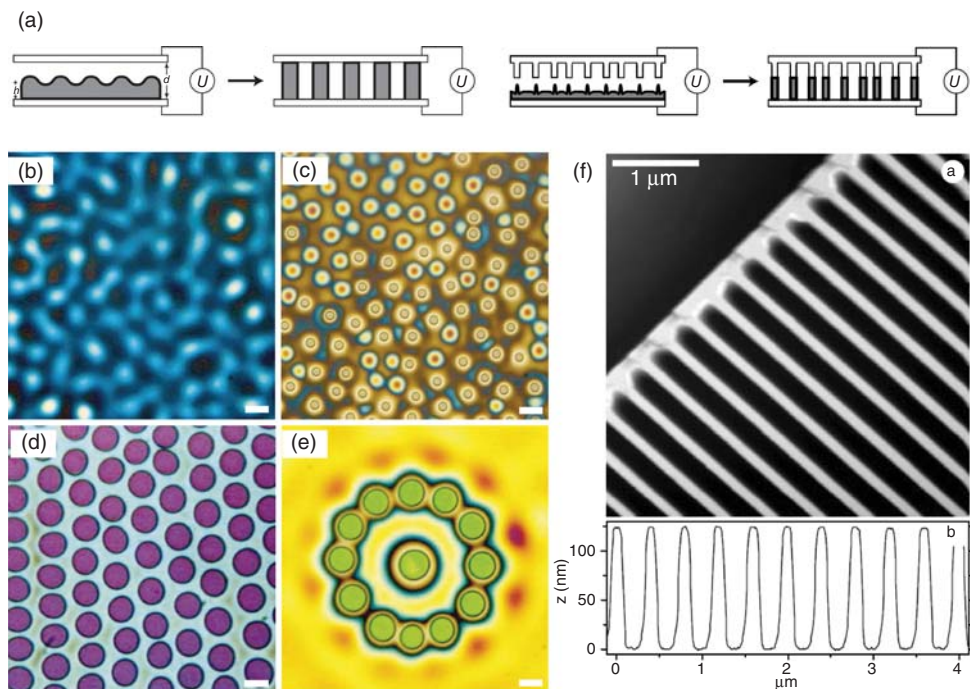
Figure 2.17 (a) Schematic representation of the capacitor device used to study EHDI triggered by external applied electric field. (b–e) Optical microscopic images of polystyrene films exposed to an electric field. (b,c) A polystyrene film with initial thickness of 93 nm was annealed for 18 h at 170 °C with an applied voltage $U = 50$ V. The interelectrode distance in (b) is larger than in (c). (d,e) Initial film thickness is 193 nm. (e) A second-order effect observed for a nucleated instability in a pattern of 12 pillars lies on a circle with a radius of 2λ. The scale bars correspond to 10 µm in (a) and (b) and to 5 µm in (c) and (d) [14].

replaced by two-phase fluidic layers, that is, a polymer layer and an air layer as shown in Figure 2.18a. During the experiment, the AC voltage is replaced by DC voltage.

In the OEHI process, the instability sites can be confined effectively by light-induced tangential stresses, including tangential electrical forces and the interfacial shear stress caused by the optically induced heterogeneous electric field and the temperature gradient, while the instability evolution is controlled by the parameters of the applied DC voltage, that is, the duration and amplitude [118]. A simulation result illustrating velocity and forces appearing in OEHI is shown in Figure 2.18g. Both the experimental results and theoretical/numerical analyses demonstrated that the EHD instability sites are nucleated firstly at the dark areas [116–118]. By adjusting the duration and electric field sufficiently to induce EHD states' transition, a multipoint "virtual dispenser" drawing femtoliter droplets with controllable size from a dielectric fluidic thin film has been reported [118]. Two droplet dispensing mechanisms, which correspond to different EHD states: Taylor
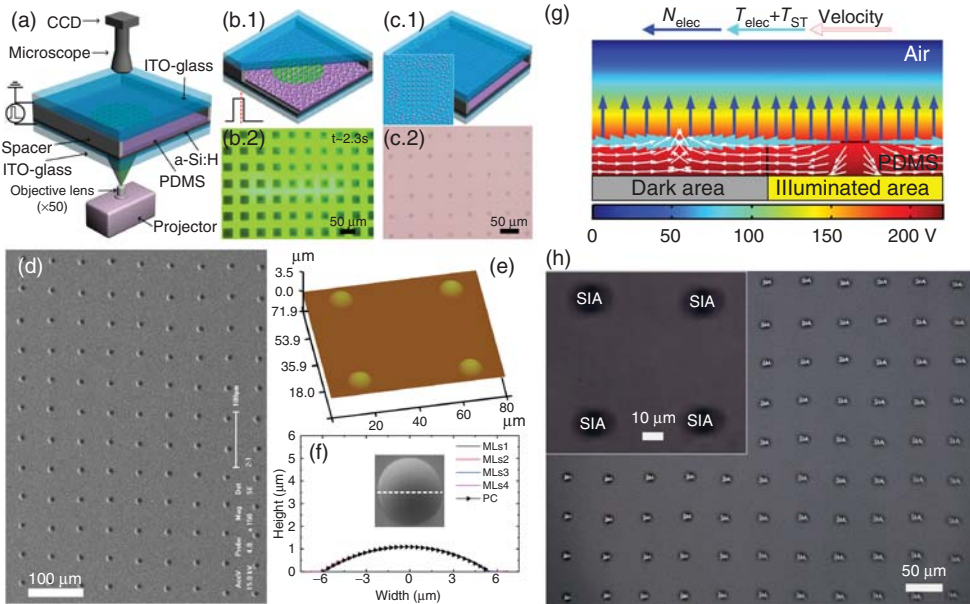
Figure 2.18 (a) A typical experimental setup and structure of the optoelectronics chip used to conduct OEHI. (b.2) is a microscope image taken within 2.3 s after the pulse voltage is applied in the pulse voltage-triggered OEHI process. (c.2) Polydimethylsiloxane (PDMS) microlens array on the upper ITO glass surface fabricated by pulse voltage-triggered OEHI. (d–f) are SEM and AFM images of microlens array shown in (c.2). (g) Simulated velocity and forces as they appear in OEHI. (h) Microscope picture showing images of the "SIA" focused by each lens in the MLA. The inset is a zoom image [118].

cone formation and optically induced EHD jet, have also been demonstrated [118]. Because of the surface tension effect, the dispensed droplets can self-organize into a spherical morphology, which can be further used as a microlens (Figure 2.18h) [118]. When the liquid bridges generated during OEHI evolution process satisfy the stability criteria, the pillar arrays are organized in an orderly manner, so an arbitrary pattern can be fabricated as shown in Figure 2.19 [116, 117].

2.4
Summary

Since the demonstration of ODEP in 2005, OEK-based technologies have attracted considerable attention and advanced from theory to experimental reality. The combination of programmable light patterns and photosensitive materials, which function as the media coupling multiphysic fields in an OEK chip, endows this technology with the capability of subjecting micro- and nanoscale wires and particles, single cells, and DNAs to massively parallel
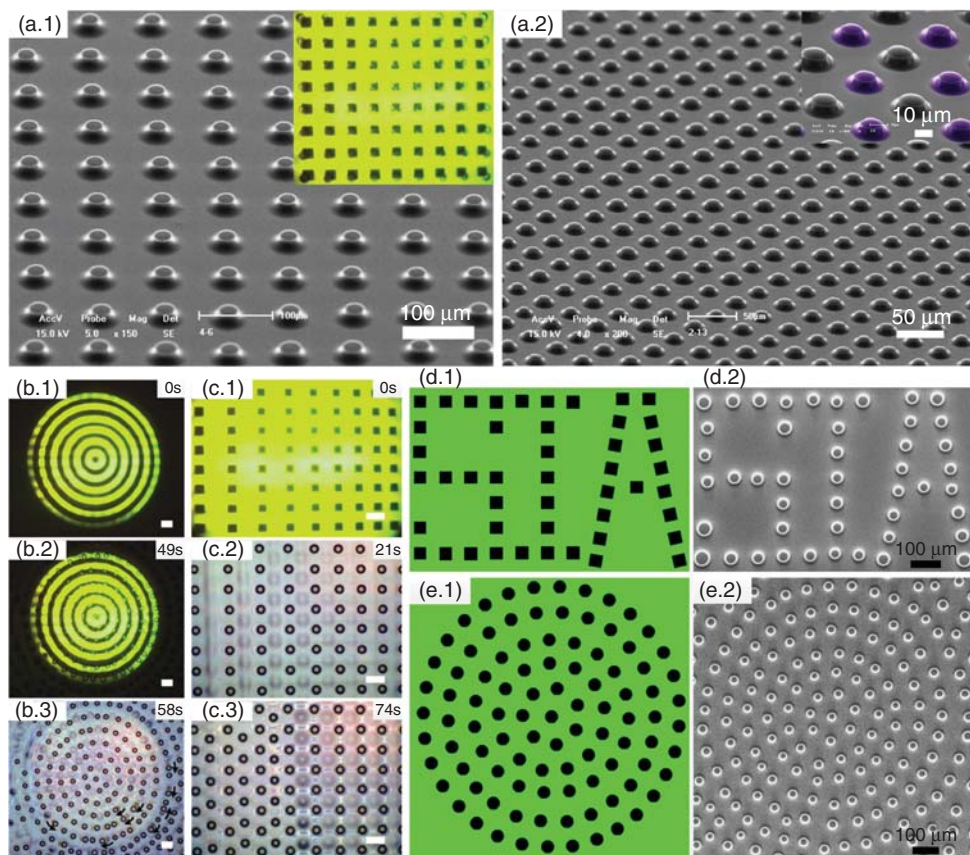
Figure 2.19 (a) Two kinds of ordered micropillar arrays fabricated by OEHI. (b) OEHI triggered by different aperiodic projected light images and pillars are organized accordingly. (Panels (a), (d), and (e) from Ref. [117]. Panels (b) and (c) from Ref. [116].)

manipulation in a real-time reconfigurable manner. This new technology has already overcame inherent technical vulnerabilities of existing methods such as optical tweezers- and metal electrodes-based DEP, and enabled researchers to study single-cell behavior, develop pharmaceutical products, and assemble sensor units in a more flexible and automated manner. This chapter has presented the theory and operational principles of OEK devices and their major applications in cell trapping, cell sorting, optically induced electroporation, cell inherent properties' study, polymer thin film, and micro- or nanoparticles' manipulation and assembly by various OEK-based mechanisms.

In addition, some other unconventional applications of OEK technology have also been reported. For example, Starovoytov *et al.* presented the possibility of light addressable electrical stimulation of cultured neurons with a similar structure to OEK device by replacing the transparent ITO electrode with a floating one [119, 120]. Suzurikawa *et al.* [34] reported the production of

microscale pH gradient in OEK chips. Wang *et al.* demonstrated the polymerization of prepolymer in an OEK device for the fabrication of poly(ethylene glycol) diacrylate (PEGDA) microstructures [121, 122]. The existence of the light-addressable temperature gradient focusing for sample preconcentration has also been proved by studying the balance of electrical forces and temperature gradients induced by laser illumination [123]. The manipulation of air bubbles in OEK device driving by thermocapillary flow has also been studied [62]. All of these applications have expanded the capabilities of OEK technologies.

However, even though these research results have pointed to many promising applications, there are still several obstacles to overcome in order for the utilization of OEK technology to become for pervasive among researchers and potentially becoming a widely accepted cell manipulation method. The following are several critical areas that require further exploration in order to advance OEK technology for more prevalent acceptance by biological researchers. (i) A systematic study of the influence of the various physical fields in an OEK chip on cellular viability should be carried out. AC electric field exposure typically used for DEP manipulation does not damage DS19 murine erythroleukemia cells and cell alterations; if they appear during the process, they can be mitigated [124]. Even though careful selection of DEP parameters could minimize the negative effect on following cell detection [125], the collaborative effects of light, AC electric field, and temperature field have not been studied. (ii) The mechanism of deposition or concentration of nanoparticles or biological macromolecules by "optically induced ACEO" is not fully understood. Much more systematic experimental and theoretical work should be investigated in this area. (iii) The enclosed environment for ODEP-based cell manipulations restricts direct scanning of cell membrane surface by cell patch clamp [126] or atomic force microscopy (AFM) [127]. The combination of an OEK device and a traditional microfluidic chip provides a possible way to solve this problem. Positive research results related to these three areas could enable OEK to become a widely used cell and DNA manipulation method in a foreseeable future.

References

1. Hertel, T., Martel, R., and Avouris, P. (1998) Manipulation of individual carbon nanotubes and their interaction with surfaces. *J. Phys. Chem. B*, **102**, 910–915.

2. Leong, T.G. *et al.* (2009) Tetherless thermobiochemically actuated microgrippers. *Proc. Natl. Acad. Sci. U.S.A.*, **106**, 703–708.

3. Waugh, R.E., Mantalaris, A., Bauserman, R.G., Hwang, W.C., and Wu, J.H.D. (2001) Membrane instability in late-stage erythropoiesis. *Blood*, **97**, 1869–1875.

4. Bausch, A.R., Moller, W., and Sackmann, E. (1999) Measurement of local viscoelasticity and forces in living cells by magnetic tweezers. *Biophys. J.*, **76**, 573–579.

5. Ahmed, D. *et al.* (2013) Tunable, pulsatile chemical gradient generation via acoustically driven oscillating bubbles. *Lab Chip*, **13**, 328–331.

6. Lin, S.C.S., Mao, X.L., and Huang, T.J. (2012) Surface acoustic wave (SAW)

acoustophoresis: now and beyond. *Lab Chip*, **12**, 2766–2770.

7. Kessler, J.O. (1985) Hydrodynamic focusing of motile algal cells. *Nature*, **313**, 218–220.

8. Ashkin, A., Dziedzic, J.M., Bjorkholm, J.E., and Chu, S. (1986) Observation of a single-beam gradient force optical trap for dielectric particles. *Opt. Lett.*, **11**, 288–290.

9. Gascoyne, P.R.C. and Vykoukal, J. (2002) Particle separation by dielectrophoresis. *Electrophoresis*, **23**, 1973–1983.

10. Desai, J.P., Pillarisetti, A., and Brooks, A.D. (2007) Engineering approaches to biomanipulation. *Annu. Rev. Biomed. Eng.*, **9**, 35–53(Annual Reviews).

11. Hughes, M.P. (2002) Strategies for dielectrophoretic separation in laboratory-on-a-chip systems. *Electrophoresis*, **23**, 2569–2582.

12. Kuiper, S. and Hendriks, B.H.W. (2004) Variable-focus liquid lens for miniature cameras. *Appl. Phys. Lett.*, **85**, 1128.

13. Pollack, M.G., Shenderov, A.D., and Fair, R.B. (2002) Electrowetting-based actuation of droplets for integrated microfluidics. *Lab Chip*, **2**, 96–101.

14. Schäffer, E., Thurn-Albrecht, T., Russell, T.P., and Steiner, U. (2000) Electrically induced structure formation and pattern transfer. *Nature*, **403**, 874–877.

15. Manaresi, N. *et al.* (2003) A CMOS chip for individual cell manipulation and detection. *IEEE J. Solid-State Circuits*, **38**, 2297–2305.

16. Wu, M.C. (2011) Optoelectronic tweezers. *Nat. Photonics*, **5**, 322–324.

17. Neuman, K.C. and Nagy, A. (2008) Single-molecule force spectroscopy: optical tweezers, magnetic tweezers and atomic force microscopy. *Nat. Methods*, **5**, 491–505.

18. Chiou, P.Y., Ohta, A.T., and Wu, M.C. (2005) Massively parallel manipulation of single cells and microparticles using optical images. *Nature*, **436**, 370–372.

19. Kumar, A., Williams, S.J., Chuang, H.S., Green, N.G., and Wereley, S.T. (2011) Hybrid opto-electric manipulation in microfluidics-opportunities and challenges. *Lab Chip*, **11**, 2135–2148.

20. Mizuno, A., Nishioka, M., Ohno, Y., and Dascalescu, L. (1993) Liquid microvortex generated around laser focal point in an intense high-frequency electric-field. *IEEE Trans. Ind. Appl.*, **3**, 1774–1778

21. Nakano, M., Kurita, H., Komatsu, J., Mizuno, A., and Katsura, S. (2006) Stretching of long DNA molecules in the microvortex induced by laser and ac electric field. *Appl. Phys. Lett.*, **89**, 133901–133903.

22. Hayward, R.C., Saville, D.A., and Aksay, I.A. (2000) Electrophoretic assembly of colloidal crystals with optically tunable micropatterns. *Nature*, **404**, 56–59.

23. Gong, T.Y. and Marr, D.W.M. (2004) Photon-directed colloidal crystallization. *Appl. Phys. Lett.*, **85**, 3760–3762.

24. Ozkan, M., Bhatia, S., and Esener, S.C. (2002) Optical addressing of polymer beads in microdevices. *Sens. Mater.*, **14**, 189–197.

25. Pei-Yu, C., Zehao, C., and Wu, M. C. (2003) A novel optoelectronic tweezer using light induced dielectrophoresis 2003 IEEE/LEOS International Conference on Optical MEMS, pp. 8–9.

26. Wang, W., Lin, Y.-H., Wen, T.-C., Guo, T.-F., and Lee, G.-B. (2010) Selective manipulation of microparticles using polymer-based optically induced dielectrophoretic devices. *Appl. Phys. Lett.*, **96**, 113302.

27. Wang, W. *et al.* (2009) Bulk-heterojunction polymers in optically-induced dielectrophoretic devices for the manipulation of microparticles. *Opt. Express*, **17**, 17603–17613.

28. Hsu, H.Y. *et al.* (2010) Phototransistor-based optoelectronic tweezers for dynamic cell manipulation in cell culture media. *Lab Chip*, **10**, 165–172.

29. Yang, S.-M. *et al.* (2010) Dynamic manipulation and patterning of microparticles and cells by using TiOPc-based optoelectronic dielectrophoresis. *Opt. Lett.*, **35**, 1959–1961.

30. Jamshidi, A. *et al.* (2008) Dynamic manipulation and separation of individual semiconducting and metallic nanowires. *Nat. Photonics*, **2**, 85–89.

31. Hwang, H. and Park, J.K. (2009) Dynamic light-activated control of local chemical concentration in a fluid. *Ann. Chem.*, **81**, 5865–5870.

32. Chiou, P.Y., Wong, W., Liao, J.C., and Wu, M.C. (2004) Cell addressing and trapping using novel optoelectronic tweezers. Proceeding of the IEEE Micro Electronics, pp. 21–24.

33. Chiou, P.Y., Ohta, A.T., Jamshidi, A., Hsu, H.Y., and Wu, M.C. (2008) Light-actuated ac electroosmosis for nanoparticle manipulation. *J. Microelectromech. Syst.*, **17**, 525–531.

34. Suzurikawa, J., Nakao, M., Kanzaki, R., and Takahashi, H. (2010) Microscale pH gradient generation by electrolysis on a light-addressable planar electrode. *Sens. Actuators, B*, **149**, 205–211.

35. Lu, Y.S., Huang, Y.P., Yeh, J.A., Lee, C., and Chang, Y.H. (2005) Controllability of non-contact cell manipulation by image dielectrophoresis (iDEP). *Opt. Quantum Electron.*, **37**, 1385–1395.

36. Liang, W. *et al.* (2014) Rapid and label-free separation of Burkitt's lymphoma cells from red blood cells by optically-induced electrokinetics. *PLoS One*, **9**, e90827.

37. Choi, W., Kim, S.H., Jang, J., and Park, J.K. (2007) Lab-on-a-display: a new microparticle manipulation platform using a liquid crystal display (LCD). *Microfluid. Nanofluid.*, **3**, 217–225.

38. Hwang, H. *et al.* (2008) Interactive manipulation of blood cells using a lens-integrated liquid crystal display based optoelectronic tweezers system. *Electrophoresis*, **29**, 1203–1212.

39. Lin, Y.H. and Lee, G.B. (2010) An integrated cell counting and continuous cell lysis device using an optically induced electric field. *Sens. Actuators, B*, **145**, 854–860.

40. Lin, Y.H. and Lee, G.B. (2008) Optically induced flow cytometry for continuous microparticle counting and sorting. *Biosens. Bioelectron.*, **24**, 572–578.

41. Lin, Y.H., Chang, C.M., and Lee, G.B. (2009) Manipulation of single DNA molecules by using optically projected images. *Opt. Express*, **17**, 15318–15329.

42. Pauzauskie, P.J., Jamshidi, A., Valley, J.K., Satcher, J.H., and Wu, M.C. (2009) Parallel trapping of multiwalled carbon nanotubes with optoelectronic tweezers. *Appl. Phys. Lett.*, **95**, 113104.

43. Lee, M.W., Lin, Y.H., and Lee, G.B. (2010) Manipulation and patterning of carbon nanotubes utilizing optically induced dielectrophoretic forces. *Microfluid. Nanofluid.*, **8**, 609–617.

44. Lau, A.N.K. *et al.* (2009) Antifouling coatings for optoelectronic tweezers. *Lab Chip*, **9**, 2952–2957.

45. Valley, J.K. *et al.* (2009) Parallel single-cell light-induced electroporation and dielectrophoretic manipulation. *Lab Chip*, **9**, 1714–1720.

46. Hung, S.H., Lin, Y.H., and Lee, G.B. (2010) A microfluidic platform for manipulation and separation of oil-in-water emulsion droplets using optically induced dielectrophoresis. *J. Micromech. Microeng.*, **20**, 045026.

47. Wang, X.B., Hughes, M.P., Huang, Y., Becker, F.F., and Gascoyne, P.R.C. (1995) Non-uniform spatial distributions of both the magnitude and phase of AC electric fields determine dielectrophoretic forces. *Biochim. Biophys. Acta, Gen. Subj.*, **1243**, 185–194.

48. Pethig, R., Talary, M.S., and Lee, R.S. (2003) Enhancing traveling-wave dielectrophoresis with signal superposition. *IEEE Eng. Med. Biol.*, **22**, 43–50.

49. Jones, T.B. and Jones, T.B. (2005) *Electromechanics of Particles*, Cambridge University Press.

50. Gascoyne, P.R.C., Wang, X.B., Huang, Y., and Becker, F.F. (1997) Dielectrophoretic separation of cancer cells from blood. *IEEE Trans. Ind. Appl.*, **33**, 670–678.

51. Kirby, B.J. (2010) *Micro-and Nanoscale Fluid Mechanics: Transport in Microfluidic Devices*, Cambridge University Press.

52. Park, H.M. and Lee, W.M. (2008) Helmholtz-Smoluchowski velocity for viscoelastic electroosmotic flows. *J. Colloid Interface Sci.*, **317**, 631–636.

53. Ramos, A., Morgan, H., Green, N.G., and Castellanos, A. (1999) AC electric-field-induced fluid flow in microelectrodes. *J. Colloid Interface Sci.*, **217**, 420–422.

54. Valley, J.K., Jamshidi, A., Ohta, A.T., Hsu, H.Y., and Wu, M.C. (2008) Operational regimes and physics present in optoelectronic tweezers. *J. Microelectromech. Syst.*, **17**, 342–350.

55. Chiou, P.-Y. (2005) *Massively Parallel Optical Manipulation of Single Cells, Micro-and Nano-Particles on Optoelectronic Devices*, University of California.

56. Green, N.G., Ramos, A., Gonzalez, A., Castellanos, A., and Morgan, H. (2001) Electrothermally induced fluid flow on microelectrodes. *J. Electrostat.*, **53**, 71–87.

57. Castellanos, A., Ramos, A., Gonzalez, A., Green, N.G., and Morgan, H. (2003) Electrohydrodynamics and dielectrophoresis in microsystems: scaling laws. *J. Phys. D: Appl. Phys.*, **36**, 2584–2597.

58. Ramos, A., Morgan, H., Green, N.G., and Castellanos, A. (1998) AC electrokinetics: a review of forces in microelectrode structures. *J. Phys. D: Appl. Phys.*, **31**, 2338–2353.

59. Einstein, A. (1956) *Investigations on the Theory of the Brownian Movement*, Courier Dover Publications.

60. Zheng, L.F., Li, S.D., Brody, J.P., and Burke, P.J. (2004) Manipulating nanoparticles in solution with electrically contacted nanotubes using dielectrophoresis. *Langmuir*, **20**, 8612–8619.

61. Ohta, A.T. *et al.* (2007) Optically controlled cell discrimination and trapping using optoelectronic tweezers. *IEEE J. Sel. Top. Quantum Electron.*, **13**, 235–243.

62. Hu, W.Q., Ishii, K.S., and Ohta, A.T. (2011) Micro-assembly using optically controlled bubble microrobots. *Appl. Phys. Lett.*, **99**, 094103.

63. Douglass, M.R. *et al.* (2010) Quantifying heat transfer in DMD-based optoelectronic tweezers with infrared thermography. *Proc. SPIE*, **7596**, 759609–759609-8.

64. Jaeger, M.S., Mueller, T., and Schnelle, T. (2007) Thermometry in dielectrophoresis chips for contact-free cell handling. *J. Phys. D: Appl. Phys.*, **40**, 95–105.

65. Park, S.Y., Kalim, S., Callahan, C., Teitell, M.A., and Chiou, E.P. (2009) A light-induced dielectrophoretic droplet manipulation platform. *Lab Chip*, **9**, 3228–3235.

66. Hsan-yin, H. *et al.* (2010) Thermo-sensitive microgels as in-situ sensor for temperature measurement in optoelectronic tweezers. 23rd IEEE International Conference on Micro Electro Mechanical Systems (MEMS 2010), pp. 1123–1126.

67. Jamshidi, A. *et al.* (2008) Optofluidics and optoelectronic tweezers. *Proc. SPIE*, **6993**, 69930A.

68. Hsu, H. *et al.* (2011) Micro Electro Mechanical Systems (MEMS). 24th International Conference on IEEE 2011, pp. 63–66.

69. Jamshidi, A. *et al.* (2009) Metallic nanoparticle manipulation using optoelectronic tweezers. 2009 IEEE 22nd International Conference on Micro Electro Mechanical Systems. MEMS 2009, pp. 579–582.

70. Hwang, H. *et al.* (2008) Reduction of nonspecific surface-particle interactions in optoelectronic tweezers. *Appl. Phys. Lett.*, **92**, 151101.

71. Park, S. *et al.* (2008) Floating electrode optoelectronic tweezers: Light-driven dielectrophoretic droplet manipulation in electrically insulating oil medium. *Appl. Phys. Lett.*, **92**, 151101–1511013.

72. Stutzmann, M., Jackson, W.B., and Tsai, C.C. (1985) Light-induced metastable defects in hydrogenated amorphous-silicon – a systematic study. *Phys. Rev. B*, **32**, 23–47.

73. Carlson, D.E. and Wronski, C.R. (1976) Amorphous silicon solar-cell. *Appl. Phys. Lett.*, **28**, 671–673.

74. Hishikawa, Y. *et al.* (1991) Interference-free determination of the optical-absorption coefficient and the optical gap of amorphous-silicon thin-films. *Jpn. J. Appl. Phys., Part 1-Regul. Pap. Short Notes Rev. Pap.*, **30**, 1008–1014.

75. Adachi, S. (1999) *Optical Properties of Crystalline and Amorphous Semiconductors: Materials and Fundamental Principles*, Kluwer Academic Publishers, Boston, MA, pp. 207–208.

76. Liang, W., Wang, S., Dong, Z., Lee, G.-B., and Li, W.J. (2012) Optical spectrum and electric field waveform dependent Optically-Induced Dielectrophoretic (ODEP) micromanipulation. *Micromachines*, **3**, 492–508.

77. Okamoto, H., Kida, H., Nonomura, S., Fukumoto, K., and Hamakawa, Y. (1983) Mobility-lifetime product and interface property in amorphous-silicon solar-cells. *J. Appl. Phys.*, **54**, 3236–3243.

78. Liang, W. *et al.* (2013) Simultaneous separation and concentration of micro- and nano-particles by optically induced electrokinetics. *Sens. Actuators, A*, **193**, 103–111.

79. Tien, M.-C., Ohta, A.T., Yu, K., Neale, S.L., and Wu, M.C. (2009) Heterogeneous integration of InGaAsP microdisk laser on a silicon platform using optofluidic assembly. *Appl. Phys. A-Mater. Sci. Process.*, **95**, 967–972.

80. Lee, M.-W., Lin, Y.-H., and Lee, G.-B. (2010) Manipulation and patterning of carbon nanotubes utilizing optically induced dielectrophoretic forces. *Microfluid. Nanofluid.*, **8**, 609–617.

81. Carrara, S. and De Micheli, G. (2011) *Nano-Bio-Sensing*, Springer.

82. Wu, J., Lian, M., and Yang, K. (2007) Micropumping of biofluids by alternating current electrothermal effects. *Appl. Phys. Lett.*, **90**, 234103.

83. Sigurdson, M., Wang, D.Z., and Meinhart, C.D. (2005) Electrothermal stirring for heterogeneous immunoassays. *Lab Chip*, **5**, 1366–1373.

84. Jamshidi, A. *et al.* (2009) NanoPen: dynamic, low-power, and light-actuated patterning of nanoparticles. *Nano Lett.*, **9**, 2921–2925.

85. Hwang, H. and Park, J.K. (2009) Rapid and selective concentration of microparticles in an optoelectrofluidic platform. *Lab Chip*, **9**, 199–206.

86. Scudellari, M. (2009) A closer look at the single cell. *Nat. Rep. Stem Cells.* http://www.nature.com/stemcells/2009/0905/090507/full/stemcells.2009.71.html

87. Puliafito, A. *et al.* (2012) Collective and single cell behavior in epithelial contact inhibition. *Proc. Natl. Acad. Sci. U.S.A.*, **109**, 739–744.

88. Yates, F. and Daley, G.Q. (2006) Progress and prospects: gene transfer into embryonic stem cells. *Gene Ther.*, **13**, 1431–1439.

89. Neale, S.L. *et al.* (2009) Trap profiles of projector based optoelectronic tweezers (OET) with HeLa cells. *Opt. Express*, **17**, 5232–5239.

90. Valley, J.K., Shao, N.P., Jamshidi, A., Hsu, H.Y., and Wu, M.C. (2011) A unified platform for optoelectrowetting and optoelectronic tweezers. *Lab Chip*, **11**, 1292–1297.

91. Huang, K.W., Su, T.W., Ozcan, A., and Chiou, P.Y. (2013) Optoelectronic tweezers integrated with lensfree holographic microscopy for wide-field interactive cell and particle manipulation on a chip. *Lab Chip*, **13**, 2278–2284.

92. Neale, S. L., Mody, N., Selman, C. & Cooper, J. M. Optoelectronic tweezers for the measurement of the relative stiffness of erythrocytes. *Proc. SPIE* (Optical Trapping and Optical Micro-manipulation IX) **8458** (2012) 845827.

93. Chau, L.H. *et al.* (2013) Self-rotation of cells in an irrotational AC e-field in an opto-electrokinetics chip. *PLoS One*, **8**, e51577.

94. Zhao, Y. *et al.* (2013) Distinguishing cells by their first-order transient motion response under an optically induced dielectrophoretic force field. *Appl. Phys. Lett.*, **103**, 183702 (183704 pp.).

95. Yen-Sheng, L., Yuan-Peng, H., Yeh, J.A., Chengkuo, L., and Yu-Hua, C. (2005) Controllability of non-contact cell manipulation by image dielectrophoresis (iDEP). *Opt. Quantum Electron.*, **37**, 1385–1395.

96. Hwang, H., Lee, D.H., Choi, W.J., and Park, J.K. (2009) Enhanced discrimination of normal oocytes using optically induced pulling-up dielectrophoretic force. *Biomicrofluidics*, **3**, 014103.

97. Choi, W., Nam, S.W., Hwang, H., Park, S., and Park, J.K. (2008) Programmable manipulation of motile cells in optoelectronic tweezers using a grayscale image. *Appl. Phys. Lett.*, **93**, 143901.

98. Lin, Y.H. and Lee, G.B. (2009) An optically induced cell lysis device using dielectrophoresis. *Appl. Phys. Lett.*, **94**, 033901.

99. Grad, M., Bigelow, A.W., Garty, G., Attinger, D., and Brenner, D.J. (2013) Optofluidic cell manipulation for a biological microbeam. *Rev. Sci. Instrum.*, **84**, 014301.

100. Chau, L. H. *et al.* (2012) Inducing self-rotation of Melan-a cells by ODEP. 2012 7th IEEE International Conference on Nano/Micro Engineered and Molecular Systems (NEMS), pp. 195–199.

101. Ohta, A.T. *et al.* (2010) Motile and non-motile sperm diagnostic manipulation using optoelectronic tweezers. *Lab Chip*, **10**, 3213–3217.

102. Zhao, Y., Lai, H.S.S., Zhang, G., Lee, G.-B., and Li, W.J. (2014) Rapid determination of cell mass and density using digitally-controlled electric field in a microfluidic chip. *Lab Chip*, **14**, 4426–4434.

103. Hoeb, M., Rädler, J.O., Klein, S., Stutzmann, M., and Brandt, M.S. (2007) Light-induced dielectrophoretic manipulation of DNA. *Biophys. J.*, **93**, 1032–1038.

104. Lin, Y.-H., Chang, C.-M., and Lee, G.-B. (2009) Manipulation of single DNA molecules by using optically projected images. *Opt. Express*, **17**, 15318–15329.

105. Nakano, M., Kurita, H., Komatsu, J., Mizuno, A., and Katsura, S. (2006) Stretching of long DNA molecules in the microvortex induced by laser and ac electric field. *Appl. Phys. Lett.*, **89**, 133901–133901-133903.

106. Reiter, G. (1992) Dewetting of thin polymer-films. *Phys. Rev. Lett.*, **68**, 75–78.

107. Schaffer, E., Harkema, S., Roerdink, M., Blossey, R., and Steiner, U. (2003) Thermomechanical lithography: pattern replication using a temperature gradient driven instability. *Adv. Mater.*, **15**, 514–517.

108. Chou, S.Y. and Zhuang, L. (1999) Lithographically induced self-assembly of periodic polymer micropillar arrays. *J. Vac. Sci. Technol., B*, **17**, 3197–3202.

109. Lin, Z.Q., Kerle, T., Russell, T.P., Schaffer, E., and Steiner, U. (2002) Structure formation at the interface of liquid/liquid bilayer in electric field. *Macromolecules*, **35**, 3971–3976.

110. Wu, N. and Russel, W.B. (2009) Micro- and nano-patterns created via electro-hydrodynamic instabilities. *Nano Today*, **4**, 180–192.

111. Lei, X.Y. *et al.* (2003) 100 nm period gratings produced by lithographically induced self-construction. *Nanotechnology*, **14**, 786–790.

112. Wu, N., Pease, L.F., and Russel, W.B. (2006) Toward large-scale alignment of electrohydrodynamic patterning of thin polymer films. *Adv. Funct. Mater.*, **16**, 1992–1999.

113. Deshpande, P., Pease, L.F., Chen, L., Chou, S.Y., and Russel, W.B. (2004) Cylindrically symmetric electrohydrodynamic patterning. *Phys. Rev. E*, **70**, 041601.

114. Deshpande, P., Sun, X.Y., and Chou, S.Y. (2001) Observation of dynamic behavior of lithographically induced self-assembly of supramolecular periodic pillar arrays in a homopolymer film. *Appl. Phys. Lett.*, **79**, 1688–1690.

115. Lei, C., Lei, Z., Deshpande, P., and Chou, S. (2005) Novel polymer patterns formed by lithographically induced self-assembly (LISA). *Langmuir*, **21**, 818–821.

116. Wang, F. *et al.* (2014) Optically induced electrohydrodynamic instability-based micro-patterning of fluidic thin films. *Microfluid. Nanofluid.*, **16**, 1097–1106.

117. Wang, F. *et al.* (2013) Non-ultraviolet-based patterning of polymer structures by optically induced electrohydrodynamic instability. *Appl. Phys. Lett.*, **103**, 214101–214101-5.

118. Wang, F. *et al.* (2014) Exploring pulse-voltage-triggered optically-induced electrohydrodynamic instability for femtolitre droplet generation. *Appl. Phys. Lett.*, **104**, 264103.

119. Starovoytov, A., Choi, J., and Seung, H.S. (2005) Light-directed electrical stimulation of neurons cultured on silicon wafers. *J. Neurophys.*, **93**, 1090–1098.

120. Suzurikawa, J. *et al.* (2007) Light-addressable electrode with hydrogenated amorphous silicon and low-conductive passivation layer for stimulation of cultured neurons. *Appl. Phys. Lett.*, **90**, 093901.

121. Wang, S., Liang, W.F., Dong, Z.L., Lee, V.G.B., and Li, W.J. (2011) Fabrication of micrometer- and nanometer-scale polymer structures by visible light induced Dielectrophoresis (DEP) Force. *Micromachines*, **2**, 431–442.

122. Liu, N. *et al.* (2014) Extracellular-controlled breast cancer cell formation and growth using non-UV patterned hydrogels via optically-induced electrokinetics. *Lab Chip*, **14**, 1367–1376.

123. Akbari, M., Bahrami, M., and Sinton, D. (2012) Optothermal sample preconcentration and manipulation with temperature gradient focusing. *Microfluid. Nanofluid.*, **12**, 221–228.

124. 125. Wang, X.J., Yang, J., and Gascoyne, P.R.C. (1999) Role of peroxide in AC electrical field exposure effects on Friend murine erythroleukemia cells during dielectrophoretic manipulations. *Biochim. Biophys. Acta, Gen. Subj.*, **1426**, 53–68.

125. Yang, L., Banada, P.P., Bhunia, A.K., and Bashir, R. (2008) Effects of dielectrophoresis on growth, viability and immuno-reactivity of Listeria monocytogenes. *J. Biol. Eng.*, **2**, 6–6.

126. Hamill, O.P., Marty, A., Neher, E., Sakmann, B., and Sigworth, F.J. (1981) Improved patch-clamp techniques for high-resolution current recording from cells and cell-free membrane patches. *Pflugers Arch.-Eur. J. Physiol.*, **391**, 85–100.

127. Li, M. *et al.* (2014) Nanoscale imaging and mechanical analysis of fc receptor-mediated macrophage phagocytosis against cancer cells. *Langmuir*, **30**, 1609–1621.

3
Manipulation of DNA by Complex Confinement Using Nanofluidic Slits

Elizabeth A. Strychalski and Samuel M. Stavis

3.1
Introduction

Nanofluidic technology for DNA manipulation is premised on the use of nanoscale confinement to control individual DNA molecules in a way that allows analysis, for example, of contour length [1, 2], topology [3, 4], sequence [5, 6], or bound proteins [7]. The importance of these analytical applications in separation science and genetic sequencing has motivated the development of new nanofluidic devices and methods. However, in the case of nanofluidic structures incorporating nanoslits, this progress has occurred without a complete understanding of the physical behavior of DNA molecules in nanoscale confinement. Lacking this knowledge, advances in nanofluidic technology for DNA manipulation and analysis have arguably followed from and been inspired by conventional benchtop analytical technologies, without a clear focus on how to best exploit DNA behavior in engineered nanofluidic confinement. Indeed, early nanofluidic technologies for DNA manipulation, such as the post array [8] and entropic trap array [2], incorporated nanoslits and may be considered as artificial gels for DNA electrophoresis.

This chapter considers the benefits of refocusing on understanding and exploiting the fundamental physical behavior of DNA molecules in nanoscale slitlike confinement. This is a topic of enduring interest in polymer science and increasing importance in nanofluidics. Looking to the past, a complete understanding of the physical behavior of confined DNA molecules is needed to optimize existing nanofluidic devices and methods for DNA analysis. Looking to the future, a better understanding of the fundamentals may shift the perspective and approach from nanofluidic analogs of benchtop analytical technologies to the rational design of more inherently nanofluidic devices and methods. In particular, this approach will inform a promising new trend in nanofluidic technology for DNA analysis in which more complex nanofluidic structures are engineered for structural control of DNA molecules.
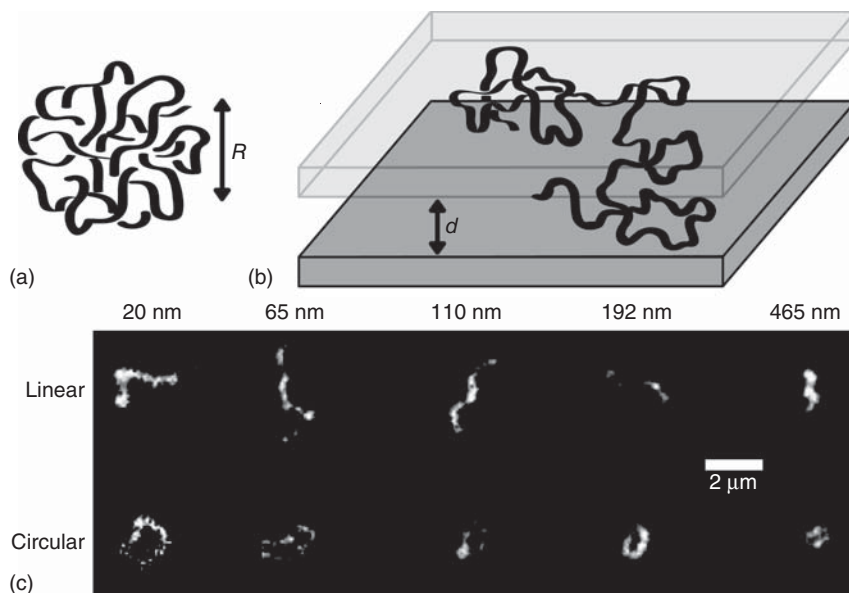
Figure 3.1 DNA molecules confined to nanoslits. (a) A DNA molecule in free solution forms a random coil with a characteristic size R. (b) The molecule is squeezed between the surfaces of a nanoslit with depth $d < R$. (c) Fluorescence images show linear and circular DNA molecules confined to nanoslits of different depths, with the confining nanoslit surfaces parallel to the page. (Panel (c) adapted with permission from Figure 1 of Lin *et al*. [9] Copyright 2012 American Chemical Society.)

There are three fundamental categories of nanofluidic confinement. This chapter focuses on the nanoslit, which results in the uniaxial, or slitlike, confinement of a DNA molecule (Figure 3.1). This seemingly simple geometrical arrangement belies the utility of nanoslits for DNA analysis [1, 2, 10–14]. These have been demonstrated despite the fact that the physical behavior of a DNA molecule confined to a nanoslit remains incompletely understood. Nanoslits tend to be the most accessible nanofluidic structures to fabricate, requiring only low-resolution photolithography and standard chemical etching processes to transfer an exposed nanoslit pattern into a device substrate to a slit depth d. From both of these fundamental and practical perspectives, a DNA molecule in nanofluidic slitlike confinement is a particularly interesting system to consider.

While a nanoslit confines a DNA molecule in one dimension only, other structures confine in additional dimensions. Progress in DNA analysis using nanochannels, which result in biaxial confinement, has been reviewed recently [15, 16]. Relative to nanoslits, nanochannels are more difficult to fabricate, requiring either high-resolution lithography or nonlithographic approaches that can complicate integration into analytical devices. Nanocavities introduce a third dimension of confinement, resulting in triaxial confinement of DNA molecules [17]. Nanocavities have not been widely implemented using top-down lithographic fabrication

techniques. Hybrid confinement schemes involving seminanochannels (the edge of a nanoslit) [18], nanoslits with embedded seminanochannels (nanotrenches) [3, 19], or seminanocavities (nanopits) are also considered in this chapter [20, 21]. Nanoslits with embedded pillars arrays constitute yet another scheme of hybrid confinement, but these structures have often been associated with batch manipulation and analysis of DNA molecules to understand DNA−gel interactions during separations [12] and are therefore not the focus on this chapter.

In the spirit of refocusing on fundamentals, the application of forces external to the nanofluidic confinement is largely neglected here. Typically, electrokinetic or hydrodynamic forces are applied at fluid reservoirs to transport DNA molecules through a nanofluidic device, and such forces will certainly be needed in many practical nanofluidic methods for DNA analysis. However, the use of such external forces adds tremendously to the physical complexity of the system, making a complete understanding of DNA behavior in a nanoslit even more challenging. Moreover, these forces add technological complexity to the design, fabrication, and operation of a nanofluidic device. To the extent that a nanofluidic structure alone can control the physical behavior of a DNA molecule for analysis, the control arises from thermodynamic, hydrodynamic, and surface interactions between the DNA molecule and the confining structure. It stands to reason that, without external forces, nanofluidic technology for DNA analysis must be based on exploiting spontaneous nanoscale phenomena, such as diffusion, conformational entropy, and surface interactions, to control the conformation and transport of a DNA molecule. This new perspective is supported by recent literature, which has demonstrated largely unexplored aspects of nanofluidic technology that exploit only the spontaneous physical behavior of DNA molecules in confining structures for DNA analysis [4, 18, 20, 22]. Moreover, the underlying physical behavior of a DNA molecule in a confining system without external forces remains relevant once external forces are reintroduced. Therefore, to develop a complete understanding of DNA behavior in nanoslits for the purpose of DNA analysis, it is appropriate to first study the simpler case.

Nanofluidic DNA analysis has generally focused on long (kilobase pairs to megabase pairs), double-stranded, B-form, DNA molecules for several reasons. First and foremost, this type of DNA molecule is of fundamental importance in the life sciences, as it encodes genetic information within cells. Therefore, such molecules are of central concern in genetic analysis, for example, in health care and forensic applications, which have provided much of the impetus for the development of nanofluidic technology for DNA analysis.

Second, this type of DNA molecule is a useful model polymer for physical analysis. This type of DNA molecule is long enough and, as a semiflexible polymer, stiff enough to be significantly confined and manipulated by typical nanofluidic structures. Depending on the contour length, which is approximately $10-100\,\mu m$ for the experimental studies considered here, the characteristic size R may extend through the nanometer length scale and into the micrometer length scale. A monovalent electrolyte buffer solution of appreciable ionic strength results in a persistence length p of approximately $50\,nm$ [23, 24]. Considering

these characteristic length scales for a DNA molecule, various regimes of slitlike confinement are technologically accessible. These regimes are traditionally described as strong [25, 26] for $d < 2p$, moderate [27, 28] for $2p < d < 2R$, and weak for $d > 2R$. A DNA molecule also has a significant electrostatic charge, as a polyelectrolyte with a bare charge density of $-2e$ per base pair, where e is the elementary charge. Electrostatic effects [18], which are ubiquitous near charged surfaces and in electrolyte solutions at the nanoscale [29], and electrokinetic effects [30, 31] may therefore be studied and exploited for nanofluidic DNA analysis.

Third, this type of DNA molecule satisfies several practical concerns of the experimentalist who seeks to study fundamental phenomena and develop new nanofluidic technology for DNA analysis. Such DNA molecules are readily available commercially with a well-defined contour length, topology, genetic sequence, and chemical modification. As a result, the related structural properties and behavior are at least reasonably well controlled, if not well understood, to test nanofluidic tools for DNA analysis. Good fluorescent dye molecules are also available commercially and usually label the DNA contour, sometimes with genetic [5, 6, 32 – 34] or epigenetic [35] specificity. This enables the analysis of limited attributes of the spatiotemporal behavior, structure, and sequence of a DNA molecule measured directly by fluorescence microscopy with high sensitivity and fidelity.

3.2
Slitlike Confinement of DNA

The confinement of a single DNA molecule to a nanoslit alters the behavior of the molecule relative to an unconfined state in free solution. A linear DNA molecule confined to a nanoslit at thermodynamic equilibrium has, for example, a different free energy, size, diffusivity, and relaxation time. Importantly, the effects of confinement cannot be understood independently of interactions, such as electrostatic, chemical, or hydrodynamic, with the confining surfaces. These interactions may strongly influence DNA behavior in ways that differ significantly from those expected from purely steric, geometric confinement. In principle, all of the changes in DNA behavior as confinement is varied may be exploited for DNA analysis. In practice, the emerging trend toward more complex nanofluidic structures based on slitlike confinement shows promise for DNA analysis.

For a DNA molecule confined to a nanoslit, the free energy of confinement F relative to the unconfined state in free solution is of fundamental importance. However, at the current state of the art, the variation of F with confinement is not understood clearly, has not been measured quantitatively, and remains a topic of ongoing investigation. Taking a simplified view of this system, as a DNA molecule is forced from free solution into slitlike confinement, the change in free energy ΔF arises in part from the difference in the entropic contribution associated with conformation. In free solution, the DNA molecule is able to sample the largest

possible physical volume by thermal fluctuations in conformation. Therefore, the DNA molecule has the most conformational microstates available to it, the most conformational entropy, and the least conformational entropic free energy. In a confining nanoslit, the physical volume that the DNA molecule is able to sample by thermal fluctuations is decreased (Figure 3.1a). Therefore, the DNA molecule has fewer conformational microstates available to it, less conformational entropy, and more conformational entropic free energy. Because of the finite width w and electrostatic interactions of the DNA contour [36], excluded volume interactions further reduce the number of conformational microstates available to a DNA molecule, increasing F. While excluded volume interactions are expected qualitatively to increase with confinement [37−39], the quantitative influence of these interactions on F is not clear. Furthermore, DNA−surface interactions may strongly affect F. If the molecule is attracted to (repulsed from) the surfaces of a nanofluidic structure, for example, these surface interactions can result in a net decrease (increase) in ΔF [40]. Even though substantially screened in slitlike confinement [41, 42], hydrodynamic interactions may also affect DNA behavior [43]. Recent theoretical and computational predictions have largely ignored relevant DNA−surface interactions, while recent experimental measurements have not necessarily controlled these interactions strictly or accounted for the effects appropriately in interpretations of the experimental results. In the absence of direct measurements of free energy, predictions of free energy have been assessed indirectly through DNA size measurements, as discussed below.

There are several related metrics for the size R of a DNA molecule confined to a nanoslit, including the root-mean-square end-to-end radius R_e, the radius of gyration R_g, and the components of R_g in the plane parallel to the confining surfaces of the slit $R_{g||}$. The predicted relation between R and d may be derived from the relation between F and d. In this way, Odijk [26] used a scaling argument to predict a relation of $R_e(d) \sim d^{-0.25}$ in moderate and strong confinement. Other recent theoretical and computational studies of $R(d)$ have not been fully consistent with this prediction. Tang *et al.* [44] used Brownian dynamics simulations that accounted for the effects of optical diffraction, and predicted a relation of $R_{g||}(d) \sim d^{-0.13\pm0.06}$ (average $\pm$ standard deviation), as fitted here. Chaudhuri and Mulder [45] used a mean field approach that mapped a confined polymer onto an anisotropic Gaussian chain and predicted a relation of $R_{g||}(d) \sim d^{-0.25}$ in both moderate and strong confinement. Cifra [46] used an analytic wormlike chain model and predicted a relation of $R_{g||}(d) \sim d^{-0.25}$ in moderate confinement, with a transition at $d \approx p$ to a relation of $R_{g||}(d) \sim d^{-0.15}$ in strong confinement. Dai *et al.* [47] combined scaling arguments and a wormlike chain model to predict a relation of $R_{g||}(d) \sim d^{-0.25}$ through the transition between strong and moderate confinement and a gradual saturation of $R_{g||}(d)$ near $d \approx w$. Chen *et al.* [43] reported a relation of $R_{g||}(d) \sim d^{-0.25}$ across strong and moderate confinement using a semi-flexible chain model incorporating hydrodynamic interactions. The discrepancies between these predictions for linear DNA molecules indicate that the many variable parameters relevant to this system have not been modeled consistently.

For circular DNA molecules, Micheletti and Orlandini [48] used Monte Carlo simulations to identify a relation of $R_{g||}(d) \sim d^{-0.26\pm0.04}$ (average $\pm$ standard deviation).

Such predictions can be assessed by experimental measurements of $R_{g||}(d)$, which have yielded complicated results. An initial study by Strychalski *et al.* [49] reported a monotonic increase of $R_{g||}(d)$ as d decreased from moderate to strong confinement. By contrast, Bonthuis *et al.* [50] reported a nonmonotonic trend as d decreased, in which $R_{g||}(d)$ initially decreased from weak to moderate confinement, subsequently increased by $R_{g||}(d) \sim d^{-0.23\pm0.03}$ in moderate confinement, and then abruptly saturated near $d \approx 2p$. Tang *et al.* [44] revisited the topic and reported a monotonic and gradual increase of $R_{g||}(d)$ through the $d \approx 2p$ transition between moderate and strong confinement. A more quantitative study by Strychalski *et al.* [51] superseded the initial study of Strychalski *et al.* [49] and reported relations of $R_{g||}(d) \sim d^{-0.16\pm0.01}$ and $R_{g||}(d) \sim d^{-0.17\pm0.01}$ (average $\pm$ standard deviation) for linear DNA samples with different ratios of DNA base pairs to fluorescent dye molecules. Strychalski *et al.* [51] also fitted the $R_{g||}(d)$ data reported by Tang *et al.* [44], which produced a relation of $R_{g||}(d) \sim d^{-0.17\pm0.01}$ (average $\pm$ standard deviation). Lin *et al.* [9] reported a relation of $R_{g||}(d) \sim d^{-0.22\pm0.02}$ for linear DNA. However, the data published by Lin *et al.* [9] were fitted here over the same range of $d \approx (65-465)$ nm used by Strychalski *et al.* [51], and a significantly different relation of $R_{g||}(d) \sim d^{-0.17\pm0.01}$ (average $\pm$ standard deviation) was obtained. The experimental relations for circular DNA molecules reported by Strychalski *et al.* [51] and Lin *et al.* [9] are in similar disagreement. In contrast to the direct measurements of Tang *et al.* [44], Strychalski *et al.* [51], and Lin *et al.* [9], Dai *et al.* [47] inferred a relation of $R_{g||}(d) \sim d^{-0.24\pm0.04}$ through strong and moderate confinement. This inference assumed the relation $R \sim (D\tau)^{1/2}$, where R is the chain radius, D is the diffusivity, and τ is the rotational relaxation time. Dai *et al.* [47] used the values of D and τ reported by Tang *et al.* [44] Beyond a power law scaling relation, Strychalski *et al.* [52] used an empirical piecewise linear relation to identify an abrupt transition in $D(d)$ between strong and moderate confinement for circular DNA at $d \approx 3p$ and a potential transition at $d \approx 2p$ for linear DNA. To summarize these experimental measurements, DNA size, as measured by $R_{g||}$, generally increased with decreasing d. However, none of these measurements is entirely consistent with any of the recent predictions, and further research is needed to reach a quantitative, consensus relation for $R_{g||}(d)$.

As the conformation of a DNA molecule fluctuates due to thermal motion, the instantaneous value of $R_{g||}$ also fluctuates. This results in a distribution over time of DNA sizes for a given d. The Flory distribution of R_g for a flexible polymer with excluded volume and a dimensionality of two [28] was derived originally from the free energy penalties of contracting a polymer with excluded volume in a mean field approach or extending an ideal polymer with entropic elasticity. This distribution has been used successfully to model the experimentally measured histograms of $R_{g||}$ values for semiflexible DNA molecules in microfluidic and nanofluidic slits

that ranged in depth from nearly free solution ($d > 2R_g$ (free solution)) toward the two-dimensional limit ($d < p$) [44, 50, 51, 53].

Slitlike confinement influences the relaxation behavior of a DNA molecule. Thermal fluctuations of the DNA conformation are associated with the stretch and rotational relaxation times of the molecule, which are the longest relaxation times and equal according to the simple polymer models of Rouse and Zimm [54]. Hsieh *et al.* [24, 54] observed that these relaxation times increase with decreasing d, increasing contour length, or decreasing ionic strength of the solvent. These results were supported by Lin *et al.* [53] and Tang *et al.* [44] for linear DNA molecules and extended to circular DNA molecules by Lin *et al.* [9] The relaxation times reported by Bonthuis *et al.* for linear DNA molecules were significantly faster with a qualitatively different trend from other experimental studies [44, 50]. The stress relaxation time describes the time required for a DNA molecule to return to thermodynamic equilibrium after a perturbation. Because nanofluidic DNA analysis has often required linearizing a molecule, it is important to understand how a DNA molecule responds to a stretching force. Building on the work of Bakajin *et al.* [10], Balducci *et al.* [55] used electric fields and post arrays to stretch DNA molecules in nanoslits and observed two distinct stress relaxation times associated with the effects of confinement within the linear force extension regime. Tang *et al.* [56] suggested that these distinct relaxation times give rise to two different strain rates, observed using cross-slot flow as DNA molecules elongated through a coil-stretch transition. The origin of these two distinct relaxation times is not yet fully understood [29].

The center of mass diffusivity of a DNA molecule is altered by confinement to a nanoslit. Several experimental studies have examined the dependence of DNA diffusivity in nanoslits on d, contour length, topology, and the ionic strength of the solvent [41, 53, 57, 58]. The diffusion of linear DNA molecules from strong to moderate confinement was presented by Balducci *et al.* [41], showing that diffusivity decreases with decreasing d and increasing contour length. Strychalski *et al.* [57] extended these results to smaller d and shorter contour lengths, while Lin *et al.* [58] subsequently reported similar behavior for circular DNA molecules. Dai *et al.* [59] included short-length scale correlations in simulations of D for linear DNA across strong and moderate confinement to better reconcile simulations and experimental measurements. Other characteristics of the system, such as temperature, solvent properties, and DNA – surface interactions, may also influence DNA diffusivity in nanoslits but have not been studied systematically.

The ionic strength of the solvent has important consequences for DNA behavior in slitlike confinement. A charged object in solution, such as a surface or DNA molecule, accumulates a layer of more tightly bound counterions, which in turn attracts a layer of more loosely bound coions [29]. The electrical potential in solution varies across this double layer between its values in the bulk solvent and at the charged object. This distance is described by the Debye length and is usually approximately 1 – 10 nm in typical experimental systems for nanofluidic DNA analysis [12]. This length determines the length scale beyond which electrostatic interactions are screened and appears, for example, in calculations of w and p of a

DNA molecule in solution [24]. Experimental measurements by Hsieh *et al.* [24] found that larger ionic strengths resulted in faster diffusion and relaxation times and smaller inferred sizes for DNA molecules in moderate confinement in 450-nm deep nanoslits. Lin *et al.* [9] reported the additional findings that linear and circular DNA molecules of the same contour length behaved similarly, as d and the ionic strength were varied. These measurements used ionic strengths for which the Debye length was relatively small compared to d. When the Debye length becomes a significant fraction of d, its effects at the surfaces of the nanoslit may be significant for DNA behavior [60] and should be considered more explicitly. The Debye length may also be so large as to overlap within a nanofluidic structure, although this has been avoided in general for DNA analysis.

3.3
Differential Slitlike Confinement of DNA

Differential slitlike confinement introduces the use of more complex nanofluidic structures to enable structural control of a DNA molecule for analysis. Consider, for example, a binary confinement scheme in which a DNA molecule is confined to adjacent nanoslits with different depths. A DNA molecule fully on the shallower of these nanoslits is at thermodynamic equilibrium, unaffected by the deeper nanoslit. When the DNA molecule diffuses to the interface between these nanoslits, however, the molecule becomes subject to a thermodynamic force that arises from the finite temperature of the system. This force is driven by the difference in free energy for that DNA molecule on each of the two nanoslits and is applied locally to the portion of the molecule at the interface between the nanoslits. This force spontaneously transports the DNA molecule from the shallower nanoslit to the deeper nanoslit to reach a new equilibrium at a lower F (Figure 3.2a). If this energy barrier ΔF to return to the shallower nanoslit is

(a)   (b)
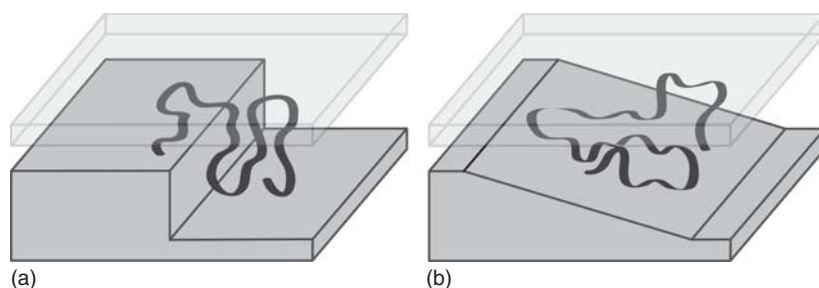
Figure 3.2 Differential slitlike confinement. (a) A DNA molecule is subject to a force due to a change in free energy ΔF at the interface between adjacent nanoslits with different depths. As a result, the molecule is transported spontaneously from the shallower nanoslit to the deeper nanoslit. (b) The same molecule is subject to ΔF more gradually in a ramp between those same nanoslits. The gradient in F over the characteristic size of the molecule determines the magnitude and effect of the force.

large relative to the thermal energy of the DNA molecule, the molecule will tend to stay in the deeper nanoslit. If ΔF is relatively small, the molecule will overcome the energy barrier and move back and forth between the two nanoslits, with the lower energy state on the deeper nanoslit preferred over time. Even though a DNA molecule is perturbed from thermodynamic equilibrium between regions of differing confinement, ΔF can be engineered, if desired, to keep these forces relatively small and allow the DNA molecule to remain near equilibrium. This allows fundamental studies of DNA behavior at or near thermodynamic equilibrium, while still acting on DNA molecules for analysis. In this way, ΔF between structurally more and less confining regions can be used to transport and manipulate the conformation of DNA molecules for analysis.

This behavior inherent to the nanofluidic confinement of a DNA molecule becomes more useful as many structures that confine DNA molecules differently are combined in a single nanofluidic device. These more complex structures impose correspondingly more complex changes in F on a confined DNA molecule. In this way, a nanofluidic structure can be designed to implement the forces needed for DNA analysis, which arise spontaneously from the interaction of a DNA molecule in solution with the confining structure. A variety of useful capabilities for DNA analysis can be achieved in complex slitlike confinement that cannot be achieved in a simple nanoslit without external forces. Those that have been demonstrated experimentally so far include DNA self-organization, self-transport, self-concentration, and self-separation [4, 20, 22].

3.4
Experimental Studies

Few experimental studies have examined DNA behavior in more complex nanofluidic structures designed for DNA analysis, and only three have done so without applying external forces to manipulate DNA molecules at or near thermodynamic equilibrium (Figure 3.3).

The simplest of these structures consists of only two depths. Reisner *et al.* [20] reported the interaction of DNA molecules at equilibrium with nanopits embedded periodically in a surface of a nanoslit (Figure 3.3a). The nanoslits ranged in depth from 50 to 100 nm, while the nanopits were 100–500 nm wide squares and 100 nm deep. These nanopits were arrayed across the nanoslit in a square lattice with pit-to-pit spacing between 500 nm and 20 μm. These structures amounted to regions of semicavity confinement within slitlike confinement and allowed nanoscale self-organization of a DNA molecule across one or more nanopits depending on the relationship between the nanofluidic geometry and DNA contour length (Figure 3.3b). ΔF between the deeper, narrower nanopits and shallower, wider nanoslits resulted in stable equilibrium conformations for each DNA molecule in the structure. Reisner *et al.* argued that this device could provide convenient, long-term storage for DNA molecules. The examined nanopits embedded in a nanoslit, while compelling, do not provide a structural
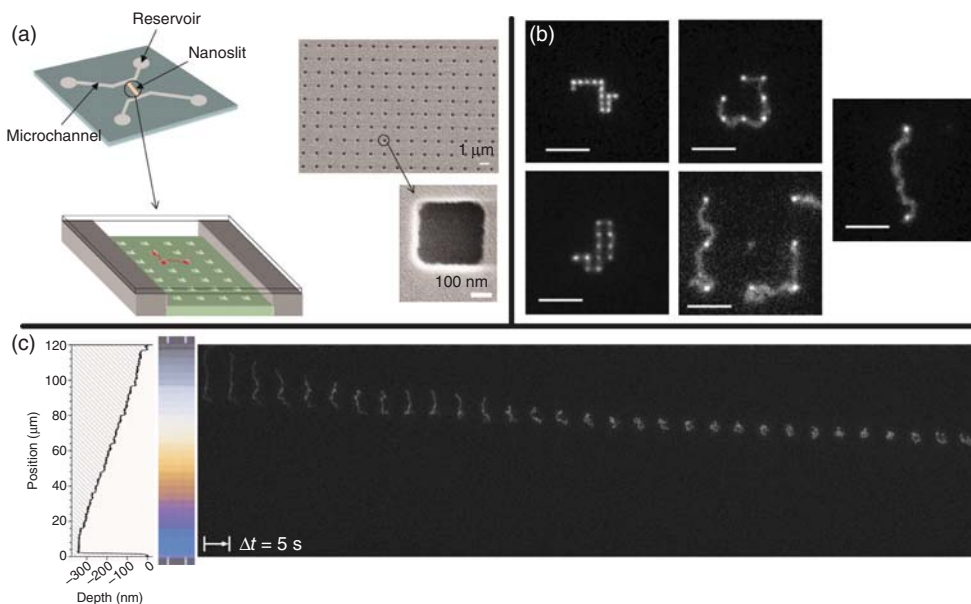
Figure 3.3 Complex nanofluidic structures for structural control of DNA molecules. (a) A nanopit array in a nanoslit enabled semi-cavity confinement based on the slitlike confinement of DNA molecules [20]. (b) Fluorescence images show DNA molecules partitioning spontaneously into the nanopits in a manner that depended on the DNA contour length and device dimensions (scale bars: 5 μm). (Adapted with permission from Figures 1 and 2 of Reisner *et al.* [20].)

(c) Surface profilometry shows the depth profile of a nanofluidic staircase, whose 30 nanoslit depths are visible as different colors due to white light interference in a bright field image. As shown in a series of fluorescence images, a DNA molecule elongated across many adjacent nanoslits during spontaneous transport down a nanofluidic staircase. (Adapted from Figure 5 of Stavis *et al.* [4] with permission from The Royal Society of Chemistry.)

means to transport the center of mass of DNA molecules distances larger than the DNA contour length or a few lattice spacings, as molecules spontaneously change configuration across multiple nanopits due to thermal fluctuations.

A more structurally complex nanofluidic confinement scheme was the nanofluidic staircase of Stavis *et al.* [4, 61] and Strychalski *et al.* [51] (Figure 3.3c). This device was used to study the transport and size of linear and circular DNA molecules near equilibrium and consisted of 30 adjacent nanoslits whose depths ranged from 4 to 342 nm and stepped down like a staircase across a distance of 120 μm. A DNA molecule confined initially to a nanoslit at the top of this staircase was spontaneously transported to deeper nanoslits and toward the bottom of the staircase across a lateral distance many times greater than the DNA contour length. The transport was driven by the center of mass diffusion of the DNA molecules and the stepped gradient in free energy across the staircase. This controlled self-transport was therefore termed *entropophoresis* and provided a means for the structural nanofluidic transport of DNA molecules for analysis.

Continuously varying, non-nanofluidic slitlike confinement was implemented by Leslie *et al.* [22], who introduced convex lens-induced confinement for observing DNA molecules at equilibrium in solution and confined between a convex lens and planar cover slip. The slitlike confinement varied smoothly from 0 to 2 µm deep across a lateral distance of 25 µm radially outward from the contact point between the lens and cover slip. DNA molecules experienced a gradient in free energy, diffusing thermally and becoming excluded entropically from a region near the contact point. Measuring the spatial distribution of a population of nominally identical DNA molecules as a function of distance from the contact point gave information on DNA size, as well as an estimate of the potential of mean force in weak confinement, which is related to the free energy.

While the nanopit array, staircase, and convex lens-induced confinement relied on differential structural confinement to control DNA behavior, Krishnan *et al.* [18] used electrostatic confinement to spontaneously organize and elongate DNA molecules. The edges and corners of nanofluidic structures can result in the superposition of electrical double layers. Krishnan *et al.* [18] observed DNA molecules become trapped and elongated at the chamfered edges of a nanoslit, reportedly due to dielectrophoresis in these double layers. This effect weakened as the overlap of the electrical double layers decreased with increasing d from 100 to 500 nm or increasing ionic strength of the solvent. Because structural and electrostatic confinements are closely related, the effects reported by Krishnan *et al.* may, in principle, be exploited generally in complex nanofluidic structures.

Additional work has introduced complex nanofluidic geometries for DNA manipulation but relied on hydrostatic or electrokinetic forces to act on the DNA molecules during measurement. The following methods represent the broader scope of complex structures fabricated with top-down processes, which have been used to shape both fluid flow and electric fields, in addition to providing complex nanoscale confinement. Several studies solved the relevant problem of overcoming the large ΔF encountered by a DNA molecule between microscale and nanoscale confinement. The earliest of these is the nanofluidic ramp fabricated via diffraction gradient lithography by Cao *et al.* [62]. This structure and the electric field gradient in the ramp elongated DNA molecules to facilitate the entrance of the molecules into nanochannels from a microchannel. Reisner [63] used a direct-write technique to create similar structures. Strychalski *et al.* [49] accomplished the same goal through an unconventional nanofabrication process termed *nanoglassblowing*, which resulted in funnel-shaped entrances to nanoslits with a continuously curving geometry over long distances. A number of other studies have also used nanopits or nanotrenches embedded in nanoslits with hydrodynamic flow to manipulate DNA molecules. These include reports by Bonis-O'Donnell *et al.* [64] to observe DNA transport across nanopits, Mikkelsen *et al.* [3] for topology-dependent separation of linear and circular DNA molecules using nanotrenches, and Shelton *et al.* [19] to influence the transport of DNA molecules using nanotrenches with more complex shapes. DNA molecules have also been stretched entropically through a nanoslit connecting less confining regions for analysis [33, 65], as well as driven electrokinetically through entropic

trap arrays for batch [2, 13, 66] and continuous [67] separation of mixtures of different DNA molecules.

3.5
Design of Complex Slitlike Devices

The use of complex nanofluidic structures for DNA manipulation and analysis relies on tailoring the interaction between the molecule and confining structure to control transport and conformation. The ability to transport DNA molecules is essential for separations or to position a molecule for measurement. The conformation can be chosen to favor a particular interaction between a DNA molecule and a confining structure, such as a post or nanochannel entrance, during transport or to enable measurements of a portion of the DNA contour.

Transport depends largely on the relationship between the size of the DNA molecule in confinement and the distance over which the confining dimensions of the structure change. The salient size metric here can be thought of simply as the physical extent of the DNA molecule. For example, in a nanotrench or nanochannel, the relevant size of the DNA molecule is its extent along the trench or channel. In a nanoslit, this can be the longest axis of the anisotropic ellipsoid formed by the DNA molecule [51].

If the confining structure does not change over this characteristic size of the DNA molecule, then the molecule will experience no gradient in F. This was the case for the study of Persson *et al*. [68], who analyzed individual DNA molecules in a hybrid nanochannel-nanoslit structure with a single depth of 60 nm and a width that tapered gradually from 1 μm to 100 nm over a distance of 450 μm. This taper was long relative to the approximately 10 μm size of a confined DNA molecule, which resulted in a negligibly shallow gradient in F over the size of the molecule. The DNA molecule, therefore, remained effectively stationary over the timescale of a measurement.

If, however, the nanofluidic structure changes dramatically across the size of the DNA molecule, the molecule is said to undergo "entropic recoil" from the more confining region to the less confining region. In this binary confinement scheme, such as the entropic trap of Han *et al*. [69] (Figure 3.2a) or Turner *et al*.'s [70] nanoslit containing a region of dense posts, the center of mass transport of the DNA molecule occurs relatively quickly.

These experimental observations suggest that the speed of DNA transport can be controlled by designing a structure that imposes the desired gradient in F across the size of the molecule. While binary differential confinement enacts an abrupt change in F, this change can also be spread across a distance in the confining structure that is larger than the size of the DNA molecule to impose a more gradual change in F (e.g., Figure 3.2b). Even though this has yet to be tested experimentally in the literature, finer spatial control over changes in confinement, in principle, enables finer control over DNA transport.

In addition to varying the gradient in *F* across a DNA molecule, transport can be controlled by varying the distance that a molecule must diffuse between changes in *F*. On average, the center of mass diffusion of a DNA molecule is a relatively slow process compared to the spontaneous transport between structurally more and less confining regions. For example, a larger DNA molecule that spans multiple steps in a nanofluidic staircase always experiences forces transporting the molecule toward deeper nanoslits and, consequently, moves relatively rapidly down a nanofluidic staircase. A smaller DNA molecule that fits entirely on a single nanoslit, by contrast, must diffuse across each nanoslit between the application of forces, causing the molecule to move relatively slowly down the staircase (Figure 3.4) [4, 51]. Properties of the system that affect DNA diffusivity, such as the solvent viscosity, temperature, or DNA–surface interactions, affect the average time for a DNA molecule to diffuse between changes in *F* and therefore also influence the rate of transport through complex structures.

Control over the conformation of a DNA molecule may also be important for analysis. With regard to influencing transport, for example, it has been suggested that DNA conformation before collisions within post arrays impacts separation [71]. With regard to single-molecule measurements, stretching of a DNA molecule may be required to measure the contour length or image a portion of the DNA contour with or without information regarding its location along the contour length. Complex structures can perturb a DNA molecule from its conformation at thermodynamic equilibrium to result in a near-equilibrium conformation that exposes portions of the contour to analysis. In binary differential confinement, a portion of the DNA contour is isolated transiently as the molecule is extended locally at the interface between the nanoslits (Figure 3.2a). Stretching a DNA molecule through a nanoslit connecting less confining regions [33, 65] or between nanopits [20] (Figure 3.3b) in a nanoslit also exposes the DNA contour for measurement. However, these schemes do not necessarily
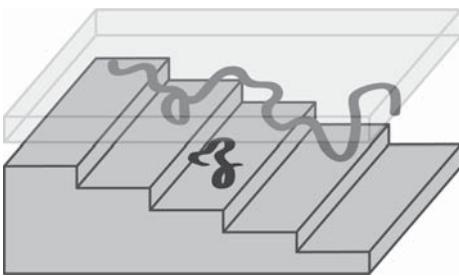
Figure 3.4 Structural control of transport and conformation using a nanofluidic staircase. A DNA molecule with a longer contour length (gray) simultaneously spans many adjacent nanoslits of a nanofluidic staircase, so that the molecule moves relatively rapidly down the staircase with an elongated conformation [4]. A DNA molecule with a shorter contour length (black) must diffuse across a nanoslit between forces applied at the depth changes between nanoslits, so that the molecule moves relatively slowly down the staircase.

allow determination of the location of that portion of the DNA contour along the entire contour length. This can be achieved in slitlike confinement, for example, using simultaneous extension across many nanoslits, so that the DNA molecule is subject to forces at intervals along the contour length (Figure 3.4). An example of this behavior occurred for a DNA molecule confined transiently near the top of a nanofluidic staircase (Figure 3.3c) [4].

3.6
Fabrication of Complex Slitlike Devices

Even though conventional, top-down, lithographic fabrication processes have been used to fabricate nanofluidic structures for DNA analysis, these processes are not amenable to creating complex nanofluidic structures with many different nanoscale depths in a single device. Typically, each depth requires separate steps for alignment, exposure, and etching of a device wafer. Complex structures must then be built up in a succession of these levels using, for example, electron beam lithography for nanopits or nanotrenches [3, 20], ion beam milling for nanotrenches [19], or diffraction gradient lithography for ramps [62], in addition to the levels of contact photolithography to define the microfluidic channels and nanoslits. Regions of the structure that must be etched two or more times due to the alignment process can further restrict the functionality of complex nanofluidic structures fabricated in this way. These limitations motivate a new approach to achieve complex nanofluidic structures that remains compatible with conventional fabrication methods.

One such approach is nanoglassblowing, which results in smooth, curving surfaces that can join microfluidic and nanofluidic device regions [49]. For nanoglassblowing, the device is patterned using contact lithography, etched to the shallowest desired depth, and a thin cover wafer is fusion-bonded to enclose the structure. A subsequent annealing step both finalizes the bond and heats air trapped inside the device that pushes on the softened cover wafer. The cover wafer bows outward, with wider device regions becoming deeper than narrower device regions. Regions narrower than a critical size retain their original cross section. Even though nanoglass blowing remains the sole reported method for fabricating continuously curving surfaces in a device across the length scales relevant to microfluidics and nanofluidics, it is not ideal for creating complex nanofluidic structures; this is due to the challenge of characterizing bonded devices and constraints on the final structure from the local coupling between the device widths and depths. Another method achieves continuously varying slitlike confinement of DNA molecules over a restricted lateral distance using a convex lens brought into close proximity to a planar cover slip [22]. While elegant, convex lens-induced confinement is outside of the laboratory on a chip concept for DNA analysis.

Grayscale photolithography has emerged as a promising approach to fabricate complex nanofluidic structures. The first demonstration by Cao *et al.* [62] via

diffraction gradient lithography delivered a continuous intensity gradient for the exposure of photoresist and, therefore, resulted in a ramp structure. However, this method is limited to fabricating ramps and by the need to pattern grayscale regions separately. Another approach to grayscale photolithography used a direct-write technique and 32 grayscale intensities [63]. Even though this technique could conceivably pattern arbitrary structures, the drawbacks discussed by Reisner include the need for intensive characterization of the fabrication process, low throughput, and stitching errors within the grayscale regions. Stavis *et al*. [61] introduced a fabrication process that enabled grayscale patterning of the entire nanofluidic device in a single layer. This method has the advantages of earlier grayscale demonstrations without the disadvantages. Stavis *et al*. [61] used optical projection lithography and a diffractive photomask with arrays of subresolution pixels to expose 30 grayscale intensities simultaneously. No alignment was required between different device depths, which allowed patterning of structures without redundantly or incompletely etched regions between different nanoscale depths.

For several reasons, the most straightforward and versatile fabrication technique demonstrated so far for creating complex nanofluidic structures is grayscale photolithography. Grayscale photolithography is, in general, compatible with conventional fabrication processes and can be used in conjunction with them, which is especially true for the method reported by Stavis *et al*. [61] Grayscale photolithography can be incorporated as a layer in a multilayer fabrication process that requires specialized tools for particular device features. For example, grayscale photolithography for nanoscale depths that vary laterally over micrometers or more might create the overall device per Stavis *et al*. [61], while a separate layer using electron beam lithography might define nanoscale-depth variation across nanoscale lateral dimensions. Furthermore, grayscale methods rely on the same established and well-characterized thin film pattern transfer processes as conventional fabrication, such as reactive ion etching, to define device depths precisely. Another advantage of grayscale photolithography is its favorable scaling with an increasing number of nanoscale depths in a complex geometry; for Stavis *et al*. [61], the identical fabrication process yields a device with one to an arbitrarily large number of nanoscale depths, limited by the mask specifications available from the mask supplier and the performance of the projection photolithography tool.

Characterizing complex nanofluidic structures presents practical challenges during and after fabrication. Complex geometries must be measured thoroughly, because nanoscale variations in depth, surface roughness, and other characteristics across a single device can critically affect DNA behavior and, consequently, the utility of a device for DNA analysis. Scanned probe measurement methods, such as surface profilometry or atomic force microscopy, give quantitative nanoscale depth and surface roughness measurements, but performing line or area scans across large regions is time consuming. Methods to visualize large areas of a device, such as scanning electron microscopy (SEM) or optical profilometry, can be useful to ascertain approximate device dimensions. However, imaging insulating substrates, such as fused silica, can be difficult without an

environmental SEM or a coating to reduce charging, such as carbon or gold, and optical profilometry does not generally offer the nanoscale-depth resolution needed for adequate characterization of complex structures for DNA analysis.

After a device is enclosed by a cover wafer, characterization of the dimensions becomes more difficult. Scanned probe measurements across the cover wafer over a device have been reported to estimate the depth of an enclosed structure fabricated using nanoglassblowing [49]. Optical interferometry can be used to visualize changes in depth in a complex nanofluidic geometry, which is essentially a thin film of air of varying thickness before filling the device with fluid. Monochromatic light interferes with itself to reveal changes in depth across a device as minima and maxima in intensity [22]. White light interference results in a striking color pattern across a device that can be used to visualize depth changes of approximately 10 nm and infer device depth locally (Figure 3.3c) [49, 61]. A more invasive but quantitative approach to determining device depth is to perform quantitative fluorescence measurements on a device filled with a uniform and uncharged fluorescent dye solution. Deeper regions will result in an optical path that excites more of the fluorescent dye molecules at a given location, resulting in brighter images for deeper than shallower regions. Such fluorescence measurements offer a means to determine depths that are too shallow for optical interferometry, but can also foul the surfaces of the device with dye molecules. Another measurement technique uses a readily available object, for example, a lambda-phage DNA molecule or nanoparticle of known size under standard conditions, as a reference material.

3.7
Experimental Conditions

A DNA molecule in a nanofluidic structure is typically labeled along its contour with fluorescent dye molecules and observed by fluorescence microscopy. The dimeric cyanine bis-intercalator YOYO-1 is often chosen as the label for its large increase in brightness upon complexing with a DNA molecule, good compatibility with common fluorescence excitation wavelengths and filter sets, and emission spectrum that generally corresponds to lower device autofluorescence [72]. Despite the frequent use and noted benefits of YOYO-1, several measurement challenges for DNA analysis have been identified recently [15, 51]. Among these, it has not been possible to measure the exact number or specific location of dye molecules along the DNA contour. This information is important, because labeling the DNA molecule with YOYO-1 alters the physical properties of the DNA molecule, increasing the contour length and potentially affecting the persistence length in an uncertain manner [73−75]. Changes in these characteristic length scales of a DNA molecule have consequences for the design of nanofluidic structures for DNA analysis. An additional measurement challenge pertains to the quantitative analysis of typical fluorescence images of a DNA molecule, which appears as an extended object that is blurred by the optical diffraction

limit and thermal fluctuations during image exposure, as well as pixelated by the finite camera pixel size used to capture the image [51]. Advanced microscopy techniques, such as super-resolution and total internal reflection fluorescence, enable the measurement of a DNA molecule with better spatial resolution than that allowed by the optical diffraction limit in more conventional methods. Progress in both image analysis and fluorescence measurement methods will translate directly into improvements in nanofluidic DNA analysis.

After labeling, DNA molecules are typically dispersed in an aqueous solvent composed of a monovalent electrolyte buffer solution for analysis. This solvent influences the properties and behavior of a confined DNA molecule through a variety of mechanisms. The ionic strength affects the conditions under which a double-stranded DNA molecule will denature. As discussed earlier, the ionic strength sets the Debye length, which is relevant to electrostatic and excluded volume interactions within a DNA molecule, as well as to nanofluidic analysis that exploits electrostatic confinement [18]. The ionic strength also influences the stability of bis-intercalated fluorescent labels, such as YOYO-1, bound to a DNA molecule. In particular, a high ionic strength may destabilize the DNA-YOYO-1 complex, which presents a challenge to quantitative fluorescence analysis based on the stoichiometric dye molecule concentration during labeling of the DNA molecules [73]. In addition to the ionic strength, p is strongly influenced by counterion valence, becoming much smaller for counterions of higher valence [76]. Because multivalent counterions may result in condensed DNA conformations, monovalent electrolyte buffer solutions are typically used to maintain coiled DNA conformations for nanofluidic analysis. Specific buffer interactions with DNA molecules must also be identified and characterized. For example, the commonly used electrophoresis buffer Tris Borate Ethylenediaminetetraacetic Acid (EDTA) contains boric acid, which can increase the negative electrical charge density of a DNA molecule [77]. This buffer interaction may increase p and excluded volume interactions, which increases the size of DNA molecules confined to nanoslits [44]. Tris Acetate EDTA and Tris EDTA buffers are also commonly used but do not present this specific interaction.

The solvent also mediates surface interactions beyond the effects expected from purely geometric confinement. For nanoslits fabricated in planar fused silica or silicon dioxide, a DNA molecule interacts with the surfaces through silanol groups (SiOH) at a density of $4-5\,\text{nm}^{-2}$ [78]. These groups deprotonate in a pH-dependent manner, with $\approx$19% of the isolated silanol groups deprotonating freely ($pK_a \approx 4.9$) for typical solvents for DNA analysis and $\approx$81% of the geminal and vicinal silanol groups deprotonating under more basic conditions ($pK_a \approx 8.5$) [79]. Silanol protonation may increase attractive interactions between the confining surfaces and a negatively charged DNA molecule [80, 81]. For example, the commonly used double-stranded lambda-phage DNA has 12-base single-stranded segments at both five-prime ends that can interact attractively with the protonated silanols of fused silica surfaces [82–84]. Therefore, for some experimental systems, a careful selection of solution pH is essential to avoid attractive surface interactions.

Nonattractive DNA−surface interactions simplify the operation of a nanofluidic device for DNA analysis and allow the more reasonable neglect of surface interactions during the interpretation of experimental results. Recent studies have demonstrated a variety of methods to modify nanoslit surfaces to influence DNA−surface interactions. Although meant primarily as a means to prevent photodegradation of DNA molecules during fluorescence imaging, the proteins glucose oxidase and catalase, as used, for example, by Tang *et al.* [44], Dai *et al.* [47], and Lin *et al.* [9], may have also coated the surfaces. Blends of polymers and surfactants, such as POP-6, have also been used to mitigate DNA−surface interactions [9]. Rasmussen *et al.* [14] cleaned and blocked nanoslit surfaces by flushing a solution containing sodium dodecyl sulfate and bovine serum albumin before digesting proteins in chromosomal DNA and stretching the DNA molecule along a nanoslit. Persson *et al.* [85] created a lipid bilayer within nanochannels to observe DNA−protein interactions without prohibitive fouling of the surfaces by the proteins. As a practical matter, however, a wider repertoire of techniques would be useful to tailor surface attributes and interactions. Much of this work must proceed empirically, as the behavior of a realistic polymer in a liquid at a surface is an open problem.

The complex nanofluidic structures that have been demonstrated so far for structural control of DNA molecules have required initialization of the system using externally applied forces. DNA molecules were transported hydrodynamically into the nanoslit of Reisner *et al.* [20] before the molecules were spontaneously arranged in the nanopits. The nanofluidic staircase experiments of Stavis *et al.* [4, 61] and Strychalski *et al.* [51] transported DNA molecules electrokinetically to the top of the staircase before entropophoresis. The convex lens-induced confinement of Leslie *et al* [22]. required displacement of the lens. Other approaches to initialization could also be successful, as long as work is done on a DNA molecule to increase F in a manner that allows the molecule to relax spontaneously to lower energy states through interactions with the confining structure.

3.8
Conclusion

The recent development of complex nanofluidic structures is a promising new trend for DNA manipulation and analysis. Following initialization, this nanofluidic technology can provide complex structural control over the spontaneous transport, organization, separation, concentration, and conformation of DNA molecules. Even though these capabilities have been demonstrated using a specific class of DNA molecule, the fundamental insights and practical experience gained in developing and optimizing complex nanofluidic structures for DNA analysis should translate readily to other biopolymers. The rational design of these structures depends on an improved fundamental understanding of DNA

behavior in nanoscale confinement at or near thermodynamic equilibrium, which is a topic of broad interest beyond the focused discussion presented here.

Disclaimer

Certain commercial equipment, instruments, or materials are identified to adequately specify experimental procedures. Such identification implies neither recommendation nor endorsement by the National Institute of Standards and Technology nor that the materials or equipment identified are necessarily the best available for the purpose.

Official contribution of the National Institute of Standards and Technology; not subject to copyright in the United States.

References

1. Cross, J.D., Strychalski, E.A., and Craighead, H.G. (2007) Size-dependent DNA mobility in nanochannels. *J. Appl. Phys.*, **102**(2), 024701.

2. Han, J. and Craighead, H.G. (2000) Separation of long DNA molecules in a microfabricated entropic trap array. *Science*, **288**(5468), 1026–1029.

3. Mikkelsen, M.B. *et al.* (2011) Pressure-driven DNA in nanogroove arrays: complex dynamics leads to length- and topology-dependent separation. *Nano Lett.*, **11**(4), 1598–1602.

4. Stavis, S.M. *et al.* (2012) DNA molecules descending a nanofluidic staircase by entropophoresis. *Lab Chip*, **12**(6), 1174–1182.

5. Welch, R.L. *et al.* (2012) Denaturation mapping of Saccharomyces cerevisiae. *Lab Chip*, **12**(18), 3314–3321.

6. Nyberg, L.K. *et al.* (2012) A single-step competitive binding assay for mapping of single DNA molecules. *Biochem. Biophys. Res. Commun.*, **417**(1), 404–408.

7. Lim, S.F. *et al.* (2013) Chromatin modification mapping in nanochannels. *Biomicrofluidics*, **7**(6), 064105.

8. Volkmuth, W.D. and Austin, R.H. (1992) DNA electrophoresis in microlithographic arrays. *Nature*, **358**(6387), 600–602.

9. Lin, P.K. *et al.* (2012) Effects of topology and ionic strength on double-stranded DNA confined in nanoslits. *Macromolecules*, **45**(6), 2920–2927.

10. Bakajin, O.B. *et al.* (1998) Electrohydrodynamic stretching of DNA in confined environments. *Phys. Rev. Lett.*, **80**(12), 2737–2740.

11. Levy, S.L. and Craighead, H.G. (2010) DNA manipulation, sorting, and mapping in nanofluidic systems. *Chem. Soc. Rev.*, **39**(3), 1133–1152.

12. Salieb-Beugelaar, G.B. *et al.* (2009) Electrophoretic separation of DNA in gels and nanostructures. *Lab Chip*, **9**(17), 2508–2523.

13. Strychalski, E.A., Lau, H.W., and Archer, L.A. (2009) Nonequilibrium separation of short DNA using nanoslit arrays. *J. Appl. Phys.*, **106**(2), 024915.

14. Rasmussen, K.H. *et al.* (2011) A device for extraction, manipulation and stretching of DNA from single human chromosomes. *Lab Chip*, **11**(8), 1431–1433.

15. Persson, F. and Tegenfeldt, J.O. (2010) DNA in nanochannels-directly visualizing genomic information. *Chem. Soc. Rev.*, **39**(3), 985–999.

16. Reisner, W., Pedersen, J.N., and Austin, R.H. (2012) DNA confinement in nanochannels: physics and biological applications. *Rep. Prog. Phys.*, **75**(10), 106601.

17. Nykypanchuk, D., Strey, H.H., and Hoagland, D.A. (2002) Brownian

motion of DNA confined within a two-dimensional array. *Science*, **297**(5583), 987–990.

18. Krishnan, M. *et al.* (2008) Electrostatic self-assembly of charged colloids and macromolecules in a fluidic nanoslit. *Small*, **4**(11), 1900–1906.

19. Shelton, E. *et al.* (2011) Controlling the conformations and transport of DNA by free energy landscaping. *Appl. Phys. Lett.*, **99**(26), 263112.

20. Reisner, W. *et al.* (2009) Directed self-organization of single DNA molecules in a nanoslit via embedded nanopit arrays. *Proc. Natl. Acad. Sci. U.S.A.*, **106**(1), 79–84.

21. Klotz, A.R., Brandao, H.B., and Reisner, W.W. (2012) Diffusion resonance of nanoconfined polymers. *Macromolecules*, **45**(4), 2122–2127.

22. Leslie, S.R., Fields, A.P., and Cohen, A.E. (2010) Convex lens-induced confinement for imaging single molecules. *Anal. Chem.*, **82**(14), 6224–6229.

23. Bouchiat, C. *et al.* (1999) Estimating the persistence length of a worm-like chain molecule from force-extension measurements. *Biophys. J.*, **76**(1), 409–413.

24. Hsieh, C.C., Balducci, A., and Doyle, P.S. (2008) Ionic effects on the equilibrium dynamics of DNA confined in nanoslits. *Nano Lett.*, **8**(6), 1683–1688.

25. Odijk, T. (1983) On the statistics and dynamics of confined or entangled stiff polymers. *Macromolecules*, **16**(8), 1340–1344.

26. Odijk, T. (2008) Scaling theory of DNA confined in nanochannels and nanoslits. *Phys. Rev. E*, **77**(6), 060901.

27. Daoud, M. and Degennes, P.G. (1977) Statistics of macromolecular solutions trapped in small pores. *J. Phys.*, **38**(1), 85–93.

28. de Gennes, P.-G. (1985) *Scaling Concepts in Polymer Physics*, 2nd edn., Cornell University Press, Ithaca and London.

29. Dorfman, K.D. *et al.* (2012) Beyond gel electrophoresis: microfluidic separations, fluorescence burst analysis, and DNA stretching. *Chem. Rev.*, **113**(4), 2584–2667.

30. Chou, C.F. *et al.* (2002) Electrodeless dielectrophoresis of single- and double-stranded DNA. *Biophys. J.*, **83**(4), 2170–2179.

31. Zhou, C. *et al.* (2011) Collapse of DNA in ac electric fields. *Phys. Rev. Lett.*, **106**(24), 248103.

32. Su, T.X. *et al.* (2011) Transition between two regimes describing internal fluctuation of DNA in a nanochannel. *PLOS One*, **6**(3), e16890.

33. Jo, K. *et al.* (2007) A single-molecule barcoding system using nanoslits for DNA analysis. *Proc. Natl. Acad. Sci. U.S.A.*, **104**(8), 2673–2678.

34. Lam, E.T. *et al.* (2012) Genome mapping on nanochannel arrays for structural variation analysis and sequence assembly. *Nat. Biotechnol.*, **30**(8), 771–776.

35. Cipriany, B.R. *et al.* (2012) Real-time analysis and selection of methylated DNA by fluorescence-activated single molecule sorting in a nanofluidic channel. *Proc. Natl. Acad. Sci. U.S.A.*, **109**(22), 8477–8482.

36. Reisner, W. *et al.* (2007) Nanoconfinement-enhanced conformational response of single DNA molecules to changes in ionic environment. *Phys. Rev. Lett.*, **99**(5), 058302.

37. Van Vliet, J.H., Luyten, M.C., and Ten Brinke, G. (1992) Scaling behavior of dilute polymer solutions confined between parallel plates. *Macromolecules*, **25**(14), 3802–3806.

38. Cifra, P. (2009) Channel confinement of flexible and semiflexible macromolecules. *J. Chem. Phys.*, **131**(22), 224903.

39. Douglas, J.F., Wang, S.Q., and Freed, K.F. (1987) Flexible polymers with excluded volume at a penetrable interacting surface. *Macromolecules*, **20**(3), 543–551.

40. Freed, K.F. *et al.* (2010) General approach to polymer chains confined by interacting boundaries. *J. Chem. Phys.*, **133**(9), 094901.

41. Balducci, A. *et al.* (2006) Double-stranded DNA diffusion in slitlike nanochannels. *Macromolecules*, **39**(18), 6273–6281.

42. Jones, J.J., van der Maarel, J.R.C., and Doyle, P.S. (2013) Intrachain dynamics of large dsDNA confined to slitlike channels. *Phys. Rev. Lett.*, **110**(6), 068101.

43. Chen, Y.L. *et al.* (2014) Dynamics and conformation of semiflexible polymers in strong quasi-1D and-2D confinement. *Macromolecules*, **47**(3), 1199–1205.

44. Tang, J. *et al.* (2010) Revisiting the conformation and dynamics of DNA in slitlike confinement. *Macromolecules*, **43**(17), 7368–7377.

45. Chaudhuri, D. and Mulder, B. (2011) Size and shape of excluded volume polymers confined between parallel plates. *Phys. Rev. E*, **83**(3), 031803.

46. Cifra, P. (2012) Weak-to-strong confinement transition of semi-flexible macromolecules in slit and in channel. *J. Chem. Phys.*, **136**(2), 024902.

47. Dai, L. *et al.* (2012) A systematic study of DNA conformation in slitlike confinement. *Soft Matter*, **8**(10), 2972–2982.

48. Micheletti, C. and Orlandini, E. (2012) Numerical study of linear and circular model DNA chains confined in a slit: metric and topological properties. *Macromolecules*, **45**(4), 2113–2121.

49. Strychalski, E.A., Stavis, S.M., and Craighead, H.G. (2008) Non-planar nanofluidic devices for single molecule analysis fabricated using nanoglassblowing. *Nanotechnology*, **19**(31), 315301.

50. Bonthuis, D.J. *et al.* (2008) Conformation and dynamics of DNA confined in slitlike nanofluidic channels. *Phys. Rev. Lett.*, **101**(10), 108303.

51. Strychalski, E.A. *et al.* (2012) Quantitative measurements of the size scaling of linear and circular DNA in nanofluidic slitlike confinement. *Macromolecules*, **45**(3), 1602–1611.

52. Strychalski, E.A., Stavis, S.M., and Geist, J. (2013) A localized transition in the size variation of circular DNA in nanofluidic slitlike confinement. *AIP Adv.*, **3**(4), 042115.

53. Lin, P.K. *et al.* (2007) Static conformation and dynamics of single DNA molecules confined in nanoslits. *Phys. Rev. E*, **76**(1), 011806.

54. Hsieh, C.C., Balducci, A., and Doyle, P.S. (2007) An experimental study of DNA rotational relaxation time in nanoslits. *Macromolecules*, **40**(14), 5196–5205.

55. Balducci, A., Hsieh, C.C., and Doyle, P.S. (2007) Relaxation of stretched DNA in slitlike confinement. *Phys. Rev. Lett.*, **99**(23), 238102.

56. Tang, J., Trahan, D.W., and Doyle, P.S. (2010) Coil-stretch transition of DNA molecules in slitlike confinement. *Macromolecules*, **43**(6), 3081–3089.

57. Strychalski, E.A., Levy, S.L., and Craighead, H.G. (2008) Diffusion of DNA in nanoslits. *Macromolecules*, **41**(20), 7716–7721.

58. Lin, P.K. *et al.* (2011) Partial hydrodynamic screening of confined linear and circular double-stranded DNA dynamics. *Phys. Rev. E*, **84**(3), 031917.

59. Dai, L. *et al.* (2013) Revisiting blob theory for DNA diffusivity in slitlike confinement. *Phys. Rev. Lett.*, **110**(16), 168105.

60. Pennathur, S. *et al.* (2007) Free-solution oligonucleotide separation in nanoscale channels. *Anal. Chem.*, **79**(21), 8316–8322.

61. Stavis, S.M., Strychalski, E.A., and Gaitan, M. (2009) Nanofluidic structures with complex three-dimensional surfaces. *Nanotechnology*, **20**(16), 165302.

62. Cao, H. *et al.* (2002) Gradient nanostructures for interfacing microfluidics and nanofluidics. *Appl. Phys. Lett.*, **81**(16), 3058–3060.

63. Reisner, W. (2006) *Statics and Dynamics of DNA in Nanofabricated Devices*, Princeton University.

64. Bonis-O'Donnell, J.T.D. *et al.* (2009) Pressure-driven DNA transport across an artificial nanotopography. *New J. Phys.*, **11**(7), 075032.

65. Yeh, J.-W. *et al.* (2012) Entropy-driven single molecule tug-of-war of DNA at micro-nanofluidic interfaces. *Nano Lett.*, **12**(3), 1597–1602.

66. Thomas, J.D.P. *et al.* (2013) Ratchet nanofiltration of DNA. *Lab Chip*, **13**(18), 3741–3746.

67. Fu, J.P. *et al.* (2007) A patterned anisotropic nanofluidic sieving structure for continuous-flow separation of DNA and proteins. *Nat. Nanotechnol.*, **2**(2), 121–128.

68. Persson, F. *et al.* (2009) Confinement spectroscopy: probing single DNA molecules with tapered nanochannels. *Nano Lett.*, **9**(4), 1382–1385.

69. Han, J., Turner, S.W., and Craighead, H.G. (1999) Entropic trapping and escape of long DNA molecules at sub-micron size constriction. *Phys. Rev. Lett.*, **83**(8), 1688–1691.

70. Turner, S.W.P., Cabodi, M., and Craighead, H.G. (2002) Confinement-induced entropic recoil of single DNA molecules in a nanofluidic structure. *Phys. Rev. Lett.*, **88**(12), 128103.

71. Park, S.-G., Olson, D.W., and Dorfman, K.D. (2012) DNA electrophoresis in a nanofence array. *Lab Chip*, **12**(8), 1463–1470.

72. Stavis, S.M. (2012) A glowing future for lab on a chip testing standards. *Lab Chip*, **12**(17), 3008–3011.

73. Gunther, K., Mertig, M., and Seidel, R. (2010) Mechanical and structural properties of YOYO-1 complexed DNA. *Nucleic Acids Res.*, **38**(19), 6526–6532.

74. Murade, C.U. *et al.* (2009) Interaction of oxazole yellow dyes with DNA studied with hybrid optical tweezers and fluorescence microscopy. *Biophys. J.*, **97**(3), 835–843.

75. Nyberg, L. *et al.* (2013) Heterogeneous staining: a tool for studies of how fluorescent dyes affect the physical properties of DNA. *Nucleic Acids Res.*, **41**(19), e184.

76. Baumann, C.G. *et al.* (1997) Ionic effects on the elasticity of single DNA molecules. *Proc. Natl. Acad. Sci. U.S.A.*, **94**(12), 6185–6190.

77. Stellwagen, N.C., Gelfi, C., and Righetti, P.G. (2000) DNA and buffers: the hidden danger of complex formation. *Biopolymers*, **54**(2), 137–142.

78. Iler, R.K. (1979) *The Chemistry of Silica*, John Wiley & Sons, Inc., New York.

79. Ong, S.W., Zhao, X.L., and Eisenthal, K.B. (1992) Polarization of water-molecules at a charged interface – 2nd harmonic studies of the silica water interface. *Chem. Phys. Lett.*, **191**(3–4), 327–335.

80. Vandeventer, P.E. *et al.* (2012) Multiphasic DNA adsorption to silica surfaces under varying buffer, pH, and ionic strength conditions. *J. Phys. Chem. B*, **116**(19), 5661–5670.

81. Melzak, K.A. *et al.* (1996) Driving forces for DNA adsorption to silica in perchlorate solutions. *J. Colloid Interface Sci.*, **181**(2), 635–644.

82. Isailovic, S., Li, H.W., and Yeung, E.S. (2007) Adsorption of single DNA molecules at the water/fused-silica interface. *J. Chromatogr. A*, **1150**(1–2), 259–266.

83. Allemand, J.F. *et al.* (1997) pH-dependent specific binding and combing of DNA. *Biophys. J.*, **73**(4), 2064–2070.

84. Kang, S.H., Shortreed, M.R., and Yeung, E.S. (2001) Real-time dynamics of single-DNA molecules undergoing adsorption and desorption at liquid-solid interfaces. *Anal. Chem.*, **73**(6), 1091–1099.

85. Persson, F. *et al.* (2012) Lipid-based passivation in nanofluidics. *Nano Lett.*, **12**(5), 2260–2265.

4
Microfluidic Approaches for Manipulation and Assembly of One-Dimensional Nanomaterials

Shaolin Zhou, Qiuquan Guo, and Jun Yang

4.1
Introduction

Nanowires (NWs) and nanotubes (NTs) are two major categories of one-dimensional (1D) nanomaterials that have been used to construct varieties of nanodevices with extraordinary performance and unprecedented potential in terms of sensitivity, low energy consumption and response time, and so on [1, 2]. So far, two strategies for nanostructure assembly and nanodevice fabrication are attributed to the top-down and bottom-up approaches, respectively. The conventional top-down approaches mainly comprise photolithography, E-beam lithography, focused ion beams lithography, and so on, with advantages such as mass production, accurate control over feature size, and structural geometry as well as compatibility with the other postprocessing technique and semi-conductor process, but also with limitations in material diversity and process versatility. By contrast, the bottom-up approaches offer more flexibility in materials selection and corresponding process adjustment. Conventionally, 1D nanomaterials including NWs and NTs can be synthesized by a variety of bottom-up techniques that enable to precisely and effectively control or tune the material properties including dimension, shape, elasticity, atomic composition, doping concentration, and hydrophobicity. As a result, with advantages of those assembling techniques as well as different types of NWs/NTs, varieties of 1D nanomaterial-based electronic or biological/chemical devices can be prototyped, for example, the field effect transistors, single virus detectors, and photodetectors as well as flexible electronic sensors. In this area, a reliable, low-cost, and efficient assembly method that is capable of NWs/NTs assembly with reasonable align-ment, density, uniformity, and even selective control of the NW/NT type is still challenging but essential for robust and high-quality nanodevices fabrication and integration.

To date, the bottom-up NWs/NTs assembly approaches developed by researchers can be classified by two different ways of taxonomy separately into two categories [1, 3–11]: (i) the *Deterministic assembly* and (ii) *Stochastic assembly*, or the (i) *Assembly during growth* and (ii) *Assembly after growth*. As

the name implies, *Stochastic assembly* is usually realized by dispersing the NWs in a volatile solution and drying out the NW-containing liquid droplets so that NWs are randomly distributed on a substrate, while the *Deterministic assembly* approach with higher reliability and higher yield is performed by predefining the locations, dimension, and even the specific NW/NT type. Meanwhile, the *Assembly during growth* in the second taxonomy means that NWs/NTs are usually assembled and aligned in parallel with the process of NWs/NTs synthesis/growth, for example, by prelocating the catalyst to confine the growth space of NWs [12–15], electric field-assisted seeding and growth system [16, 17], air flow-directed growth system [18, 19], or direct growth on a crystal or atomic structures-based surface [20–24], by electrospinning [25–27] or superaligning [28, 29]. Somehow, there are limited types of materials that can be directly employed by the aforementioned approaches, and the uniformity of grown NWs turns out to be relatively poor. On the contrary, the other strategy of *Assembly after growth* is able to manipulate NWs/NTs individually and assemble them into complex architectures for nanodevices fabrication in a highly controllable and flexible way. Overall, most well-known methods of controllable and deterministic 1D nanomaterial assembly are based on the *Assembly after growth* concept, including the intermolecular force-assisted assembly [30–32], electrostatic interaction-assisted assembly [33–36], assembly with magnetic fields [37–39], assembly with electric fields [40–43], shear force-assisted assembly [44–46], Langmuir–Blodgett technique [47–49], bubble-blown technique [50], assembly by contact/roll printing [51–53], the knockdown process [54], and the microflow-assisted assembly techniques [1, 11].

Particularly, those *Assembly after growth* techniques are usually performed in specific solutions and the NWs suspension is first prepared by mixing or dispersing the NWs together with the solution after certain surface modification. The NWs suspension could be further condensed or diluted to tune its concentration to certain level. The NWs settle down randomly to a substrate surface when the prepared suspension is directly deposited onto a smooth substrate, since the adhesion and reorganization are only dependent on the physical and/or chemical interactions, van der Waals forces, hydrophobic force or hydrogen bonding interactions. Therefore, if some external forces or mechanism could be employed to assist the assembly process, for example, the shear forces, electric or magnetic forces as were adopted in aforementioned deterministic assembly techniques, NWs will be reoriented by the external force and thus become aligned in accordance with the direction of external force when residing onto substrate surface. In this chapter, we focus on the process of 1D nanomaterials assembly assisted by shear force of microflow, that is, the microflow-assisted or microfluidic 1D nanomaterial manipulation and assembly, especially recent advances that are able to realize precise control of density, width, and location of assembled NWs array through combination of both fluidic shear force within the well-designed microfluidic channels and the mechanism of hydrodynamic focusing (HF).

4.2
Microfluidic Assembly

Generally, the microfluidic or micro flow-assisted assembly of NWs/NTs is carried out in such a parallel process that virtually all NWs are reoriented by shear force along the flow direction when the NWs suspensions are confined to pass through the predetermined paths of microfluidic channel, shown in Figure 4.1a. Specifically, the degree of NW assembly or surface coverage of NWs can be controlled by the flow rate and duration. For example, increased flow rate leads to substantially narrowed or focused distribution of NWs flow as well as better alignment of NWs due to larger shear force. Moreover, cross arrays or complex structures of NWs can be assembled by changing the microflow direction sequentially in a layer-by-layer process, shown in Figure 4.1b. Under certain circumstances, the substrate of microchannel can also be chemically functionalized to selectively or preferentially deposit specific types of NWs onto certain designated areas to form arrays. Results in Figure 4.2 show that InP NWs preferentially reside onto a surface functionalized with $-NH_2$ monolayer along the direction of microchannel flow. As a result, the related methodologies or design may be employed to further assemble microsystems or devices with more complex structures, that is, the guiding mechanism in "railed microfluidics" [55], programmable geometrical design [56], and so on.

In addition, for the sake of getting ordered NWs array or even single NW alignment, other mechanism or machinery can be incorporated into the microfluidic techniques to assist the NWs assembly process in a tunable and controllable manner. One alternative is the magnetic microfluidic assembly technique that

(a) Parallel array

(b) First layer Second layer Crossed array
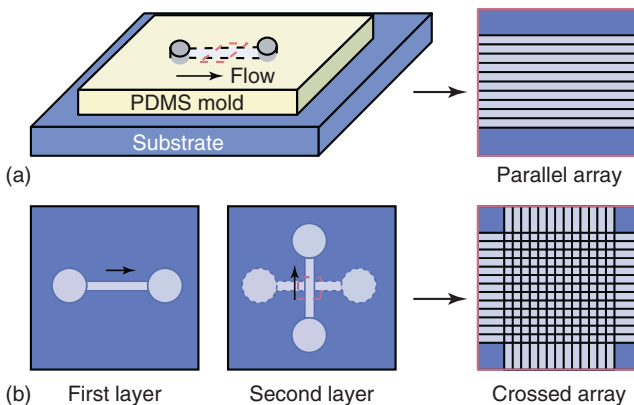
Figure 4.1 The schematic of the microfluidic technique of NWs assembly. (a) NWs are aligned in parallel within the PDMS microchannel and reside on to a flat substrate. (b) The cross NWs arrays with complex geometries are obtained with changed flow direction in a sequential layer-by-layer assembly process. (Reprinted with permission from Ref. [45]. ©2001 American Association for the Advancement of Science.)
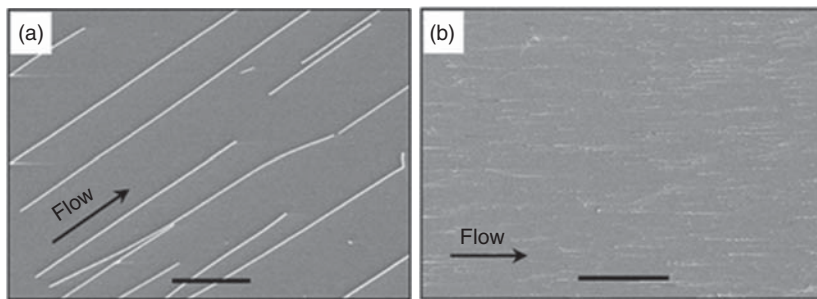
Figure 4.2 SEM images of NWs aligned in parallel along the microchannel flow by the microfluidic assembly technique. The substrates in both (a) and (b) are functionalized with NH_2-terminated monolayer for preferential deposition of InP NWs. (Reprinted with permission from Ref. [45]. © 2001 American Association for the Advancement of Science.)

introduces magnetic force into microflow to capture target iron-ended NTs onto predetermined metal pattern or uses magnetic fluids to assemble the nonmagnetic NWs suspended in the magnetic solution [1, 57]. In this chapter, we mainly focus on review of a recent advance in this area that is able to precisely position a single NW onto predetermined locations with designated orientation using the mechanism of HF, which acts as microfluidic "hydro-tweezers" to ensure parallel NWs assembly and scalable integration of NW-based devices. First of all, the mechanism, the related design, and behaviors of HF are introduced. Then, the HF-based NW(s) assembly technique is demonstrated in detail, including the basic concepts and principles, AgNWs synthesis, microfluidic channels fabrication as well as the procedure of NW(s) assembly by symmetrical and nonsymmetrical HF.

4.2.1
Hydrodynamic Focusing

4.2.1.1 Concept and Mechanism

HF is a common microfluidic technique that has been intensively used in a variety of applications for chemical/biological analyses, such as flow cytometry including on-chip flow cytometry [58], single-molecule detection and measurement [59], and laminar mixers [60]; microfluidic optical waveguides [61]; fluorescent light sources [62]; flow switch [63]; and generation of microdroplets and bubbles [64, 65].

Figure 4.3 shows the schematic of a HF device with inner nozzle jointed to the middle of the outer nozzle [66, 67]. The sample flow Q_i is constrained laterally at the center of the microchannel and sandwiched by two neighboring sheath flows from the side channels. The flow inside microfluidic channel is assumed to be laminar due to negligible diffusion and mixing between the focused stream and sheath. The sample flows Q_i are then stably wrapped in-between two sheath flows Q_{s1} and Q_{s2}, so that a stable two-phase flow configuration can be maintained in
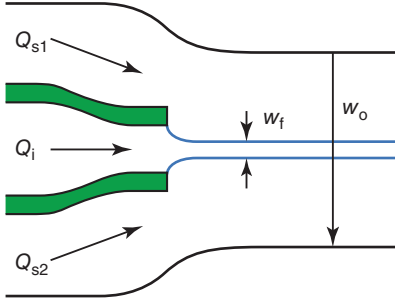
Figure 4.3   The schematic of hydrodynamic focusing device. Q_i is the volumetric sample flow rate; Q_{s1} and Q_{s2} are the volumetric flow rates of two sheath flows; w_f and w_o are the widths of the focused stream and the outlet channel, respectively.

HF devices. According to the mass conservation law, the relationship between the width of the hydrodynamically focused stream (w_f) and the volumetric flow rates of the inlet channel (Q_i) and the side channels (Q_{s1} and Q_{s2}) can be expressed as

$$\frac{w_e}{w_o} = \frac{Q_i}{\gamma(Q_i + Q_{s1} + Q_{s2})} \tag{4.1}$$

where the velocity ratio is $\gamma = v_f/v_o$, w_o is the width of the outlet channel, and v_f and v_o are the average flow rate of the focused stream and the flow in the outlet channel, respectively. Therefore, the width of the focused stream (w_f) turns out to be controllable through adjustment of flow ratio of the sheath flow with regard to the sample flow, that is, the sample stream gradually broaden out along with lower flow ratio, while the focused stream narrow down along with increased flow ratio.

Typically, the commonly used HF techniques in applications mentioned above can be generally classified into two categories: (i) multiphase flow focusing (i.e., liquid–liquid or liquid–gas) and (ii) liquid single-phase flow focusing. Further, they can be classified into two-dimensional (2D) and three-dimensional (3D) HF by architecture or the *symmetrical focusing* and *asymmetric focusing* by symmetry.

4.2.1.2   **2D and 3D Hierarchy**

Traditionally, the HF devices are developed and intensively applied in a 2D assembly. Figure 4.4 shows the typical 2D HF design. Figure 4.4a shows a HF chamber of microfluidic cytometer fabricated by hot embossing. Figure 4.4b shows stably focused sample flow is obtained when an appropriate relative sheath and sample flow rate is applied. However, the planar nature of 2D microfluidic architecture fabricated by the conventional polydimethylsiloxane (PDMS) soft lithography limits the HF within the 2D device plane by horizontally compressing the inner sample flow into a thin "sheet" between two sheath flows that are injected from both sides of the sample flow. Consequently, there arises an inability to focus the sample flow vertically or in the out-of-plane direction, or the third dimension. For example, in the application of planar microflow cytometers for cell/particle counting, the cells or particles may not be able to pass the focused stream one by one even though the stream width is focused to the same order of the cell size, but not the out-of-plane direction. In this situation, the approach to solve this issue happened in 2D HF devices is the 3D HF, that is, the 3D hierarchy design.
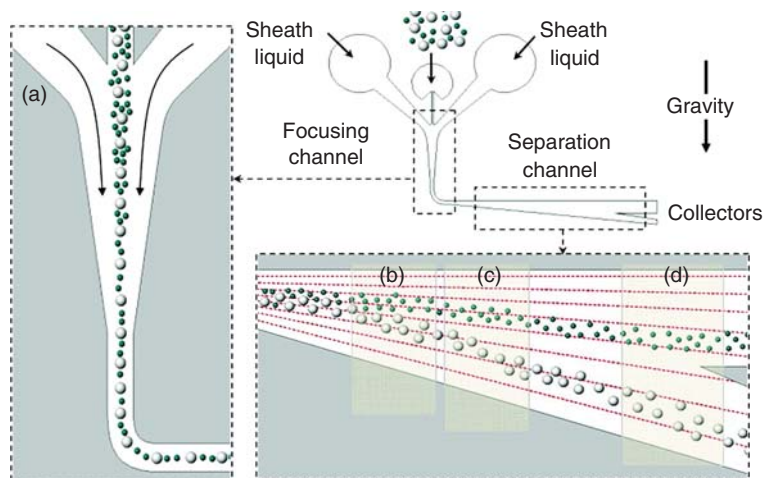
Figure 4.4 A typical 2D hydrodynamic focusing setup for particle sorting. (a) The 2D-designed chamber for hydrodynamic focusing and focused sample flow by the side sheath flows and (b–d) separated sample flow in subsequent channel. (Reprinted with permission from Ref. [68]. © 2007 American Chemical Society.)

Recently, the 3D HF hierarchy with complex architecture has been frequently used and fabricated by conventional microfabrication technologies. Reference [68] reported a typical design of HF in 3D hierarchy, in which vertical focusing can be accomplished with a two-level design for the microfluidic channels. In that 3D hierarchy, the sample stream enters only into the bottom layer, while low-conductivity buffer enters from another channel that is wider and taller than the sample stream. Low-conductivity buffer forms a sheath flow around the top and side part of the outlet channel, forcing the sample into a narrow stream at the bottom of the channel adjacent to the electrodes (see Figure 4.5).

In addition, another strategy aims to decrease the device fabrication and integration complexity and yet enable the HF in a single layer of planar microfluidic device by a novel fluid manipulation technique termed as *microfluidic drifting* [70]. Overall, the device is formed by four inlets for sample and sheath flows, one outlet, and a 90° curved joint. The 3D HF hierarchy is achieved sequentially by a two-step process. The first step aims at focusing the sample flow downstream vertically by the mechanism of microfluidic drifting, which also refers to the lateral drift of the sample flow. In this way, the ultimate cross-sectional profile of the drifted sample flow at the exit of curve channel is then determined by the flow rate. Specifically, the degree of lateral drift of the sample flow is determined by the flow rates of both vertically focused sheath flow and sample flow, as well as the compression ratio in the vertical direction that can be controlled by the flow rate ratio of vertically focused sheath flow over the sample flow. During the experimental process, the sample flow drifts laterally to the opposite side of the channel when it passes through the curved microfluidic channel due to by the transverse
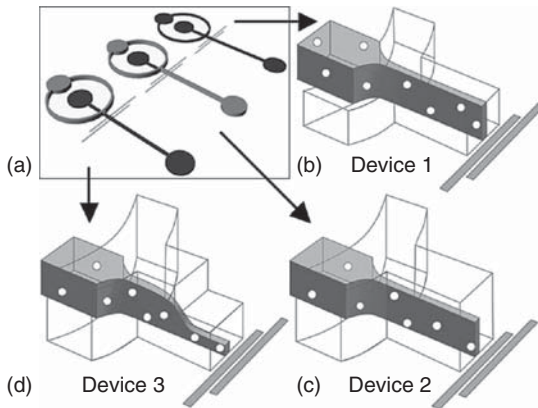
Figure 4.5 (a) The typical 3D hierarchy of hydrodynamic focusing setup for cytometry. Dark gray regions are thin (typically 90 μm) and light gray regions are tall (typically 200 μm). (b) 2D focused flow device 1, showing a ribbon of particle-laden fluids crossing the sensing electrodes. (c) 2D focused flow device 2, which has a tall outlet channel. (d) 3D focused flow in device 3 is caused by stepping the outlet channel back down to the lower level. (Reprinted with permission from Ref. [69]. © 2008 AIP Publishing LLC.)
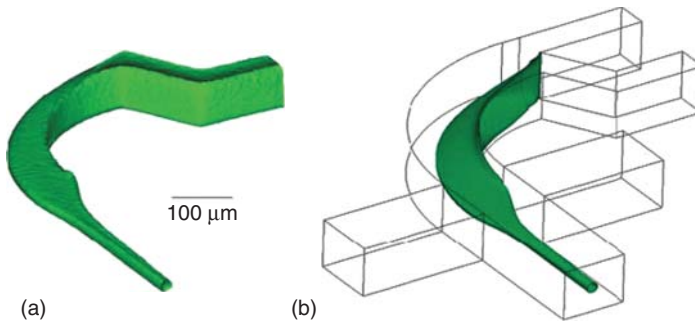
Figure 4.6 The 3D hierarchy of "microfluidic drifting" technique for hydrodynamic focusing. (a) The architecture by confocal microscopy and (b) the CFD simulated result. (Reprinted with permission from Ref. [70]. © Royal Society of Chemistry 2007.)

secondary flow induced by the centrifugal force. The sample flow reaches its maximum at the exit of the curved joint. Right at this point, the flow starts to be compressed by the horizontally focused sheath flows. Figure 4.6 shows the simulation result of 3D focused sample flow obtained by the computational fluid dynamic (CFD) method, and the microfluidic drifting around the curve joint is demonstrated. As a result, this effective and robust 3D HF method is able to tune the cross-sectional widths of the vertically and horizontally focused flow in two directions as well as the horizontal shift in an easy-to-implement way.

4.2.1.3 Symmetrical and Asymmetrical Behavior

Fundamentally, two types of behaviors exist for HF according to the flow symmetry: symmetrical focusing and asymmetrical focusing, shown in Figure 4.7.
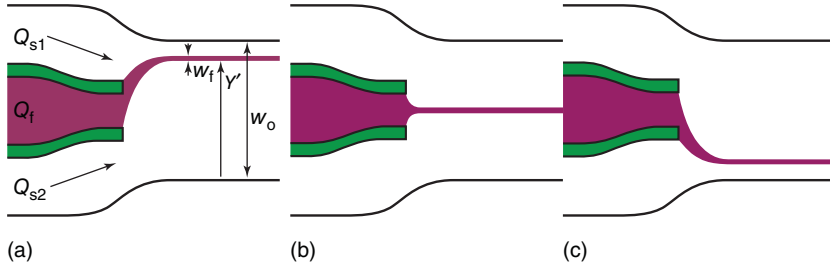
Figure 4.7 Two types of hydrodynamic focusing. (a) Asymmetric hydro-tweezers created by unequaling sheath flows; (b) symmetric hydrodynamic focusing caused by sheath flows with the same flow rate; and (c) the other working state of asymmetric hydro-tweezers. (Reprinted with permission from Ref. [11]. © 2011 IOP Publishing Ltd.)

Specifically, shown in Figure 4.7a, in the 2D asymmetric HF technique, the sample flow (supplied from the inlet channel) is constrained by two unequal sheath flows, that is, sheath flows with different volumetric flow rates. In symmetric HF, shown in Figure 4.7b, the sample flow is constrained laterally at the center of the microchannel sandwiched by two neighboring sheath flows from the side channels with the same volumetric flow rate.

In other words, the mechanism of HF is equivalent to that of hydro-tweezers, where two sheath flows act as the two "blades." In the symmetric mode of operation, the hydro-tweezers can be opened up and closed down by adjusting the flow ratio of the sheath flow against the sample flow; for example, when the flow ratio is high, the focused stream narrow down until the hydro-tweezers close. In the asymmetric mode, the hydro-tweezers are movable by balancing the flow rate of two sheath flows; for example, when one "blade" becomes stronger to surpass the other one, the focused stream will be pushed away from the increased sheath flow, resulting in the movement of hydro-tweezers, shown in Figure 4.7a,c. The widths of sample flow and sheath in both behaviors can be predicted from Eq. (4.1) and the following equation:

$$\frac{Y'}{w} = \frac{Q_{s2}}{\gamma'(Q_i + Q_{s1} + Q_{s2})} \tag{4.2}$$

where Y' denotes position of one sheath flow in the outlet channel, shown in Figure 4.7a. As a result, the widths of sample flow and two sheath flows are determined by the ratio of individual flow rate to the overall flow rate, and the two states of symmetrical and asymmetrical HF could be directly switched by adjusting the flow rate.

4.2.2
HF-Based NW Assembly

4.2.2.1   The Principle
HF mentioned earlier is one of the most frequently utilized techniques in microfluidics. The fact that stable and laminar microflow usually occurs at low Reynolds

number (Re) enables HF for efficient NWs assembly. In a typical HF process for NW assembly, NWs are injected to produce a suspension sample flow and DI water without NWs are used as sheath flows. When the sample flow carrying NWs is squeezed by two sheath flows into a narrow tube at a constant velocity, moving NWs are gradually forced to deposit on substrate surface with high accuracy and throughput. This is the basis of this chapter. When sample flow containing NWs is hydrodynamically focused by the sheath flows, the focused width can be tuned by the flow ratio R ($R = (Q_{s1} + Q_{s2})/Q_i$), and the position can be tuned by flow share R' ($R' = Y'/w_o$, see Figure 4.7a). Sometimes, the substrate is chemically treated so that NWs in the sample flow can preferentially reside onto the treated area. The shear force of microflow compels NWs to be aligned along the flow direction before immobilized on the substrate. Since NWs are only injected into the sample flow, only the focused stream could induce NW coating underneath. The width, density, and positions of the NW array can be controlled by changing and adjusting the working state of HF.

4.2.2.2 Device Design and Fabrication

Preparation or growth of NWs is the first step for microfluidic assembly of 1D nanomaterial. Hereinto, AgNWs are synthesized first and chosen as example NWs in the microfluidics-based HF assembly process due to their high electrical and thermal conductivity as well as the relatively high yields, good dispersion, and uniformity during the synthesis of NWs. Further, AgNWs have been one of the most widely exploited materials for applications ranging from catalysis and electronics to photonics and photography.

Here, AgNWs are synthesized for assembly during a solution-based process by reducing $AgNO_3$ with EG (ethylene glycol, HO14CH214CH2OH, Sigma-Aldrich) when PVP (polyvinylpyrrolidone, Sigma-Aldrich) injected into the refluxed EG. The first is to introduce growth seeds into the reaction mixture, that is, when silver nitrate is reduced in the presence of the seeds, silver nanoparticles (NPs) with a bimodal size distribution that are formed through heterogeneous and homogeneous nucleation serve as seeds for subsequent AgNWs growth. During the second stage, high-aspect-ratio AgNWs with uniform diameters are synthesized in a self-seeding process using PVP as the coordination reagent and the seeds of silver NPs formed before. Evolution of silver into anisotropic nanostructures within a highly isotropic medium is affected by several factors: (i) molar ratio of PVP to $AgNO_3$; (ii) refluxing temperature; (iii) injection rate for the solution; and so on. Figure 4.8 shows one type of long NWs with a diameter of 100 ± 5 nm and a length of ~15 μm.

For device fabrication, both the conventional photolithography and soft lithography processes using PDMS (Sylgard 184 silicone elastomer kit, Dow Corning Corporation) are employed for microfluidic channel or devices prototyping, shown in Figure 4.9. First, the master or mold with designed structure of microchannels is fabricated on SU-8 in a UV photolithographic process. The typical procedure mainly includes (i) wafer preparation by thorough rinsing, drying, and coating with HDMS; (ii) spin-coating resist of SU-8; (iii) soft baking;
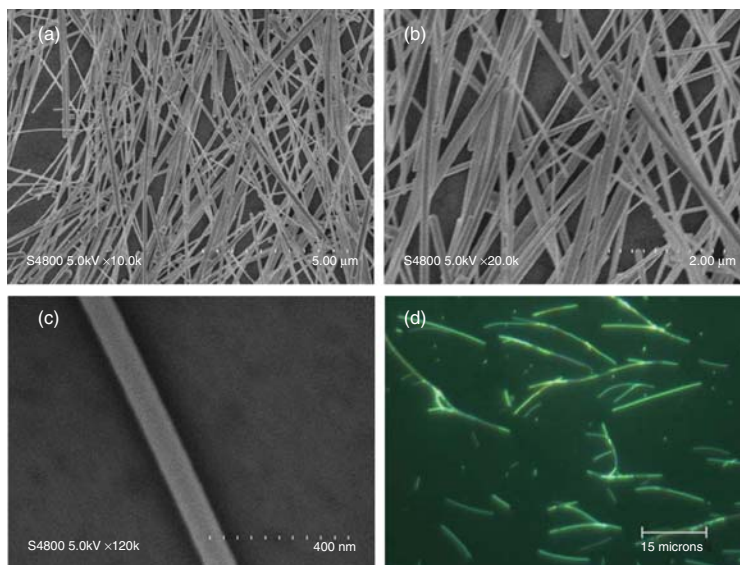
Figure 4.8 Synthesized long AgNWs under different magnifications with SEM and optical microscope.
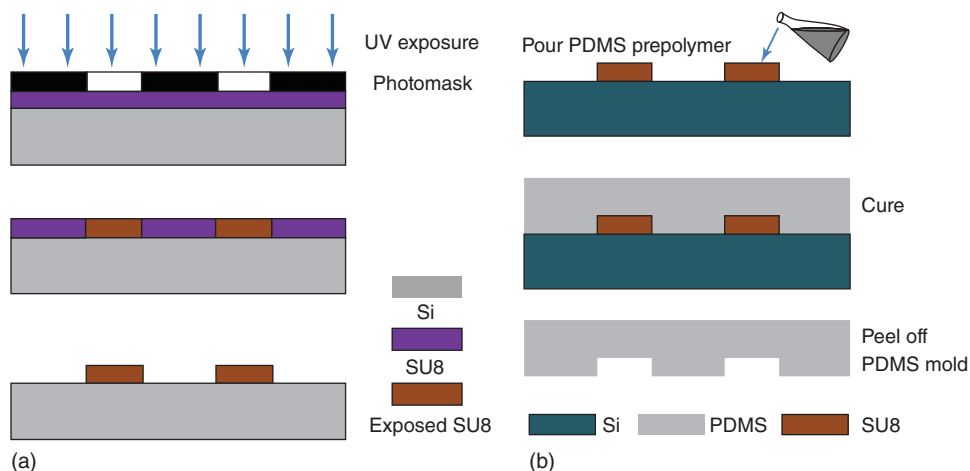
Figure 4.9 The typical procedure of photolithography and soft lithography for microfluidic devices fabrication. (a) Mold fabrication by photolithography and (b) mold transfer during a soft lithographic process.

(iv) UV exposure using a mask aligner; (v) post baking; (vi) development; and (vii) hard baking. Then the microfluidic channels for HF are fabricated in a mold transfer process by soft lithography, shown in Figure 4.9b. First PDMS is prepared by mixing precursor and curing agent in ratio of 10 : 1. Then, the PDMS is poured onto mold structure after degassing. When completely cured,
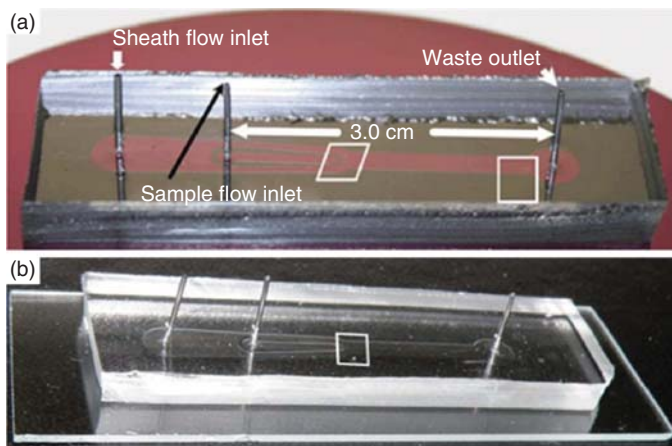
Figure 4.10 The fabricated hydrodynamic focusing device on a silicon substrate.

the PDMS structures replicated from the mold are released. Finally, holes are punched and tubes are inserted to make the inlet and outlet. Figure 4.10 shows the fabricated microfluidic devices for HF on silicon/glass substrate.

4.2.2.3 NW Assembly by Symmetrical Hydrodynamic Focusing

Before started, the AgNWs suspensions are prepared first by mixing NWs with pure ethanol solution. For efficient and selective assembly of NWs, the microfluidic device also needs to be treated with 3-aminopropyltriethoxysilane (APTES) to functionalize the cleaned surface with an NH_2-terminated monolayer. One specific recipe in recent advance is pumping 1 mM alcohol solution of 3-APTES (Sigma-Aldrich) and leaving for 10 h, followed by heating the device at 120 °C for 10 min [11, 67].

For assembly by both the symmetrical and asymmetrical HF, the AgNWs solution is diluted in advance as needed and checked for uniformity. Therefore, the symmetrical HF can be performed in such a way that the ethanol suspension dispersed with NWs is injected from the center channel as the sample flow, and DI water is injected into the outer channel as the sheathing "blades." A typical schematic of symmetrical HF is shown in Figure 4.3. Two sheath flows that sandwich the sample flow have the same volumetric flow rate. The sample flow is then focused hydrodynamically into a narrow stream constrained by water flows from the sheath channels, as can be seen in the experimental setup in Figure 4.10. The volumetric flow rates of the sample flow and sheath flows are generally controlled by two external pumps. The flow width is controllable by adjusting the ratio of sample flow rate over sheath flow rate. The pressure is always maintained to be constant at the outlet to keep flow stable by immersing the outlet at the bottom of water. To achieve a steady and uniform AgNWs distribution onto the substrate, the focused sample velocity is usually fixed at a certain value.

Table 4.1 Three recipes of NWs assembly by symmetrical hydrodynamic focusing.

Flow protocol	Sheath flow $(Q_{s1} + Q_{s2})$(ml h^{-1})	Sample flow Q_i (ml h^{-1})	Flow rate ratio R	$r = w_f/w_o$	Focused width (μm)	Flow duration (min)
1	1.5	0.06	25	0.038	92.3	40
				0.036	86	
2	1.75	0.05	35	0.028	66.7	40
				0.027	65	
3	2.0	0.04	50	0.020	47.1	40
				0.021	51.1	

The upper rows in columns 5 and 6 show the theoretical data obtained from Eq. (4.1), while the bottom rows in columns 5 and 6 were obtained from experiments.
Reprinted with permission from Ref. [11]. © 2011 IOP Publishing Ltd.

To start the experiment, the focused stream is adjusted and maintained at a constant value of velocity, and the AgNWs are then forced to follow the flow direction and some AgNWs gradually reside on the substrate due to the interaction between AgNWs and the treated substrate surface. Shear force exerted on AgNWs is the driving force to align AgNWs along the flow direction before immobilized on the substrate surface. Table 4.1 lists three examples of protocols during the experiment of symmetrical HF cited from the Refs. [11, 67]. Figure 4.11 shows the optical microscopic images of three states and results of NWs assembly corresponding to the protocols listed in Table 4.1.

Obviously, it can be observed from results in Table 4.1 and Figure 4.11 that when the sheath flow rate increases over that of the sample flow, that is, the flow ratio R increases, the width of focused sample flow decreases accordingly, namely the focused sample stream becomes narrowed and the hydro-tweezers shrunk. Results also suggest that the focused stream could be scaled up to be as wide as the size of the outlet channel when $R \to 0$, and further down to ∼0.02% of the outlet channel size when R is adjusted to be around 120. Figure 4.12 shows the relationship between theoretically predicted and experimentally recorded values of the normalized width of focused sample stream r and the flow rate ratio of the sheath flow over the sample flow R. In addition, the width of focused sample flow can be also determined as a function of the size of the outlet channel w_o according to Eq. (4.1). The further decreased w_o accordingly leads to further focused sample flow as well as the decreased width of the NW pattern, which is the basic mechanism for single NW assembly by HF. Besides, experimental results in Figure 4.13 also indicate that the AgNWS pattern with varied density can be obtained by controlling the flow duration.

4.2.2.4 NW Assembly by Asymmetrical Hydrodynamic Focusing

In principle, asymmetrical HF is realized by the two sheath flows with unequal flow rates, shown in Figure 4.14. Similarly as the symmetrical HF, the NWs suspension of sample flow is input from the middle channel, while two fluids are separately injected as sheath flows from two sides. The sample flow dispersed with
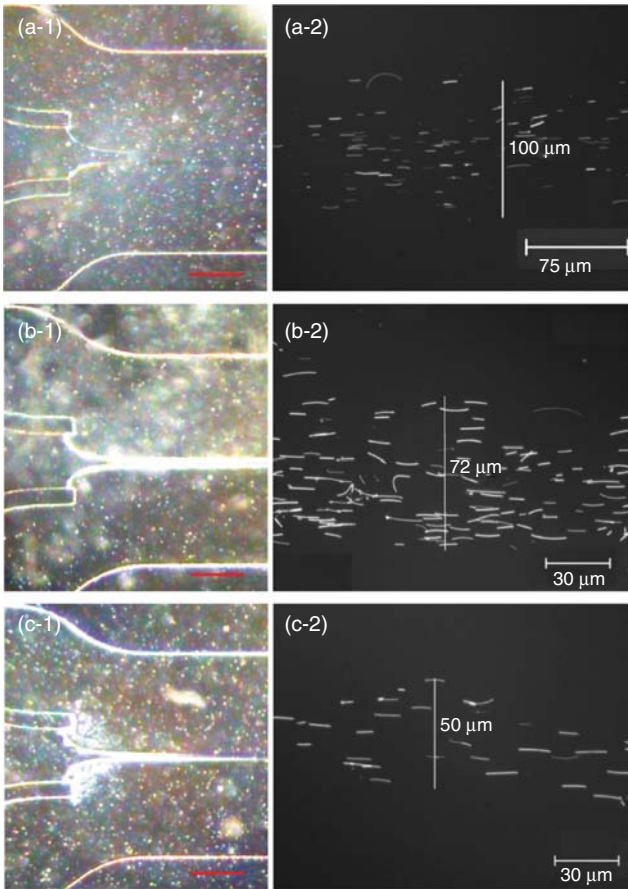
Figure 4.11 Microscopic images of three states of symmetrical hydrodynamic focusing in Table 4.1 and the results of NWs patterns assembled on substrate. (a-1) and (a-2) The state of protocol 1 and corresponding AgNWs pattern on the substrate. (b-1) and (b-2) The state of protocol 2 and its AgNWs result. (c-1) and (c-2) The state of protocol 3 plus the AgNWs assembly result. The scale bar in the flow figures (a-1), (b-1), and (c-1) is 600 µm. The outlet channel width $w_o = 2.4$ mm. (Reprinted with implied permission from Ref. [11]. © 2011 IOP Publishing Ltd.)

NWs is then hydrodynamically focused by two offset sheath flows, and the focused flow width can be tuned by the flow ratio of sheath flows over sample flow. The different point is that the focused flow can be displaced and the position can be dynamically tuned by the flow ratio of two sheath flows. Laminar flow is another essential point to the asymmetrical HF as turbulence may occur to induce mixing between the sample flow and sheath flows. The nature of the flow totally depends on the Reynolds number. In the flows for NWs assembly, the Reynolds number is usually less than unity, which indicates that the dominant condition is laminar flow. Therefore, the two sheath flows are adjusted to displace the focused stream
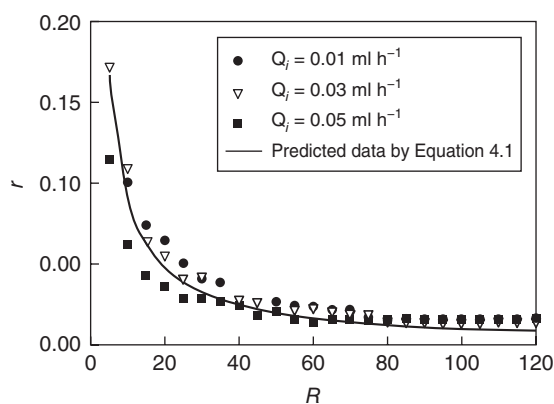
Figure 4.12 Experimental and theoretical data of the normalized width of the focused stream $r = w_f/w_o$ with respect to the flow rate ratio R. (Reprinted with implied permission from Ref. [11]. © 2011 IOP Publishing Ltd.)
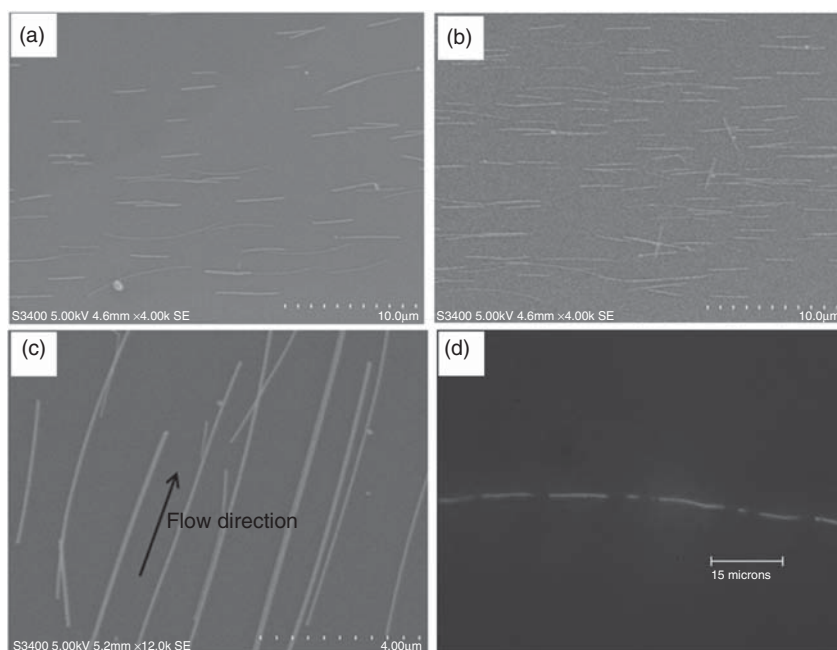
Figure 4.13 SEM-characterized results of assembled AgNWs patterns with different density. (a) The pattern was obtained with 20-min flow duration. (b) The pattern was obtained with 40-min flow duration. (c) Well-aligned local AgNWs arrays. (d) The single NW assembled on the substrate surface.
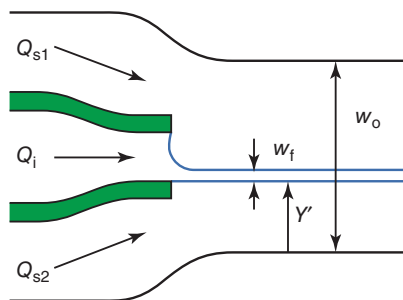
Figure 4.14   The schematics of asymmetric hydrodynamic focusing for NWs assembly.

across the microchannel section and the NWs in the sample can be forced to follow the differently defined streamlines along the flow direction in a similar way as the symmetrical HF process. However, AgNWs carried in the sample stream can be coated on in a series of discrete wide lanes with certain distance apart from each other.

Similarly, the substrate surface is chemically treated so that NWs in the sample flow can be preferentially deposited on it. Shear force in the flow is also the driving force to align the NWs in the flow direction before they are immobilized on the substrate. As one sheath flow rate becomes higher than the other one, it squeezes both the sample flow and the other sheath flow to spatially tune their width. Similarly, the width of the focused stream is directly determined by the ratio of relative flow rate of the sample flow to the sum of both sheath flows, and its position is determined and balanced by two focusing flows. Table 4.2 lists four typical recipes of protocols in the experiment of asymmetric HF, and Figure 4.15 shows the corresponding states of asymmetrical HF with the sample flow displaced at different positions by two sheath flows with different ratio and the total flow rate fixed at $2.25 \, \text{ml h}^{-1}$. In addition, since the position of the focused stream is directly determined by the sheath flow ratio, the patterned AgNWs can be assembled at different

Table 4.2   Four recipes of NWs assembly by the asymmetrical hydrodynamic focusing.

Flow steps	Sheath flow Q_{s1} (ml h^{-1})	Sheath flow Q_{s2} (ml h^{-1})	Sample flow Q_i (ml h^{-1})	R	$r = w_f/w_o$	Focused width (µm)	$R' = r'$	Y' (µm)	Flow duration (min)
1	0.25	2	0.2	11.25	0.082	82	0.82	820	20
					0.076	76	0.81	810	
2	0.75	1.5	0.2	11.25	0.082	82	0.61	610	20
					0.075	75	0.61	610	
3	1.5	0.75	0.2	11.25	0.082	82	0.31	310	20
					0.075	75	0.32	320	
4	2	0.25	0.2	11.25	0.082	82	0.10	100	20
					0.077	77	0.10	100	

Note: the upper rows in columns 6−9 show the theoretical predictions in Eq. (4.2), while the bottom rows in columns 6−9 are experimental results.
Reprinted with permission from Ref. [11] © 2011 IOP Publishing Ltd.
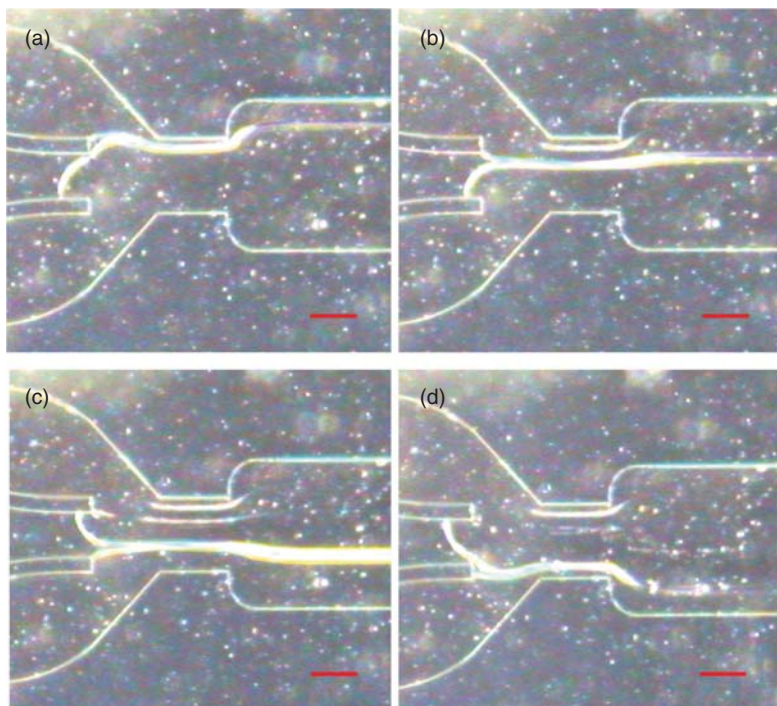
Figure 4.15 Several states of asymmetric hydrodynamic focusing for multiple AgNWs stripe assembly, corresponding to recipes listed in Table 4.2. Figures (a–d) correspond to flow-tuning steps of 1–4, respectively. The scale bar in the flow figures is 300 μm. The outlet channel width $w_o = 1.0$ mm. (Reprinted with permission from Ref. [11]. © 2011 IOP Publishing Ltd.)

locations across the microchannel, so that the density, position, and width of the AgNWs array are all controllable. Figure 4.16 shows arrays of AgNWs horizontally assembled at different level across the microchannel by the asymmetric HF method.

4.3
Summary

Robust and controllable assembly of 1D nanomaterial is promising as a bottom-up approach for high-quality nanodevices fabrication and integration. So far, a variety of strategies have been employed for the sake of assembly of different types of NWs/NTs with reasonable control of alignment, density, uniformity, and even selective control of the material type. Further, most of the current approaches are based on the assembly after growth strategies that aim to align the synthesized NWs/NTs by resorting to certain mechanism or external force. Among them is one attractive type of microflow-assisted 1D nanomaterial assembly technique
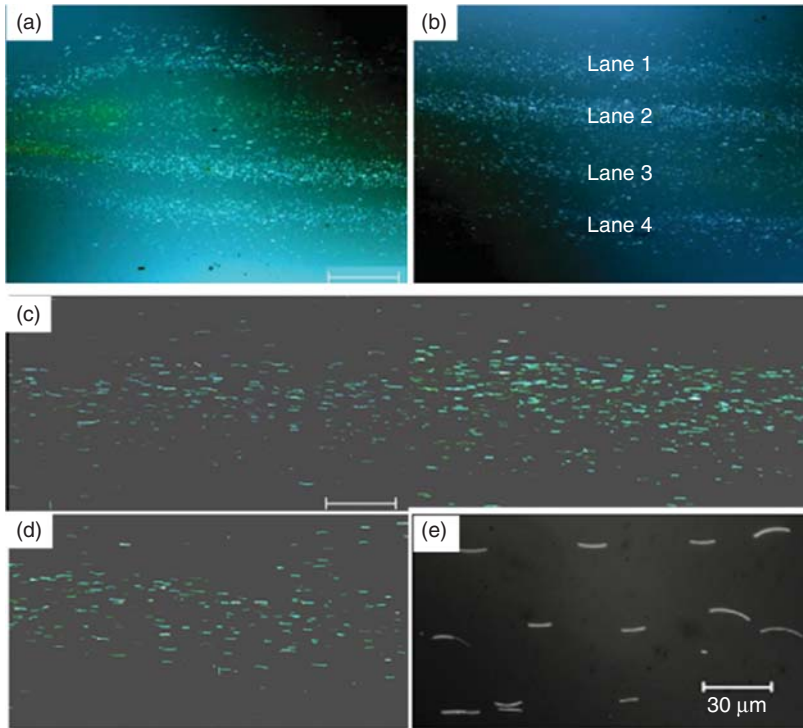
Figure 4.16 Arrays of AgNWs assembled by the asymmetric hydrodynamic focusing. (a) The AgNWs assembled by sample flow offset from each other. (b) The AgNWs stripes down the microchannel. Scale bar in (a) and (b) is 150 μm. (c) Lane 1 in (b); (d) Lane 2 in (b); and (e) single AgNWs separately deposited on predefined lines of the substrate. (Reprinted with permission from Ref. [11] © 2011 IOP Publishing Ltd.)

based on the mechanism of HF. This chapter provides a brief introduction on present NWs assembly routes and focuses on one promising microfluidic assembly technique that utilizes the mechanism of HF. As a result, the HF NWs assembly technique that is able to align both large-scale NW arrays and single lines of NWs in a controllable, efficient, and cost-effective manner may pave a new way for potential applications such as massive production/fabrication of nanoelectronics, nanoelectromechanical systems (NEMSs), biosensors, and material science.

References

1. Wang, M.C.P. and Gates, B.D. (2009) Directed assembly of nanowires. *Mater. Today*, **12**, 34–43.
2. Liu, M., Wu, Z., Lau, W.M., and Yang, J. (2012) Recent advances in directed assembly of nanowires or nanotubes. *Nano-Micro Lett.*, **4**, 142–153.
3. Long, Y.Z., Yu, M., Sun, B., Gu, C.Z., and Fan, Z. (2012) Recent advances in large-scale assembly of semiconducting inorganic nanowires and nanofibers for

electronics, sensors and photovoltaics. *Chem. Soc. Rev.*, **41**, 4560–4580.

4. Liu, X., Long, Y.Z., Liao, L., Duan, X., and Fan, Z. (2012) Large-scale integration of semiconductor nanowires for high performance flexible electronics. *ACS Nano*, **6**, 1888–1900.

5. Fan, Z., Ho, J.C., Takahashi, T., Yerushalmi, R., Takei, K., Ford, A.C., Chueh, Y.L., and Javey, A. (2009) Toward the development of printable nanowire electronics and sensors. *Adv. Mater.*, **21**, 3730–3743.

6. Huang, L., Jia, Z., and O'Brien, S. (2007) Orientated assembly of single-walled carbon nanotubes and applications. *J. Mater. Chem.*, **17**, 3863–3874.

7. Erdem Alaca, B. (2009) Integration of one-dimensional nanostructures with microsystems: an overview. *Int. Mater. Rev.*, **54**, 245–282.

8. Liu, Z., Jiao, L., Yao, Y., Xian, X., and Zhang, J. (2010) Aligned, ultralong single-walled carbon nanotubes: from synthesis, sorting, to electronic devices. *Adv. Mater.*, **22**, 2285–2310.

9. Zhou, X., Boey, F., and Zhang, H. (2011) Controlled growth of single-walled carbon nanotubes on patterned substrates. *Chem. Soc. Rev.*, **40**, 5221–5231.

10. Ma, Y., Wang, B., Wu, Y., Huang, Y., and Chen, Y. (2011) The production of horizontally aligned single-walled carbon nanotubes. *Carbon*, **49**, 4098–4110.

11. Liu, M., Chen, Y., Guo, Q., Li, R., Sun, X., and Yang, J. (2011) Controllable positioning and alignment of silver nanowires by tunable hydrodynamic focusing. *Nanotechnology*, **22**, 125302.

12. Chai, J., Wang, D., Fan, X., and Buriak, J.M. (2007) Assembly of aligned linear metallic patterns on silicon. *Nat. Nanotechnol.*, **2**, 500–506.

13. Messer, B., Song, J.H., and Yang, P. (2000) Microchannel networks for nanowire patterning. *J. Am. Chem. Soc.*, **122**, 10232–10233.

14. Shan, Y. and Fonash, S.J. (2008) Self-assembling silicon nanowires for device applications using the nanochannel-guided "grow-in-place" approach. *ACS Nano*, **2**, 429–434.

15. Shan, Y., Kalkan, A.K., Peng, C.Y., and Fonash, S.J. (2004) From Si source gas directly to positioned, electrically contacted Si nanowires: the self-assembling "grow-in-place" approach. *Nano Lett.*, **4**, 2085–2089.

16. Cheng, C., Gonela, R.K., Gu, Q., and Haynie, D.T. (2005) Self-assembly of metallic nanowires from aqueous solution. *Nano Lett.*, **5**, 175–178.

17. Zhang, Y., Chang, A., Cao, J., Wang, Q., Kim, W., Li, Y., Morris, N., Yenilmez, E., Kong, J., and Dai, H. (2001) Electric-field-directed growth of aligned single-walled carbon nanotubes. *Appl. Phys. Lett.*, **79**, 3155–3157.

18. Huang, S., Cai, X., and Liu, J. (2003) Growth of millimeter-long and horizontally aligned single-walled carbon nanotubes on flat substrates. *J. Am. Chem. Soc.*, **125**, 5636–5637.

19. Wang, X., Li, Q., Zheng, G., Ren, Y., Jiang, K., and Fan, S. (2010) Selective fabrication of quasi-parallel single-walled carbon nanotubes on silicon substrates. *Nanotechnology*, **21**, 395602.

20. Ding, L., Tselev, A., Wang, J., Yuan, D., Chu, H., McNicholas, T.P., Li, Y., and Liu, J. (2009) Selective growth of well-aligned semiconducting single-walled carbon nanotubes. *Nano Lett.*, **9**, 800–805.

21. Xiao, J., Dunham, S., Liu, P., Zhang, Y., Kocabas, C., Moh, L., Huang, Y., Hwang, K.C., Lu, C., and Huang, W. (2009) Alignment controlled growth of single-walled carbon nanotubes on quartz substrates. *Nano Lett.*, **9**, 4311–4319.

22. Chen, J., Gao, F., Zhang, L., and Huang, S. (2009) Catalyst-free growth of oriented single-walled carbon nanotubes on mica by ethanol chemical vapor deposition. *Mater. Lett.*, **63**, 721–723.

23. Wu, H., Chen, L., and Tsai, C. (2006) Self-assembled epitaxial silicon nanowires grown along easy-glide directions on Si (001). *Micro Nano Lett.*, **1**, 25–28.

24. Cui, R., Zhang, Y., Wang, J., Zhou, W., and Li, Y. (2010) Comparison between copper and iron as catalyst for chemical vapor deposition of horizontally aligned ultralong single-walled carbon nanotubes on silicon substrates. *J. Phys. Chem. C*, **114**, 15547–15552.

25. Yan, H., Liu, L., and Zhang, Z. (2009) Alignment of electrospun nanofibers using dielectric materials. *Appl. Phys. Lett.*, **95**, 143114.

26. Kim, G.H. and Kim, W.D. (2006) Formation of oriented nanofibers using electrospinning. *Appl. Phys. Lett.*, **88**, 233101.

27. Bazbouz, M.B. and Stylios, G.K. (2008) Alignment and optimization of nylon 6 nanofibers by electrospinning. *J. Appl. Polym. Sci.*, **107**, 3023–3032.

28. Xiao, L., Zhang, Y., Wang, Y., Liu, K., Wang, Z., Li, T., Jiang, Z., Shi, J., Liu, L., and Li, Q.Q. (2011) A polarized infrared thermal detector made from superaligned multiwalled carbon nanotube films. *Nanotechnology*, **22**, 025502.

29. Jiang, K., Wang, J., Li, Q., Liu, L., Liu, C., and Fan, S. (2011) Superaligned carbon nanotube arrays, films and yarns: a road to applications. *Adv. Mater.*, **23**, 1154–1161.

30. Lee, J., Wang, A.A., Rheem, Y., Yoo, B., Mulchandani, A., Chen, W., and Myung, N.V. (2007) DNA assisted assembly of multisegmented nanowires. *Electroanalysis*, **19**, 2287–2293.

31. Mbindyo, J.K.N., Reiss, B.D., Martin, B.R., Keating, C.D., Natan, M.J., and Mallouk, T.E. (2001) DNA-directed assembly of gold nanowires on complementary surfaces. *Adv. Mater.*, **13**, 249–254.

32. Kovtyukhova, N.I. and Mallouk, T.E. (2002) Nanowires as building blocks for self-assembling logic and memory circuits. *Chem. Eur. J.*, **8**, 4354–4363.

33. Myung, S., Lee, M., Kim, G.T., Ha, J.S., and Hong, S. (2005) Large-scale "surface-programmed assembly" of pristine vanadium oxide nanowire-based devices. *Adv. Mater.*, **17**, 2361–2364.

34. Heo, K., Cho, E., Yang, J.E., Kim, M.H., Lee, M., Lee, B.Y., Kwon, S.G., Lee, M.S., Jo, M.H., and Choi, H.J. (2008) Large-scale assembly of silicon nanowire network-based devices using conventional microfabrication facilities. *Nano Lett.*, **8**, 4523–4527.

35. Kang, J., Myung, S., Kim, B., Oh, D., Kim, G.T., and Hong, S. (2008) Massive assembly of ZnO nanowire-based integrated devices. *Nanotechnology*, **19**, 095303.

36. Lee, M., Im, J., Lee, B., Myung, S., Kang, J., Huang, L., Kwon, Y.K., and Hong, S. (2006) Linker-free directed assembly of high-performance integrated devices based on nanotubes and nanowires. *Nat. Nanotechnol.*, **1**, 66–71.

37. Hangarter, C., Rheem, Y., Yoo, B., Yang, E., and Myung, N. (2007) Hierarchical magnetic assembly of nanowires. *Nanotechnology*, **18**, 205305.

38. Hangarter, C.M. and Myung, N.V. (2005) Magnetic alignment of nanowires. *Chem. Mater.*, **17**, 1320–1324.

39. Yoo, B., Rheem, Y., Beyermann, W.P., and Myung, N.V. (2006) Magnetically assembled 30 nm diameter nickel nanowire with ferromagnetic electrodes. *Nanotechnology*, **17**, 2512.

40. Freer, E.M., Grachev, O., and Stumbo, D.P. (2010) High-yield self-limiting single-nanowire assembly with dielectrophoresis. *Nat. Nanotechnol.*, **5**, 525–530.

41. Duan, X., Huang, Y., Cui, Y., Wang, J., and Lieber, C. (2001) Indium phosphide nanowires as building blocks for nanoscale electronic and optoelectronic devices. *Nature*, **409**, 66–69.

42. Li, M., Bhiladvala, R.B., Morrow, T.J., Sioss, J.A., Lew, K.K., Redwing, J.M., Keating, C.D., and Mayer, T.S. (2008) Bottom-up assembly of large-area nanowire resonator arrays. *Nat. Nanotechnol.*, **3**, 88–92.

43. Liao, L., Bai, J., Cheng, R., Zhou, H., Liu, L., Liu, Y., Huang, Y., and Duan, X. (2011) Scalable fabrication of self-aligned graphene transistors and circuits on glass. *Nano Lett.*, **12**, 2653–2657.

44. Duan, X., Niu, C., Sahi, V., Chen, J., Parce, J.W., Empedocles, S., and Goldman, J.L. (2003) High-performance thin-film transistors using semiconductor nanowires and nanoribbons. *Nature*, **425**, 274–278.

45. Huang, Y., Duan, X., Wei, Q., and Lieber, C.M. (2001) Directed assembly of one-dimensional nanostructures into functional networks. *Science*, **291**, 630–633.

46. M. C. McAlpine, R. S. Friedman, and C. M. Lieber, Nanoimprint lithography for hybrid plastic electronics, *Nano Lett.*, . **3**, 443-445, 2003.

47. Whang, D., Jin, S., Wu, Y., and Lieber, C.M. (2003) Large-scale hierarchical organization of nanowire arrays for integrated nanosystems. *Nano Lett.*, **3**, 1255–1259.

48. Wang, D. and Dai, H. (2006) Germanium nanowires: from synthesis, surface chemistry, and assembly to devices. *Appl. Phys. A Mater. Sci. Process.*, **85**, 217–225.

49. Acharya, S., Panda, A.B., Belman, N., Efrima, S., and Golan, Y. (2006) A semiconductor-nanowire assembly of ultrahigh junction density by the Langmuir-Blodgett technique. *Adv. Mater.*, **18**, 210–213.

50. Yu, G., Cao, A., and Lieber, C.M. (2007) Large-area blown bubble films of aligned nanowires and carbon nanotubes. *Nat. Nanotechnol.*, **2**, 372–377.

51. Fan, Z., Ho, J.C., Jacobson, Z.A., Yerushalmi, R., Alley, R.L., Razavi, H., and Javey, A. (2008) Wafer-scale assembly of highly ordered semiconductor nanowire arrays by contact printing. *Nano Lett.*, **8**, 20–25.

52. Kim, Y.K., Park, S.J., Koo, J.P., Kim, G.T., Hong, S., and Ha, J.S. (2007) Control of adsorption and alignment of V_2O_5 nanowires via chemically functionalized patterns. *Nanotechnology*, **18**, 015304.

53. Yang, J., Lee, M.S., Lee, H.J., and Kim, H. (2011) Hybrid ZnO nanowire networked field-effect transistor with solution-processed InGaZnO film. *Appl. Phys. Lett.*, **98**, 253106.

54. Pevzner, A., Engel, Y., Elnathan, R., Ducobni, T., Ben-Ishai, M., Reddy, K., Shpaisman, N., Tsukernik, A., Oksman, M., and Patolsky, F. (2010) Knocking down highly-ordered large-scale nanowire arrays. *Nano Lett.*, **10**, 1202–1208.

55. Chung, S.E., Park, W., Shin, S., Lee, S.A., and Kwon, S. (2008) Guided and fluidic self-assembly of microstructures using railed microfluidic channels. *Nat. Mater.*, **7**, 581–587.

56. Tolley, M.T., Krishnan, M., Erickson, D., and Lipson, H. (2008) Dynamically programmable fluidic assembly. *Appl. Phys. Lett.*, **93**, 254105.

57. Shim, J.S., Yun, Y.H., Rust, M.J., Do, J., Shanov, V., Schulz, M.J., and Ahn, C.H. (2009) The precise self-assembly of individual carbon nanotubes using magnetic capturing and fluidic alignment. *Nanotechnology*, **20**, 325607.

58. Huh, D., Gu, W., Kamotani, Y., Grotberg, J.B., and Takayama, S. (2005) Microfluidics for flow cytometric analysis of cells and particles. *Physiol. Meas.*, **26**, R73–R98.

59. Wang, T.-H., Peng, Y., Zhang, C., Wong, P.K., and Ho, C.-M. (2005) Single-molecule tracing on a fluidic microchip for quantitative detection of low-abundance nucleic acids. *J. Am. Chem. Soc.*, **127**, 5354–5359.

60. Knight, J.B., Vishwanath, A., Brody, J.P., and Austin, R.H. (1998) Hydrodynamic focusing on a silicon chip: mixing nanoliters in microseconds. *Phys. Rev. Lett.*, **80**, 3863–3866.

61. Wolfe, D.B., Conroy, R.S., Garstecki, P., Mayers, B.T., Fischbach, M.A., Paul, K.E., Prentiss, M., and Whitesides, G.M. (2004) Dynamic control of liquid-core/liquid-cladding optical waveguides. *Proc. Natl. Acad. Sci. U.S.A*, **101**, 12434–12438.

62. Vezenov, D.V., Mayers, B.T., Wolfe, D.B., and Whitesides, G.M. (2005) Integrated fluorescent light source for optofluidic applications. *Appl. Phys. Lett.*, **86**, 041104.

63. Gwo-Bin, L., Chen, I.H., Bin-Jo, K., Guan-Ruey, H., and Bao-Herng, H. (2001) Micromachined pre-focused 1× N flow switches for continuous sample injection. *J. Micromech. Microeng.*, **11**, 567.

64. Gañán-Calvo, A.M. and Gordillo, J.M. (2001) Perfectly monodisperse microbubbling by capillary flow focusing. *Phys. Rev. Lett.*, **87**, 274501.

65. Anna, S.L., Bontoux, N., and Stone, H.A. (2003) Formation of dispersions using "flow focusing" in microchannels. *Appl. Phys. Lett.*, **82**, 364–366.

66. Lee, G.-B., Hung, C.-I., Ke, B.-J., Huang, G.-R., Hwei, B.-H., and Lai, H.-F. (2001) Hydrodynamic focusing for a micromachined flow cytometer. *J. Fluids Eng.*, **123**, 672.

67. Liu, M. (2010) Self-assembly of nanowires and microparts for integration of NMES/MEMS. PhD thesis. The University of Western of Ontario.

68. Huh, D., Bahng, J.H., Ling, Y., Wei, H.-H., Kripfgans, O.D., Fowlkes, J.B., Grotberg, J.B., and Takayama, S. (2007) Gravity-driven microfluidic particle sorting device with hydrodynamic separation amplification. *Anal. Chem.*, **79**, 1369–1376.

69. Scott, R., Sethu, P., and Harnett, C.K. (2008) Three-dimensional hydrodynamic focusing in a microfluidic Coulter counter. *Rev. Sci. Instrum.*, **79**, 046104.

70. Mao, X., Waldeisen, J.R., and Huang, T.J. (2007) "Microfluidic drifting"-implementing three-dimensional hydrodynamic focusing with a single-layer planar microfluidic device. *Lab Chip*, **7**, 1260–1262.

5
Optically Assisted and Dielectrophoretical Manipulation of Cells and Molecules on Microfluidic Platforms

Yen-Heng Lin and Gwo-Bin Lee

5.1
Introduction

Recently, micromachining techniques and micro-electro-mechanical systems (MEMS) technology have allowed for the miniaturization of biomedical and chemical analysis devices and systems, such that a small amount of fluid can be analyzed on a single microfluidic chip. Fluid-based microsystem technologies have been further developed and comprehended with the advent of micro-total-analysis systems (μ-TAS) [1, 2]. With the use of μ-TAS, a small amount of fluids can be transported, mixed, and manipulated in a hand-sized device using several driving forces, including optical [3], electrokinetic [4], gravity [5], pneumatic [6], electromagnetic [7], piezoelectric [8], and electrothermal (ET) approaches [9]. Among them, the electrokinetic force is one of the most important driving forces in the microfluidic systems due to its broad applications and compatibility with many currently used standard electronic instruments.

Electrokinetic forces can be classified as electroosmosis, electrophoresis, dielectrophoresis (DEP), electrowetting on dielectric (EWOD), and alternating current (AC) electroosmosis, depending on their operating conditions. For example, an electrokinetic force can serve as a micropump driving fluids through a microchannel. This is known as *electroosmotic flow* (*EOF*) [10]. The EOF is generated by the formation of an electrical double layer (EDL) on the surface of the microchannel. When an electrical potential is applied along the microchannel, the charge inside the EDL will move due to the electrostatic force, and thus, drive the fluid through the channel accordingly [11]. This EOF is commonly used in capillary or microchannel-based platforms for a variety of applications, including precise sample injection [12] and sample separation, if combined with electrophoretic operation [13]. For instance, an electrokinetic sample injection technique with a cross-channel layout for microchip capillary electrophoresis (CE) applications has been demonstrated; and furthermore, a multi-T-form injection system that could replace conventional cross-, double-, and triple-T-form injection systems

in micro CE biochips has been proposed [12]. This approach will allow precise sample injections to be performed inside microchannels.

Alternatively, if charged molecules are placed in the microchannel with an electrical potential across two ends of the microchannel, they may experience an electrophoretic force, which is mainly determined by its size and charges. Note, if the EDL exists, the EOF occurs as well, when the electrophoretic force is generated. Molecules with positive charges, negative charges, and no charge can be separated in the combination of the EOF and the electrophoretic force.

In contrast to the EOF, bulk fluid can also be driven by alternating current electroosmosis (ACEO). Similar to the EOF, surface charges are first induced at the electrode–electrolyte interface, thus, forming the EDL. When an AC electric field is applied, tangential components of the electric field drive the charged ions in the EDL, which produce the alternating current electroosmosis flow (ACEOF) due to fluid viscosity [14–17]. This ACEOF is commonly used in the manipulation of cells, particles, and molecules.

Another common fluid transportation method generated by the electrokinetic force is termed *EWOD*. When an external electrical potential is applied between a liquid and solid interface or between two immiscible liquids (such as oil and water), the surface energy at the interface is modified due to the redistribution of the charges at the surface. Therefore, an accumulation of the charges at the interface changes the contact angle from hydrophobic to more hydrophilic, and a liquid droplet can be moved between hydrophobic and hydrophilic areas accordingly [18]. This approach has shown its great potential for manipulation of droplets and molecules inside the droplets.

In contrast to the aforementioned methods manipulating bulk fluid, the electrokinetic force can be also used to control substances suspended in fluid. This is called a *DEP force*, which was first reported by Pohl [19, 20]. When particles or cells in a medium are applied with an AC electric field, a dipole moment is induced in the particles/cells. The dipole moment interacts with the applied AC electric field to generate the DEP force, which can be either an attractive or repulsive force, depending on relative particle polarizability compared with the suspending medium. Note that the magnitude of the DEP force depends on the dielectric and electric properties of the particle and the medium, as well as the sizes of the particles [21].

DEP forces are very effective when used in microfluidic systems for manipulation of cells and molecules. For instance, the manipulation of cells and molecules using the DEP force has been extensively explored on behalf of biological applications, such as separating live and dead cells [22], isolating viruses [23], separating live and dead bacteria [24], preconcentrating DNA [25], and many other applications. However, conventional DEP manipulation requires complicated photolithography and delicate thin-film deposition processes to form the metal planar electrodes or three-dimensional microstructures used to generate

the required electric field. Different geometric configurations of the electrodes require tedious fabrication processes in order to redesign and fabricate another electrode pattern, thus, limiting its practical applications.

By contrast, a new technology fuses optoelectronics and biomedicine fields to form a new optoelectronic platform for cell and molecule manipulation, which is commonly referred to as *optoelectronic tweezer*s (*OET*s) [3] or *optically induced dielectrophoresis* (*ODEP*) [26]. This technology uses optical images (stationary or moving) to define "virtual" electrodes and serves as a powerful tool, which can be used to manipulate substances suspended in fluid. A beam of light is commonly used to illuminate the surface of a photoconductive material (usually amorphous silicon). This forms a nonuniform electric field, which generates a dielectrophoretic force. The advantage of this platform is that it allows for a high degree of manipulation and enables dynamic changes in the layouts of the driving electrodes, thereby providing a new approach for cell and molecule manipulation. Furthermore, when compared with other optical manipulation techniques like optical tweezers [27], it merely requires 10^5 times lower light intensity [3]. By contrast, optical tweezers manipulate objects by focusing a laser light on the object to generate an optical force. However, a high-intensity laser may cause damage to the manipulated biological objects, and in addition, a sophisticated laser light source system and a precision $x-y$ stage are commonly required [28, 29]. Thus, the ODEP platform can provide relative flexibility for biomedical applications, and may serve as a user-friendly and affordable tool for further biological and nanotechnology applications.

An ODEP platform contains several forces during the process. When the light source illuminates the photoconductive layer, three major forces are generated simultaneously, including ODEP, optically induced alternating current electroosmosis (OACEO), and ET forces. The magnitude of each force depends on the applied driving frequency of the AC electric field. Typically, when the applied frequency is greater than 10 kHz, the ODEP force is larger and more dominant than the OACEO force. The ET force is generated from the absorption of light energy in the amorphous silicon layer. Hence, the intensity of light directly influences the magnitude of the ET force. Typically, the ET force generated from commercially available projectors is much lower than the ODEP and OACEO forces produced in this platform.

Among the electrokinetic phenomena in microfluidics, the ODEP platform has attracted considerable attention due to its convenience, flexibility, and ease of control. The following sections will discuss, further in depth, the ODEP platform, including the fundamental physical phenomena, the experimental setup of the platform, and several potential biomedical and nanotechnology applications, such as cell manipulation, colloidal manipulation, molecule manipulation, gel formation, and manipulation of nanoparticles. Current challenges and future perspectives are also explored.

5.2

Operating Principle and Fundamental Physics of the ODEP Platform

5.2.1

ODEP Force

A schematic diagram of an ODEP microfluidic chip is presented in Figure 5.1. The ODEP force is generated through the photoconductive effect to change the resistance of the bottom substrate when light is illuminated. An AC electrical potential is first applied between the upper indium tin oxide (ITO) glass substrate and the lower ITO glass layer, which is coated with a photoconductive layer to generate a parallel, uniform electric field. When a substance experiences such an electric field, dipoles are induced on the substance's surface. However, there is no net force in this case. When light is illuminated on the photoconductive layer, electron-hole pairs are generated, causing a decrease in the resistance of the photoconductive layer and the forming of a nonuniform electric field. The substance suspended in the fluid with the induced dipoles is either attracted or repelled by the nonuniform electric field. The interaction between the dipole and
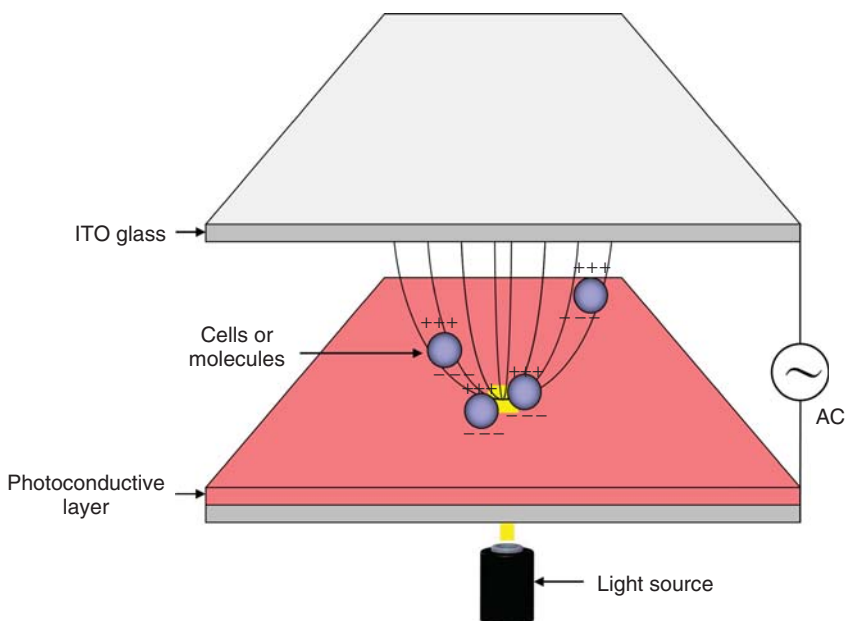

Figure 5.1 Schematic illustration of the ODEP platform. It consists of a top ITO glass, a bottom ITO glass with a photoconductive layer, a light source, and a function generator to provide the AC electric signal. The ODEP force will be induced while a light source illuminates the photoconductive layer, such that cells or molecules in the surrounding medium can be manipulated [3].

the nonuniform electric field generates the ODEP force, which can be expressed as follows [21]:

$$F_{\text{DEP}} = 2\pi r^3 \varepsilon_{\text{m}} \text{Re}(f_{\text{CM}}) \nabla E^2 \tag{5.1}$$

where r is the radius of cells or molecules, ε_{m} is the permittivity of the media surrounding the cells or molecules, E is the root-mean-square value of the local electric field, and $\text{Re}(f_{\text{CM}})$ is the real part of the Clausius–Mossotti factor [21], that is,

$$f_{\text{CM}}(\omega) = \frac{\varepsilon_{\text{p}}^* - \varepsilon_{\text{m}}^*}{\varepsilon_{\text{p}}^* + 2\varepsilon_{\text{m}}^*} \tag{5.2}$$

where ε_p^* is the complex permittivity of the cells or molecules and ε_m^* is the complex permittivity of the surrounding medium. Furthermore, the complex permittivity can be expressed as follows [21]:

$$\varepsilon^* = \varepsilon - j(\sigma/\omega) \tag{5.3}$$

It indicates that the magnitude of the complex permittivity is dependent on the permittivity (ε) and conductance (σ) of the cells or molecules and the medium, the applied driving angular frequency (ω), and the size of the cells or molecules as well. Note that the magnitude and direction (attraction or repulsion) of the ODEP force can be changed by regulating the driving frequency.

5.2.2
Optically Induced ACEO Flow

ACEOF is an electrokinetic effect generating from the interaction between ions in the EDL and the tangential component of the AC electric field inside the EDL. The ions can drag bulk fluid surrounding them and produce a net fluid motion. The generation of the ACEOF depends on the applied driving frequency of the AC electric field. As schematically shown in Figure 5.2, the configuration of the ACEOF is similar to a pair of parallel plates with a larger electrode area on the top plate and a smaller electrode area on the bottom plate. Since the configuration of the top and bottom electrodes is asymmetric, the tangential AC electric fields are produced in the EDL to generate the ACEOF [14].

Similar to the ODEP platform, when a light pattern (virtual electrodes) illuminates on the bottom photoconductive layer while an AC electrical potential is applied to the top and bottom plates, the asymmetric electric field is formed to produce the ODEP and OACEO (as schematically shown in Figure 5.3). The magnitude of the OACEO force depends on the driving frequency of the AC electric field, for example, which is dominant when the applied frequency ranges from 10 to 1 kHz [30–32]. Similar to ACEOF, the fluid in the EDL (close to the photoconductive layer) is driven by the alternating current electroosmosis flow (OACEOF). The fluid slip velocity in the boundary layer generated by the electrostatic force can be represented by the Helmholtz–Smoluchowski equation [30]:

$$v_{\text{slip}} = -\frac{\varepsilon \zeta E_{\text{t}}}{\eta} \tag{5.4}$$
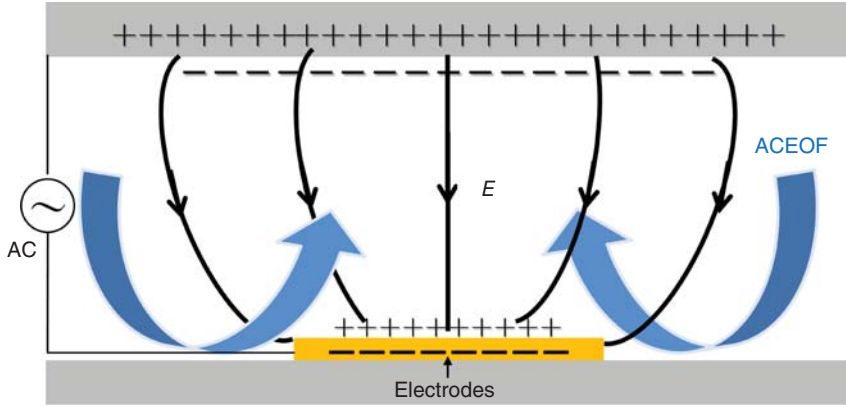
Figure 5.2 Schematic illustration of the ACEOF (cross-sectional view). It consists of a pair of parallel plates with a larger electrode area on the top plate and a smaller electrode area on the bottom plate. Since the configuration of the top and bottom electrodes is asymmetric, the tangential AC electric fields are produced in the electrical double layer to generate the ACEOF [14].
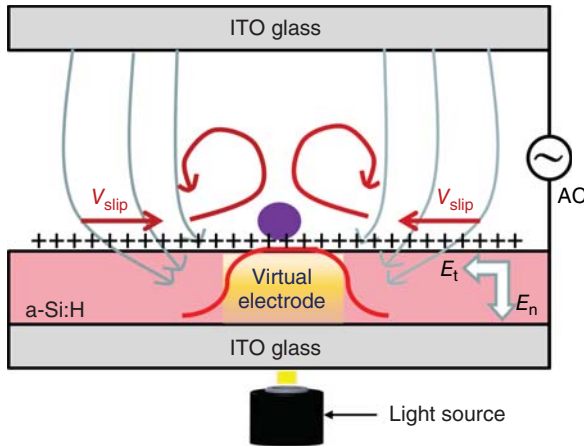
Figure 5.3 Schematic illustration of the OACEOF. When a light pattern (virtual electrodes) illuminates on the bottom photoconductive layer (a-Si:H) while an AC electrical signal is applied to the top and the bottom plates, the asymmetric electric field is formed to produce the OACEOF [30].

where v_{slip} is the slip velocity, ε is the permittivity of the fluid, ζ is the zeta potential at the interface between the liquid and the channel wall, E_t is the tangential component of the electric field, and η is the fluidic viscosity.

The zeta potential is dependent on the material and the surface properties of the microchannel, the type of electrolyte, and the ionic strength. Since the OACEOF is a phenomenon induced by a fluid on the suspended substance, the driving force is not affected by the substance size. Even submicron substances can be driven by

OACEOF effectively, which can compensate for the DEP force that cannot drive submicron substances since it is strongly dependent on the substance size.

5.2.3
Electrothermal (ET) Force

Mizuno *et al.* [33] first observed the ET force acting on a microfluidic system. This phenomenon can be regarded as heat generated by changes in the electrical properties of the fluid from optical illumination. In the ODEP platform, the light source illuminating the photoconductive layer generates localized heating on the substrate and causes gradients of the electrical permittivity and conductivity in the fluid (as schematically shown in Figure 5.4) [35]. The interaction between an external AC electric field and these gradients generates a body of force acting on the fluid. The time-averaged body of force can be expressed as follows [34]:

$$f_{\text{ET}} = \frac{1}{2}\text{Re}\left[\frac{\sigma\varepsilon\,(\alpha - \beta)}{\sigma + i\omega\varepsilon}(\nabla T \cdot E_0)E_0^* - \frac{1}{2}\varepsilon\alpha|E_0|^2\nabla T\right] \tag{5.5}$$

where Re is the real part of the complex term, E_0 is the electric field, E_0^* is its complex conjugate, T is the temperature, ω is the applied angular frequency, σ is the fluid conductivity, ε is the fluid permittivity, β is $(1/\sigma)(d\sigma/dT)$, and α is $(1/\varepsilon)(d\varepsilon/dT)$. As expected, the ET phenomena are highly dependent on the illuminated light intensity in the ODEP platform because of the Joule heating [35]. Typically, the operating power intensity of an ODEP light source is in the order of several W cm^{-2}. At this intensity, the ET force is much weaker than the ODEP force and OACEOF at the same operating conditions [36].

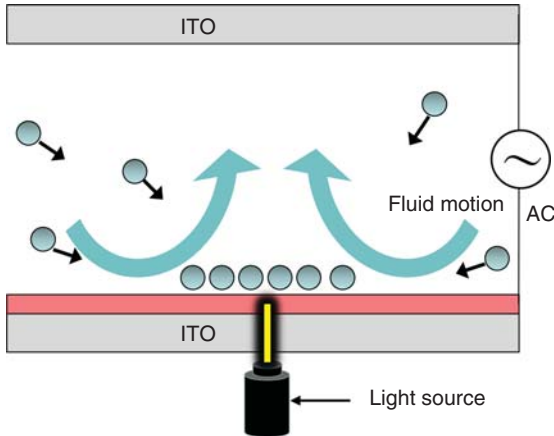**Figure 5.4** Schematic illustration of the optically induced ET. The light source illuminating the photoconductive layer generates localized heating on the bottom ITO substrate and causes gradients of the electrical permittivity and conductivity in the fluid. The interaction between an external AC electric field and these gradients generates a body of force acting on the fluid [34].
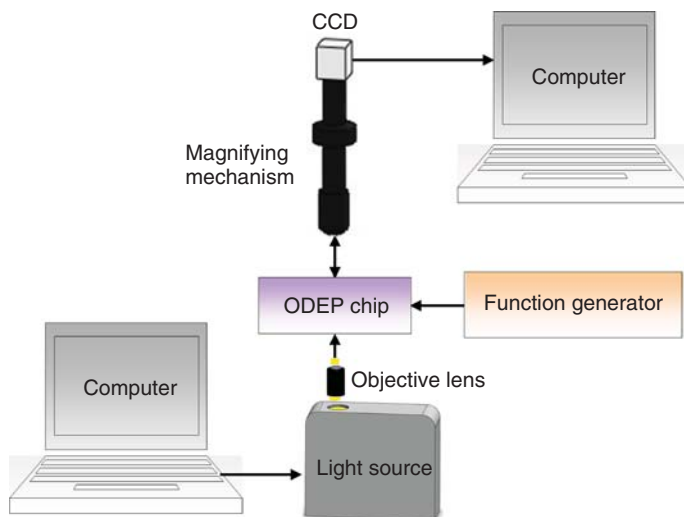
Figure 5.5 Main components of the ODEP platform including an image-magnifying mechanism with an image acquisition system (CCD), a light source (could be a projector, a laser, or a LCD panel), an ODEP microfluidic chip, and a function generator.

5.2.4
Experimental Setup of an ODEP Platform

As schematically shown in Figure 5.5, the ODEP platform consists of six major parts: a light source, a light control unit, a photoconductive microfluidic chip, optical lens, a function generator, and an image acquisition system. The light source and the light control unit are used to provide a configurable light pattern illuminating on the photoconductive layer. The optical lens is used to shrink and collimate the light image appropriately onto the photoconductive layer. A function generator is connected to the photoconductive microfluidic chip to provide an AC electric field and generate the required ODEP force. An image acquisition system, typically consisting of an image-magnifying mechanism and a charge-coupled device (CCD) camera, is used to observe and record experimental phenomena. The focus of this section will now change to the light pattern generation and the photoconductive microfluidic chip.

5.2.4.1 **Light Source**
When generating a proper ODEP force, there are two common methods to control and provide the light patterns. The first method is to use a light source, such as halogen, mercury, light-emitting diode (LED), or laser, in combination with a light control unit. For example, a digital micromirror device (DMD) [3, 30], a liquid crystal display (LCD) [26, 31, 32, 37], or an x−y stage [9] can be used to generate the required light patterns and achieve virtual electrodes. A modulator provides

an interface between the DMD (or LCD) and the user for changing the light pattern illuminating the substrate. Another method is to use a commercially available projector (either DMD or LCD-based devices) to generate the changeable light patterns, which provide a similar effect such as the one provided by the combination of the light source, the light control unit, and the modulator. The advantage of the former method is that all of the components, such as the light source and the light control unit, can be modified or replaced by other components for different applications. However, sophisticated optical setup and programming processes are required for the modulator. On the other hand, in the case of a commercially available projector, the light source and the light modulator setup is built in the digital projector, making it more user-friendly for a common user who is not familiar with the optical setup. Another alternative for illuminating the light patterns is the combination of a laser and a precision x−y stage. A laser can generate a coherent spot of light, and the position of the spot can be precisely controlled by moving the x−y stage. The advantage of this method is that the contrast ratio of light and dark parts is relatively higher than the aforementioned two approaches. In addition, it is not necessary to adjust the focus point between the photoconductive layer and the laser head when using a laser. Consequently, the setup is rather delicate and the cost of equipment is relatively high as well.

5.2.4.2 Materials of the Photoconductive Layer

The crucial component of an ODEP microfluidic chip is the photoconductive layer, which is precoated onto the ITO substrate. When a light beam shines on the photoconductive layer, electron-hole pairs are generated, causing a decrease in the impedance of the layer. Optical images work as reconfigurable "virtual" electrodes since the pattern of the light beam can be properly adjusted. ODEP forces that originate in the nonuniform electric field then manipulate the cells or molecules. Several types of photoconductive materials have been reported in literature and can be used in the ODEP platform, including amorphous silicon [3, 26, 30−32, 35, 37], polymer (such as poly(3-hexylthiophene) (P3HT) and [6,6]-phenyl C61-butyric acid methyl ester (PCBM)) [38, 39], titanium oxide phthalocyanine (TiOPc) [40], and phototransistors [41]. Noted as one of the most commonly used materials due to its high stability and durability, amorphous silicon is generally deposited using a plasma-enhanced chemical vapor deposition (PECVD) process, to a thickness of $0.5 - 1\,\mu m$. It is acknowledged that amorphous silicon has a shorter carrier diffusion length than the crystalline silicon, thus, the lateral spatial resolution of the light-defined virtual electrode is higher than that of the crystalline silicon.

In addition, the amorphous silicon layer has different photoconductive responses to different colors. It shows a greater photoconductive response to excitation with green light over red and blue lights [42] which provides a further manipulation strategy for particle separation. For instance, separation of cells or microparticles utilizing spatial difference of ODEP forces could be demonstrated with this approach when shining lights with different wavelengths. This technique

may be useful for a variety of applications, such as cell-based assays and sample pretreatment using microparticles.

The fabrication process of the ODEP chip begins with an ITO glass substrate. A buffer layer is usually deposited to improve the ohmic contact and adhesion with the ITO layer, and the amorphous silicon is then deposited subsequently. Note that molybdenum and heavily doped amorphous silicon (n$^+$) are materials commonly used for the buffer layer. Finally, an isolation layer, usually silicon nitride, is deposited onto the amorphous silicon, using the PECVD process, which serves as electric isolation while used in liquid afterward.

Instead of amorphous silicon, a polymer can also be used as the photoconductive material of the ODEP chip. Photoconductive polymers are recognized as excellent materials for a variety of applications, such as solar cells and laser printer heads. A thin polymer layer, such as a blended film of regioregular P3HT and PCBM ester, which is a well-known bulk heterojunction structure, can be used as a photoconductive layer [38]. The fabrication process of the polymer ODEP chip also starts with an ITO glass substrate. After the spin coating of the conductive polymers, the ODEP chip can be formed under a relatively low temperature. Note that the use of the photoconductive polymers may open up a new route for ODEP applications since it does not require expensive facilities and high-temperature fabrication processes.

In addition to using the photoconductive polymer on an ITO glass, the use of an ITO/polyethylene naphthalate (PEN) substrate to replace ITO glass can achieve a completely flexible ODEP chip, which may allow for a roll-to-roll fabrication process [39]. Poly(3,4-ethylenedioxythiophene):poly(styrenesulfonate) (PEDOT:PSS), which is a photoconductive polymer commonly used as an interfacial buffer layer, is spin-coated onto the ITO layer. After a mixing process, the solution of P3HT and PCBM is spin-coated onto the treated ITO substrate or PEN substrate, a "slow solvent vapor treatment" process [38] is then used to solidify the film. Finally, a lithium fluoride (LiF) layer is thermally deposited onto the P3HT:PCBM film as a water/oxygen-proof layer. The fabrication process of this kind of polymer ODEP chip is relatively simple, which could be performed in a relatively low temperature. However, some processes, including the P3HT:PCBM film process, need to be conducted in a nitrogen-filled glove box.

The photoconductive layer of the polymer ODEP chip can also be TiOPc, which is also an organic photoconductive material composed of phthalocyanine pigments [40]. TiOPc has been widely used as an electrophotographic-sensitive component in laser printers. The fabrication process of the TiOPc ODEP chip is quite simple. All complicated processes, including PECVD, ion implantation, reactive ion etching, and a nitrogen-filled glove box, can be avoided by using this process. Only a one-step spin coating process is needed to spray the organic photoconductive material onto the ITO substrate. After spin coating, the TiOPc is solidified by baking for several tens of minutes.

Unfortunately, the aforementioned photoconductive material can only operate in media with low conductivity (typically $<0.01-0.1\,\mathrm{S\,m^{-1}}$) [41]. The conductivity of physiological buffers or a cell culture medium is much higher (approximately $1.4\,\mathrm{S\,m^{-1}}$); thus, it is necessary to replace a high-conductivity medium when cell manipulations are conducted with the previously mentioned photoconductive materials. A phototransistor-based device, which has 500 times the photoconductivity of amorphous silicon, can replace the traditional photoconductive materials for cell manipulation in a cell culture medium or physiological buffer solutions [41]. However, the fabrication process of such a device is relatively complex when compared with other methods. As a result, a highly photoconductive material with a simple fabrication process and inexpensive fabrication cost is still in great need.

Another alternative to tackle this issue is to replace the medium before and after the ODEP manipulation process. ODEP has been demonstrated to generate sufficient forces for manipulating cells by projecting a light pattern onto photoconductive materials which creates virtual electrodes. As mentioned previously, the production of the ODEP force usually requires a medium that has a suitable electrical conductivity and an appropriate dielectric constant. Hence, a proper medium (such as $0.2\,\mathrm{M}$ sucrose solution) is commonly required. Consequently, this requires a complicated medium replacement process before one is able to manipulate cells. Furthermore, this medium (such as the $0.2\,\mathrm{M}$ sucrose solution) may not be suitable for the long-term viability of cells. The integration of microfluidic devices with an ODEP device has been demonstrated such that the critical medium replacement process can be automated and the cells could be subsequently manipulated using projected optical images [43].

5.3
Applications of the ODEP Platform

Cells are the basic biological unit in our body. Each cell contains significant amounts of useful information in nuclear DNA, mitochondrial DNA, messenger RNA, proteins, and many others. The ODEP platform is a convenient manipulation tool for cell study. The platform can perform several crucial cell manipulation functions even at the single-cell level. This includes cell position manipulation, cell separation, cell electroporation, and cell lysis. Furthermore, the ODEP platform can also be used for manipulation of micro- or nanometer-scale particles, molecules, and droplets. These applications will be briefly introduced in the following sections.

5.3.1
Cell Manipulation

The most commonly used working medium for cell manipulation is sucrose, because it is isotonic and has a relatively low conductivity. Cells in such a medium

frequently experience a positive (attractive) ODEP force with an operating frequency ranging from 10 kHz to 1 MHz. This force is a result of the interaction between the induced dipole of the cell and the applied nonuniform electric field. The nonuniform electric field originates from a suitable light pattern projected on a photoconductive layer. Thus, the reconfigurable virtual electrodes (light patterns) can manipulate cells, which can be moved around by projecting a dynamic, moving light pattern [44, 45]. In addition, the ODEP platform can be integrated with a microfluidic system formed with flexible polydimethylsiloxane (PDMS) materials, so that some pneumatic microfluidic components, such as microvalves, micropumps, or micromixers, can be integrated on a single chip. For example, a single-cell sample preparation platform using ODEP and microvalves has been demonstrated with this approach [46]. Quantitative reverse-transcription polymerase chain reaction (RT-qPCR) was subsequently performed to detect beta-actin mRNA from the single-cell sample prepared by such a platform.

5.3.2
Cell Separation

ODEP can also be used to separate cells, which is vital in the cell study. Different dielectric properties of cells can be distinguished using optical images. For instance, because of their different dielectric properties, live B cells are selectively concentrated from both, a group of live and dead B cells, using a series of optical images of broken concentric rings [47]. In addition, HeLa and Jurkat cells can also be separated through different drag forces generated by scanning line images. When the line image is scanned, the Jurkat cells have sufficient ODEP force to be retained by the leading line, whereas the HeLa cells do not experience sufficient force. Accordingly, scanning lines provide enough force to drag the HeLa cells, while the Jurkat cells stay in position. This principle is also used to separate rare circulating tumor cells (CTCs) from a leukocyte background [48]. The isolation of prostate cancer cells and human oral cancer cells from leukocytes with a high recovery rate has been demonstrated using another light pattern animations. Furthermore, discrimination between normal and starved abnormal oocytes has been demonstrated using the ODEP platform for *in vitro* fertilization [49]. The combination of gravity, an upward ODEP force, and a frictional force provides differences in moving velocities that enhance discrimination by dragging cells with a moving light line. Note that the cell viability still stays a critical issue after the separation of cells after ODEP operation.

5.3.3
Cell Rotation

Optical images in the ODEP platform can likewise induce the self-rotation of cells caused by a rotating electric field [50] or an uneven distribution of the cell's mass [51]. The electrorotation of cells has been successfully demonstrated by rotating

Ramos and yeast cells in their pitch axes and can be determined by the medium and cells' electrical properties, as well as the frequency of the applied electric field. The rotational speed of the cells also depends on the voltage, the applied frequency, and the cells' distance from the optical image center. The self-rotation phenomenon may be used to characterize the dielectric and physical properties of cells.

5.3.4
Cell Electroporation

Another useful biotechnological technique, electroporation, can also be performed by using an ODEP platform. Exogenous molecules can be delivered into cells by applying an external electric field to prompt pores on the cell membrane to open temporarily. Conversely, traditional methods using electroporation cuvettes lack selectivity. It is challenging to selectively perform electroporation on a single cell located in a group of cells; however, this is possible with a light addressable electric field. After genes are delivered with the ODEP platform, the viability of the cells is further confirmed in the integrated microfluidic channels [52]. Furthermore, a cell-selective, user-friendly gene transfection can be performed by illuminating multitriangle optical patterns on a photoconductive substrate, which can induce the highest electric field [53]. The ODEP platform, therefore, demonstrates the ability to selectively deliver nucleic acids or genes into cells. This has a variety of applications in genetic research, including in gene recombination, stem cells, cancer research, and gene therapy.

5.3.5
Cell Lysis

Pore opening on the cell membrane can be reversible or irreversible depending upon the strength of the applied electric field. When the transmembrane potential induced on a cell membrane is higher than about 1 V, irreversible electroporation takes place and causes cell lysis [54]. When a DC voltage is applied, the transmembrane potential can be expressed as follows: [54].

$$\Delta\varphi = 1.5\,aE\cos\theta, \tag{5.6}$$

where a represents the cell radius, E represents the strength of the applied electric field, and θ is the angle between the applied electric field and a line normal to the point of interest on the cell membrane [54]. Therefore, the ODEP platform can also be used to selectively disrupt the membrane of a specific cell in a group of cells [55]. Note that the transmembrane potential could be also induced while an AC voltage is applied [56]. Therefore, optically induced cell lysis could be performed in DC or AC electric fields. Furthermore, continuous cell lysis could be also performed in a microfluidic chip to enhance the throughput of the cell lysis [57].

5.3.6

Manipulation of Micro- or Nanoscale Objects

Besides cell manipulation, the ODEP platform demonstrates a great ability to handle micro- or nanoscale objects. When manipulating nanoparticles using the ODEP platform, the dominant forces become OACEOF and ET, rather than DEP. This is because the ODEP force is strongly related to the particle size (to the power of third order). For example, nanoparticles such as spherical metallic nanocrystals and carbon nanotubes [58] can be collected and patterned by the ODEP platform using a combination of the OACEOF, ET, and DEP effects [35]. The OACEOF and ET force can be used to collect particles over a longer working range, while the ODEP force can attract particles within a shorter working range. The ability to manipulate and collect nanoparticles into a specific position has been demonstrated with surface-enhanced Raman scattering (SERS) microscopy [35, 59, 60]. Gold nanoparticles can be concentrated, firstly, by shining a laser spot onto the ODEP substrate surface. The SERS signal can be measured subsequently with laser excitation. As schematically shown in Figure 5.6, a single laser can achieve both aggregation of gold nanoparticles and Raman excitation. The integrated platform can greatly enhance the SERS signal and has the ability to
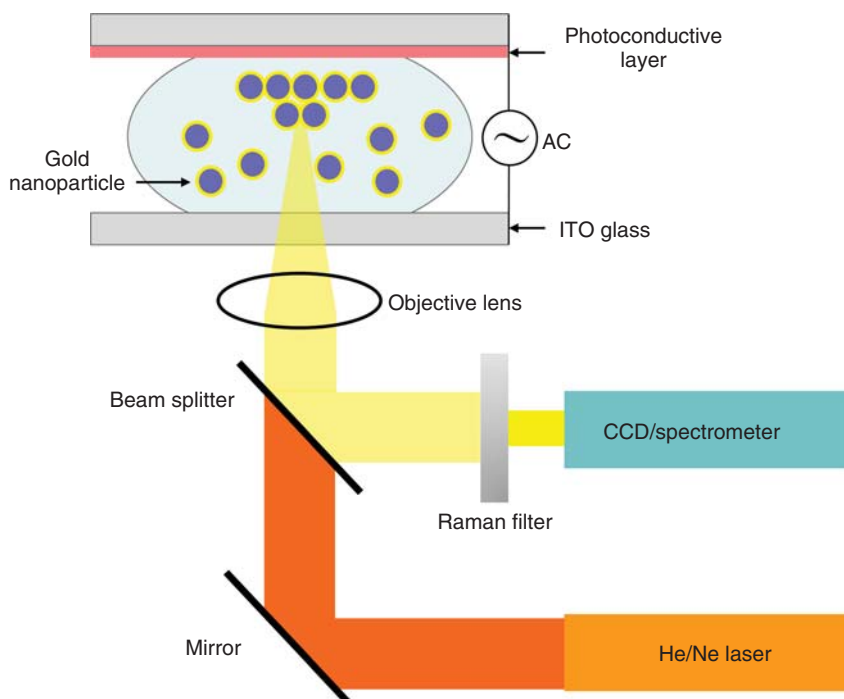

Figure 5.6 Schematic illustration of the combination of the ODEP platform and the SERS platform. A single laser source can be used to collect gold nanoparticles and excite SERS signal, so that the signal can be enhanced in the integrated platform [60].

perform in situ SERS measurements in a specific region (hot spot) with a small sample volume [60].

Microscale particles can also be manipulated in a very similar manner. For microparticle manipulation, the ODEP force increases with increasing the particle size. The applied frequency is also an important parameter in controlling the magnitude of the OACEO and ODEP forces. Generally speaking, a lower applied frequency (<10 kHz) causes a larger OACEO force [31, 32, 35, 59, 60]. Depending on the driving frequency, these forces can be used to separate a mixture of micro- and nanoscale particles [31]. With a lower applied frequency (<300 Hz), both micro- and nanoparticles can be concentrated in the illumination spot because of a stronger OACEOF force and a weaker ODEP force. With a higher applied frequency (>10 kHz), microparticles are repelled by the light spot while nanoparticles are concentrated within the region of light. Particles of differing sizes can, therefore, be separated by fine-tuning the applied frequency.

With the ability to perform simultaneous manipulation of micro- and nanoparticles, sandwiched immunoassays for the detection of protein biomarkers can be conducted using the ODEP SERS platform [59]. Monoclonal antibody-coated polystyrene microspheres could be used as the supporting material for this assay. Polyclonal antibody-conjugated Ag nanoparticles with a fluorescent dye are utilized as a SERS probe. All of the sample-handling processes for the immunoassay, including sample incubation, washing, and concentration, can be performed using the ODEP platform with combinations of ACEOF, ET, and ODEP forces. Afterward, an immunocomplex consisting of probe metallic nanoparticles, protein biomarkers, and supporting microspheres is formed. The concentration of target proteins can then be measured with SERS laser excitation.

Alternatively, the immunocomplex can be detected by using a flow cytometric approach. Optically induced flow cytometry can be comprehended by using the ODEP platform [26]. As illustratively shown in Figure 5.7, first, cells or

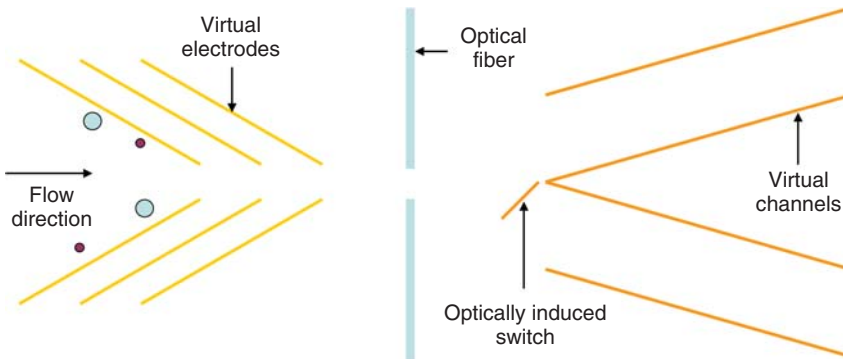**Figure 5.7** Schematic illustration of the optically induced microflow cytometry. Cells or microparticles are lined up through symmetric virtual electrodes with a repelling DEP force. Then, the number of the focused cells or microparticles is counted using buried optical fibers. Finally, different-sized cells or microparticles are directed into different virtual channels using an optically induced switch [26].

microparticles are lined up using a series of symmetrical virtual electrodes, which are optical patterns illuminated on the photoconductive substrate. Then, they are continuously counted by using a couple of buried optical fibers and sorted by an optically induced dynamic switch, which is also an optical pattern providing repelling forces on cells or microparticles. No complicated lithography and metal patterning processes are needed to predefine the electrodes. Thus, this technique has great potential for future use in optically induced, bead-based immunoassays.

5.3.7
Manipulation of Molecules

The ODEP platform can also be used to manipulate molecules. The size of a molecule is similar to that of a nanoparticle (typically several to several tens of nanometers). Therefore, certain manipulation mechanisms are similar. One of the most promising applications for molecule manipulation is to control the local concentration of specific molecules [61]. The applied magnitude of the driving voltage, driving frequency, type of the molecule, and bulk concentration of the molecule are fundamental factors for controlling the local concentration of molecules. The forces involved in molecule manipulation in the ODEP platform are OACEOF, electrostatic forces between the polarized molecules, the affinity among molecules, and the interaction force between the molecule and the EDL on the substrate's surface. One of the most significant manipulation factors is the applied driving frequency. When the applied frequency is around 100 Hz, the molecules in the illumination area move away from the light spot (repelling force) and cause molecule depletion in that area. When the molecules are stained with fluorescent dyes, the intensity of fluorescence decreases in that area. If the applied voltage and the illuminated light are turned off, the fluorescent signal recovers due to the diffusion of molecules. The molecular diffusion rate can be then explored by measuring the fluorescent recovery rate [62]. Alternatively, when the applied frequency is set to be around 1 kHz to several tens of kilohertz, the molecules aggregate inside the illumination area (attractive force), and the concentration of molecules can thus be controlled accordingly.

Another interesting application of concentrating molecules in a certain illumination area is to pattern a poly-(ethylene) glycol diacrylate (PEGDA)-based hydrogel on top of photoconductive substrates [63]. The PEGDA prepolymer and the photoinitiator (2-dimethoxy-2-phenyl-acetophenone) are dissolved in deionized (DI) water and introduced in the ODEP platform. When a light pattern illuminates the photoconductive layer, the induced electric field concentrates the PEGDA molecule. Then, three-dimensional polymer structures are formed by the combined effect of the light and the applied electric field, which activate the cross-linking of PEGDA precursor molecules. It has been estimated that the OACEOF and ODEP forces are much higher than the ET force acting on the PEGDA molecules, at an applied signal of around 10 kHz [63]. Under similar operating conditions, DNA molecules can also be concentrated inside an illumination area in the ODEP platform [30].

The other strategy to manipulate a single strand of DNA molecules with the ODEP platform is to bind polystyrene beads on the two ends of a single strand of DNA molecule, and fix one end of the DNA onto the substrate while moving the bead on the other end using optical images [64]. Thus, a single strand of DNA molecule is indirectly manipulated and stretched by a projected light animation, which has been preprogrammed using computer software. The manipulation force can be estimated in the ODEP platform through Stokes' law, which involves a bead moving at a terminal velocity, that is, the drag force acting on the bead is in balance with the applied ODEP force. The manipulation force for DNA extension in the ODEP platform is around several tens of piconewtons, which is smaller than the force generated by optical tweezers. However, the setup of the ODEP platform is much less expensive and simpler than that of optical tweezers. Furthermore, the ODEP platform requires less illumination power when compared with the optical tweezers.

5.3.8
Droplet Manipulation

Emulsions of droplets have a variety of applications in biomedical and chemical analyses, including polymerase chain reactions (PCRs) in droplets [65], protein crystallization [66], synthesis of nanoparticles [67], and many others. The use of isolated droplets as microreactors provides advantages such as a high-throughput analysis, contamination-free operation between each reactor, and a quick reaction time due to the compact volume of the droplet. In the ODEP platform, both water-in-oil [68–70] and oil-in-water [71] emulsion droplets can be manipulated using optical images. Droplet transportation, separation by size, merging, and mixing can be achieved using the ODEP platform. The size of most emulsion droplets is around several tens to several hundreds of micrometers; therefore, the dominant manipulation force is the ODEP force when the operating parameters are around 10–100 kHz in frequency and above 10 Vpp (peak-to-peak voltage) in voltage. Because aqueous droplets have higher permittivity and conductivity than the surrounding electrical insulation oil, the water-in-oil droplets experience a positive DEP (i.e., are attracted by the optical image), and vice versa for the oil-in-water droplets.

Another droplet manipulation method is EWOD, which involves a reduction in the contact angle of the droplet through an applied external electrical potential. It allows for transportation, division, and merging of individual droplets over a planar electrode. The EWOD technique can also be integrated with ODEP, such that both the droplets and their contents (such as beads or cells) can be manipulated individually [72, 73]. As schematically represented in Figure 5.8, this platform allows microenvironments created by individual droplets to be used to encapsulate cells for detailed study. Stimulants such as drugs, nutrients, and salts can be added to the cells' original microenvironments by merging with another droplet containing such stimulants using EWOD. After stimulation, specific cell(s) can be distinguished from the rest of the population using ODEP, and isolated into
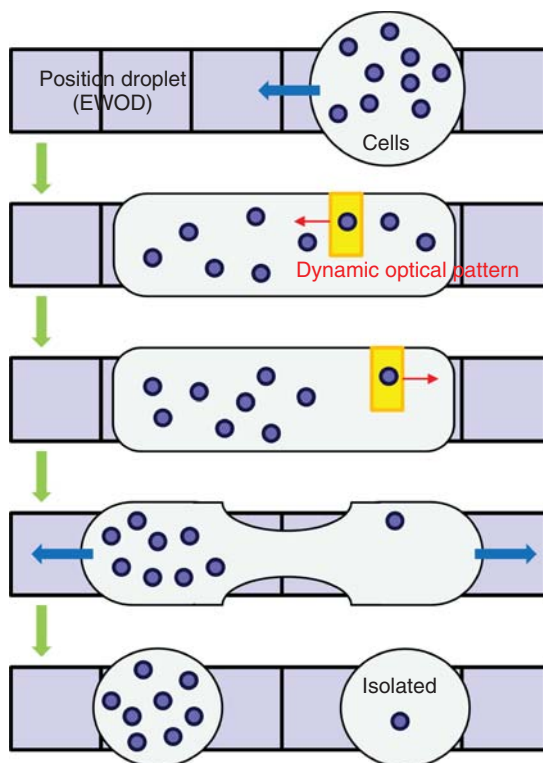
Figure 5.8 Schematic function of the combination of ODEP platform and the EWOD. The entire microenvironments can be driven by the EWOD electrodes, whereas the contents in the microenvironments can be manipulated by the optical images in ODEP platform [72].

a separate droplet using EWOD. The integrated platform is a promising tool for single-cell studies involving multiplex environmental stimuli.

5.4
Conclusion

Manipulation of cells and molecules are essential technologies for biomedical and nanotechnology applications. It can be achieved by applying an AC voltage to generate either bulk fluid or attractive/repelling forces on cells and molecules. Alternatively, ODEP technology, using optical images to define various kinds of "virtual" electrodes to manipulate cells and molecules, has attracted considerable attention and recently made substantial impacts. It simplifies the complicated process of fabricating microelectrodes in conventional DEP devices. When a light image is illuminated onto the surface of photoconductive materials (such as amorphous silicon, polymers, TiOPc, and phototransistors), under an AC voltage, a nonuniform electric field is formed to induce ODEP forces at the optical "virtual"

electrodes, which enables the manipulation of the cells and molecules. This ODEP manipulation of cells and molecules can be extremely useful when performed on microfluidic platforms; thus, it can be used for a variety of applications, including cell manipulation, cell separation, cell rotation, cell electroporation, and cell lysis. In addition, it can be used for manipulation of molecules and nanoparticles, making it an enabling technology in this promising field. It can be also used for manipulation of droplets containing cells or particles. It is envisioned that this technology will continue to advance and become a user-friendly, flexible technology for biomedical and nanotechnology applications.

References

1. Whitesides, G.M. (2006) The origins and the future of microfluidics. *Nature*, **442** (27), 368–373.

2. Quake, S.R. and Scherer, A. (2000) From micro- to nanofabrication with soft materials. *Science*, **290** (5496), 1536–1540.

3. Chiou, P.Y., Ohta, A.T., and Wu, M.C. (2005) Massively parallel manipulation of single cells and microparticles using optical images. *Nature*, **436** (7049), 370–372.

4. Ramos, A., Morgan, H., Green, N.G., and Castellanos, A. (1998) Ac electrokinetics: a review of forces in microelectrode structures. *J. Phys. D: Appl. Phys.*, **31** (18), 2338–2353.

5. Huh, D., Bahng, J.H., Ling, Y., Wei, H.H., Kripfgans, O.D., Fowlkes, J.B., Grotberg, J.B., and Takayama, S. (2007) Gravity-driven microfluidic particle sorting device with hydrodynamic separation amplification. *Anal. Chem.*, **79** (4), 1369–1376.

6. Unger, M.A., Chou, H.P., Thorsen, T., Scherer, A., and Quake, S.R. (2000) Monolithic microfabricated valves and pumps by multilayer soft lithography. *Science*, **288** (5463), 113–116.

7. Pamme, N. (2006) Magnetism and microfluidics. *Lab Chip*, **6** (1), 24–38.

8. Bransky, A., Korin, N., Khoury, M., and Levenberg, S. (2009) A microfluidic droplet generator based on a piezoelectric actuator. *Lab Chip*, **9** (4), 516–520.

9. Williams, S.J., Kumar, A., Green, N.G., and Twereley, S. (2010) Optically induced electrokinetic concentration and sorting of colloids. *J. Micromech. Microeng.*, **20** (1), 015022(11 pp).

10. Wong, P.K., Wang, T.H., Deval, J.H., and Ho, C.M. (2004) Electrokinetics in micro devices for biotechnology applications. *IEEE-ASME Trans. Mechatron.*, **9** (2), 366–376.

11. Wang, X., Cheng, C., Wang, S., and Liu, S. (2009) Electroosmotic pumps and their applications in microfluidic systems. *Microfluid. Nanofluid.*, **6** (2), 145–162.

12. Fu, L.M., Yang, R.J., Lee, G.B., and Liu, H.H. (2002) Electrokinetic injection techniques in microfluidic chips. *Anal. Chem.*, **74** (19), 5084–5091.

13. Wainright, A., Nguyen, U.T., Bjornson, T., and Boone, T.D. (2003) Preconcentration and separation of double stranded DNA fragments by electrophoresis in plastic microfluidic devices. *Electrophoresis*, **24** (21), 3784–3792.

14. Ramos, A., Morgan, H., Green, N.G., and Castellanos, A. (1999) AC electric-field-induced fluid flow in microelectrodes. *J. Colloid Interface Sci.*, **217** (2), 420–422.

15. Islam, N., Lian, M., and Wu, J. (2007) Enhancing microcantilever capability with integrated AC electroosmotic trapping. *Microfluid. Nanofluid.*, **3** (3), 369–375.

16. Bhatt, K.H., Grego, S., and Velev, O.D. (2005) An AC electrokinetic technique for collection and concentration of particles and cells on patterned electrodes. *Langmuir*, **21** (14), 6603–6612.

17. Studer, V., Pepin, A., Chen, Y., and Ajdari, A. (2004) An integrated AC

electrokinetic pump in a microfluidic loop for fast and tunable flow control. *Analyst*, **129** (10), 944–949.

18. Lee, J. and Kim, C.J. (2000) Surface-tension-driven microactuation based on continuous electrowetting. *J. Microelectromech. Syst.*, **9** (2), 171–180.

19. Pohl, H.A. (1951) The motion and precipitation of suspensoids in divergent electric fields. *J. Appl. Phys.*, **22** (7), 869–871.

20. Pohl, H.A. (1978) *Dielectrophoresis*, Cambridge University Press, Cambridge.

21. Morgan, H., Hughes, M.P., and Green, N.G. (1999) Separation of submicron bioparticles by dielectrophoresis. *Biophys. J.*, **77** (1), 516–525.

22. Doh, I. and Cho, Y.H. (2005) A continuous cell separation chip using hydrodynamic dielectrophoresis (DEP) process. *Sens. Actuators A*, **121** (1), 59–65.

23. Morgan, H. and Green, N.G. (1997) Dielectrophoretic manipulation of rod-shaped viral particles. *J. Electrost.*, **42** (3), 279–293.

24. Lapizco-Encinas, B.H., Simmons, B.A., Cummings, E.B., and Fintschenko, Y. (2004) Dielectrophoretic concentration and separation of live and dead bacteria in an array of insulators. *Anal. Chem.*, **76** (6), 1571–1579.

25. Chou, C.F., Tegenfeldt, J.O., Bakajin, O., Chan, S.S., and Cox, E.C. (2002) Electrodeless dielectrophoresis of single- and double-stranded DNA. *Biophys. J.*, **83** (4), 2170–2179.

26. Lin, Y.H. and Lee, G.B. (2008) Optically induced flow cytometry for continuous microparticle counting and sorting. *Biosens. Bioelectron.*, **24** (4), 572–578.

27. Ashkin, A., Dziedzic, J.M., Bjorkholm, J.E., and Chu, S. (1986) Observation of a single-beam gradient force optical trap for dielectric particle. *Opt. Lett.*, **11** (5), 288–290.

28. Yan, Z., Jureller, J.E., Sweet, J., Guffey, M.J., Pelton, M., and Scherer, N.F. (2012) Three-dimensional optical trapping and manipulation of single silver nanowires. *Nano Lett.*, **12** (10), 5155–5161.

29. Irrera, A., Artoni, P., Saija, R., Gucciardi, P.G., Iatì, M.A., Borghese, F., Denti, P., Iacona, F., Priolo, F., and Marago, O.M.

30. Chiou, P.Y., Ohta, A.T., Jamshidi, A., Hsu, H.Y., and Wu, M.C. (2008) Light-actuated AC electroosmosis for nanoparticle manipulation. *J. Microelectromech. Syst.*, **17** (3), 525–531.

31. Hwang, H. and Park, J.K. (2009) Rapid and selective concentration of microparticles in an optoelectrofluidic platform. *Lab Chip*, **9** (2), 199–206.

32. Hwang, H., Park, Y.H., and Park, J.K. (2009) Optoelectrofluidic control of colloidal assembly in an optically induced electric field. *Langmuir*, **25** (11), 6010–6014.

33. Mizuno, A., Nishioka, M., Ohno, Y., and Dascalescu, L.D. (1995) Liquid microvortex generated around a laser focal point in an intense high-frequency electric field. *IEEE Trans. Ind. Appl.*, **31** (3), 464–468.

34. Green, N.G., Ramos, A., Gonzalez, A., Castellanos, A., and Morgan, H. (2001) Electrothermally induced fluid flow on microelectrodes. *J. Electrost.*, **53** (2), 71–87.

35. Jamshidi, A., Neale, S.L., Yu, K., Pauzauskie, P.J., Schuck, P.J., Valley, J.K., Hsu, H.Y., Ohta, A.T., and Wu, M.C. (2009) NanoPen: dynamic, low-power, and light-actuated patterning of nanoparticles. *Nano Lett.*, **9** (8), 2921–2925.

36. Hwang, H. and Park, J.K. (2011) Optoelectrofluidic platforms for chemistry and biology. *Lab Chip*, **11** (1), 33–47.

37. Choi, W., Kim, S.H., Jang, J., and Park, J.K. (2007) Lab-on-a-display: a new microparticle manipulation platform using a liquid crystal display (LCD). *Microfluid. Nanofluid.*, **3** (2), 217–225.

38. Wang, W., Lin, Y.H., Guan, R.S., Wen, T.C., and Guo, T.F. (2009) Bulk-heterojunction polymers in optically induced dielectrophoretic devices for the manipulation of microparticles. *Opt. Express*, **17** (20), 17603–17613.

39. Lin, S.J., Hung, S.H., Jeng, J.Y., Guo, T.F., and Lee, G.B. (2012) Manipulation of micro-particles by flexible polymer-based optically-induced dielectrophoretic devices. *Opt. Express*, **20** (1), 583–592.

(2011) Size-scaling in optical trapping of silicon nanowires. *Nano Lett.*, **11** (11), 4879–4884.

40. Yang, S.M., Yu, T.M., Huang, H.P., Ku, M.Y., Hsu, L., and Liu, C.H. (2010) Dynamic manipulation and patterning of microparticles and cells by using TiOPc-based optoelectronic dielectrophoresis. *Opt. Lett.*, **35** (12), 1959–1961.

41. Hsu, H.Y., Ohta, A.T., Chiou, P.Y., Jamshidi, A., Neale, S.L., and Wu, M.C. (2010) Phototransistor-based opto-electronic tweezers for dynamic cell manipulation in cell culture media. *Lab Chip*, **10** (2), 165–172.

42. Lin, W.Y., Lin, Y.H., and Lee, G.B. (2010) Separation of micro-particles utilizing spatial difference of optically induced dielectrophoretic forces. *Microfluid. Nanofluid.*, **8** (2), 217–229.

43. Lee, G.B., Wu, H.C., Yang, P.F., and Mai, J.D. (2014) Automated medium replacement in an integrated optofluidic device resulting in higher cell viability after optically-induced dielectrophoresis sorting. *Lab Chip*, **14** (15), 2837–2843

44. Lu, Y.S., Huang, Y.P., Yeh, J.A., Lee, C., and Chang, Y.H. (2005) Controllability of non-contact manipulation by image dielectrophoresis (iDEP). *Opt. Quantum Electron.*, **37** (13-15), 1385–1395.

45. Ohta, A.T., Chiou, P.Y., Han, T.H., Liao, J.C., Bhardwaj, U., McCabe, E.R.B., Yu, F., Sun, R., and Wu, M.C. (2007) Dynamic cell and microparticle control via optoelectronic tweezers. *J. Microelectromech. Syst.*, **16** (3), 491–499.

46. Huang, K.W., Wu, Y.C., Lee, J.A., and Chiou, P.Y. (2013) Microfluidic integrated optoelectronic tweezers for single-cell preparation and analysis. *Lab Chip*, **13** (18), 3721–3727.

47. Ohta, A.T., Chiou, P.Y., Phan, H.L., Sherwood, S.W., Yang, J.M., Lau, A.N.K., Hsu, H.Y., Jamshidi, A., and Wu, M.C. (2007) Optically controlled cell discrimination and trapping using optoelectronic tweezers. *IEEE J. Sel. Top. Quantum Electron.*, **13** (2), 235–242.

48. Huang, S.B., Wu, M.H., Lin, Y.H., Hsieh, C.H., Yang, C.L., Lin, H.C., Tseng, C.P., and Lee, G.B. (2013) High-purity and label-free isolation of circulating tumor cells (CTCs) in a microfluidic platform by using optically-induced-dielectrophoretic (ODEP) force. *Lab Chip*, **13** (7), 1371–1383.

49. Hwang, H., Lee, D.H., Choi, W., and Park, J.K. (2009) Enhanced discrimination of normal oocytes using optically induced pulling-up dielectrophoretic force. *Biomicrofluidics*, **3** (1), 014103.

50. Liang, Y.L., Huang, Y.P., Lu, Y.S., Hou, M.T., and Yeh, J.A. (2010) Cell rotation using optoelectronic tweezers. *Biomicrofluidics*, **4** (4), 043003.

51. Chau, L.H., Liang, W., Cheung, F.W.K., Liu, W.K., Li, W.J., Chen, S.C., and Lee, G.B. (2013) Self-rotation of cells in an irrotational AC e-field in an opto-electrokinetics chip. *PLoS One*, **8** (1), 51577.

52. Valley, J.K., Neale, S., Hsu, H.Y., Ohta, A.T., Jamshidi, A., and Wu, M.C. (2009) Parallel single-cell light-induced electroporation and dielectrophoretic manipulation. *Lab Chip*, **9** (12), 1714–1720.

53. Wang, C.H., Lee, Y.H., Kuo, H.T., Liang, W.F., Li, W.J., and Lee, G.B. (2014) Dielectrophoretically-assisted electroporation using light-activated virtual microelectrodes for multiple DNA transfection. *Lab Chip*, **14** (3), 592–601.

54. Lee, S.W. and Tai, Y.C. (1999) A micro cell lysis device. *Sens. Actuators, A*, **73** (1–2), 74–79.

55. Lin, Y.H. and Lee, G.B. (2009) An optically-induced cell lysis device using dielectrophoresis. *Appl. Phys. Lett.*, **94** (3), 033901.

56. Chen, C., Evan, J.A., Robinson, M.P., Smye, S.W., and O'Toole, P. (2008) Measurement of the efficiency of cell membrane electroporation using pulsed ac fields. *Phys. Med. Biol.*, **53** (17), 4747–4757.

57. Lin, Y.H. and Lee, G.B. (2010) An integrated cell counting and continuous cell lysis device using optically induced electric field. *Sens. Actuators, B*, **145** (2), 854–860.

58. Hsu, M.C. and Lee, G.B. (2014) Carbon nanotube-based hot-film and temperature sensors assembled by optically-induced dielectrophoresis. *IET Nanobiotechnol.*, **8** (1), 44–50.

59. Hwang, H., Chon, H., Choo, J., and Park, J.K. (2010) Optoelectrofluidic sandwich immunoassays for detection of human tumor marker using surface-enhanced

Raman scattering. *Anal. Chem.*, **82** (18), 7603–7610.

60. Hwang, H., Han, D., Oh, Y.J., Cho, Y.K., Jeong, K.H., and Park, J.K. (2011) In situ dynamic measurements of the enhanced SERS signal using an optoelectrofluidic SERS platform. *Lab Chip*, **11** (15), 2518–2525.

61. Hwang, H. and Park, J.K. (2009) Dynamic light-activated control of local chemical concentration in a fluid. *Anal. Chem.*, **81** (14), 5865–5870.

62. Hwang, H. and Park, J.K. (2009) Measurement of molecular diffusion based on optoelectrofluidic fluorescence microscopy. *Anal. Chem.*, **81** (21), 9163–9167.

63. Liu, N., Liang, W., Liu, L., Wang, Y., Mai, J.D., Lee, G.B., and Li, W.J. (2014) Extracellular-controlled breast cancer cell formation and growth using non-UV patterned hydrogels via optically-induced electrokinetics. *Lab Chip*, **14** (7), 367–1376.

64. Lin, Y.H., Chang, C.M., and Lee, G.B. (2009) Manipulation of single DNA molecules by using optically projected images. *Opt. Express*, **17** (17), 15318–15329.

65. Curcio, M. and Roeraade, J. (2003) Continuous segmented-flow polymerase chain reaction for high-throughput miniaturized DNA amplification. *Anal. Chem.*, **75** (1), 1–7.

66. Chen, D.L., Gerdts, C.J., and Ismagilov, R.F. (2005) Using microfluidics to observe the effect of mixing on nucleation of protein crystals. *J. Am. Chem. Soc.*, **127** (27), 9672–9673.

67. Hung, L.H., Choi, K.M., Tseng, W.Y., Tan, Y.C., Shea, K.J., and Lee, A.P. (2006) Alternating droplet generation and controlled dynamic droplet fusion in microfluidic device for CdS nanoparticle synthesis. *Lab Chip*, **6** (2), 174–178.

68. Park, S., Pan, C., Wu, T.H., Kloss, C., Kalim, S., Callahan, C.E., Teitell, M., and Chiou, E.P. (2008) Floating electrode optoelectronic tweezers: Light-driven dielectrophoretic droplet manipulation in electrically insulating oil medium. *Appl. Phys. Lett.*, **92** (15), 151101.

69. Park, S.Y., Kalim, S., Callahan, C., Teitell, M.A., and Chiou, E.P. (2009) A light-induced dielectrophoretic droplet manipulation platform. *Lab Chip*, **9** (22), 3228–3235.

70. Lee, D.H., Hwang, H., and Park, J.K. (2009) Generation and manipulation of droplets in an optoelectrofluidic device integrated with microfluidic channels. *Appl. Phys. Lett.*, **95** (16), 164102.

71. Hung, S.H., Lin, Y.H., and Lee, G.B. (2010) A microfluidic platform for manipulation and separation of oil-in-water emulsion droplets using optically induced dielectrophoresis. *J. Micromech. Microeng.*, **20** (4), 045026.

72. Shah, G.J., Ohta, A.T., Chiou, E.P.Y., Wu, M.C., and Kim, C.J. (2009) EWOD-driven droplet microfluidic device integrated with optoelectronic tweezers as an automated platform for cellular isolation and analysis. *Lab Chip*, **9** (12), 1732–1739.

73. Valley, J.K., Pei, S.N., Jamshidi, A., Hsu, H.Y., and Wu, M.C. (2011) A unified platform for optoelectrowetting and optoelectronic tweezers. *Lab Chip*, **11** (7), 1292–1297.

6
On-Chip Microrobot Driven by Permanent Magnets
for Biomedical Applications

Masaya Hagiwara, Tomohiro Kawahara, and Fumihito Arai

6.1
On-Chip Microrobot

A microfluidic chip is a device that performs various functions in simulating a laboratory environment within the small size of a chip. Use of a microfluidic chip makes it possible to perform high-throughput screening, separation, detection, and reaction of various liquid solutions in a small confined space by taking advantage of the ability to use very small quantities of samples and conduct analyses at low cost and over short time frames. The applications of microfluidic chips are increasing rapidly to include such things as single-cell analysis, evaluation, and cultivation. However, a fluid is not always a suitable tool for precise manipulation of objects, such as cells, and evaluation of mechanical interactions is complicated by the difficulties of precise fluid control.

Micromechanical manipulators are widely used in medical and life science applications because of their high accuracy, high power output, and flexibility of manipulation. However, this manipulation is conducted in an open-air environment because of the huge size of the manipulator, and this leads to cell contamination issues. In addition, the manipulation requires a high degree of operator skill because the manipulator to be controlled has six degrees of freedom.

To take advantage of the features of both microfluidic devices and micromechanical manipulators, Arai *et al.* [1] proposed in 2000 that a microrobot be implemented on a microfluidic chip. On-chip robots have great potential to perform powerful and accurate cell manipulations for a broad range of biological applications with high throughput by taking advantage of flow control of microfluidic chips. In addition, the cost of an on-chip robot is generally low because of the small size of the manipulator and the microfluidic chip. Thus, an on-chip robot can be disposed of after an operation is conducted to prevent cell contamination. The closed environment of a microfluidic chip also helps to prevent cell contamination and provides a stable environment for the robot's actuations.
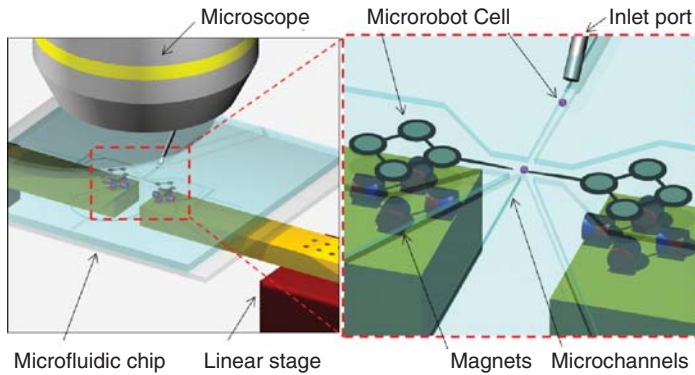
Figure 6.1 Conceptual illustration of an on-chip robot.

Figure 6.1 illustrates the concept of an on-chip robot. Microrobots are placed on a microfluidic chip and are actuated by a noncontact power source. The microrobots then manipulate cells inserted under a microscope, in the same way that a micromechanical manipulator does. The differences are that the microrobot manipulator is significantly smaller in size and that the environment is more stable than that in which a micromechanical manipulator operates, because of the confined space of the microfluidic chip. In addition, cells flow continuously to the microrobot manipulation area. As a result, the on-chip robot can conduct flow processes in the same way as an industrial manufacturing line and achieve high-throughput cell manipulations.

There are many types of actuation sources for on-chip robots, including optics [2–6] and electromagnetics [7–11]. These noncontact actuators can achieve precise cell control; however, in practical use, the order of magnitude of output forces is less than micronewtons. Thus, the applications and the target cell size are limited. On the other hand, a permanent magnet possesses a magnetic field that is more than 10 times the strength of the magnetic field of an electromagnetic coil of the same size. A magnetically driven microtool (MMT) actuated by a permanent magnet can output a force on the order of millinewtons with a drive unit of small size. Therefore, an MMT can be applied to a wide range of cell manipulations, such as cell cutting, arranging, and rotating.

6.2
Characteristics of Microrobot Actuated by Permanent Magnet

It is essential for an MMT to follow the drive magnet precisely to achieve accurate cell manipulations on a microfluidic chip. However, when the permanent magnet actuates an MMT beneath the microfluidic chip, there is an area within which the MMT is not driven when the magnet passes under the MMT. The size of this "dead band" was found to reach 500 μm when a nickel-based MMT (diameter = 1.0 mm, height = 0.05 mm) was driven by a permanent neodymium
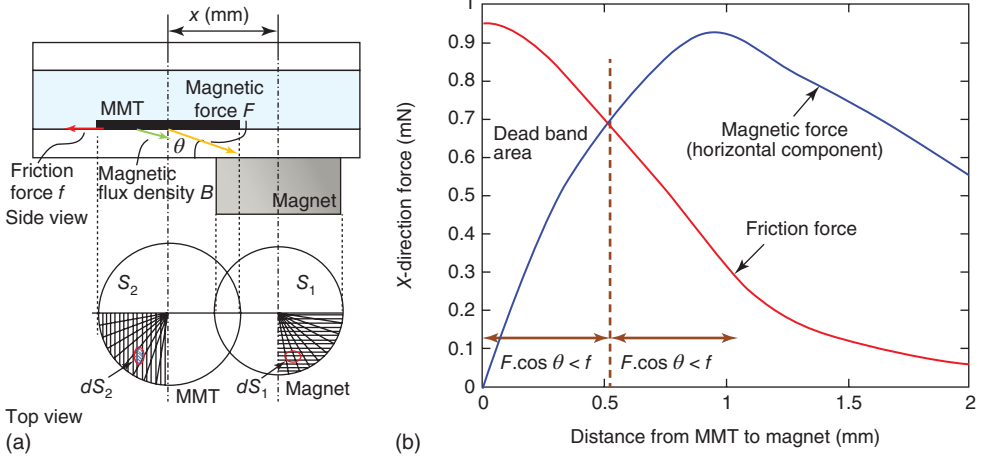
Figure 6.2 Analysis of static force on the MMT. (a) Model of forces on the MMT. (b) Simulation results.

$(\text{Nd}_2\text{Fe}_{14}\text{B})$ magnet (diameter $= 1.0$ mm, height $= 1.0$ mm, grade $= $ N40). This large dead band interferes with the precise positioning of the MMT on a microfluidic chip and diminishes the effectiveness of the control of the MMT because of the low response rate of the driver unit.

To counter the reason for the presence of the dead band and to predict its size for a given MMT and magnet, a static force model was developed for the MMT (Figure 6.2a) [12]. The gravitational force, buoyant force, and van der Waals' force are ignored in this model because these are relatively small in comparison to the magnetic force applied to the MMT. For the calculation of the magnetic force, the magnet and the MMT are subdivided into the very small elemental areas dS_1 and dS_2, respectively. The vector B, which is the magnetic flux density in the small elemental area of the MMT (dS_2), can then be computed as the sum of the vectors of the flux from each small elemental area dS_1 in the magnet area S_1:

$$\vec{B} = \iint d\vec{B} \cdot dS_1 / S_1 \qquad (6.1)$$

where dB is the magnetic flux density radiated from each small elemental area of the magnet dS_1.

However, it is quite difficult to express the magnetic flux density distribution around a magnet by a single formula because the magnetic flux density B has a complicated nonlinear distribution as a result of its dependence on the size, shape, and the material properties of the magnet. Therefore, a cubic spline interpolation from experimentally measured data is used to predict the magnetic flux density distribution around the magnet. The pressure P on the small elemental area of the MMT (dS_2) can be expressed as follows:

$$\vec{P} = v(M \cdot \nabla)\vec{B} \qquad (6.2)$$

where v is the MMT volume and M is the magnetization.

The total magnetic force F on the MMT can be calculated as the sum of the elemental forces, which is calculated as the product of the pressure P and the elemental area dS_2:

$$\overrightarrow{F} = \iint \overrightarrow{P} \cdot dS_2 \tag{6.3}$$

The drive force of the MMT is the horizontal component of the F vector, and the friction force on the MMT can be expressed as the product of the vertical component of the F vector and the static friction coefficient, μ. The MMT can move when the drive force is greater than the friction force:

$$\left|\overrightarrow{F}\right| \cos\theta - \left|\overrightarrow{F}\right| \sin\theta \times \mu > 0 \tag{6.4}$$

where θ is the angle of the vector F from the horizontal line.

Figure 6.2b shows the simulation results for a neodymium magnet of size ϕ 1.0×1.0 mm and a nickel MMT of size ϕ 1.0×0.05 mm. The saturation magnetization, which is a material constant, is 5.12×105 A m^{-1} for Ni. As Figure 6.2b shows, the magnetic force in the horizontal direction initially increases with the distance from the magnet and then starts to decrease. In the region where the center of MMT and magnet are within a certain distance, the friction force is greater than the drive force. Thus, the MMT does not move, despite the movement of the magnet. When the distance from the magnet reaches about 500 μm, the drive force exceeds the friction force and the MMT starts to follow the magnet. These simulation results correspond to the measured dead band size mentioned earlier (543.0 μm).

These results indicate that the major reason for the presence of the dead band is static friction. As it is clear that the reason for the low positioning accuracy and low controllability is static friction, the next challenge is determining how to reduce the friction on the MMT.

6.3
Friction Reduction for On-Chip Robot

6.3.1
Friction Reduction by Drive Unit

Two disadvantages of an MMT driven by a permanent magnet are low positioning accuracy and low response rate in the drive stage. The poor performance of an MMT in this situation can be attributed to the fact that the applied friction force is relatively large in comparison to the component of the magnetic force in the driving direction as described in the previous section.

To counter the large friction force, a horizontally arranged permanent magnet drive was developed [12]. When the MMT is set such that the permanent magnet pole is parallel to the driving direction of a magnet that has the same size as the MMT, the magnetic force in the downward direction is considerably
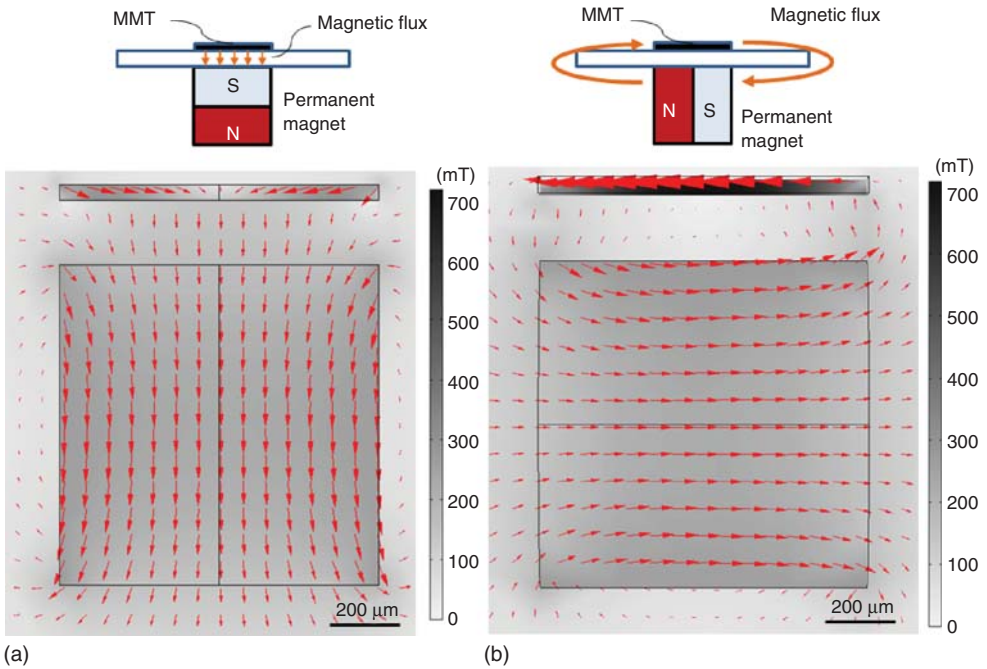
Figure 6.3 Results of FEM analysis of the magnetic flux density distribution. (a) Conventional method and (b) HPD.

reduced. Here, we refer to the driving method used for the MMT in such a setup as horizontal polar drive (HPD). Figure 6.3 shows the magnetic flux density distributions determined using the finite element method (FEM). Compared to the results for the conventional drive unit (Figure 6.3a), there is considerably less magnetic flux in the vertical direction around the center of the MMT using HPD (Figure 6.3b). As a result, the friction on the MMT is reduced, and we achieved a 10-fold improvement in positioning accuracy and a fivefold increase in the response rate of the MMT.

However, HPD is only available with one degree of freedom (DOF). In cell manipulations, more than two DOFs are required for precise control. Therefore, we extended the HPD to multi-DOF precise control actuation by combining four magnets under HPD conditions. Figure 6.4a illustrates the concept of a multi-DOF MMT driven by HPD, and Figure 6.4b shows the actual design. Under HPD conditions, two pairs of magnets are positioned with their polar axes normal to each other. Cell manipulation is conducted on the head of the extended part. Figure 6.4c shows the FEM results for the magnetic flux density of the MMT. These results show that the magnets independently actuate the circular disc portion of the MMT, as shown in Figure 6.3b. By combining two pairs of magnets under HPD conditions, we achieve the same levels of positioning accuracy and response rate with a three-DOF $(x - y - \theta)$ MMT as with a one-DOF MMT.
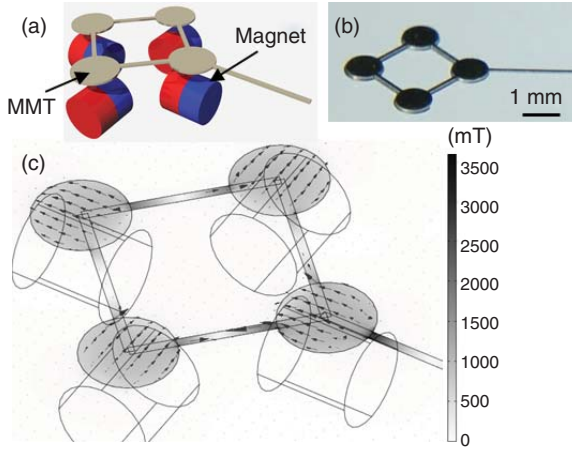
Figure 6.4 Multi-DOF MMT. (a) Concept, (b) actual picture, and (c) FEM analysis results for magnetic flux density.

6.3.2
Friction Reduction by Ultrasonic Vibrations

When ultrasonic vibration is applied to the sliding surface of a moving object, the direction of the friction on the object switches thousands to millions of times per second, and as a result, the effective friction decreases significantly [13–15]. Littmann *et al*. [14, 15] developed an analytical model to explain the phenomenon of friction reduction and demonstrated that the friction reduction ratio depends on the ratio of the velocities of the moving object and the sliding surface. Kumar *et al*. [16] also developed an analytical model for friction reduction and expressed the friction reduction ratio as follows:

$$F_a/F_0 = 2/\pi \sin^{-1} \frac{V_s}{a\omega} \approx \frac{2 \cdot V_s}{\pi \cdot a\omega} \tag{6.5}$$

where F_0 is the frictional force in the absence of vibration, F_a is resultant average frictional force with vibration, V_s is the velocity of the sliding object, and a and ω are the amplitude and angular frequency of the vibration, respectively.

By applying this phenomenon to the microfluidic chip, the effective friction on the MMT can be reduced considerably [17]. Figure 6.5 illustrates the concept of driving an MMT with ultrasonic vibration. Radially displaceable piezoelectric ceramic is attached to the glass substrate under the microfluidic chip and oscillates the sliding surface of the MMT.

6.3.3
Experimental Evaluations of MMT

6.3.3.1   **Positioning Accuracy Evaluation**
Because friction reduction using ultrasonic vibration is compatible with HPD, the design shown in Figure 6.4a was employed for the evaluation experiments. Four
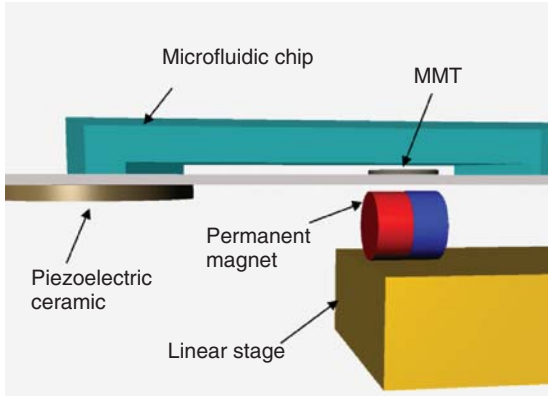
Figure 6.5 Concept of driving an MMT with ultrasonic vibration.

neodymium (Nd2Fe14B) magnets (diameter = 1.0 mm, grade = N40) were set on an x−y linear stage to serve as the drive magnet. A commercially available piezo-electric ceramic (W-40, MKT Taisei Co.) with dimensions of φ 42.0 × 3.5 mm was attached to the glass substrate to oscillate the microfluidic chip and improve the positioning accuracy. The resonance frequency of the ceramic was 55 kHz, and the electrostatic capacitance was 4600 pF. When a 300-V_{p-p} (peak-to-peak) AC voltage was applied at the resonance frequency, the piezoelectric ceramic was oscillated at an amplitude of 1.4 μm.

The linear stage was actuated in a circular trajectory with a constant drive veloc-ity, and the corresponding MMT positions were measured using a CCD camera. Four columnar neodymium magnets φ 1.0 mm × 1.0 mm in size were used as the drive unit. Figure 6.6a shows the MMT positioning accuracy without vibration by the piezoelectric ceramic versus the target circular trajectory (radius = 0.5 mm). The drive velocity of the linear stage was 0.785 mm s^{-1} in the x−y direction. Mea-surements were obtained at 100 points. The maximum error between the targets with respect to the actual MMT position was approximately 120 μm. However, when vibration was applied to the microfluidic chip, the MMT movement was significantly improved. Figure 6.6b shows the MMT positioning accuracy when 300 V_{p-p} was applied to the piezoelectric ceramic at a frequency of 55 kHz. The drive stage configuration was same as that shown in Figure 6.6a, but the maxi-mum error between the targets with respect to the actual trajectory was 9.5 μm, which reflects a positioning accuracy more than 10 times greater than in the case without vibration.

According to Eq. (6.5), the friction reduction ratio is a function of the vibration amplitude and the velocity of the MMT. Figure 6.6c shows the positioning error of the MMT from the target, excluding measurement error and stage error deter-mined by the root-mean-square method, for various applied voltages (15, 75, 150, 225, and 300 V_{p-p}) and drive velocities (0.16, 0.47, 0.79, 1.57, 2.36, 3.14, 3.93, 4.71, and 5.50 mm s^{-1}). The errors were measured at 100 points using a CCD camera, and values were interpolated from the measured data using cubic spline curves.
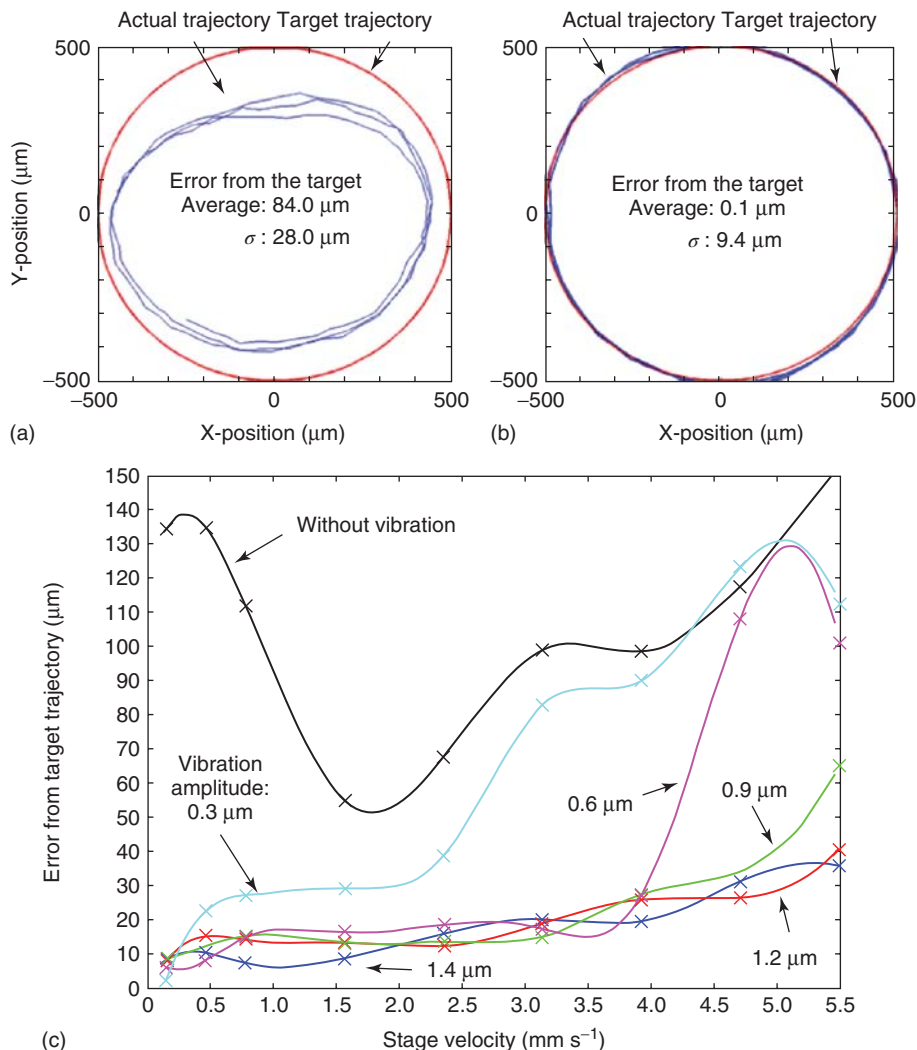
Figure 6.6 Results of evaluation of the MMT positioning error from the target trajectory. (a) Comparison of the target and actual trajectories without vibration. (b) Comparison of the target and actual trajectories with vibration. (c) Correlation of the maximum positioning error and the drive velocity for various vibration amplitude.

The positioning error increases with increasing stage velocity and decreases with increasing applied voltage, which represents the vibration amplitude at the sliding surface. In the case without vibration, the result corresponds to the Stribeck curve [18], and it is reasonable that the positioning error should increase with increasing friction. The results in the case with vibration broadly correspond to Eq. (6.5); however, the positioning accuracy at lower applied voltages is more precise than at higher voltages applied in the region of the low

stage velocity. This can be attributed to the fact that the positioning accuracy approaches the amplitude of the vibrations. In fact, the positioning accuracy of the MMT was 1.1 μm when the vibration amplitude was 0.3 μm and the stage velocity was 0.16 mm s^{-1}, but it is impossible to achieve this accuracy when the applied vibration amplitude was 1.4 μm, as shown in Figure 6.6c. Consequently, the error of MMT at a stage velocity of 0.16 mm s^{-1} was less than 1% of that without vibration when a vibration of 0.3 μm amplitude was applied.

6.3.3.2 Output Force Evaluation

Another advantage of static friction reduction pertains to the output force of the MMT. Figure 6.7a shows the experimentally measured output force of the MMT with and without ultrasonic vibration. The output force of the MMT with ultrasonic vibration (150 Vp−p, 55 kHz) was double that without vibration. Compared to other types of microactuators, the output force of an MMT is considerably higher and can reach magnitudes on the order of millinewtons. Increasing the maximum force enables the MMT to apply to the force required for tasks such as cell cutting and mechanical stimulation of microorganisms.

The actual friction on the MMT can be calculated from Kumar's equation (6.5) and the following force balances:

$$F_{\text{out}} = F_{\text{drive}} - F_0 \tag{6.6}$$

$$F'_{\text{out}} = F_{\text{drive}} - F_{\text{a}} \tag{6.7}$$

The unknown quantities in these equations are the drive force applied by the permanent magnet (F_{drive}), the friction without vibration (F_0), and the friction with vibration (F_{a}). We can calculate the unknown quantities from Eqs. (6.5−6.7). Figure 6.7b shows the calculated amounts of friction F_0 and F_{a}. Because of the friction reduction due to ultrasonic vibration, the friction decreased by a factor of nearly one thousand from the original amount, from 3.2 mN to 3.6 μN.
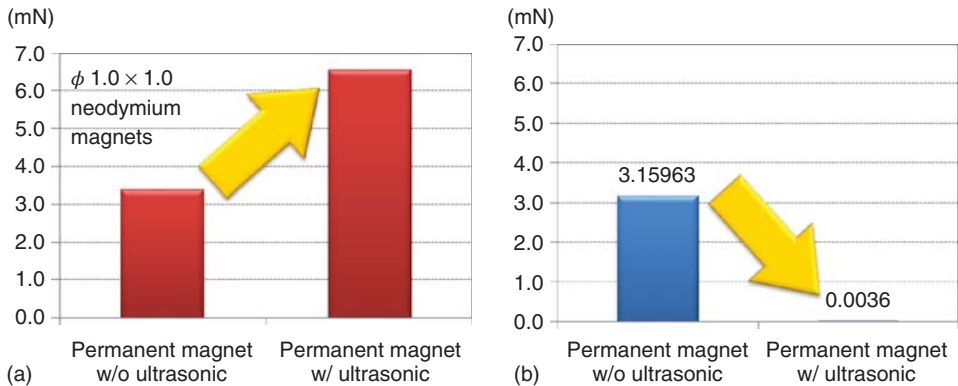

Figure 6.7 Force comparison with and without vibration. (a) Experimentally measured output force and (b) calculated friction force.

6.4

Fluid Friction Reduction for On-Chip Robot

6.4.1
Fluid Friction Reduction by Riblet Surface

By reducing static friction using the drive unit arrangement described and ultra-sonic vibration, the MMT was able to achieve a minimum positioning accuracy of 1.1 μm and a power output force of several millinewtons [12, 17]. However, as Eq. (6.5) shows, the friction reduction ratio depends on the MMT velocity and decreases as the velocity of the MMT increases. The fluid friction force, on the other hand, increases rapidly as the velocity of the MMT increases. As a result, the error between the MMT and the drive stage increases considerably when the stage velocity exceeds 3.1 mm s^{-1} (3 Hz), as shown in Figure 6.6c. Thus, the fluid friction on the MMT has to be reduced to achieve precise manipulation of the MMT at high speeds.

A riblet-shaped surface, consisting of regularly arrayed V grooves, can be employed on the MMT to reduce the fluid friction force [19]. The basic principle of reducing the fluid friction force using riblets is that squeezing liquid past the V grooves generates upward fluid force on the riblet surface and increases the lubricant film thickness. As a result, the shear stress decreases and the fluid friction force decreases. By employing a riblet surface on the MMT, the fluid friction can be reduced in high-speed actuation.

6.4.2
Principle of Fluid Friction Reduction Using Riblet Surface

Figure 6.8 presents the definitions of the variables associated with a riblet surface. To simplify the calculations, the surface facing the velocity direction is classified as Region I, and the rear surface is classified as Region II. The height $h(x)$ at any arbitrary position x is expressed as follows:

$$h(x) = h_1 - (h_1 - h_2)\frac{x}{B} = h_1\{a - (a - 1) \cdot \overline{x}\}$$
$$\because a = h_1/h_2, \qquad \overline{x} = x/B \tag{6.8}$$

From Eq. (6.8), we can obtain the following expression by derivation:

$$dx = -\frac{B}{h_2(a - 1)}dh \tag{6.9}$$

Here, we assume that the fluid pressure at the boundaries of Region I and Region II is 0; that is, $P(0) = P(B) = 0$. The following expression can then be derived from the Reynolds equation:

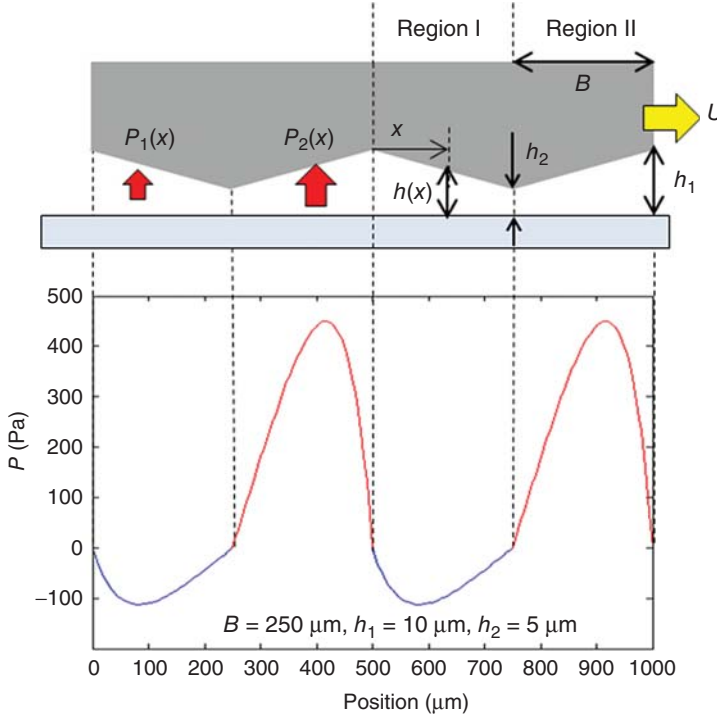$$\frac{d}{dx}\left(\frac{h^3}{\eta}\frac{dP}{dx}\right) = 6U\frac{dh}{dx} \tag{6.10}$$

Figure 6.8   Definition of the variables for the riblet and pressure distribution on the riblet surface.

where η is the viscous resistance.

For

$$I_2(x) = \int_0^x \frac{dx}{h^2}, I_3 = \int_0^x \frac{dx}{h^3}, h_m = \frac{I_2(B)}{I_3(B)},$$

$$I_2(x) = \frac{B}{h_2(a-1)}\left(\frac{1}{h} - \frac{1}{h_1}\right), \ I_3(x) = \frac{B}{2h_2(a-1)}\left(\frac{1}{h^2} - \frac{1}{h_1^2}\right),$$

and $h_m = \dfrac{I_2(B)}{I_3(B)} = \dfrac{2h_1 h_2}{h_1 + h_2},$

$$P(x) = 6\eta U\{I_2(x) - h_m I_3(x)\}$$

$$= 6\eta U\left[\frac{B}{h_2(a-1)}\left(\frac{1}{h} - \frac{1}{h_1}\right) - \frac{2h_1 h_2}{h_1 + h_2}\left\{\frac{B}{2h_2(a-1)}\left(\frac{1}{h^2} - \frac{1}{h_1^2}\right)\right\}\right]$$

$$(6.11)$$

To simplify the equations, we set $\overline{h} = \frac{h}{h_2} = a - (a-1) \cdot \overline{x}$, which yields the following expression:

$$P = \frac{6\eta UB}{h_2^2} \frac{1}{a-1} \left\{ \frac{1}{\overline{h}} - \frac{1}{a} - \frac{a}{1+a} \left(\frac{1}{\overline{h}^2} - \frac{1}{a^2} \right) \right\} \tag{6.12}$$

For Region II, in the same manner as for Region I, we obtain the following expression:

$$P = \frac{6\eta UB}{h_1^2} \frac{1}{a-1} \left\{ \frac{a}{1+a} \left(\frac{1}{\overline{h}^2} - \frac{1}{a^2} \right) - \frac{1}{\overline{h}} + \frac{1}{a} \right\} \tag{6.13}$$

Figure 6.8 shows the fluid pressure distribution calculated using Eqs. (6.12) and (6.13) for $B = 250\,\mu m$, $h_1 = 10\,\mu m$, $h_2 = 5\,\mu m$, $U = 5\,mm\,s^{-1}$, and $\eta = 0.882 \times 10^3$ Pa·s (water). The upward force is generated on Region I, and the negative force is generated on Region II. When the total fluid pressure is integrated over the surface area, the total force is always upward. This upward force increases the lubricant film thickness and decreases the fluid force.

6.4.3
Optimal Design of Riblet to Minimize the Fluid Friction

According to the Stribeck curve, the more the lubricant film thickness increases, the more the fluid friction decreases [18]. Therefore, designing the riblet shape (the height h_1 and the width B in Figure 6.8) to maximize the lubricant film thickness (h_2) minimizes the friction on the MMT. Three forces arise in the vertical direction during MMT movement on a microfluidic chip: the force of gravity ($F_{gravity}$), the magnetic force in the vertical direction (F_{magnet}), and the fluid force on the riblet (F_{fluid}). These three forces are balanced during MMT movement if the velocity of the MMT does not change, and thus, the lubricant film thickness remains same. That is,

$$F_{gravity} + F_{magnet} + F_{fluid} = 0 \tag{6.14}$$

The forces $F_{gravity}$ and F_{magnet} are easily measured, and F_{fluid} can be calculated using Eq. (6.12) or (6.13). Therefore, we can determine the optimal combination of h_1 and B that maximizes h_2 while satisfying Eq. (6.14).

In summary, this optimization problem can be expressed as follows:

- **Maximize:** h_2 (lubricant film thickness)
- **With respect to:** h_1, B (riblet shape)
- **Subject to:** $F_{gravity} + F_{magnet} + F_{fluid} = 0$ (force balance in the vertical direction).

The gravitational force ($F_{gravity}$) of the MMT was approximately $5\,\mu N$, and the vertical component of the magnetic force (F_{magnet}), which was experimentally measured, was $23\,\mu N$. Figure 6.9 shows the calculation results for h_2 under the constraints of Eq. (6.14). On the basis of this calculation result, the film thickness h_2 does not depend on the riblet width B and is maximized at $2.7\,\mu m$ when
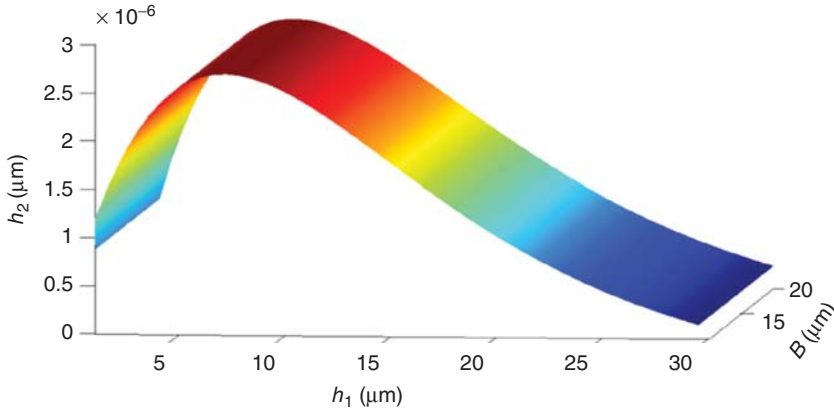
Figure 6.9   Result of riblet design optimization to maximize the lubricant film thickness h_2 ($U = 100\,\text{mm s}^{-1}$).

$h_1 = 8.0\,\mu\text{m}$. Note that the width of the riblet (B) has little effect on h_2 because the total MMT area is fixed; thus, as the width increases, the number of riblets decreases.

6.4.4
Fluid Force Analysis on MMT with Riblet Surface

It is expected that a riblet surface will reduce the fluid friction force on an MMT and that the degree to which the fluid friction is reduced will increase with increasing MMT velocity because of the higher lubricant film thickness, whereas the fluid force simply increases as the velocity of the object increases. Development of a model for the fluid force on the MMT helps us to understand the mechanisms of fluid friction and MMT behavior in high-speed actuations [19].

Figure 6.10 shows the forces on the MMT during actuation at high speed. Assuming that the MMT is actuated under full-film lubrication conditions, the forces in the horizontal direction are the shear force between the glass substrate and the MMT (F_t), the fluid drag force (D), and the x component of the magnetic force (F_{Mx}). Therefore, the equation of motion of the MMT is expressed as follows:

$$m\frac{dU}{dt} = F_{\text{Mx}} - D(U) - F_t(U) \tag{6.15}$$

where U is the drive velocity of the MMT and m is the mass of the MMT. The fluid drag force and the shear force are functions of U and increase as U increases, whereas the magnetic force is not affected by the velocity.

Fluid drag force (D)

The fluid drag force D is expressed as follows:
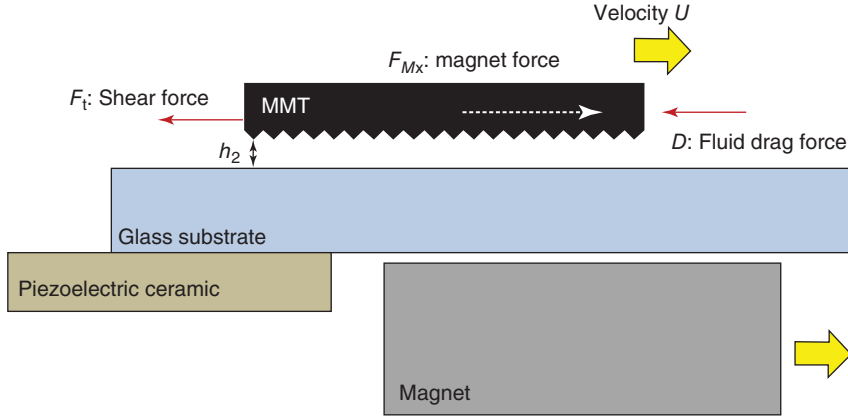
$$D(U) = \frac{C_D}{2}\rho U^2 A \tag{6.16}$$

Figure 6.10 Model for forces on the MMT.

where A is the area of the MMT, ρ is the density of the fluid, and C_D is the drag coefficient, the value of which is approximated as follows when the Reynolds number (Re) is approximately 1.0 [20]:

$$C_D = 1 + 10Re^{-2/3} \tag{6.17}$$

$$Re = \frac{UL}{\upsilon} \tag{6.18}$$

where L is the representative length of the channel and υ is the kinetic viscosity of the fluid.

Shear force (F_t)

A shear force F_t on the MMT exists due to the velocity gradient between the glass substrate and the MMT surface:

$$F_t = \mu\frac{dU}{dh_2} \cdot A \tag{6.19}$$

where μ is the fluid viscosity and h_2 is the lubricant film thickness. The value of h_2 can be calculated from Eqs. (6.12–6.14).

Figure 6.11 shows the calculation results for h_2 for the optimal riblet depth and width. The results show that the lubricant film thickness increases with increasing MMT velocity. However, in the low-speed region (less than $7\,\text{mm s}^{-1}$), h_2 is less than the surface roughness of the MMT ($R_z = 0.15\,\text{mm}$). In this region, the MMT is no longer levitated, and the lubricant condition is the boundary lubrication or mixed-film lubrication [21].

Under conditions of boundary lubrication or mixed-film lubrication, the MMT comes into contact with the glass substrate, and Coulomb friction is created. However, the Coulomb friction will be reduced significantly by the ultrasonic vibration induced by the piezoelectric ceramic. The effective Coulomb friction can be expressed as shown in Eq. (6.5). Figure 6.12 shows the calculation results for $D + F_t$
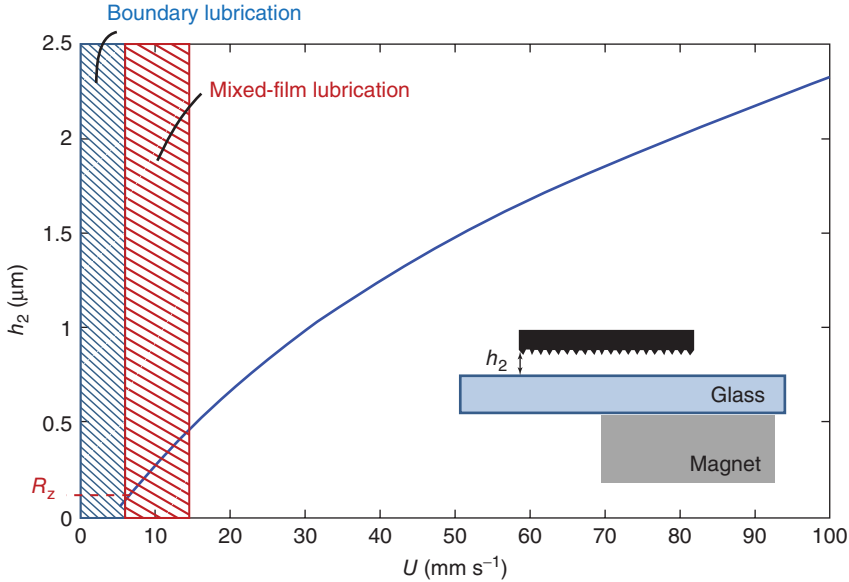
Figure 6.11 Calculated levitation height over velocity.

on the MMT for the optimized and nonoptimized riblet designs. For the latter, the surface roughness $R_z = 0.15\,\mu m$. In the low-speed region, Coulomb force is applied to the MMT because the MMT comes into contact with the glass substrate. However, the Coulomb friction is balanced by the effect of vibration, and the drag force is also low in the low-speed region. As a result, the resistance on the MMT remains low for both the optimized and nonoptimized riblet designs. On the other hand, much less fluid force is applied on the MMT in the high-speed region with the optimized riblet design than with the nonoptimized design, because the lubricant film thickness is much higher with the optimized design than with the nonoptimized design. As a result, the shear force on the MMT with the optimized riblet design is much smaller under fluid lubrication conditions.

In high-speed actuation, the inertial force tends to be a problem, but scale effects prevent the inertial force on the MMT from increasing. The red dashed line in Figure 6.12 shows the maximum inertial force applied on the MMT when the MMT actuates with a ±0.5-mm stroke sine wave. The maximum inertial force is half of the fluid force at $100\,mm\,s^{-1}$ and has little effect on the MMT movement, compared to the fluid force due to the low weight of the MMT (5 mg). Therefore, an MMT with an optimal riblet surface can be expected to follow the drive stage precisely with less resistance during high-speed actuation.

The dots and error bars in Figure 6.12 indicate the measured fluid force on the MMT with the optimal riblet surface. The results indicate that the simulation results agree reasonably well with the experimental data. The differences between the experimental values and the calculated values may be due to the Reynolds number being different at different MMT velocities, whereas the drag coefficient
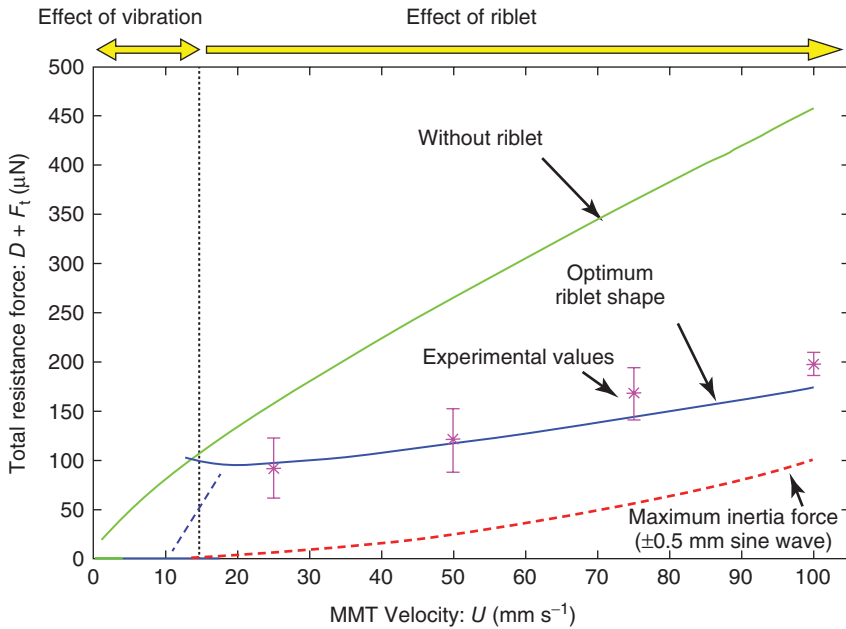
Figure 6.12 Calculated fluid force on the MMT and experimentally measured fluid force for the optimal riblet shape.

and velocity gradient were held constant in the calculations. The fluid condition may change during testing if the Reynolds number changes. In addition, a certain amount of experimental error is introduced by the 2.5-µm/pix resolution of the CCD camera, pulsation of the syringe pump, and the size distribution of the commercially produced permanent magnets.

6.4.5
Fabrication Process of MMT with Riblet Surface Using Si–Ni Composite Structure

Precise three-dimensional fabrication is required to produce the optimal riblet shape. However, it is quite difficult to produce micrometer-sized riblets on an MMT by Ni electroplating. Therefore, a composite structure of Si and Ni was employed [19].

Figure 6.13 illustrates the process used to fabricate the Ni–Si composite MMT with a riblet surface. First, SiO_2 was sputtered on to a 200-µm-thick Si wafer with (100) crystal orientation (thickness = 300 nm). Then, HMDS was spin-coated on the SiO_2 to bond OFPR and SiO_2 properly. Next, OFPR-800 200 cp (TOKYO OHKA KOGYO CO., LTD.) was spin-coated on the HMDS (thickness = 4 µm). The OFPR was exposed, and 9-µm-pitched stripes (2 µm widths of OFPR and 7 µm gaps) were patterned. Acid treatment was then performed using a 10 : 1 buffered hydrogen fluoride (BHF) solution to etch the SiO_2. After the OFPR was removed with acetone, anisotropic wet etching of the Si was conducted with a 50% solution

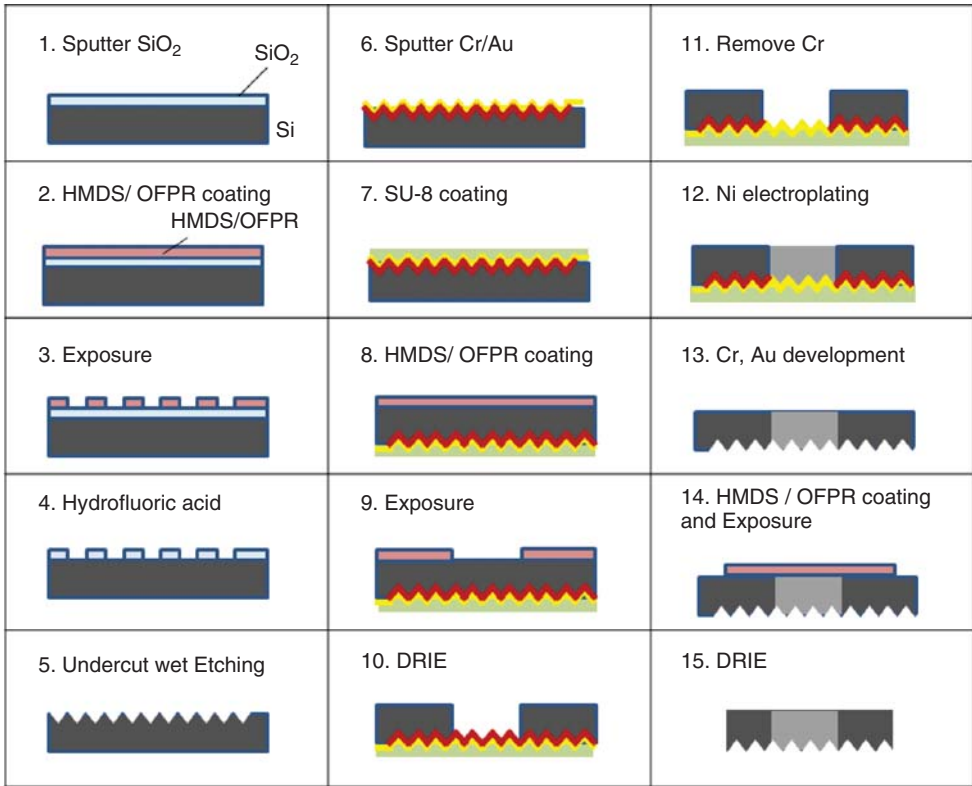| 1. Sputter SiO$_2$	6. Sputter Cr/Au	11. Remove Cr
2. HMDS/ OFPR coating	7. SU-8 coating	12. Ni electroplating
3. Exposure	8. HMDS/ OFPR coating	13. Cr, Au development
4. Hydrofluoric acid	9. Exposure	14. HMDS / OFPR coating and Exposure
5. Undercut wet Etching	10. DRIE	15. DRIE

Figure 6.13   Fabrication process for an MMT with riblet surface.

of potassium hydroxide (KOH). The etching direction was 54.7° for the Si with (100) crystal orientation. Therefore, the depth of the V grooves could be controlled by the pitch of the stripe mask and the etching time. Undercutting was intentionally employed to reduce the horizontal area of the stripe mask. The optimal riblet shape was then fabricated on the Si wafer (process 5 in Figure 6.13). The optimal riblet shape determined as described in the previous section was then fabricated precisely. Figure 6.14a shows a scanning electron microscope (SEM) image of the Si after wet etching. Note that a certain amount of the horizontal area (approximately 1 μm wide) was left to prevent failure of the fabrication. If all of the horizontal area had been etched, the mask would have peeled off, and the V shape would have been gone in a matter of seconds.

Next, Cr/Au was sputtered on to the riblet surface (thickness = 300 nm), and SU-8 was spin-coated on the riblet surface as a support layer. After HMDS and OFPR were coated on the opposite surface (thickness = 4 μm), it was exposed to a pattern of a circular shape for Ni actuation. Deep reactive ion etching (DRIE) was then conducted to penetrate the Si.

After the Cr film was removed by Cr etchant, Ni was formed by electroplating. The Si–Ni composite structure of the MMT was fabricated after the Cr/Au and
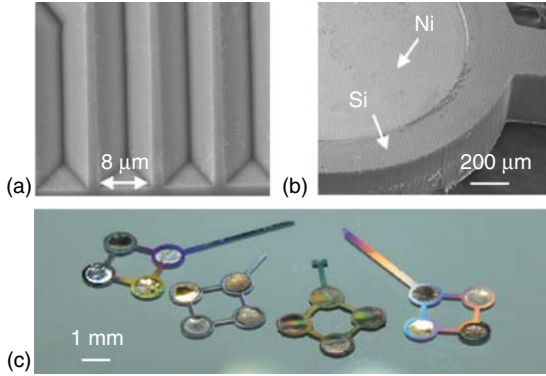
Figure 6.14 Fabricated MMT. (a) SEM image of riblet surface after wet etching. (b) SEM image of fabricated microrobot with optimal riblet surface. (c) Fabricated MMT. Rainbow colors are shown because of light interference from the riblet surface.

Ni support sheet were removed by Cr and Au etchant. Finally, to form the MMT shape, HMDS and OFPR were again coated and exposed to pattern the MMT shape, and DRIE was conducted to form the whole shape of the MMT. Figure 6.14b shows an SEM image of a fabricated MMT with an optimized riblet. The riblet shape was patterned on the Si and Ni surface, and the Ni was surrounded by Si. Figure 6.14c shows the fabricated MMT. Rainbow colors are shown because of light interference from the riblet surface. An MMT fabricated in this manner can be used for various applications by changing the tip shape, depending on the application, such as cutting, sorting, capturing, or stimulating. Figure 6.14c shows various types of MMTs with riblet surfaces for various applications.

6.4.6
Evaluation of Si–Ni Composite MMT with Optimal Riblet

An experiment was conducted to evaluate the effect of the riblet surface. The linear stage, whose actuation speed is up to $400\,\mathrm{mm\,s^{-1}}$, was actuated as a one-DOF sine wave with a ± 0.5-mm stroke, from 0.1 to 100 Hz. The corresponding MMT positions were measured using a high-speed camera (1000 frames/s) through the microscope, and the stage position was recorded through the encoder. The camera resolution was $2.5\,\mu\mathrm{m/pix}$. The four columnar neodymium magnets ($\phi\,1.0\,\mathrm{mm}\times 1.0\,\mathrm{mm}$, magnetic flux density at the magnet surface $=176\,\mathrm{mT}$) were used as the drive unit for HPD conditions [12]. A voltage of $150\,\mathrm{V_{p-p}}$ was applied to piezoelectric ceramics to induce ultrasonic vibrations and reduce Coulomb friction on the MMT [17]. A culture solution (Medium 199 with follicular fluid) was used for the liquid.

The riblets have an orientation, and thus, the MMT actuation must differ from the drive direction. Therefore, the frequency characteristic was measured for a Si–Ni MMT with riblets in two different directions, as well as a Ni MMT and a Si–Ni composite MMT without riblets. In addition, Si pillars whose contact
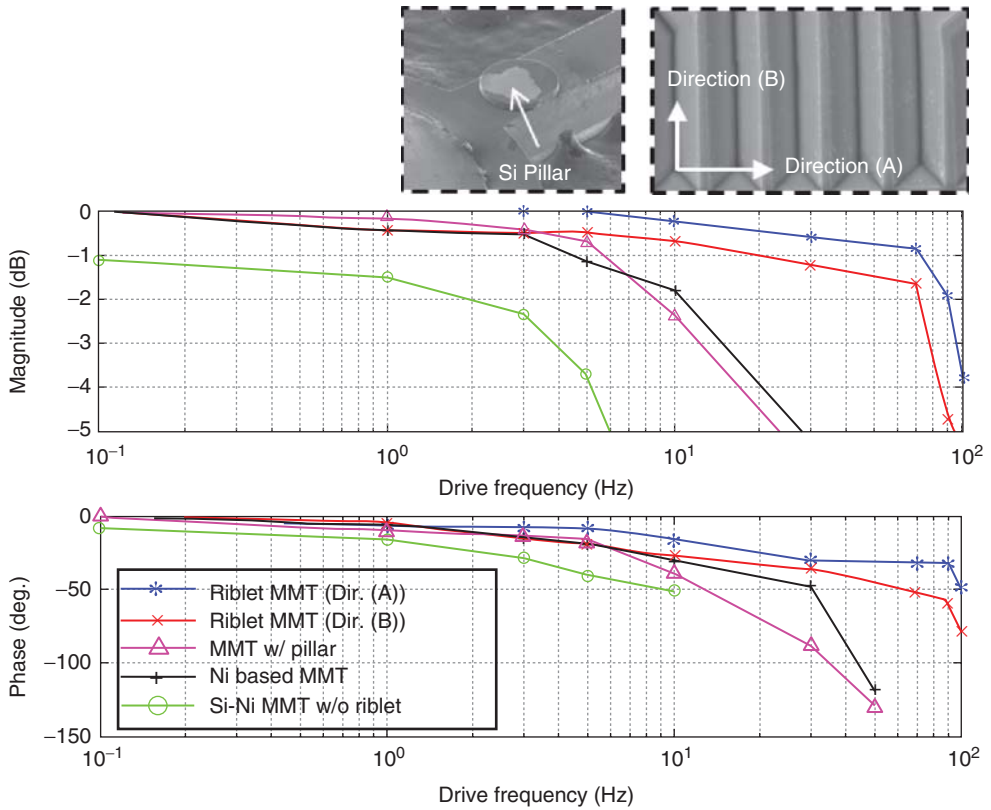
Figure 6.15 Drive frequency characteristics of the microrobots with and without riblet surface.

area was the same as that of the riblets were fabricated on an MMT instead of V grooves to evaluate the effect of contact area reduction on the driving performance of the MMT.

Figure 6.15 shows the frequency response characteristics of the various MMTs tested in the experiment. The magnitude graph shows the MMT amplitude with respect to the stage amplitude in decibels, and the phase graph shows the MMT phase lag from the stage movement. The results show that the MMT with the optimal riblet surface can follow the stage up to 90 Hz (maximum speed = 282.6 mm s^{-1}) in direction (A) (magnitude = less than 2 dB, maximum error = 140.5 μm), while the conventional Ni-based MMT does not move after 10 Hz. In addition, the Si–Ni composite MMT without riblets experiences delays at 3 Hz and does not move at all after 5 Hz. These results show that the riblet surface improves the drive speed of the MMT by a factor of 10.

On the other hand, the MMT driven parallel to the riblet grooves (direction (B)) can be actuated properly up to 70 Hz. Compared to the results for the MMT with riblets moving in direction (A), the drive capability of the MMT driven parallel to

the riblets was worse; however, the following response was considerably improved, compared to that of the MMT without riblets, because the fluid cannot escape from the V grooves when the fluid flows parallel to the V grooves, and this helps to maintain a thicker lubricant film [22]. As a result, the fluid friction on the MMT can be kept low, and the MMT can achieve high-speed actuation.

The results for the MMT with the Si pillars indicate that the MMT initially followed the drive stage precisely but that the magnitude decreased significantly after 5 Hz and that it did not move after 10 Hz. The results were very similar to those for the Ni MMT, although the contact area of the MMT with pillars was much smaller than that of the Ni MMT. This is because there is no effect of contact area under fluid lubricant conditions, because the MMT and glass substrate are no longer in contact. In the low-speed region, the lubrication with boundary conditions and appropriate Coulomb friction was applied on the MMT. In this case, the effect of the contact area may be substantial; however, the effect of the vibration by piezoelectric ceramic is quite high and it covered the effect of the contact area reduction. From this result, the small contact area of the riblet does not contribute to the high-speed actuation of MMT.

6.5
Applications of On-Chip Robot to Cell Manipulations

Cell manipulations in the confined space of a microfluidic chip are highly important in the field of biotechnology because of the low contamination capability, repeatability, and high throughput possible. On-chip robots offer great advantages over human handling in the treatment of biological cells, because their functioning is not dependent on operator skill and is capable of high throughput and high repeatability. In addition, microfluidic chips supply flow processes to high-speed microrobots that permit high-throughput manipulations.

With MMTs that can achieve precise positioning up to 1.1 μm, high-speed actuation up to 90 Hz, and high-power-output force on the order of several millinewtons, a wide range of applications for cell manipulations can be achieved using microfluidic chips. Several applications of cell manipulation by MMTs on microfluidic chips are presented in this section.

6.5.1
Oocyte Enucleation

Cloning has been actively investigated for use in food production, organ transplantation, and the development of genetically similar laboratory animals. Enucleation of oocytes is a cloning process that is time consuming and requires operator skill. As currently performed, manually operated micromanipulators with glass capillaries are used to remove a nucleus under a microscope. However, the conventional manual manipulation method tends to have problems with contamination, a low success rate, and low repeatability. As a result, complicated cell
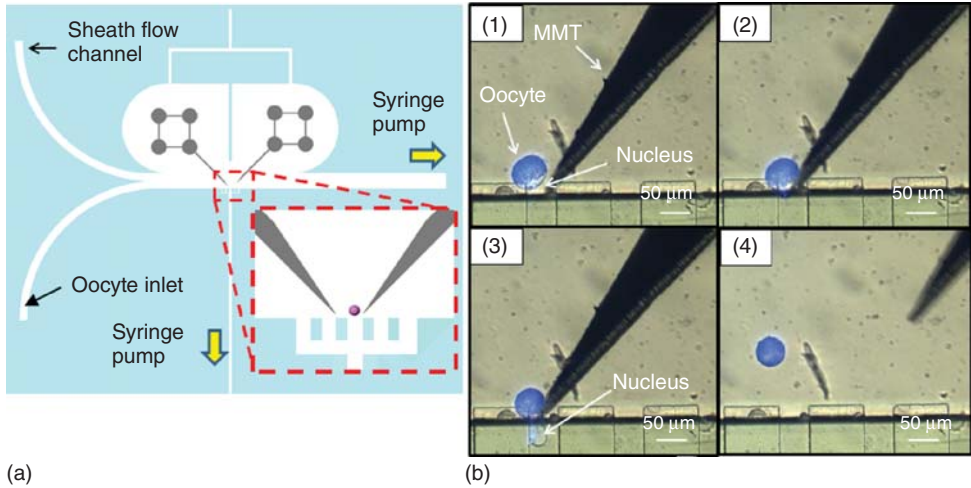
Figure 6.16   Enucleation of oocyte by on-chip robots. (a) Design for the microfluidic chip for use in enucleation. (b) Experimental results of enucleation.

manipulation work can only be carried out by skilled people. Oocyte enucleation performed by an MMT on a microfluidic chip is described below.

Figure 6.16a illustrates the design of a microfluidic chip for enucleation of oocytes. The oocytes are inserted at the inlet port and flow in a channel 100-μm high and 200-μm wide. The height of the channel to the nucleus collection port is lower (50 μm) so that the area containing the nucleus cannot escape from the MMT in the z-direction. The dual-arm MMT then rotates the oocyte, and the area containing the nucleus is drawn into the channel. The dual-arm MMT cuts the oocyte with the tip of the blade and the nucleus flows into the nucleus collection port. The remaining oocyte flows into the oocyte collection port to be used in subsequent processes. The sheath flow channel is set for the oocyte to flow along the polydimethylsiloxane (PDMS) wall and reaches the manipulation area properly. The sheath flow restricts the fluid from the oocyte inlet port from flowing to the area where the MMT is placed, and thus, the oocyte can keep flowing along the wall. In addition, the center PDMS wall between the dual-arm MMTs prohibits fluid flow from occurring in the MMT actuation area.

Figure 6.16b shows experimental results for swine oocyte enucleation. The oocyte that was inserted at the inlet flowed to the narrow channel and became lodged because the oocyte was not small enough to enter the channel, which was 50-μm wide and high (Figure 6.16b (1)). After the nucleus position was confirmed, the oocyte was rolled by the MMT and pushed back to the narrow channel so that the nucleus-containing area was trapped in the channel (Figure 6.16b (2)). The tip of the MMT then pressed (Figure 6.16b (3)) and cut the oocyte. The nucleus was successfully removed, and the oocyte retained its circular shape even after the cutting (Figure 6.16b (4)). The processing time, which is from the time when

the oocyte reached the narrow channel to the time when the oocyte was cut, was less than 10 s, and the portion of the oocyte removed was approximately 20% of the original size.

6.5.2
Multichannel Sorting

Sorting specific cells out of mixtures is required in cell observation and analysis of cells. Flow cytometers, also called *cell sorters*, which are used to assay individual cells and separate or collect cells from suspensions [23], present problems of cost, size, and adaptability. Mechanical sorting of microparticles into multiple channels is a good example of an application of a high-speed on-chip robot [19]. Figure 6.17a shows the design of a multiple-channel sorting chip using MMTs. The cells or particles are inserted from the inlet and delivered to the channel area. A pair of MMTs then blocks all the channels except for the desired one, so that the particle flows into the desired channel with the fluid flow. The sorted particle can be observed at the observation port located downstream of the channel. The advantage of this sorting device is that it can perform completely label-free sorting because only mechanical phenomena are involved. By integrating a high-speed vision sensor, the chip can be made to sort by size, shape, and color into multiple channels. Figure 6.17b shows the actual sorting microfluidic chip. The size of the device is only 30×30 mm. The microfluidic chip was made of PDMS using photolithography.

Figure 6.17c shows experimental results of the sorting of ϕ 70-μm polystyrene beads into 30 branches. The flow rate of the polystyrene beads was 7.5 mm s^{-1}, and a high-speed vision sensor was integrated into the device to detect each particle and shift the MMT to the next channel. The polystyrene beads were successfully separated into the channels, one by one, and could be observed at the observation port. Because of the high-speed actuation of the microrobot and the flow control of the microfluidic chip, the sorting throughput was increased significantly.

6.5.3
Evaluation of Effect of Mechanical Stimulation on Microorganisms

In the biosciences, mechanical stimulation of single cells has become essential to the investigation of the functions and mechanical characteristics of cells [24, 25]. In particular, investigation of the effect of mechanical stimulation offers significant potential for increasing understanding of the characteristics of aquatic microorganisms, in fields such as neurology and biofuel technology [26]. Because the mechanical characteristics of a number of aquatic microorganisms are not yet fully understood, a mechanical approach is essential to improve our understanding of cell interaction, the growth of cells, and the functions of mechanoreceptors. Even though fluidic force has been actively employed for stimulating cells on microchips for experimental convenience [27, 28], a
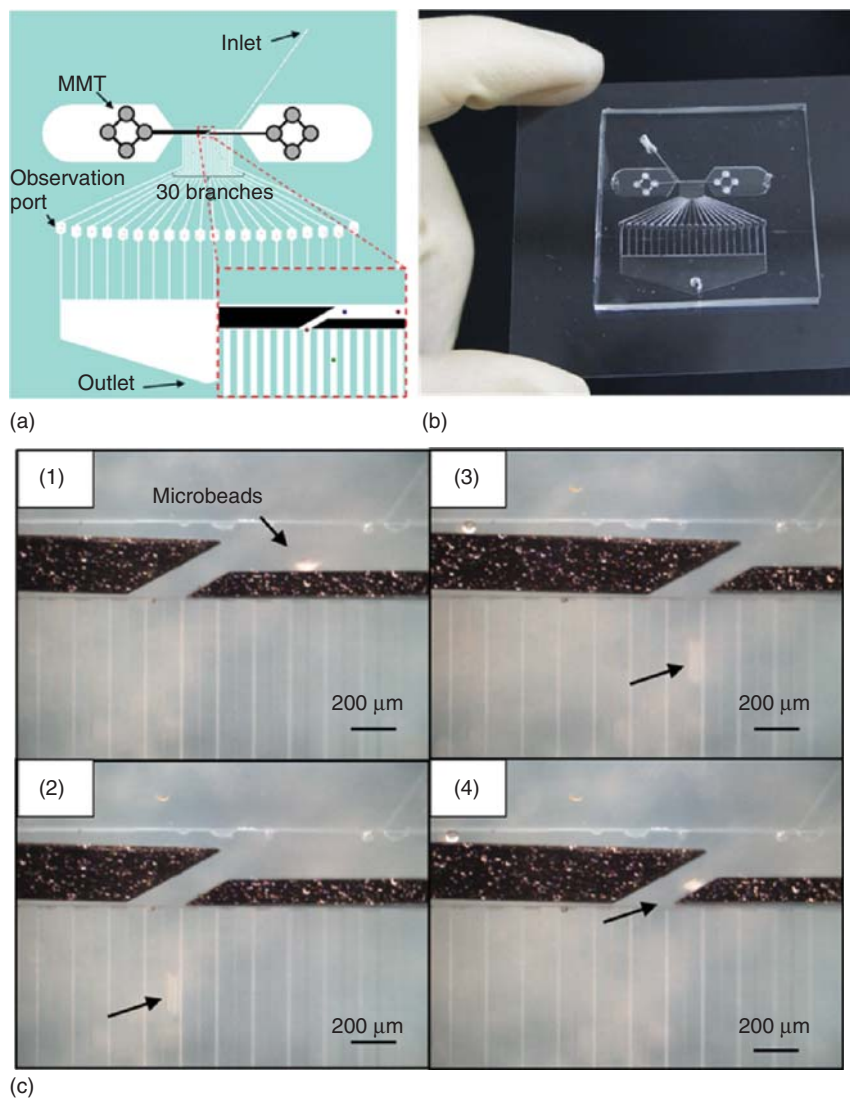
Figure 6.17 Multiple-channel mechanical sorting by on-chip robots. (a) Design of the sorting chip. (b) Actual microfluidic chip and MMTs. (c) Experimental results of sorting with ϕ 70-µm polystyrene beads.

mechanical probe is a stronger tool with which to apply a force to a specific part of a single cell as a stimulus.

An on-chip microrobot capable of force-sensing using a magnetically driven microrobot was developed to evaluate the effect of stimulating microorganisms on a microfluidic chip [29]. Using a noncontact actuated microrobot with a force-sensing structure (i.e., a beam structure), we can apply a millinewton-order force

to a single cell using the strong magnetic force of permanent magnets and then estimate the applied force from the deformation of the beam. In doing so, we use a completely closed biochip, and therefore, we can avoid contamination and maintain stable experimental conditions during our measurements. This is important because it is necessary to continuously observe the chemical reactions occurring in microorganisms in response to stimulation.

Figure 6.18a shows a frame model of the force-sensing structure. This structure is not a cantilever structure, and it is necessary to keep the microrobot heading straight when it is pushed toward microorganisms. In addition, a mechanism to magnify the beam deformation was placed within the frame to increase the sensitivity of the camera's force sensing. A small probe was attached to the tip of the force-sensing structure to push at a specific place on a cell. Figure 6.18b shows a fabricated microrobot with a 5-μm-wide force-sensing structure. The Si wafer was almost vertically etched by DRIE with a margin of fabrication error within 1%.
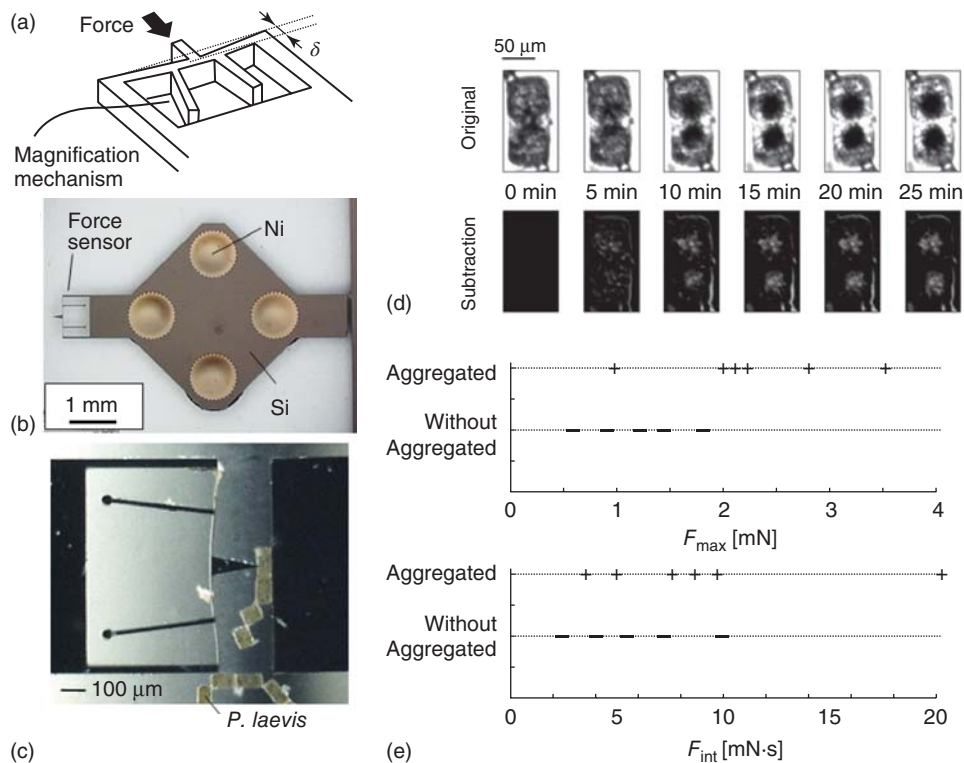

Figure 6.18 Mechanical stimulating MMT with force sensor. (a) Force sensor structure. (b) Fabricated MMT with force sensor. (c) Stimulation of *P. laevis* by on-chip robot with force sensor. (d) Investigation of the effect of stimulation for *P. laevis*. (e) Relation of chloroplast agglomeration to force applied to *P. laevis*.

We applied the microrobot to actual microorganisms. *Pleurosira laevis*, which is found in freshwater, is a centric diatom. This cylindrically shaped single cell has a vitriform structure (a silicic outer shell) that is approximately 1.3-μm thick, 100-μm long, and 40–80-μm wide. This type of microorganism exhibits unique behavior: when the cell is stimulated, the chloroplasts within it agglomerate around the nucleus. Furthermore, this agglomeration behavior is transmitted to other connected cells. From the perspective of neurology and algae-based biofuels, investigation of this behavior will be useful in understanding the communication mechanisms between aquatic microorganisms. The agglomeration behavior is caused by optical and electrical stimulation, but the mechanism of this behavior is still not fully understood [30].

Figure 6.18c shows an overview of the experiment. We confirmed that the robot developed had sufficient force to break the outer shell of *P. laevis*; the pushing force was therefore adjusted to avoid damage to the cell. As a result, we succeeded in stably stimulating a single cell of *P. laevis*. The applied force was then estimated. After stimulation, the chloroplast agglomeration was observed using the CCD camera, as shown in the original images in Figure 6.18d. From these images, the microrobot-stimulated movement of the chloroplasts was clearly confirmed. Then, to evaluate the degree of chloroplast agglomeration, subtraction images were generated by subtracting each image from the first image (at 0 min), and a summation of the pixel value of each subtraction image was plotted, as shown in Figure 6.18d. By setting an appropriate threshold value, we could determine whether agglomeration occurred. Figure 6.18e shows a summary of the experiments for 11 cells, where F_{max} is the maximum force value of each stimulation and F_{int} is calculated by integration of the time series of the applied force. The results suggest that the effect of the maximum force was greater than that of the total pushing force, although there were individual differences among the cells. In fact, lengthy stimulation with a small force did not induce chloroplast agglomeration. This indicates that we should apply stimulation at least until receptors reach a lower limit for activation. Furthermore, momentary stimulation could be effective in emphasizing the difference in stimulant response between cells for the purposes of more specific evaluation.

6.6
Summary

The combination of robotics and microfluidics has great potential for biomedical innovations. Both physical control and environmental control enable high-throughput continuous physical cell manipulations. In this chapter, we introduced MMTs for high-power, high-precision, high-speed use as on-chip robots. Using MMTs, a wide range of cell manipulations can be accomplished. The final goal is fully automated cell manipulation by integrating high-speed sensors and a feedback control of drive stages. Then, a production-line manufacturing can be developed on a small chip.

References

1. Arai, F., Ogawa, M., Fukuda, T., Horio, K., Sone, T., Itoigawa, K., and Maeda, A. 2000 High-speed random separation of microobject in microchip by laser manipulator and dielectrophoresis. Proceedings of the 13th International Conference on Micro Electro Mechanical Systems (MEMS 2000), pp. 727-732.

2. Bustamante, C., Macosko, J.C., and Wuite, G.J.L. (2000) Grabbing the cat by the tail: manipulating molecules one by one. *Nat. Rev.*, **1**, 130–136.

3. Ishijima, A. and Yanagida, T. (2001) Single molecule nanobioscience. *Trends Biochem. Sci*, **26** (7), 7.

4. Arai, F., Ichikawa, A., Ogawa, M., Fukuda, T., Horio, K., and Itoigawa, K. (2001) High-speed separation system of randomly suspended single living cells by laser trap and dielectrophoresis. *Electrophoresis*, **22**, 6.

5. Eriksson, E., Sott, K., Lundqvist, F., Sveningsson, M., Scrimgeour, J., Hanstorp, D., Goksor, M., and Graneli, A. (2010) A microfluidic device for reversible environmental changes around single cells using optical tweezers for cell selection and positioning. *Lab Chip*, **10**, 9.

6. Werner, M., Merenda, F., Piguet, J., Salathé, R.P., and Vogel, H. (2011) Microfluidic array cytometer based on refractive optical tweezers for parallel trapping, imaging and sorting of individual cells. *Lab Chip*, **11** (14), 2432.

7. Abbott, J.J., Peyer, K.E., Lagomarsino, M.C., Zhang, L., Dong, L., Kaliakatsos, I.K., and Nelson, B.J. (2009) How should microrobots swim? *Int. J. Rob. Res.*, **28** (11-12), 1434–1447.

8. Zhang, L., Peyer, K.E., and Nelson, B.J. (2010) Artificial bacterial flagella for micromanipulation. *Lab Chip*, **10** (17), 2203–2216.

9. Yesin, K.B. (2006) Modeling and control of untethered biomicrorobots in a fluidic environment using electromagnetic fields. *Int. J. Rob. Res.*, **25** (5-6), 527–536.

10. Pawashe, C., Diller, E., Floyd, S., and Sitti, M. (2011) Assembly and disassembly of magnetic mobile-robots towards deterministic 2-D reconfigurable micro-systems. *Proc. IEEE Int. Conf. Rob. Autom.*, **6**, 43–54.

11. Sakar, M.S., Steager, E.B., Kim, D.H., Kim, M.J., Pappas, G.J., and Kumar, V. (2010) Single-cell manipulation using ferromagnetic composite microtransporters. *Appl. Phys. Lett.*, **96** (4), 043705.

12. Hagiwara, M., Kawahara, T., Yamanishi, Y., and Arai, F. (2010) Driving method of microtool by horizontally arranged permanent magnets for single cell manipulation. *Appl. Phys. Lett.*, **97** (1), 013701-1–013701-3.

13. Kutomi, H., Daugela, A., Gerberich, W.W., Fujii, H., and Wyrobek, T.J. (2003) Nanoscale friction reduction and fatigue monitoring due to ultrasonic excitation. *Tribol. Int.*, **36**, 255–259.

14. Littmann, W., Storck, H., and Wallaschek, J. (2001) Sliding friction in the presence of ultrasonic oscillations: superposition of longitudinal oscillations. *Arch. Appl. Mech.*, **71**, 549–554.

15. Storck, H., Littmann, W., Wallaschek, J., and Mracek, M. (2002) The effect of friction reduction in presence of ultrasonic vibrations and its relevance to travelling wave ultrasonic motors. *Ultrasonics*, **40**, 379–383.

16. Kumar, V.C. and Hutchings, I.M. (2004) Reduction of the sliding friction of metals by the application of longitudinal or transverse ultrasonic vibration. *Tribol. Int.*, **37**, 833–840.

17. Hagiwara, M., Kawahara, T., Yamanishi, Y., Masuda, T., Feng, L., and Arai, F. (2011) On-chip magnetically actuated robot with ultrasonic vibration for single cell manipulations. *Lab Chip*, **11** (12), 2049–2054.

18. Lu, X., Khonsari, M.M., and Gelinck, E.R.M. (2006) The stribeck curve: experimental results and theoretical prediction. *J. Tribol.*, **128**, 789–794.

19. Hagiwara, M., Kawahara, T., Iijima, T., and Arai, F. (2013) High-speed magnetic microrobot actuation in a microfluidic chip by a fine V-groove surface. *IEEE Trans. Rob.*, **29** (2), 363–372.

20. Tritton, D.J. (1959) Experiments on the flow past a circular cylinder at low Reynolds numbers. *J. Fluid Mech.*, **6**, 25.

21. Zhu, D. and Hu, Y.Z. (2001) Effects of rough surface topography and orientation on the characteristics of EHD and mixed lubrication in both circular and elliptical contacts. *Tribol. Trans.*, **44** (3), 391–298.

22. Yuan, S., Huang, W., and Wang, X. (2011) Orientation effects of micro-grooves on sliding surface. *Tribol. Int.*, **44**, 1047–1054.

23. Bonner, W.A., Hulett, H.R., Sweet, R.G., and Herzenberg, L.A. (1972) Fluorescence activated cell sorting. *Rev. Sci. Instrum.*, **43** (3), 6.

24. Meyer, C.J., Alenghat, F.J., Rim, P., Fong, J.H., Fabry, B., and Ingber, D.E. (2000) Mechanical control of cyclic AMP signalling and gene transcription through integrins. *Nat. Cell Biol.*, **2**, 666–668.

25. Itabashi, T., Terada, Y., Kuwana, K., Kan, T., Shimoyama, I., and Ishiwata, S. (2012) Mechanical impulses can control metaphase progression in a mammalian cell. *Proc. Natl. Acad. Sci. U.S.A.*, **109**, 7320–7325.

26. Teixeira, R.E. (2012) Energy-efficient extraction of fuel and chemical feedstocks from algae. *Green Chem.*, **14**, 419–427.

27. Lu, H., Koo, L.Y., Wang, W.M., Lauffenburger, D.A., Griffith, L.G., and Jensen, K.F. (2004) Microfluidic shear devices for quantitative analysis of cell adhesion. *Anal. Chem.*, **76**, 5257–5264.

28. Park, J.Y., Yoo, S.J., Hwang, C.M., and Lee, S.H. (2009) Simultaneous generation of chemical concentration and mechanical shear stress gradients using microfluidic osmotic flow comparable to interstitial flow. *Lab Chip*, **9**, 2194–2202.

29. Kawahara, T., Sugita, M., Hagiwara, M., Arai, F., Kawano, H., Ishikawa, I., and Miyawaki, A. (2013) On-chip microrobot for investigating the response of aquatic microorganisms to mechanical stimulation. *Lab Chip*, **13**, 1070–1078.

30. Shihira-Ishikawa, I., Nakamura, T., Higashi, S., and Watanabe, M. (2007) Distinct responses of chloroplasts to blue and green laser microbeam irradiations in the centric diatom Pleurosira laevis. *Photochem. Photobiol.*, **83**, 1101–1109.

7

Silicon Nanotweezers for Molecules and Cells Manipulation and Characterization

Dominique Collard, Nicolas Lafitte, Hervé Guillou, Momoko Kumemura, Laurent Jalabert, and Hiroyuki Fujita

7.1
Introduction

In modern life, technologies enabling detection of biological samples at a low threshold for health and ecological concerns are in high demand. Besides approaches using high-throughput analyses of thousands of assays at the same time [1], detection limits are improved when the analysis is performed in tiny volumes, as demonstrated by microfluidic chip [1, 2] for biological diagnostics [3] and drug screening [4]. Nevertheless, even if the detection is performed in a small chamber, many reactions simultaneously occur and the readout remains noisy and the result uncertain. To clear away this uncertainty, the detection and analysis have to be performed at even the smaller scale by directly interrogating individual entities, single cells [5], and molecules [6].

Biophysical method proves to be very appropriate to address individual molecules and cells and sense their response to their surrounding [7]. Filamentary molecules such as DNA change their conformation during local hybridization or specific proteins interaction, a physical change that is detectable by mechanical measurements. Any alteration of cell function induced by a disease state can significantly modify the biomechanical properties of cells, stiffening for arthritis, asthma, malaria, for example, while cancer is characterized by cell softening [8].

These biomechanical measurements are usually performed either with micropipettes and microplates [9], optical tweezers [10, 11], magnetic tweezers [12, 13], or atomic force microscopes (AFMs) [14, 15]. These biophysical instruments reveal many fundamental biological phenomena with amazing precision, but they are sophisticated and require experienced manipulation skills and controlled environments. The samples have to be prepared one at a time, to anchor them on cover glass or to bind functionalized microbeads at their extremities for their optical or magnetic manipulation. These constraints hardly fit with routine biosensing operations.

Nevertheless, the achievements of AFM in biophysics incited us to exploit further the possibilities offered by silicon micromachining technology; Micro-electro-mechanical-systems (MEMS) devices can integrate accurate molecular level engineering tools [16−18], are compatible with microfluidics [19], and are produced at a cheaper cost using parallel processes. The concept of silicon nanotweezers (SNTs) arose from successful minute trapping of DNA bundle between microfabricated opposing sharp tips [19], in 2003. Thus, further integration of actuation and sensing to this trapping method provides SNT with the capability of biomechanical characterization of molecules and cells. Since then, the SNT has been continuously improved in terms of sensitivity/repeatability and capability of perform electrical [20] and mechanical measurements of diverse types of biological samples (DNA [21, 22], gelatin [23], fibronectin filaments [24], epithelial cells, myotubes) in various environments (air, vacuum, liquid, and irradiation [25]).

In this chapter, SNT is presented as a generic microdevice allowing bio-mechanical assays of filamentary molecules and cells. SNT operations and design are presented in Section 7.2, Section 7.3 details the SNT microfabrication process; the operations and applications to molecules and cell characterization are described in Sections 7.4 and 7.5, respectively, before concluding remarks in Section 7.5.

7.2
SNT Operation and Design

The routine analysis of biological molecules or cells requires a versatile instrument capable of (i) manipulating of the samples inside their environment and (ii) sensing the reaction of the trapped samples to their environments. In a first step, these samples need to be trapped inside biological liquid with minute procedure and, then, delivered into diverse solutions or environments in which targeted characteristic or reaction can be measured. Meanwhile characteristic or reaction is detected and monitored in real time by the direct sensing of physical modifications, either mechanical or electrical.

Silicon technology-based nanotweezers can integrate these features and achieve the goal for systematic diagnosis of biological molecules and cells. On the one hand, the SNT are small enough and *de facto* compatible with microfluidic technologies for manipulation of the samples in liquid. On the other hand, MEMS fabrication enables the fabrication of special tips for trapping/manipulation and electromechanical actuator and sensor for the interactions with the physical properties of the sample.

7.2.1
Design

Figure 7.1 shows a three-dimensional (3D) illustration of the SNT. The device consists of three parts:

- The two tips
- A series of electrostatic comb-drive actuators
- A differential capacitive sensor.

The two tips are either sharp for filamentary molecules trapping or flat for circulating cell manipulation, and they act as electrodes for both trapping and electrical measurements. For example, DNA molecules are trapped by dielectrophoresis [21, 26] as described in Section 7.4, and their conductivity can be measured under various humidity conditions [20].

One tip is fixed and the other one is moved with the electrostatic actuator. Finally, the mechanical motion is measured using two capacitances with gaps that vary in proportion to the electrode displacement.

7.2.1.1   Electrostatic Actuation

The actuation is provided by electrostatic forces in an interdigitated comb architecture, one of the most widely used forces in the submicrometer-size design [27–29] (Figure 7.1a). The total stroke is rather shorter than what is possible in a parallel plate architecture [30], but the generated force is exclusively dependent on the actuation voltage, which allows simple control of the actuation. The design of a comb-drive actuator requires the study of the electrostatic forces generated between the two electrodes with respect to the targeted application [31]. The final force equation depending on the physical dimensions of the actuator is given by

$$F_{es} = \frac{1}{2} \frac{\varepsilon_0 N_a t}{g} \times V_{act}^2 = \alpha \times V_{act}^2 \tag{7.1}$$

where ε_0 is the vacuum permittivity (we consider the relative permittivity of air $= 1$), N_a is the number of comb fingers, t is the device thickness, g is the lateral gap between fingers, and V_{act} is the actuation voltage. Numerical values of the SNT design can be found in Table 7.1. Because of its electrostatic feature, the actuator generates only attractive forces between its two electrodes, that is, displacements in one direction only. For large strokes and "open/close" displacements required in the case of cell trapping, the design is modified and integrates two actuators, as described in Section 7.5.

7.2.1.2   Mechanical Structure

The mobile part of the tweezers is suspended by flexible beams (Figure 7.1d). Commonly integrated in microsystem designs, folded-beam springs are designed to minimize beams areas, decrease their mechanical stiffness, and enhance displacement ranges [28, 32]. In the current design, three sets of folded-beam suspensions support the different part of the system (the actuator, the mobile tip, and the sensor) and provide the electrical connections for the actuation and sensing. Their sum gives the total stiffness k of the device, such as $k = 2 \times k_1 + 2 \times k_2 + 2 \times k_3$.

(a)　Comb-drive actuator

(b)　Differential capacitive sensor

(c)　100 μm
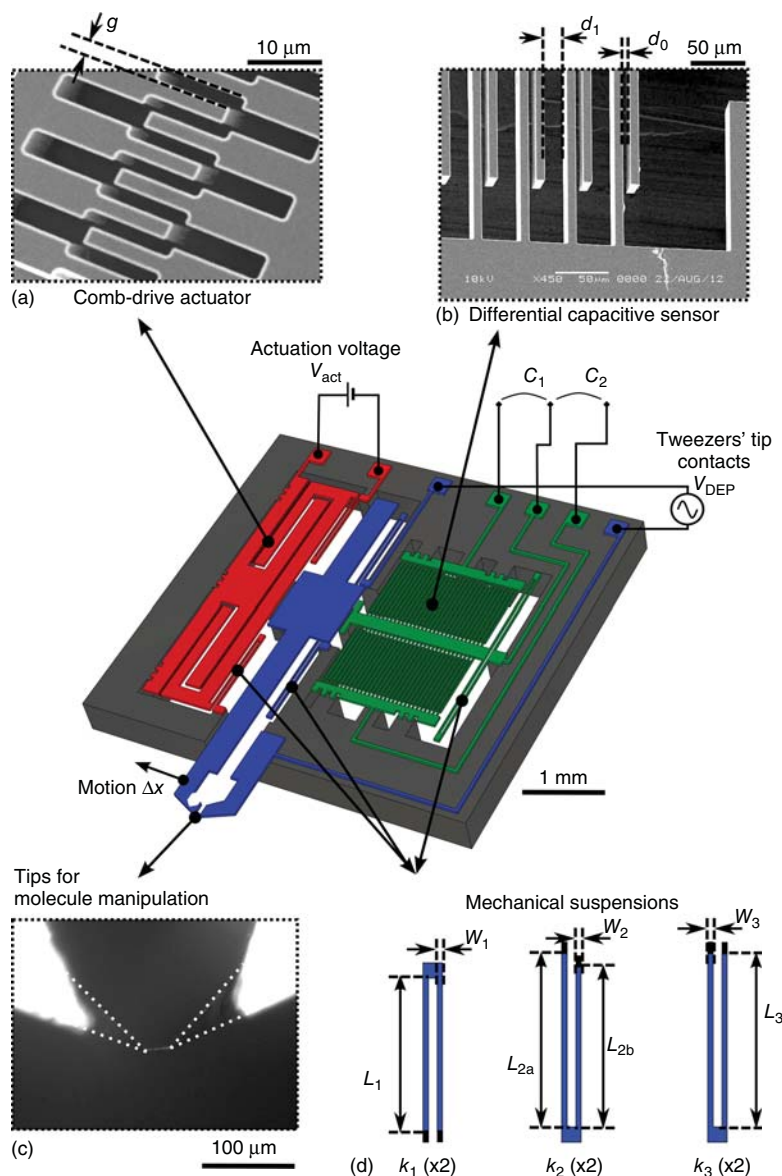
(d)　k_1 (x2)　k_2 (x2)　k_3 (x2)

Figure 7.1 3D view of silicon nanotweezers (SNTs) description. The key parts are shown in colors: in red, the actuator; in blue, the tips; and in green, the sensor. (a) Scanning electronic microscopy (SEM) image of the actuator consisting of 880 pairs of inter-digitated combs separated by a 2-μm gap, and organized in 2 series. (b) SEM image of the integrated sensor of 2 opposing series of 30 combs. (c) Microscope image of the tweezers' tips with a small DNA bundle in between. (d) Design of the three sets of suspensions, k_1 for the actuator polarization, k_2 for the mobile arm, and k_3 for central sensor plate. Overall dimensions are $4.5 \times 4.5 \times 0.5$ mm.

Table 7.1 Numerical values of dimensions and parameters of the SNT.

SOI wafer dimensions	
Device layer silicon thickness	30 μm
Bulk layer thickness	300 or 500 μm
Comb-drive actuator	
N_a	440
G	2 μm
Mechanical suspensions	
L_1, L_{2a}	900 μm
L_{2b}, L_3	1000 μm
w_1, w_2, w_3	15 μm
Capacitive sensor	
N_b	30
L	585 μm
d_0	5 μm
d_1	20 μm

These values are defined in Figure 7.1 and used in Eqs. (7.1–7.3).

Assuming rigid trusses, folded flexure designs are considered as a series of two clamped-clamped beams and the equivalent spring constant in the lateral direction can be found from [28, 32]

$$k_1 = 2 \frac{E \times t_1 \times w_1^3}{L_1^3} \; ; \; k_2 = \frac{E \times t_2 \times w_2^3}{L_{2a}^3} + \frac{E \times t_2 \times w_2^3}{L_{2b}^3} \; ; \; k_3 = 2 \frac{E \times t_3 \times w_3^3}{L_3^3} \quad (7.2)$$

A very compliant system is ideally suitable for the sensing of mechanical properties of biological molecules. For example, the equivalent rigidity of biological macromolecules can be very low, that is, about $30 \, \mu\mathrm{N\,m^{-1}}$ for one λ-phage DNA (16.5-μm length or 48.5 kbp) [33, 34]. On the other hand, a minimum stiffness is required to (i) survive the fabrication processes, (ii) support the system weight, and (iii) prevent attractive and sticking surface forces in the comb-drive actuator and the capacitive sensor. These constraints are justified in Section 7.3 presenting the SNT process.

7.2.1.3 Capacitive Sensor

The tip displacement is measured by a differential capacitance sensor, which is suitable for bulk micromachining and compact integration [35]. The sensor is designed in a triplate configuration with transverse combs. A central electrode is mechanically connected to the mobile tip and moves in between two fixed electrodes creating two differential capacitances, C_1 and C_2, related to the displacement, x (Figure 7.1b). For small displacements, as $x \ll d_0 < d_1$, a first-order approximation gives a linear relationship between $\Delta C = C_2 - C_1$ and x [2, 7, 21, 31], that is

$$\Delta C \cong 2\varepsilon_0 N_b L t \left(\frac{1}{d_0^2} - \frac{1}{d_1^2} \right) x = \beta \times x \quad (7.3)$$

where N_b is the number of capacitance electrodes in opposition, t is the device thickness, L is the electrode length, and d_0 and d_1 are the initial distances between repeating combs. Theoretically, C_1 and C_2 are equal, such that differential measurements eliminate offset values and common mode enabling full-range sensing and a significant noise/perturbation rejection.

All dimensions and parameters of the SNT are summed up in Table 7.1. The Young's modulus and the density of the silicon are 165 GPa and 2329 kg m^{-3}, respectively, and the permittivity ε_0 is 8.85×10^{-12} kg^{-1} m^{-3} A^2 s^4. Theoretical calculations give a first-order approximation for a proper characterization and modeling of the SNT.

7.2.2
Operation

After clean-room fabrication, tweezer chips are bonded on a printed circuit board (PCB), for electrical connection with measurement instruments and mounted on a robotized stage, as illustrated in Figures 7.6–7.8 for molecular and cellular applications, respectively. On the one hand, the actuation of the tip is quite straightforward; a voltage applied to the actuator generates a force that induces a displacement of the tip. On the other hand, the sensing of the motion requires the measurement of the differential capacitance ΔC according to Eq. (7.3).

7.2.2.1 Instrumentation

We developed two instrumentation chains for static and dynamic measurements (Figure 7.2), that can be used separately or simultaneously. In both methods, the idea is to create and measure alternating currents through the capacitances C_1 and C_2. Because of the size of the sensor, the currents turn out to be only few picoamperes and are converted into voltages V_1 and V_2, by two low-noise current-to-voltage (A/V) preamplifiers with $10^{-8}/10^{-9}$ gain (Signal Recovery, model 5182). The low input impedance of the preamplifier (virtual ground) ensures an accurate current conversion [36]. The detection level is enhanced using lock-in amplifiers (NF LI 5640 or Ametek SR7270).

For static actuation (Figure 7.2a), a sinusoidal input signal, V_{ref} supplied by the internal reference of a lock-in amplifier is applied to the central plate of the capacitive sensor (port C_0). The amplitude of the detected voltage, V_{out}, is directly related to ΔC and x by the acquisition chain gain:

$$V_{out} = G(i_{C2} - i_{C1}) = G \cdot \frac{\partial V_{ref}}{\partial t} \cdot \Delta C = G \cdot 2\pi \cdot f_{ref} \cdot V_{ref} \cdot \beta \times x \tag{7.4}$$

where V_{ref} and f_{ref} are respectively the amplitude and frequency of the signal applied on C_0 (usually 1 V$_{RMS}$ and 10 kHz), G is the preamplifier gain, and β is the sensor gain (Eq. (7.3)).

In dynamic mode (Figure 7.2b), the motion $x(t)$ of the central electrode C_0 creates the dynamics currents, i_{C1} and i_{C2}. C_0 is polarized with a DC voltage V_{ref}
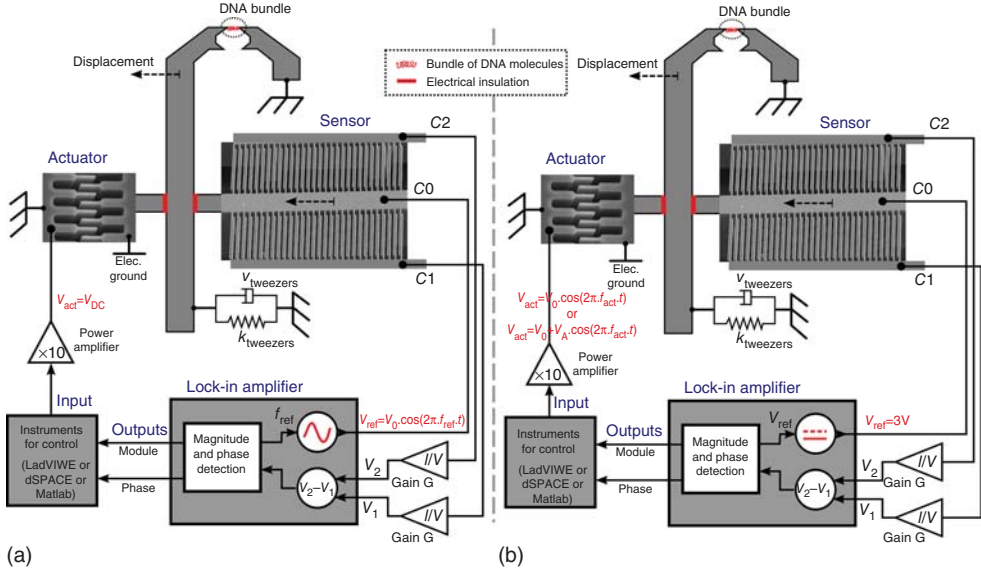
Figure 7.2 Electromechanical scheme of the tweezers and electrical connections for actuation and displacement sensing in static mode (a) and dynamic configurations (b). SEM images illustrate the actuator and the sensor. Red lines represent electrical insulation between parts, and differences between the two configurations are highlighted in red.

(usually 3 V) and the output voltage V_{out} is then related to the velocity of the motion $\frac{\partial x}{\partial t}$:

$$V_{out} = G(i_{C2} - i_{C1}) = G \cdot V_{ref} \cdot \frac{\partial \Delta C}{\partial t} = G \cdot V_{ref} \cdot \beta \times \frac{\partial x}{\partial t} \tag{7.5}$$

The dynamic response of the device is characterized by a harmonic analysis sweeping the working bandwidth of the SNT. A sinusoidal signal (at the frequency f) is provided to the actuator electrodes V_{act}, and generates oscillations at the frequency $2f$ because of the quadratic dependence of the force with the actuation voltage (Eq. (7.1)). The lock-in amplifier acquires the amplitude and the phase of the oscillations using the second harmonic mode detection.

7.2.2.2 Characterization

Using the aforementioned configurations controlled by a Personal computer (PC) equipped with LabVIEW programs and Universal serial bus (USB)/General purpose interface bus (GPIB)/Ethernet interfaces, SNTs are characterized in real time in static and dynamic modes (Figure 7.3).

Figure 7.3b plots the output signal of the sensor for actuations from 0 to 40 V. For small actuations (0–20 V), the curve shows a quadratic behavior in agreement with Eq. (7.1). The conversion output signal to equivalent displacement can be fitted with optical measurement (not shown in the figure) and the sensing gain β identified.
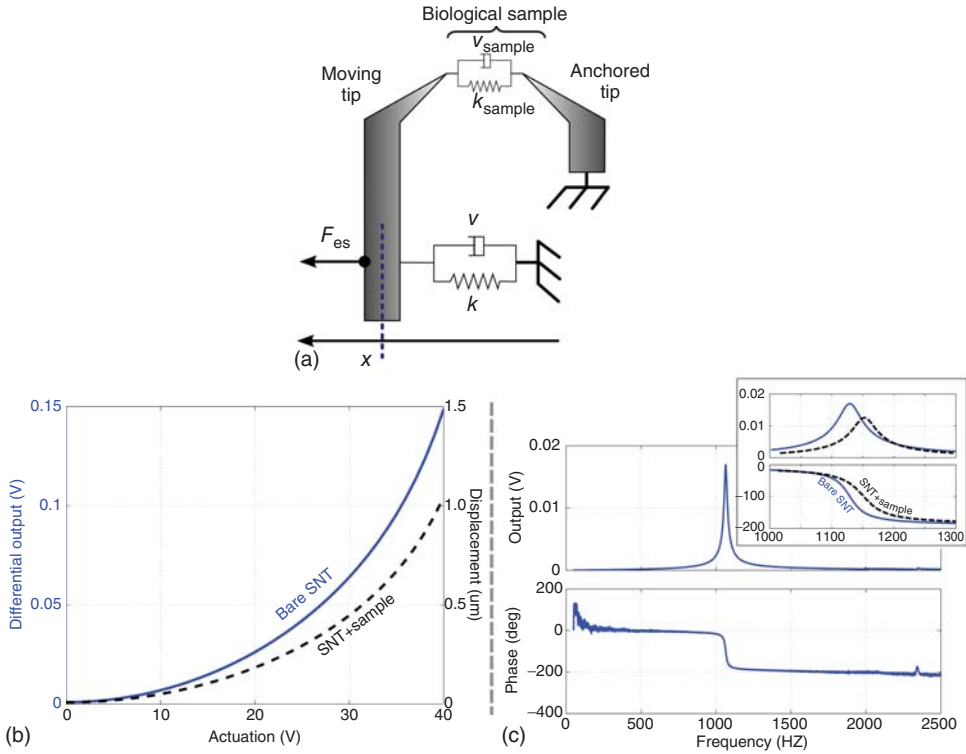
Figure 7.3 Equivalent dynamic model (a) and experimental responses of the SNT (b,c). Blue lines are experimental data, while dashed lines are simulated responses of the SNT when biological sample would be trapped.

However, for voltage actuations higher than 20 V, the displacement measurement is overestimated by the sensor. The condition $x \ll d_0$ is not anymore respected.

Figure 7.3c shows the frequency response of the SNT, that is, output amplitude and phase versus a sinusoidal actuation of 3 V_{PP}. The plot outlines a resonance mode around 1150 Hz. As desired, it turns out that this first mechanical resonant mode moves in the direction of the gripping ability. The maximum displacement at the peak is about 25 nm. A second resonant mode can be noticed on the phase curve around 2400 Hz. The second mode has been rejected out of SNT sensing operation bandwidth to avoid any artifact due to frequency mixing. This frequency response has been optimized by recursive works between mechanical designs and finite element simulations [31].

7.2.2.3 Modeling

Before the quantitative analysis of biological samples, model parameters need to be extracted from the device characterizations. The main resonance can be accurately fitted with a second-order differential equation, stemmed from a

Table 7.2 Theoretical and identified model parameter values of the SNT.

Parameters	Theoretical	Identified
Mechanical parameters		
M (kg)	360×10^{-9}	360×10^{-9}
k (N·m^{-1})	49.3	~25
ν (N·s·m^{-1})	—	$\sim 100 \times 10^{-6}$
Comb-drive actuator		
α (N V^{-2})	29.2×10^{-9}	$\sim 35.5 \times 10^{-9}$
Capacitive sensor		
β (F m^{-1})	412.2×10^{-9}	$\sim 227.5 \times 10^{-9}$

Identified values are approximate values since they change slightly depending upon the devices and the fabrication. Each device needs to be characterized as Figure 2.3 shows.

damped mass-spring system with three mechanical parameters: M, the mass of the mobile part; k, the equivalent stiffness of the system; and ν, the losses mainly due to viscous dragging of air in tiny space of the design.

These parameters with the sensor and actuator gains (β and α) are identified through standard recursive fitting of SNT responses with a least squares method. Table 7.2 sums up and compares the theoretical and experimental values of the model. Disparities are explained by the fabrication process that causes small changes in the device dimensions. Small dimensions as the sensor gaps and suspension widths are more significantly affected inducing reduced sensor gain and mechanical stiffness. Finally, with a proper model, the SNT can be used as a sensor for detecting and measuring mechanical properties of biological molecules or cells (Sections 7.4 and 7.5).

7.3
SNT Process

7.3.1
MEMS Fabrication versus the Design Constrains and User Applications

The SNT is based on two symmetric arms ended with flat or sharp tips. Depending on the design, single or both arms can be actuated by supplying AC voltage on arrays of comb drives. A capacitive sensor measures the position and velocity of a single arm.

The displacement of movable structures depends on the design of gaps (comb drives, capacitive sensor), but also on the ratio between the width and the height of suspended structures that is defining the stiffness of silicon springs thence sensing performances, as modeled in Section 7.3. Therefore, precise alignments, vertical etching, and reduced underetching are critical process constrains.

By changing the design, the same flowchart can be used for fabricating single- or double-actuation SNT using a 2(3)-mask process for flat (sharp) tips

engineering. Additional steps are needed in case of sharp tips fabrication, such as nitride patterning, local oxidation of silicon (LOCOS) oxidation, and Tetramethy-lammonium hydroxide (TMAH) etching, all other process parameters remaining the same than for flat tip fabrication.

The fabrication of sharp tips SNTs will be described based on two major improvements compared to previous design [37]. Here, the edges of the tips are forming an angle of 130° (instead of 180°). This "chopstick" configuration adds to the versatility of SNT without the need for external manipulator tool [38]. Another major improvement consists of a one-step plasma overetching that allows controlling the gap between the tips from a few nanometers up to tens of micrometers without changing the design of the masks.

Such a design is suitable for (i) trapping molecules by Liquid Dielectrophoresis (LDEP) from a droplet, (ii) being used as a microgripper to pick and place objects, and (iii) operating in opened microfluidics cavities. In the later case, the angle forming the tips prevents from liquid-flow perturbations since only the thinnest parts of the tips are immersed instead of thick arms. Moreover, the pyramidal cross section of the tips made in (111) planes brings more rigidity.

7.3.2
Sharp Tip Single Actuator SNT Process Flow

MEMS is fabricated from (100) oriented Silicon On Insulator (SOI) wafer (Ultrasil) either type N or P, having resistivity between 0.01 and $10\,\Omega$ cm. SOI layer thicknesses are 30, 2, and 400 µm for the top silicon, the buried oxide (BOX), and the handle wafer, respectively. The process steps are illustrated in Figure 7.4.

7.3.2.1   Nitride Deposition
After standard Piranha solution (SPM) cleaning and Buffered hydrofluoric acid (BHF) to remove the dirty oxide, 50-nm-thick silicon nitride layer is deposited by low-pressure chemical vapor deposition (LPCVD) at 800 °C by reacting silane and ammonia gases. Nitride patterns will be used as sacrificial mask for LOCOS. Residual stress is not an issue.

7.3.2.2   Defining Crystallographic Alignment Structures
Sharp tips are formed by wet etching of (100) silicon revealing (111) facets [1;4]. Therefore, the alignment of nitride patterns in (110) direction on the (100) surface is of utmost importance for the symmetric aspect of the opposing tips.

Several approaches can be considered to process the wafer:

- Cut the wafer and align nitride patterns with the (110) planes of a one-fourth wafer.
- Dicing at 45° with accurate alignment with (110) flat.
- Using a mask aligner with flat edge detection and 45° wafer rotation capabilities.
- TMAH etching on dummy areas to reveal crystallographic planes. This method needs an additional mask level.
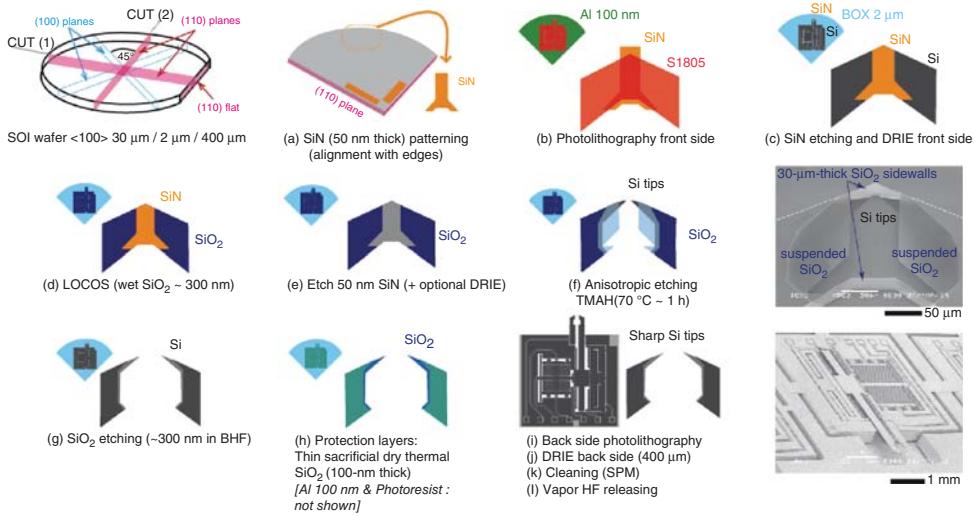
Figure 7.4 Three-mask process flowchart schematics for fabricating SNT. The sharp tips are designed with a 130° angle and the gap is adjusted by a one-step dry etching. SEM images shows sharp tip obtained hereafter TMAH etching (top), and the final device after releasing in vapor HF (bottom).

7.3.2.3 Photolithography (Level 1) – Nitride Patterning for LOCOS

A thin (500 nm) photoresist (Shipley S1805) is spin-coated on the SiN layer and baked at 110 °C for 1 min. UV exposure is performed on single-sided Karl Suss MJB-3 photomask aligner. Development time is fixed to 1 min in diluted TMAH (2.38%) (Figure 7.4a).

Nitride is etched by inductively coupled plasma reactive ion etching (ICP-RIE) by mixing SF_6 with C_4F_8 (5:1). The chamber pressure is fixed to 5 mTorr. Directional etching is obtained by setting Radio-frequency (RF) platen/coil powers at 50 W/600 W, respectively. Such nonselective recipe will overetch the silicon top layer by a few hundreds of nanometers in a few seconds and cannot be precisely controlled on the overall wafer. The residual polymers are removed by plasma oxygen.

7.3.2.4 Photolithography (Level 2) – Sensors and Actuators

Evaporated Al thin film (~100 nm) is used as a sacrificial mask for deep reactive ion etching (DRIE). A thin (500 nm) photoresist (Shipley S1805) is spin-coated on the Al layer and baked at 110 °C for 1 min. As the index of refraction of aluminum is 200 times larger than that of nitride, the UV exposure time has to be reduced accordingly (*http://refractiveindex.info*). Development time is fixed to 1 min in diluted TMAH (2.38%). Hard bake is not needed. The 100-nm-thick Al layer is wet-etched in a commercial Al etchant for about 4 min (Figure 7.4b).

7.3.2.5 DRIE Front Side

Overhanging nitride film surrounding the Al patterns on the tip area is removed by ICP-RIE, followed by plasma oxygen. Such dry cleaning process prevents from the formation of black silicon during DRIE (Figure 7.4c).

Diffusion pump oil is used to stick the one-fourth wafer on a glass holder. The holder is mechanically clamped on the chuck. Kapton tape is used to maintain the wafer on the holder. The Diffusion pump (DP) oil aims at enhancing the heat transfer from the wafer to the chuck. The wafer is cooled by flowing He between the chuck and the glass holder with a leak-up rate below $5\,\mathrm{mTorr\,min^{-1}}$. In addition, the chuck is cooled by a chiller (set at $18\,°C$). Despite its poor thermal conductivity, glass holder is chosen for its very low etching rate compared to silicon.

DRIE process is based on a Bosch process. It consists of repeating sequences of isotropic etching of silicon (SF_6/O_2 gas) followed by a passivation step based on Teflon-like coating on the sidewalls (C_4F_8 gas). Mixing 10% O_2 with SF_6 gases is known to enhance the etching rate [39]. Vertical sidewalls are obtained when the ICP-RIE parameters are balanced in the way of keeping Teflon on the sidewalls while etching Teflon and Si at the bottom of the opened areas. Passivation is obtained by setting the platen power to $0\,W$. Switching from passivation to isotropic etching requires a platen power of around $20\,W$ that yields a slight directional etching at the bottom of opened areas. Typically, the SF_6/O_2 etching step generates underetching of about $300\,nm$ and indeed reduces the width of final structures.

The electromagnetic field distribution in the chamber should be as "flat" as possible to guaranty good etching uniformity on the overall wafer. The high-density plasma distribution is usually not uniform and depends on the performance and engineering of the coil element surrounding the chamber walls. The coil RF power controls the dissociation rate of gas molecules thence the "chemical" etching. The "physical" one depends on the mean free path of reactive species (inversely proportional to the chamber pressure), and the platen RF power that drives the bombardment of ions with the substrate.

In addition, the etching rate depends on the wafer size and the total opened area on the wafer (amount of reactive ions regarding the surface to be etched). Narrow gap between patterns will reduce the etching rate (called *aspect ratio-dependent etching*). When reaching the dielectric stop layer (BOX), accumulation of charges leads to unwanted notching effect that reduces locally the width of patterns and modifies the final performance of the device (stiffness of springs, nonvertical sidewalls for capacitive sensor, and comb drives).

The DRIE ends with plasma oxygen to remove passivation layers especially on the sidewalls. The pressure is then increased to about $20\,mTorr$ to get multidirectional ashing. The wafer is cleaned in acetone/ethanol/Deionised (DI) water to remove the DP oil traces, then in commercial aluminum etchant to remove the sacrificial mask. Before oxidation, the wafer is cleaned in SPM for 30 min at $130\,°C$ to remove metallic residues and residual polymers while keeping the nitride film on top of the silicon (at the tip area). The dirty thin oxide layer is removed in BHF for a few seconds.

A LOCOS process of ~350 nm is performed by wet oxidation (H_2O/O_2) at 1100 °C for 90 min (Figure 7.4d).

7.3.2.6 Sharp Tip Fabrication and Gap Control

The 50-nm-thick nitride on the tip area is etched by ICP-RIE similarly to step 3. The slight overetching of silicon is not an issue. The final gap depends on the initial nitride width W_{SiN} and the top silicon layer thickness h, which is given in the form of a simple equation as follows [37] (Figure 7.4e and 7.4f):

$$gap = W_{SiN} - 2h \qquad (7.6)$$

Interestingly, the gap can be controlled by the overetching depth d of the top silicon layer while keeping the same mask design $W_{SiN} \leq 2h$ (no gap). In that case, the gap is given by

$$gap = W_{SiN} - 2(h - d) \qquad (7.7)$$

Typically, for $W_{SiN} = 60\,\mu m$ and $h = 30\,\mu m$, a 10-μm gap is obtained with an overetching depth (d) of 5 μm. Gap adjustment can be done either before or after the TMAH wet etching as shown in Figure 7.5 (top). This approach is suitable for creating on-demand gaps ranging from several tens of micrometers down to submicrometers. Nanogaps can be obtained from slight joint tips (no gap) that are mechanically broken during wafer manipulation or wire bonding as shown in Figure 7.5 (bottom).
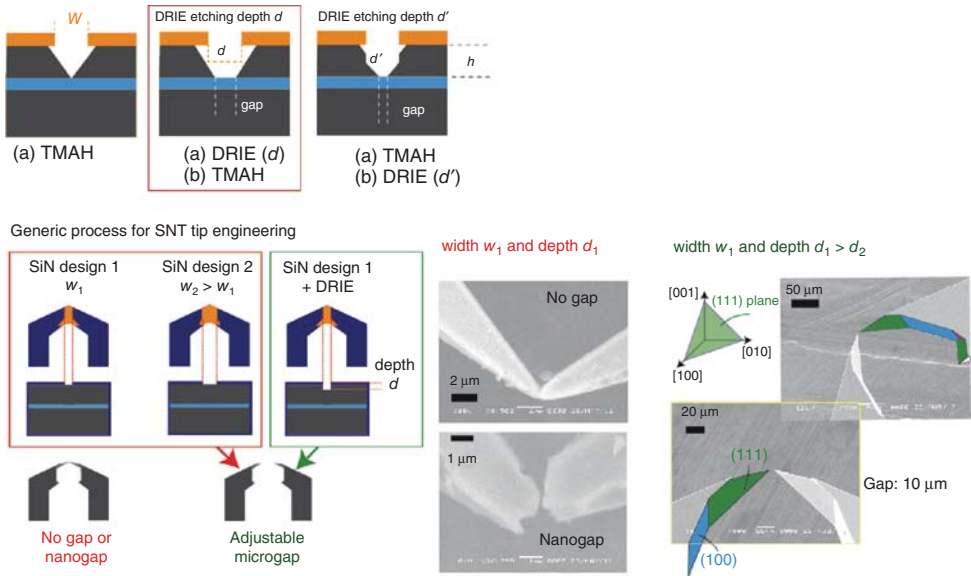
Figure 7.5 One-step gap adjustment by tuning the overetching of nitride layer but keeping the same photomasks/design. Nanogaps can be created by mechanical breakage of "no-gap" tips. (When detaching SNTs from the wafer or due to ultrasonication during the wire-bonding on a PCB.)

Wet anisotropic etching is performed in TMAH (15%) at 70 °C for about 60 min depending upon the remaining silicon top layer thickness $h - d$. (111) facets form a triangular cross-sectional shape ending with apexes of $\sim$10 nm in diameter. The thick oxide sidewalls (from LOCOS) act as a etch barrier. Here, tips are designed with a 130° angle to create "chopstick" rather than facing tips [21]. Here, the 130° angle brings more versatility especially for inserting the tips in opened microfluidics even under continuous liquid flow. As only apexes of pyramidal tips are immersed, the lower pressure on the tips reduces flow perturbation while keeping good actuation/sensing performances in liquid.

The remaining 300-nm-thick sacrificial oxide is then removed in BHF, rinsed, and dried.

The top silicon structures are then protected by three consecutive layers (Figure 7.4h): (i) by conformal thermal oxidation at 1050 °C for 30 min (that aims also at sharpening the tips at the final step); (ii) by evaporating a thin Al film (100 nm); (iii) by spin-coating 2-μm-thick photoresist hardly baked on a hot plate (130 °C) for 30 min.

7.3.2.7 Photolithography (Level 3) and Rearside DRIE

Sacrificial 100-nm-thick Al film is evaporated on rearside followed by photolithography (level 3) and wet Al etching. The handling silicon (400-μm-thick) is etched by DRIE for about 2.5 h (etching rate of 3 μm min^{-1}). The one-fourth wafer is carefully removed from the glass holder in acetone, rinsed in ethanol, and dried in an oven. Aluminum is removed in Al etchant (40 °C). A final SPM cleaning is done at 110 °C for 10 min to prevent bubbling, then rinsed in DI water and dried in an oven (Figure 7.1j–k).

7.3.2.8 Releasing in Vapor HF

The buried and sacrificial oxides are removed in Vapor HF. Vapor Hydrofluoric acid (HF) can be performed by either commercial vapor HF machines or homemade setup operated under continuous airflow in a closed draft. The equipment for the later case consists of a Teflon container half-filled with 50% HF solution, capped with a multiholes plastic plate handling the wafer, and again capped with a transparent plastic lid [40]. A 40 W light is placed on the top of the lid at a certain distance. Vapor HF is based on a compromise between the fast chemical etching of SiO_2 in HF at room temperature and the resulting water formation that has to be evaporated by heating up with the light. Usually, "high-temperature" vapor HF tends to reduce the etching rate, but avoids the formation of water droplets and therefore the sticking of suspended beams. Thence, a trade-off is obtained by empiric adjustment of height position of the light (heating) (Figure 7.4l).

Isotropic vapor HF process generates $1 - 2$ μm underetching that is suitable to prevent short circuits when an option of 50-nm-thick Al is evaporated on front side.

7.3.3
Concluding Remarks on the Silicon Nanotweezers Microfabrication

A 3-mask generic process was developed to produce SNTs with sharp tips, and can be simplified to 2-mask process for flat tips. The sharp tips are designed with a 130° angle for "chopstick" capability. Micro- to nanogap can be fabricated on demand (depending on the application) by tuning a one-step dry etching, keeping the design of the original masks.

7.4
DNA Trapping and Enzymatic Reaction Monitoring

The SNT concept, summarized by the integration of grippers, actuator, and sensor in a tiny device, allows a wide range of biosensing capabilities. In order to keep the advantages of the integration and performance of the tweezers, they are operated in air with only their tips immersed in the solutions. Two configurations are currently used for the characterization of molecules. One corresponds to operation in droplets, as illustrated in Figure 7.6a. In the second configuration, Figure 7.7a, the tips are inserted in a lateral slit of a microfluidic chamber. The results presented in this section have been obtained with a previous design of the SNT [21] that were stiffer that our current version detailed in Section 7.2 [24].

DNA trapping is an appropriate illustration of SNT operation in liquid, the procedure is here detailed for the "in-droplet" configuration in Figure 7.6. The trapping of bundles of molecules by DEP with the silicon tweezers follows the technique developed by Hashiguchi *et al.* [19], inspired from pioneering experiments of Washizu and Kurosawa [26]. A small droplet of DNA solution (Figure 7.6a,b) is first deposited on a microscope coverslip. (48 502 bp λ-DNA, TAKARA BIO INC., Shiga, Japan, diluted 1 : 1 with DI water). The tweezers, mounted on a PCB, are maintained at a fixed position. The tips of tweezers are smoothly brought into contact with the surface of the droplet by moving the coverslip upward with a 3D mechanical stage (Figure 7.6b). When the tips are immersed, but still forming a meniscus, an AC electric field (1 MHz, 1 V μm^{-1}) is applied between the two arms of the tweezers. Because of the intense electric field, DNA molecules are stretched and attracted toward the tips and finally form a bundle between them. The diameter of the bundle varies by DEP time, and can range from several tens of nanometers (10 s DEP) to ≥300 nm (5 min DEP). Even a single DNA molecule can be trapped with DEP with very short pulses (5 ms) [41]. The strong DNA binding to the aluminum-coated tips prevents the bundle from being washed away due to the surface tension of the solution. The DNA bundle is then accessible for visualization under an optical microscope in real time (Figure 7.6c) or a scanning electron microscope [20]. The bundle is ready for mechanical [21] and electrical characterizations [20], and subsequent assays, when reinserted in solution with reactants as shown in Figure 7.7.
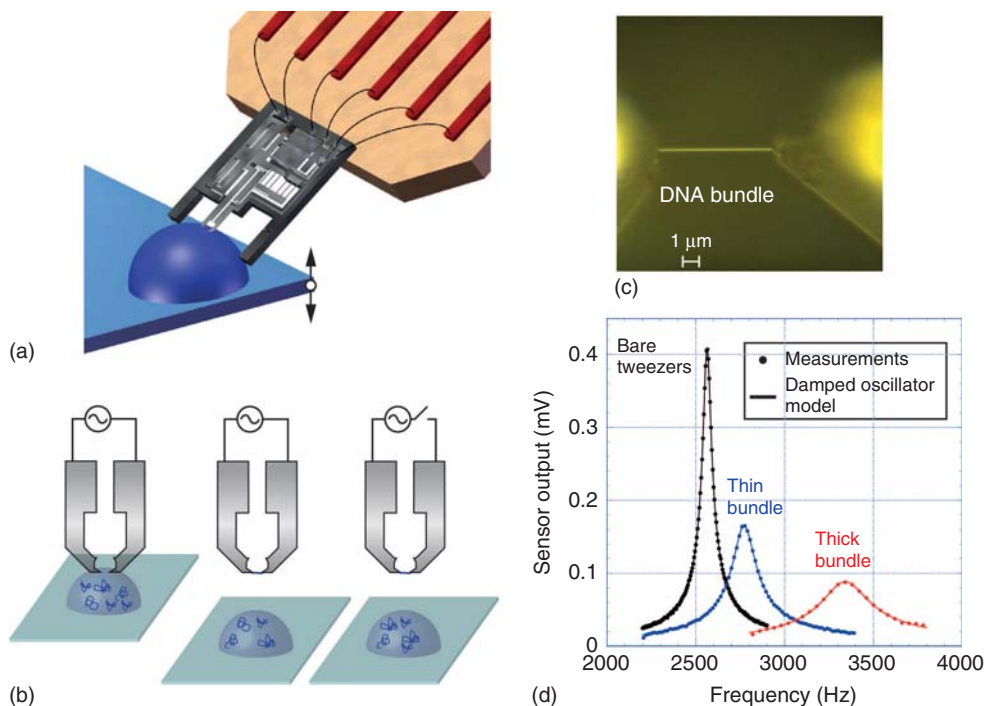
(a)

(b)

(c)

DNA bundle

1 µm

(d)

Figure 7.6 Operation of SNT in solution droplet and DNA characterization in air. (a) Schematic view of "in-droplet" operation. The SNT is mounted on a PCB and a droplet of DNA solution is deposited on a cover plate maintained by a micromanipulator. (b) Trapping of a DNA bundle by Dielectrophoresis (DEP) and retrieving from the solution. (c) Optical real-time visualization of the retrieved DNA bundle (magnification 5000). (d) Frequency response of the SNT with a two different DNA bundles and compared to the bare SNT response. Best extracted damped oscillator models are plotted with measurements for the three curves.

The first characterization method with SNT is illustrated by the measurement of the mechanical properties of DNA in air, Figure 7.6d. After the DEP trapping, Figure 7.6a, the mechanical characterization is carried out by the frequency response of the SNT holding the bundle. As detailed in Section 7.2 and with the measurement setup of Figure 7.2b, a sinusoidal voltage of constant amplitude and frequency scanning (step-by-step frequency increase) is supplied to the actuator and the capacitive current of the displacement sensor is recorded. With the bundle trapped between the two tips, the resonance of the tweezers shifts to higher frequencies due to the added stiffness brought by the bundle. At the same time, the quality factor of the resonance is degraded, the maximum displacement is lowered, and the peak extends to a wider frequency range. This degradation indicates the presence of viscous losses in the DNA bundle during its deformation. The SNT behaves as a damped oscillator consisting of an oscillating mass attached to a mechanical spring and a damper, as shown in Figure 7.3.

Table 7.3 Mechanical characteristics of tweezers and DNA bundles.

	SNT	Thin bundle	Thick bundle
M (kg)	$1.9 \cdot 10^{-7}$ [a]	ε [b]	ε [b]
F (Hz)	2563.42	2771.67	3341.11
Q	55.83	22.65	13.01
K (N m^{-1})	49.3 [c]	8.30 [d]	34.4 [d]
ηv (N s m^{-1})	$5.49 \cdot 10^{-5}$ [c]	$9.11 \ 10^{-5}$ [e]	$2.52 \cdot 10^{-4}$ [e]
T (s) [f]	$1.11 \cdot 10^{-6}$	$1.10 \ 10^{-5}$	$7.32 \cdot 10^{-6}$

a) SNT mass is calculated from processed device dimensions.
b) DNA bundle mass is negligible.
c) Truncated value.
d) Bundle alone stiffness, truncated value.
e) Bundle alone viscosity, truncated value.
f) Relaxation time: $\eta \, K^{-1}$.

Using this damped oscillator model, the resonance frequency and the quality factor are extracted by least squares optimization [42]. For the tweezers alone and with the two different attached bundles, the model matches the measurements with a remarkable accuracy as shown in Figure 7.6d. As the tweezers and bundle undergo the same deformation, their mechanical components add up (Figure 7.3), and the total stiffness and viscosity are calculated from the resonance frequency and quality factor of the oscillating system. The bundle characteristics are then deduced by subtracting the bare tweezers contribution from the total stiffness and viscosity. The resonance frequency and quality factor extracted from the three experiments of Figure 7.6d are given in Table 7.3. The calculated stiffness and viscosity of the SNT and the two trapped bundles are also mentioned with their relaxation time. The precise extraction of the frequency determines the bundle stiffness with a resolution of 0.5 mN m^{-1} that is suitable to detect tiny structural alterations of the bundle and thus provides the tweezers with very sensitive ambient sensing capabilities.

The second example presents the real-time sensing of enzymatic reaction on DNA bundle. Following the trapping protocol of Figure 7.6b, the DNA bundle is inserted into a lateral cavity containing a Hind-III restriction enzyme solution. This cavity is formed by a structured Polydimethylsiloxane (PDMS) layer, obtained by molding [43] and reported on a glass cover slide. The cavity is maintained by a motorized microrobot to ensure a smooth immersion of the SNT tips grabbing the DNA, as illustrated in Figure 7.7a. The slit and the microfluidic cavity are 200 μm in height to ensure an easy pipetting of the solution and to control the evaporation.

The Hind-III restriction enzyme cuts (digests) double-strand λ-DNA (seven restriction sites per molecule). The bundle digestion is measured by the real-time frequency response of the tweezers + DNA system. Figure 7.7b shows the frequency response of MEMS tweezers at the beginning and the end of the DNA digestion. As digestion proceeds, F decreases due the reduction of the stiffness
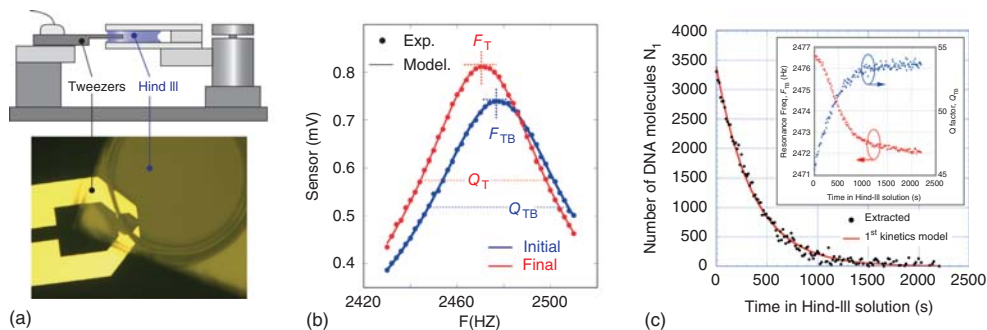
Figure 7.7 Operation of SNT in slit and biomechanical detection of enzymatic reaction. (a) Setup with the SNT inserted in a cavity by a lateral slit. (b) Frequency response of the SNT with the bundle at the beginning and end of the enzymatic reaction. (c) Evolution of the number of DNA molecules (modeled) as the Hind-III digestion is going on. Inset: Corresponding measured resonance frequency and quality factor.

of the attached DNA bundle. At the same time, Q increases as the viscous losses in the bundle are reduced with the shrinkage of bundle cross section. During the reaction, frequency response of the tweezers is continuously recorded, and resonance frequency (F_{TB}) and quality factor (Q_{TB}) are extracted from dumped resonator model in real time, as shown in the inset of Figure 7.7c. The evolution of the stiffness and the viscous losses of the DNA bundle are calculated, as for the first example with DNA bundle in air, by subtracting the bare SNT characteristic given by F_T, Q_T, from the global SNT + DNA one (F_{TB}, Q_{TB}). The decrease of the bundle stiffness with the digestion time is plotted in Figure 7.7c and compared to first-order kinetics model. The result here presented in terms of equivalent number of λ-DNA, by dividing the bundle stiffness by the equivalent rigidity, is about $30\,\mu N\,m^{-1}$ of one λ-phage DNA [33].

This second example shows the ability of the SNT to sense biomolecular reaction in real time by monitoring the evolution of the mechanical characteristic of the trapped bundle as the reaction proceeds. This direct biomechanical detection opens the way of systematic biotests at the molecular level by an integrated MEMS device.

7.5
Cell Trapping and Characterization

7.5.1
Introducing Remarks

As it was mentioned in Introduction, cell mechanical properties are of crucial importance in cell biology and medicine. They are indeed implied in both fundamental process, such as cell differentiation and numerous pathologies, such as cancers and heart diseases. Several tools have been developed in the past to study

quantitatively their mechanical properties. This section presents the potential of SNT as a versatile, quantitative, and integrated tool to evaluate the mechanical properties of cells.

7.5.2
Specific Issues

Cells are complex, inhomogeneous, and nonlinear materials whose mechanical properties cannot be described by simple discrete elements [44, 45]. Models need to be developed to describe precisely their mechanical properties. In general, cells can be considered as soft, and strains from 50% to 100% can be applied for force ranging from 10^{-7} to 10^{-6} N. For smaller strains, the forces are of the order of few tens of nanonewtons, which are in the challenging lower range of the force sensitivity achievable with SNT. From the mechanical characterization of cells in the large strain limit, one can expect a better understanding of complex inhomogeneous hyperelastic and viscous materials. In the lower strain limit, i.e. small deformations and small forces, the mechanical properties of the individual components such as the cell cortex, the cytoskeleton, and stress fibers or individual adhesion, such as focal contacts may be adressed.

In order to perform mechanical analysis on single cells, SNT needs to be able to measure quantitatively forces ranging from 10 to 100 nN, which are the expected range of forces in the lower strain limit. SNT must also be able to apply large strains in order to measure the complex mechanical behaviors. In contrast with other applications, most of the relevant information is contained in the absolute force measurement, nevertheless the dynamic properties will provide qualitative insight of the viscoelastic properties of the biomaterials. Therefore, the dynamic control of the resonance of the SNT in contact with the cell is also of importance to characterize fully the mechanical properties of the biological objects. Moreover, the high-bandwidth tracking of the dynamic parameters allows the positioning of the SNT tips with a resolution below 100 nm, which is very useful for mechanical characterizations on spread cells.

Of course, SNT needs to operate in an environment compatible with cell survival and proper development, that is, in liquid and at a temperature close to 37 °C. The ability to observe the living object with usual phase contrast or live fluorescence greatly facilitates the interpretations of the data. Living cells are known to be biochemically tightly regulated objects. The measurement of the mechanical properties as a function of the biochemical environment is also a requirement to provide a versatile, quantitative, and fast platform for the biomechanical characterization of single cells.

7.5.3
Design of SNT

We implemented some of these requirements on the design of SNT shown in Figure 7.8a. The SNTs have two mobile arms with parallel kinetics that can be
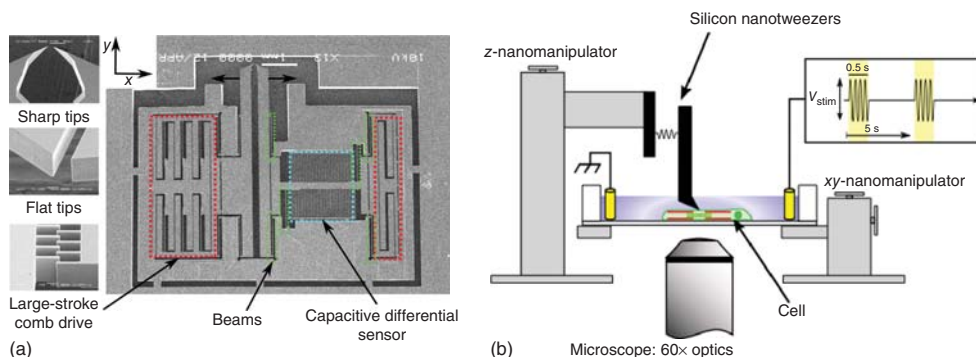
Figure 7.8 SNT and platform for cell manipulation and characterization. (a) SEM image of SNT for cell characterization that integrates a left and right actuation by large-stroke comb drives (red), distributed beams (green) for pure harmonic spectra and a high stiffness in (y) and a differential position sensor (light blue) are highlighted. Arrows show tips motion: the SNT can open. On the left, close-up view of two tips design and long-stroke comb-drive actuator are displayed. (b) Experimental setup integrated on a fluorescence microscope and with nanomanipulators for the addressing of cells with electrical stimulation capability.

opened independently by the application of a voltage. Black arrows in Figure 7.1 indicate their respective directions of displacement. Silicon beams support mechanically the system and define the force and stiffness sensitivity of the system; they are highlighted in green in the figure. In this double-arm design, only on arm integrates a capacitive displacement sensor that is shown in light blue in the figure.

The ability of the SNT to apply large strain on the biological sample is achieved by electrostatic comb drives detailed on the lower left image of Figure 7.8a. For a typical object size of the order of 10 µm, the displacement of the SNT must be of about the same length. Therefore, the comb length has to accommodate this stroke that makes the process challenging, and at the same time, the gap between the facing combs need to be kept at the critical dimension of the lithography and DRIE etching in order to minimize the actuation voltage.

More other, in order to prevent lateral instabilities that could occur at the higher driving voltage and could destroy the MEMS, the design must implement a large ratio of the spring constants, k_y/k_x and a parallel kinematics, where the directions x and y are defined in Figure 7.8a. The beams used in this design are clamped-clamped that may not be optimal for large displacements [28] but ensure a parallel kinematics being evenly distributed on the suspended structures. Actuation voltage up to 100 V could be applied without observing any side instabilities that appeared above 110 V. We have also used folded flexure design, which, for the same footprint, offers a softer rigidity and a higher force sensitivity but is more subject to side instabilities.

The double actuation was initially designed to increase further the applied strain and to work both in compression and extension with cells in

Table 7.4 Typical properties of the fabricated SNT.

Properties	Design	Measured (avg)
Stiffness (left)	$88\,\mathrm{N\,m^{-1}}$	$83\,\mathrm{N\,m^{-1}}$
Stiffness (right)	$56\,\mathrm{N\,m^{-1}}$	$47\,\mathrm{N\,m^{-1}}$
Sensor sensitivity	$100\,\mathrm{fF\,\mu m^{-1}}$	$52\,\mathrm{fF\,\mu m^{-1}}$
Comb-drive gain (right)	$75\,\mathrm{nN\,V^{-2}}$	$47\,\mathrm{nN\,V^{-2}}$
Comb-drive gain (left)	$140\,\mathrm{nN\,V^{-2}}$	$49\,\mathrm{nN\,V^{-2}}$
Stroke (left)	$1.6\,\mathrm{nm\,V^{-2}}$	$0.56\,\mathrm{nm\,V^{-2}}$
Stroke (right)	$1.3\,\mathrm{nm\,V^{-2}}$	$1\,\mathrm{nm\,V^{-2}}$

Qualitative agreement between the designed values and the measured values is observed. Deviation may come from process inhomogeneities.

suspension. The drift in the mechanical properties of the SNT due to nonlinear effects [46, 47] needed an optimized design methodology. One arm, carefully calibrated in displacement, is used to apply a large strain (generally above 30%) while the other arm, with an integrated capacitive displacement sensor, senses the force transduced or generated by the living material. This provides the advantage of working with a sensitive arm always close or within few nanometers from its reference position. The mechanical properties of the sensor are thus well established and Table 7.4 summarizes the mechanical properties of the SNT designed to perform single-cell analysis.

7.5.4
Instrumentation

We advocate the use of SNT for single-cell studies in particular, because it allows the gathering of complementary information with one single tool. Thus, their development should greatly contribute to the convergence of the conflicting views on the mechanical properties of these complex materials [48, 49]. In addition, the control strategies that have been presented in Section 7.2 [24] will provide original methods to deepen our understanding of the active behaviors of these systems [9, 50].

We focused the instrumentation on the simultaneous recording of the dynamic and static properties. In phenomenological models, the dynamic properties inform us on the stiffness and dissipation at the resonance frequency, whereas the static properties are related directly to the force. The dynamic properties are recorded using a digital PLL (phase-locked loop) implemented with LabVIEW, and the static properties are measured using a lock-in technique at the highest possible frequency. The whole system is optimized for high bandwidth. The dynamic properties are used to approach the surfaces and monitor soft contact with fragile cells. The system's dynamic properties allow the reversible approach and touch of the surface within 20 nm by using a robotized nanopositioning system.

7.5.5
Experimental Platform

The experimental platform, onto which the SNT, the robotized nanopositioning system, and the cells are placed, is designed to be fully compatible with standard microscopy technique, Figure 7.8b. The platform replaces the stage of an inverted microscope, and both transmission microcopy and fluorescence microscopy can be performed on the biological cells while performing the mechanical characterization. This is a major advantage compared with other techniques such as AFM that does not allow real-time high-resolution microscopy.

The chamber into which the live cell needs to be inserted must be open for the SNT to penetrate into the culture medium. The interface, subject to very strong capillary forces, is a major source of noises and drawbacks that make this emerging technology still an art. If no change of the biochemical composition of the medium is required, then large volumes are used and the evaporation and the resulting drift of the meniscus are minimized. For spread cells, the SNT can be used with a single arm, the substrate onto which the cell adhere being used as a reference frame. Strains are applied using the robotized nanopositioning system. It is only for the case of cells in suspensions that the two arms are required and that great care must be taken to subtract the contribution of the meniscus from the mechanical properties. Without care, the capillary forces can be as high as several micronewtons [51, 52] prevailing biologically relevant contributions. Several strategies are being developed to minimize the effect of capillary force. The precise control of the meniscus is an efficient way if the thickness of the water layer is very shallow as in the setup of Figure 7.7 for molecular application in Section 7.4.

7.5.6
Cells in Suspension

To perform mechanical characterization on cells in suspension, an SNT with double actuation and flat tips (Figure 7.8a, middle left) is mounted and calibrated on the setup. For the evaluation of the instrument, fresh cells are collected from the culture dish and pipetted in the microdish on the platform. In principle, the cells could have been outputs of a pathological cell-sorting device connected to the microdish. The SNT is approached to the vicinity of the surface thanks to the robotized arm until the continuous monitoring of the resonance parameters of the vibrating arm indicates by a rapid decrease of the resonance amplitude that the contact of the surface is established. Cells in suspension generally form sphere of approximately 10 µm in diameter. There is no need in this case to work very close to the surface and the SNT is raised at about 1 µm above the glass surface. At this height, the influence of the surface is not observed on the dynamic properties and there is no risk to touch the surface and damage the SNT. An appropriate cell is selected optically. Applying a voltage on the comb drives open the gap wide and the cell is placed in between the SNT arms. The monitoring of the resonance properties prevents any damage to the cell or to the SNT, Figure 7.9a. The actuation
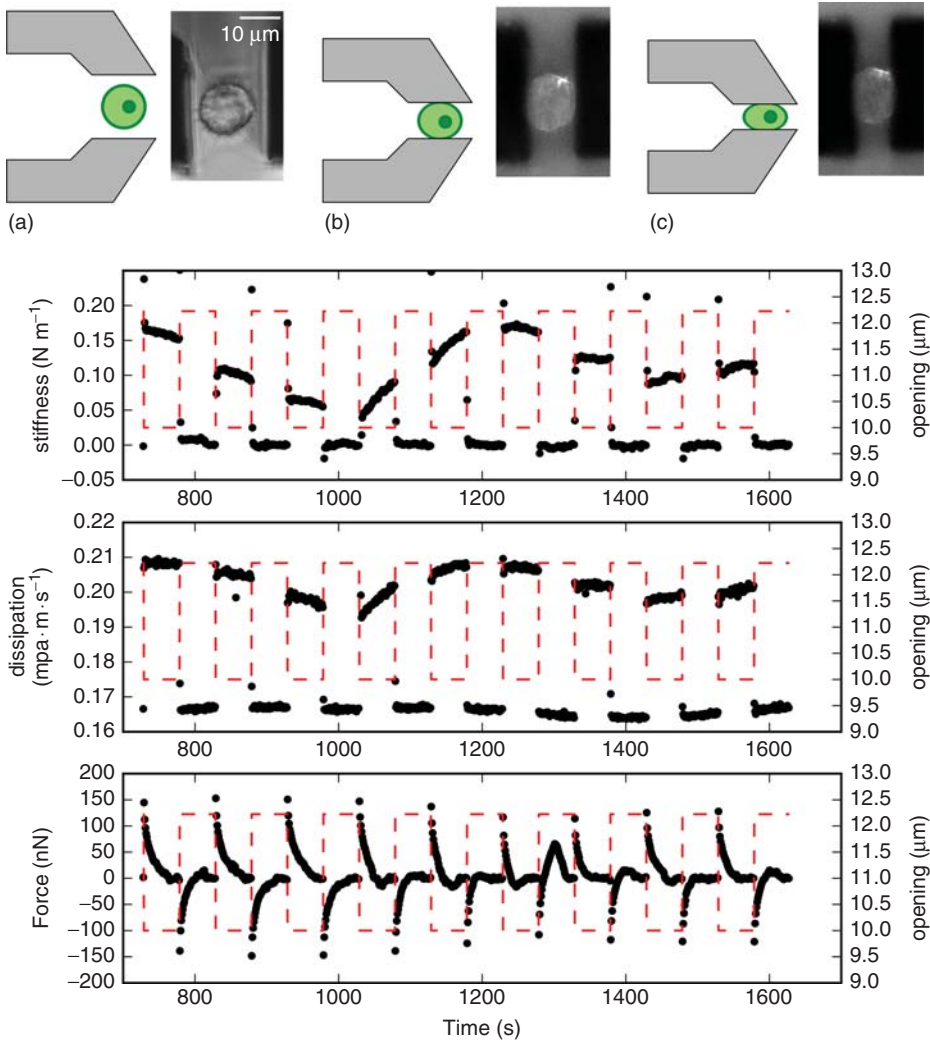
Figure 7.9 Repeated compressions and release of a single cell in suspension. (a) The initial diameter of the cell is 13 μm. (b,c) Schematics and fluorescence image of the cell in compressed state. The upper arm is used for the mechanical stimulations and the lower arm senses the stiffness of the cell, its dissipation (dynamic properties at the resonance frequency), and the absolute force (static) acting on the cell. The opening of the SNT is plotted as a dashed line.

voltage is reduced until an increase of the resonance frequency is observed. At this point, the cell is slightly strained (Figure 7.9b) by the SNT and the voltage is memorized. The cell is then fully strained by reducing the actuation voltage to 0 V (Figure 7.9c). In the experiment depicted in Figure 7.9, the amplitude of compression was about 2 μm and the strain was about 20%. Compression and extensions

are repeated several times and the stiffness, dissipation coefficient, and force are recorded as a function of time along the experiment. The cell's mechanical parameters are not constant over time. This is probably due to biochemical signaling and plastic flow of the cytoskeleton. These parameters are the results of the interplay of the mechanical properties of the cell cortex, cell cytoskeleton, and nucleus as well as the cell adhesion onto the SNT surface and are hard to model a priori. Nevertheless, we can expect that different cell types, or cells at different stages of some pathology will show different fingerprints. The goals of further research in this direction will aim to determine the "fingerprint" of cells in various physiological and pathological conditions and deepen our understanding of the interplay of the mechanical components of the inhomogeneous material.

7.5.7
Spread Cells

Our next target is to study cells spread onto a surface. In that case, adhesive cells organize their cytoskeleton to form fibers known as *stress fibers*. Stress fibers are supposed to be responsible for the generation of force in cells [53, 54], and thus are very interesting molecular objects to explore using nanomechanical tools. It remains a challenge because the forces generated by these objects are of the order of nanonewtons [55, 56], just lower than the detection limit of our system. Another challenge is to stimulate a single stress fiber embedded into the cell body without damaging the cell. For that purpose, we use only one arm of the SNT and use the substrate onto which the cell adheres as a reference. Instead of using flat tips, we use sharp tips that provide high spatial resolution. Figure 7.10a shows a spread cell onto which the tip of the SNT is pushed on the side of the cell by moving the robotized nanopositioner. Away from the nucleus, the spread cell has a thickness of a few hundreds of nanometers, and the flatness and thermal drift of the whole may become an issue like in submicron SPM techniques. Figure 7.10a shows the recording of the cell stiffness as a function of time. The same qualitative behaviors are observed at different positions offset by 5 μm in the y-direction as depicted in the figure (circle and cross). The behaviors of the curves are as expected: immediately after pushing the cell, stiffness is added to the dynamic system. After about 10 s which the stiffness increases suggesting that there is some sort of stiffening in the system that may be induced by either the flow of the deformed cytoskeleton or the biochemical response of the cell. The retraction of the SNT tip recovers the initial stiffness proving that the drift is negligible. A second indentation is performed that shows the added stiffness but not the peak as observed in the first indentation suggesting that the stiffening process does not occur or that the second indentation is not large enough to trigger it (square). The evolution of the stiffness on the long time is not trivial and should be correlated with high-resolution fluorescence microscopy of Green Fluorescent Protein (GFP)-labeled proteins for better understanding.

The SNT platform has shown sufficient stability to perform cell indentation at heights of few hundreds of nanometers above a surface. Live-cell fluorescence
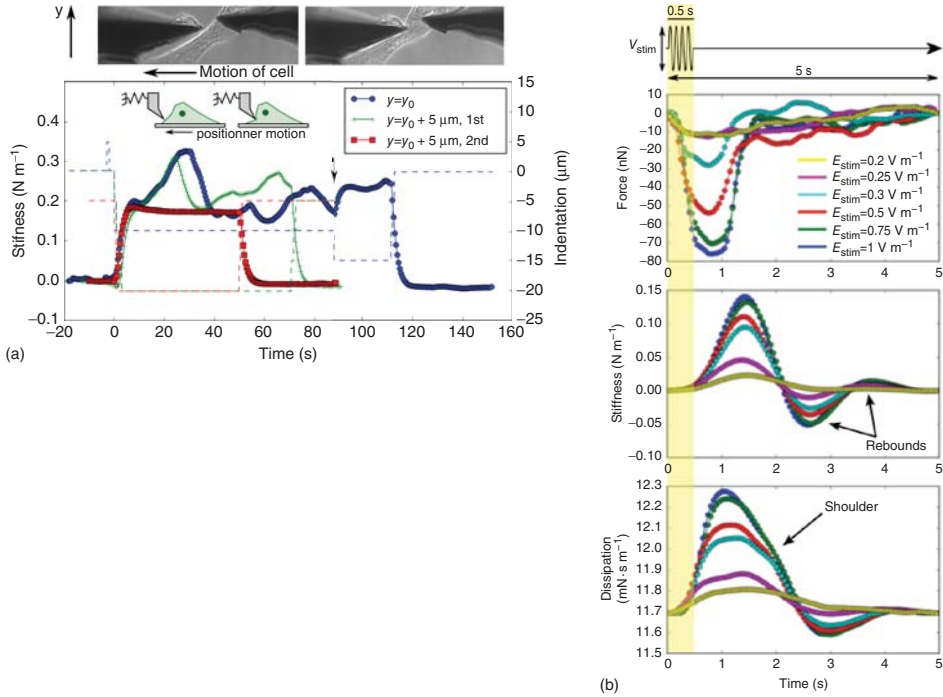
Figure 7.10 Characterization of adherent cells, epithelial A breast cancer cell line, Michigan Cancer Foundation-7 (MCF), and myotubes. (a) Indentation on fixed cells with a sharp tip. The fluorescence images on top represent the extreme positions of the indentation. Cells are epithelial MCF expressing GFP-life act. Only the left sensitive tip was used. The cells are moved toward the tips by using nanopositioners. The stiffness is recorded as the indentation progresses, for three consecutive scans with different tip heights. (b) Various mechanical responses measured by the SNT in contact with the contracting myotube. The yellow-shaded area indicates the duration of the excitation signal (0.5 s). The inset shows the characteristics of the stimulation signal. The arrows highlight complex structures in the myotube response. Here, only the amplitude was varied, period = 5 s, pulse period = 50 ms, N_b of repeat = 10.

microscopy would greatly help to decipher the time evolution of the mechanical signals that are observed.

7.5.8
Cell Differentiation

The last type of living system that we studied with the SNT was C2C12 cells differentiated into contractile myotubes. The contractile properties of the cell were evaluated according to the stimulating voltage that triggers membrane depolarization and the contraction of the myotube. The simultaneous recordings of the mechanical parameters are shown in Figure 7.10b. SNT allowed

quantitative determination of the minimal electric field that is required to trigger the myotube contraction. In addition, the dynamics of the contraction can be studied quantitatively. Fine structures are observed in the stiffness or dissipation coefficients of the systems that suggest nontrivial mechanical events in the myotubes even several seconds after the stimulation. Noteworthy, optically no activity was observed after the stress relaxation by the myotube that occurs independently of the strength of the electric field about 1 s after the end of the stimulation.

7.5.9
Concluding Remarks for Cell Characterization with SNT

In conclusion, we would highlight the versatility of the SNT to study various living systems and obtain relevant information regarding their mechanical properties as a function of parameters such as strain, time, or external stimulations such as electric fields in the case of myotubes. The platform is compatible with state-of-the-art microscopy and the combination of the methods should contribute significantly to the advancement of fundamental knowledge of the mechanical properties of these complex materials that are heterogeneous and out of equilibrium.

The use of the platform as a diagnostic tool for diseases altering the mechanical properties of cells should be possible after some improvements such as the microfluidic integration and the control of the meniscus that can complicate the measurements. Nevertheless the system is mature for the gathering of the cell line's mechanical fingerprint that could allow later fast and low-cost diagnosis of many diseases.

7.6
General Concluding Remarks and Perspectives

The advantage of MEMS technology for scientific instruments critically depends on its small size. MEMS instruments have sizes ranging from a few tens of nanometers to a few tens of micrometers, which are in the same range as macromolecules, organelles, cells, and small tissues. In addition to their small size, however, there are other advantages also. MEMS technology enables us to integrate sensors, actuators, and microfluidic devices in the close vicinity of the structures that interact with samples. Sensors can directly measure electromechanical properties of the sample. Actuators are used to manipulate the sample and apply force to it. Microfluidic devices allow quick exchange of liquid surrounding the sample; the chemical reaction can be controlled and measured easily. Furthermore, MEMS technology is capable of making many devices on a small chip. Parallel processing becomes feasible to efficiently extract multiple parameters from the sample or to analyze different samples at the same time.

Silicon nanotweezers combined with the microfluidic system are the typical example featuring such advantages. The tips are as small as tens of nanometers and sharp enough to electrically attract and capture molecules. Once filamentary

molecule(s) is captured between tips, with separation of few micrometers, it is possible to apply force or vibration to know the stiffness and viscosity of the sample. The measurement can be performed continuously during the chemical reaction between the sample and surrounding solutions that are easily replaced by integrated microfluidic elements. The microfluidic integration also allows us to minimize the amount of the solution and stabilize the motion of the tweezers. Please note that the minimum amount of measured sample can be as little as a single molecule or very few numbers of molecules. In addition, labeling is not required. Those features make the continuous monitoring of chemical reaction applicable to the wide variety of materials.

Of course, the system is still in the emerging phase and there are technical challenges to solve.

1) The automation of procedures. This is basically easy to solve. Automated $X-Y-Z$ stages can position both tweezers and the microchamber with submicrometer accuracy. Also, the pumps and valves of the microfluidic system can be controlled by PC via electrical signals. Measurements and data acquisition can also be done by PC digitally.

2) Further improvement of stability and sensitivity through the optimization of device structures and bioassay protocols.

3) The interaction between the meniscus surface and tweezers' tips, which affects the stability of resonant characteristics. The shape of meniscus and the interfacial line of air and liquid on the tips may change due to evaporation, the surface tension of the meniscus, which can depend on the absorption of sample molecules on its surface, and the surface hydrophobicity of the tips. We have stabilized the meniscus by introducing pressure-controlled microfluidic channel and coating the designated part of tips with a hydrophobic film. In the future, the combination of tweezers with droplet-based digital microfluidic system [57] can be investigated.

4) The capturing method of target molecules has much room to improve. For the DNA case, the number of captured DNA may differ one trial to another. On the basis of the calibration of the initial amount of DNA, it is possible to normalize the result; such procedure will be established. The attachment of other filamentary molecules or nanofibers is also the issue. Good "adhesive" coating to firmly fix the sample between tips needs to be found. For example, PLL is positively charged and can attract fibers that have negative charges.

5) If the tweezers are used as the tool to manipulate and examine the properties of the sample, some robotics approach may be interesting. There are robotic systems called *master–slave manipulators*. The operator moves the master manipulator, and the remotely located slave robot follows the motion. Some feedback of force and/or displacement can be sent to the master for the operator to feel the reaction. The scales of the master and the slave are not necessarily the same. Therefore, if the slave robot is replaced by our silicon nanotweezers, the operator can "touch" cells or molecules and "feel" the response when they are stretched or squeezed. Even a visual feedback through the microscope can be added.

To conclude, the silicon nanotweezers can be applied to handle various objects other than DNA molecules. More generally, the MEMS tools with features such as microscale, integrated functionality, automation, and parallelism, will be utilized not only in nanoscientific instrumentation but also in miniaturized analysis devices for the precise detection and monitoring at the point of concern in real time and with low cost.

Acknowledgments

References

1. Bubendorf, L., Kononen, J., Koivisto, P., Schraml, P., Moch, H., Gasser, T.C., Willi, N., Mihatsch, M.J., Sauter, G., and Kallioniemi, O.P. (1999) Survey of gene amplifications during prostate cancer progression by high-throughout fluorescence in situ hybridization on tissue microarrays. *Cancer Res.*, **59** (4), 803–806.

2. Manz, A., Graber, N., and Widmer, H.M. (1990) Miniaturized total chemical analysis systems. *Sens. Actuators, B: Chem.*, **1**, 244–248.

3. Jakeway, S., de Mello, A., and Russell, E. (2000) Miniaturized total analysis systems for biological analysis. *Fresenius J. Anal. Chem.*, **366**, 525–539.

4. Hong, J., Edel, J.B., and deMello, A.J. (2009) Micro- and nanofluidic systems for high-throughput biological screening. *Drug Discovery Today*, **14** (3), 134–146.

5. Kim, S.H., Yamamoto, T., Fourmy, D., and Fujii, T. (2011) Electroactive microwell arrays for highly efficient single-cell trapping and analysis. *Small*, **7** (22), 3239–3247.

6. Craighead, H. (2006) Future lab-on-a-chip technologies for interrogating individual molecules. *Nature*, **442** (7101), 387–393.

7. Bao, G. and Suresh, S. (2003) Cell and molecular mechanics of biological materials. *Nat. Mater.*, **2** (11), 715–725.

8. Guz, N., Dokukin, M., Kalaparthi, V., and Sokolov, I. (2014) If cell mechanics can be described by elastic modulus: study of different models and probes used in indentation experiments. *Biophys. J.*, **107** (3), 564–575.

9. Mitrossilis, D., Fouchard, J., Pereira, D., Postic, F., Richert, A., Saint-Jean, M., and Asnacios, A. (2010) Real-time single-cell

response to stiffness. *Proc. Natl. Acad. Sci. U.S.A.*, **107** (38), 16518–16523.

10. Fuller, D., Gemmen, G., Rickgauer, J., Dupont, A., Millin, R., Recouvreux, P., and Smith, D. (2006) A general method for manipulating DNA sequences from any organism with optical tweezers. *Nucleic Acids Res.*, **34** (2), e15.

11. Mills, J.P., Qie, L., Dao, M., Lim, C.T., and Suresh, S. (2004) Nonlinear elastic and viscoelastic deformation of the human red blood cell with optical tweezers. *Mech. Chem. Biosyst.*, **1** (3), 169–180.

12. Strick, T., Allemand, J., Bensimon, D., Bensimon, A., and Croquette, V. (1996) The elasticity of a single supercoiled DNA molecule. *Science*, **271** (5257), 1835–1837.

13. Wang, N., Butler, J.P., and Ingber, D.E. (1993) Mechanotransduction across the cell surface and through the cytoskeleton. *Science*, **260** (5111), 1124–1127.

14. Lee, G.U., Chrisey, L.A., and Colton, R.J. (1994) Direct measurement of the forces between complementary strands of DNA. *Science*, **266** (5186), 771–773.

15. Cross, S.E., Jin, Y.-S., Rao, J., and Gimzewski, J.K. (2007) Nanomechanical analysis of cells from cancer patients. *Nat. Nanotechnol.*, **2** (12), 780–783.

16. Mita, M., Kawara, H., Toshiyoshi, H., Endo, J., and Fujita, H. (2005) Bulk micromachined tunneling tips integrated with positioning actuators. *J. Microelectromech. Syst.*, **14** (1), 23–28.

17. Sun, Y., Nelson, B., Potasek, D., and Enikov, E. (2002) A bulk microfabricated multi-axis capacitive cellular force sensor using transverse comb drives. *J. Micromech. Microeng.*, **12** (6), 832–840.

18. Kim, K., Liu, X., Zhang, Y., and Sun, Y. (2008) Nanonewton force-controlled manipulation of biological cells using a monolithic MEMS microgripper with two-axis force feedback. *J. Micromech. Microeng.*, **18** (5), 055013.

19. Hashiguchi, G., Goda, T., Hosogi, M., Hirano, K., Kaji, N., Baba, Y., Kakushima, K., and Fujita, H. (2003) DNA manipulation and retrieval from an aqueous solution with micromachined nanotweezers. *Anal. Chem.*, **75** (17), 4347–4350.

20. Yamahata, C., Collard, D., Takekawa, T., Kumemura, M., Hashiguchi, G., and Fujita, H. (2008) Humidity dependence of charge transport through DNA revealed by silicon-based nanotweezers manipulation. *Biophys. J.*, **94** (1), 63–70.

21. Yamahata, C., Collard, D., Legrand, B., Takekawa, T., Kumemura, M., Hashiguchi, G., and Fujita, H. (2008) Silicon nanotweezers with subnanometer resolution for the micromanipulation of biomolecules. *J. Microelectromech. Syst.*, **17** (3), 623–631.

22. Kumemura, M., Collard, D., Yamahata, C., Sakaki, N., Hashiguchi, G., and Fujita, H. (2007) Single DNA molecule isolation and trapping in a microfluidic device. *ChemPhysChem*, **8** (12), 1875–1880.

23. Collard, D. (2013) Silicon nanotweezers for biomechanical and bioelectrical assays. *Front. Biosci. (Elite Ed.)*, **5**, 955–965.

24. Lafitte, N., Haddab, Y., Le Gorrec, Y., Guillou, H., Kumemura, M., Jalabert, L., Collard, D., and Fujita, H. (2015) Improvement of silicon nanotweezers sensitivity for mechanical characterization of biomolecules using closed-loop control. *IEEE/ASME Trans. Mechatron.* **20** (3), 1418–1427.

25. Perret, G., Chiang, P.-T., Lacornerie, T., Kumemura, M., Lafitte, N., Guillou, H., Jalabert, L., Lartigau, E., Fujii, T., Cleri, F., Fujita, H., and Collard, D. (2013) Silicon nanotweezers with a microfluidic cavity for the real time characterization of DNA damage under therapeutic radiation beams. *Conf. Proc. IEEE Eng. Med. Biol. Soc.*, **2013**, 6820.

26. Washizu, M. and Kurosawa, O. (1990) Electrostatic manipulation of DNA in microfabricated structures. *IEEE Trans. Ind. Appl.*, **26** (6), 1165–1172.

27. Tang, W.C., Nguyen, T.-C.H., and Howe, R.T. (1989) Laterally driven polysilicon resonant microstructures. *Sens. Actuator*, **20**, 25–32.

28. Legtenberg, R., Groeneveld, A., and Elwenspoek, M. (1996) Comb-drive actuators for large displacements. *J. Micromech. Microeng.*, **6** (3), 320–329.

29. Dai, W., Lian, K., and Wang, W. (2007) Design and fabrication of a SU-8 based

electrostatic microactuator. *Microsyst. Technol.-Micro-Nanosyst.-Inf. Storage Process. Syst.*, **13** (3), 271–277.

30. Hung, E.S. and Senturia, S.D. (1999) Extending the travel range of analog-tuned electrostatic actuators. *J. Microelectromech. Syst.*, **8** (4), 497–505.

31. Lafitte, N. (2012) Modeling and control of MEMS tweezers for the characterization of enzymatic reactions on DNA molecules. PhD dissertation. Universite de Franche Comte. *https://tel.archives-ouvertes.fr/tel-00711961v1*.

32. Zhou, G. and Dowd, P. (2003) Tilted folded-beam suspension for extending the stable travel range of comb-drive actuators. *J. Micromech. Microeng.*, **13** (2), 178–183.

33. Smith, S., Cui, Y., and Bustamante, C. (1996) Overstretching B-DNA: the elastic response of individual double-stranded and single-stranded DNA molecules. *Science*, **271** (5250), 795–799.

34. Bustamante, C., Bryant, Z., and Smith, S.B. (2003) Ten years of tension: single-molecule DNA mechanics. *Nature*, **421** (6921), 423–427.

35. Sun, Y., Fry, S.N., Potasek, D.P., Bell, D.J., and Nelson, B.J. (2005) Characterizing fruit fly flight behavior using a micro-force sensor with a new comb-drive configuration. *J. Microelectromech. Syst.*, **14** (1), 4–11.

36. Collard, D., Yamahata, C., Legrand, B., Takekawa, T., Kumemura, M., Sakaki, N., Hashiguchi, G., and Fujita, H. (2007) Towards mechanical characterization of biomolecules by MNEMS tools. *IEEJ Trans. Electr. Electron. Eng.*, **2** (3), 262–271.

37. Hashiguchi, G., Mihara, Y., Fukino, T., Hara, T., and Fujita, H. (2008) Nano-grippers and method of producing same. US Patent 7, 322,622 B2.

38. Boggild P. (2003) Fabrication and application of nano-manipulators with induced growth. US Patent 20, 020,061,662 A1.

39. Jansen, H., Gardeniers, H., de Boer, M., Elwenspoek, M., and Fluitman, J. (1999) A survey on the reactive ion etching of silicon in microtechnology. *J. Micromech. Microeng.*, **6** (1), 14–28.

40. Fukuta, Y., Fujita, H., and Toshiyoshi, H. (2003) Vapor hydrofluoric acid sacrificial release technique for micro electro mechanical systems using labware. *Jpn. J. Appl. Phys.*, **42** (1), 3690–3694.

41. Kumemura, M., Collard, D., Sakaki, N., Yamahata, C., Hosogi, M., Hashiguchi, G., and Fujita, H. (2011) Single-DNA-molecule trapping with silicon nanotweezers using pulsed dielectrophoresis. *J. Micromech. Microeng.*, **21** (5), 054020.

42. Tilmans, H. (1996) Equivalent circuit representation of electromechanical transducers. 1. Lumped-parameter systems. *J. Micromech. Microeng.*, **6** (1), 157–176.

43. Fujii, T. (2002) PDMS-based microfluidic devices for biomedical applications. *Microelectron. Eng.*, **61**, 907–914.

44. Caille, N., Thoumine, O., Tardy, Y., and Meister, J.-J. (2002) Contribution of the nucleus to the mechanical properties of endothelial cells. *J. Biomech.*, **35** (2), 177–187.

45. Zeng, X. and Li, S. (2011) Multiscale modeling and simulation of soft adhesion and contact of stem cells. *J. Mech. Behav. Biomed. Mater.*, **4** (2), 180–189.

46. Cho, H., Jeong, B., Yu, M.-F., Vakakis, A.F., McFarland, D.M., and Bergman, L.A. (2012) Nonlinear hardening and softening resonances in micromechanical cantilever-nanotube systems originated from nanoscale geometric nonlinearities. *Int. J. Solids Struct.*, **49** (15), 2059–2065.

47. Ekinci, K.L. and Roukes, M.L. (2005) *Rev. Sci. Instrum.*, **76** (6), 061101.

48. Hoffman, B.D., Massiera, G., Van Citters, K.M., and Crocker, J.C. (2006) The consensus mechanics of cultured mammalian cells. *Proc. Natl. Acad. Sci. U.S.A.*, **103** (27), 10259–10264.

49. Hoffman, B.D. and Crocker, J.C. (2009) Cell mechanics: dissecting the physical responses of cells to force. *Annu. Rev. Biomed. Eng.*, **11**, 259–288.

50. Mitrossilis, D., Fouchard, J., Guiroy, A., Desprat, N., Rodriguez, N., Fabry, B., and Asnacios, A. (2009) Single-cell response to stiffness exhibits muscle-like behavior. *Proc. Natl. Acad. Sci. U.S.A.*, **106** (43), 18243–18248.

51. Velev, O.D., Denkov, N.D., Paunov, V.N., Kralchevsky, P.A., and Nakayama, K. (1993) Direct measurement of lateral capillary forces. *Langmuir*, **9** (12), 3702–3709.

52. Cooray, H., Cicuta, P., and Vella, D. (2012) The capillary interaction between two vertical cylinders. *J. Phys. Condens. Matter*, **24**, 284104.

53. Pellegrin, S. and Mellor, H. (2007) Actin stress fibres. *J. Cell Sci.*, **120** (20), 3491–3499.

54. Burridge, K. (1981) Are stress fibers contractile. *Nature*, **294** (5843), 691–692.

55. Sabass, B., Gardel, M.L., Waterman, C.M., and Schwarz, U.S. (2008) High resolution traction force microscopy based on experimental and computational advances. *Biophys. J.*, **94** (1), 207–220.

56. Riveline, D., Zamir, E., Balaban, N.Q., Schwarz, U.S., Ishizaki, T., Narumiya, S., Kam, Z., Geiger, B., and Bershadsky, A.D. (2001) Focal contacts as mechanosensors: externally applied local mechanical force induces growth of focal contacts by an mDia1-dependent and ROCK-independent mechanism. *J. Cell Biol.*, **153** (6), 1175–1185.

57. Moon, H., Wheeler, A.R., Garrell, R.L., Loo, J.A., and Kim, C.-J.C. (2006) An integrated digital microfluidic chip for multiplexed proteomic sample preparation and analysis by MALDI-MS. *Lab Chip*, **6** (9), 1213–1219.

8
Miniaturized Untethered Tools for Surgery

Evin Gultepe, Qianru Jin, Andrew Choi, Alex Abramson, and David H. Gracias

8.1
Introduction

Miniaturization has a presence in every aspect of our lives from the smart phones that operate much faster than our 10-year-old computers, to the drones that ship groceries to remote areas. Consequently, it is no surprise that miniaturization has also emerged as a significant enabler in the biomedical sciences. Owing to recent advances in micro- and nanotechnologies, we have better techniques to observe and understand our bodies as well as treat the diseases that affect us. For example, we now use nanometer-sized contrast agents that can help identify diseases [1] or robotic systems that aid in surgical operations [2]. In this chapter, we summarize important advances in miniaturization of relevance to surgery. Specifically, we focus on untethered tools, which are miniaturized surgical devices that do not require any physical connections to the external world.

Depending on the anatomical part where they are being used, the dimensions of untethered surgical tools cover a wide size range, from the macro- to the molecular scale, as depicted in Figure 8.1. As with all miniaturized devices, the operation and application principles of these tools, too, depend on their size. The fundamental reason behind this size dependency is the relative importance of the governing physical forces at different size scales [4]. Importantly, when the size of the device gets smaller, the magnitude of forces related to the mass of the body, such as inertia, becomes less important compared to that of forces related to the surface, such as viscosity.

One of the biggest advantages of utilizing untethered tools for surgical operations is the possibility to minimize, if not completely avoid, the fulcrum effect, which represents a significant limitation to surgical dexterity in minimally invasive procedures [5]. When the manipulation of the surgical device does not rely on any tethers that are connected to the outside of the body, motion dexterity is not limited by the size of the incision site or the distance from it. This enhanced dexterity allows the untethered tools to reach small, narrow conduits; even pass through curved and twisted routes. This improved maneuverability also extends the application range of minimally invasive operations. For example, the utiliza-
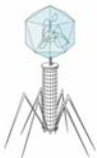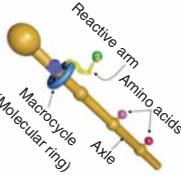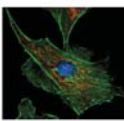
Size	Macro	Micro	Nano	Molecular
Tools	PillCam® COLON	μ-Grippers	Bacteriophage	Synthetic ribosomes
Anatomical part	Organs	Tumors	Cells	Organelles

Figure 8.1 Applicability of untethered surgical tools at different size scales. Macroscale tools, for example, PillCam® Colon (By permission from Given Imaging (a Covidien company)) can operate in large organs, such as the colon. Microscale tools, such as μ-grippers (credit: Evin Gultepe) , can operate on multicellular structures such as tumors. Nanoscale tools, such as a synthetic bacteriophage (from Database Center for Life Science) , can be used to operate on a single cell (credit: Darryl Leja, NHGRI from *www.genome.gov*). Molecular machines can be used in organelles (credit: Bruce Blaus); the image shows a synthetic ribosome. (© 2013 Landes Bioscience [3].)

tion of capsule endoscopes render it possible to get information such as *in situ* optical images or pH data of the gastrointestinal (GI) tract by simply swallowing a rather large pill without requiring sedation [6]; such information was previously only retrievable through long, endoscopic procedures.

While the miniaturization of surgical tools is not a new area of development, when it comes to untethered surgical tools the field is relatively young and still emerging. One of the main reasons behind this delay is the challenge in supplying power to an untethered surgical device. When a device is not connected to any wires, the power required for its operation can be supplied by either the energy stored on the device, such as a battery, or wireless energy harvesting, using, for example, electromagnetic radiation or ultrasonic waves. Both of these power supply modalities have their own challenges in miniaturization. While battery technologies have advanced significantly in the past decade and are still the dominant source of energy for most untethered medical devices, they are also major contributors to the overall weight and size of the devices [7, 8]. On the other hand, alternative energy harvesting methods are still in their infancy with pronounced challenges in supplying adequate reliable power as well as patient safety during power transmission [9].

Another obstacle for untethered miniaturized tools is the engineering challenge in designing and manufacturing the moving parts within surgical tools [10]. Even though micro- and nanomanufacturing methods have been rapidly advancing in the recent years, miniaturized fabrication still relies predominantly on planar

lithography. This planar fabrication paradigm, however, is not adequate for building small, three-dimensional (3D) parts with multiple degrees of freedom in a high-throughput manner, and alternative fabrication methods are still in development [11, 12].

In the following sections, we detail the application areas of miniaturized untethered surgical tools and also explain their operation principles with specific examples. We also discuss the advantages and disadvantages of these tools and point out important directions of their development.

8.2
Macroscale Untethered Surgical Tools

We classify macroscale untethered surgical devices as those that range in size from 1 mm to 10 cm in at least one dimension. These devices find utility in anatomical environments with easy external access and wide internal channels [13]. For example, these devices can be used in colonoscopies [14], laparoscopies [15, 16], and percutaneous coronary interventions [17]. In order for a macrodevice to perform untethered surgical operations *in vivo*, it must possess multiple functionalities. Specifically, such a macrodevice must be able to perform the following tasks: (i) locomotion: capacity to be directed to a desired location; (ii) communication: maintain a wireless link to the outside world; (iii) actuation: ability to perform mechanical functions on command; and (iv) supply of power: store or acquire sufficient power to perform said tasks.

These design parameters are the main challenges in developing macroscale untethered surgical devices. It is important to understand these challenges in the frame of reference of an untethered device. First, since it is not possible to manually maneuver the device with a tether, just the task of reaching the anatomical target poses a challenge [18]. Second, without wires or tethers, it is not straightforward to send signals to the device for actuation or movement. Third, these untethered devices must contain an on-board activation mechanism in order to complete their operation. For example, a biopsy device must be activated at the area of interest in order to take a tissue sample [19–21]. Finally, untethered devices must have enough stored or harvested energy to power their operation. For example, a capsule endoscopy camera must contain sufficient battery power to take video data throughout the targeted area of the digestive tract [6].

These challenges can be addressed by either designing the whole device appropriately [18] or adding different modules into the device [20]. Since the beginning of miniaturization efforts in the medical sciences, several methods have been developed to address these challenges. Each of these methods provides valuable insight into the possible configurations and combinations that can be used to create a functional untethered surgical device.

8.2.1
Localization and Locomotion without Tethers

Many surgical tasks are required on specific target areas inside the body which require the untethered tool to be maneuvered until it reaches a predetermined location. When devices such as biopotential measurement machines [22] or drug delivery micropumps [23] are localized on external body parts, the process of localization is relatively trivial. On the other hand, when untethered devices operate inside the body, their localization and locomotion becomes challenging. In the case of macroscale devices, they are typically limited to large, open spaces inside the body, such as the digestive tract [14], the arteries [17], or the inside the eye [24]. In order to reach their target locations, these devices rely on localization methods, such as insertion and incision [15, 16], and/or locomotive modules, such as legs [25] and propellers [26].

8.2.1.1 Localization

In order for devices to reach their target areas, they can be inserted through either an orifice, as is the case with endoscopic capsules [14], or an incision, as is the case with drug-eluting stents [27], laparoscopy tools [15, 16], and intraocular measurement tools [24]. For example, it has been reported that a wireless robot for networked laparoscopy can be implanted or inserted into the body to assist with the operation (Figure 8.2a) [15]. This 2-megapixel remote-controlled robotic camera, which is only 12 mm in diameter, can be implanted in the wall of the abdomen so as to provide a 360° view of the area of interest with a focus range of up to

———————————————————————————————→

Figure 8.2 Macroscale untethered devices. (a) Optical images of an implantable wireless laparoscopy camera. This camera uses robotic manipulation and has a 360° viewing angle. (Credit: © (2013) IEEE. Reprinted with permission from [15].) (b) An optical image of a capsule utilizing multilegged locomotion. The legs move at once and push against the tissue nearby, creating a force of 0.67 N and propelling the capsule forward. (Credit: © (2009) IEEE. Reprinted with permission from Ref. [25].) (c) Optical images of a surgical assistance tool used in procedures such as laparoscopies. This tool can perform multiple functionalities including clamping, cauterizing, and drug delivery by replacing the head of the tool with different attachments. Scale bar represents 5 mm. (Credit: © (2009) IEEE. Reprinted with permission from Ref. [28].) (d) Time lapse optical images of a drug-eluting capsule utilizing magnetic activation. The magnets located on the top and bottom of the capsule compress it when in the presence of a magnetic field in order to deliver the drug cargo. (Credit: © (2013) IEEE. Reprinted with permission from Ref. [29].) (e) An optical image of a magnetic field-activated biopsy capsule razor on a graph paper (left). Schematic representation of the working principle of the capsule (right). The razor cocks in the presence of an external magnetic field and returns to its original position when the magnet is removed, slicing away the tissue in its path. (Credit: Reprinted with permission from Ref. [30], originally published by ASME.) (f) Optical images of a gripping robot used to manipulate cells in a microfluidic chip. The robot is localized via a magnet and can be used for enucleation, scale bar (left): 1 mm, scale bar (right): 100 μm. (Credit: © (2013) IEEE. Reprinted with permission from Ref. [31].)

(a)

(b)

(c)
- Wheel
- Top jaw
- Bottom jaw
- Collar
- Wheel

- Top jaw
- Staple
- Bottom jaw
- Collar

(d)

(1) t = 0 sec (2) t = 6 sec (3) t = 10 sec

(e)

External magnet

Abdominal wall
Lumen wall

Capsule

1   2   3

(f)

Oocyte
Glass needle
Micro-robot

(1) Gripping (2) Piercing (3) Cutting

(4) After cutting (5) Pushing (6) Enucleation
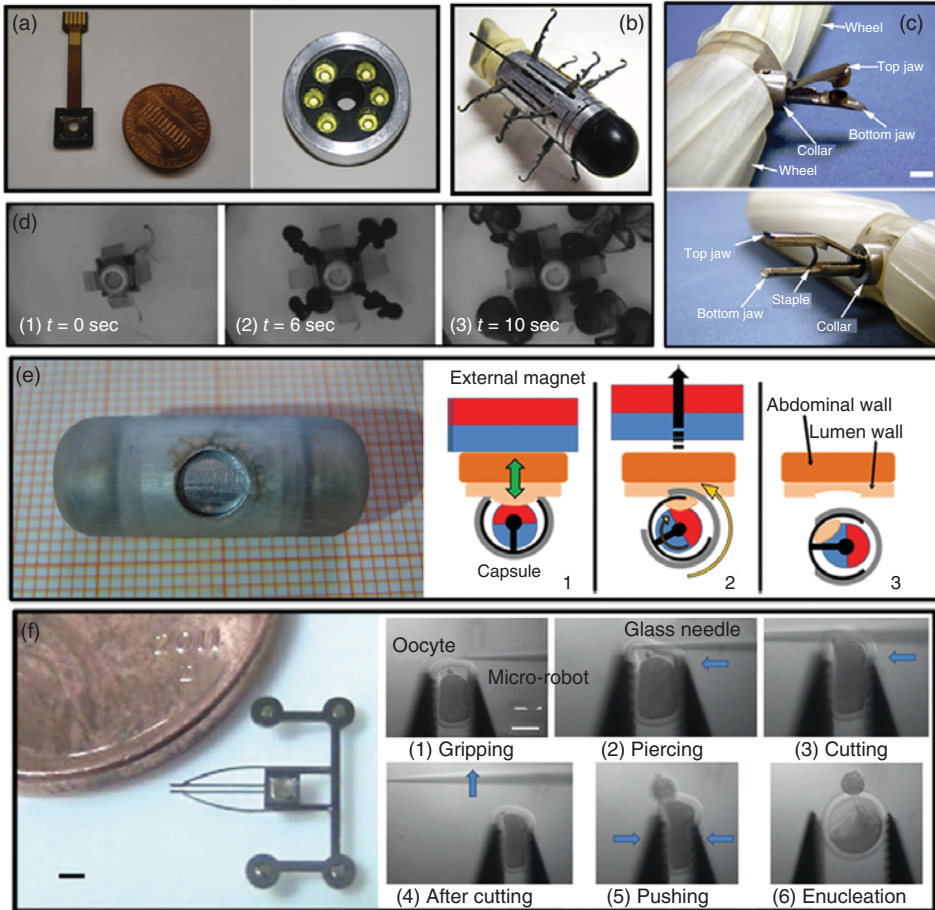
100 mm. This device can replace wired cameras that interfere with other surgical instruments, and it will require fewer personnel to operate.

Another reported device, the intraocular oxygen sensor, allows for efficient and minimally invasive surgeries without requiring a tether [24]. An inadequate supply of oxygen to the eye can be a sign of retinal vein occlusions, diabetic retinopathy, macular degeneration, and glaucoma. This untethered device could potentially replace the invasive oxygen measurement devices currently on the market, such as fiber-optic probes and electrodes. By making a small incision in the sclera, this sensor can be placed in the vitreous humor and maneuvered via an external magnetic field. The sensor, which is coated with an iridium phosphorescent complex, quenches light in the presence of oxygen. The results are then read by a luminescence sensor outside the eye without requiring an incision for each measurement as with current commercially available methods.

8.2.1.2 Locomotion

While many untethered macroscale devices, including the ones listed earlier, are implanted and localized by a doctor, there are other devices that must find their way to their target in the body autonomously. Unless natural body movements, such as peristalsis, are enough to move the device as in the case of commercially available endoscopic capsules, such as the PillCam® or EndoCapsule, untethered tools require specialized modules for locomotion. There are several methods of locomotion currently utilized by surgical devices including magnetic [30], worm-like [32], legged [25], and propeller-based [26] locomotion; however, some of these methods require excessive amounts of space and power. In addition, such paradigms can be challenging to implement in 3D spaces *in vivo* and in the absence of visual feedback.

When a device contains magnetic modules, it can be manipulated via an external magnetic field. For example, the intraocular oxygen sensor mentioned in Section 8.2.1.1 is made out of a ferromagnetic material, cobalt–nickel, and therefore can be moved to different areas of the eye in order to take several measurements [24]. In another example, a biopsy device contains a magnet for both actuation and locomotion [30]. When exposed to a magnetic field, the device is concurrently actuated and drawn toward the wall of the tissue, so that it is more likely to obtain a tissue sample. For devices that already contain magnets, magnetic locomotion seems simple and effective. However, for the precise control of such a device, magnetic locomotion requires additional equipment and operational controls outside of the body.

A mechanical earthworm represents an excellent example of worm-like locomotion [32]. This mechanical worm, which is 50 mm in length and 10 mm in diameter, moves by anchoring a section of the device at one end to a surface while compressing the body of the device using a spring. The spring then concurrently expands and releases its hold from the surface, causing the worm to move forward. Even though the device requires only a 1.55 V battery with a current of 0.07 mA to move, it requires the entire length of the device to be dedicated to the locomotion mechanism.

Multilegged devices use more energy than earthworm devices, but allow for smaller designs. It has been demonstrated that a multilegged capsule can provide the necessary power for movement in a tubular environment such as the intestine by using several small legs pushing in unison (Figure 8.2b) [25]. These legs rotate 110° and, when pushing together, exert a force of 0.67 N. The legs run on 430 mW of power and can be housed in a chamber 26 mm in length and 11 mm in diameter. In a slightly different mechanism, the legs rotate into the capsule instead of rotating perpendicular to the capsule [33]. Even though this mechanism requires a chamber 45 mm in length and 16 mm in diameter, each of the legs is able to produce 2.6 N of force on 500 mW of power. Both of these legged mechanisms can easily move a device through a tubular organ, yet they require relatively large capsules in which to be housed.

One of the smallest methods of macrolocomotion has been achieved using a propeller. It has been shown that a 3.8-mm-diameter propeller can be attached to a variety of untethered devices [26]. The propeller can be turned on and off via a microcontroller, and it runs on a 17 mm × 10 mm × 3 mm battery of 3.7 V with 400 mA. This propeller allows an untethered macrodevice to swim though any area that contains liquid. Even though the propeller method requires more power than the multilegged or earthworm devices, its small size makes it ideal for smaller locomotive devices.

8.2.2
Powering and Activating a Small Machine

Most macroscale devices contain enough room to hold several components, and each one of these components requires both a source of energy and a method of activation. For the energy required for their operations and locomotion, untethered devices typically utilize one of these most common energy supply methods: stored chemical energy, stored mechanical energy, and external magnetic fields. While stored chemical energy provides long-lasting power for electronics in the form of batteries [34], stored mechanical energy in the form of springs and external magnetic fields via magnetic modules provides short, powerful bursts of energy [20, 29]. Some devices have been shown to rely on less-common sources, such as wireless power transfer [35, 36], piezoelectricity [37, 38], or biofuel cells [39].

In many cases, a combination of these energy sources is used to power, activate, and control an untethered device together. While batteries are generally used to power the circuit board as well as the other electronic parts, the springs and magnets are used for other specialized tasks.

8.2.2.1 Stored Chemical Energy
Many macroscale untethered surgical devices contain specialized batteries in order to power the electronics and mechanical equipment; examples include commercial pill cameras [14], legged capsules [25], and biopsy contraptions [19]. For example, a surgical task assistance robot using a 185 mA lithium organic cell battery in order to power locomotive motors and communication electronics

has been reported (Figure 8.2c) [16]. This device, only 100-mm long and 20-mm wide, can perform simple surgical tasks such as cauterizing and clamping blood vessels.

A bioadhesive patch-releasing capsule, 19 mm in diameter and 50 mm in length, relying on both chemical and mechanical stored energies has been developed [34]. This capsule's battery, which measures 22 mm × 12 mm × 4 mm, is about twice as big as a watch battery and releases twice as much power, about 320 mA of current at 3.7 V. While the power from the battery is used for communication and control purposes; it is not sufficient for the mechanical needs of the capsule. In order to physically apply the bioadhesive patch, this capsule must rely on additional sources of energy.

8.2.2.2 Stored Mechanical Energy

Another way of storing energy, particularly for mechanical tasks, utilizes the potential energy of compressed springs. Compressed springs take up little to no room inside the device compared to the amount of power they can release; however, they can be released only once. Because of this limitation, compressed springs are normally used to power an actuated process and are hooked up to the remote communications system. Still, compressed springs are versatile and can perform a multitude of actions.

Compressed springs are typically used to change the physical configuration of the device to complete a task. The bioadhesive patch-releasing capsule utilizes a system of compressed springs in order to push the stored bioadhesive patch out of the capsule and onto a portion of the surrounding tissue [34]. Compressed springs are an ideal source of power for this action, because the task requires energy in the form of one swift motion. Similarly, the InteliSite® drug delivery capsule utilizes compressed springs to push a cap off a capsule to release its stored contents [40]. In another example, springs have been shown to rotate a razor in order to sample a tissue piece [20]. This untethered biopsy device receives 8 N of force from compressed springs to propel the razor blade at 12 mm s^{-1} speed, similar to surgical scissors.

Stored mechanical energy allows devices to perform energy-intensive mechanical tasks with little to no compromise on space inside the device. Still, by using compressed springs, the devices are limited to performing the action only once. When a device is required to perform an energy-intensive task multiple times, a different source of energy is needed.

8.2.2.3 External Magnetic Field

Incorporating different sizes and configurations of magnets into the design of an untethered device allows for remote power and activation capabilities. Unlike the stored energy systems, the power supplied by this method can be rerouted during the operation by changing the properties of the applied magnetic field. Typically, magnetic fields are used to perform mechanical actions: they can establish removable barriers [41]; or they can serve as compression [29] or trigger mechanisms [30].

Certain devices use magnets in the same way as compressed springs are used. In this type of application, the magnets are used only once. For example, a wireless insufflation device has utilized magnets as a removable barrier between an acid and a base, acting as a switch [41]. The presence of any external magnetic field causes the magnets to move, allowing the acid to mix with the base. This reaction releases CO_2 gas, resulting in insufflation. In this case, the strength of the magnetic field is inconsequential, as long as the field is strong enough to move the magnets. On the other hand, there are devices that depend on the gradient of the magnetic field strength to control the outcome of an action. For example, in the case of the soft drug delivery capsules, the strength of the external magnetic field determines the amount of the released drug (Figure 8.2d) [29]. When an external magnetic field is applied to the soft capsule, two magnets on either side of the capsule compress the entire device, squeezing the drug out. When the maximum field strength, $\sim$0.07 T, is applied, then the entire load, approximately 800 mm^3, is released and distributed to an area of up to 33 mm away from the capsule.

Elsewhere, a biopsy capsule required a much smaller magnetic field strength than the soft capsule, because this device harnesses the power of the magnetic field in a different way [30]. The device contains two cylindrical magnets, where each magnet is polarized along its axis into two semicircular prisms (Figure 8.2e). One of the magnets is anchored to the device while the other magnet is attached to a razor, free to rotate inside the capsule. When an external magnetic field of 100 mT is applied to the device, the free magnet rotates and cocks the razor. When the magnetic field is removed, the stationary magnet applies 5.3 mN of torque on the free magnet and forces the razor to recoil back to its original position, cutting the tissue on its way. Because it does not contain any circuitry or batteries, this capsule is smaller than the typical capsule endoscopes, only 9 mm in diameter and 24 mm in length.

In another study, an on-chip enucleation robot has been reported to use magnets for actuation without containing any circuitry inside the device [31]. This robot houses a permanent magnet at the center in order to actuate its gripping mechanism. In conjunction with a 0.1 V electrical magnet, this device can be positioned with an accuracy of 3.0 μm and can perform tasks such as cell transportation and enucleation (Figure 8.2f).

8.2.2.4 Other Sources of Energy

While many of the devices used in surgery rely on the aforementioned sources of power, some devices do rely on less-common sources, such as wireless power transfer, biofuel cells, and piezoelectricity. For example, wireless power transfer can be used as a replacement for batteries [35, 36]. The advantage is a constant, endless stream of energy, but the setup, in these cases, requires additional pieces of equipment both inside and outside the capsule, such as a generator or an MRI, respectively. Biofuel cells, unlike wireless power transfer mechanisms, garner energy from the environment around the device [39]. Devices can use glucose and oxygen from the bloodstream in order to power small electronics

and replace a battery. Several different biofuel cells have been created, but they tend to work best under the native conditions for the enzymes used in the process, typically in moderate temperatures, $25-50\,°C$ and neutral pH [42]. Finally, piezoelectricity can also be used interchangeably with batteries as has been reported in a magnetically coupleable robotic surgical device [37]. It is also possible for piezoelectric materials to solely power a device by utilizing their sensitivity to mechanical stress. For example, a device using ultrasonic crystals and sonomicrometry has been developed to monitor patients during cardiac operations [38]. In general, these alternative sources of power allow for flexibility and creativity when designing new devices that cannot or choose not to use conventional power sources.

8.3
Microscale Untethered Surgical Tools

As we shrink down from the macro to the submillimeter scale, untethered devices become an increasingly powerful asset to the surgeon's toolkit. In this section, we discuss some of the applications of untethered microtools, as well as the potential modes to control the movement of these devices.

8.3.1
Applications

The dream of miniaturizing tools and operating from within the body to perform targeted surgical procedures while minimizing damage to other regions has been a long-standing goal in medical research. Because of the small size scale of untethered microdevices, it is conceivable that such devices can traverse narrow channels to access hard-to-reach areas of the body, and perform operations such as angioplasties and biopsies.

8.3.1.1 Angioplasty
An important application of untethered microtools is the treatment of coronary artery disease (CAD) in which an artery is blocked by plaque. One way this blockage can be treated is with stent implantation to expand the artery and keep it from renarrowing. Coronary balloon angioplasties have been around since the 1970s, but early versions of stents were difficult to transport to the site of interest, and successful deployment was not easy. Figure 8.3a shows a schematic of the general procedure in which a stent is placed inside an artery: The balloon is expanded to deploy the stent and then deflated for removal once the stent is in place [43]. With advances in microfabrication, the design of stents has improved to have smaller dimensions and deploy more reliably, providing surgeons with more powerful tools to perform their procedures [52].

Figure 8.3b shows a thermo-moisture-responsive biocompatible polyurethane thin-film shape memory polymer (SMP) stent [44]. In order to prevent the occurrence of restenosis, or the renarrowing of an artery, most stents are designed

Angioplasty

Surgical wound closure

Biopsy

Micro-Manipulation
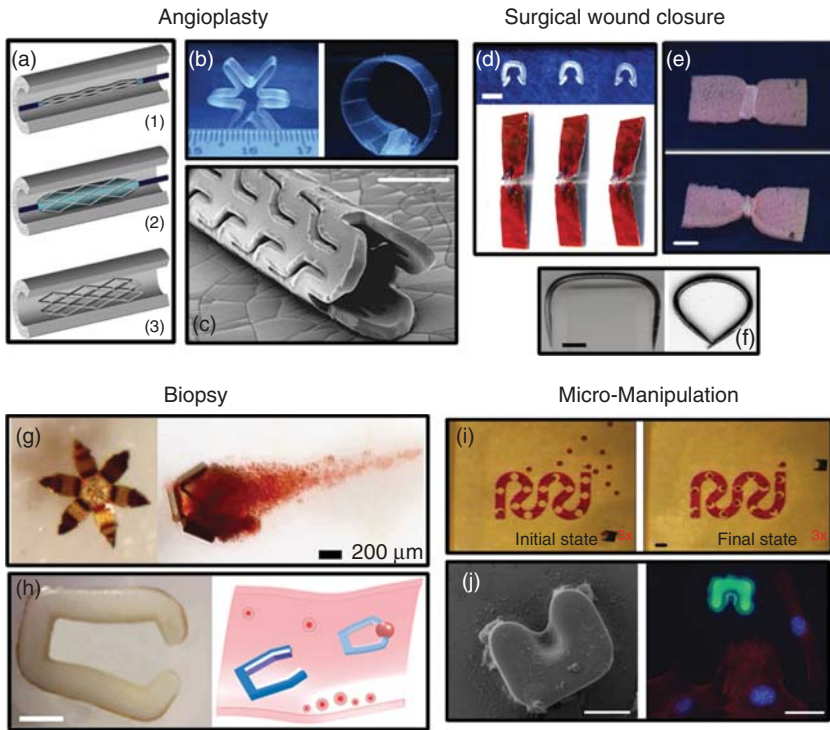
Figure 8.3 Surgical applications of untethered microscale tools. (a) Diagram depicting the deployment of an expanding balloon stent. (Reprinted from Ref. [43] with permission from Elsevier.) (b) Optical image of a water-responsive shape memory polymer being expanded from a collapsed form. (Reprinted from Ref. [44] with permission from SPIE.) (c) SEM (scanning electron microscopy) image of a biocompatible stent. Scale bar represents 1 mm. (Reprinted from Ref. [45] with permission from ASME.) (d) Optical image of the INSORB® staple holding two pieces of simulated tissue together. Scale bar represents 4 mm. (Reprinted from Ref. [46] with permission from Elsevier.) (e) Optical image showing a shape memory polymer wire wrapped around a sponge and tightening upon absorption of water. Scale bar represents 1 cm. (Reprinted from Ref. [44] with permission from SPIE.) (f) Optical image of a thermo-responsive shape memory alloy staple closing upon heating. Scale bar represents 1 mm. (©IOP Publishing. Reprinted from Ref. [47] with permission of IOP Publishing. All rights reserved.) (g) Optical image of a gold plated thermally actuated microgripper capturing a tissue sample for biopsy. Scale bar represents 200 μm. (Reprinted from Ref. [48] with permission from PNAS.) (h) Optical image (left) of a magnetic nanoparticle embedded hydrogel microgripper for blood clot removal and schematic (right) showing closing of the microgripper using an external rotating magnetic field. Scale bar represents 200 μm. (© (2013) IEEE. Reprinted with permission from Ref. [49].) (i) Optical images of a microrobot placing zirconia beads from a random arrangement into a specific pattern. Scale bar represents 1 mm. (Reprinted from Ref. [50] with permission from Elsevier.) (j) SEM image (left) and fluorescence microscopy image (right) of a single-cell-sized microrobot pusher that can be used to move small objects or deliver drugs to individual cells. Scale bar, left 15 μm; right 30 μm. (Reprinted from Ref. [51] by permission of SAGE.)

to expand, but not to retract. The prevention of restenosis is important to keep stents in place, but proves to be a significant problem when stents need to be removed and replaced. The demonstrated thermo-moisture-responsive stent can be mechanically expanded and then retracted to a significantly smaller diameter in an aqueous environment when the polymer absorbs water, thereby facilitating easy removal. However, since the human body is an aqueous environment, shrinkage of this device would be triggered soon after implantation, making it somewhat impractical until further improvements are made; this stent contraction mechanism should be looked upon primarily as a novel shape change mechanism. Figure 8.3c shows an electron micrograph of a poly(L-lactide)/triethylcitrate (PLLA/TEC) stent in its collapsed form [45]. PLLA is a popular biomaterial for medical devices, because it is both biocompatible and biodegradable, and TEC serves as a plasticizer to increase the stent's flexibility [53–55]. A higher TEC content changes the mechanical properties of the stent to have lower elastic modulus and tensile strength [45]. This particular stent has an inner diameter of 1.4 mm, and expands up to 3.5 mm, but the design can be adjusted to accommodate various vascular applications by varying the parameters of the stent such as the diameter, length, and thickness. Such versatility can open up new possibilities for expanding biocompatible structures beyond vascular use.

8.3.1.2 Surgical Wound Closure

Following a surgery, it is usually necessary to close up any open wounds to prevent infection and further complications. Currently, the most common methods for wound closure are suturing and stapling. Over the years, there has been a drive in medical technology to create biocompatible and/or bioabsorbable forms of wound closure. These forms are convenient since they eliminate the need for an extra operation in order to remove the closure material.

An example of a recent biocompatible and bioabsorbable wound closure device is the INSORB® staple [56]. This polylactide–polyglycolide copolymer staple is implanted underneath the skin (subcuticular) using a customized stapling device (Figure 8.3d). Once the staple is in place, it gets absorbed into the skin within a few weeks so removal is not necessary. In addition, since the staple is placed underneath rather than above the skin surface, the unattractive railroad scar that conventional percutaneous metal staples create can also be avoided.

Another wound closure device using a water-responsive polyurethane SMP has been reported [46]. Figure 8.3e shows the SMP wire tightening around a sponge. The SMP is heated and stretched before implantation, and the absorption of water into the polymer causes significant shrinkage within the material, resulting in a tightening effect. Unlike most shape recovery techniques which require embedding of magnetic components, such as Fe_3O_4 or carbon black, to trigger a heating response, this SMP is only made of polyurethane and recovers its parent shape when immersed in water. The drawback of this wire is that the human body is aqueous and absorption of water could trigger shrinking before the surgeon has finished placing it in the desired position.

A popular shape memory alloy, NiTi or Nitinol, can also be used as an alternative to staple closure. Unlike the polymers mentioned earlier, this alloy does not shrink, nor does it get absorbed into the body. It does, however, have a thermomechanical property which causes it to change shape in the presence of a sufficient temperature change. In the fixator depicted in Figure 8.3f, the staple is fabricated in the closed position, and while under the martensite finish temperature, M_f, the staple can be mechanically altered into an open state [47]. When an electric current passes through the backbone of the staple, it raises the temperature above the martensite finish temperature and triggers shape recovery back to the parent conformation, effectively closing the wound. However, the electrical current that was used to heat the NiTi fixator was fairly high (15 A for 0.1 s), which could damage the tissue surrounding the fixator.

Functionally, it is also possible to add a therapeutic effect to untethered microdevices in order to expedite the healing process or to aid in the treatment of a localized condition such as an ulcer or inflammation. Toward this goal, porous polymer microgrippers have been used to load and deliver sustained doses of drugs, such as doxorubicin and mesalamine to localized areas via a combined chemical and mechanical approach [57]. On introduction from a cold state, these polymer grippers can grab onto tissue at physiological temperatures and under flow were shown to remain in place more securely and consequently release drug over prolonged periods as compared to flat therapeutic patches.

8.3.1.3 Biopsy

Biopsies are procedures used to retrieve a cellular sample from a location of interest for further diagnosis. There are many narrow channels within the human body where a biopsy may be needed, but the size and shape of the biopsy location is a limiting factor for the surgeon. Untethered microtools offer a solution to this problem since they are able to navigate small and complex passages. Further, beyond getting to the biopsy site, collateral tissue damage must also be minimized. If too many biopsies are performed in a certain area or too much tissue is removed, excessive damage will occur at the target site, which may cause complications. Since untethered microdevices are smaller than conventional biopsy forceps, they excise smaller samples. With less damage done per biopsy, more biopsies over a larger area can be performed, leading to a more thorough examination.

Thermo-responsive untethered microgrippers have been used to excise tissue samples (Figure 8.3g) [48]. These microgrippers utilize the residual stress in a thin-film bilayer to power the closing motion of the microgripper arms. A biochemical or thermosensitive polymer trigger layer prevents the release of the stress until the microgripper is exposed to an appropriate temperature or biochemical environment. When exposed to these specific stimuli, the polymer softens, dissolves, or delaminates, triggering self-actuation of the microgripper. A thin layer of gold encapsulates a ferromagnetic nickel layer used to aid in magnetic retrieval which keeps the microgrippers bioinert. Recently, such microgrippers were used to perform a biopsy in the bile duct of a live pig, demonstrating their *in vivo* utility [58].

Figure 8.3h shows a hydrogel-based microgripper composed of a temperature-responsive hydrogel embedded with both 20- to 30-nm-diameter Fe_3O_4 nanoparticles and multiwall carbon nanotubes [49]. The magnetic Fe_3O_4 nanoparticles allowed the microgrippers to be guided into position and served as a heating source, while the carbon nanotubes shortened the thermal response times by enhancing mass transport of water molecules. When an alternating magnetic field was applied to the microgripper, the hydrogel heated up, causing a nonhomogeneous shrinking response, resulting in closure of the gripper.

8.3.1.4 Micromanipulation

The manipulation of small objects may not seem to have an obvious relationship with surgery; however, it is an important feature that must be enabled for the progression of this field. The end goal would be to construct a surgical station inside the body or to treat individual cells, but this futuristic goal cannot be achieved unless there is a method to pick and place objects at will.

In the world of manipulating objects at the small scale, we must start with the basic concept of pushing objects into place. A microrobot embedded with neodymium magnetic powder was able to be maneuvered using an electromagnet [50]. This microrobot took a random arrangement of 500-μm zirconia beads, and pushed each bead into specific locations in a patterned arrangement (Figure 8.3i). This robot had dimensions of $1000\,\mu m \times 1000\,\mu m \times 50\,\mu m$, with $50\,\mu m$ being the height of the robot. The front of the microrobot had a U-shaped indent to aid in pushing a spherical bead, but it could be shaped differently to push objects of varying sizes and dimensions. When moving zirconia beads into the pattern, the positioning errors of the microrobot ranged between 70 and $120\,\mu m$ only, providing state-of-the-art accuracy.

An even smaller magnetic micromanipulation robot has been reported with dimensions of $30\,\mu m \times 30\,\mu m \times 10\,\mu m$, with $10\,\mu m$ being its height (Figure 8.3j) [51]. This size scale is small enough to manipulate and push single cells around, or even deliver therapeutic drugs to individual cells. In this method, drugs loaded onto microbeads can be pushed to a specific location for targeted drug delivery. Similar to Go's microrobot, Steager's microrobot also has a U-shaped frontal end, which can be used to push drug-releasing microbeads to a location of interest. These devices offer future potential in transporting controlled drug release systems through small passages within the body.

8.3.2
Locomotion

Without the ability to move untethered microdevices to a desired position, we would have to rely on random events or natural body motions to get the devices into place. In order to increase the efficiency and effectiveness of surgical tasks with these tools, there is a need to develop mechanisms to move these devices in precise trajectories. However, the challenge of moving such objects at the small scale is enormous.

At the microscale, the Reynolds number (*Re*), which is a dimensionless number expressing the ratio between inertial and viscous forces, becomes very low. $Re = \rho u L/\mu$, where ρ (kg m^{-3}) is the density of the fluid, u (m s^{-1}) is the velocity, L (m) is the characteristic length, and μ (Pa s) is the dynamic viscosity of the fluid. At the microscale, both L and u typically have values between 10^{-6} and 10^{-4}, which leads to a Reynolds number $\ll 1$. Microdevices in water face a viscosity comparable to that of honey at the macroscale due to the decreasing Reynolds number. The low Reynolds number makes conventional swimming methods such as stroke-based propulsion challenging, so new creative methods of locomotion must be utilized. It is noteworthy that recent studies have shown that conventional swimming methods could work in non-Newtonian fluids such as extracellular matrix [59].

8.3.2.1 Magnetic Force

One of the most popular methods to move objects at the microscale is by using magnetic forces. An external magnetic field can be applied with either an electromagnet or a permanent magnet. In the case of an electromagnet, the strength of the applied field is dependent on the amplitude of the current, and rotating fields can be created using three orthogonal coil pairs with a sinusoidal alternating current. A permanent magnet has a fixed strength, and the distance between the magnet and the magnetic object must be adjusted to increase or decrease the magnetic force.

Figure 8.4a shows a mimicked flagellum using a soft magnetic head (Cr/Ni/Au film) and a helical InGaAs/GaAs/Cr tail [60]. A soft magnet is one that has a relatively narrow hysteresis loop and therefore, can be demagnetized easily. The helical shape converts rotary motion to a linear propulsion motion when a rotating magnetic field is introduced. Depending on the conditions of the surrounding environment, the size of the head matters. A flagellum with a larger head swims slower than one with smaller head at low frequencies due to higher viscous drag. However, with the higher nickel mass of a larger head, a stronger magnetic torque can be achieved, which would result in increased maximum velocity in high-frequency environments. For a 38-μm-long artificial bacterial flagellum, the maximum velocity in water was 18 μm s^{-1} using a 2.0 mT field.

In Figure 8.4b, we can see a hydrogel microgripper moving through a curved microfluidic PDMS channel. In this study, a Helmholtz coil was used to generate a magnetic field of 10 mT, resulting in velocities of 2 mm s^{-1} [49]. Figure 8.4c shows a metallic microgripper navigating through a complex coiled tube using a direct magnet [48]. This type of environment complexity can be similar to the small coiled ducts within the human body.

Figure 8.4d shows a tumbling magnetic robot. This device is dumbbell shaped with opposite polarization direction on the dumbbell ends. This causes a rotation in the vertical plane when an external magnetic force is applied, and when the magnetic field is switched to the opposite direction, the microdevice tumbles forward. Using a Helmholtz coil, this group was able to achieve translational speeds of 0.38 mm s^{-1} limited by the response speed of the experimental setup.

Magnetic force

0s   2s   4s   6s   8s   10s

(a)

(b)

(c)

End

Start

(d)

Electromechanical

100 μm

B   A

(e)

Electrodes

(f)

(g)

Optical tweezers

(h)

Focused laser

Micro-particle

(i)

Particle 1

Particle 2

Cell

Obstacle

(j)

1   Initial scene   G

2   G

3   G

4   Path followed by the gripper formation   G

Biological tissue

(k)

(m)

0.00 s   (l)

0.80 s
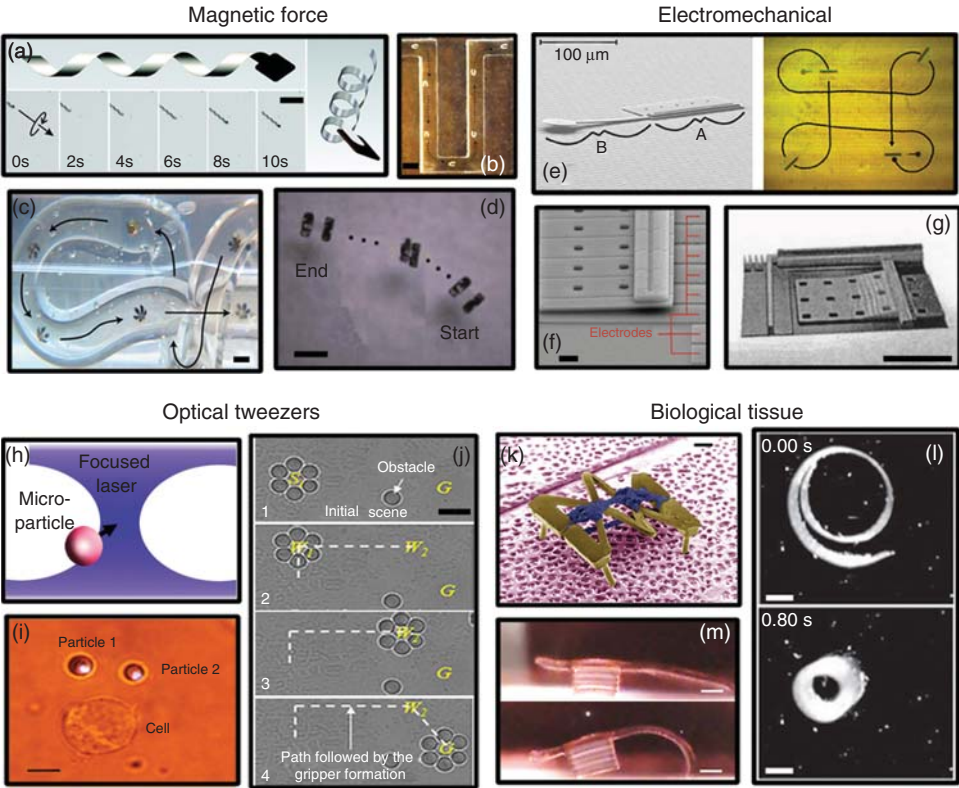
Figure 8.4 Locomotion methods for untethered microtools. (a) Images of a magnetic artificial helical flagellum, which translates rotational motion into linear propulsion (top and right). The bottom portion shows time-lapsed optical images of an artificial flagellum in motion; scale bar represents 40 μm. (Reprinted with permission from Ref. [60] ©American Chemical Society.) (b) Overlaid optical images of a hydrogel microgripper maneuvering through a narrow PDMS channel. Scale bar represents 1.5 mm. (©IEEE (2013). Reprinted with permission from Ref. [49].) (c) Overlaid optical images of a metallic microgripper traversing a curved and tortuous glass capillary. Scale bar represents 500 μm. (Reprinted from Ref. [48] with permission from PNAS.) (d) Optical image of a magnetic tumbling robot showing controlled steering capabilities. Scale bar represents 400 μm. (Reprinted from Ref. [61] with kind permission from Springer Science and Business Media.) (e) Electron micrograph of a scratch drive actuator showing turning capabilities. The labels A and B show the untethered scratch drive actuator and cantilevered steering arm segments, respectively. (© (2006) IEEE. Reprinted with permission from Ref. [62].) (f) Electron micrograph of the electrode pad for scratch drive actuators. Scale bar represents 18 μm. (©IEEE. Reprinted with permission from Ref. [63].) (g) Optical surface profiler image of an SDA body bending downward due to an applied voltage. Scale bar represents 50 μm. (©The Institution of Engineering and Technology. Reprinted from Ref. [64].) (h) The schematic of a non-centered microparticle reorienting itself to the center of the beam waist in an optical tweezer. (i) Optical image of two chemically loaded particles trapped by optical tweezers dragging a cell using chemotaxis. Scale bar represents 10 μm. (© (2013) IEEE. Reprinted with permission from Ref. [65].) (j) Optical images of optical tweezers trapping six 5-μm beads to grab the bead in the center and transport it around an obstacle. Scale bar represents 10 μm. (© (2013) IEEE. Reprinted with permission from Ref. [66].) (k) SEM image of a hopping microrobot powered by insect dorsal vessel tissue. Scale bar represents 500 μm. (Reprinted from Ref. [67] with kind permission from Springer Science and Business Media.) (l) Optical image of rat cardiomyocyte-driven curling of thin films. Scale bar represents 1 mm. (From Ref. [68]. Reprinted with permission from AAAS.) (m) Optical images of contracting rat cardiomyocyte tissue moving a biobot forward. Scale bar represents 1 mm. (Reprinted by permission from Macmillan Publishers Ltd: Nature Publishing Group. Ref. [69].)

The tumbling robot was able to operate on various surfaces, such as normal paper, a penny in silicon oil, and biological tissue in saline [61].

Magnetic colloids with an average size of 90 μm have been shown to self-assemble at the interface of two immiscible fluids to form smart aster clusters [70]. The asters can form different patterns such as a 2-mm-diameter ring or linear segments at different magnetic field intensities and frequencies. Breaking the symmetry of the aster generates asymmetric hydrodynamic flow at the interface, leading the aster to move at a speed ranging from 0.1 to 0.6 cm s^{-1}. In this study, the speed of the aster and cluster of asters was controlled by varying the magnetic field intensity while the direction of motion was determined by the field direction. The asters can perform locomotion and gripping operations to capture, transport, and manipulate particles, even as big as 1-mm glass beads, at the interface of two liquids.

8.3.2.2 Electromechanical

In the field of electromechanical motion at the microscale, an interesting option is scratch drive actuation. Scratch drive actuators (SDAs) all share a similar L-shaped

design, where the short end is called the *bushing* and the long end responds to an applied voltage. When a voltage is applied to the substrate via electrodes, the resulting potential causes the body of the SDA to curve downward and pushes the bushing forward. When the voltage is removed, the body springs back while the bushing remains in place, causing an overall forward motion.

A cantilevered steering arm attached to an SDA gives it turning capabilities (Figure 8.4e) [62]. When the steering arm is raised, the device behaves like a generic SDA, moving forward in a straight line. However, when the cantilever is brought into contact with the substrate, the device turns radially from the contact point of the arm. Electrodes on the substrate can be seen in Figure 8.4f [63], and the bending of the long end of an SDA due to an applied voltage can be seen in Figure 8.4g [64]. Even though SDAs require electrodes on the substrate to deliver the potential difference, the device itself is untethered. Furthermore, advances in thin-film electronics may allow SDAs to traverse curved surfaces.

8.3.2.3 Optical Tweezers

Optical tweezers utilize a highly focused beam of light to trap particles at the focal point. Objects that are trapped in the beam waist, or the focal point, experience a net force of zero because the momentum of photons acting upon the particles cancels each other out within the trap. As the laser moves, the focal point moves with it. This causes a short interval where the particle may not be in the center of the beam. The force imbalance caused by the photons pushes the particle back toward the center of the beam (Figure 8.4h). The benefit of optical tweezers is that they are able to manipulate many small objects simultaneously at high response speeds with great control. Also, multiple particles can be moved together or separately at the same time with the same laser. However, the extended direct exposure of the laser to live cells during manipulation poses a risk of photodamage, resulting in reduced functionality or even cell death. To get around this problem, optical tweezers can be used to manipulate objects that influence the movement of cells indirectly.

An example of this method is the application of chemoattractive poly(lactic-co-glycolic acid) (PLGA) microparticles (100 nm to 100 μm) which releases a chemical gradient to induce chemotaxis of cells toward the particle [65]. In this case, photodamage of the cells is avoided because the cell movement is influenced by controlled positioning of optically trapped microparticles. Figure 8.4i shows an image of two chemoattractive microparticles above a cell to induce a net upward cell migration. The trapping force of the optical tweezers, as well as the maximum manipulation velocity of the particle is linearly proportional to laser power, reaching about 19.5 pN and 270 μm s^{-1}, respectively, at a laser power of 1000 mW [71].

In another study, it was reported that a circular formation of dielectric beads can grip a cell in order to maneuver it [66]. In this method, a cell is surrounded with optically trapped dielectric beads, and the coordinated movement of the entire set of dielectric beads carries the contents along a desired path as illustrated in Figure 8.4j. This would be analogous to moving a ping pong ball across

a table by first placing an upside down cup over it and moving the cup to a new location.

8.3.2.4 Biologic Tissue Powered

The idea of integrating biological tissue into engineered devices is an exciting field which utilizes cells or tissues to carry out desired functions, such as walking or contracting. Figure 8.4k shows a pantograph-shaped microrobot (PSMR) [67]. The PSMR's frame is created using PDMS molding techniques, and a whole piece of insect dorsal vessel tissue excised from the final stage larvae of inchworms (*Ctenoplusia agnata*) is wrapped around the PSMR front to back using tweezers. When the dorsal vessel is wrapped around the robot, it moves autonomously at 25 °C due to the independent contractions of the insect tissue. PSMR's average velocity is 26.4 μm s^{-1}, moving 66.1 μm per stroke. With the addition of crustacean cardioactive peptide, the frequency of contractions can be increased to achieve even higher moving velocities [72].

Aside from insect tissue, rat tissue has also shown motion-inducing capabilities. For example, neonatal rat ventricular cardiomyocytes can be used to contract thin films of PDMS (Figure 8.4l) [68]. In another study, rat cardiomyocytes were also used to maneuver a biobot, a cube-shaped base with a hybrid hydrogel/rat cardiomyocytes cantilever, to induce movement [69]. The contractions of the rat cardiomyocytes cause the long end of the biobot to retract against the surface, pushing the base forward in small increments (Figure 8.4m). This biobot can achieve an average velocity of 236 μm s^{-1}, moving 337 μm per power stroke, while the rat cardiomyocytes beat at a frequency of 1.50 Hz. By varying the thickness and curvature of the cantilever, different types of movement for the biobot could be derived, resulting in varying average velocities and power strokes.

8.4
Nanoscale Untethered Surgical Tools

Apart from minimizing the invasiveness of the procedure, nanoscale tools also offer superior precision when compared to macro- or microscale tools. For example, by capturing a single cell, diagnostic details such as protein overexpression or gene mutation of this specific cell can be detected during the analysis. This information might get overlooked in conventional biopsies where the analysis is based on the cumulative, averaged data collected from large numbers of cells. Nanoscale tools could also potentially reach and operate on hard-to-reach parts of the body, such as vascular capillaries and hence significantly minimize the invasiveness of the surgical functions, such as incision, cell manipulation, or drug delivery. However, they could also potentially reach unwanted areas of the body, such as unintentionally crossing the blood–brain barrier. In addition, since they are too small to be retrieved after introduction to the body, toxicity is an important factor that must be considered.

While there has been tremendous progress in nanomanufacturing in the past decades, there are still challenges in the development of nanoscale tools for surgical applications, mainly powering their operation and facilitating localization. When the tool size is in the nanometer scale, the use of conventional energy storage systems for power supply is very limited. There exists the possibility of utilizing preloaded energy, such as thin-film stress or carry-on fuels. However, these methods are often only available for one-time actuation or for short intervals, to be released completely or rapidly depleted at the desired location. For repeated operations, it is necessary to harvest power either by acquiring fuel from the local environment, or through an external field.

Localization is another challenge especially when it comes to *in vivo* applications. For example, in the complex vascular network, maneuvering nanoscale tools becomes difficult with only limited feedback from the device. As a result, it is hard to deliver the device and operate it at a specific area *in vivo*. Because of this lack of control, nanoscale tools still remain mostly in the proof-of-concept stage or are currently used for *in vitro* applications.

Figure 8.5 Untethered nanoscale devices. (a) SEM image (left) of the tapered sharp tip of an InGaAs/GaAs/Cr/Pt rolled-up nanojet and optical microscopy image (right) of its bubble propelled corkscrew motion. Scale bar: 250 nm. (Reprinted with permission from Ref. [74]. Copyright 2012 American Chemical Society.) (b1) SEM image of a microdriller embedded into porcine liver tissue after drilling and (b2) SEM image of a resulting hole drilled in the tissue. ([75] – Published by The Royal Society of Chemistry.) (c) Optical image of a rotating nickel nanowire transporting a blood cell toward an epidermal cell driven by magnetic field. Scale bar: 30 μm. (Reprinted from Ref. [76] Copyright 2012 with permission from Elsevier.) (d) Optical image of single-cell gripper with a captured red blood cell, scale bar: 10 μm. (Reprinted with permission from Ref. [77]. Copyright 2014 American Chemical Society.) (e) Dark field images showing the formation of an assembled chain pattern composed of AuRu microrods in a 3.7 MHz acoustic field. Note that cartoon superimposed is intended to show the alignment of the rods and is not to scale or in proportion to the aspect ratio of the AuRu rods. (Reprinted with permission from Ref. [78] Copyright 2012 American Chemical Society.) (f) Stacked images showing aligned bovine red blood cells manipulated by surface acoustic waves. Scale bar represents 50 μm. (Reprinted from Ref. [79].) (g) Computer-aided graphic image showing ultrasound-triggered PFH-loaded microbullets cleaving kidney tissue. (Reprinted with permission from Ref. [80] Copyright © 2012 Wiley-VCH Verlag GmbH & Co. KGaA, Weinheim.) (h) SEM image of hematite peanut particles, and schematics of reversible docking and release of a sphere triggered with blue light. Scale bar represents 1 μm. (Reprinted with permission from Ref. [81]. Copyright 2013 American Chemical Society.) (i) Optical image (top) of a red blood cell attached to a flexible magnetic filament for controlled motion. Schematic (bottom) showing a flexible filament composed of magnetic particles linked by double-stranded DNA. Total filament length is 24 μm. (Reprinted by permission from Macmillan Publishers Ltd: Nature [82], Copyright 2005.) (j) Conceptual diagram showing palindromic bistable rotaxane molecules tethered onto the surface of a gold microcantilever controlling reversible deflection of cantilevers through electrochemical switching. (Reprinted with permission from Ref. [83]. Copyright 2005 American Chemical Society.) (k) Conceptual diagram showing a synthetic ribosome made from rotaxane that could pick up amino acids and synthesize a sequence-specific peptide. (© 2013 Landes Bioscience [3].)
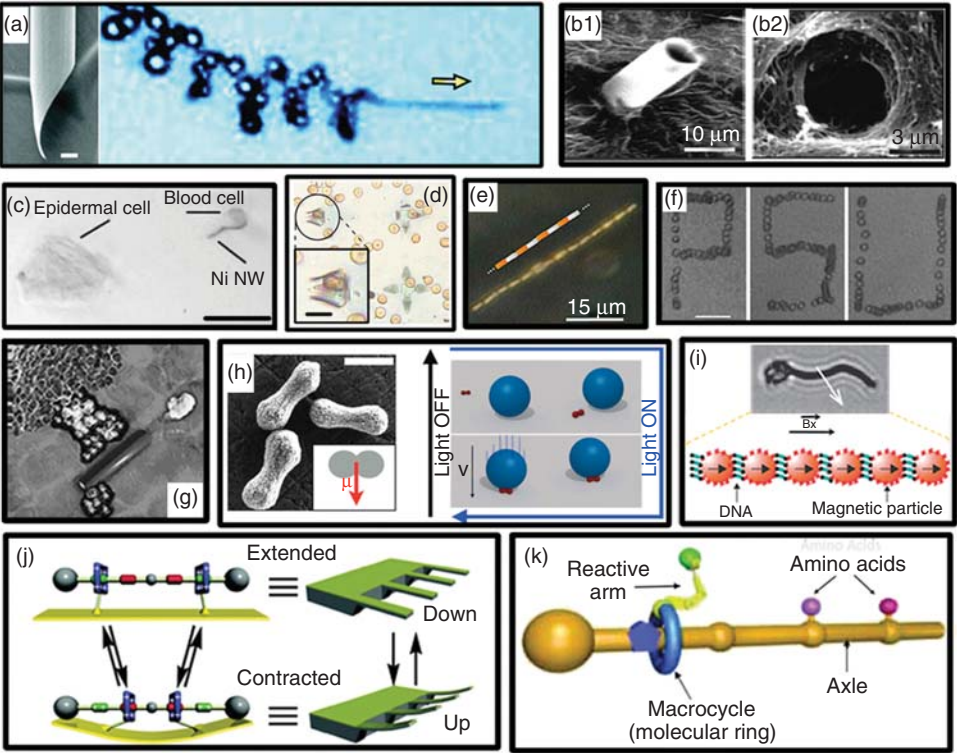
In this section, we discuss untethered nanoscale surgical tools developed in recent years, categorized by their actuation methods. Their fabrication process, key parameters, and functions are also detailed.

8.4.1
Fuel-Driven Motion

Chemicals suitable for fuels need to satisfy two criteria to be used by surgical tools: (i) the reaction needs to be catalyzed by the device and (ii) the reaction should generate momentum in form of bubbles, temperature or electrostatic gradients in liquid. In order to utilize chemicals in the environment, nanoscale tools usually contain a catalytic component, such as platinum. The chemical reaction occurs at the interface between the catalyst, a part of the device, and fuels that are available in the environment or carried by the device itself.

Bubble propulsion is one of the most well-studied mechanisms that utilize catalytic fuels for locomotion of nanoscale devices. In this technique, bubbles, usually oxygen or hydrogen, are generated to propel the device. For example, platinum coatings on the device can catalyze the decomposition of hydrogen peroxide into oxygen and water. In tubular-shaped devices, oxygen bubbles accumulated in the confined tube nucleate on the inner surface and escape into the liquid environment at a high speed. As a result, the recoiling force propels the device toward the direction opposite to the platinum end [73].

The propulsion trajectory can be adjusted by changing the tube design. For example, it has been shown how conical tubes of InGaAs/GaAs/Cr/Pt with tapered tips lead to a corkscrew-shaped trajectory, ideal for facilitating a drilling action [74]. These nanoscale drillers, with diameters in the range of $280-600$ nm, could achieve speeds as high as $180\,\mu m\,s^{-1}$ (Figure 8.5a). The ultrasharp tips enable the tubes to drill to paraformaldehyde-fixed HeLa cells.

In addition to oxygen, hydrogen bubbles can also be generated in acidic conditions to power nanoscale devices. For example, in the case of polyaniline/zinc bilayer microtubes, zinc segments of the tubes reacted with acidic environment and produced hydrogen [84]. In this case, the speed of the propulsion is determined by the pH of the solution. At a pH of -0.2, the 5-μm-diameter devices were shown to move at an ultrahigh speed of $1000\,\mu m\,s^{-1}$, dropping to $140\,\mu m\,s^{-1}$ at pH 0.4, and $10\,\mu m\,s^{-1}$ at pH 1.3; these devices have potential relevance in acidic *in vivo* environments, such as the stomach.

With modified surfaces or controlled external fields, nanoscale devices powered by bubble propulsion can perform a variety of tasks. It has been reported that catalytic nanorobots can be used to capture, transport, and release murine CAD cells to specified locations, when directed by an external magnetic field [85]. Furthermore, these nanoscale devices can be used to detect biomolecules in bulk solutions. For instance, in another study, a nanoscale device with a single-strand DNA probe was shown to successfully isolate a targeted nucleic acid from a microliter of raw biological sample [86]. The same group also developed an

antibody-modified device that could selectively isolate cancer cells *in vitro* by recognizing the overexpressed surface antigen on pancreatic cancer cells [87].

The versatile functionalities of devices powered by catalytic fuels demonstrate promising applications in diagnostics and drug delivery. However, the use of toxic chemicals, such as hydrogen peroxide, is a major concern for biomedical applications. For *in vivo* applications, it is necessary to develop biocompatible or low-toxicity fuels.

Other than the bubble propulsion, self-phoresis due to anisotropy in shape or composition is another mechanism that can be used to propel a device. Self-phoretic motion is the autonomous motion of dispersed particles in fluid, driven by fluid pumping induced from a concentration gradient or an electric field. The different chemical reactions at opposite ends of the device will generate a chemical concentration gradient or electric field along the device. At the particle–liquid interface, water diffuses from the lower solute or ion concentration end to the higher concentration end. This osmotic flow results in the motion of the particle relative to the liquid, observed as self-phoresis. A self-phoresis induced by a local electric field through electrochemical reactions has been reported [88]. In their work, nanorods with gold and platinum segments were shown to move autonomously in the direction of the platinum end in hydrogen peroxide solution attributed to a bipolar electrochemical mechanism [89]. They reported speeds of $20 \, \mu m \, s^{-1}$, more than 10 times the length of the device per second. Utilizing this mechanism, $Ni/(Au_{50}Ag_{50})/Ni/Pt$ nanoshuttles were used to pick up, transport, and release drug-loaded PLGA particles to a designated location through magnetic guidance [90]. The paramagnetic nickel segment on the nanorods allowed magnetic attraction of iron oxide encapsulated in PLGA. These nanoshuttles show potential to increase the penetration depth into the tumors and enhance the targeting precision in drug delivery.

Propulsion can also emerge from a self-diffusiophoretic mechanism. A diffusion-induced local flow can be generated due to the concentration gradient between different catalytic sections without involving any electrochemical reaction. In a recent study, it has been shown that Janus particles, which are 2-μm polystyrene beads with one face coated with platinum, can aggregate into a doublet containing two Janus particles with different orientation combinations [91]. In a 10% w/v H_2O_2 solution, the doublet moved autonomously in a variety of cyclonical trajectories. The trajectory of the motion was determined by the translational and rotational diffusion coefficients of the solute. The averaged translational speed of doublets ranged from 1.3 to $6.0 \, \mu m \, s^{-1}$, while their angular velocity ranged from 0 to $1.3 \, rad \, s^{-1}$.

8.4.2
Magnetic Field-Driven Motion

The use of external magnetic fields allows fuel-free locomotion and complex maneuvering; hence, this process has great potential for *in vivo* applications. To allow external magnetic control, the device must contain a ferromagnetic

part and the shape of the device is also important. It is noteworthy to recall the difficulties in moving micro- or nanoscale devices in body fluids. As discussed earlier, the Reynolds number is very low for devices with small characteristic lengths at low velocities, resulting in negligible net movements. However, nature provides us insights into the design of nanoscale devices. Flagella on eukaryotic cells and cilia on microorganisms are able to rotate and create traveling waves resulting in net propulsion. Inspired by nature, human-engineered flagella-like, helical, or asymmetric structures have been shown to enable rotation under external fields and propel the device.

Magnetic field-driven microdrillers have been used to drill tissue pieces *ex vivo* (Figure 8.5b) [75]. These microdrillers were made from titanium, chromium, and iron thin films; each 5-nm thick. While the titanium–chromium bilayer facilitated the roll-up process needed to form a tubular driller shape, the iron layer provided the ferromagnetic property, facilitating the microdrillers' rotation under an external magnetic field. As the frequency of the rotational magnetic field increased, the orientation of the microdriller changed from parallel to perpendicular to the substrate. The tissue drilling lasted from tens of minutes to a few hours. The drillers were shown to perforate porcine liver tissue reaching approximately 25-µm depth. Locomotion and drilling operations of these microdrillers could be controlled by changing the magnetic field direction and frequency.

In another example, nickel nanowires with diameters of 100–200 nm were used to transport cargo under a rotating magnetic field [76]. Owing to shape anisotropy, the nanowires rotated under the applied field and generated waves to propel themselves. These nanowires performed push and pull operation in either contact or noncontact mode. In contact mode, the nanowires utilized their van der Waals attraction to transport their cargo. The cargo could be released by altering the direction of the field and reducing its frequency at the same time. Figure 8.5c depicts the transport of preattached red blood cells toward an epidermal cell by such a nanowire. In noncontact mode, the rotating nanowires induced local fluid flow around the particles, in order to push or pull the cargo in short range.

Another fuel-free cargo-towing study [92] shows that nanowires with two segments of nickel and silver could pick up and transport drug-loaded PLGA particles, then attach them onto targeted HeLa cells, and release the encapsulated drug by precise magnetic field guidance. In this study, ferromagnetic nanoparticles were encapsulated in PLGA to allow magnetic attraction by the nanowire under a magnetic field. The nanowires, prepared by template electrodeposition, were 5–6 µm in length and 200 nm in diameter. The nickel segment promoted rotation under an external rotating magnetic field. The flexible silver filament attached to the nickel segment of the nanowire deformed and generated a local hydrodynamic flow to propel the wire in the direction of the nickel segment [93]. While the nanowires could rotate due to their anisotropic shape, the spherical nanoparticles could not propel themselves under a magnetic field because the flow over a sphere caused reciprocal motion at low Reynolds number [94]. The nanowires were used to carry micrometer-sized spherical particles, such as PLGA particles,

which are commonly used drug delivery vehicles that can encapsulate hydrophilic or hydrophobic medications, at speeds of $10\,\mu m\,s^{-1}$. These studies show that the nanowires are capable of delivering drugs to specific targets in a fuel-free manner.

Recently, single-cell grippers have been described including those that can isolate and capture individual murine cell or red blood cells [77]. These grippers were made from biocompatible silicon monoxide and silicon dioxide. They could be designed in a variety of sizes, from 70 to $10\,\mu m$, in order to accommodate different cell sizes. The gripping motion was actuated by the release of thin-film stress as soon as the grippers were released from the substrate. Cells in the vicinity of the closing gripper were captured and stayed alive after being trapped. When enabled with appropriate magnetic locomotion and triggering, these single-cell grippers have the potential to be used for single-cell capture *in vivo*. Figure 8.5d demonstrates the capture of 7-μm-sized red blood cells.

8.4.3
Acoustic Wave-Driven Motion

In addition to magnetic fields, acoustic waves can deliver energy wirelessly to power nanoscale devices. Acoustic energy, including ultrasonic energy, has been used extensively in biomedical applications, such as internal organ imaging, tissue heating, and drug delivery [95]. The use of acoustic energy is advantageous in biomedical applications, because it can pass through tissue and be applied to manipulate different types of particles, such as cells, regardless of their magnetic, optical, or electrical properties.

It has been reported that metallic microrods can be actuated by ultrasonic waves in the range of megahertz to perform unidirectional motion, in-plane rotation, and pattern formation [78]. These microrods can be made from a single metal, for example, gold, ruthenium, or platinum, or two metal segments, for example, gold and ruthenium or gold and platinum, by template-assisted electrodeposition. Their lengths were $1-3\,\mu m$ with diameters around $300\,nm$. The speed of directional motion varied based on the location at the levitation plane, as well as the frequency of the acoustic wave. Levitated at the nodal plane of the acoustic field, the microrods performed fast in-plane rotation and axial directional motion at resonance frequency, with speeds as high as $200\,\mu m\,s^{-1}$. The microrods could aggregate into long head-to-tail chains, spin around their axes, and be propelled unidirectionally (Figure 8.5e). Moreover, metallic microrods could also align into a ring pattern in which the microrods orbit around the center of the ring. This motion was achieved at the nodal plane of the acoustic field, regardless of the ionic strength of the solution, making it possible to be used in biological fluids. The mechanism of these movements is not completely understood quantitatively, but it has been hypothesized that the asymmetry of microrods is important in order to form a local acoustic pressure gradient, driving directional motion and vortex formation.

Precise locomotion of micro- or nanoparticles, such as cells, can be achieved through acoustic tweezers. Acoustic tweezers establish a standing wave pattern,

trap particles at the wave pressure nodes, and achieve locomotion by changing the wavelength. For example, acoustic waves generated by orthogonal pairs of chirped interdigital transducers (IDTs) could form a desired wave pattern on liquid surfaces for 2D locomotion [79]. In this study, the particles are trapped at the pressure node of the wave field, and precise manipulation of location is achieved by changing the wavelength determined by the frequency of the IDTs. While the current set up in this study could manipulate microscale objects with a resolution of a few microns, a higher frequency is required to control nanoscale objects. Figure 8.5f shows the stacked images of the acronym "PSU" (for Pennsylvania State University), formed from 6-μm bovine red blood cells using IDTs.

Furthermore, the acoustic energy supply can be combined with other types of energy sources to power nanoscale devices. For example, emulsified perfluorohexane (PFH) is biologically inert and stable in a liquid environment, and it can vaporize upon ultrasound triggering. When combined with ultrasound waves, PFH works as nontoxic carry-on fuel. It has been reported that a 40-μm-long microbullet rolled up from a nanometer-scale Ti/Ni/Au thin film could be functionalized with thiolated cysteamine to store PFH emulsions in the tube through electrostatic attraction [80]. Once triggered by an ultrasound wave, the PFH vaporized immediately and created bubbles that propel the bullet at a remarkably high speed of 6.3 m s^{-1} in the initial 55.6 μs. Because of the significant momentum 2.69×10^{-11} N s, as a result of this propulsion, the bullet could penetrate, deform, and cleave biological tissue. In Figure 8.5g, the computer-aided image illustrates cleavage of a lamb kidney tissue by such a microbullet.

8.4.4
Light-Driven Motion

Using light as an energy source to move nanoscale objects is another attractive idea since control methods for light activation have been very well developed. The wavelength, energy density, exposure time, and location of the light wave can be precisely modified to achieve a desired functionality. Different forms of light, such as near infrared or laser, have been demonstrated to be useful in a variety of medical applications. For example, the precise energy delivery to a small targeted area by laser has been used for ocular, neural, and cosmetic surgeries for decades [96].

In a recent study, it has been shown that hematite dockers that could transport larger colloidal particles could be switched on and off by light and steered by an applied magnetic field [81]. The peanut-shaped hematite particles, typically 1.5 μm long and 0.6 μm wide, have a permanent magnetic moment perpendicular to their long spindle axis, allowing for magnetic manipulation. When these hematite particles were immersed in 1% hydrogen peroxide solution and exposed to blue light, which induced photocatalytic decomposition of hydrogen peroxide, the resulting chemical gradient induced the diffusiophoresis of surrounding colloids. In a basic solution with 8.5 pH, a hematite particle attracted 5-μm-sized colloidal particles and docked on the colloidal surface (Figure 8.5h). The resulting

composite could be steered by an external magnetic field to the desired location. The attraction between the colloids and the hematite particles could be disabled by turning off the blue light. A 1-µm hematite particle was able to carry a cargo made from various materials up to 20 µm in size.

White light has also been used as a switch to stop and start the motion of catalytic microengines. For example, illumination of bright white light was shown to stop a catalytic micromotor in hydrogen peroxide fuel [97]. The authors attribute the mechanism to the fact that light illumination depleted hydrogen peroxide fuel locally, reducing bubble generation rate. At the same time, the light also decomposed the surfactant in the solution so that the fuel could not wet the catalytic wall effectively. Therefore, increasing the white light intensity slowed down the reaction. Consequently, switching the light off was found to power the engine back again.

8.4.5
Nano-Bio Hybrid Systems

The combination of natural molecules and fabricated nanoscale structures provides enormous opportunities for surgical applications. Biomolecules such as enzymes, DNA, and ATP can function as catalysts, mechanical components, or power generators of nanoscale devices enabling considerable functionality. For example, a hybrid bio-nanoscale device was shown to generate and consume hydrogen peroxide *in situ*, instead of using it from the environment [98]. This system was made from carbon nanotubes with covalently immobilized glucose oxidase and catalase. Once glucose was added to the solution, the glucose oxidase could convert glucose into hydrogen peroxide, which was subsequently converted to water and oxygen by the on-board catalase enzyme. The oxygen bubbles were able to propel carbon nanotube aggregates at the speed of approximately $0.2 – 0.8 \, cm \, s^{-1}$. The speed decreased with the depletion of the glucose fuel.

In another example, researchers have shown controlled red blood cell motion by attaching cells to artificial magnetic flagella [82]. The flagella filaments were made of superparamagnetic colloidal particles linked by double-stranded DNA enabling the flexibility (Figure 8.5i). The superparamagnetic colloid particles could acquire a magnetic dipole under an applied magnetic field. Through the dipolar interaction between the particles, and the interaction between the dipole and the external sinusoidal magnetic field, the filament would deform and rotate, functioning as a flagellum to propel the red blood cell. This system also shows the potential to precisely position microscale and nanoscale objects using a nano-bio hybrid device.

8.4.6
Artificial Molecular Machines

Artificial molecular machines are molecules that can harness useful mechanical or chemical work from molecular-level motion such as chemical group circumrotation or positional changes between multiple states. For instance, in a bistable

molecule, there are multiple equilibrium states in which the chemical groups at two different locations can both attract a third part of the molecule. Upon addition of an oxidation or reduction reagent to the system, the location of the third group can switch between the two sites. Even though the location change of the third group is in the nanometer range, it could still generate a small amount of work on the order of 10^{-18} J per molecule. Even though this value is small, it has been suggested that if a large number of such multistable molecules are integrated into organized assembly, they could overcome thermal noise and perform significant work at nano-, micro-, or even macroscopic level, such as 10^3 kJ mol^{-1} [99].

Figure 8.5j shows a specially designed "artificial molecular muscle" made from palindromic bistable rotaxane. The rotaxane was synthesized with a pair of mobile rings encircling a single dumbbell [83]. The distance between the two rings could change from 4.2 to 1.4 nm upon chemical or electrochemical stimulation. This displacement could generate a bending moment on the attached surface. A cantilever coated with a monolayer of 6 billion rotaxane molecules was observed to undergo a reversible 35-nm deflection upon adding a chemical oxidant and a reductant. The corresponding force per molecule in this deflection was calculated to be 10.2 pN. This study demonstrates the capability of artificial molecular machines to convert chemical energy to ordered mechanical movements.

Another artificial molecule, the "synthetic ribosome," was shown to successfully synthesize a sequence-specific peptide from individual amino acids [100]. The synthetic ribosome was also made from a rotaxane molecule, with a molecular ring threaded onto a molecular axle. The amino acids were attached on the strand in sequence-specific order through weak phenolic ester linkages. Under catalysis, the thiolate-functionalized ring could pick up one amino acid from the strand at a time, transfer it to a peptide elongation site, regenerate the catalytic thiolate group to pick up the next amino acid and elongate the peptide chain (Figure 8.5k). Eventually, when the last amino acid on the strand was cleaved, the macrocycle ring left the strand, producing a sequence-specific synthesized peptide. In this work, milligrams of peptide have been synthesized using approximately 10^{18} molecular machines. Even though the reaction takes relatively long time, approximately 12 h for each amide bond, and the peptide is still short, this current study is a valuable proof of concept that extends the capability of artificial molecular machines in monomer and chemical synthesis [3].

8.5
Conclusion

In summary, miniaturized untethered surgical tools provide an alternative approach to conventional surgical devices that allows for more precise and less invasive surgical operations. Depending on their size scale, a variety of approaches have been developed for localization, locomotion, and activation of such tools. Among the methods we presented here, many are conceptual and could not possibly be implemented in a clinical setting, in their present form.

Nevertheless, they are instructive as model systems that explore the boundaries of what might be possible in surgery at small size scales. In contrast, some other approaches have already been demonstrated in animal (microgripper biopsy) or even human (PillCam®) studies and would likely find greater utility in patients in the coming decades. Further, it is clear from the examples discussed in this chapter that certain aspects of fictional concepts such as "swallow the surgeon" or the "fantastic voyage" could be closer to reality than ever before.

Acknowledgments

References

1. Wang, Y.-X.J. (2011) Superparamagnetic iron oxide based MRI contrast agents: current status of clinical application. *Quant. Imaging Med. Surg.*, **1**, 35–40.

2. Gastrich, M.D., Barone, J., Bachmann, G., Anderson, M., and Balica, A. (2011) Robotic surgery: review of the latest advances, risks, and outcomes. *J. Rob. Surg.*, **5**, 79–97.

3. Sleator, R.D. (2013) Synthetic ribosomes: making molecules that make molecules. *Bioengineered*, **4**, 63–64.

4. Abbott, J.J., Nagy, Z., Beyeler, F., and Nelson, B.J. (2007) Robotics in the small, part I: microbotics. *IEEE Rob. Autom. Mag.*, **14**, 92–103.

5. Nisky, I., Huang, F., Milstein, A., Pugh, C.M., Mussa-Ivaldi, F.A., and Karniel, A. (2012) Perception of stiffness in laparoscopy – the fulcrum effect. *Stud. Health Technol. Inf.*, **173**, 313–319.

6. Van Gossum, A., Munoz-Navas, M., Fernandez-Urien, I., Carretero, C., Gay, G., Delvaux, M., Lapalus, M.G., Ponchon, T., Neuhaus, H., Philipper, M. *et al.* (2009) Capsule endoscopy versus colonoscopy for the detection of polyps and cancer. *New Engl. J. Med.*, **361**, 264–270.

7. Bazaka, K. and Jacob, M.V. (2012) Implantable devices: issues and challenges. *Electronics*, **2**, 1–34.

8. Rasouli, M. and Phee, L.S.J. (2010) Energy sources and their development for application in medical devices. *Expert Rev. Med. Devices*, **7**, 693–709.

9. Wei, X. and Liu, J. (2008) Power sources and electrical recharging strategies for implantable medical devices. *Front. Energy Power Eng. China*, **2**, 1–13.

10. Fernandes, R. and Gracias, D.H. (2009) Toward a miniaturized mechanical surgeon. *Mater. Today*, **12**, 14–20.

11. Bogue, R. (2011) Assembly of 3D micro-components: a review of recent research. *Assembly Automat.*, **31**, 309–314.

12. Leong, T.G., Zarafshar, A.M., and Gracias, D.H. (2010) Three-dimensional fabrication at small size scales. *Small*, **6**, 792–806.

13. Dario, P., Carrozza, M.C., Benvenuto, A., and Menciassi, A. (2000) Micro-systems in biomedical applications. *J. Micromech. Microeng.*, **10**, 235.

14. Ciuti, G., Menciassi, A., and Dario, P. (2011) Capsule endoscopy: from current achievements to open challenges. *IEEE Rev. Biomed. Eng.*, **4**, 59–72.

15. Castro, C.A., Alqassis, A., Smith, S., Ketterl, T., Sun, Y., Ross, S., Rosemurgy, A., Savage, P.P., and Gitlin, R.D. (2013) A wireless robot for networked laparoscopy. *IEEE Trans. Biomed. Eng.*, **60**, 930–936.

16. Hawks, J.A., Kunowski, J., and Platt, S.R. (2012) In vivo demonstration of

surgical task assistance using miniature robots. *IEEE Trans Biomed. Eng.*, **59**, 2866–2873.

17. Ranade, S.V., Miller, K.M., Richard, R.E., Chan, A.K., Allen, M.J., and Helmus, M.N. (2004) Physical characterization of controlled release of paclitaxel from the TAXUS^{TM} Express2^{TM} drug-eluting stent. *J. Biomed. Mater. Res. Part A*, **71A**, 625–634.

18. Than, T.D., Alici, G., Zhou, H., and Li, W. (2012) A review of localization systems for robotic endoscopic capsules. *IEEE Trans. Biomed. Eng.*, **59**, 2387–2399.

19. Kong, K., Cha, J., Jeon, D., and Cho, D. (2005) A rotational micro biopsy device for the capsule endoscope. 2005 IEEE/RSJ International Conference in Intelligent Robots Systems, 2005 (IROS 2005), pp. 1839–1843.

20. Kong, K., Jeon, D., Yim, S., and Choi, S. (2012) A robotic biopsy device for capsule endoscopy. *J. Med. Devices*, **6**, 031004.

21. Simi, M., Gerboni, G., Menciassi, A., and Valdastri, P. (2012) Magnetic mechanism for wireless capsule biopsy. *J. Med. Devices*, **6**, 017611.

22. Griss, P., Enoksson, P., Tolvanen-Laakso, H.K., Merilainen, P., Ollmar, S., and Stemme, G. (2001) Micromachined electrodes for biopotential measurements. *J. Microelectromech. Syst.*, **10**, 10–16.

23. Mousoulis, C., Ochoa, M., Papageorgiou, D., and Ziaie, B. (2011) A skin-contact-actuated micropump for transdermal drug delivery. *IEEE Trans. Biomed. Eng.*, **58**, 1492–1498.

24. Ergeneman, O., Dogangil, G., Kummer, M.P., Abbott, J.J., Nazeeruddin, M.K., and Nelson, B.J. (2008) A magnetically controlled wireless optical oxygen sensor for intraocular measurements. *IEEE Sens. J.*, **8**, 29–37.

25. Valdastri, P., Webster, R.J., Quaglia, C., Quirini, M., Menciassi, A., and Dario, P. (2009) A new mechanism for mesoscale legged locomotion in compliant tubular environments. *IEEE Trans. Robot.*, **25**, 1047–1057.

26. Tortora, G., Valdastri, P., Susilo, E., Menciassi, A., Dario, P., Rieber, F., and Schurr, M.O. (2009) Propeller-based wireless device for active capsular endoscopy in the gastric district. *Minimally Invasive Ther. Allied Technol.*, **18**, 280–290.

27. NIH (2014) How Are Stents Placed? *http://www.nhlbi.nih.gov/health/health-topics/topics/stents/risks.html* (accessed 10 April 2015).

28. Platt, S.R., Hawks, J.A., and Rentschler, M.E. (2009) Vision and task assistance using modular wireless in vivo surgical robots. *IEEE Trans. Biomed. Eng.*, **56**, 1700–1710.

29. Yim, S., Goyal, K., and Sitti, M. (2013) Magnetically actuated soft capsule with the multimodal drug release function. *IEEE/ASME Trans. Mechatron.*, **18**, 1413–1418.

30. Simi, M., Gerboni, G., Menciassi, A., and Valdastri, P. (2013) Magnetic torsion spring mechanism for a wireless biopsy capsule. *J. Med. Devices*, **7**, 041009.

31. Ichikawa, A., Sakuma, S., Shoda, T., Arai, F., and Akagi, S. (2013) On-chip enuleation of oocyte using untethered micro-robot with gripping mechanism. 2013 International Symposium on Micro Nano Mechatronics Human Science (MHS), Nagoya, Japan, pp. 1–3.

32. Kim, B., Lee, M.G., Lee, Y.P., Kim, Y., and Lee, G. (2006) An earthworm-like micro robot using shape memory alloy actuator. *Sens. Actuators, A*, **125**, 429–437.

33. Chen, W., Yan, G., Wang, Z., Jiang, P., and Liu, H. (2013) A wireless capsule robot with spiral legs for human intestine. *Int. J. Med. Rob.*, **10**, 147–61.

34. Quaglia, C., Tognarelli, S., Sinibaldi, E., Funaro, N., Dario, P., and Menciassi, A. (2014) Wireless robotic capsule for releasing bioadhesive patches in the gastrointestinal tract. *J. Med. Devices*, **8**, 014503.

35. Li, H., Yan, G., and Ma, G. (2008) An active endoscopic robot based on wireless power transmission and electromagnetic localization. *Int. J.*

Med. Robot. Comput. Assist. Surg., **4**, 355–367.

36. Yan, G., Ye, D., Zan, P., Wang, K., and Ma, G. (2007) Micro-robot for endoscope based on wireless power transfer. ICMA 2007 International Conference in Mechatronics Automation. pp. 3577–3581.

37. Farritor, S., Rentschler, M., Dumpert, J., Platt, S., and Oleynikov, D. (2007) Magnetically coupleable robotic surgical devices and related methods. US Patent App. 11/766,720, filed Jun. 21, 2007 and issued Jan. 3, 2008.

38. Moores, W.Y., LeWinter, M.M., Long, M., William, B., Grover, M., Mack, R., and Daily, P.O. (1984) Sonomicrometry: its application as a routine monitoring technique in cardiac surgery. *Ann. Thoracic Surg.*, **38**, 117–123.

39. Nelson, B.J., Kaliakatsos, I.K., and Abbott, J.J. (2010) Microrobots for minimally invasive medicine. *Annu. Rev. Biomed. Eng.*, **12**, 55–85.

40. McGirr, M.E., McAllister, S.M., Peters, E.E., Vickers, A.W., Parr, A.F., and Basit, A.W. (2009) The use of the InteliSite® Companion device to deliver mucoadhesive polymers to the dog colon. *Eur. J. Pharm. Sci.*, **36**, 386–391.

41. Gorlewicz, J.L., Battaglia, S., Smith, B.F., Ciuti, G., Gerding, J., Menciassi, A., Obstein, K.L., Valdastri, P., and Webster, R. (2013) Wireless insufflation of the gastrointestinal tract. *IEEE Trans. Biomed. Eng.*, **60**, 1225–1233.

42. Calabrese Barton, S., Gallaway, J., and Atanassov, P. (2004) Enzymatic biofuel cells for implantable and microscale devices. *Chem. Rev.*, **104**, 4867–4886.

43. McGarry, J., O'donnell, B., McHugh, P., and McGarry, J. (2004) Analysis of the mechanical performance of a cardiovascular stent design based on micromechanical modelling. *Comput. Mater. Sci.*, **31**, 421–438.

44. Huang, W., Yang, B., Liu, N., and Phee, S. (2007) Water-responsive programmable shape memory polymer devices. International Conference Smart Materials Nanotechnology Engineering, p. 64231S.

45. Grabow, N., Schlun, M., Sternberg, K., Hakansson, N., Kramer, S., and Schmitz, K.-P. (2005) Mechanical properties of laser cut poly (L-lactide) micro-specimens: implications for stent design, manufacture, and sterilization. *J. Biomech. Eng.*, **127**, 25–31.

46. Huang, W., Song, C., Fu, Y., Wang, C., Zhao, Y., Purnawali, H., Lu, H., Tang, C., Ding, Z., and Zhang, J. (2013) Shaping tissue with shape memory materials. *Adv. Drug Delivery Rev.*, **65**, 515–535.

47. Song, C., Campbell, P., Frank, T., and Cuschieri, A. (2002) Thermal modelling of shape memory alloy fixator for medical application. *Smart Mater. Struct.*, **11**, 312.

48. Leong, T.G., Randall, C.L., Benson, B.R., Bassik, N., Stern, G.M., and Gracias, D.H. (2009) Tetherless thermobiochemically actuated microgrippers. *Proc. Natl. Acad. Sci. U.S.A.*, **106**, 703–708.

49. Kuo, J.-C., Tung, S.-W., and Yang, Y.-J. (2013) A hydrogel-based intravascular microgripper manipulated using magnetic fields. The 17th International Conference in Solid State Sensors, Actuators Microsystems Transducers and Eurosensors XXVII, pp. 1683–1686.

50. Go, G., Kwak, D., Piao, L., Choi, H., Jeong, S., Lee, C., Park, B.J., Ko, S.Y., Park, J., and Park, S. (2013) Manipulation of micro-particles using a magnetically actuated microrobot. *Mechatronics*, **23**, 1037–1043.

51. Steager, E.B., Sakar, M.S., Magee, C., Kennedy, M., Cowley, A., and Kumar, V. (2013) Automated biomanipulation of single cells using magnetic microrobots. *Int. J. Robot. Res.*, **32**, 346–359.

52. O'Brien, B. and Carroll, W. (2009) The evolution of cardiovascular stent materials and surfaces in response to clinical drivers: a review. *Acta Biomater.*, **5**, 945–958.

53. Gogolewski, S., Jovanovic, M., Perren, S., Dillon, J., and Hughes, M. (1993) Tissue response and in vivo degradation of selected polyhydroxyacids: Polylactides (PLA), poly (3-hydroxybutyrate)(PHB),

and poly (3-hydroxybutyrate-co-3-hydroxyvalerate)(PHB/VA). *J. Biomed. Mater. Res.*, **27**, 1135–1148.

54. Labinaz, M., Zidar, J.P., Stack, R.S., and Phillips, H.R. (1995) Biodegradable stents: the future of interventional cardiology? *J. Interventional Cardiol.*, **8**, 395–405.

55. Zilberman, M., Schwade, N., Meidell, R., and Eberhart, R. (2001) Structured drug-loaded bioresorbable films for support structures. *J. Biomater. Sci., Polym. Edn.*, **12**, 875–892.

56. Incisive Surgical, I (2014) *www.insorb.com* (accessed 10 April 2014).

57. Malachowski, K., Breger, J., Kwag, H.R., Wang, M.O., Fisher, J.P., Selaru, F.M., and Gracias, D.H. (2014) Stimuli-responsive theragrippers for chemomechanical controlled release. *Angew. Chem.*, **53**, 8045–9.

58. Gultepe, E., Randhawa, J.S., Kadam, S., Yamanaka, S., Selaru, F.M., Shin, E.J., Kalloo, A.N., and Gracias, D.H. (2013) Biopsy with thermally-responsive untethered microtools. *Adv. Mater.*, **25**, 514–519.

59. Schamel, D., Mark, A.G., Gibbs, J.G., Miksch, C., Morozov, K.I., Leshansky, A.M., and Fischer, P. (2014) Nano-propellers and their actuation in complex viscoelastic media. *ACS Nano*, **8** (9), 8794–8801.

60. Zhang, L., Abbott, J.J., Dong, L., Peyer, K.E., Kratochvil, B.E., Zhang, H., Bergeles, C., and Nelson, B.J. (2009) Characterizing the swimming properties of artificial bacterial flagella. *Nano Lett.*, **9**, 3663–3667.

61. Jing, W., Pagano, N., and Cappelleri, D.J. (2013) A novel micro-scale magnetic tumbling microrobot. *J. Micro-Bio Robot.*, **8**, 1–12.

62. Donald, B.R., Levey, C.G., McGray, C.D., Paprotny, I., and Rus, D. (2006) An untethered, electrostatic, globally controllable MEMS micro-robot. *J. Microelectromech. Syst.*, **15**, 1–15.

63. Donald, B.R., Levey, C.G., McGray, C.D., Rus, D., and Sinclair, M. (2003) Power delivery and locomotion of untethered microactuators. *J. Microelectromech. Syst.*, **12**, 947–959.

64. Li, L., Brown, J., and Uttamchandani, D. (2004) Flexing of scratch drive actuator plates: modelling and experimentation. IEEE Proceedings in Science, Measurement Technology, pp. 137–141.

65. Gou, X., Yang, H., Yan, X., Wang, Y., and Sun, D. (2013) Dynamics analysis and automated control of cell chemotaxis movement using a robot-aided optical manipulation tool. IEEE International Conference in Robotics Automation (ICRA), 2013, pp. 1706–1711.

66. Chowdhury, S., Thakur, A., Svec, P., Wang, C., Losert, W., and Gupta, S.K. (2013) Automated manipulation of biological cells using gripper formations controlled by optical tweezers. *IEEE Trans. Autom. Sci. Eng.*, **11**, 338–347.

67. Akiyama, Y., Odaira, K., Sakiyama, K., Hoshino, T., Iwabuchi, K., and Morishima, K. (2012) Rapidly-moving insect muscle-powered microrobot and its chemical acceleration. *Biomed. Microdevices*, **14**, 979–986.

68. Feinberg, A.W., Feigel, A., Shevkoplyas, S.S., Sheehy, S., Whitesides, G.M., and Parker, K.K. (2007) Muscular thin films for building actuators and powering devices. *Science*, **317**, 1366–1370.

69. Chan, V., Park, K., Collens, M.B., Kong, H., Saif, T.A., and Bashir, R. (2012) Development of miniaturized walking biological machines. *Sci. Rep.*, **2**, 857.

70. Snezhko, A. and Aranson, I.S. (2011) Magnetic manipulation of self-assembled colloidal asters. *Nat. Mater.*, **10**, 698–703.

71. Gou, X., Wang, X., Yang, H., Yan, X., Wang, Y., Fahmy, T.M., and Sun, D. (2012) Dynamic control of cell migration using optical tweezers and microfluidic channel. 12th IEEE Conference Nanotechnology (IEEE NANO), pp. 1–5.

72. Akiyama, Y., Odaira, K., Iwabuchi, K., and Morishima, K. (2011) Long-term and room temperature operable bio-microrobot powered by insect heart tissue. IEEE 24th International Conference in Micro-Electro-Mechanical Systems (MEMS), pp. 145–148.

73. Ismagilov, R.F., Schwartz, A., Bowden, N., and Whitesides, G.M. (2002) Autonomous movement and self-assembly. *Angew. Chem.*, **114**, 674–676.

74. Solovev, A.A., Xi, W., Gracias, D.H., Harazim, S.M., Deneke, C., Sanchez, S., and Schmidt, O.G. (2012) Self-propelled nanotools. *ACS Nano*, **6**, 1751–1756.

75. Xi, W., Solovev, A.A., Ananth, A.N., Gracias, D.H., Sanchez, S., and Schmidt, O.G. (2013) Rolled-up magnetic microdrillers: towards remotely controlled minimally invasive surgery. *Nanoscale*, **5**, 1294–1297.

76. Zhang, L., Petit, T., Peyer, K.E., and Nelson, B.J. (2012) Targeted cargo delivery using a rotating nickel nanowire. *Nanomedicine*, **8**, 1074–1080.

77. Malachowski, K., Jamal, M., Jin, Q., Polat, B., Morris, C., and Gracias, D.H. (2014) Self-folding single cell grippers. *Nano Lett.*, **14**, 4164–70.

78. Wang, W., Castro, L.A., Hoyos, M., and Mallouk, T.E. (2012) Autonomous motion of metallic microrods propelled by ultrasound. *ACS Nano*, **6**, 6122–6132.

79. Ding, X., Lin, S.-C.S., Kiraly, B., Yue, H., Li, S., Chiang, I.-K., Shi, J., Benkovic, S.J., and Huang, T.J. (2012) On-chip manipulation of single microparticles, cells, and organisms using surface acoustic waves. *Proc. Natl. Acad. Sci. U.S.A.*, **109**, 11105–11109.

80. Kagan, D., Benchimol, M.J., Claussen, J.C., Chuluun-Erdene, E., Esener, S., and Wang, J. (2012) Acoustic droplet vaporization and propulsion of perfluorocarbon-loaded microbullets for targeted tissue penetration and deformation. *Angew. Chem. Int. Ed.*, **51**, 7519–7522.

81. Palacci, J., Sacanna, S., Vatchinsky, A., Chaikin, P.M., and Pine, D.J. (2013) Photoactivated colloidal dockers for cargo transportation. *J. Am. Chem. Soc.*, **135**, 15978–15981.

82. Dreyfus, R., Baudry, J., Roper, M.L., Fermigier, M., Stone, H.A., and Bibette, J. (2005) Microscopic artificial swimmers. *Nature*, **437**, 862–865.

83. Liu, Y., Flood, A.H., Bonvallet, P.A., Vignon, S.A., Northrop, B.H., Tseng, H.-R., Jeppesen, J.O., Huang, T.J., Brough, B., Baller, M. *et al.* (2005) Linear artificial molecular muscles. *J. Am. Chem. Soc.*, **127**, 9745–9759.

84. Gao, W., Uygun, A., and Wang, J. (2012) Hydrogen-bubble-propelled zinc-based microrockets in strongly acidic media. *J. Am. Chem. Soc.*, **134**, 897–900.

85. Sanchez, S., Solovev, A.A., Schulze, S., and Schmidt, O.G. (2011) Controlled manipulation of multiple cells using catalytic microbots. *Chem. Commun.*, **47**, 698–700.

86. Kagan, D., Campuzano, S., Balasubramanian, S., Kuralay, F., Flechsig, G.-U., and Wang, J. (2011) Functionalized micromachines for selective and rapid isolation of nucleic acid targets from complex samples. *Nano Lett.*, **11**, 2083–2087.

87. Balasubramanian, S., Kagan, D., Hu, C.-M.J., Campuzano, S., Lobo-Castañon, M.J., Lim, N., Kang, D.Y., Zimmerman, M., Zhang, L., and Wang, J. (2011) Micromachine-enabled capture and isolation of cancer cells in complex media. *Angew. Chem. Int. Ed.*, **50**, 4161–4164.

88. Paxton, W.F., Kistler, K.C., Olmeda, C.C., Sen, A., St Angelo, S.K., Cao, Y., Mallouk, T.E., Lammert, P.E., and Crespi, V.H. (2004) Catalytic nanomotors: autonomous movement of striped nanorods. *J. Am. Chem. Soc.*, **126**, 13424–13431.

89. Wang, Y., Hernandez, R.M., Bartlett, D.J. Jr,., Bingham, J.M., Kline, T.R., Sen, A., and Mallouk, T.E. (2006) Bipolar electrochemical mechanism for the propulsion of catalytic nanomotors in hydrogen peroxide solutions. *Langmuir*, **22**, 10451–10456.

90. Kagan, D., Laocharoensuk, R., Zimmerman, M., Clawson, C., Balasubramanian, S., Kang, D., Bishop, D., Sattayasamitsathit, S., Zhang, L., and Wang, J. (2010) Rapid delivery of drug carriers propelled and navigated by catalytic nanoshuttles. *Small*, **6**, 2741–2747.

91. Ebbens, S., Jones, R.A., Ryan, A.J., Golestanian, R., and Howse, J.R. (2010)

Self-assembled autonomous runners and tumblers. *Phys. Rev. E*, **82**, 015304.

92. Gao, W., Kagan, D., Pak, O.S., Clawson, C., Campuzano, S., Chuluun-Erdene, E., Shipton, E., Fullerton, E.E., Zhang, L., Lauga, E. *et al.* (2012) Cargo-towing fuel-free magnetic nanoswimmers for targeted drug delivery. *Small*, **8**, 460–467.

93. Pak, O.S., Gao, W., Wang, J., and Lauga, E. (2011) High-speed propulsion of flexible nanowire motors: theory and experiments. *Soft Matter*, **7**, 8169–8181.

94. Purcell, E.M. (1977) Life at low Reynolds number. *Am. J. Phys.*, **45**, 3–11.

95. Pitt, W.G., Husseini, G.A., and Staples, B.J. (2004) Ultrasonic drug delivery – a general review. *Expert Opin. Drug Deliv.*, **1**, 37–56.

96. Fitzpatrick, R.E. and Goldman, M.P. (1995) Advances in carbon dioxide laser surgery. *Clin. Dermatol.*, **13**, 35–47.

97. Solovev, A.A., Smith, E.J., Bof' Bufon, C.C., Sanchez, S., and Schmidt, O.G. (2011) Light-controlled propulsion of catalytic microengines. *Angew. Chem. Int. Ed.*, **50**, 10875–10878.

98. Pantarotto, D., Browne, W.R., and Feringa, B.L. (2008) Autonomous propulsion of carbon nanotubes powered by a multienzyme ensemble. *Chem. Commun.*, (13), 1533–1535.

99. Coskun, A., Banaszak, M., Astumian, R.D., Stoddart, J.F., and Grzybowski, B.A. (2012) Great expectations: can artificial molecular machines deliver on their promise? *Chem. Soc. Rev.*, **41**, 19–30.

100. Lewandowski, B., De Bo, G., Ward, J.W., Papmeyer, M., Kuschel, S., Aldegunde, M.J., Gramlich, P.M.E., Heckmann, D., Goldup, S.M., D'Souza, D.M. *et al.* (2013) Sequence-specific peptide synthesis by an artificial small-molecule machine. *Science*, **339**, 189–193.

9

Single-Chip Scanning Probe Microscopes

Neil Sarkar and Raafat R. Mansour

The progress of technology from the Neolithic Revolution to the Industrial Revolution has always been concurrent with improvements in the precision and accuracy with which we are able to manufacture and inspect things. For roughly half a century, the microelectronics industry has enjoyed exponential scaling in critical dimensions, as predicted by the widely cited Moore's law [1]. Today, the fabrication of features with dimensions of several hundreds of atoms has become routine, as semiconductor manufacturing has entered the nanometer regime. By contrast, conventional manufacturing, inspection, and metrology tools have not benefitted from dimensional scaling, and so they are encountering limitations in ultimate resolution, stability, and throughput. It is interesting to note that the cost of test for an individual transistor has exceeded the cost of manufacture per transistor, in part due to this disparity in scaling.

The concept of controlling the atomic structure of matter was proposed as early as 1959 by Richard Feynman in his renowned talk *There's Plenty of Room at the Bottom:*

> But I am not afraid to consider the final question as to whether, ultimately---in the great future---we can arrange the atoms the way we want; the very atoms, all the way down!

Imaging individual atoms remained an elusive goal until the introduction of the scanning tunneling microscope (STM) in 1982 by Binnig, Rohrer, Gerber, and Weibel [2, 3]. This instrument provided for the first time the ability to view the atoms of flat samples in real space, and the history of its development was described by its inventors at their Nobel Prize lecture in 1987 [4]. In 1989, scientists marked a milestone in the ability to structure the world around us by demonstrating the ability to position individual atoms with atomic precision using an STM [5]. These landmark experiments ushered in numerous tip-based imaging modalities, known collectively today as the family of scanning probe microscopes (SPMs).

SPMs are widely regarded as the workhorse instruments of nanoscience. Their principle of operation is simple and elegant. A sharp tip is maintained in close proximity to a sample with a feedback controller that uses a tip−sample

interaction measurement as its process variable. As the tip is scanned over the sample surface, the control effort is recorded. An image of the sample's surface structure thus emerges as a three-dimensional (3D) plot of this control effort.

Conventional SPMs suffer from several drawbacks that present a barrier to their widespread adoption by industry. The most widely used SPMs are atomic force microscopes (AFMs). Commercially available AFMs rely on piezoelectric elements to scan a cantilever in three dimensions. The use of these materials imposes several constraints on the system design. For instance, the strain produced by these actuators is small, so their size is several orders of magnitude larger than the achievable scan range. Large, bulky scanner designs are susceptible to thermal drift and poor vibration immunity. In addition, the mass of such scanners limits their mechanical bandwidth. Furthermore, the creep and hysteresis stemming from material properties in piezoelectric positioning systems manifest as image distortion. Even though phenomenological and empirical models have been developed to mitigate creep, it remains a dominant parasitic effect at the nanometer scale. Closed-loop control of the scanners employing externally mounted capacitive position sensors can mitigate this issue; however, the tip−sample interaction occurs several millimeters away from the position sensor, introducing errors in positioning accuracy. The cantilever's position is typically read by a laser that is reflected from its rear surface. This imposes further constraints on the instrument design. For instance, if probes are to be operated in parallel to improve throughput, the system becomes prohibitively large due to the free-space paths of the optical configuration.

For SPMs to address the rigorous demands of metrology at the nanometer scale, they must be smaller, faster, and more stable.

The emerging tools that are the focus of this chapter are based on the assertion that all of the mechanical and electrical components that are required for an SPM to capture an image can be scaled and integrated onto a single chip. The principles of electro-thermo-mechanical microsystem design can be applied to yield a chip-scaled instrument that independently acquires images of underlying samples, without the need for off-chip scanners or sensors. Furthermore, the performance of such an instrument stands to benefit from integration and volumetric scaling of the scanner and sensor components by a factor of 1E-6. These tools are called *single-chip scanning probe microscopes* (*sc-SPMs*).

Figure 9.1a is an image of an sc-AFM that measures 0.25 mm^3 in volume. The device is die-bonded to a carrier printed circuit board (PCB) and wire-bonded. Through-silicon vias (TSVs) are an alternative to wire bonding that may obviate the need for a coarse approach mechanism by allowing the user to simply place the sc-AFM on a sample of interest; to date, sc-SPMs have not been fabricated in a complementary metal oxide semiconductor (CMOS) process that offers TSVs as an option. At present, there are several alternatives to engaging the tip and sample. An ultrasonic motor may be used to position the sample, or a manual micrometer may be used to position the sc-AFM. The vertical actuators that are integrated on-chip have a 30-μm range of motion, a feature that significantly relaxes the

(a)

(b)

(c)

(d)

(e)

(f)
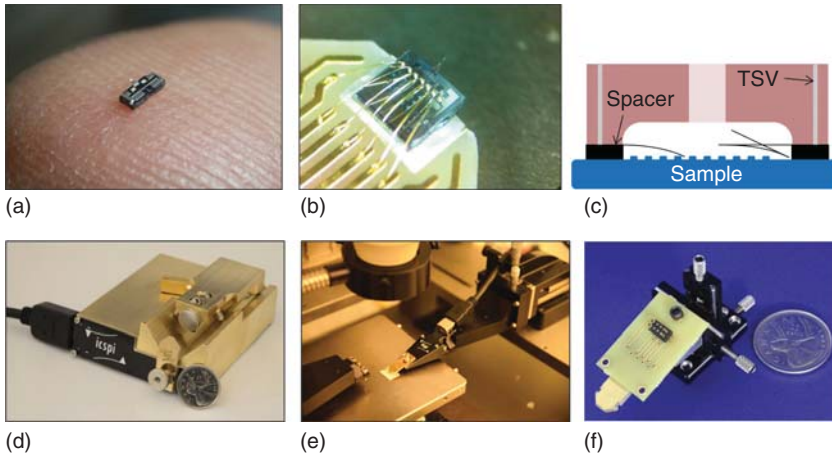
Figure 9.1 (a) An sc-SPM on a fingertip, (b) die-bonded and wire-bonded device, (c) TSV technology may be used instead of a coarse approach mechanism, (d) an ultrasonic motor may be used to engage the sample and tip, (e) a 3D-printed adapter may be used to install the AFM on a probe station, and (f) a miniature manual micropositioning system may be used to engage the tip and sample.

constraints on the coarse approach mechanism. Lateral actuators are capable of scanning over a $40\,\mu m \times 10\,\mu m$ range.

The remainder of this chapter is organized as follows: after a brief review of scanning probe microscopy in Section 9.1, the role of microelectromechanical system (MEMS) in SPM will be discussed in Section 9.2. The manufacturing process that is used to fabricate sc-SPMs will then be described in Section 9.3. In Section 9.4, the modeling effort and design process for sc-AFMs are illustrated using vertical actuators as an example. Section 9.5 chronicles the incremental progress in the design and operation of sc-SPMs and includes imaging performance of AFM modes.

9.1
Scanning Probe Microscopy

The fundamental concept behind scanning probe microscopy is akin to the action of "feeling" an object; the idea is so intuitive that it is difficult to point to its origin. In an SPM, a sharp tip is moved in three dimensions over an object while measuring its interaction with the surface. The measured quantities are used to control the tip–sample separation, and they are stored and processed to reveal an image of the underlying sample. The physical implementation is reminiscent of the phonograph, invented in 1877 by Thomas Edison as described in [6] and possibly the earliest example of a system that could track topology using a stylus to recover information. In 1928, Synge introduced the concept for a scanning probe near-field optical microscope [7]. In 1933, the concept of quantitative measurements of surfaces using stylus profilometry was introduced by Abbott and Firestone [8]. In 1972, the Topografiner [9] yielded the first measurements of

surface microtopography using electronic tip–sample interactions. Imaging was performed using field emission currents, although tunneling currents were measured in a static mode of operation. The Topografiner was not sufficiently isolated from ambient vibration to produce STM images. Also in 1972, Ash and Nicholls used microwave radiation to demonstrate super-resolution imaging; a resolution of $150\,\mu m$ was obtained using a radiation with $\lambda = 3$ cm (that is, $\lambda/200$) [10].

The invention of the STM in 1982 [2] was quickly followed by the publication of atomic resolution images of silicon by its inventors [11]. Binnig and Rohrer received the Nobel Prize for their invention in 1986, and they are generally credited for the explosive growth of SPMs that followed. In the STM, a sharp, conductive tip is biased with respect to the sample to give rise to a tunneling current when the tip–sample separation is between 4 and 7 Å. Within tunneling range, there is a highly nonlinear dependence of tunneling current on this gap, and this phenomenon is exploited to track topology. A ~ 1 Å change in the tip–sample separation results in a ~ 10-fold change in the tunneling current. Reviews of calculation methods for the tunneling current are presented in [12]. STMs require that the sample has a clean conductive surface, and they have been largely relegated to vacuum operation because many materials grow a native oxide under ambient conditions. Nevertheless, a large number of semiconductors and metals have been investigated using this invaluable tool [13].

In 1986, the AFM was invented by Binnig [14] and the first images acquired with the instrument were published by Binnig *et al.* [15]. In the first AFM, a diamond tip placed on a gold cantilever interacted with the sample. The tip–sample interaction force deflected the cantilever, and modulated a tunneling current that flowed between the cantilever and a sharp tip that was mounted on top of it. Even though the inventors anticipated that the instrument could achieve atomic resolution, it took 5 years before Giessibl and Bielefeldt [16] demonstrated it. In addition to studies of insulating samples, the AFM can achieve atomic resolution under ambient conditions, unlike the STM which requires ultrahigh vacuum except for a few special cases such as highly oriented pyrolytic graphite (HOPG). This is due to the fact that in air, the surface layer of solids constantly changes due to adsorption and desorption of atoms and molecules. Since there are no conductivity requirements in AFM, one can image virtually any flat surface without the need for surface preparation. Giessibl [17] provides a review of the common modes of operation in AFM, while Poggi *et al.* [18] review several applications of the instrument.

A large number of SPMs have been developed based on a range of tip–sample interaction mechanisms. In [19], a chronologically ordered listing of SPM modalities is tabulated. Even though a discussion of each type of SPM is beyond the scope of this chapter, it should be noted that most of these modalities can be integrated in a CMOS–MEMS process. In fact, many of the modes are supported by the devices that are presented herein. For example, a CMOS–MEMS AFM with a shielded conductive path to its tip can be used as a scanning capacitance microscope, scanning attractive force microscope, "frictional" force microscope, electrostatic force microscope, scanning electrochemical microscope, or a Kelvin probe force microscope. Even though the measurement setup for each type of microscope may vary,

a similar device may be used in all modes. This example underscores the versatility of the CMOS−MEMS manufacturing process, which is described in Section 9.3.

9.2
The Role of MEMS in SPM

The high-volume, high-yield manufacturing precision achieved by the semiconductor industry in the fabrication of integrated circuits (ICs) remains unsurpassed by any other technological endeavor. At the time of this writing, the production of <15-nm thin lines is underway. The deposition, lithography, and etching techniques borrowed from the IC industry have also enabled the batch fabrication of micromechanical components with exquisite dimensional control. Just as the improvement in IC performance is incremental [1], so too are the resolution of fabrication and metrology tools that address the challenges at this length scale. SPMs are the highest resolution tools available for imaging surfaces, and their performance is no exception; the instrument's speed, resolution, and stability all depend on improvements manufacturing precision of its constituents. For example, as cantilevers and scanners are miniaturized, the speed and stability of SPMs improve. In Ando *et al.* [20], a small scanner with a first resonance of 60 kHz and small MEMS cantilevers with resonance frequencies from 450 to 650 kHz were used to generate video rate (80 ms/frame) images of samples to capture the motion of molecules.

Progress in MEMS has had a profound impact on the SPM community, as a natural consequence of the physical laws of scaling. Micromachining technology has played a significant role in the progress of AFMs, since the tip−sample interaction force is detected by the deflection of a cantilever beam. The first micromachined cantilevers were built at Stanford [21] out of SiO_2 and Si_3N_4. Today, single-crystal silicon cantilevers based on a design presented in 1991 [22] are most common. In 1993, atomic resolution AFM images were obtained using a cantilever with an integrated piezoresistive strain sensor [23]. The optimization of a piezoresistive cantilever for AFM is discussed in [24]. MEMS cantilevers with integrated optical gratings are discussed in [25]. The FIRAT probe is a micromachined membrane that is actuated electrostatically, and includes an integrated diffraction grating. The grating is illuminated by a laser, and the far-field patterns are measured with a photodetector. Cantilevers with integrated electrostatic actuation and capacitive detection are discussed in [26]. Heated AFM probes for thermomechanical data storage and topology imaging were presented in [27, 28]. A piezoelectrically transduced cantilever was presented in [29]. A MEMS-based ring resonator with integrated transduction and >1 MHz natural frequency was discussed in [30]. Ultrasharp tips can be integrated into silicon cantilevers with various methods, including oxide sharpening and anisotropic wet etching.

Probes that have been developed to support other modes of SPM also enjoy the benefits of microfabrication. A surface-micromachined polyimide thermocouple probe for scanning thermal microscope (SThM) was presented in [31]. A silicon-micromachined probe for KPFM was presented in [32]. Probes for magnetic force microscope (MFM) are discussed in [33, 34]. Several probes for scanning

microwave microscopy (SMM) have been described in the literature as well [35–41].

One approach to improving the bandwidth of SPMs is to use a fixed array of probes that is collectively scanned using a piezoelectric actuator. In this configuration, the probe usually incorporates a sensor for tip–sample interaction measurements, since the laser-based beam-bounce technique is not amenable to array operation. A 5×5 array of AFMs was implemented in an SOI (silicon on insulator) process incorporating piezoresistive sensing for each cantilever [42]. Data storage applications were investigated as part of the "Millipede" program at IBM [43]. The Millipede represents the largest and densest 2D array (32×32, 1024 cantilevers) of AFM cantilevers to date. A PZT cantilever array with piezoresistive detection was reported in [44]. Electrostatically [45] and electrothermally actuated dip-pen nanolithography arrays have also been reported. Arrays of thermocouple probes were reported in [46]. A stand-alone single-chip AFM unit including an array of cantilevers with individual 1-DOF (degrees of freedom) actuation, detection, and control has been reported as well [47, 48]. It is important to note that all of these methods ultimately rely on a conventional AFM for scanning.

Several attempts have been made to incorporate the scanning and sensing functions on-chip. The first microfabricated STM device was a millimeter-scale piezoelectric multimorph with 3-DOF actuation, reported in [49]. This scanner achieved atomic resolution on a HOPG sample, with an impressive 20 frames per second imaging bandwidth. The maximum scan range of the device was $\sim 45\,nm \times 300\,nm \times 7500\,nm$, and its stiffness in the tip–sample approach direction was $3\,N\,m^{-1}$. Another approach is based on the SCREAM (silicon crystal reactive etching and metallization) process developed at Cornell. The approach is based on high-aspect-ratio electrostatic comb drives for actuation and selective oxidation for the formation of tips and for lateral electrical isolation of suspended microstructures [50]. A scan range of $200\,nm \times 200\,nm$ was reported, along with an image of a step feature on a grating structure. Since these devices were intended for STM measurements, no sensors were required on the chips – that is, they are examples of scanners only. It is therefore not surprising that these were the first miniature SPMs. To the best of the authors' knowledge, no other mode of SPM operation has been reported without the use of a conventional SPM for scanning. A two-axis electrostatically driven kinematic stage with an integrated cantilever is discussed in [51]; the device does not incorporate a sensor, so imaging results were not achieved. A 2-DOF probe with an integrated junction field effect transistor (JFET) was presented in [52]. A CMOS-MEMS probe with open-loop 3-DOF positioning and integrated force sensing was presented in [53].

9.3
CMOS–MEMS Manufacturing Processes Applied to sc-SPMs

There is a rich body of literature on various aspects of CMOS technology, including several texts on fabrication aspects [54, 55]. Process technology from

a MEMS perspective is also the subject of several texts and review articles [56–58]. By appropriately combining the deposition, lithography, and etch steps in CMOS with those needed for MEMS, it is possible to fabricate an integrated microsystem in a single process sequence. The devices we consider in this research are based on the cofabrication of CMOS and MEMS, an area that is the subject of a number of commercial and academic research thrusts [59, 60]. A review of the development of CMOS–MEMS processes, with emphasis on strategies for robust co-integration, has been published by Fedder *et al.* [61], and a textbook on the subject was published by Baltes *et al.* [62]. Mansour [63] provides a review of CMOS–MEMS technology applied to radio frequency (RF) applications.

When compared to conventional MEMS processes, the integrated approach offers several advantages. The excellent lithographical resolution in CMOS processes offers submicron minimum feature sizes that can be exploited in micromechanical structures. The local integration of preamplifiers with piezoresitive, temperature, or force sensing tips stands to improve the signal-to-noise ratio of the measurement. Integrated electronics may be used to multiplex signals to and from the SPMs to reduce pin count, thus enabling the practical realization of large arrays of SPMs. The unique capability to integrate temperature and position sensors within actuators is used for closed-loop scanning operation. Importantly, the use of CMOS manufacturing processes with minimal postprocessing steps offers a path toward high-volume, low-cost production of sc-SPMs.

Chip-scaled SPM instruments rely on the concerted operation of various subcomponents, each of which exploits a range of material properties. Table 9.1 contains a list of these material properties, along with their values in several MEMS processes.

Even though a range of material properties and features are available in CMOS–MEMS processes, there is an important caveat: *none* of these properties are optimized with SPMs in mind. The goal of a CMOS process is to improve the quality and yield of CMOS electronics, which are intended to perform consistently over a wide range of temperature and to be insensitive to strain from packaging. These requirements dictate a low temperature coefficient of resistivity (TCR) and gauge factor. The residual stress in CMOS processes must be lowered to mitigate bowing issues as wafer sizes scale upward. These are examples of CMOS requirements that are in contradiction with the needs of single-chip SPMs. Furthermore, the values in the table are not all available in a single process. They represent the overall range that is available in a variety of CMOS–MEMS processes, as measured and presented in the literature. Thus, even though piezoresistivity, a Seebeck coefficient, some residual stress, and a TCR are all available for the MEMS designer to exploit, none of these values are comparable to those obtained in a process that has been optimized to leverage these effects. This reality presents challenges to the design of CMOS–MEMS SPMs.

Table 9.1 Material properties available in a CMOS-MEMS process.

Design feature	Material property	Range of values in CMOS–MEMS processes
Lateral and vertical bimorphs	CTE, $\alpha^{a)}$	Al: 23.1, oxide: 0.5, W: $4.5 \times \mu\,K^{-1}$
Vertical bimorphs	Residual stress, $\sigma_0^{b)}$	Oxide: -485 to $+250$, Al: $+73$ to $+232$, poly: -583 to $+203$ Mpa
Lateral flexures, resonant cantilevers	Young's modulus $E^{c)}$	Si: $155-180$, poly: $130-175$, Al: 69, oxide: $57-70 \times$ Gpa
Lateral flexures, lateral actuators	Aspect ratio$^{d)}$	Up to $10:1$ (released)
Resistive heater	Resistivity$^{e)}$	$0.76-90 \times 10^{-3}\ \Omega\,cm$
Resistive thermometer	TCR$^{f)}$	-5.0 to $+4.38 \times 10^{-3}\ K^{-1}$
Thermocouple (Seebeck)	α_S	Poly: -366.9 to $+380$, Al: $-1.7 \times \mu V\,K^{-1}$
Integrated piezoresistor	Gauge factor, GF	Poly: $5-17$ PPM ε^{-1}
Dielectric structural layer (isolation)	Dielectric breakdown voltage $^{g)}$	Intermetal, >200 V, gate: >9 V
Thermal shunt path, isolation path	Thermal conductivity $\kappa^{h), \,i)}$	Oxide: $0.5-1.5$, poly: $18-45.6$, Al: 237, W: $174 \times W\,m^{-1}\,K^{-1}$
Sharp, conductive tips	Native oxide	All materials have native oxide
Electrothermal actuators	Volumetric heat capacity, ρc	Al: 2.4, oxide: $1.25-1.5 \times 10^6\ K\,m^{-3}\,K^{-1}$
Bulk piezoresistor	Piezoresistive coefficient	π_{44}:p-Si:$62-138$, n-Si:-19 to-9.7 π_{11}:n-Si,-38 to 102.2 p-Si, $1.1-6.6$

a) A large difference in coefficient of thermal expansion (CTE) causes a greater bending moment upon heating.
b) Residual stress is needed to generate a self-assembled out-of-plane displacement. This is required for the tip to engage the sample in one type of approach.
c) A high Young's modulus improves the out-of-plane stiffness of lateral flexures and increases the resonant frequency of cantilevers.
d) A high aspect ratio increases the linear range of flexures and prevents out-of-plane buckling under moderate loads.
e) The resistivity determines whether the desired heater resistance can be obtained in a reasonable footprint.
f) The TCR of a resistive heater should be low to avoid thermal runaway and nonlinearity in the transfer function of the actuator.
g) A structural insulating material is critical as it allows for electrical routing throughout the instrument to various sensors and actuators.
h) A material with high thermal conductivity can be used to provide thermal shunt paths from "hot spots" to the substrate, and reduce thermal coupling to nearby sensors.
i) A material with low thermal conductivity can be used to thermally isolate structures from one another, or from the substrate (to improve efficiency at the cost of bandwidth).

9.4
Modeling and Design of sc-SPMs

The design of sc-SPMs requires models that predict quantities in the electrical, thermal, and mechanical domains for various components of the instruments.

Each of the many parts of a chip-scaled SPM has performance specifications that are influenced by effects in these three domains. To build a model for a single element, one must consider solutions of the constitutive equations in each domain, and the nature of the coupling *between* domains (interdomain coupling). The components are further interconnected to one another in various ways; the SPMs consist of many elements that are coupled *within* each of the domains (intradomain coupling). Lumped element models of various components are developed using analytical expressions as a starting point. When a lumped element model fails to capture important distributed effects, models are enhanced to incorporate them. The models are then interconnected to shed light on how the coupling between elements impacts device performance. A comprehensive model of the SPM therefore seeks to capture the interplay of the components within various domains; the model ultimately serves to guide the design process to enhance the desired effects and suppress the parasitic ones.

Every component of the CMOS-MEMS SPMs can be modeled using lumped element equivalent circuits according to the principles described by Senturia [64]. In the electrical domain, the use of the $e \rightarrow V$ convention implies that the voltage is the across variable and the current is the through variable. In the mechanical domain, the $e \rightarrow V$ convention implies that the force is the across variable and the velocity is the through variable. In a circuit representation, a capacitor replaces the compliance of the spring that stores potential energy, while an inductor is the analog of the mass that stores kinetic energy. The effort and flow variables are conjugate power variables, meaning that their product in a given circuit element is equal to the power in that element. In the thermal domain, the thermal convention implies that the temperature is the across variable and the heat current is the through variable. A thermal capacitor stores heat energy and a thermal resistor represents the reciprocal of thermal conduction. The effort and flow variables in the thermal convention are not conjugate power variables, so one must use the heat energy to keep track of energy flow.

At a glance, while a CMOS–MEMS SPM is scanning a sample, the nature of each distinct building block in the instrument is obscured by its monolithic construction undergoing continuous, coordinated flexural deformations. The behavior of such a system, simultaneously responding to a multitude of inputs and generating a multitude of outputs, would be difficult to capture in a single continuum model. In fact, the meshing process alone for such a device could take hours. The problem becomes tractable when it is divided into various subcomponents that are each intended to serve a single purpose.

The elements of an SPM that must be modeled are self-heated resistors, lateral quasi-static electrothermal actuators, flexural suspensions, thermal shunt paths and thermal isolation paths, vertical dynamic electrothermal actuators, resistive and thermocouple-based temperature sensors, flexural resonant cantilevers, and piezoresistive strain sensors. Several of these components are depicted in Figure 9.2.
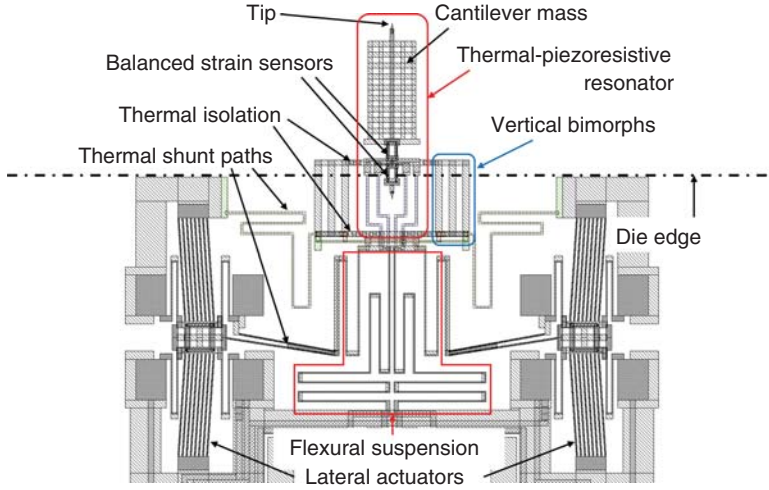
Figure 9.2 Layout capture of an sc-AFM with various components indicated.

A detailed description of the model development for each component of sc-SPMs is beyond the scope of this chapter. Instead, the lumped element model of the vertical actuator is developed here as an example.

Vertical electrothermal actuators are used to adjust the tip – sample separation. The static deflection of the vertical actuator is an important quantity, since it is plotted to reveal sample topology. Vertical actuators in this work are based on the thermal bimorph principle.

The following are some examples of design constraints:

1) The out-of-plane stiffness of the z-actuator is typically the "weakest link" in the overall out-of-plane stiffness budget, because the actuator must be compliant enough to deflect in this direction. Depending upon the type of SPM, k_z may vary from <1 to >50 N m^{-1}.

2) The range of motion of the z-actuator has several impacts on the instrument's performance. A large deflection in the z-direction increases the height of topographical features that can be imaged, and also relaxes the constraint on the resolution of the coarse approach mechanism. A large range of motion may be achieved at the cost of stiffness. The range-to-stiffness trade-off can be illustrated for the case of a constant-temperature, tip-loaded bimorph:

$$z_{\max} = \frac{ML^2}{2EI}, \quad k_z = \frac{3EI}{L^3}. \tag{9.1}$$

In other words, if the length is increased, the range increases as L^2 while the stiffness decreases as $\frac{1}{L^3}$.

3) The bandwidth of the z-actuator is necessarily the highest among all actuators in the SPM. For instance, in order to track topology, the z-actuator must deflect several times to track sample topology within a single line scan. In

addition, for dynamic modes of operation, the actuator must excite a resonant mode in a flexural cantilever, which is usually above the bandwidth of the actuator. The *bandwidth* may be defined as the location of the thermal pole set by the thermal RC time constant, which can also be related to the length of the actuator.

$$f_{-3\text{dB}} = \frac{1}{2\pi\tau} = \frac{1}{2\pi R_{\text{th}} C_{\text{th}}} = \frac{\kappa}{2\rho c_{\text{p}} L^2}. \tag{9.2}$$

4) The open-loop position resolution can be defined simply as

$$\Delta z = \frac{z_{\text{max}}}{2^n}, \tag{9.3}$$

where z_{max} is the maximum achievable deflection and n is the number of bits of resolution of the digital-to-analog converter (DAC) that is driving the actuator. This is an oversimplification that does not consider noise contributions to the position resolution of a closed-loop system. Nevertheless, the trade-off between position resolution and range is revealed in this expression.

These constraints are intended to illustrate that the z-actuator performance is the result of design trade-offs that are defined on a case-by-case basis for each type of SPM. Some additional constraints are hard limits that are defined by the process, such as the thermal budget and operating voltage. There are, of course, various other constraints that may be defined in terms of material properties and geometry. Some examples are power efficiency, work per unit volume, thermomechanical noise, maximum strain, and damping (squeeze film and thermoelastic).

9.4.1
Electrothermal Model of Self-Heated Resistor

Joule heating that occurs in self-heated resistors is the source of power for all of the actuators used in this work. The heaters are treated as localized sources of heat, and their placement within the actuator influences the time- and position-dependent temperature distribution. Because the polysilicon material used in CMOS processes possesses a TCR, the local temperature influences the electrical resistance. This is a source of feedback from the thermal domain to the electrical domain, and it results in a nonlinearity in the voltage-to-position transfer function of the device. A more significant nonlinearity stems from the fact that the heat power is proportional to the square of the voltage input. Both of these effects are captured in the lumped element model.

The electrothermal model of a self-heating resistor is shown in Figure 9.3, along with scanning electron microscope (SEM) images that capture the static voltage-to-deflection function of an actuator.

The governing equation of this first-order system is [64]

$$C_{\text{th}} \frac{dT_{\text{R}}}{dt} = -\frac{T_{\text{R}}}{R_{\text{th}}} + \frac{V^2}{R_0(1 + \alpha_{\text{R}} T_{\text{R}})}. \tag{9.4}$$
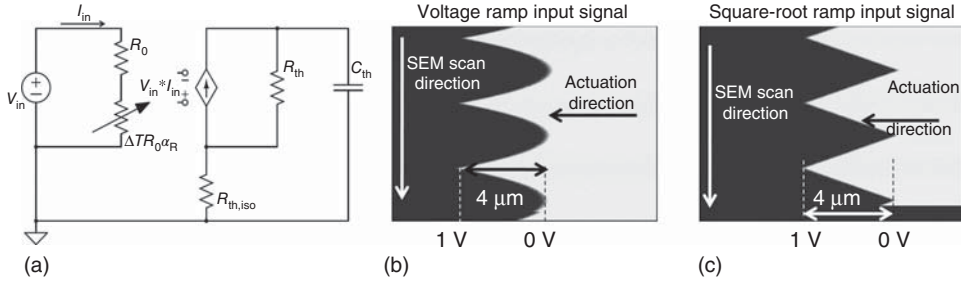
Figure 9.3 (a) Electrothermal representation of a self-heated resistor. (b) A SEM image captured over the course of three cycles of a ramp signal applied to a lateral actuator. (c) A square-root ramp signal may be used to linearize the actuator's output.

This expression contains two nonlinearities that affect the voltage-to-temperature (and therefore voltage-to-position) transfer function of actuators that are used in the SPMs. The first nonlinearity is the V^2 dependence, which may be removed with a nonlinear inversion by taking the square root of the voltage signal before it is applied to the heater. The second nonlinearity results from the presence of the temperature term below V^2.

Since the TCR is small, the following approximation can be made:

$$\frac{V^2}{R_0(1 + \alpha_R T_R)} \approx \frac{V^2}{R_0}(1 - \alpha_R T_R). \tag{9.5}$$

Substituting back into Section 9.4 and collecting terms gives

$$\frac{dT_R}{dt} = -\frac{1}{R_{th}C_{th}}\left(1 + \frac{\alpha_R R_{th} V^2}{R_0}\right) T_R + \frac{V^2}{R_0}. \tag{9.6}$$

The thermal time constant for this system, assuming a constant V^2, is

$$\tau_V = \frac{R_{th}C_{th}}{\left(1 + \frac{\alpha_R R_{th} V^2}{R_0}\right)}. \tag{9.7}$$

which depends on the value of the input voltage. The steady-state temperature rise of this linear system with negative feedback is

$$T_{ss} = \frac{\frac{R_{th} V^2}{R_0}}{\left(1 + \frac{\alpha_R R_{th} V^2}{R_0}\right)}. \tag{9.8}$$

If the resistor has a positive temperature coefficient, the value of the denominator increases with applied voltage, implying that the slope of $T_{ss}(V)$ decreases, and stable operation is possible. For negative temperature coefficients, the situation is reversed, and there is a possibility of "thermal runaway" at sufficiently high voltages. The term *thermal runaway* is used to describe the situation in which there is a positive feedback between the input voltage and the temperature, making it possible for the temperature to rise at a fixed input voltage. Beyond a characteristic threshold voltage, this would result in catastrophic device failure due to overheating.

9.4.2
Electrothermal Model of Vertical Actuator

The electrical model of the actuator calculates the amount of joule heating in a resistor that is subject to an applied voltage, and the temperature dependence of this resistor is captured through feedback from the thermal domain. The input voltage may be divided into a DC component and an AC component. The DC component is applied to track topology, while the AC component is used in dynamic modes. In frequency modulation atomic force microscope (FM-AFM) and amplitude modulation atomic force microscope (AM-AFM), the AC component places the cantilever in resonance to increase the tip−sample force sensitivity. An AC signal may also be used to force a nonresonant oscillation, and subsequently demodulate and filter the output in order to improve noise performance.

For quasi-static operation, the thermal model is similar to that of a self-heating resistor. A simplified schematic of the thermal model with a single lumped capacitor is shown in Figure 9.4. If the temperature gradient is sought, the difference between the end points of the model may be used to determine the slope of the temperature function.

Lumped parameter models like the one presented earlier are useful when the wavelength of interest is larger than the geometry being considered. As the frequency of the thermal excitation source is increased (as in dynamic AFM imaging modes), the full solution to the heat equation shows that the AC temperature has an exponential dependence on position, as well as a phase dependence. To capture this behavior, a distributed parameter model is developed. The methodology shown here is borrowed from the concept of transmission lines in the field of microwave engineering.

The model begins with a section of the thermal conduction path with the values of the components scaled to match its length, as shown in Figure 9.5. After Kirchhoff's voltage law is applied to this model, one takes the limit as the length of the section approaches zero. The value for the characteristic impedance of the line is

$$Z_0 = \frac{V_0^+}{I_0^+} = \frac{V_0^-}{I_0^-} = \frac{R_{th}}{\gamma} = \sqrt{\frac{R_{th}}{G_{th} + j\omega C_{th}}}. \tag{9.9}$$
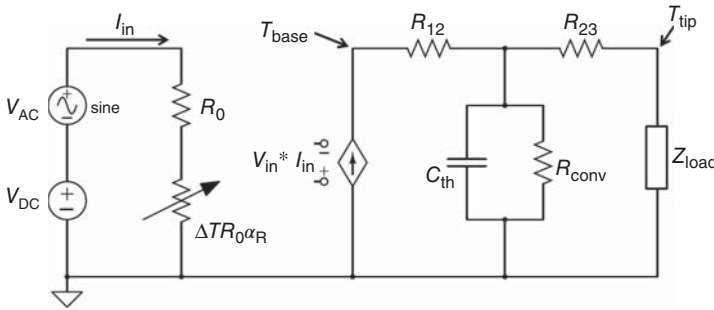
Figure 9.4 Electrothermal model of a vertical actuator.
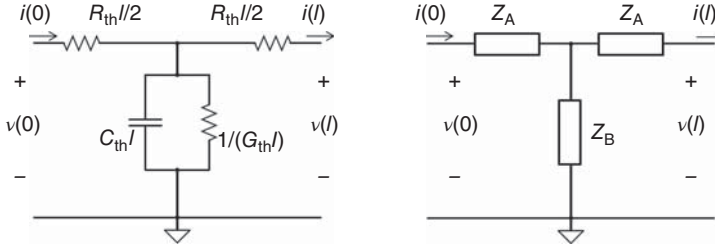
Figure 9.5 Thermal transmission line model.

where $\gamma = \alpha + j\beta = \sqrt{R_{th}(G_{th} + j\omega C_{th})}$ is the complex propagation constant. The series impedance in the model is

$$Z_A = \frac{R_{th}}{\gamma} \frac{e^{\gamma L} - 1}{e^{\gamma L} + 1} = Z_0 \tanh \frac{\gamma L}{2}. \tag{9.10}$$

The value for the shunt impedance is

$$Z_B = \frac{R_{th}}{\gamma} \frac{2e^{\gamma L}}{e^{\gamma L} - 1} = \frac{Z_0}{\sinh \gamma L}. \tag{9.11}$$

The voltage waveform representing the temperature on the line in the time domain is

$$V(x) = \frac{I(0)R_{th}}{\gamma} e^{-\gamma x}. \tag{9.12}$$

It is assumed that the current $I(0)$ is known and expressed in terms of the forward voltage in the line. The voltage may be evaluated at any number of points along the line and its value may be applied to the corresponding nodes in the mechanical domain.

9.4.3
Electro-Thermo-Mechanical Model

The temperature distribution is coupled to the mechanical domain through a voltage source that represents the thermal moment induced in the beam. Here, we consider the static case in which a temperature gradient exists over the length of the actuator. The slope of the temperature between nodes of the thermal model is represented by

$$m_{th} = \frac{\Delta T_{tip} - \Delta T_{base}}{L}. \tag{9.13}$$

The value for the tip angle is calculated by direct integration of the static Euler–Bernoulli beam equation with a gradient in the moment load. Integrating once again yields the tip displacement. Energy methods are used to calculate the effective linear spring constant of the beam, which results in a capacitance of

$$C_{y, m\_th} = \frac{1}{k} = \frac{L^3}{4EI} \left[\frac{1}{3} + \frac{Lm_{th} + 2}{\left(L^2 m_{th}^2 + 3Lm_{th} + 3\right)} \right]. \tag{9.14}$$
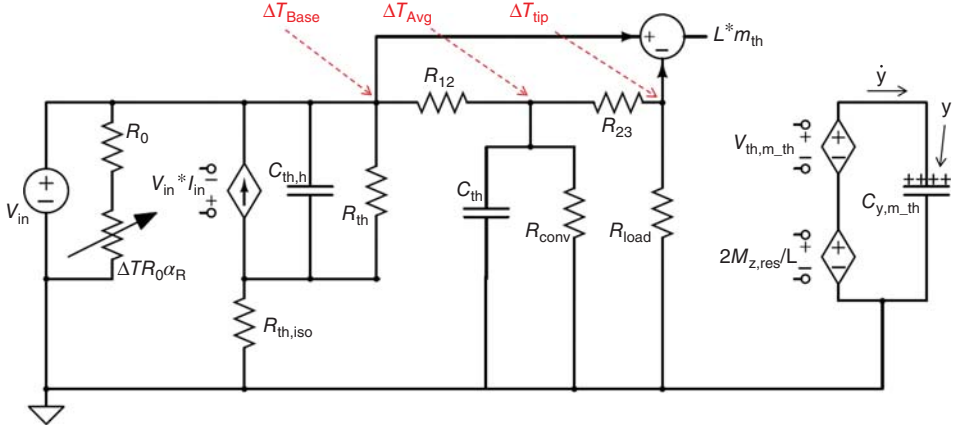
Figure 9.6 Electro-thermo-mechanical model of deflection.

The corresponding voltage source is

$$V_{\text{th,m\_th}} = \frac{q}{C} = 2S_{\text{M\_z,th}} \frac{L^2 m_{\text{th}}^2 + 3Lm_{\text{th}} + 3}{L(Lm_{\text{th}} + 3)} \Delta T. \tag{9.15}$$

The complete quasi-static model of the electrothermal bimorph is shown in Figure 9.6. The model accounts for thermal gradients and provides a realistic estimation of the tip-referred force and deflection by considering the strain energy produced by thermal bending moments. The quasi-static nature of the model means that it ignores the dynamics in the mechanical domain, which is why there is no lumped resistor to represent damping and no lumped inductor to represent effective mass. The charge on the capacitor instantaneously follows the voltage on the source, scaled by a judiciously chosen compliance factor. Note that the resistor used to capture convection is tied directly to ground, since it is not affected by thermal isolation.

The lumped models developed earlier provide qualitative insight to guide the design of sc-SPM devices. To provide quantitative information, the values of lumped parameters are fitted to experimental data and various simulation results. In the electrical domain, CMOS CAD tools (e.g., Cadence) may be used to extract parasitic capacitance and resistance of wiring and pads in order to minimize cross talk between actuators and sensors. In the thermal domain, test structures are used to extract thermal conductivity and heat capacity of CMOS materials, and transient thermal analysis is performed using finite element analysis (FEA) software. In the mechanical domain, FEA software may be used to estimate the overall tip-referred stiffness of the instruments. Lumped parameter values for effective mass and damping of a given resonant mode may be extracted from a combination of FEA (modal analysis) and measurements in air and vacuum. Details on models and simulation strategies are provided in [65–68].

9.5
Imaging Results

Several modalities of SPM have been implemented using the CMOS-MEMS approach, including contact-mode AFM [69], intermittent contact with higher harmonic detection [70], AM-AFM [68], FM-AFM [67], SMM [71], scanning thermal microscopy [72], and Kelvin probe force microscopy [73]. The most widely used SPM modality is by far the AM-AFM mode, owing to its versatility, ease of implementation, and robustness under a range of imaging conditions. This section highlights the imaging results obtained with contact, intermittent-contact, and AM-AFM modes using single-chip instruments. The evolution of the instrument design is shown in Figure 9.7, and the impact of incremental design improvements on imaging performance is also discussed.

The first scanner design (Figure 9.7a) obtained 3 DOFs by serially cascading lateral and vertical electrothermal actuators. This design pattern was problematic for a number of reasons. First, the actuators were directly coupled in the thermal domain, forcing the heat from the vertical actuator to traverse the lateral actuators in order to reach thermal ground (substrate). The result was that a voltage applied to the z-actuator moved the tip in the x, y, and z directions simultaneously. Because of the long mechanical path from tip to sample, the tip-referred stiffness of this design is too low to overcome attractive tip−sample interaction forces (van der Waals forces), giving rise to pull-in effects. The lateral compliance of the device is also low, causing lateral "stiction" to features on the sample. These factors contributed to poor imaging performance.
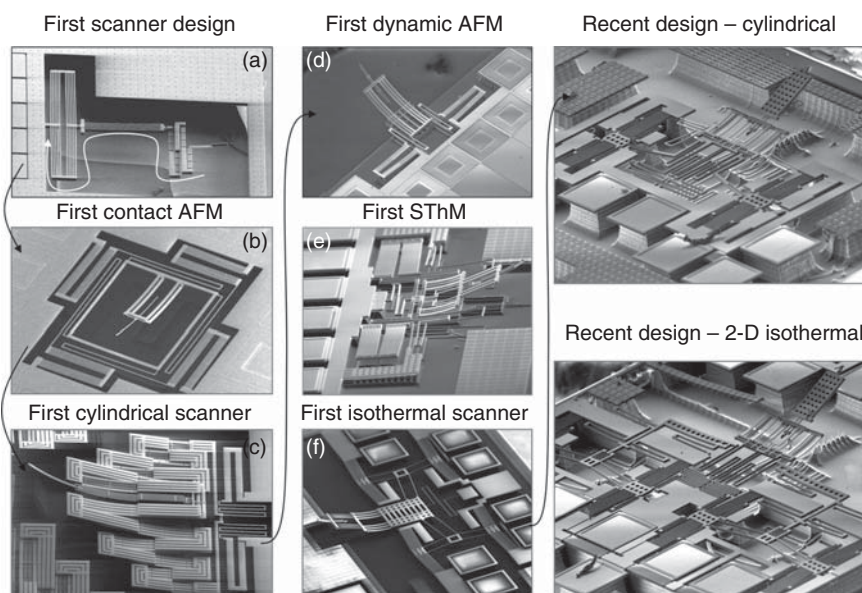
Figure 9.7 Incremental progress in the design of sc-SPMs.

The first contact-mode AFM images were obtained with the device shown in Figure 9.7b. To mitigate thermal coupling effects, all lateral actuators have a direct path to thermal ground; however, thermal coupling through the flexural suspension was still observed. The flexures that decouple the *x*- and *y*-axes in this design are guided-end beams whose compliance is lower than the piezoresistive strain sensing beam. Thus, the strain from tip–sample interaction forces is not preferentially captured by the sensors, and is instead "lost" in the flexural suspension. In addition, the lateral rigidity of the piezoresistive beams was not sufficient to overcome stiction effects. The sample geometry was restricted by the central location of the tip and surrounding wire bonds, and the tip–sample region was not observable during imaging experiments. The images of AFM calibration standards shown in Figure 9.8 were obtained in the contact mode of operation, and significant postprocessing was required to remove artifacts from sticking effects and thermal coupling.

A cylindrical coordinate scanner is shown in Figure 9.7c. When voltages V_a and V_b are applied to the lateral actuators, a radial tip displacement (r) arises from the common-mode voltage $(V_a + V_b)/2$ while a tangential tip displacement (θ) arises from the differential voltage $(V_a - V_b)$. Constraints on the sample geometry and tip–sample region visibility were removed and a significantly increased scan range was achieved; however, the out-of-plane stiffness of the design was lower than $0.1\,\mathrm{N\,m^{-1}}$ and imaging performance was poor. The scanner in Figure 9.7d

Image of 2D periodic grating obtained with single-chip AFM (3-micron period)

Image of triangular grating obtained with single-chip AFM (3-micron period)

Image of 2D periodic grating obtained with conventional AFM

Image of triangular grating obtained with conventional AFM
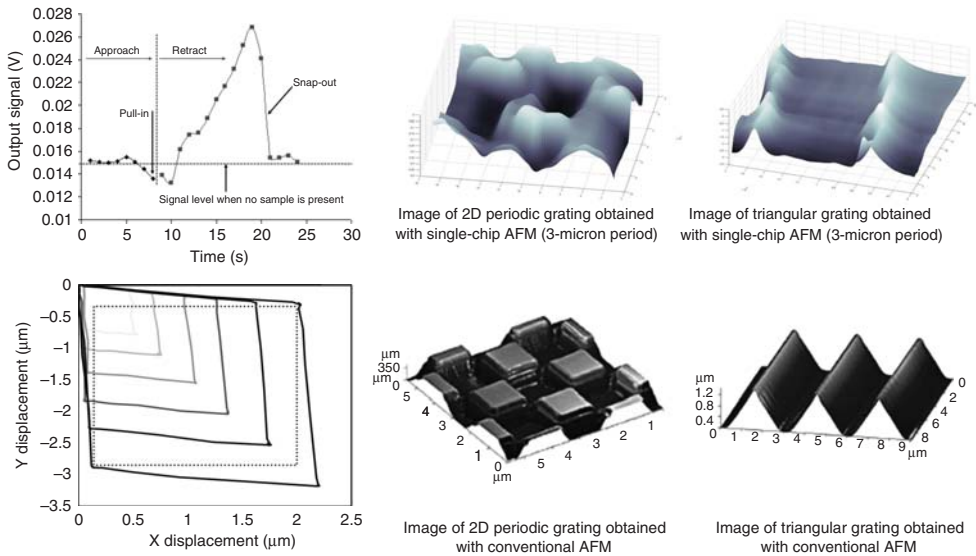
Figure 9.8 Contact-mode AFM approach curves (top left) are used to establish that the instrument can detect attractive and repulsive forces from tip–sample interaction. Thermal coupling between the lateral actuators results in a scan pattern that deviates from the intended orthogonal pattern (bottom left). Images obtained with the first sc-AFM in contact mode, compared to those obtained with a conventional instrument.
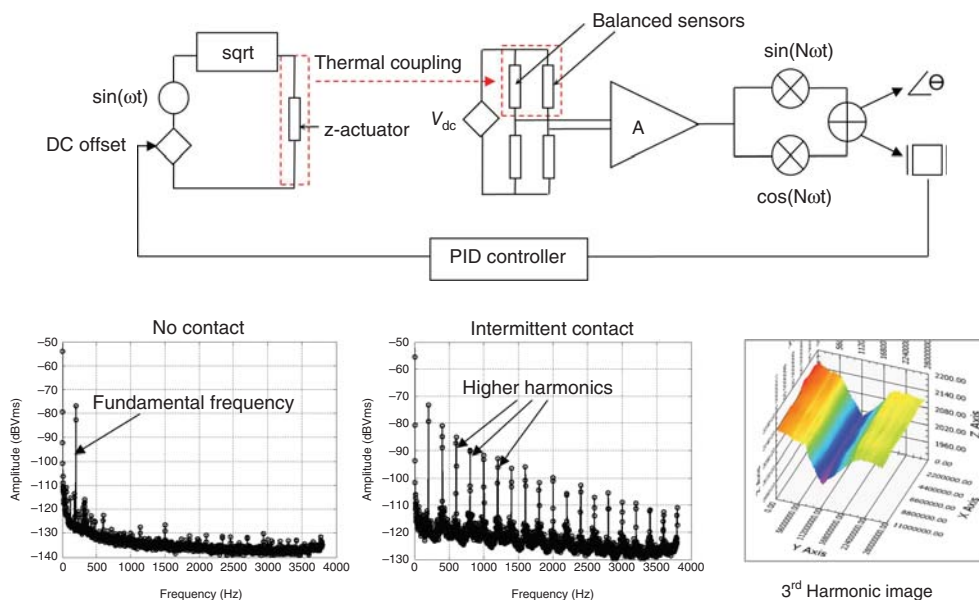
Figure 9.9 Schematic of the higher-harmonic detection mode. Higher harmonics of the fundamental (forcing) frequency are observed when the tip is in intermittent contact with the sample. An image was obtained in this mode using the third harmonic.

remedies the stiffness issue while providing an improved geometry, with the cantilever and tip suspended over the die edge. This instrument was used to obtain images in the higher-harmonic detection mode. An AC signal was applied to force the oscillation of the z-actuator to bring it into intermittent contact with an underlying sample. When the cantilever impacts the sample, several higher harmonics are observed, some of which are above the thermal time constant of the actuator. The frequency separation between the piezoresistive signal and the parasitic thermal coupling signal results in reduced thermal cross talk. Furthermore, the increased stiffness of the design mitigates pull-in, and lateral sticking is suppressed by large oscillation amplitudes. The measurement setup, observed signals, and imaging performance are shown in Figure 9.9.

Dynamic AFM operation was explored using the device in Figure 9.7g. The lateral actuators were augmented with higher stiffness and improved work per unit volume, while the tip-referred out-of-plane stiffness was increased to $\sim 0.5\,\mathrm{N\,m}^{-1}$. A temperature coefficient of natural frequency was observed in the first resonant mode of the device. To mitigate this deleterious effect, the device was operated with an "isothermal scanning" method, in which the sum of powers dissipated by lateral actuators was held constant over the course of a line scan. A calibration procedure was followed to capture the temperature coefficient of resistivity of the self-heating resistors, thereby compensating nonlinear power dissipation. Imaging results in the AM-AFM mode with a cylindrical coordinate scanner operating isothermally are shown in Figure 9.10. An AFM calibration standard with 20-nm
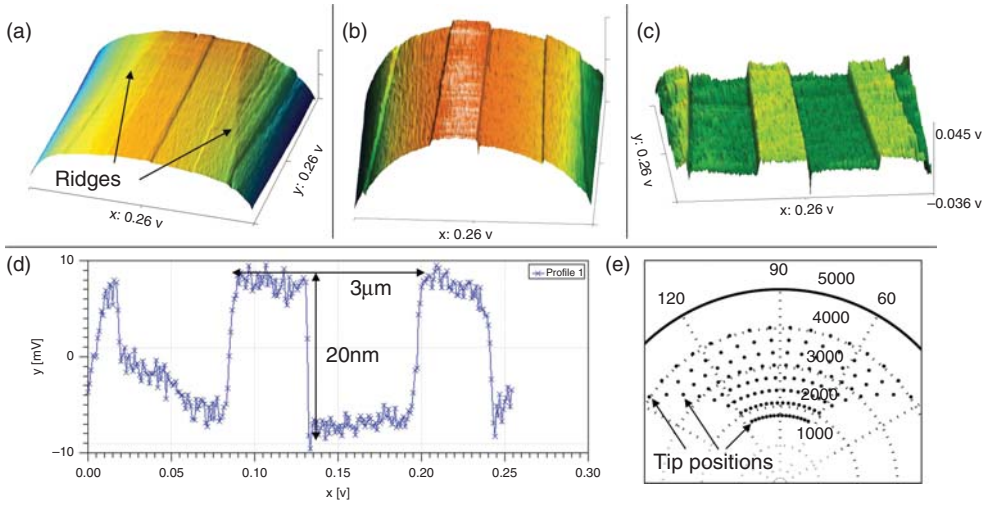
Figure 9.10 (a–c) Images of 20-nm steps on a silicon AFM calibration standard. Ridge artifacts appear in the image when calibration is performed over a smaller scan range than the image. Postprocessing with a polynomial flattening step removes curvature in the image. (d) Line profile extracted from the image in (c) shows pk–pk noise of ~3 nm. (e) The tip trajectory during isothermal scanning results in image distortion.

step heights and 3-μm pitch was imaged under ambient conditions without vibration isolation.

Because of the isothermal constraint, the cylindrical coordinate scanners described above must follow a trajectory that leads to significant image distortion, as shown in Figure 9.10. To mitigate this distortion, scanners that maintain constant temperature under 2-DOF actuation were designed (Figure 9.7h). Both cylindrical and Cartesian coordinate versions of these devices achieve 2D isothermal operation while mitigating image distortion. An AFM calibration standard with 50-nm pits on a 1-μm pitch was imaged with these scanners as shown in Figure 9.11.
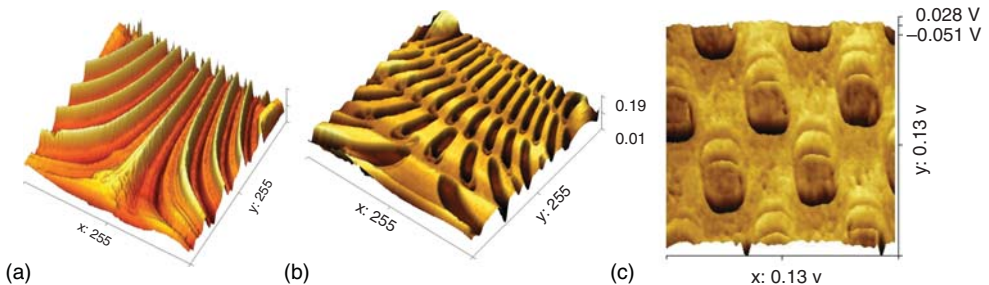
Figure 9.11 (a,b) Images of AFM calibration standards obtained with cylindrical scanners suffer from distortion due to the tip trajectory. (c) An image of the same calibration standard as the center image (50-nm deep pits in a Si sample) obtained using a 2-DOF isothermal scanner. No postprocessing was performed in this image.

9.6
Conclusion

SPMs have been widely adopted by the nanoscience research community and are routinely used to manipulate matter with atomic resolution; however, the high cost, poor drift performance, susceptibility to creep and hysteresis, and low throughput of conventional instruments have limited their adoption in the industrial metrology community.

An emerging tool in this area is the sc-SPM, which has achieved resolution comparable to state-of-the-art tools at a small fraction of the size and cost. For high-throughput applications, the scanners must be operable in massively parallel arrays and the speed of individual scanners must be increased. The isothermal scanning methods described so far are well suited to array operation, as they suppress thermal cross talk between SPMs by assuring constant heat generation while traversing arbitrary tip trajectories. As the speed and resolution of sc-SPMs improves with every design cycle, these tools may have a significant impact on the emerging nanotechnology enterprise.

References

1. Moore, B.G.E. (1975) Cramming more components onto integrated circuits. *Electron. Mag.*, **38** (8), 114.
2. Binnig, G., Rohrer, H., Gerber, C., and Weibel, E. (1982) Surface studies by scanning tunneling microscopy. *Phys. Rev. Lett.*, **49** (1), 57–61.
3. Ogletree, F., Binnig, G., Rohrer, H., and Rüshlikon, I.B.M. (2006) 25 Years of Scanning Probe Microscopes : How Instrumental Developments Revolutionized Surface Science and Nanotechnology Imaging and Manipulation Facility.
4. Binnig, G. and Rohrer, H. (1987) Scanning tunneling microscopy-from birth to adolescence (Nobel Lecture). *Angew. Chem. Int. Ed. Engl.*, **26**, 606–614.
5. Eigler, D.M. and Schweizer, E.K. (1990) Positioning single atoms with a scanning tunneling microscope. *Nature*, **344**, 524–526.
6. Read, O. and Welch, W.L. (1959) *From Tin Foil to Stereo: Evolution of the Phonograph*, H.W. Sams.
7. Synge, E.A. (1928) A suggested method for extending microscopic resolution into the ultra-microscopic region. *Philos. Mag. Ser. 7*, **6** (35), 356–362.
8. Abbott, F.A. and Firestone, E.J. (1933) Specifying surface quality: a method based on accurate measurement and comparison. *Mech. Eng.*, **55**, 569–572.
9. Young, R. (1972) The topografiner: an instrument for measuring surface microtopography. *Rev. Sci. Instrum.*, **43** (7), 999.
10. Ash, E.A. and Nicholls, G. (1972) Superresolution aperture scanning microscope. *Nature*, **237** (5357), 510–512.
11. Binnig, G., Rohrer, H., Gerber, C., and Weibel, E. (1983) 7× 7 reconstruction on Si (111) resolved in real space. *Phys. Rev. Lett.*, **50** (2), 120.
12. Hofer, W., Foster, A., and Shluger, A. (2003) Theories of scanning probe microscopes at the atomic scale. *Rev. Mod. Phys.*, **75** (4), 1287–1331.
13. Stroscio, J.A. and Kaiser, W.J. (1993) *Scanning Tunneling Microscopy*, Elsevier Science.
14. G. K. Binnig (1988) Atomic force microscope and method for imaging surfaces with atomic resolution. US Patent 4724318.
15. Binnig, G., Quate, C., and Gerber, C. (1986) Atomic force microscope. *Phys. Rev. Lett.*, **56** (9), 930–933.

16. Giessibl, F.J., Bielefeldt, H., Hembacher, S. and Mannhart, J. (2001) Imaging of atomic orbitals with the atomic force microscope-Experiments and simulations. *Ann. Phys. (Leipzig)*, (10), 887–910.

17. Giessibl, F.J. (2003) Advances in atomic force microscopy. *Rev. Mod. Phys.*, **75** (3), 949–983.

18. Poggi, M.A., Gadsby, E.D., Bottomley, L.A., King, W.P., Oroudjev, E., and Hansma, H. (2004) Scanning probe microscopy. *Anal. Chem.*, **76** (12), 3429–3443.

19. Wickramasinghe, H.K. (2000) Progress in scanning probe microscopy. *Acta Mater.*, **48** (1), 347–358.

20. Ando, T., Kodera, N., Takai, E., Maruyama, D., Saito, K., and Toda, A. (2001) A high-speed atomic force microscope for studying biological macromolecules. *Proc. Natl. Acad. Sci. U.S.A.*, **98** (22), 12468–12472.

21. Albrecht, T.R., Akamine, S., Carver, T.E., and Quate, C.F. (1990) Microfabrication of cantilever styli for the atomic force microscope. *J. Vac. Sci. Technol., A: Vac. Surf. Films*, **8** (4), 3386.

22. Wolter, O., Bayer, T., and Greschner, J. (1991) Micromachined silicon sensors for scanning force microscopy. *J. Vac. Sci. Technol., B Microelectron. Nanom. Struct.*, **9** (2), 1353.

23. Tortonese, M., Barrett, R.C., and Quate, C.F. (1993) Atomic resolution with an atomic force microscope using piezoresistive detection. *Appl. Phys. Lett.*, **62** (8), 834.

24. Harley, J.A. and Kenny, T.W. (2000) 1 = F noise considerations for the design and process optimization of piezoresistive cantilevers. *J. Microelectromech.*, **9** (2), 226–235.

25. Kocabas, C. and Aydinli, A. (2005) Design and analysis of an integrated optical sensor for scanning force microscopies. *IEEE Sens. J.*, **5** (3), 411–418.

26. Blanc, N., Brugger, J., and De Rooij, N.F. (2007) Scanning force microscopy in the dynamic mode using microfabricated capacitive sensors. *J. Vac. Sci. Technol.*, **14** (2), 901–905.

27. Chui, B.W., Stowe, T.D., Goodson, K.E., Kenny, T.W., Mamin, H.J., Terris, B.D., Ried, R.P., and Rugar, D. (1998) Low-stiffness silicon cantilevers with integrated heaters and piezoresistive sensors for high-density AFM thermomechanical data storage. *J. Microelectromech. Syst.*, **7** (1), 69–78.

28. King, W.P. (2005) Design analysis of heated atomic force microscope cantilevers for nanotopography measurements. *J. Micromech. Microeng.*, **15** (12), 2441–2448.

29. Itoh, T., Lee, C., and Suga, T. (1996) Deflection detection and feedback actuation using a self-excited piezoelectric Pb(Zr,Ti)O3 microcantilever for dynamic scanning force microscopy. *Appl. Phys. Lett.*, **69** (14), 2036.

30. Algré, E., Xiong, Z., and Faucher, M. (2012) MEMS ring resonators for laserless AFM with sub-nanoNewton force resolution. *J. Microelectromech. Syst.*, **21** (2), 385–397.

31. Li, M.-H., Wu, J.J., and Gianchandani, Y.B. (2001) Surface micromachined polyimide scanning thermocouple probes. *J. Microelectromech. Syst.*, **10** (1), 3–9.

32. Chu, L.L., Takahata, K., Selvaganapathy, P.R., Gianchandani, Y.B., and Shohet, J.L. (2005) A micromachined kelvin probe with integrated actuator for microfluidic and solid-state applications. *J. Microelectromech. Syst.*, **14** (4), 691–698.

33. Hartmann, U. (Aug. 1999) Magnetic force microscopy. *Annu. Rev. Mater. Sci.*, **29** (1), 53–87.

34. Al-Khafaji, M., Rainforth, W., Gibbs, M., Bishop, J.E.L., and Davies, H.A. (1996) The effect of tip type and scan height on magnetic domain images obtained by MFM. *Magn. IEEE Trans.*, **32** (5), 4138–4140.

35. Talanov, V.V., Scherz, A., Moreland, R.L., and Schwartz, A.R. (2006) A near-field scanned microwave probe for spatially localized electrical metrology. *Appl. Phys. Lett.*, **88** (13), 134106.

36. Reznik, A.N. and Talanov, V.V. (2008) Quantitative model for near-field scanning microwave microscopy: application to metrology of thin film dielectrics. *Rev. Sci. Instrum.*, **79** (11), 113708.

37. Tabib-Azar, M., Shoemaker, N.S., and Harris, S. (1993) Non-destructive characterization of materials by evanescent

microwaves. *Meas. Sci. Technol.*, **4** (5), 583–590.

38. Tabib-Azar, M., Su, D.-P., Pohar, A., LeClair, S.R., and Ponchak, G. (1999) 0.4 μm spatial resolution with 1 GHz (λ=30 cm) evanescent microwave probe. *Rev. Sci. Instrum.*, **70** (3), 1725.

39. Lai, K., Ji, M.B., Leindecker, N., Kelly, M.A., and Shen, Z.-X. (2007) Atomic-force-microscope-compatible near-field scanning microwave microscope with separated excitation and sensing probes. *Rev. Sci. Instrum.*, **78** (6), 063702.

40. Yang, Y., Lai, K., Tang, Q., Kundhikanjana, W., Kelly, M.A., Zhang, K., Shen, Z., and Li, X. (2012) Batch-fabricated cantilever probes with electrical shielding for nanoscale dielectric and conductivity imaging. *J. Micromech. Microeng.*, **22** (11), 115040.

41. Lai, K., Kundhikanjana, W., Kelly, M.A., and Shen, Z.X. (2008) Calibration of shielded microwave probes using bulk dielectrics. *Appl. Phys. Lett.*, **93** (12), 123105.

42. Lutwyche, M., Andreoli, C., Binnig, G., Brugger, J., Drechsler, U., Haeberle, W., Rohrer, H., Rothuizen, H., and Vettiger, P. (1998) Microfabrication and parallel operation of 5×5 2D AFM cantilever arrays for data storage and imaging. Proceedings MEMS 98 IEEE, The Eleventh Annual International Workshop on Micro Electro Mechanical Systems. An Investigation Micro Structures Sensors, Actuators, Machines and Systems (Cat.98CH36176), pp. 8–11.

43. Vettiger, P., Cross, G., Despont, M., Drechsler, U., Durig, U., Gotsmann, B., Haberle, W., Lantz, M.A., Rothuizen, H.E., Stutz, R., and Binnig, G.K. (2002) The 'millipede' – nanotechnology entering data storage. *IEEE Trans. Nanotechnol.*, **1** (1), 39–55.

44. Kim, Y. (2003) PZT cantilever array integrated with piezoresistor sensor for high speed parallel operation of AFM. *Sens. Actuators, A*, **103** (1-2), 122–129.

45. Bullen, D. and Liu, C. (2006) Electrostatically actuated dip pen nanolithography probe arrays. *Sens. Actuators, A*, **125** (2), 504–511.

46. McNamara, S., Basu, A.S., Lee, J., and Gianchandani, Y.B. (2005) Ultracompliant thermal probe array for scanning non-planar surfaces without force feedback. *J. Micromech. Microeng.*, **15** (1), 237–243.

47. Barrettino, D., Hafizovic, S., Volden, T., Sedivy, J., Kirstein, K., Hierlemann, A., and Baltes, H. (2004) CMOS monolithic atomic force microscope. 2004 Symposium on VLSI Circuits. Digest Technical Paper (IEEE Cat. No.04CH37525), 306–309.

48. Hafizovic, S., Barrettino, D., Volden, T., Sedivy, J., Kirstein, K.-U., Brand, O., and Hierlemann, A. (2004) Single-chip mechatronic microsystem for surface imaging and force response studies. *Proc. Natl. Acad. Sci. U.S.A.*, **101** (49), 17011–17015.

49. Akamine, S., Albrecht, T.R., Zdeblick, M.J., and Quate, C.F. (1989) Microfabricated scanning tunneling microscope. *IEEE Electron Device Lett.*, **10** (11), 490–492.

50. Xu, Y., MacDonald, N., and Miller, S. (1995) Integrated micro-scanning tunneling microscope. *Appl. Phys. Lett.*, **67**, 2305–2307.

51. Jingyan, D. and Ferreira, P. (2009) Electrostatically actuated cantilever with SOI-MEMS parallel kinematic XY stage. *J. Microelectromech. Syst.*, **18** (3), 641–651.

52. Amponsah, K. and Lal, A. (2012) Multiple tip nano probe actuators with intergrated JFETS. 25th International Conference on Micro Electro Mechanical Systems (MEMS), 2012 IEEE, Paris, France, February, 2012, pp. 1356–1359.

53. Liu, J., Draghi, L., Bain, J. A., Schlesinger, T. E., and Fedder, G. K. (2010). Three-DOF CMOS-MEMS probes with embedded piezoresistive sensors. 2010 IEEE 23rd International Conference Micro Electro Mechanical Systems, January, 2010, 284–287.

54. Sze, S.M. (1983) *VLSI Technology*, McGraw-Hill.

55. Jäger, R.C. (2002) *Introduction to Microelectronic Fabrication*, Prentice Hall PTR.

56. Madou, M. (2011) *Fundamentals of Microfabrication: The Science of Miniturization*, Taylor & Francis Limited.

57. Kovacs, G.T.A. (1998) *Micromachined Transducers Sourcebook*, WCB/McGraw-Hill, New York.

58. Bustillo, J.M., Howe, R.T., and Muller, R.S. (1998) Surface micromachining for microelectromechanical systems. *Proc. IEEE*, **86** (8), 1552–1574.

59. Hagleitner, C., Hierlemann, A., Lange, D., Kummer, A., Kerness, N., Brand, O., and Baltes, H. (2001) Smart single-chip gas sensor microsystem. *Nature*, **414** (6861), 293–296.

60. Giner, J., Uranga, A., Muñóz-Gamarra, J.L., Marigó, E., and Barniol, N. (2012) A fully integrated programmable dual-band RF filter based on electrically and mechanically coupled CMOS-MEMS resonators. *J. Micromech. Microeng.*, **22** (5), 055020.

61. Fedder, G.K., Howe, R.T., and Quevy, E.P. (2008) Technologies for cofabricating MEMS and electronics. *Proc. IEEE*, **96** (2), 306–322.

62. Baltes, H., Brand, O., Fedder, G.K., Hierold, C., Korvink, J.G., and Tabata, O. (2008) *CMOS-MEMS: Advanced Micro and Nanosystems*, Wiley-VCH Verlag GmbH.

63. Mansour, R.R. (2013) RF MEMS-CMOS device integration. *IEEE Microwave Mag.* 2012, 39–56.

64. Senturia, S.D. (2000) *Microsystem Design*, Springer.

65. Sarkar, N., Trainor, K., and Mansour, R.R. (2012) Temperature compensation in integrated CMOS-MEMS scanning probe microscopes. *Micro Nano Lett.*, 7 (4), 297.

66. N. Sarkar, R. Mansour, and K. Trainor (2012) Forced oscillation and higher harmonic detection in an integrated cmos-mems scanning probe microscope. Hilton Head Workshop 2012, Hilton Head Island, pp. 1–4.

67. Sarkar, N., Lee, G., and Mansour, R. (2013) CMOS-MEMS dynamic FM atomic force microscope. 2013 Transducers and Eurosensors XXVII: The 17th International Conference on Solid-State Sensors, Actuators and Microsystems (TRANSDUCERS & EUROSENSORS XXVII), IEEE.

68. Sarkar, N. and Mansour, R.R. (2014) Single-chip atomic force microscope with integrated Q-enhancement and isothermal scanning. 2014 IEEE 27th International Conference on Micro Electro Mechanical Systems (MEMS), pp. 789–792.

69. Sarkar, N. and Mansour, R. (2008) A CMOS-MEMS scanning probe microscope with integrated position sensors. 2008 1st Microsystems Nanoelectronics Research Conference, October 2008, pp. 77–80.

70. N. Sarkar, R. R. Mansour, and K. Trainor Forced oscillation and higher harmonic detection in an integrated CMOS-MEMS scanning probe microscope. Proceedings of Hilton Head Workshop, pp. 307–310, 2012.

71. Azizi, M., Sarkar, N., and Mansour, R.R. (2013) Single-chip CMOS-MEMS dual mode scanning microwave microscope. *IEEE Trans. Microwave Theory Tech.*, **61**, 4621–4629.

72. Sarkar, N. (2013) *Single-Chip Scanning Probe Microscopes*, University of Waterloo.

73. Lee, G. (2013) Design, fabrication and validation of a CMOS-MEMS kelvin probe force microscope. Master thesis. University of Waterloo.

10
Untethered Magnetic Micromanipulation

Eric Diller and Metin Sitti

The ability to manipulate small objects in remote spaces has emerged as a relevant but challenging task for microfluidics, biotechnology, and medical applications. Moving and studying individual cells in microfluidic environments, building three-dimensional (3D) assemblies in microfactories, and delivering therapeutic agents inside the human body are three areas of particular interest that are difficult to address with precision, speed, and flexibility using conventional manipulation techniques. Recent advances in remote actuation and control techniques have led to the development of mobile untethered microrobots that can move and interact with their environment at tiny size scales. Increased capabilities of these systems for precise motion, sensing, and the recent inclusion of simple on-board tools have resulted in devices that can manipulate objects in their environment with the precision and control expected from a robotic system. Moreover, mobile microrobots could be manufactured cost effectively in large numbers, which could enable distributed and parallel manipulation schemes.

In this chapter, we discuss the methods and state of the art in microscale manipulation in remote environments using untethered microrobotic devices. We focus on manipulation at the size scale of tens to hundreds of microns, where small size leads to a dominance of microscale physical effects and challenges in fabrication and actuation. To motivate the challenges of operating at this size scale, we first include coverage of the physical forces relevant to microrobot motion and manipulation below the millimeter-size scale. We then introduce the actuation methods commonly used in untethered manipulation schemes, with particular focus on magnetic actuation due to its wide use in the field. As manipulation techniques using these untethered microrobots are dependent on precise motion of microrobots through the environment, we provide details of magnetic field creation, magnetic actuation, and locomotion. We then cover notable examples of micromanipulation using untethered microrobotic agents. We divide these manipulation techniques into two types: contact manipulation, which relies on direct pushing or grasping of objects for motion, and noncontact manipulation, which relies indirectly on induced fluid flow from the microrobot motion to move objects without any direct contact. We conclude with a summary and prospects for future work in this field.

10.1
Physics of Micromanipulation

Here we discuss some of the physical forces acting on microdevices during object manipulation processes. All entities, regardless of size, experience the same physical forces and are governed by the same laws. However, the relative strength of physical effects can change dramatically with scale. Scaling down the size of an object isometrically with a characteristic size L would scale its surface area and volume with L^2 and L^3, respectively. This means that the surface-area-to-volume ratio increases at small length scales, and therefore surface area-related forces and dynamics dominate at the micro- or nanoscale. Here, we analyze some of the relevant physical forces acting on microscale objects, such as sliding friction, surface adhesion, and fluid drag effects. These forces will dictate some of the unique challenges in microscale manipulation and the constraints and opportunities in designing microrobotic devices to perform motion, grasping, and manipulation.

10.2
Sliding Friction and Surface Adhesion

10.2.1
Adhesion

Adhesion is defined as the pull-off force required to separate two surfaces in contact in a given environment, for example, air, liquid, or vacuum. Under ambient conditions, these forces can be due to van der Waals interactions, capillary effects, hydrogen bonding, covalent bonding, electrostatic charging, or Casimir forces [1]. Capillary forces can be very significant when there are fluid–fluid boundaries. Electrostatic effects are often small compared to van der Waals forces [2]. In this chapter, we give details on van der Waals interactions, because object manipulation is assumed to be under liquid, which minimizes capillary and electrostatic forces.

To determine the adhesive force between materials 1 and 2, the work of adhesion, W_{12}, must be determined for the pair utilizing their intrinsic surface energies γ_1 and γ_2 as [3, 4]

$$W_{12} = \gamma_1 + \gamma_2 - \gamma_{12} = 2\sqrt{\gamma_1\gamma_2}.$$

Adhesion modeling for micro- and nanoparticle manipulation is discussed in [3, 5, 6], where the Johnson–Kendall–Roberts (JKR), Derjaguin–Muller–Toporov (DMT), and Dugdale (D) models are the three main contact mechanics models at the micro- or nanoscale. To determine which of the three models is most appropriate to use, a dimensionless parameter λ, often called the *elasticity* , or

Tabor parameter, is introduced as

$$\lambda = \left(\frac{8 R_e W_{12}^2}{\pi h^3 K^2} \right)^{1/3}, \text{ where}$$

$$K = \frac{4}{3} \left(\frac{1 - \nu_1^2}{E_1} + \frac{1 - \nu_2^2}{E_2} \right)^{-1} \text{ and}$$

$$R_e = (R_1^{-1} + R_2^{-1})^{-1},$$

where R_e is the effective radius of contact of the two spherical objects of radii R_1 and R_2, $h = 0.165$ nm is a typical separation distance between the points of contact of the two materials' atoms, and K is the equivalent elastic modulus of contact, based on each material's Young's modulus (E_1 and E_2) and Poisson's ratio (ν_1 and ν_1) [4]. Values of several of these properties for different materials commonly seen in microrobotics can be found in [7]. The elasticity parameter λ is then used to determine the appropriate model to use as $\lambda < 0.6$ for DMT, $\lambda > 5$ for JKR, and the D model for intermediate λ values. The pull-off force for the DMT model ($\lambda < 0.6$) is given as

$$P_{DMT} = -2\pi R W_{12},$$

the pull-off force for the JKR model ($\lambda > 5$) is given as

$$P_{JKR} = -\frac{3}{2}\pi R W_{12},$$

and the pull-off force for the DMT model (intermediate λ) is given as

$$P_D = -\left(\frac{7}{4} - \frac{1}{4} \frac{4.04\lambda^{1/4} - 1}{4.04\lambda^{1/4} + 1} \right) \pi R W_{12}.$$

When immersed completely in a fluid, the capillary and electrostatic contributions to the pull-off force are reduced due to the lack of air–fluid interfaces and dispersion of electrical charges. The van der Waals, double layer, steric, hydrophobic, and other intermolecular forces in liquid will thus dominate and now will include fluid interaction forces [4]:

$$W_{132} = W_{12} + W_{33} - W_{13} - W_{23}.$$

Positive or negative total work of adhesion values W_{132} can result from different material and liquid layer combinations. Negative values imply that the two surfaces repel each other, whereby the surfaces minimize their energy by contacting the fluid, not each other. As an example of this case, a glass surface is used with polystyrene beads for manipulation in [8]. The range of immersed work of adhesion when immersed in water is -45 mJ m$^{-2} < W_{132} < -3.1$ mJ m^{-2}. As this range is assured to be negative, the adhesion is negative between these two surfaces. This repulsion can aid in object motion, as the motion will be governed primarily by fluid interactions. For irregularly shaped particles, the pull-off force will also be greatly reduced from its perfectly smooth value.

10.2.1.1 van der Waals Forces

van der Waals forces are due to instantaneous fluctuating dipole moments that act on nearby atoms within a material to generate an induced dipole moment. Dispersion (London) forces act on all molecules, and are quantum mechanical in origin. Orientation (Keesom) forces result from attraction between permanent dipoles, such as the case with water, and are negligible for nonpolar molecules. Induction (Debye) forces are between permanent and induced dipoles.

van der Waals forces always exist, and are considered long-range adhesive forces, acting at ranges of 0.2–20 nm. The forces between two identical materials are always attractive, but can be repulsive for certain cases involving different materials. Thus, the van der Waals force is an important consideration for microscale manipulation tasks.

For the case of an atomically smooth sphere–plane contact geometry, van der Waals forces can be modeled as

$$F_{\text{vdW}}(h) = -\frac{AR}{6h^2},$$

where R is the sphere radius, h is the sphere–plane separation distance, and A is the Hamaker constant. The Hamaker constant is found as

$$A = \pi^2 C \rho_1 \rho_2,$$

where C is the coefficient in the particle–particle pair interaction, and ρ_1 and ρ_2 are the number of atoms in the two interacting bodies per unit volume. Hamaker constants do not vary widely between different materials, and mostly lie in the range of $0.4–4 \times 10^{-19}$ J. Values for some materials can be found in [9]. Force relations for other contact geometries and additional details of van der Waals interactions are given in [4].

The Hamaker constant for disparate materials with constants A_1 and A_2 in contact can be found as

$$A_{12} = \sqrt{A_1 A_2}.$$

For two solids with constants A_1 and A_2 separated by a liquid with constant A_3, the Hamaker constant can be found as

$$A_{132} = \left(\sqrt{A_{11}} - \sqrt{A_{33}} \right) \left(\sqrt{A_{22}} - \sqrt{A_{33}} \right).$$

The relation of van der Waals force for very small separations can be investigated approximately using the Lennard–Jones potential, which is a simple model that predicts the change from attraction to repulsion at very small interatom spacings due to Pauli repulsion. The relation for two atoms separated by distance r_{s} is of the form

$$w(r_{\text{s}}) = -\frac{A_{\text{L}}}{r_{\text{s}}^6} + \frac{B_{\text{L}}}{r_{\text{s}}^{12}},$$

where w is the interaction potential and $A_{\text{L}} = 10^{-77}$ Jm^6 and $B_{\text{L}} = 10^{-134}$ Jm^{12} [4]. The interaction force using this potential can be computed as

$$F(r_{\text{s}}) = -\frac{dw(r_{\text{s}})}{dr_{\text{s}}}.$$

The van der Waals force is reduced by the surface roughness because the two rigid surfaces are locally further separated. Taking b_r as the root-mean-square roughness of two surfaces separated by distance h, the force is attenuated as [10]

$$F_{vdW, \, rough}(h); \; \left(\frac{h}{h + b_r/2} \right)^2 F_{vdW}(h),$$

where h is measured to the top of the surface roughness. Typical roughness values are approximately 2 nm for a polished silicon wafer, and 1 μm for a polished metal surface.

For micromanipulation of small objects, contact adhesion between the object and the manipulator is a common issue for part release. The preceding analysis can be used to identify some material property and surface geometry choices to minimize this adhesion to ensure repeatable and precise object release. Two major factors are the surface energy or Hamaker constant of the object and gripper and the area of contact between the two surfaces. While material choices are often limited due to the fabrication techniques used, addition of contact area reduction features, such as local surface roughness, can greatly reduce gripper–object adhesion [11].

10.2.2
Sliding Friction

Friction can play a large part in the behavior of micro-objects in contact with mobile microrobots, solid surfaces in the environment, or other micro-objects during part assembly. Friction at the macroscale is often modeled as being independent of interface contact area. However, at the microscale, friction can be adhesion-controlled or load-controlled. The friction can thus be both load and contact area dependent as

$$f = \tau_f A_f + \mu_f N,$$

where τ_f is the interfacial shear strength, A_f is the real contact area, μ_f is the coefficient of friction, and N is the normal load. The interfacial shear stress can be approximated as one-third of the effective interface shear modulus [12]. The real contact area is difficult to calculate, and may depend largely on the surface roughness. For relatively hard surfaces with low adhesion, that is, $\lambda < 0.6$, the contact area A_f can be found using the DMT model as [4]

$$A_f = \pi \left[\frac{R_s}{K} \left(L_w + 2\pi R_s W_{12} \right) \right]^{2/3},$$

where K is the interface stiffness and L_w is the vertical load on the sphere. For relatively soft surfaces with high adhesion, that is, $\lambda > 5$, the contact area is found as [4]

$$A_f = \pi \left[\frac{R_s}{K} \left(L_w + 3\pi R_s W_{12} + \sqrt{6\pi R_s W_{12} L_w + \left(3\pi R_s W_{12} \right)^2} \right) \right]^{2/3}.$$

The shear stress is thus

$$S = \frac{f}{A_f} = \tau_f + \mu_f \frac{N}{A_f}.$$

When two rough objects contact, the actual contact area is less than the apparent contact area because contact only occurs at certain asperity points. For cases when the normal contact force is dominated by adhesion, a common method to reduce friction is to reduce the contact area by adding small geometric features or ridges on surfaces in contact to serve as contact points with reduced contact area [13]. This is particularly important for micromanipulation tasks involving the release of objects in a precise position.

10.3
Fluid Dynamics Effects

Micromanipulation tasks are often conducted in a fluid medium. The motion of microrobots by any method thus is subject to fluid forces. In this section, we cover the governing equations of fluid mechanics, focusing on simplifications for motion at the microscale. Of particular interest for microrobot and micro-object manipulation, we introduce fluid drag relations for translating and rotating bodies.

Using the principles of conservation of momentum, a fluid flow is governed by pressure, viscous, and body (gravitational) forces. This balance of forces is assembled in the Navier–Stokes equation as

$$-\nabla P_f + \mu \nabla^2 u + \rho g = \rho \frac{Du}{Dt},$$

where P_f is the fluid pressure, μ is the fluid viscosity, u is the fluid velocity, ρ is the fluid density, and g is the acceleration due to gravity. Here, $\frac{Du}{Dt}$ refers to the material derivative of the fluid velocity. This governing equation assumes the liquid as a continuous, incompressible, Newtonian medium, and neglects effects such as Brownian motion. The continuum model of fluid mechanics is valid at all scales in the realm of microrobotics. Solutions to this equation, using appropriate fluid boundary conditions, give the fluid velocity vector field. In many applications, the gravitational (body) force term can be neglected, and we use a change of variables to analyze the relative magnitude of the remaining terms. Here, we use the nondimensional variables $u^* = u/u_\infty$ and $P_f^* = P_f L_c/\mu u_\infty$, and divide by $\mu u_\infty/L_c$ to isolate the terms on the left-hand side of the equation. Here, u_∞ is a characteristic velocity of the fluid (such as the free-stream velocity) and L_c is a characteristic length, such as an object dimension. Thus, we arrive at the nondimensional form of the Navier–Stokes equation as follows:

$$-\nabla P_f^* + \mu \nabla^2 u^* = \left(\frac{\rho u_\infty L_c}{\mu} \right) \frac{Du}{Dt}.$$

The term within parentheses on the right-hand side of this equation is known as the *Reynolds number* $Re = \rho u_\infty L_c / \mu$, and is often interpreted as the ratio of fluid inertial to viscous forces. Thus, when Re becomes small, viscous forces dominate over inertial forces, resulting in creeping flow (Stokes flow), and can be thus described by

$$\nabla P_f^* = \mu \nabla^2 u^*.$$

Fluid flow at the microscale, with small characteristic length L_c, is thus dominated by viscous forces. This flow would correspond to that seen at larger scales for low density, slow, or fast viscosity flows. Stokes flow has no dependence on time, and thus the solution for steady boundary conditions over all time only requires knowledge of the fluid state at a single time. In addition, the flow is time reversible. Thus reciprocal motions, where a motion and its opposite are repeated over time, will result in no net forces exerted on the fluid. This is known as the *Scallop theorem* [14], and is a notable difference when comparing microscale and larger scale swimming methods.

The Stokes flow equation can be solved exactly by finding the Green's function (here called a *stokeslet*), numerically by a boundary element method, or by experimental characterization. The solutions to several interesting cases are now given. These fluid flow solutions are used in modeling microrobot or micro-object motion through fluids as well as in studies of the fluid flow generated by moving microrobots for manipulation.

10.3.1
Viscous Drag on a Sphere

The fluid drag on any object at the microscale can be approximated by the drag on a sphere. As opposed to macroscale high-Re drag analysis, which includes multiple competing drag contributors such as viscous drag, form drag, and so on, Stokes flow drag is relatively simple, as it results only from viscous fluid forces. The drag force across a wide range of laminar flows can be found using the empirically derived Kahn–Richardson formulation for a sphere, F_{KR}, which is valid for a large range of small to moderate Reynolds numbers ($0 < Re < 10^5$) [15]. For small Re, this force can be simplified by using the viscous drag equation for a sphere at low Reynolds number [16], which provides results within 2.5% of the Kahn–Richardson model:

$$F_{drag} \approx 6\pi \mu R U,$$

where R is the radius of the sphere and U is the fluid velocity.

Thus, the fluid drag force on a sphere in the low-Re regime is proportional to the fluid viscosity, the sphere radius, and the fluid velocity. This simple model can also be applied approximately to nonspherical shapes using a sphere of equivalent radius.

10.4
Magnetic Microrobot Actuation

Actuation using magnetic fields has emerged as a leading method for mobile microrobotics. As compared with other driving methods, magnetic actuation can operate at a long distance using computer-controlled coils that are outside the operation workspace. This allows for a great deal of versatility in designing microrobotic systems.

For micromanipulation, a microrobot must be able to control its position and orientation in 2D or 3D space. Owing to its ability to penetrate most materials (including biological materials), a magnetic field is well suited to remotely power and control microrobots in inaccessible spaces. It is possible to independently apply magnetic forces and torques onto a magnetic microrobot using the magnetic field and its spatial gradient, leading to a wide range of microrobot design and actuation possibilities.

Magnetic forces and torques are applied to move a microrobot using fields created using magnetic coils or permanent magnets outside the workspace. The magnetic force $\vec{F}_m$ exerted on a microrobot with magnetic moment $\vec{m}$ in a magnetic field $\vec{B}$, assuming no electric current is flowing in the workspace, is given by

$$\vec{F}_m = (\vec{m}\cdot\nabla)\vec{B},$$

and the magnetic torque $\vec{T}_m$ is given by

$$\vec{T}_m = \vec{m} \times \vec{B}.$$

Thus, magnetic torques are generated from the magnitude and direction of the applied field, and they act to bring a magnetic moment into alignment with the applied field. Magnetic forces, however, are generated from the magnetic spatial field gradient, and operate on a magnetic moment in a less-intuitive manner. By controlling both the magnetic field and its gradients in the microrobot workspace, it is possible to provide independent magnetic torques and forces.

10.5
Locomotion Techniques

Motion of microrobots for manipulation tasks requires precision and accuracy. Most of the manipulation methods described in this chapter depend directly on the path of the microrobot in two or three dimensions to move objects. Thus, locomotion techniques must overcome environmental factors such as high adhesion and friction, viscous drag, and other disturbances for repeatable micro-object manipulation. We introduce several methods for motion that are used in manipulation and transport of micro-objects, and are still the subject of active research.

10.5.1
Motion in Two Dimensions

Approaches to crawling or walking on 2D surfaces use a combination of magnetic gradient pulling forces, induced torques, and internal deflections to achieve translation across a 2D surface. While magnetic forces can be used to move microrobots, such forces are relatively weak compared with those resulting from magnetic torques [17]. Thus, many actuation methods make use of strong magnetic torques for crawling in two dimensions. One major challenge addressed in these designs is overcoming high surface friction and adhesion. Many designs use oscillatory motions to interrupt adhesion contact with the substrate to achieve repeatable and constant motion. A few examples here illustrate the methods in the literature that overcome these challenges for motion and manipulation tasks.

The MagMite system [18] uses low-strength, high-frequency fields to excite a resonant microrobot structure for smooth crawling motion. Speeds of tens of millimeters per second are achieved in an air environment, and lower speeds in liquid. The $300\,\mu\text{m} \times 300\,\mu\text{m} \times 70\,\mu\text{m}$ microrobot consists of two magnetic masses, which are free to vibrate relative to each other, connected by a meandering microfabricated spring. Oscillations at high frequency help to periodically break the friction and adhesion with the surface. Because of the small size of the microrobot, the resonant frequency of this oscillation is several kilohertz. The MagMite is steered by applying a small DC field that orients the entire microrobot in the plane.

A thin microrobot can be driven by the magnetostrictive response of certain materials. Magnetostriction is the internal realization of magnetic field-induced stress, analogous to the piezoelectric effect, which is induced by electric field. By driving with a 6 kHz pulsed magnetic field, a steady walking motion is achieved, with stated velocities up to $75\,\text{mm s}^{-1}$ achieved in the Mobile Microrobotics Challenge (reviewed at the end of this chapter) in 2010 [19]. Using controlled gradient fields, limited 2D path following is also achieved with this method.

A magnetic torque-based approach has been implemented, which allows for a simple magnetic microrobot to translate using stick-slip actuation, termed the *Mag-µBot system* [20]. One major advantage is that the pulsed stepping motion results in small steps with a known step size. By regulating the pulsing frequency and angle sweep of each step, step sizes can be reduced to several microns. In addition, the microrobot can be driven using large steps in conjunction with magnetic field gradients at speeds of several hundred millimeters per second, albeit with less-precision control capability. A similar approach has also been used in [21] at a smaller length scale down to tens of microns.

10.5.2
Motion in Three Dimensions

Microrobots moving in three dimensions must rely on swimming forces or externally generated pulling forces, such as those created from a magnetic field gradient. Swimming in low-*Re* environments requires methods different

from large-scale swimming. Since the first published in-depth study of the fluid mechanics of such swimming in 1951 [22], many fluid dynamics studies have been conducted to understand these propulsion styles, as reviewed in [23]. In helical swimming, propulsion is generated by a rotary motion. The fluid mechanics of such helical swimming devices has been studied in depth, and the reader is referred to [24, 25] for a full review. In short, torque is generated in microrobotic helical swimmers using a magnetic head or tail and a uniform rotating magnetic field. The tail of such a swimmer is typically fabricated to be stiff, and can be formed using stress-engineered curling thin films [26], wound wire [27], by glancing angle deposition [28], or microstereolithography [29], among others.

Manipulating a rigid-body magnetic microrobot in 3D levitation requires a high level of control. This has been accomplished with a set of electromagnetic coils arranged around the workspace, which can simultaneously control the field and field gradient directions. Building on the work of Meeker *et al.* [30], a system capable of manipulating microscale robots uses eight independently controlled electromagnets, dubbed the OctoMag system. Such a system can achieve 5-degree-of-freedom (DOF) control of a simple magnetic microrobot for levitation in liquid. The sixth DOF, rotation about the magnetization vector, has only been demonstrated for special arrangements of magnets on the microrobot device [31]. In the OctoMag system, precise 3D position and 2-DOF orientation control of soft magnetic or permanent microrobots is demonstrated in a workspace of several centimeters, in a high-viscosity silicone oil.

10.5.3
Magnetic Actuation Systems

Magnetic fields for actuating magnetic microrobots are typically supplied by magnetic coils next to or surrounding the microrobot workspace. As compared with permanent magnets, electromagnetic coils have the advantage that they can deliver varying fields with no moving parts, and can be designed in a variety of ways to create spatially uniform magnetic fields and gradients to create a large workspace.

Magnetic coils are often designed to surround all or part of the microrobot workspace. The field created is assumed to be proportional to the current through the coils, an assumption valid if there are no nearby materials with nonlinear magnetization hysteresis characteristics.

The magnetic field produced by a cylindrical coil is found by applying the Biot–Savart law for each turn over the path S as [32]

$$\vec{B} = \frac{\mu_0 N_t I}{4\pi} \int_S \frac{d\vec{l} \times \vec{a}_R}{|\vec{r}|^2},$$

where $\vec{B}$ is the magnetic field at the microrobot's position due to the electromagnets, N_t is the number of wire turns in the coil, $d\vec{l}$ is an infinitesimal line segment along the direction of integration, $\vec{a}_R$ is the unit vector from the line segment to

the point in space of interest, and $|\vec{r}|$ is the distance from the line segment to the point of interest. The field from multiple field sources can be added linearly to determine the total field (assuming the workspace is free from soft magnetic materials).

10.5.4
Special Coil Arrangements

By pairing two coils along a single direction, a condition of high spatial field or gradient uniformity can be obtained. Thus, the field can be assumed to be constant in magnitude and direction in the workspace. To maximize the area of field uniformity using such a coil pair, a Helmholtz configuration is used, where the space between the two parallel coils is equal to the coil radius [33]. By driving both coils equally in the same direction, a large region of uniform field is created between the two.

To maximize the area of field gradient uniformity, a Maxwell configuration is used, where the space between the two parallel coils is $\sqrt{2/3}$ times the coil radius and the coils are driven in equal but opposite directions. Maxwell and Helmholtz coil pairs can be used together to achieve uniform fields and gradients in one workspace.

Alternative coil configurations have some advantages over Helmholtz or Maxwell configurations, such as an increased level of controllable microrobot DOFs, at the expense of field uniformity [34]. To calculate the fields and gradients created from a general coil system, we can use the following relations:

$$\vec{B} = \boldsymbol{B}\vec{I}$$

$$\frac{\partial \vec{B}}{\partial x} = \boldsymbol{B}_x \vec{I}\,; \qquad \frac{\partial \vec{B}}{\partial y} = \boldsymbol{B}_y \vec{I}\,; \qquad \frac{\partial \vec{B}}{\partial z} = \boldsymbol{B}_z \vec{I}\,,$$

where each element of $\vec{I}$ is current through each of the c coils, $\boldsymbol{B}$ is a $3 \times c$ matrix mapping these coil currents to the magnetic field vector $\vec{B}$, and $\boldsymbol{B}_x$, $\boldsymbol{B}_y$, $\boldsymbol{B}_z$ are the $3 \times c$ matrices mapping the coil currents to the magnetic field spatial gradients in the x, y, and z directions, respectively. These mapping matrices are calculated for a given coil arrangement using the equations before or by treating the coils as magnetic dipoles in space and are calibrated through workspace measurements as outlined in [30, 34].

Thus, using the aforementioned equations for a desired field and force on a single magnetic microrobot, we arrive at

$$\begin{bmatrix} \vec{B} \\ \vec{F} \end{bmatrix} = \begin{bmatrix} \boldsymbol{B} \\ \vec{m}^{\mathrm{T}} \boldsymbol{B}_x \\ \vec{m}^{\mathrm{T}} \boldsymbol{B}_y \\ \vec{m}^{\mathrm{T}} \boldsymbol{B}_z \end{bmatrix} \vec{I} = \boldsymbol{A}\vec{I}\,,$$

where A is the $6 \times c$ matrix mapping the coil currents $\vec{I}$ to the field $\vec{B}$ and force $\vec{F}$. The equation can be solved if A is full rank, that is, the number of coils c is greater than or equal to six. The solution can be accomplished for $c < 6$ through the pseudo-inverse, which finds the solution that minimizes the two-norm of $\vec{I}$ as

$$\vec{I} = A^+ \begin{bmatrix} \vec{B} \\ \vec{F} \end{bmatrix}.$$

If $c < 6$, then the solution will be a least-squares approximation. Having greater than six coils leads to a better-conditioned A matrix, which means a more isotropic workspace, reduction of singularity configurations, and lower coil current requirements. Systems designed to create such arbitrary 3D forces and torques have been created with six or eight coils arranged around the workspace in a packed configuration, first shown in [30] for manipulation of magnetic seeds in the brain and more recently for microrobot actuation (the OctoMag system) in [34]. The OctoMag system is designed to provide easy access to one face, so all coils are on one side of the workspace. Another system with a set of eight coils completely surrounding the microrobot workspace is shown in Figure 10.1. The distance of each coil to the center of the workspace is the same for all coils, and they are arranged along the vertices of a cube, with the four lower coils rotated 45° about the z-axis to break symmetry (which would result in a singular A matrix).
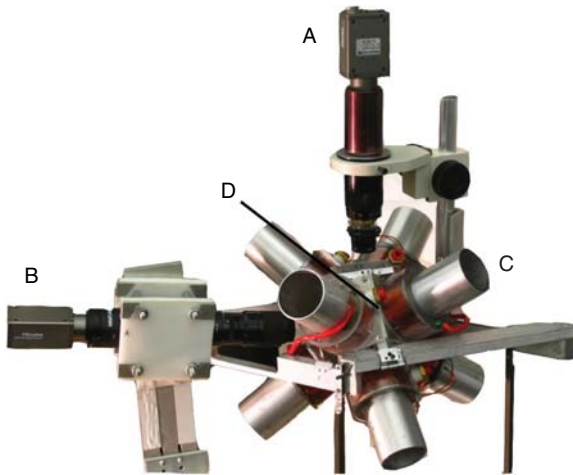
Figure 10.1 Eight-coil system, capable of applying 5-DOF magnetic force and torque in a several-centimeter-sized workspace. This system is capable of applying fields of strength 25 mT and field gradients up to 1 T m^{-1} using optional iron cores. (A) Top camera. (B) Side camera. (C) Magnetic coils. (D) Workspace. (Reprinted by Permission of SAGE from Ref. [7].)

**10.6
Manipulation Techniques**

Manipulation of microscale objects by mobile microrobots can be classified into two categories. The first method involves moving an object through direct contact. This could include pushing or grasping in two or three dimensions, and can be executed by nearly any microrobot which can move through its environment. The second method moves objects without directly touching them by using induced fluid flows in the environment. By translating or rotating in a fluid medium, a boundary layer of moving fluid will be developed, which can be used to move objects through fluid drag. This second method potentially offers unique capabilities for manipulating fragile objects over long distances, with high precision. The two classes of micromanipulation are illustrated in Figure 10.2.

10.6.1
Contact Micromanipulation

Contact-based manipulation uses direct pushing of an object to move it. As a simple and intuitive method, it can be implemented by nearly any type of mobile microrobot that moves in two or three dimensions, as shown schematically in Figure 10.2a.

10.6.1.1 **Direct Pushing**
The simplest method is to use a microrobot with a blunt or concave face to push an object. A simple example of this type of manipulation is shown in Figure 10.3, where a magnetic microrobot moving in two dimensions is shown to push plastic

(a) Contact manipulation   (b) Non-contact manipulation
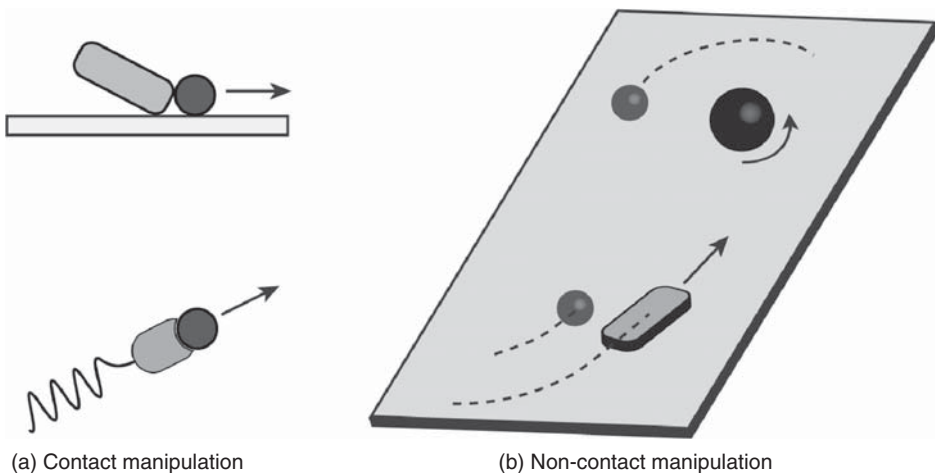
Figure 10.2 Manipulation techniques. (a) Contact manipulation in two or three dimensions relies on direct pushing of an object. (b) Noncontact manipulation using rotating or translating microrobots relies on secondary fluid effects to move objects.
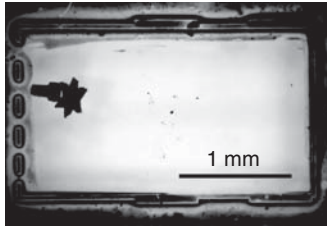
Figure 10.3 Direct-contact manipulation using a star-shaped microrobot pushing pegs into gaps in the wall in a 2D assembly demonstration. The environment is SU-8 photoresist polymer walls on a silicon substrate. The microrobot size is 500 μm.

peg-shaped objects in a simple-assembly experiment. In this case, the microrobot geometry is designed with special guiding features to aid the pushing procedure. A star shape is chosen to trap an object of arbitrary geometry as it is pushed, allowing for robust manipulation over long distances. The design is also symmetric, allowing the microrobot to manipulate objects by moving forward or backward, giving additional versatility.

The ability for a microrobot to push an object, and the speed with which it pushes, depend on the pushing force of the microrobot, the object surface contact friction, and fluid drag effects. Figure 10.4 shows the forces acting on a mobile magnetic microrobot pushing a spherical object. Here, the microrobot is moved using magnetic forces and torques, and the motion is hindered by fluid drag and contact friction with the substrate, as well as by the contact force with the microsphere. Depending on the operating environment, contact friction and adhesion with the substrate can dominate the behavior of the system. This effect is even more pronounced as the size scale is reduced. Operation in liquid environments greatly reduces the magnitude of the adhesion force, resulting in far more reliable and repeatable operation.

While the forces acting during this type of contact manipulation are numerous, one easily controlled method to regulate the object pushing speed is through the use of varying microrobot force during pushing. This was investigated for a rectilinear magnetic microrobot pushing millimeter-scale hydrogel blocks on an acrylic surface in water, as shown in Figure 10.5. Here, the microrobot moves by
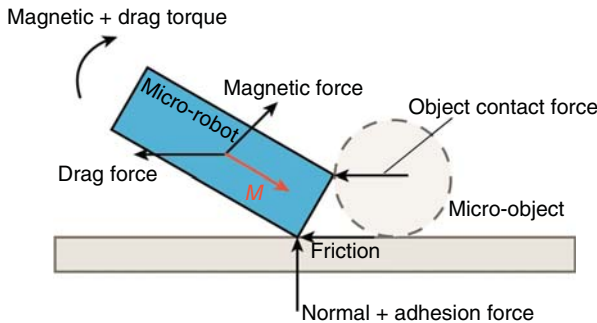
Figure 10.4 Free body diagram of a mobile magnetic microrobot with magnetization M pushing a spherical object on a flat substrate. Magnetic, fluid drag, and contact forces act on the microrobot to determine its motion during the pushing operation.
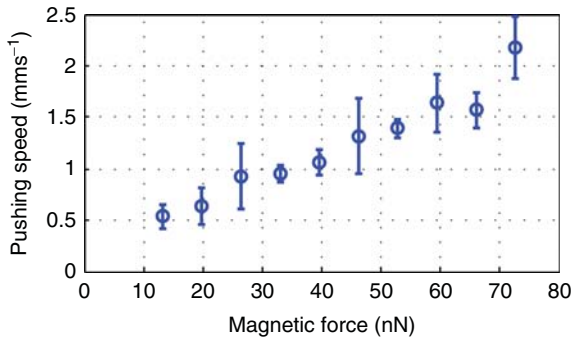
Figure 10.5 Contact manipulation speed as a function of the magnetic pulling force exerted on the microrobot. Microrobot size is 1 mm × 1 mm × 0.3 mm, and gel size is 1 mm × 1 mm × 0.15 mm. The microrobot moves through a periodic sawtooth waveform of magnetic field which periodically breaks surface friction. (Reprinted from Ref. [35] with permission.)

stick-slip crawling with an additional magnetic pulling force, which is varied. The average microgel pushing speed is plotted, and is shown to increase roughly linearly with magnetic force, indicating that the pushing is dominated by this applied magnetic force, and is dragged by fluid drag and friction, which are proportional to the speed. Such results indicate that the manipulation can be easily controlled and served under computer control, using the applied magnetic force as a regulating input to the system.

Some useful applications of direct manipulation have been investigated. In Figure 10.6, a magnetic microrobot is seen to have manipulated a number of colored microgels into a close-fitting array in two dimensions. In this experiment, air bubbles are seen attached to the microrobot, the substrate, and the microgels. Care must be taken to avoid contact between the air bubble and two solid surfaces due to the capillary forces that will form at the interface. This experiment demonstrates the ability to perform precision manipulation and assembly with teleoperated mobile microrobots.

An example of direct-contact manipulation using biological materials is shown in Figure 10.7. Here, cell-laden microgels are patterned into 2D and layered 3D assemblies. Multiple gel geometries and cell types are manipulated in the same assembly, showing the capability for programmable assembly of arbitrary cell
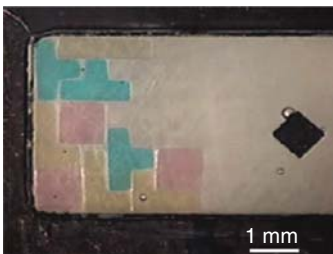
Figure 10.6 Magnetic microrobot assembly of hydrogel blocks into an ordered array in two dimensions. The microrobot is the black square on the right, and the assembly area is framed by a Poly(methyl methacrylate) (PMMA) wall 300 μm in height.
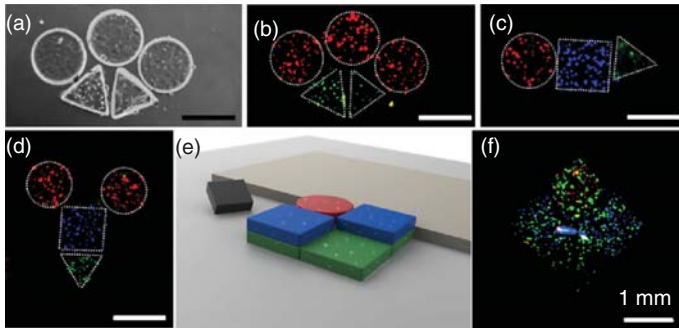
Figure 10.7 Assembly of cell-encapsulating microgels in two and three dimensions. (a) Optical image of five microgels assembled by mobile microrobot in a fluid environment. (b–d) Fluorescent microscope images of the assembled structures. (e,f) Cartoon schematic and fluorescent microscope image of a layered 3D microgel assembly. (Adapted from Ref. [35] with permission.)

types. This example with multiple cell types patterned into arbitrary patterns could be used for tissue engineering, cell interaction, or pharmaceutical study.

To extend contact pushing to true 3D motion, a more controlled microrobot–object contact geometry is needed. The cage-like manipulator shown on a helical swimming robot in Figure 10.8 enables such motion. Here, a swimming helical microrobot is shown to pick up spherical objects and carry them in three dimensions to a target location. This type of manipulation allows for long-range transport and release of objects through any arbitrary fluid medium. Transport is highly robust to disturbances as the object being carried is fully caged on the front of the microrobot. Release is performed by swimming the microrobot backward. Fluid flow then pushes the object out from the cage, allowing for rough placement of objects near a target location.

10.6.1.2 Grasping Manipulation

To achieve greater control over object motion and orientation, the part can be grasped. Such grasping will allow for dexterity in manipulation, robust cargo transport, and precision part assembly. Tethered microgrippers are commonly used for grasping microscale objects, but do not allow for access to remote spaces such as inside microfluidic channels. A method to achieve untethered gripping is shown in Figure 10.9, featuring a magnetically driven gripping motion, based on patterned magnetization of the gripping arm tips. The design can be moved as a mobile microrobot using weak applied fields and field gradients, and is opened and closed by large applied fields as shown. This device relies on flexible materials and patterned magnetization to achieve a simple design with advanced functionality.

As a demonstration of the capabilities of such a gripper for manipulation and assembly of millimeter-scale components, a simple-assembly task is shown in Figure 10.10. Additional assembly demonstrations are given in [37]. In these
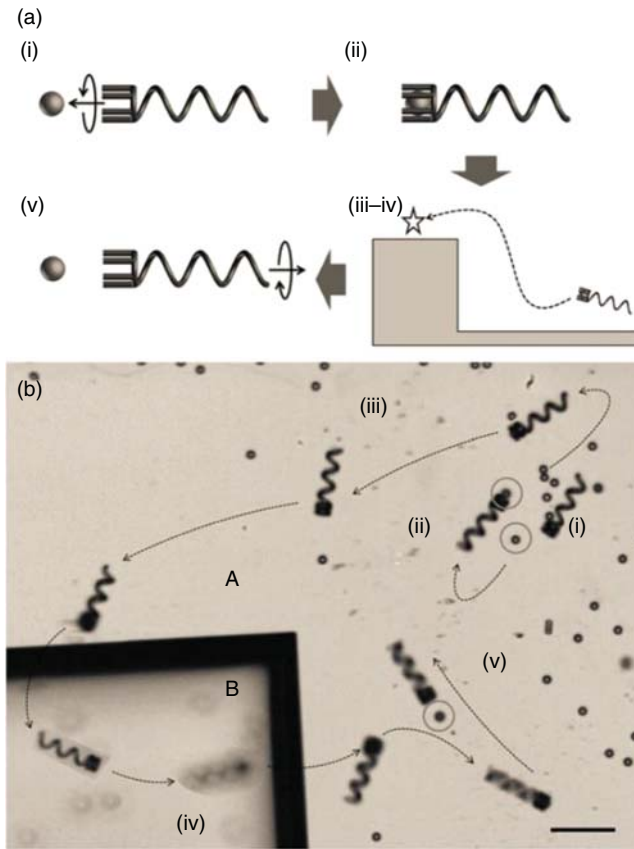
Figure 10.8   Cage-like manipulator on a helical swimming microrobot. (a) Here, the microrobot is shown to approach an object and pick it up for motion in three dimensions. Release is accomplished by reversing directions. (b) Experimental demonstration. Scale bar is 50 μm. (Reprinted from Ref. [36] with permission from John Wiley and sons.)

assembly examples, high adhesion between the gripper and the objects to be grasped is avoided by operating in a liquid environment.

Other untethered grasping microrobots have been demonstrated, actuated by chemical reactions or temperature change [38, 39], showing potential for targeted drug delivery using magnetic motion.

10.6.2
Noncontact Manipulation

A second method of manipulation uses fluid drag as a secondary effect from microrobot motion to move an object. In low-*Re* environments commonly seen by mobile microrobots, the fluid flow is viscous in nature and can move objects in a robust and consistent manner. Such manipulation is termed   *noncontact*
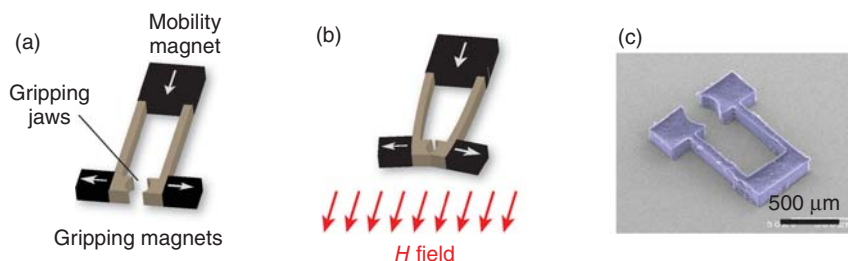
Figure 10.9 (a) Schematic showing the operation of gripping mobile microrobots. (b) Magnets on the tips of the long arms allow the gripping jaws to open and close in an applied *H* field. The gripper can be moved like a mobile microrobot using low-strength fields and gradients which act on the "mobility magnet." (c) image of a fabricated gripper. (Portions adapted from Ref. [37]. Reprinted with permission from Wiley-VCH.)
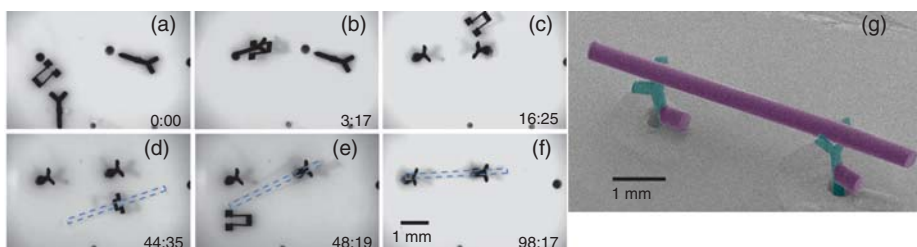
Figure 10.10 Manual assembly of out-of-plane 3D parts by a mobile microgripper. (a–c) The mobile gripper picks up parts lying on the substrate and inserts them vertically into holes in the substrate. (d–f) The gripper places a nylon rod across the top of the two posts to complete the assembly. (g) SEM (scanning electron microscopy) image of the completed three-part out-of-plane structure. Times during the experiment are shown in minutes:seconds. (Portions adapted from Refs. [37]. Reprinted with permission from Wiley-VCH.)

fluid-based manipulation. Microrobots can induce fluid flow in their surroundings by translating or rotating. These motions can be independent of, or coupled to, the microrobot motion through the environment in a manner which allows for controlled manipulation and transport of objects over long distances with a high level of precision.

10.6.2.1 Translation

Microrobots moving along a straight line by any motion method will drag fluid along with them as a boundary layer. The boundary layer for a typical 250-µm magnetic microrobot translating on a flat surface is shown in Figure 10.11.

An image of this type of noncontact manipulation using a magnetic microrobot translating on a flat surface is shown in Figure 10.12. Here, a polystyrene microsphere is moved a distance D_s when the microrobot translates nearby.

The distance D_s moved during this process is determined by how close the microrobot moves to the micro-object. Such a relationship is explored in Figure 10.13, where the manipulation distance D_s is compared with the
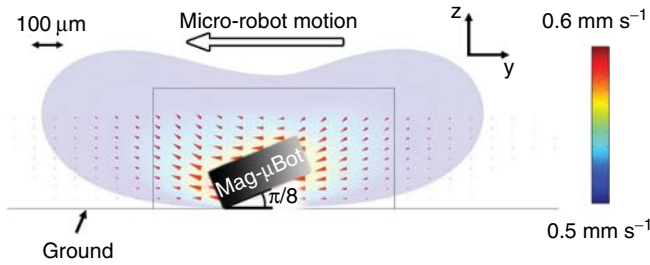
Figure 10.11 Fluid boundary layer analysis of a translating magnetic microrobot, calculated using finite element modeling (FEM). (From Ref. [40].) The image shows a side view of the fluid field as the microrobot moves to the left at an inclined angle from the surface to simulate the operational stance of the crawling microrobot. Arrows show fluid flow in the analysis plane, and background color indicates the fluid velocity. Fluid flow is analyzed using COMSOL Multiphysics (COMSOL Inc.). (Reprinted with permission of IEEE.)
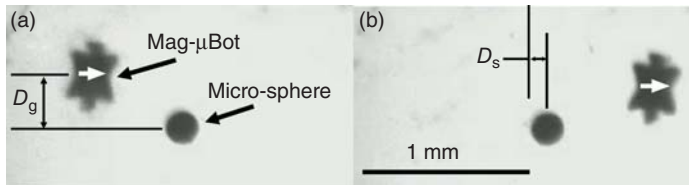
Figure 10.12 Noncontact fluid-based manipulation of a spherical polystyrene object by a star-shaped microrobot translating under magnetic control. The arrow on the microrobot indicates the microrobot magnetization and motion direction. (a) Micro-robot approaches the sphere. (b) Movement of the sphere after the microrobot has passed. (Reprinted from Ref. [40] with permission of IEEE.)

robot−object gap distance D_g. Here, simulation results use the flow field from Figure 10.11 and a Runge−Kutta solver (ODE23s in MATLAB, Mathworks, Inc.) to calculate the object trajectory as the microrobot moves by. Close experimental and simulation results are seen, due to the relatively simple and time-independent nature of low-Re fluid flows.

10.6.2.2 Rotation

Rotating microrobots can induce a fluid flow of high speed for object manipulation. By combining spinning and rolling motions, mobile microrobots can translate through the environment while inducing rotatory flow fields for manipulation. Three examples of spinning and rolling microrobots are shown in Figure 10.14. Here, the induced fluid flow causes objects to be trapped nearby the microrobot as it moves over large distances. Here, the objects can be robustly dragged over arbitrary paths in two dimensions and deposited at a goal location. The final pane of the figure shows the manipulation of bacteria by a small magnetic microrobot, exhibiting the capabilities of this type of manipulation for
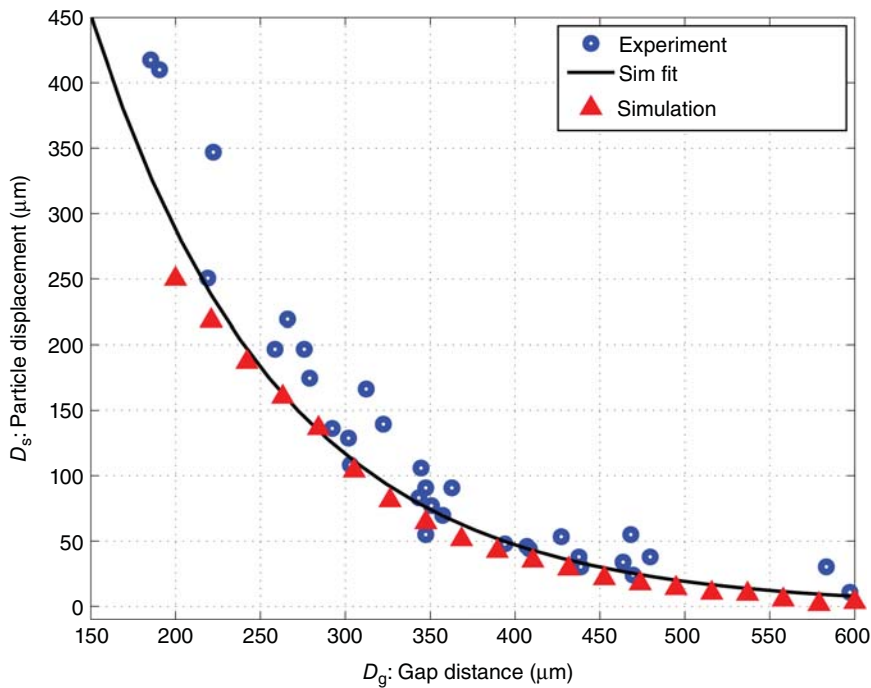
Figure 10.13 Particle displacement D_s induced by a translating microrobot, which comes within a horizontal gap of size D_g of the object. (From Ref. [40].) Simulation and experimental results are from a star-shaped microrobot pushing a 210-μm microsphere. (Reprinted with permission of IEEE.)
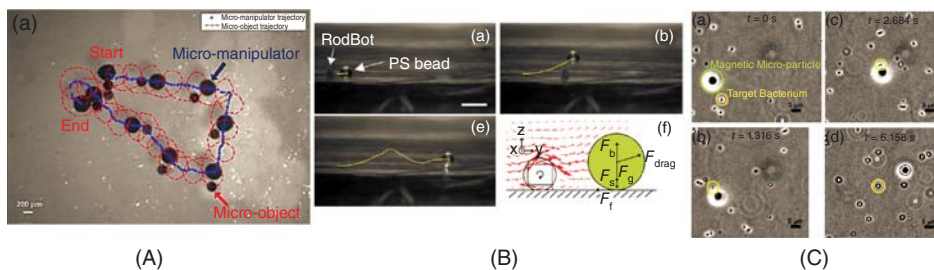
Figure 10.14 Noncontact manipulation examples. (A) A spherical magnetic microrobot manipulator is shown to carry an object in a circular orbit as it translates along the substrate by rolling. The object can be dropped at a target location by rolling the manipulator away at low speed. (From Ref. [41]. Reprinted with permission of AIP.) (B) Out-of-plane manipulation of an object by "RodBot," a magnetic manipulator. RodBot can pull objects along a unique 3D trajectory by rolling along the surface. (From Ref. [42] RodBot has also been used to perform automated protein crystal harvesting in three dimensions [43]. Republished with permission of AIP Publishing LLC.) (C) A spherical magnetic manipulator is shown to manipulate individual and groups of living cells in two dimensions. (Reproduced from Ref. [44] with permission from The Royal Society of Chemistry.)
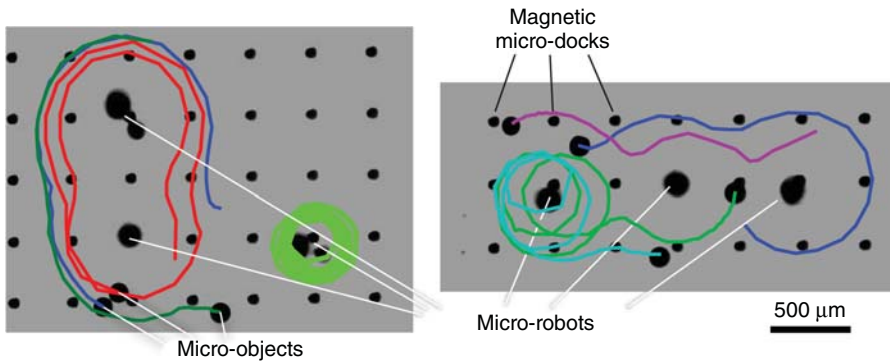
Figure 10.15   Multiple objects are manipulated using a team of three microrobots which rotate in place. The fluid flow fields generated by multiple nearby microrobots form more complex geometry depending on the microrobot arrangement. Microrobot positions are fixed on magnetic traps built in the substrate, to allow for parallel operation without independent magnetic control. (From Ref. [41]. Reprinted with permission of AIP.)

the transport of biological entities. Noncontact manipulation could be preferable for the manipulation of bacteria or individual cells due to its low-impact nature, which could prevent cell damage.

10.6.2.3   Parallel Manipulation

The benefits of using rotary microrobot motion for noncontact manipulation can be extended through the use of teams of multiple microrobots in parallel. This scheme, as shown in Figure 10.15, allows for the manipulation of objects over larger distances along a desired path. In this example, microrobots are "docked" at prescribed locations on the substrate using magnetic traps embedded in the surface. This allows a uniform magnetic field to drive all microrobots in parallel. By changing the position of the microrobots on the docks, the manipulation paths can be changed. The use of many microrobots in parallel could thus lead to reconfigurable virtual fluid channels for long-range transportation of objects in fluidic environments.

10.6.3
Mobile Microrobotics Competition

The state of the art of micromanipulation using untethered microrobotic devices has been advanced greatly in recent years. Much of this success is due to a large increase in the number of research groups around the world focusing on this challenging problem. One significant contributor to the increased interest is the Mobile Microrobotics Challenge event held annually since 2007. First sponsored by the US National Institute for Standards and Technology (NIST) and held at the RoboCup robotic soccer competition as the RoboCup Nanogram Demonstration Competition, the event has been continued under independent

sponsorship supported by the US National Science Foundation. The event is now held yearly at the International Conference on Robotics and Automation, and has been very successful at attracting both experienced and new research groups to the field for friendly competition. Of particular note is the involvement of both undergraduate- and graduate-level students representing both student groups and more formal research groups.

One of the events in the competition since its inception has involved the manipulation of an object or objects in a 2D confined environment. Microrobots, under $500\,\mu m$ in size, may be driven by any remote actuation method, and the competition has seen electrostatic, electrowetting, magnetic, optothermal approaches used, among others. Many new ideas have been demonstrated at the competition to accomplish these challenges, which have increased in difficulty over the course of the competition.

10.7
Conclusions and Prospects

This chapter has provided an overview of the scale-dependent physics, actuation techniques, and manipulation techniques used for the manipulation of microscale objects using untethered microrobotic devices. We showed the state of the art in manipulation of objects in two and three dimensions using microrobots, which move and grasp using a variety of methods for precision pushing, grasping, transport, and assembly of objects in remote confined spaces. Direct contact-based manipulation has shown its advantages for simple and intuitive manipulation in two or three dimensions, and can allow for dexterous manipulation of objects using grasping manipulators. Noncontact manipulation has also emerged as a flexible, gentle, and fast manipulation method for object transport and positioning tasks with low risk of object damage from contact.

Future work in untethered micromanipulation will increase the dexterity and precision of manipulation. The creation of more complex assemblies of parts for microfluidic, microfactory, or potential medical applications will require fast grasping and release of objects with full 6-DOF motion capability, in addition to automated feedback control. The potential for parallel manipulation using teams of mobile microrobots working as a team should be leveraged to increase throughput of an object transport or assembly task, and to take advantage of heterogeneous microrobot teams consisting of unique individuals designed for a specific manipulation or assembly task.

Progress in the field will be gauged by speed, precision, and capability. Manipulation of arbitrary objects (referring to both geometry and material) will be increasingly important for applications where functional microassemblies are required. Events such as the yearly Mobile Microrobotics Competition will help to disseminate results, standardize challenging manipulation and assembly tasks, and motivate the field.

References

1. Fearing, R. (1995) Survey of sticking effects for micro parts handling. IEEE/RSJ International Conference on Intelligent Robots and Systems, pp. 212–217.

2. Arai, F., Ando, D., Fukuda, T., Nonoda, Y., and Oota, T. (1995) Micro Manipulation Based on Micro Physics – Strategy Based on Attractive Force Reduction and Stress Measurement, in *IEEE/RSJ International Conference on Intelligent Robots and Systems*, vol. **2**, pp. 236–241.

3. Gauthier, M., Regnier, S., Rougeot, P., and Chaillet, N. (2006) Forces analysis for micromanipulations in dry and liquid media. *J. Micromechatron.*, **3** (3-4), 389–413.

4. Israelachivili, J. (1992) *Intermolecular and Surface Forces*, Academic Press.

5. Sitti, M. and Hashimoto, H. (2003) Teleoperated touch feedback from the surfaces at the nanoscale: modeling and experiments. *IEEE/ASME Trans. Mechatron.*, **8** (2), 287–298.

6. Maugis, D. (1992) Adhesion of spheres: the JKR-DMT transition using a Dugdale model. *J. Colloid Interface Sci.*, **150** (1), 243–269.

7. Diller, E., Giltinan, J., and Sitti, M. (2013) Independent control of multiple magnetic microrobots in three dimensions. *Int. J. Rob. Res.*, **32** (5), 614–631.

8. Floyd, S., Sitti, M., and Pawashe, C. (2009) Two-dimensional contact and non-contact micro-manipulation in liquid using an untethered mobile magnetic micro-robot. *Trans. Rob.*, **25** (6), 1332–1342.

9. Diller, E. and Sitti, M. (2013) Microscale mobile robotics. *Found. Trends Rob.*, **2** (3), 143–259.

10. Sitti, M. and Hashimoto, H. (2000) Controlled pushing of nanoparticles: modeling and experiments. *IEEE/ASME Trans. Mechatron.*, **5** (2), 199–211.

11. Arai, F., Fukuda, T., Iwata, H., and Itoigawa, K. (1996) Integrated micro endeffector for dexterous micromanipulation. Proceedings of the Seventh International Symposium on Micro Machine and Human Science, pp. 149–156.

12. Sümer, B. and Sitti, M. (2008) Rolling and spinning friction characterization of fine particles using lateral force microscopy based contact pushing. *J. Adhes. Sci. Technol.*, **22** (5), 481–506.

13. Hagiwara, M., Kawahara, T., Iijima, T., and Arai, F. (2013) High-speed magnetic microrobot actuation in a microfluidic chip by a fine V-groove surface. *Trans. Rob.*, **29** (2), 363–372.

14. Purcell, E. (1977) Life at low Reynolds number. *Am. J. Phys*, **45** (1), 3–11.

15. Richardson, J. and Harker, J. (2002) *Chemical Engineering*, vol. **2**, 5th edn, Butterworth and Heinemann.

16. Munson, B., Young, D., and Okiishi, T. (2002) *Fundamentals of Fluid Mechanics*, 4th edn, John Wiley & Sons, Inc.

17. Cugat, O., Delamare, J., and Reyne, G. (2003) Magnetic micro-actuators and systems (MAGMAS). *IEEE Trans. Magn.*, **39** (6), 3607–3612.

18. Frutiger, D.R., Vollmers, K., Kratochvil, B.E., and Nelson, B.J. (2009) Small, fast, and under control: wireless resonant magnetic micro-agents. *Int. J. Rob. Res.*, **29** (5), 613–636.

19. Jing, W., Chen, X., Lyttle, S., and Z. Fu (2011) A magnetic thin film microrobot with two operating modes. International Conference on Robotics and Automation, pp. 96–101.

20. Pawashe, C., Floyd, S., and Sitti, M. (2009) Modeling and experimental characterization of an untethered magnetic micro-robot. *Int. J. Rob. Res.*, **28** (8), 1077–1094.

21. Sakar, M. and Steager, E. (2011) Wireless manipulation of single cells using magnetic microtransporters. International Conference on Robotics and Automation, pp. 2668–2673.

22. Taylor, G. (1951) Analysis of the swimming of microscopic organisms. *Proc. R. Soc. A: Math. Phys. Eng. Sci.*, **209** (1099), 447–461.

23. Lauga, E. and Powers, T.R. (2009) The hydrodynamics of swimming microorganisms. *Rep. Prog. Phys.*, **72** (9), 096601.

24. Peyer, K.E., Tottori, S., Qiu, F., Zhang, L., and Nelson, B.J. (2013) Magnetic

helical micromachines. *Chemistry*, **19** (1), 28–38.

25. Peyer, K.E., Zhang, L., and Nelson, B.J. (2013) Bio-inspired magnetic swimming microroobts for biomedical applications. *Nanoscale*, **5**, 1259–1272.

26. Zhang, L., Abbott, J.J., Dong, L., Kratochvil, B.E., Bell, D. and Nelson, B.J. (2009) Artificial bacterial flagella: fabrication and magnetic control. *Appl. Phys. Lett.*, **94**, 064107.

27. Honda, T., Arai, K.I., and Ishiyama, K. (1996) Micro swimming mechanisms propelled by external magnetic fields. *IEEE Trans. Magn.*, **32** (5), 5085–5087.

28. Ghosh, A. and Fischer, P. (2009) Controlled propulsion of artificial magnetic nanostructured propellers. *Nano Lett.*, **9** (6), 2243–2245.

29. M. Yasui, M. Ikeuchi, and K. Ikuta (2012) Magnetic micro actuator with neutral buoyancy and 3D fabrication of cell size magnetized structure. IEEE International Conference on Robotics and Automation, pp. 745–750.

30. Meeker, D.C., Maslen, E.H., Ritter, R.C., and Creighton, F.M. (1996) Optimal realization of arbitrary forces in a magnetic stereotaxis system. *IEEE Trans. Magn.*, **32** (2), 320–328.

31. Diller, E., Giltinan, J., Lum, G.Z., Ye, Z., and Sitti, M. (2014) Six-degrees-of-freedom remote actuation of magnetic microrobots. Robotics: Science and Systems, http://www.roboticsproceedings.org/rss10/p13.html.

32. Cheng, D.K. (1992) *Field and Wave Electromagnetics*, 2nd edn, Addison-Wesley Publishing Company, Inc..

33. Rudd, M.E. (1968) Optimum spacing of square and circular coil pairs. *Rev. Sci. Instrum.*, **39** (9), 1372.

34. Kummer, M.P., Abbott, J.J., Kratochvil, B.E., Borer, R., Sengul, A., and Nelson, B.J. (2010) OctoMag: an electromagnetic system for 5-DOF wireless micromanipulation. *IEEE Trans. Rob.*, **26** (6), 1006–1017.

35. Tasoglu, S., Diller, E., Guven, S., Sitti, M., and Demirci, U. (2014) Untethered micro-robotic coding of three-dimensional material composition. *Nat. Commun.*, **5**, 3124.

36. Tottori, S., Zhang, L., Qiu, F., Krawczyk, K.K., Franco-Obregón, A., and Nelson, B.J. (2012) Magnetic helical micromachines: fabrication, controlled swimming, and cargo transport. *Adv. Mater.*, **24** (6), 811–816.

37. Diller, E. and Sitti, M. (2014) Three-dimensional programmable assembly by untethered magnetic robotic microgrippers. *Adv. Funct. Mater.*, **24** (28), 4397–4404.

38. Azam, A., Laflin, K.E., Jamal, M., Fernandes, R., and Gracias, D.H. (2011) Self-folding micropatterned polymeric containers. *Biomed. Microdevices*, **13** (1), 51–58.

39. Fusco, S., Sakar, M.S., Kennedy, S., Peters, C., Bottani, R., Starsich, F., Mao, A., Sotiriou, G.A., Pané, S., Pratsinis, S.E., Mooney, D., and Nelson, B.J. (2013) An integrated microrobotic platform for on-demand, targeted therapeutic interventions. *Adv. Mater.*, **26** (6), 952–957.

40. Pawashe, C., Floyd, S., Diller, E., and Sitti, M. (2012) Two-Dimensional Autonomous Microparticle Manipulation Strategies for Magnetic Microrobots in Fluidic Environments. *IEEE Trans. Robot.*, **28** (2), 467–477.

41. Ye, Z., Diller, E., and Sitti, M. (2012) Micro-manipulation using rotational fluid flows induced by remote magnetic micro-manipulators. *J. Appl. Phys.*, **112** (6), 064912.

42. Tung, H.-W., Peyer, K.E., Sargent, D.F., and Nelson, B.J. (2013) Noncontact manipulation using a transversely magnetized rolling robot. *Appl. Phys. Lett.*, **103** (11), 114101.

43. Tung, H.-W., Sargent, D.F., and Nelson, B.J. (2014) Protein crystal harvesting using the RodBot: a wireless mobile microrobot. *J. Appl. Crystallogr.*, **47** (2), 692–700.

44. Ye, Z. and Sitti, M. (2014) Dynamic trapping and two-dimensional transport of swimming microorganisms using a rotating magnetic micro-robot. *Lab Chip*, **14**, 2177–2182.

11

Microrobotic Tools for Plant Biology

Dimitrios Felekis, Hannes Vogler, Ueli Grossniklaus, and Bradley J. Nelson

11.1
Why Do We Need a Mechanical Understanding of the Plant Growth Mechanism?

Almost all our food, feed, fuel, and fiber are ultimately derived from plants. Furthermore, photosynthetic organisms have a major impact on the global climate since they comprise 99% of the Earth's biomass. One of the problems in agriculture is crop failure due to mechanical instability. This phenomenon, known as crop lodging, is caused by storms and can reduce harvests locally by up to 90%. To minimize this problem, farmers widely use dwarfed varieties, which provide less windage but often have the disadvantage of a reduced productivity even in years without storms. Furthermore, cell wall stability has profound effects on its digestibility, be it in the stomach of ruminants or for cellulosic biofuel production. Only by knowing the effect of individual cell wall components on the stability of the entire cell wall, we would be able to engineer more stable plants that can grow to their full potential. Thus, understanding growth processes in plants and how they interact with their environment during growth is of fundamental importance. Interactions between expanding cells at the tissue level or even the entire organism are extremely complex. Therefore, we first need a quantitative understanding of the principles of growth at the single-cell level.

Cell expansion is one of the fundamental processes in plant morphogenesis that involves changes in shape and size. Two highly coordinated mechanical processes are required for these changes: (i) the deformation and modification of the existing cell wall and (ii) the secretion and deposition of new membrane and cell wall material. Turgor pressure is the driving force for wall expansion, while the cytoskeleton and vesicle transport regulate the delivery of new cell wall material. The dynamics of the growth process itself as well as the resulting final cell size and cellular shape are controlled by the changing mechanical behavior of the cell wall.

Turgor pressure creates a tensile stress on the cell wall [1]. Since growth depends mostly on in-plane stress, it is important to directly measure in-plane elasticity.

The Young's modulus is a measure of the stiffness of a linear elastic material. In the past, several methods were deployed to assess the stiffness of plant cell walls [reviewed in 2]. Tensile tests using extensometers delivered valuable information about the elasticity of isolated cell walls and entire tissues [3–7]. The disadvantages of this method are that it is difficult to perform experiments on individual living cells and it is not possible to gain information about local differences in mechanical cell wall properties. Magnetic and optical tweezers are capable of applying and measuring piconewton forces. However, they are not indicated for micronewton forces and offer limited workspace [8, 9]. Micropipette aspiration offers a micronewton force range, but is not suitable for cells that move or rapidly elongate [10]. The atomic force microscope (AFM) has been used both as an imaging tool and for measuring forces with exceptionally high resolution [11]. However, a complete characterization of plant cells requires the application of multiscale loads (from nanonewtons to millinewtons), and the forces that can be applied by an AFM are insufficient to deform the cell walls of turgid cells enough to measure in-plane elasticity [12]. Furthermore, due to the cantilever-based nature of the AFM, the sensor is sensitive to off-axis loads and induces lateral motions when it is deflected [13]. In traditional micro- or nanoindentation, the specimen is fixed tightly on a stiff surface. An end-effector with a well-defined tip geometry indents the material until penetration and plastic deformation [14]. This technique can offer high-resolution information on the mechanical properties of the specimen. However, it is a destructive method and requires that the cell is not in a living state.

These problems are overcome by micro- or nanocompression approaches, which determine stiffness by measuring the forces that are necessary to cause small, local deformations of the cell wall. Since these methods are noninvasive, they can be used for repetitive, locally distinct measurements on living cells and tissues. Another important aspect of these techniques is the effort and time required to conduct the experiment, for example, sample preparation and end-effector localization. Experiment time affects the throughput and is critical for cells with a limited lifetime. In the micro- or nanocompression method, an end-effector mounted on a positioning system applies compressive tensile forces. Depending on the force sensing element, the range of forces varies from nano- to millinewton. The positioning capabilities of the positioner define the resolution and travel range, which can vary from nanometers to centimeters.

Our goal was to develop an automated, high-throughput, microcompression system that can apply and measure forces and generate stiffness and topography maps with high precision and accuracy. The system we have developed conducts robust microindentations and collects the resulting force and indentation data. These data serve as input to mechanophysical models that employ cell-specific geometrical parameters from measurements, such as radius and cell wall thickness. By fitting the model on the experimental data, we manage to calculate material properties for the cell wall. A schematic representation of the approach is shown in Figure 11.1.
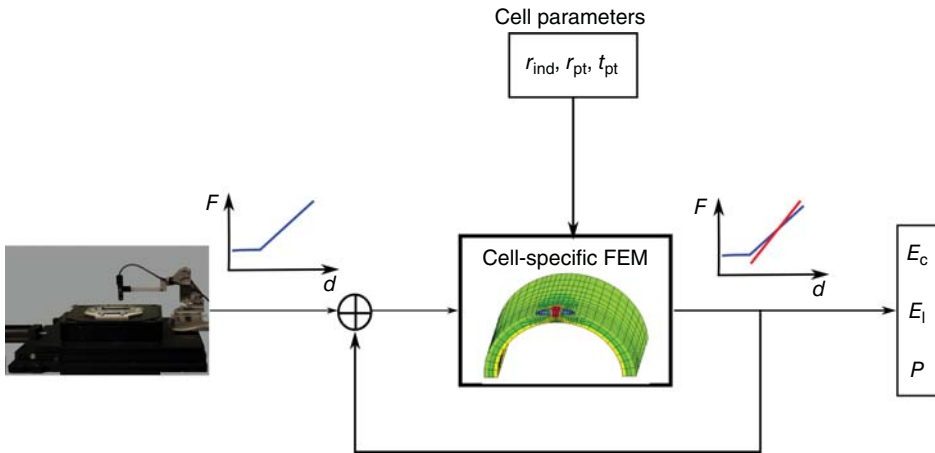
Figure 11.1 Systematic approach for characterizing material properties of the cell wall. A microrobotic system applies controlled forces and collects force and indentation data. These data – in combination with geometrical data – are used as inputs in a cell-specific mechanical model that calculates material properties of the cells. F, force; d, indentation; r_{ind}, indenter radius; r_{pt}, cell radius; t_{pt}, cell wall thickness; E_c, Young's modulus in the circumferential direction; E_l, Young's modulus in the longitudinal direction; P, turgor pressure; FEM, Finite Element Model.

11.2
Microrobotic Platforms for Plant Mechanics

Computer simulation techniques are often employed to study plant development. The simulation models include a geometrical aspect, as the cells change geometry while growing, and a biochemical aspect. It is known that development is an interplay between processes affecting these two aspects [15–18]. More specifically, growth is the result of changes in the cell's physical properties, which are controlled by gene activities, and the consequent change in geometry feeds back on gene regulation through physical forces and signal transduction cascades. Thus, it is critical to quantify mechanical properties at the cellular level and study the response of cells to external physical loads. The quantitative data will be then used as input in the predictive growth models. However, reliable tools for acquiring quantitative data for plant mechanics are lacking.

In order to develop reliable models of cellular growth, a vast quantity of experimental data must be collected to establish the statistical significance of observations and, thus, the experimental system must offer high throughput. Precision and accuracy in force and position are critical for developing reliable models of growth that rely on measured inputs. The system must be calibrated and characterized with known uncertainties for the quantities involved in the measurement. High speed is a key requirement for characterizing organisms that grow and have limited lifetime. The positioning range and resolution must suffice for characterizing organisms with diverse morphologies and high aspect ratios.

Robotic systems offer high precision and throughput at high speed through automation. Since we are interested in manipulating organisms at the microscale, we investigated microrobotics as a potential solution. A microrobot is a robotic system that performs tasks in the microworld or a system that has micron-sized dimensions. As a robotic system, a microrobot employs actuation, sensing, and control units to perform automated tasks.

Microrobotics has contributed to the investigation of single-cell mechanics by providing tools for measuring the response of cells to applied forces using robotic micromanipulation techniques. The manipulation of cells using micro-electro-mechanical system (MEMS)-based force feedback combined with visual feedback [19] was used to investigate the mechanical hardening of the zona pellucida, the extracellular membrane of oocytes, upon fertilization. This study was the first of its kind to mechanically characterize and quantify the dramatic hardening of an extracellular matrix and demonstrated the advantages of precision microrobotic manipulation in the investigation of the mechanical behavior of cells.

Microrobotic platforms enable the precise characterization and mechanical stimulation of single cells, tissues, and whole organs. System characterization and calibration allow a consistent and reliable operation. The real-time control and acquisition architecture allow for a deterministic position and force control. Visual automation methods are applied in tasks, such as sample selection and tip localization, to reduce experiment time and achieve high throughput. The system is designed in such a way that it can be integrated with various microscopy techniques to allow real-time imaging of intracellular activities during micromechanical stimulation.

11.2.1
The Cellular Force Microscope

CFM stands for *cellular force microscope* and is a mechatronic system that combines micropositioners and force sensing devices integrated with microscopes and software for the real-time control and acquisition of experimental data. The CFM is used to characterize the mechanical properties of biological cells and tissues with an increased level of automation.

Determining reasonable parameters for the experiments to be performed was of central importance in the design of the system. Lacking accurate specifications for the cell wall of *Arabidopsis thaliana*, we expected forces in the order of tens to hundreds of micronewtons. With this initial guess, we designed the CFM (Figure 11.2), which is composed of a MEMS force sensor, a data acquisition system, a three-axis positioning system, a position control unit, a high-resolution optical microscope, and a custom user interface for the control of automated tasks.

11.2.1.1 Force Sensing Technology
Depending on the requirements of the application (e.g., the required force range or whether the forces to be measured are static or dynamic), the appropriate approach and sensing technology need to be chosen. For the micromechanical
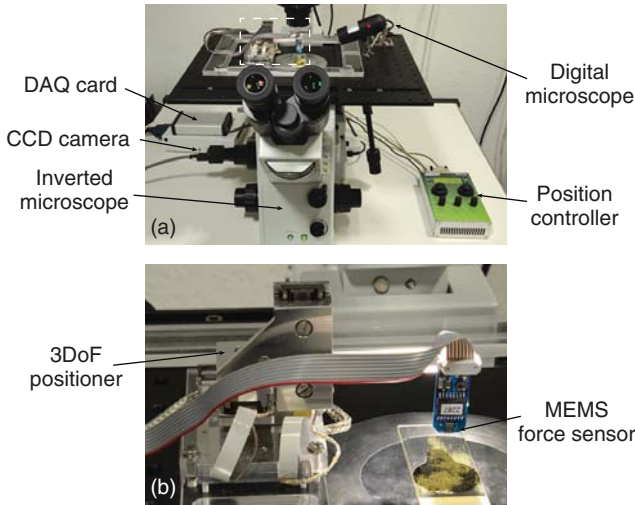
Figure 11.2 The first generation cellular force microscope (CFM) in an inverted configuration for the mechanical characterization of living cells *in situ*. DAQ, data acquisition; CCD, charged-coupled device; DoF, degree of freedom; MEMS, micro-electro-mechanical system. (Image taken from Ref. [20].)

testing of samples with micrometer-characteristic dimensions, such as individual cells or biological fibers and MEMS-based mechanisms, the measurement of quasi-static forces (< 1 kHz) in the micronewton to nanonewton range is required. The sensor needs to be compatible with different environments, such as air, liquid, and vacuum. In addition, it must be compact in size, light in weight, and easily integrable into a measurement system.

Miniature force sensors capable of measuring forces in the micronewton to nanonewton range generally fall into one of four categories: piezoresistive, piezoelectric, capacitive, and optical-based force sensors. More exotic principles, such as magnetic-based sensing [21] or tunneling microforce sensing [22], have been reported in the literature, but are currently not mature enough for the development of reliable sensors. An ideal force sensor is stable, highly sensitive to its primary input, and insensitive to variations in environmental conditions. This narrows the field of candidate technologies to piezoresistive or capacitive force-based sensing. Compared with piezoresistive sensors, the superior stability and minimal hysteresis of capacitive sensors [23] argue in favor of their suitability for use in micromechanical material testing systems [13].

The FT-S100 (FemtoTools GmBH, Figure 11.3a), a commercially available capacitive MEMS-based microforce sensing probe, was used for micromechanical investigations. The working principle of the sensor is depicted schematically in Figure 11.3b.

The sensor consists of a movable body with an attached probe suspended by four flexures within an outer frame. A force applied to the probe in x-direction results in relative motion of the body with respect to the outer frame, which is measured
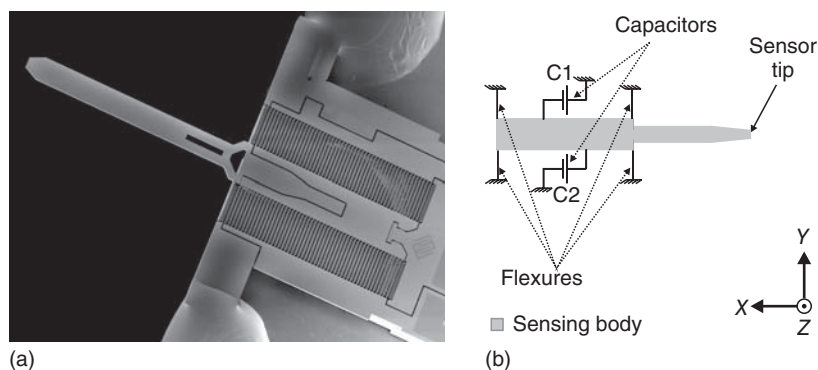
Figure 11.3 (a) Scanning electron microscope image of the FT-S100 MEMS sensor and (b) schematic of the principle of operation of a single-axis MEMS force sensor. C1 and C2, capacitors 1 and 2.

by attached capacitive electrodes as a change in capacitance. Two capacitive changes with opposite signs are differentially measured using a capacitance-to-voltage converter (MS3110, Irvine Sensors Inc.), resulting in a linear output.

Because of the symmetric design of this sensor with its four flexures, parallel motion of the movable body during deflection is possible, making this design superior to most cantilever-type sensors. Furthermore, because of its long sensing probe, the sensor can access three-dimensional (3D) structures even in depressions.

Depending on the properties to be characterized (local or global), sharp probes can be attached to the end of the force sensor tip. Tungsten probes with diameters ranging from 5 μm to 100 nm and lengths ranging from microns to millimeters are available. Extensions with various geometries (e.g., spheres or pyramids) can also be attached to the sensor tip.

11.2.1.2 Positioning System

The force sensor is mounted at the tip of an extension arm that is mounted at its base on a three-axis positioning system (Figure 11.2b). More specifically, we use an SL-2040 (SmarAct GmbH) that is capable of moving over a range of 27 mm with a resolution of 5 nm along each axis. The three-axis positioner used is based on stick-slip piezoelectric actuators.

Two modes of operation are supported by the micropositioner: the stepping mode and the scanning mode. In the stepping mode, the micropositioner achieves a travel range of 27 mm and a step size down to 50 nm in closed-loop operation. The settling time for the 50-nm step size is relatively large increasing the total time required for a given experimental procedure. The positioner can be used in the scanning mode, where the deflection of the actuator is directly controlled through the input voltage. The advantage of the latter mode is that the movement is smooth, stable, fast, and continuous. However, in this case, the range is limited by the size of the actuator, resulting in deflections ranging between 600 and 1000

nm. The positioner is interfaced to a PC via either USB or RS-232 using LabVIEW (National Instruments) for the position readout and the closed- or open-loop control.

11.2.1.3 Imaging System and Interface

The entire system is integrated with an imaging unit for the inspection of the experimental procedure and the manual localization of the sensor tip. In the CFM, the imaging system consists of an inverted microscope with a 400X magnification lens and a CCD camera that is connected through the firewire protocol to a desktop PC, as shown in Figure 11.4. In addition to the inverted microscope, a USB digital microscope is used to inspect the manual coarse positioning of the sensor probe at the area of interest.

The aforementioned components are integrated with a custom user interface (UI), designed in LabVIEW, into a complete microrobotic measurement system. The UI allows for the control of parameters, such as contact and measurement forces, speed, step size, and measurement locations, among others. Position control is performed during steering of the sensor probe at various $x-y$ locations, during control of the indentation size, and during positioning in stepping and scanning modes. Force control is performed at the moment of contact between the sensor and the sample and during indentation. Guided by the three-axis micropositioner, the sensor probe approaches the cell samples until physical contact is established. Once in contact with the cell, the probe may be operated in either a position or force control mode, resulting in measurements of either the cell's resistance to indentation or cell wall displacement, respectively.

Characterization of mechanical properties of the cell wall requires extremely precise manipulation in the nanometer range. Therefore, all the parts that constitute the system (apart from the PC) are mounted on a vibration isolation table. In order to avoid noise that stems from the environment, the measurement area is covered with an acoustically sealed box.
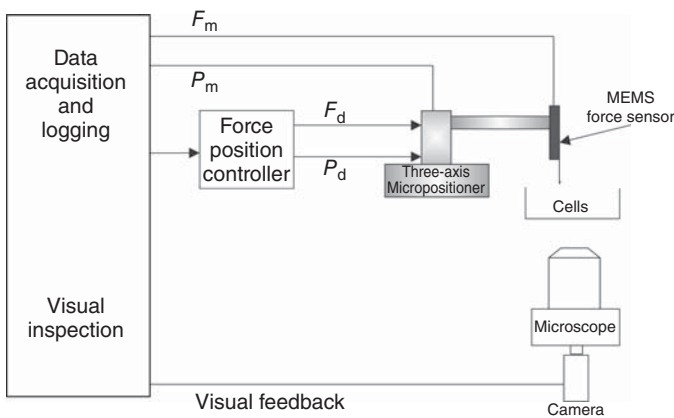
Figure 11.4 CFM schematic. F_m, P_m are the measured values and F_d and P_d are the desired values of force and position, respectively.

11.2.2
Real-Time CFM

The CFM performed well in characterizing mechanical properties of cells in the range of tens to hundreds of micrometers and micronewtons. However, a system that expands in the single micrometer and micronewton range is required for manipulating cells of a few micrometers in size. High throughput and speed are key factors for studying cells and organisms that show rapid variation in their measured material properties. To achieve high throughput, experimental procedures, such as sample selection and mechanical loading, must be automated. Using computer vision routines, the force sensing tip can be automatically positioned at the area of interest on the target cell with minimal input. The system then constructs an interactive image of the workspace at high magnification, within which the user can select the exact locations of the measurement points. The real-time CFM (RT-CFM) relies on the same fundamental principle as the original CFM, that is, MEMS-based capacitive force sensors that are moved against samples in order to perform micro- or nanocompressions. The most salient difference in the RT-CFM is that the sample moves against the sensor probe and not the reverse, as in the first-generation CFM.

11.2.2.1 **Positioning System**
The new three-axis positioner, a PI Mars P563.3CL from Physik Instrumente (PI) GmbH & Co., employs piezoelectric stack actuators connected in parallel kinematics. This positioner is capable of producing continuous movements over a range of 300 μm, in contrast with the old positioner's comparatively limited continuous movement range of only 1 μm. The positioning of the piezoelectric actuators is guided by flexures in all three axes. The piezo stage has fewer moving parts overall, resulting in more precise positioning due to a reduction of backlash (i.e., clearance between mechanical parts). Nonlinearities and undesired off-axis movements are minimized by design and are also compensated for using a parallel metrology approach. Parallel metrology allows for the detection and real-time, closed-loop correction of undesired motion along axes perpendicular to the axis of actuation (cross talk).

For position sensing, capacitive sensors with subnanometric resolution and bandwidths of up to 10 kHz are employed. Another advantage of the piezo stage is the open-frame construction that allows for the positioning system to be combined with different microscopy techniques.

Furthermore, continuous, subnanometric movement is performed throughout the entire displacement range of the actuator, unlike in the first-generation system, where such motion is limited by the actuator's size. However, the total travel range of this positioner is 300 μm compared to 27 mm for the first generation. In order to increase the positioning range to its first-generation value, a second $x-y$ positioner is used for coarse movements. The coarse positioner is actuated using stepper actuators with a resolution of 1 μm. Together, the coarse and fine positioners result in a dual-stage system featuring a 25-mm overall

range and 300 µm of continuous movement with subnanometer resolution. These specifications are superior for conducting the plant cell characterization experiments that we designed.

As opposed to the CFM, in which the sensor probe was mobile, in the RT-CFM the sample moves while the sensor remains stationary. As seen in Figure 11.5, the sensor is mounted on the SL-2040 micromanipulator in order to provide additional positioning capabilities for positioning the probe and establishing contact with the sample.

Another key aspect of the second-generation positioner is the analog position readout and analog control input. The voltage applied to the piezo actuator, and thus its position, can be controlled with an analog signal from 0 to 10 V. This feature improves communication speed and allows for the positioner to be interfaced with various analog controllers. Similarly, the position of the stage is an analog signal that can be captured by any data acquisition system with analog inputs.

11.2.2.2 Data Acquisition

In addition to the characterization of the elastic properties of cells, the viscoelastic properties of biological organisms were of interest in our investigation. In order to accurately measure these properties, we needed real-time control of the force and the position. Moreover, synchronization between force and position signals at fast acquisition speed is required. Thus, apart from the advantages in the mechanics of the positioning system described above, the second-generation microbotic measurement system needed to offer the possibility for deterministic acquisition.

The data acquisition system comprises a real-time (RT) computer connected to a field-programmable gate array (FPGA) unit. The input/output modules are connected on the FPGA backplane. With the FPGA, real-time and deterministic
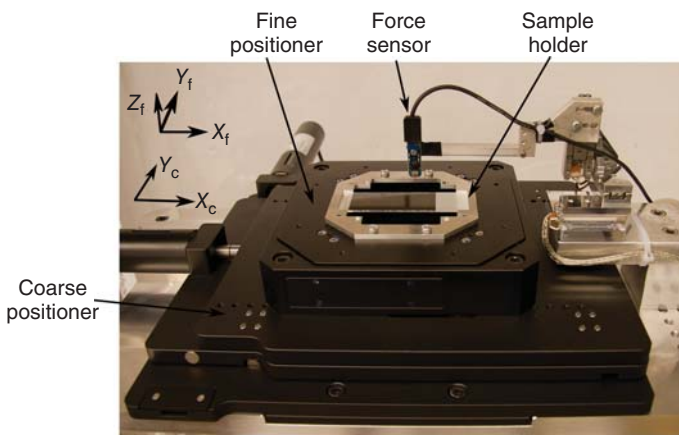
Figure 11.5 Positioners assembled in the dual-stage configuration on the RT-CFM. The sensor is mounted on the SL-2040 for contact detection. The axes of movement for both coarse (X_c, Y_c) and fine (X_f, Y_f, Z_f) positioners are shown, with Z_f being the measurement axis of the fine positioner.

acquisition of experimental data is possible, as well as implementation of real-time control of the force and position. The RT computer is used for other important but less time-sensitive operations, such as data logging, plotting, and interaction with the user. Finally, due to the faster dynamics of the piezoelectric stack actuators in combination with the real-time control, the execution time required for experiments is drastically reduced, allowing for faster measurements and, thus, higher throughput.

11.2.2.3 Automated Cell Selection and Positioning

Because of the limitations associated with manual operation and the configuration of most systems, microcompression-type techniques are generally limited in speed, throughput, and precision. Single cells are only few microns in size and finding a cell of interest by visual inspection is time consuming. Only under high magnification are the cells visible, resulting in a spatially confined workspace. Plant cells, such as pollen tubes, grow at high rates; consequently, the target locations change. Once a target cell is detected, a significant amount of time is spent in localizing the force sensing tip at the measurement location. This is a challenging task even for experienced users and occasionally results in damage to the sensor. With our previous system, the time that an average inexperienced user spent to localize the force sensor tip was more than 30 min.

In order to overcome these limitations, we automated the process using computer vision techniques. The successful coupling between computer vision and sensor positioning requires forward and inverse mappings between image and real-world coordinates. Thus, the experimental procedure begins with a calibration process of defining the sensor position within the field of view of the microscope. Then, the user defines the workspace, and the experimental sequence consisting of visual servoing, that is, vision-based robot control, and the microcompression test begins. For the experiment, the user defines the experimental parameters, for example, measurement force f_d, measurement step size z_d, and the task planner controls the task to be executed (Figure 11.6). Inputs to the task
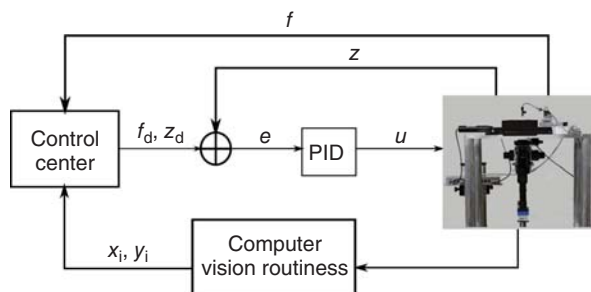
Figure 11.6 Block diagram of the RT-CFM showing the measured variables (f, z), the position output from the image processing algorithm (x_i, y_i), and the control loop. PID, proportional-integral-derivative; f_d, desired force; z_d desired position; e, error; u, control signal.

planner are x, y position coordinates of the next measurement location from the computer vision algorithms, measured force f, and position z. Depending on the user-defined parameters and the values of the inputs, the task planner switches between visual servoing in the $x-y$ plane, closed-loop scanning in the z-direction for the microcompression test, and workspace image creation among others.

Because of the limited field of view at high magnifications, a mosaicing feature automatically acquires images of complementary regions in the workspace that, when assembled, constitute a complete mosaic of the target area. The user thus has an overview of the workspace and can select the areas of interest on the interactive mosaic image. This functionality not only assists in quick target detection but also increases the speed and precision of sensor tip localization. An automated tracking algorithm follows the sensor tip with respect to the image space and uses this position as the sensor reference position.

Visual servoing is implemented using a dynamic, image-based, look-and-move architecture, combined with either a template matching or Kanade−Lucas−Tomasi [24] (KLT) algorithm for the position error quantification. A proportional-integral-derivative (PID) controller is implemented for moving the sample with the dual-stage positioner. This method decouples the visual servoing program from the positioner dynamics. The input location to the servoing program can be either a user-defined point from the mosaic image or an image coordinate determined by a tracking algorithm. The sensor tip can be positioned at the desired location with pixel resolution within fractions of a second. Users also have the option to define a large grid of points covering a region of interest over which the system makes a series of measurements at the selected locations in an automated manner.

The system is built for biomedical researchers without detailed system knowledge and, thus, the calibration process must be fast, automated, and easy to perform. We developed an automated calibration method based on the features of the sample to be measured. Using this method, the user selects a distinctive feature on a cell to initiate the calibration procedure. First, a template 80×80 pixels centered around the selected feature is created. Then the sample is moved along the x-axis, the feature is tracked, the sample is moved along the y-axis, the feature is tracked again and moved to the opposite direction along the x-axis. At each step, the displacement is recorded by the encoders and the distance of the feature in image coordinates is calculated by the template matching algorithm. In order to minimize the error stemming from the positioning uncertainty and the feature tracking algorithm, this procedure is repeated 10 times. This allows for an estimation of the pixel size and rotation matrix. Having obtained these values, we can use Equation (11.1) to pass from image to real-world coordinates.

$$\begin{bmatrix} x_s \\ y_s \end{bmatrix} = R \begin{bmatrix} x_c - x_{R_c} \\ y_c - y_{R_c} \end{bmatrix} \cdot \begin{bmatrix} ps_x \\ ps_y \end{bmatrix} + \begin{bmatrix} x_{R_s} \\ y_{R_s} \end{bmatrix}, \tag{11.1}$$

where (x_s, y_s) are the stage coordinates, (x_c, y_c) are camera coordinates, (x_{R_s}, y_{R_s}) is the reference point in stage coordinates, (x_{R_c}, y_{R_c}) is the reference point in camera coordinates, (ps_x, ps_y) is the pixel size, and R is the rotation matrix.
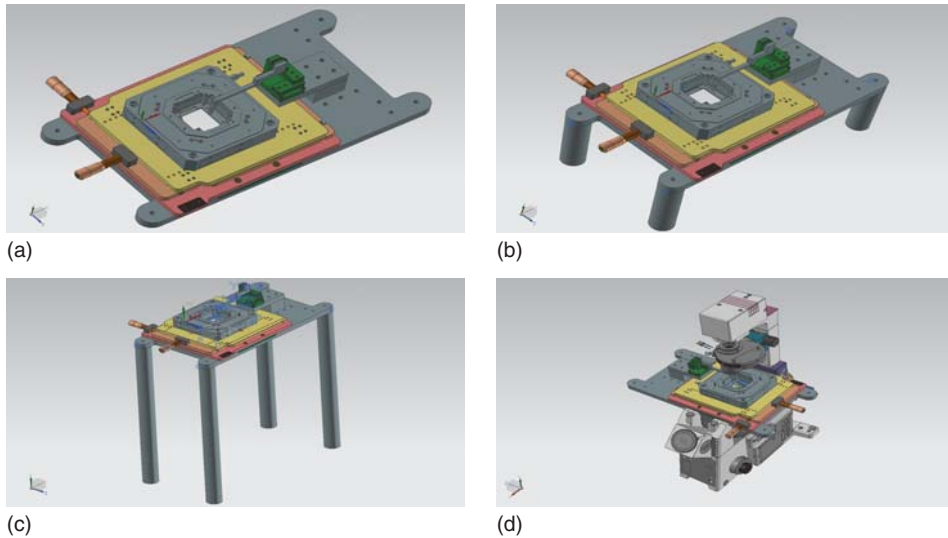
Figure 11.7 CAD rendering of the RT-CFM setup in various configurations. (a) The movable platform only, (b) for upright microscopes, (c) for custom inverted microscopes, and (d) on an Olympus inverted microscope. CAD, computer-aided design.

In order to combine the micromechanical characterization approach with various types of imaging techniques, the system is mounted on a movable platform. With this design, the system can be used in inverted (e.g., with an Olympus microscope), upright, and tilted configurations. Figure 11.7 shows a computer-aided design (CAD) model of the RT-CFM in a variety of possible configurations.

11.3
Biomechanical and Morphological Characterization of Living Cells

The first CFM was developed to measure the mechanical properties of the primary cell wall in living pollen tubes [25]. It has been applied at single-cell [20] and tissue levels [26].

The pollen tube is a highly specialized cell type that delivers the sperm cells to the ovule for fertilization. Thus, pollen tube growth is crucial to the process of sexual reproduction in plants. Upon landing on the stigmatic surface of the pistil, pollen grains hydrate and germinate, and each extrudes a polarized outgrowth to form a pollen tube. Pollen tubes elongate rapidly within specific pistil tissues, targeting ovules that are often located at distances thousands of times that of the diameter of the grain away from the stigma [27]. Pollen tubes are also of fundamental interest as they represent the fastest growing cells known to mankind [28]. Growth rates ranging from $25-30$ to $80-100$ nm s^{-1} have been reported for *in vitro* grown tobacco pollen tubes and 250 nm s^{-1} for lily pollen tubes. *In vivo*,

tobacco pollen tubes may grow to 4.5 cm within the pistil in approximately 30 h to reach the ovules [27].

Pollen tubes are easily accessible as they can be grown *in vitro*, and manipulation of the nutritional status and cell wall properties can be achieved by changes in the growth medium. The transcriptome, proteome, and ionome of pollen tubes have been described in detail, making them one of the best characterized systems for cell biology [29, 30].

We used lily and *Arabidopsis* pollen tubes for our experiments. After successfully demonstrating the use of lily pollen tubes in the CFM [20] (Figure 11.8), we turned our attention to establishing *Arabidopsis* pollen tubes as a suitable experimental system for use with the CFM. *Arabidopsis* pollen tubes hold significant potential for further studies, as they allow the use of mutants and transgenic lines to manipulate the cell wall and the cell's physiology.

11.3.1
Cell Wall Apparent Stiffness

Compression tests of the primary cell wall in pollen tubes were conducted using the CFM. The system detects contact based on force feedback. During this phase, the microrobot drives the force sensor toward the sample at controlled speed, using the stick-slip actuation. When the force measured by the force sensor reaches a threshold force value, contact is achieved and the measurement procedure automatically begins (Figure 11.9).

During the measurement procedure, the microrobot was operated in scanning mode, which offers continuous movement as opposed to the discrete steps in stepping mode. In addition, subnanometer movement resolution is possible, which provides more data points during the indentation of the tube. The force and position data were sampled during both the contact detection and measurement phases. We set a contact force threshold between 1 and 2 μN, while for the measurement phase we applied nanonewton loads, which resulted in hundreds of nanometer indentations in the cell wall. On each measurement
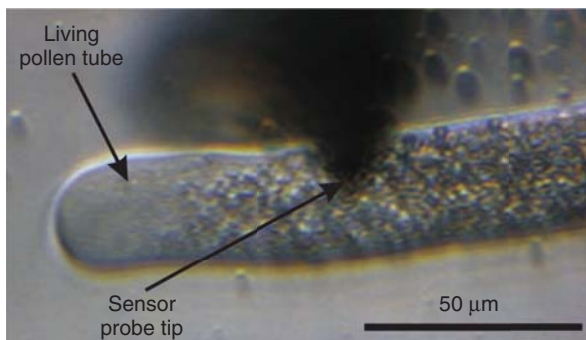
Figure 11.8 A growing lily pollen tube with the sensor tip indenting the cell.
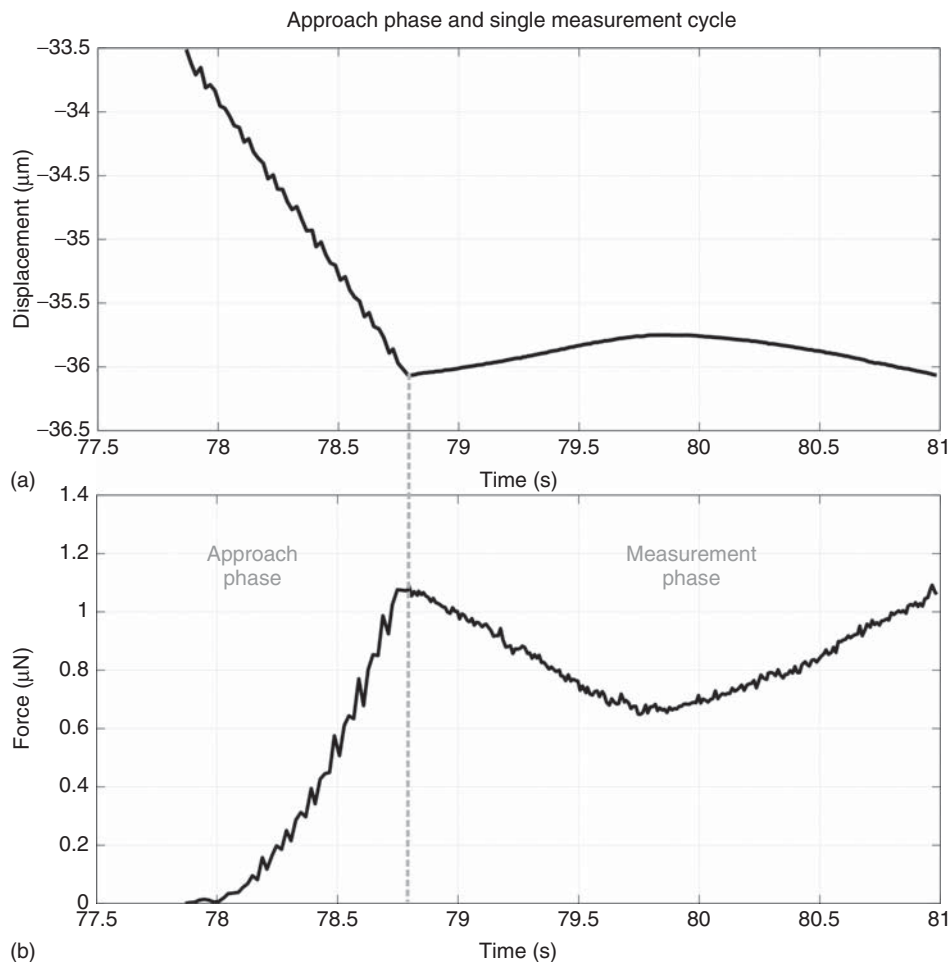
Figure 11.9 A typical CFM measurement (single scan) (a) Displacement versus time, (b) force versus time for the same data point.

point, a user-defined number of measurement cycles are performed, with each cycle consisting of a loading and an unloading movement (Figure 11.9). In the experiments presented below, data were collected from 18 different pollen tubes. All the experiments presented here are based on force feedback, and thus, the contact as well as the measurement force was user defined.

The compression test was performed vertical to the cell wall and on different points along the longitudinal axis of symmetry of the pollen tube. At each point, four measurement cycles were conducted consisting of four loadings and four unloadings, both at a speed of $0.280\,\mu\text{m}\,\text{s}^{-1}$ (Figure 11.10). While a large number of measurements at each point is desirable, the rapid growth rate of the pollen tubes limits the number of measurements possible in practice.
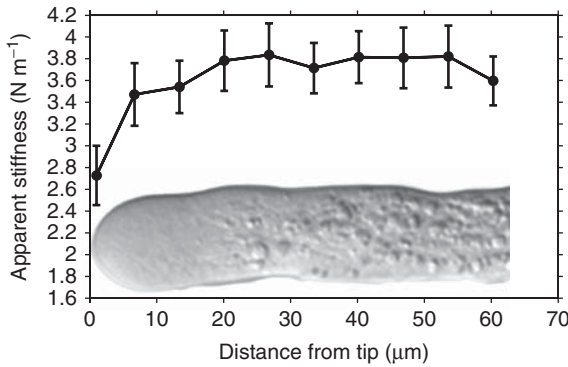
Figure 11.10 Apparent stiffness of the lily pollen tube cell wall and inlet picture of a real pollen tube. (Image taken from Ref. [20].)

From the force–displacement curves plotted in our experiments, we were able to calculate the *apparent stiffness* of the cell wall. The values reported here are the instantaneously observed stiffnesses of the entire cell, depending upon the tip geometry, contact angle between the sensor tip and the pollen tube, turgor pressure, and contact conditions. After correcting the vertical position, the stiffness was calculated by applying a linear fit to the force–indentation curve of each measurement, as shown in Figure 11.10.

For the calculation of the system's total stiffness, measurements were made in an identical system configuration (sensor, mounting parts, substrate) and under the same environmental conditions but without the pollen tube. The system stiffness was then subtracted from the collected data to determine the pollen tube stiffness.

The average stiffness value was between 2.7 and 3.8 Nm^{-1} and is depicted in Figure 11.10. A difference in the apparent stiffness from the tip to the apex is clearly visible. This finding seems to agree with the fact that in lily pollen tubes, callose is absent from the apical region and pectin is esterified at the tip but not in the shank. Thus, differences in the mechanical properties of callose and esterified and de-esterified pectin may contribute to differences in apparent stiffness. A considerable variation in pollen tube stiffnesses from different anthers was noticed, but the decrease in apparent stiffness at the tip was always measured. This may imply a difference in the mechanical properties between the tip and shank, resulting in a localization of expansion to the tips of growing pollen tubes [31, 32].

However, a difference in the apparent stiffness can be also of geometrical nature. More specifically, the sensor moves along the vertical axis (*z*-axis) and thus, due to the curvature of the pollen tube at the tip, the contact between the sensor tip and the cell wall is not vertical.

A finite element method (FEM)-based model was employed to assist in data interpretation. In brief, a quasi-static continuum mechanics model of a pollen tube is presented, the results of which agree well with the CFM measurements [20]. The initial geometry of the pollen tube is represented by a cylindrical shell, which is attached to a hemispherical shell with radius and thickness based on microscopic

data. The length of the section was chosen to be large enough to minimize the influence of boundary conditions, which are applied to the distal circular edge (Figure 11.11).

The FEM model relies on several assumptions regarding the mechanics of the cell wall. In particular, it was assumed that: (i) the material is fully compressible (i.e., all Poisson's ratios are zero), (ii) the Young's modulus in the direction normal to the surface is the same as in the longitudinal direction, (iii) all shear moduli are $E_1/22$, where E_1 denotes the longitudinal Young's modulus.

The model may be subdivided into two dynamic steps. The first step describes the inflation of a pollen tube section as a result of osmotic water uptake. The second step simulates the contact of the inflated structure during indentation with a rigid probe, that is, the MEMS-based force sensor.

In the first step, the turgor pressure is calculated. In spite of a geometry which is not perfectly cylindrical, the global deformation of a pollen tube obeys the Laplace law of stress distribution in a cylindrical pressure vessel to a high degree of approximation [20]. This formula is combined with Abaqus' linear elastic material law (*i.e.* with logarithmic strain) yielding

$$\frac{Pr}{d} = \sigma_c = E_c \cdot \log(\lambda_c) \tag{11.2}$$

$$\frac{Pr}{2d} = \sigma_l = E_l \cdot \log(\lambda_l), \tag{11.3}$$

where P is the turgor pressure, r is the radius and d is the thickness of the cylinder, σ_c and σ_l are Cauchy stresses, E_c and E_l are Young's moduli, and λ_c and

Figure 11.11 Finite element method (FEM)-based model of the pollen tube. The stress distribution in the simulated pollen tube is shown. The stress-free reference configuration (a) is pressurized and indented by a rigid probe (b). (Image modified from Ref. [20].)

λ_1 are the initial stretch ratios in the circumferential and longitudinal directions, respectively.

In the second step of the simulation, the pressurized shell is indented with a rigid probe, which has the shape of a hemisphere that is connected to a cylinder. We assumed frictionless contact between the pollen tube and the probe (the supporting plane) and calculated the apparent stiffness as the change in force over the change in vertical displacement.

The simulation resulted in values for the apparent stiffness that were very close to the apparent stiffness values measured by CFM [20]. As we assumed uniform mechanical cell wall properties for the entire pollen tube in this simulation, the observed reduction in apparent stiffness at the tip can be explained solely by the geometry of the pollen tube. The angle of tilt between the direction of indentation and the surface gradually increases in the vertical direction due to the tip's shape. This means that even if the forces were the same in magnitude, we would expect microcompression methods to report lower values on the hemispherical part of the apex, since forces are measured only in the direction of probe compression.

Turgor-induced pretension of the cell wall also affects geometry, creating a gradient in stiffness near the apex in the cylindrical portion of the tube. In this portion of the tube, there is twice as much maximum principal tension as in the hemispherical apex. As a result of this difference, the cylindrical part acts like a guitar string under high tension, which is harder to deflect than the same string under lower tension [20].

11.3.2
3D Stiffness and Topography Maps

For developing physical models that take into account the mechanics of the pollen tube during growth, it is important to study the mechanical properties of the cell wall over the area of interest of the cell. With the RT-CFM we were able to characterize the stiffness over the entire area of the pollen tube as it grows, in contrast to measurements along the pollen tube longitudinal axis that have been previously reported [20, 25, 31]. As shown in Figure 11.12 , at the beginning of the experiment, the camera calibration and sensor position are set. This procedure is done once in the setup of the system. Before each experiment, the workspace is defined, and the interactive mosaic workspace is created. The experiment continues with the measurement on the defined locations.

We combined the measured stiffness maps with topography maps of growing pollen tubes [33] (Figure 11.13). An area of $60 \times 50\,\mu$m with maximum forces reaching 1.5 µN was measured. For each measurement point, an average of 1.5 s was required. A pollen tube is characterized starting from the tip and reaching approximately 50 µm toward its shank. The reconstructed 3D topography representation of the pollen tube colored with measured stiffness values is depicted. The apparent stiffness measured on the cell wall is around 2 Nm^{-1} and depends on geometrical factors, cell wall stiffness, and turgor pressure. Around the perimeter of the pollen tube, the calculated stiffness is lower. This is due to
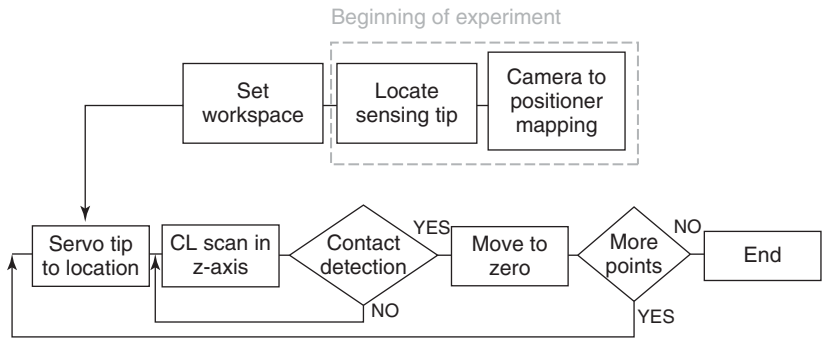
Figure 11.12 Flowchart of the experimental procedure in the RT-CFM including the calibration methods followed at the beginning of the experiment. CL, closed-loop.
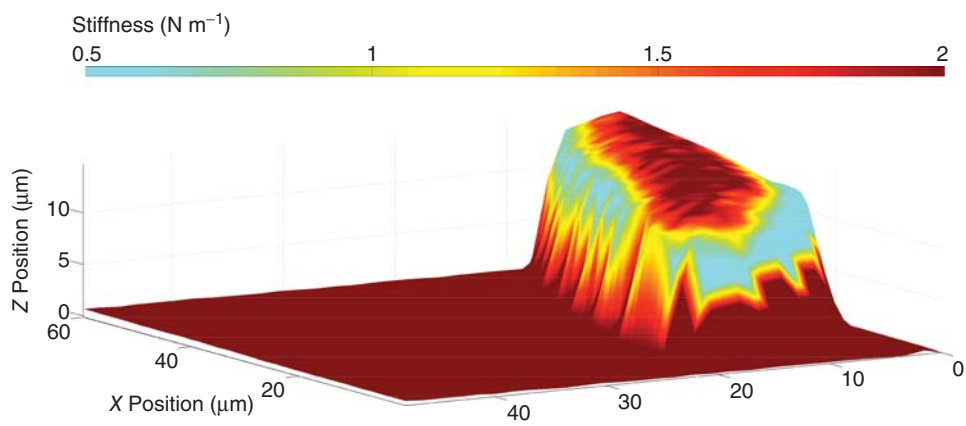
Figure 11.13 Combined 3D topography and stiffness map of a lily pollen tube growing on a glass slide. The axes denote *x*, *y*, and *z* position and the colormap is the measured stiffness in N m^{-1}. A grid of 60×50 μm is covered and the measurement force was set at 1.5 μN.

the fact that at the edges of the pollen tube, there is slippage between the sensor tip and cell wall, resulting in a miscalculation of the stiffness at those points. Moreover, the system measures along the vertical axis, and, thus, no information for the side wall stiffness can be inferred. These results demonstrate the capability of the RT-CFM to generate high-resolution topography and stiffness maps on growing organisms at micrometer dimensions. However, to get better information about the apparent stiffness at the edges, 2D force sensor will be required.

Pollen tubes change their morphology while growing, and it is essential to study the effect of growth on the mechanical properties of the cell wall. Because of their high growth rate, the measurements needed to be fast and well localized on the area of interest. The real-time control ensured the speed and determinism

of measurement, and the visual servoing functionality allowed us to accurately localize the sensor tip on the growing cell and compare successive experiments.

11.3.3
Real-Time Intracellular Imaging During Mechanical Stimulation

Even though much is known about the biosynthesis of the cell wall, the individual contributions of components to the mechanical properties of the cell wall is not well understood. A signaling network regulating pollen tube growth at the tip has been identified, relying on calcium (Ca^{2+}) and reactive oxygen species (ROS) as secondary messengers [34]. Furthermore, coordinated vesicle trafficking is critically important for the delivery of new cell wall material to the growth zone near the tip of the pollen tube. Despite intensive prior efforts over the years, controversy surrounding the exact location of exo- and endocytosis remains [35, 36].

In conjunction with the micromechanical characterization of the material properties of cells, we are interested in understanding how external mechanical stresses are perceived, influence behavior, and are in turn modified by cells. Because of its modular design, the CFM can be integrated with various types of microscopes. In combination with fluorescence microscopy, the CFM is a useful tool for quantifying the physiological responses of cells to mechanical stimulation. Ca^{2+}, for instance, is known to play a vital role in the tip growth process of pollen tubes. Fluorescent molecular markers allow us to visualize the tip-focused gradient of cytosolic Ca^{2+}, which is essential for pollen tube elongation [37], and there is evidence that directional changes are preceded by a delocalization of this gradient [38, 39]. Mechanosensitive channels have been proposed to play a role in establishing and maintaining the Ca^{2+} gradient, based on the effects of nonspecific stretch channel inhibitors such as lanthanides [34]. Even though the presence of such channels in pollen tubes still lacks molecular evidence, they have been identified in *Arabidopsis* root hairs, which employ a tip-growing mechanism similar to that of pollen tubes [40].

We showed that RT-CFM can be used to directly test the effect of mechanical stimulation on cytosolic Ca^{2+} fluxes in growing pollen tubes. Figure 11.14 shows a ratio analysis of an *Arabidopsis* pollen tube expressing the Ca^{2+} sensor YC3.60 before, during, and after mechanical stimulation with a force of 10 μN that was maintained for 20 s. Before stimulation, a regular Ca^{2+} oscillation pattern at the pollen tube tip was observed (Figure 11.14a and d). Coinciding with the first contact of the pollen tube with the sensor probe (2 μN at 153 s), this pattern was disturbed. Application of the full force (155 s) dissipated both the Förster resonance energy transfer (FRET) and the cyan fluorescent protein (CFP) signals, probably due to compression of the cytoplasm around the sensor probe (Figure 11.14b and d). Release of the mechanical stimulus resulted in a sharp peak of Ca^{2+}, followed by a phase without Ca^{2+} oscillation (Figure 11.14c and d), which was resumed 95 s after the force release but with a smaller amplitude and at a lower frequency than before stimulation (Figure 11.14d).
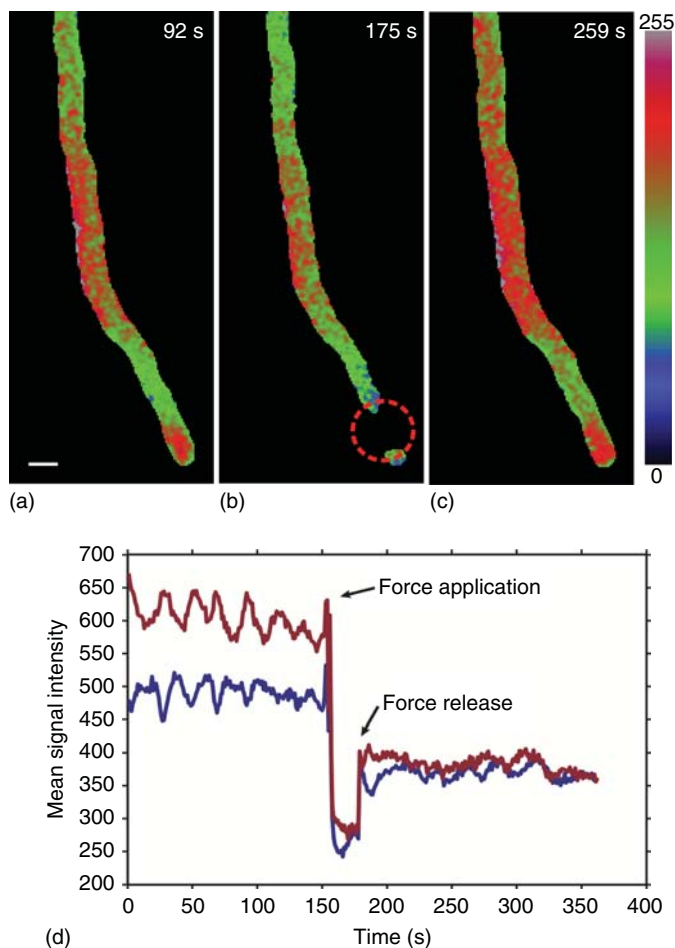
Figure 11.14 Effect of mechanical stress on the intracellular Ca^{2+} concentration. (a–c) Mechanical force was applied near the tip of an *Arabidopsis* pollen tube (dashed circle). Snapshots of the experiment are shown representing Ca^{2+} oscillation (a) before, (b) during, and (c) after the application of the mechanical stimulus, respectively. The images are shown in false color (red: high Ca^{2+} levels, blue: low Ca^{2+} levels; scale bar = 20 μm). Time points indicated at the top of the panels (a) to (c) correspond with the time in (d). (d) Ratio analysis over time. The ratio (FRET/CFP) is a measure for the intracellular Ca^{2+} levels. In (g), the FRET (red) and CFP (blue) channels are shown separately. FRET, Förster resonance energy transfer; CFP, cyan fluorescent protein.

11.4
Conclusions

In plant cells, the increase in cell volume and, thus, growth occur due to cellular expansion. Cellular expansive growth results from the combined actions of deformation of the existing cell wall by turgor pressure and the secretion and

deposition of new cell wall material by vesicle secretion. The mechanism of cell wall loosening and the contribution of upstream molecular and signaling pathways to morphogenesis remains relatively poorly understood. To characterize the mechanics of the cell wall during growth and to understand how plant cells sense, control, and tune external stimuli, characterization of the physical properties at the cellular level is essential. However, the tools for precise manipulation and testing of growing cells are largely lacking.

Our approach to this problem is a microrobotic system. Microrobotics offers the precision for delicate manipulation and stimulation of cells, high data throughput through automation of tasks, and high speed that results in reduced experiment time, which is critical for fast morphological changes and changes in the physiological state of cells. The first system, which we called the cellular force microscope (CFM), was designed to conduct highly localized measurements and compute automated stiffness and topography maps of growing cells and structures. Our experience following extensive use of the first-generation CFM suggested alterations to both improve the existing system and extend its capabilities. The second system, the real-time CFM, comprises more precise and reliable actuation technology, real-time acquisition and control architecture, and increased modularity, allowing for integration with a variety of microscope configurations. Moreover, using computer vision algorithms, we drastically reduced the experiment time and added new functionalities. The new features include automated calibration, photomosaic rendering of the workspace at high magnifications, and visual servoing achieved by selecting points from the camera stream or by tracking the silhouette of growing cells.

Using the CFM, we successfully characterized the mechanics and topography of growing pollen tubes and living plant tissues and achieved highly localized rupture of a single cell within a tissue. In combination with an FEM model of the pollen tube, we experimentally obtained values for the Young's modulus and turgor pressure in lily pollen tubes. CFM combined with fluorescence microscopy provides a tool for studying the effects of mechanical stimulation on physiological parameters. As an example, we describe a method for studying the Ca^{2+} oscillations after micromechanical stimulation at the pollen tube tip. This method will assist in revealing the existence of mechanosensitive channels in pollen tubes. In addition to Ca^{2+} sensors, molecular markers for the cytoskeleton, H^+, and ROS concentrations are available. The CFM platform is compatible with various imaging systems and enables a powerful screening technology to facilitate biomechanical and morphological characterization of developing cells.

References

1. Wei, C. and Lintilhac, P. (2007) Loss of stability: a new look at the physics of cell wall behavior during plant cell growth. *Plant Physiol.*, **145** (3), 763–772.

2. Geitmann, A. (2006) Experimental approaches used to quantify physical parameters at cellular and subcellular levels. *Am. J. Bot.*, **93** (10), 1380–1390.

3. Chanliaud, E. and Gidley, M.J. (1999) In vitro synthesis and properties of pectin/acetobacter xylinus cellulose composites. *Plant J.*, **20** (1), 25–35.

4. Cosgrove, D.J. (1993) Wall extensibility: its nature, measurement and relationship to plant cell growth. *New Phytol.*, **124** (1), 1–23.

5. Edge, S., Steele, D.F., Chen, A., Tobyn, M.J., and Staniforth, J.N. (2000) The mechanical properties of compacts of microcrystalline cellulose and silicified microcrystalline cellulose. *Int. J. Pharm.*, **200** (1), 67–72.

6. Kutschera, U. (1996) Cessation of cell elongation in rye coleoptiles is accompanied by a loss of cell-wall plasticity. *J. Exp. Bot.*, **47** (9), 1387–1394.

7. Wei, C., Lintilhac, L., and Lintilhac, P. (2006) Loss of stability, pH, and the anisotropic extensibility of *Chara* cell walls. *Planta*, **223** (5), 1058–1067.

8. Huang, C.C., Wang, C.F., Mehta, D.S., and Chiou, A. (2001) Optical tweezers as sub-pico-newton force transducers. *Opt. Commun.*, **195** (1), 41–48.

9. Zlatanova, J. and Leuba, S.H. (2003) Magnetic tweezers: a sensitive tool to study DNA and chromatin at the single-molecule level. *Biochem. Cell Biol.*, **81** (3), 151–159.

10. Hochmuth, R.M. (2000) Micropipette aspiration of living cells. *J. Biomech.*, **33** (1), 15–22.

11. Muller, D.J. and Dufrêne, Y.F. (2008) Atomic force microscopy as a multifunctional molecular toolbox in nanobiotechnology. *Nat. Nanotechnol.*, **3** (5), 261–269.

12. Burgert, I. and Keplinger, T. (2013) Plant micro- and nanomechanics: experimental techniques for plant cell-wall analysis. *J. Exp. Bot.*, **64** (15), 4635–4649.

13. Muntwyler, S.D. (2011) Microforce-sensing probes and methodologies for micromechanical and dimensional metrology. PhD thesis. ETH Zurich.

14. Pharr, G. and Oliver, W. (1992) Measurement of thin film mechanical properties using nanoindentation. *MRS Bull.*, **17** (7), 28–33.

15. Footer, M.J., Kersssemakers, J.W., Theriot, J.A., and Dogterom, M. (2007) Direct measurement of force generation by actin filament polymerization using an optical trap. *Proc. Natl. Acad. Sci. U.S.A.*, **104** (7), 2181–2186.

16. Ananthakrishnan, R. and Ehrlicher, A. (2007) The forces behind cell movement. *Int. J. Biol. Sci.*, **3** (5), 303–317.

17. Winer, J.P., Oake, S., and Janmey, P.A. (2009) Non-linear elasticity of extracellular matrices enables contractile cells to communicate local position and orientation. *PLoS ONE*, **4** (7), e6382.

18. Discher, D.E. (2005) Tissue cells feel and respond to the stiffness of their substrate. *Science*, **310** (5751), 1139–1143.

19. Sun, Y., Wan, K.T., Roberts, K.P., Bischof, J.C., and Nelson, B.J. (2003) Mechanical property characterization of mouse zona pellucida. *IEEE Trans. Nanobiosci.*, **2** (4), 279–286.

20. Vogler, H., Draeger, C., Weber, A., Felekis, D., Eichenberger, C., Routier-Kierzkowska, A.L., Boisson-Dernier, A., Ringli, C., Nelson, B.J., Smith, R.S., and Grossniklaus, U. (2012) The pollen tube: a soft shell with a hard core. *Plant J.*, **73** (4), 617–627.

21. Cherry, A., Abadie, J., and Piat, E. (2007) Microforce sensor for micro-biological applications based on a floating-magnetic principle. 2007 IEEE International Conference on Robotics and Automation, IEEE, pp. 1504–1509.

22. Wang, L., Mills, J.K., and Cleghorn, W.L. (2008) Development of an electron tunneling force sensor for the use in microassembly. 1st Microsystems and Nanoelectronics Research Conference, 2008. MNRC 2008, *IEEE*, pp. 205–208.

23. Fahlbusch, S. and Fatikow, S. (1998) Force sensing in microrobotic systems-an overview. 1998 IEEE International Conference on Electronics, Circuits and Systems, pp. 259–262.

24. Lucas, D.B. and Kanade, T. (1981) *An iterative image registration technique with an application to stereo vision*, International Joint Conference on, Artificial Intelligence, pp. 674–679.

25. Felekis, D., Muntwyler, S., Vogler, H., Beyeler, F., Grossniklaus, U., and Nelson, B.J. (2011) Quantifying growth mechanics of living, growing plant cells in situ using microrobotics. *Micro Nano Lett.*, **6** (5), 311–316.

26. Routier-Kierzkowska, A.L., Weber, A., Kochova, P., Felekis, D., Nelson, B.J., Kuhlemeier, C., and Smith, R.S. (2012) Cellular force microscopy for *in vivo measurements of plant tissue mechanics*. *Plant Physiol.*, **158** (4), 1514–1522.

27. Cheung, A.Y. and Wu, H.M. (2008) Structural and signaling networks for the polar cell growth machinery in pollen tubes. *Annu. Rev. Plant Biol.*, **59** (1), 547–572.

28. Holdaway-Clarke, T.L. and Hepler, P.K. (2003) Control of pollen tube growth: role of ion gradients and fluxes. *New Phytol.*, **159** (3), 539–563.

29. Krichevsky, A., Kozlovsky, S.V., Tian, G.W., Chen, M.H., Zaltsman, A., and Citovsky, V. (2007) How pollen tubes grow. *Dev. Biol.*, **303** (2), 405–420.

30. Hepler, P.K., Lovy-Wheeler, A., McKenna, S.T., and Kunkel, J.G. (2006) Ions and pollen tube growth, in The Pollen Tube. *Springer-Verlag*, pp. 47–69.

31. Geitmann, A. and Parre, E. (2004) The local cytomechanical properties of growing pollen tubes correspond to the axial distribution of structural cellular elements. *Sex. Plant Reprod.*, **17** (1), 9–16.

32. Zerzour, R., Kroeger, J., and Geitmann, A. (2009) Polar growth in pollen tubes is associated with spatially confined dynamic changes in cell mechanical properties. *Dev. Biol.*, **334** (2), 437–446.

33. Felekis, D., Vogler, H., Mecja, G., Muntwyler, S., Nestorova, A., Huang, T., Sakar, M.S., Grossniklaus, U., and Nelson, B.J. (2014) Real-time, automated characterization of 3D morphology and mechanics of developing plant cells. *Int. J. Rob. Res.*, doi: 10.1177/0278364914564231.

34. Dutta, R. and Robinson, K.R. (2004) Identification and characterization of stretch-activated ion channels in pollen protoplasts. *Plant Physiol.*, **135** (3), 1398–1406.

35. Silva, P.A., Ul-Rehman, R., Rato, C., Di Sansebastiano, G.P., and Malhó, R. (2010) Asymmetric localization of *Arabidopsis* syp124 syntaxin at the pollen tube apical and sub-apicalzones is involved in tip growth. BMC Plant Biol., **10** (1), 179.

36. Zonia, L. and Munnik, T. (2007) Life under pressure: hydrostatic pressure in cell growth and function. *Trends Plant Sci.*, **12** (3), 90–97.

37. Jaffe, L.A., Weisenseel, M.H., and Jaffe, L.F. (1975) Calcium accumulations within the growing tips of pollen tubes. *J. Cell Biol.*, **67** (2), 488–492.

38. Holdaway-Clarke, T.L., Feijo, J.A., Hackett, G.R., Kunkel, J.G., and Hepler, P.K. (1997) Pollen tube growth and the intracellular cytosolic calcium gradient oscillate in phase while extracellular calcium influx is delayed. *Plant Cell Online*, **9** (11), 1999–2010.

39. Malhó, R., Read, N.D., Pais, M.S., and Trewavas, A.J. (1994) Role of cytosolic free calcium in the reorientation of pollen tube growth. *Plant J.*, **5** (3), 331–341.

40. Nakagawa, Y., Katagiri, T., Shinozaki, K., Qi, Z., Tatsumi, H., Furuichi, T., Kishigami, A., Sokabe, M., Kojima, I., and Sato, S. (2007) *Arabidopsis* plasma membrane protein crucial for Ca^{2+} influx and touch sensing in roots. *Proc. Natl. Acad. Sci. U.S.A.*, **104** (9), 3639–3644.

12

Magnetotactic Bacteria for the Manipulation and Transport of Micro- and Nanometer-Sized Objects

Sylvain Martel

12.1
Introduction

The manipulation or transport of micro- and nanometer-sized objects is an important research area and one that can impact several applications. For instance, manipulation allows the assembly of structures at the nano- to the microscale while the transport of nano- and microcomponents also plays critical roles in many areas, such as for detection and analysis in microfluidic devices. These are only few examples of potential applications among many under investigation. The transport of nanoscale objects can also occur in less-friendly microenvironments where the operations must be performed under excessive constraints. This is the case for the controlled transport of nanoscale components such as liposomes or polymeric particles carrying drug molecules through microvascular networks in the human body for nonsystemic therapeutic delivery in cancer therapy, to name but only one example in the medical field alone.

For assembly, the two main approaches available are self-assembly and controlled assembly. Self-assembly is known as being a type of process in which preexisting components form an organized structure typically through local interactions between the components. Even though the characteristics of each component in self-assembly must be carefully chosen, which is not necessarily true for controlled assembly, it has the advantage of being parallel as opposed to controlled assembly, which is a serial process. Being able to increase parallelization using a huge number of coordinated transporters or manipulators would make controlled assembly a preferred choice for a larger range of applications. But expanding its applicability and overall advantage over a wider range of applications by increasing the throughput rate through parallelization is not an obvious task. To better appreciate the challenge for the implementation of parallel manipulators, one must be familiar with the controlled assembly approaches, which include but are not limited to mechanical manipulators, dielectrophoresis, and optical tweezers, to name but the main ones.

The main advantage of mechanical manipulation or transport over other methods is that it is fairly independent of the properties of the components (e.g., dielectric property) being manipulated. But the system can be bulky and complex while being hard to implement in constrained spaces including inside microfluidic channels and inside the human body. As such, swarms of microorganisms and specifically mobile bacteria acting as micromanipulators can provide an alternative to achieve mechanical microassembly and transport of components of various sizes.

12.2
Magnetotactic Bacteria

The force provided by the flagellated molecular motors of bacteria can be used for manipulation and transport of nano- to micrometer-sized objects. For precise and predictable computer-controlled transport and manipulation tasks, a specific type of flagellated bacteria known as *magnetotactic bacteria* (*MTB*) [1] has been considered. MTB are adequate microorganisms for such applications because each cell has a chain of membrane-based nanoparticles that are being referred to as *magnetosomes*. Such embedded chain acting like a miniature compass needle can be exploited to act as an embedded steering system to control the directional motion of the MTB using computer-based magnetotaxis [2, 3] control. MTB cells of strain MC-1 (one cell is depicted in Figure 12.1) have been investigated for various applications including the transport of therapeutics to solid tumors and in various microassembly tasks. The rounded MC-1 cell has a typical diameter between 1 and 2 µm. Each cell is propelled by two flagella bundles activated by rotary motors. These molecular motors are somewhat similar in design to modern rotary artificial motors. Indeed, as their macroscale engineered counterparts, such molecular motors are characterized by a rotor that rotates 360° inside a stator. Instead of a propeller, these bacteria use flagella that proved to be far more efficient for displacements in low Reynolds number hydrodynamics as it is the case at such a scale. Counterclockwise rotation of the flagella is used for forward displacements whereas clockwise rotation is used for backward displacements. The average swimming velocity of the MC-1 cells in water at room temperature has been recorded at ~200 µm s^{-1} with peak velocities at ~300 µm s^{-1} under
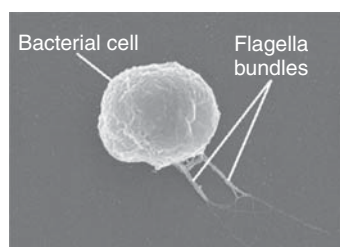
Figure 12.1 Photograph of the MC-1 bacterial cell showing the two bundle of flagella used as propelling system. The chain of magnetosomes (not visible in the figure) used for magnetotaxis directional control is embedded in the cell.

the same conditions. This is ∼10 times the velocities of many other species of flagellated bacteria.

The chain made of ∼10 aligned iron oxide nanocrystals (nanoparticles) embedded in each MC-1 cell allows the use of a weak directional magnetic field to direct the swimming direction of each bacterium. Indeed, since in their natural environment, the geomagnetic field is used to guide their migration path toward their preferred environment characterized by low oxygen concentrations, the sensibility of the chain to a magnetic directional torque is very high. This is due in great part by the embedded compass needle that is made of ∼70 nm in diameter single magnetic domain nanocrystals that are close enough to allow dipole−dipole interactions between neighbored nanoparticles.

MTB can be axial or polar. Axial MTB are characterized by flagella on both extremities of the cell whereas polar MTB have flagella on only one extremity. Unlike axial MTB that can swim in either direction along the lines of magnetic field, polar MTB swim persistently in one direction, either North-seeking or South-seeking. In the northern hemisphere, polar MTB will migrate toward the North Pole (North-seeking), whereas in the southern hemisphere, polar MTB will generally swim toward the South Pole (South-seeking). In the laboratory environment, the MTB can be programmed to be North-seeking or South-seeking by repolarizing the magnetosomes using magnetic pulses among other approaches.

Magnetotaxis directional control of the MTB is possible due to the alignment of the MC-1 magnetosomes (intracellular enveloped single magnetic domain Fe_3O_4 nanoparticles). These magnetosomes are synthesized in the cell during well-controlled cultivation parameters. A cell magnetic dipole is created when the MTB is exposed to a magnetic field and can be described by the following Langevin function:

$$\cos \Theta = L \left(\frac{m\mu_0 H}{k_B T} \right), \tag{12.1}$$

where Θ represents the angle between the direction of the cell magnetic moment m and the ambient directional magnetic field $H = \mu_0^{-1} B$, B is the magnetic field density, and μ_0 is the permeability of free space. The Boltzmann constant and the temperature are represented in Eq. (12.1) by k_B and T, respectively.

According to Eq. (12.1), the level of magnetotaxis directional control corresponds to the alignment of the cell in the applied directional magnetic field. The latter is determined by the ratio of the interactive magnetic energy with the applied field (mB) to the thermal energy ($k_B T$). The thermal energy is known to be the thermal forces associated with Brownian motion that tends to randomize the cell orientation. Besides magnetotaxis, the motion of the MC-1 cell can also be influenced by other environmental sources. For example, oxygen will influence the displacement behavior of the cell (aerotaxis). Therefore, in the absence of sufficient directional magnetic field, random motion will only take place if the bacterium is not influenced by another compatible taxis-based source. On the other hand, when operating under magnetotaxis directional control for precise and deterministic micromanipulation or transport tasks, the magnetic energy must be sufficiently

high to reduce the effect of other potential taxis-based sources that could contribute to make directional control less deterministic. Past experiments showed that a magnetic field of only ∼4 Gauss compared to the geomagnetic field in the range of 0.5 Gauss is generally sufficient to achieve highly accurate and deterministic magnetotaxis directional control.

Also, as depicted in Eq. (12.1), an elevation of the temperature will lead to a decrease of the magnetotaxis directional control efficacy which will require a higher directional field strength. But this will not be applicable here since a rise of the temperature will also impact not only the lifespan of the MC-1 cells but their swimming velocities as well. For instance, even though several hours of operations are possible in fluidic environments at room temperature, increasing the temperature to 37 °C, for example, results to a continuous decrease of the velocities of the MTB immediately after being exposed to such a temperature level from an average velocity of ∼200 μm s^{-1} to no motility after ∼40 min for the last surviving portion of the bacteria. Indeed, the population of live MC-1 cells begins to decay as soon as they are exposed to such high temperature which is not typically the case when operating around room temperature. Even though such MTB offers interesting advantages compared to an artificial version, this observation suggests that the environment and the conditions in which such bacterial actuators can operate efficiently must be taken into account for a specific task while limiting the range of possible environmental conditions in which they can operate.

The self-reproducing capability is one of the major advantages of MTB-based actuators over artificial implementations besides the self-propelled capabilities and the very low magnetic directional field required for directional control. Such self-reproducing capability provides a very low cost and highly reproducible manufacturing process compared to known artificial microactuators. On the other hand, besides environmental restrictions preventing the proper use of MTB, the lifespan, and the storage-related issues before their use are some of the main constraints imposed by MTB-based actuators. Nonetheless, being aware of these constraints, MTB can offer a suitable means compared to any other approaches for specific manipulation and transport tasks.

12.3
Component Sizes and Related Manipulation Approaches

The range of component sizes that can be manipulated by the MC-1 bacteria [4, 5] is depicted in Figure 12.2. The overall sizes of the components range from nanometers to higher than 100 μm across and can be grouped as much smaller (MS), approximately equivalent (AE), and much larger (ML) than the bacterial cell.

Accordingly, the two main manipulation approaches that can be used can be categorized as attached and nonattached manipulation, where the component is attached and not attached to the surface of the bacterial cell, respectively. For components in the MS and the AE groups, the attached manipulation
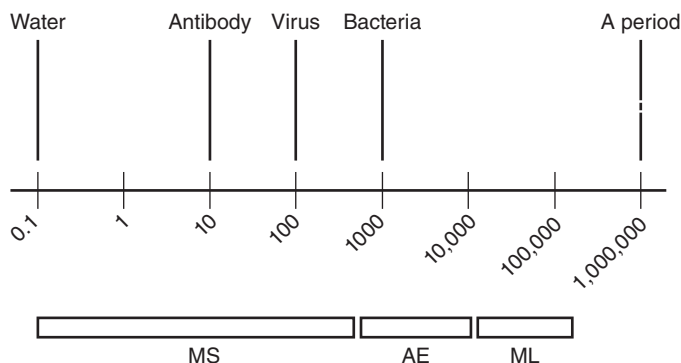
Figure 12.2 Graph showing the three approximate ranges of components that can be transported by the MC-1 cells for manipulation or microassembly purpose. The scaling is in nanometers.

approach is more suitable. Even though the attached manipulation approach could be used for components in the ML group, the nonattached manipulation approach is typically the preferred choice. The main reasons for using the nonattached manipulation approach for objects in the ML group are the ease in scaling the actuation force through the use of a larger population of MTB, maintaining the surface of the components free of bacterial cells, and the possibility to dispatch the same group of bacteria to various locations with the goal of manipulating several components without the need for additional bacteria.

12.3.1
Transport and Manipulation of MS Components

MS components are typically first attached to the surface of the bacterial cells before conducting transport or manipulation tasks. A self-assembly process is typically used to attach the components to the cells. Such self-assembly process provides high-throughput attachments of a large quantity of nanocomponents, and in most cases, it is the only or most suitable approach especially with the use of extremely high quantity of nano-objects that need to be transported or manipulated. Even though several attachment methods, also being referred to as *bioconjugation*, can be used, several factors, such as the level of specificity and the attachment strength associated with a particular method, are often (but not always) important issues.

Bioconjugation can be performed using covalent binding techniques such as carbodiimide dehydrating agent by exploiting the terminal amine group on the outer membrane of the MC-1 bacterial cell. Such terminal amine groups are ideal docking sites for specific nanometer-sized components, such as the widely used nanoliposomes that can act as nanocontainers to encapsulate molecular-sized objects. A photograph of ~70 nanoliposomes attached to the surface of an MC-1 cell is depicted in Figure 12.3. This is only one example of potential nanoscale
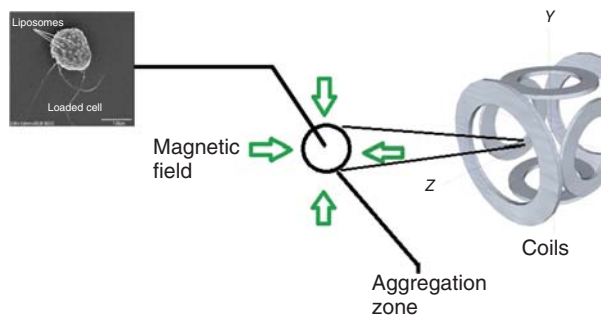
Figure 12.3 Basic approach used to aggregate nanometer-sized components attached to the magnetotactic bacterial cells (upper left corner) in a specific 3D space being referred to as *the aggregation zone.*

components that can be attached using such a method. Carbodiimide cross-linking is recognized as a versatile technique with stable chemical bonds, ease of sample preparation, high coupling efficiencies, reproducibility, relatively low cost, and most importantly, high strength bond. The dissociation energy with this approach is much higher compared to other methods, such as antibody–antigen affinity type bioconjugation including van der Waals forces, electrostatic forces, hydrogen bonds, and hydrophobic effects.

Some attachment methods may not be as specific as the carbodiimide approach. Unlike the latter that causes the nanocomponents to be attached only to the surface of the cell, other methods such as the use of polyclonal antibodies may result in one or more nano-objects to be attached to the flagella of the bacteria, affecting their motility. If losing a portion of the loaded bacteria population for manipulation or transport purpose because of a loss in motility due to nano-objects being attached to the flagella is not acceptable or desirable, then other attachment approaches should be considered. Achieving the required specificity with the use of monoclonal antibodies is another potential method but this approach may prove to be expensive and time consuming since a specific antibody must be available for each specific site on the surface of the bacterial cell. This again stresses the gained potential advantage of the carbodiimide approach in this particular case unless a specific site on the surface of the cell is an important requirement.

If a method such as carbodiimide bioconjugation is used, then the accuracy of the placement of the nanometer-scale components is restricted to the fact that they can be attached anywhere on the surface of the bacterial cell. Keeping that in mind, there are two steps for the positioning of the nanometer-scale components. The first step is concerned with their attachment sites on the surface of the cell. Unlike the use of monoclonal antibodies and as mentioned previously, the exact location of a particular nano-object on the surface of the cell cannot be predetermined but the position will be bounded by the total surface of each cell which we recall has a maximum diameter of ~2 μm for the MC-1 bacteria. In many cases, especially when all the nano-objects are identical, this is not a real constraint. The second step in the placement process is concerned with the displacement

of the bacterial carriers themselves. If the total number of nanocomponents is carried by a single bacterium, then the final position of the cluster of nanocomponents can be precisely set within a space corresponding to the overall size of the bacterial cell itself if the magnetic field is set appropriately. On the other hand, if more than one bacterium is required to carry all nanocomponents, then the level of uncertainties related to the final position of a specific nanocomponent is typically increasing with the number of bacterial carriers being used simultaneously. Such uncertainty volumetric space is bounded by the outer boundary of the aggregation of bacteria. For magnetotaxis position control, the aggregation of such bacterial carriers for transport or manipulation of nanometer-sized components can be done over a planar surface or in a three-dimensional (3D) fluidic volume.

On a planar surface, the aggregation can be formed by magnetic field lines converging to a single point. In this particular case, the planar surface acts as a boundary such that the magnetic field generated can be constant. As such, a simple magnet or a magnetized body such as a magnetized nail placed underneath the planar surface can be used.

But the transport or manipulation of nanometer-sized components by MTB allows the placement to be set in a predefined location within a 3D volumetric space. But without a planar surface or other obstacles restricting the motion of the bacteria in a particular axis, the magnetic field must be modulated through time-multiplexing sequences [6] in order to create an artificial magnetic monopole. Such multiplexing is required since creating a magnetic monopole goes against one of Maxwell's four equations for electromagnetism which states that the magnetic induction divergence in any point is zero. In other words, this is accomplished by multiplexing different static magnetic field geometries over time creating what in essence can be viewed as the addition of a fourth dimension. As such, the magnetotactic bacterial cells are sequentially exposed to different magnetic field geometries for predefined intervals in order to simulate the existence of a magnetic monopole. Such sequences of magnetic fields are generated by a special platform that has been referred to as *a magnetotaxis system* as depicted in the far right of Figure 12.3. The magnetotaxis platform typically consists of three orthogonal pairs of electric coils positioned in a Maxwell configuration.

As depicted in Figure 12.3, the coils are used to generate the time-sequenced magnetic fields that converge to the site to aggregate the nanocomponents being attached to the MC-1 cells. As the distance from the coils increases, the magnitude of the magnetic field decreases until it becomes insufficient to induce a directional torque on the chain of magnetosomes in the MC-1 cells. The locations where this occurs define the outer limit of what is referred to as *the aggregation zone*. Any MTB escaping the aggregation zone will be forced to reenter the aggregation zone due to the increased directional field inducing a sufficiently high torque on the chain of magnetosomes and toward the center of the aggregation zone. If no compatible taxis-based sources, such as oxygen gradients, are present in the aggregation zone, then random motions of the MTB within such volumetric space are expected.

To achieve a better spatial resolution for the transport of nanocomponents, the diameter of the aggregation zone must be reduced accordingly. To do so, the current circulating in the coils of the magnetotaxis system must be increased. In other words, the ability to aggregate loaded MTB into a smaller volumetric space to achieve higher positional accuracy will require higher power for the coils. Even though the power to directionally control loaded MTB is relatively low considering that precise trajectory motions can be achieved using directional magnetic fields slightly higher than the geomagnetic field, defining a small aggregation zone especially within a relatively large working space (i.e., large inner diameter of the coils) may require much higher electrical power. Offsetting the aggregation zone once the loaded bacteria have been in the aggregate can be easily achieved by modifying the electrical current ratio circulating in opposite coils. Even though 3D transport and manipulation is possible in a 3D volume, performing assembly tasks may prove to be much more challenging compared to planar assembly tasks based on the transport and manipulation of larger objects.

12.3.2
Transport and Manipulation of AE Components

Typically only one AE component can be attached per MC-1 cell. The attachment methods available are similar to the ones used for attaching MS components. Unlike the bacterial manipulation or transport of MS components, transport and manipulation of AE components is typically restricted to a 2D (planar) workspace. The main reason is the inability of a single cell to lift such relatively large objects. Unless the buoyancy of the object being manipulated can be adjusted appropriately, 3D bacterial transport may prove to be really challenging if possible.

Preliminary experimental tests showed that a single MC-1 cell could transport efficiently a component approximately three times or more the size of the bacterial cell itself, and the velocity achieved by doing so suggests that larger objects could also be manipulated by a single cell. An interesting fact from preliminary experimental observations showed that the MC-1 cell reverses the rotation of the flagella from counterclockwise to clockwise to pull an attached object much larger than the cell itself instead which results in more effective motions. This reversal is done without the need for an external command. An example of a bead approximately three times the diameter of the MC-1 cell being pulled is depicted in Figure 12.4. Again, the directional control is performed with the use of a directional magnetic field slightly higher than the geomagnetic field.

12.3.3
Transport and Manipulation of ML Components

MTB can be attached or not to ML components. For ML components approaching the size of the MTB cell but still much larger than the MC-1 cell itself, attaching the several bacteria to the components typically yields better results. Several MTB per component is required to scale the force accordingly. As such, the component
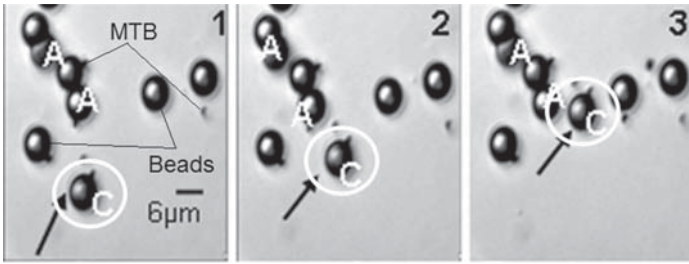
Figure 12.4 One example of a bead about three times the diameter of the MC-1 cell being pulled by one bacterium acting under directional magnetotaxis control.

must have a sufficiently large surface to accommodate the number of bacteria required to transport such component under magnetotaxis control. An example of the microassembly of such large components in the form of relatively large beads is depicted in Figure 12.5.

For larger components, not attaching the MTB becomes an option in most cases. The advantage of not attaching the bacteria is that the same batch of MTB can be dispatched successively to other components that need to be transported. Two examples of large (~100 μm across) components being transported by nonattached MC-1 cells to be assembled as microstructures are depicted in Figure 12.6.

In these examples, the components are transported one at a time. Once one component is placed at a predefined location, the aggregate of bacteria is dispatched to the next component that needs to be transported and placed next to the previously transported component in order to build the microstructure. The size of the aggregation or the number of bacteria being used is set to scale the
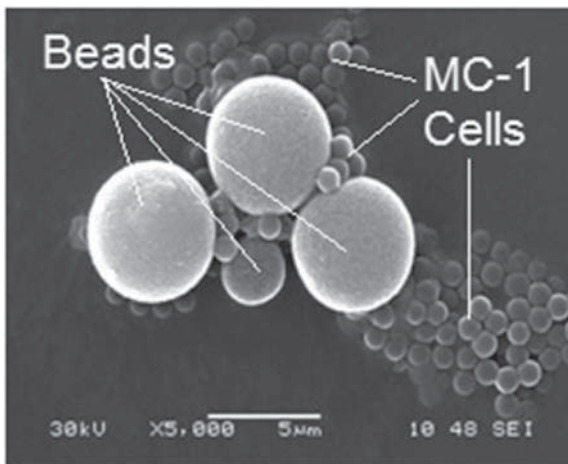
Figure 12.5 Large beads being assembled by many attached magnetotactic bacteria acting under magnetotaxis control.
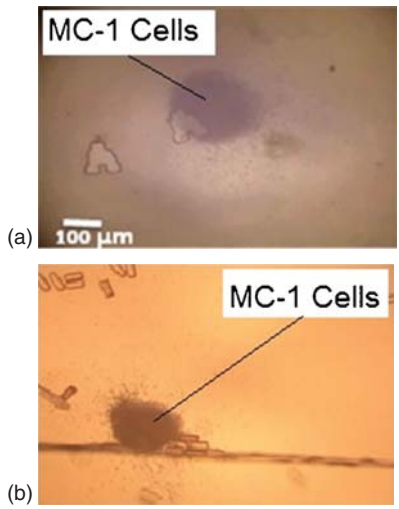
Figure 12.6 Two examples of ~100 µm across components being transported by an aggregate of a few thousands of MTB to form microstructures. (a) V-shaped components are manipulated and assembled to form the character M. (b) ~5000 MC-1 cells are used to move ~100 µm across epoxy blocks to build a miniature pyramid. These microassembly tasks were performed in a drop of water.

force required to move the component. Factors such as the size, shape, weight, and the type of surface are only few variables that can influence the efficacy of the manipulation being performed. The substrate being used can also influence the efficacy of the manipulation tasks. The placement of each component can be very precise with a level of accuracy that can be in one to a few micrometers ranges.

The fundamental method to transport such large components using an aggregate of MTB is represented by the simple schematic depicted in Figure 12.7. First, the components are placed on a substrate. Such a substrate would typically be a microscope slide where the microassembly tasks can be monitored under a microscope lens. Other materials besides glass can also be used as a substrate.
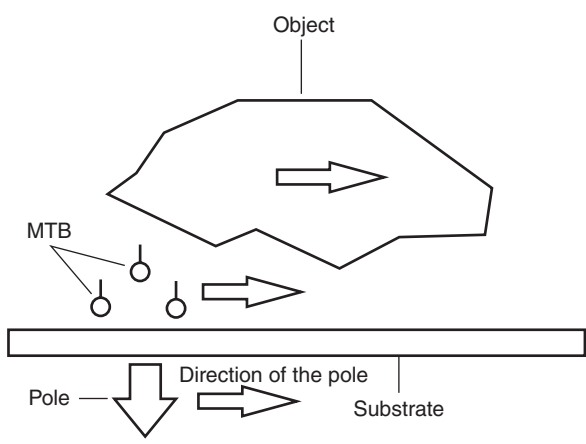
Figure 12.7 Simplified schematic showing the fundamental approach to move larger components with an aggregate of unattached magnetotactic bacteria.

Once the components are placed, a sufficient number of flagellated MTB to provide sufficient force to displace each component must be aggregated. To do so, lines of magnetic field of magnitude typically slightly higher than the geomagnetic field must be generated to converge toward the selected site of aggregation. Since the bacterial manipulation task is performed on a planar substrate, such pole can be generated with a simple permanent or electromagnet located right underneath the substrate directly under the location where the bacteria need to aggregate. This is depicted in Figure 12.7 by the arrow tagged "pole" pointing downward. Because of the presence of the substrate, the magnetotaxis system used for 3D transport is no longer required, although it can still be used for such applications.

Once the aggregation is formed on the substrate, the position of the pole can be shifted toward the object that needs to be moved. When moving, the MTB are oriented toward the substrate as depicted in Figure 12.7. When part of the bacterial aggregation is located underneath the object as depicted in Figure 12.7, the force applied on one side of the component becomes sufficient to move the object in the desired direction. For this to occur, the MTB must be able to position themselves underneath the object. As such, the substrate and/or the object itself must have a surface that is not perfectly smooth. A few micrometers are sufficient to allow the MTB to swim underneath the component that needs to be manipulated.

12.4
Conclusions and Discussion

Although not as well known as other manipulation and transport methods of nano- and micrometer-scale components in fluidic environments, the use of MTB can prove to be a suitable and advantageous alternative over all known approaches for specific cases. The self-replicating feature of the bacteria makes it an attractive solution where relatively low-cost manufacturing of a huge number of microactuators is highly desirable. Such advantage is paid by the fact that such bacterial microactuators will operate in restricted environmental conditions compared to artificial methods.

Even though the population of bacteria can be adjusted to scale the force for moving larger objects, achieving high-throughput microassembly tasks may prove to be more challenging. One alternative would be through the implementation of a large number of parallel miniature magnetotaxis systems for 2D or 3D operations being controlled by a single source for simplicity especially when a huge number or working spaces are used simultaneously. But this will limit the range of applications to relatively simple tasks that do not need closed-loop control. Although possible, much simple tasks such as transport instead of precise micromanipulation or assembly processes should initially be considered in such highly parallel approaches. Although in its infancy, further research and development in bacterial transport, manipulation, and assembly may help such approach to become an attractive solution to a wider range of applications while providing advantages that are not offered by any other known approach.

References

1. Blakemore, R.P. (1975) Magnetotactic bacteria. *Science*, **190**, 377–379.
2. Frankel, R.B. and Blakemore, R.P. (1980) Navigational compass in magnetic bacteria. *J. Magn. Magn. Mater.*, **15–18** (3), 1562–1564.
3. Debarros, H., Esquivel, D.M.S., and Farina, M. (1990) Magnetotaxis. *Sci. Prog.*, **74**, 347–359.
4. Martel S. and Mohammadi M. (2010) Using a swarm of self-propelled natural microrobots in the form of flagellated bacteria to perform complex micro-assembly tasks. IEEE International Conference on Robotics and Automation (ICRA), Anchorage, AK.
5. Martel, S., Tremblay, C., Ngakeng, S., and Langlois, G. (2006) Controlled manipulation and actuation of micro-objects with magnetotactic bacteria. *Appl. Phys. Lett.*, **89**, 233804–233806.
6. de Lanauze, D., Felfoul, O., Turcot, J.P., Mohammadi, M., and Martel, S. (2013) Three-dimensional remote aggregation and steering of magnetotactic bacteria microrobots for drug delivery applications. *Int. J. Rob. Res.*, **33** (3), 359–374.

13

Stiffness and Kinematic Analysis of a Novel Compliant Parallel Micromanipulator for Biomedical Manipulation

Xiao Xiao and Yangmin Li

13.1
Introduction

Applications related to biomedical engineering such as *in vitro* fertilization, intracytoplasmic sperm injection, genetic diagnosis, microdissection, and microinjection [1] play important roles in life science. As an important tool in these applications, micromanipulation system is a bridge that links the micro and macro world. Generally, the micromanipulation system mainly consists of micromanipulator, microscope, and control system [2] among which, micromanipulator as the execution unit is the most essential part in the whole system.

In perspective of biomanipulation, the cooperation of the micromanipulator and the microscope in a limited specimen installation space is very important. Compact structure with extraordinary manipulation abilities such as high accuracy, multidegrees of freedom, and large stroke is required, which raises a great challenge to the mechanical design of the micromanipulator.

It is known that compliant mechanism transmits motion and force by the elastic deformation of the flexures. Because of the merits of no backlash, no friction, and vacuum environment feasibility, compliant mechanism has found wide applications in ultrahigh precision positioning and manipulation [3−5].

There are two types of the structure of the compliant mechanism: (i) serial structure and (ii) parallel structure. Parallel structure is drawing more and more attention owing to its advantages of high stiffness, high accuracy, and high load capability [6]. There are many compliant parallel mechanisms that have been developed or commercialized. Awtar [7] designed a decoupled large range of parallel kinematic(XY) nanopositioner. Arai [8] proposed a hybrid two-fingered micro−nano manipulator hand for cell manipulation. Dong *et al.* [9] proposed a novel six-strut compliant parallel mechanism based on the wide-range flexure hinges. Xiao and Li [10] introduced a 3-DOF translational micro-parallel positioning stage that is driven by electromagnetic actuators. A series of commercial micro- or nanopositioning platforms are developed by PI. Inc.

In order to evaluate the performances of a compliant mechanism, analysis of stiffness and kinematics is usually needed. Stiffness is defined as the relationship between the external force and the corresponding displacement of the end-effector, which is used to evaluate the capability of resisting deformation. Therefore, it is an important performance index of the flexure-based compliant mechanism [11]. While in applications such as micropositioning and micromanipulation, the targets are usually micro- or nanosized objects. Thus, the reaction force applied on the end-effector is very small and the influence on the precision is insignificant. In this research, we define the stiffness as the relationship between the actuation force and output displacement of the end-effector.

Kinematics issue of parallel mechanism is related to the joint variables and position and orientation of the end-effector, which is the basis of many performance indexes, such as workspace, velocity, acceleration, and dexterity [12, 13]. As for compliant mechanism, the kinematics can be considered as the relationship between the input and output displacements. However, because of the flexible connections, the kinematics of the compliant mechanism is difficult to be determined. In most of the current literatures [14, 15], the kinematics of the compliant mechanism is performed by substituting the flexures with rigid kinematics joints, which result in an inaccurate kinematics model. In order to overcome these disadvantages, matrix displacement method [16] is adopted in this research.

On the basis of the above consideration and our previous works [17–19], a novel flexure-based parallel micromanipulator is proposed. And this research is concentrated on the stiffness and kinematic analysis of the micromanipulator. Modularization concept-based mechanical design is illustrated in Section 13.2. A beam flexure-based compliant P module and a cylinder flexure-based compliant 4S module are designed. On the basis of the matrix displacement method, stiffness and kinematics modeling of the micromanipulator are investigated in Sections 13.3 and 13.4. Finite element analysis (FEA) simulations are carried out, which indicate that the derived mathematic models are correct and the manipulator can be used in biomedical manipulations.

13.2
Design of the Micromanipulator

As shown in Figure 13.1, the proposed micromanipulator consists of the base, the platform, three actuators, and three identical chains. The three chains, which connect the platform and the base to form a parallel structure, are uniformly distributed in the semicylindrical space.

Each chain is made up of a compliant P(prismatic) module(active) and a compliant 4S(spherical) module(passive), which are illustrated in Figures 13.2 and 13.3. It is observed that two types of flexure elements are adopted in this design. One is beam flexure and the other is cylinder flexure. A beam flexure-based symmetrical
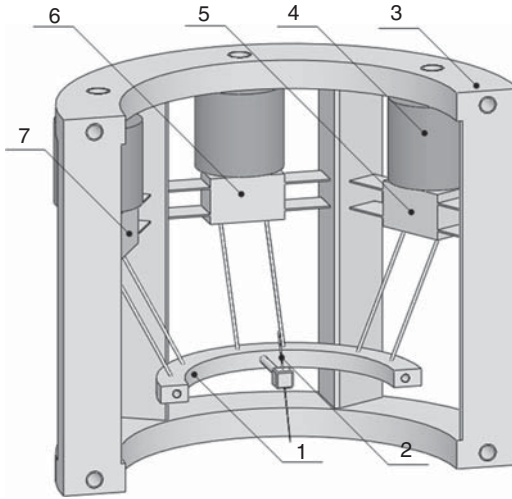
Figure 13.1 3D Model of the micromanipulator 1. Platform, 2. Pipette, 3. Base, 4. Actuator, 5. Chain 3, 6. Chain 1, 7. Chain 2.
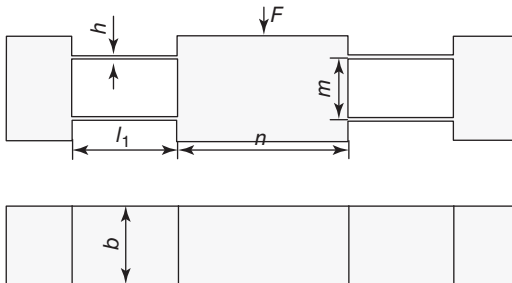
Figure 13.2 The compliant P module.

parallelogram mechanism is designed as the compliant P module for the benefits of large motion range and high linearity.

In order to reduce the difficulty of processing and manufacturing, two long cylinder flexures are utilized to construct the compliant 4S module. One end of the cylinder flexure is connected with the platform, while the other end is connected with the P module. Since the radius of the platform is much smaller than that of the base, the two long cylinder flexures are obliquely arranged with a certain angle.

Compared with the stacked stages [20], the proposed micromanipulator has a more compact design. In addition, the platform occupies little space, which is desirable in applications where installation and manipulation space are limited. Further investigations of the micromanipulator are followed by the stiffness and kinematics modeling.
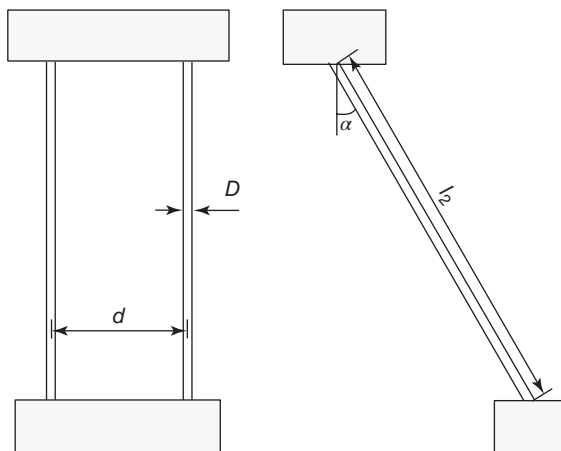
Figure 13.3 The compliant 4S module.

13.3
Stiffness Modeling of the Micromanipulator

The matrix displacement method is utilized to formulate the stiffness model of the proposed novel parallel micromanipulator. The derivation processes sequentially start from the elements to the chains and finally to the complete manipulator. As shown in Figure 13.4, a chain(chain 1) of the micromanipulator is divided into eight elements. Each element is connected by a node. The following will discuss the stiffness modeling of the micromanipulator.
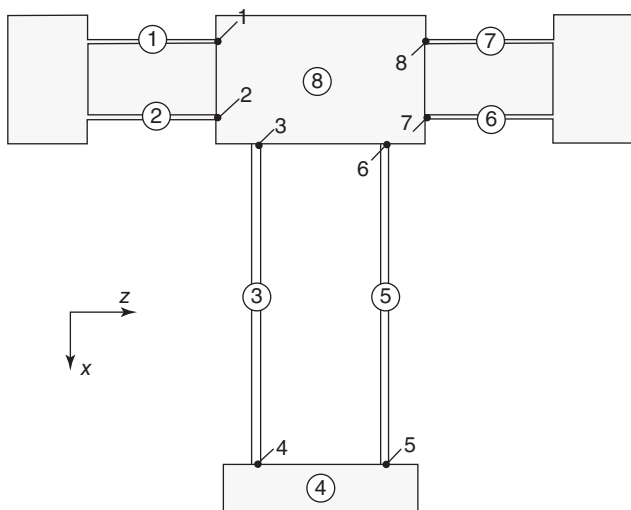
Figure 13.4 3D Model of the rigid 3-P(4S) parallel manipulator.

13.3.1
Stiffness Matrix of the Flexure Element

The flexure elements are functional elements that are used to transmit the force and displacement in compliant mechanisms. Therefore, the stiffness matrix of the flexure element is the basis of the total stiffness model of the micromanipulator. A flexure element under the loading condition is expressed in Figure 13.5.

Let the node force and the corresponding node displacement be

$$\boldsymbol{F}_n = \begin{bmatrix} f_x^n & f_y^n & f_z^n & m_x^n & m_y^n & m_z^n \end{bmatrix}^T \tag{13.1}$$

and

$$\boldsymbol{u}_n = \begin{bmatrix} u_x^n & u_y^n & u_z^n & \theta_x^n & \theta_y^n & \theta_z^n \end{bmatrix}^T, \tag{13.2}$$

respectively, where $n(n = i, j)$ is the node number. $\boldsymbol{F}_n, \boldsymbol{u}_n$ are 6×1 force vector and displacement vector, respectively.

According to the location of the flexure element in the kinematic chain, there are three different kinds of force conditions.

1) When node i is fixed and node j is free, the stiffness model of the element can be expressed as

$$\boldsymbol{F}_j = \boldsymbol{k}_j \boldsymbol{u}_j, \tag{13.3}$$

where $\boldsymbol{k}_j$ is the stiffness matrix of the flexure element.

$$\boldsymbol{k}_j = \begin{bmatrix} \frac{EA}{l} & 0 & 0 & 0 & 0 & 0 \\ 0 & \frac{12EI_1}{l^3} & 0 & 0 & 0 & -\frac{6EI_1}{l^2} \\ 0 & 0 & \frac{12EI_2}{l^3} & 0 & \frac{6EI_2}{l^2} & 0 \\ 0 & 0 & 0 & \frac{GI_p}{l} & 0 & 0 \\ 0 & 0 & \frac{6EI_1}{l^2} & 0 & \frac{4EI_1}{l} & 0 \\ 0 & -\frac{6EI_2}{l^2} & 0 & 0 & 0 & \frac{4EI_2}{l} \end{bmatrix},$$

where E and G denote the Young's modulus and shear modulus of the material; A and l denote the cross-sectional area and length of the flexure element; and I_1, I_2, and I_p denote the moment of inertia to z-axis, the moment of inertia to y-axis, and polar moment of inertia, respectively.
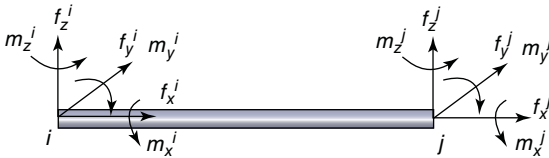
Figure 13.5 3D Model of the rigid 3-P(4S) parallel manipulator.

2) When node j is fixed and node i is free, the stiffness model of the element can be obtained by coordinate transformation as

$$F_i = T^{-1}k_j T u_i, \tag{13.4}$$

where T is the coordinate transformation matrix.

3) A more complex situation is such a case that both ends of the flexure element are applied a force. On the basis of element stiffness matrix method [21], we can get the following equation:

$$F_j = k_j u_j - f T^{-1} k_j T u_i, \tag{13.5}$$

where f is the force equilibrium matrix.

Equations (13.3)–(13.5) are three basic stiffness models of the flexure element. Elements 1, 2, 6, and 7 fit into the first two categories, while elements 3 and 5 belong to the third category.

13.3.2
Stiffness Modeling of the Compliant P Module

The compliant P module consists of elements 1, 2, 6, 7, and 8, among which 1, 2, 6, and 7 are flexure elements, 8 is rigid element.

According to Equation (13.3), the stiffness model of elements 1 and 2 can be written as

$$F_1 = k_b u_1 \tag{13.6}$$

$$F_2 = k_b u_2, \tag{13.7}$$

where k_b is the stiffness matrix of the beam flexures, which can be obtained by transforming k_j to the current coordinate system.

$$k_b = \begin{bmatrix} \dfrac{Ebh^3}{l_1^3} & 0 & 0 & 0 & \dfrac{-Ebh^3}{2l_1^2} & 0 \\ 0 & \dfrac{Eb^3h}{l_1^3} & 0 & \dfrac{Eb^3h}{2l_1^2} & 0 & 0 \\ 0 & 0 & \dfrac{Ebh}{l_1} & 0 & 0 & 0 \\ 0 & \dfrac{Ebh^3}{2l_1^2} & 0 & \dfrac{Ebh^3}{3l_1} & 0 & 0 \\ \dfrac{-Eb^3h}{2l_1^2} & 0 & 0 & 0 & \dfrac{Eb^3h}{3l_1} & 0 \\ 0 & 0 & 0 & 0 & 0 & \dfrac{G(bh^3+b^3h)}{12l_1} \end{bmatrix},$$

where b, h, and l_1 are structure parameters of the beam flexure illustrated in Figure 13.2.

According to Equation (13.4), the stiffness model of elements 6 and 7 can be obtained as

$$F_8 = T_1^{-1} k_b T_1 u_8 \tag{13.8}$$

$$F_7 = T_1^{-1} k_b T_1 u_7, \tag{13.9}$$

where T_1 is the coordinate transformation matrix, and

$$T_1 = \begin{bmatrix} -1 & 0 & 0 & 0 & 0 & 0 \\ 0 & 1 & 0 & 0 & 0 & 0 \\ 0 & 0 & -1 & 0 & 0 & 0 \\ 0 & 0 & 0 & -1 & 0 & 0 \\ 0 & 0 & 0 & 0 & 1 & 0 \\ 0 & 0 & 0 & 0 & 0 & -1 \end{bmatrix}.$$

Assuming that F_p is the external force applied on element 8 and u_p is the corresponding displacement. Then we can get the following force equilibrium equations and deformation compatibility equations.

$$F_p = \sum f_n F_n (n = 1, 2, 7, 8) \tag{13.10}$$

$$u_n = \lambda_n u_p (n = 1, 2, 7, 8), \tag{13.11}$$

where f_n and λ_n denote the force equilibrium matrix and deformation compatibility matrix, respectively. And f_n is given by

$$f_n = \begin{bmatrix} 1 & 0 & 0 & 0 & 0 & 0 \\ 0 & 1 & 0 & 0 & 0 & 0 \\ 0 & 0 & 1 & 0 & 0 & 0 \\ 0 & -z_n & y_n & 1 & 0 & 0 \\ z_n & 0 & -x_n & 0 & 1 & 0 \\ -y_n & x_n & 0 & 0 & 0 & 1 \end{bmatrix}, \tag{13.12}$$

where (x_n, y_n, z_n) are the coordinates of node $n(n = 1, 2, 7, 8)$ in the local coordinate system. It is not difficult to prove that $\lambda_n = f_n^T$. The detailed information can be also found in Ref. [22].

Substituting Equations. (13.6)–(13.9) and Equation (13.11) into Equation (13.10), we can get

$$F_p = k_p u_p, \tag{13.13}$$

where k_p is the stiffness matrix of the compliant P joint, and it can be expressed as

$$k_p = f_1 k_1 \lambda_1 + f_2 k_1 \lambda_2 + f_8 T_1^{-1} k_1 T_1 \lambda_8 + f_7 T_1^{-1} k_1 T_1 \lambda_7. \tag{13.14}$$

On the basis of Equation (13.14), we have the compliance matrix of the compliant P joint as

$$c_p = k_p^{-1}. \tag{13.15}$$

13.3.3
Stiffness Modeling of the Compliant 4S Module

The compliant 4S module consists of two cylinder flexure elements. Each cylinder flexure element is utilized as a compliant 2S branch. The 4S module

is the connection of the compliant P joint and the moving platform. Therefore, both ends of the 2S branches are under the stress state. Besides, the compliant 4S module is obliquely arranged with an angle α, the stiffness matrix of the cylinder flexure element needs to be adjusted by coordinate transformation. That is

$$k_{\mathrm{c}} = T_2^{-1} k_{\mathrm{lc}} T_2, \tag{13.16}$$

where k_{c} and k_{lc} denote the stiffness matrix of the slant circular element in current system and local coordinate system, respectively. k_{lc} can be obtained by substituting the structural parameters of the circular element into k_j. T_2 is the transformation matrix and is given by

$$T_2 = \begin{bmatrix} \cos\alpha & -\sin\alpha & 0 & 0 & 0 & 0 \\ \sin\alpha & \cos\alpha & 0 & 0 & 0 & 0 \\ 0 & 0 & 1 & 0 & 0 & 0 \\ 0 & 0 & 0 & \cos\alpha & -\sin\alpha & 0 \\ 0 & 0 & 0 & \sin\alpha & \cos\alpha & 0 \\ 0 & 0 & 0 & 0 & 0 & 1 \end{bmatrix}. \tag{13.17}$$

According to Equation (13.5), the stiffness model of elements 3 and 5 can be expressed as

$$F_4 = k_{\mathrm{c}} u_4 - f_{\mathrm{c}} T_3^{-1} k_{\mathrm{c}} T_3 u_3 \tag{13.18}$$

$$F_5 = k_{\mathrm{c}} u_5 - f_{\mathrm{c}} T_3^{-1} k_{\mathrm{c}} T_3 u_6, \tag{13.19}$$

where f_{c} and T_3 are force equilibrium matrix and coordinate transformation matrix between the two nodes of the circular element, respectively.

Let F_{c1}^p be the external force acting on element 4, and u_{c1}^p, u_{c1}^e be the displacement of elements 4 and 8. Then, we can get the following equations:

$$F_{\mathrm{c1}}^p = f_4 F_4 + f_5 F_5 \tag{13.20}$$

$$u_4 = \lambda_4 u_{\mathrm{c1}}^p \qquad u_5 = \lambda_5 u_{\mathrm{c1}}^p \tag{13.21}$$

$$u_3 = \lambda_3 u_{\mathrm{c1}}^e \qquad u_6 = \lambda_6 u_{\mathrm{c1}}^e. \tag{13.22}$$

Combining Equations (13.18)–(13.22), we have

$$F_{\mathrm{c1}}^p = m_1 u_{\mathrm{c1}}^p + m_2 u_{\mathrm{c1}}^e, \tag{13.23}$$

where

$$m_1 = f_4 k_{\mathrm{c}} \lambda_4 + f_5 k_{\mathrm{c}} \lambda_5 \tag{13.24}$$

$$m_2 = -f_4 f_{\mathrm{c}} T_3^{-1} k_{\mathrm{c}} T_3 \lambda_3 - f_5 f_{\mathrm{c}} T_3^{-1} k_{\mathrm{c}} T_3 \lambda_6. \tag{13.25}$$

Equation (13.23) is stiffness model of the compliant 4S module.

13.3.4
Stiffness Modeling of the Compliant P(4S) Chain

The stiffness model of the compliant P joint and the compliant 4S module are separately derived in the previous sections. In this section, we will analyze the two parts as a whole, that is, P(4S) chain.

Assuming that F_{c1} is the external force acting on P joint of the P(4S) chain and F_{int} is the internal force of element 8, we have

$$F_{c1} + (-F_{int}) = k_p u_{c1}^e \tag{13.26}$$

$$F_{c1}^p + f_9 F_{int} = 0, \tag{13.27}$$

where f_9 is the equilibrium matrix of the external and internal forces.

Substituting Equations (13.26) and (13.27) into Equation (13.23), we can get

$$n_1 F_{c1}^p + n_2 F_{c1} = m_1 u_{c1}^p, \tag{13.28}$$

where

$$n_1 = E - m_2 k_p^{-1} f_9^{-1} \tag{13.29}$$

$$n_2 = -m_2 k_p^{-1}. \tag{13.30}$$

Equation (13.28) is the stiffness model of the compliant P(4S) chain.

13.3.5
Stiffness Modeling of the Complete Mechanism

The micromanipulator is structured with a homogeneous distribution. Therefore, on the basis of Equation (13.28), we can easily derive the stiffness model of chains 2 and 3 as follows:

$$n_1 T_{c2} F_{c2}^p + n_2 T_{c2} F_{c2} = m_1 T_{c2} u_{c2}^p \tag{13.31}$$

$$n_1 T_{c3} F_{c3}^p + n_2 T_{c3} F_{c3} = m_1 T_{c3} u_{c3}^p, \tag{13.32}$$

where T_{c2} and T_{c3} are the coordinate transformation matrices that transform the forces and displacement from global coordinate system to the local coordinate system. They can be derived as follows:

$$T_{c2} = \begin{bmatrix} 1 & 0 & 0 & 0 & 0 & 0 \\ 0 & \cos\left(\frac{\pi}{3}\right) & -\sin\left(\frac{\pi}{3}\right) & 0 & 0 & 0 \\ 0 & \sin\left(\frac{\pi}{3}\right) & \cos\left(\frac{\pi}{3}\right) & 0 & 0 & 0 \\ 0 & 0 & 0 & 1 & 0 & 0 \\ 0 & 0 & 0 & 0 & \cos\left(\frac{\pi}{3}\right) & -\sin\left(\frac{\pi}{3}\right) \\ 0 & 0 & 0 & 0 & \sin\left(\frac{\pi}{3}\right) & \cos\left(\frac{\pi}{3}\right) \end{bmatrix} \tag{13.33}$$

$$
\boldsymbol{T}_{c3} =
\begin{bmatrix}
1 & 0 & 0 & 0 & 0 & 0 \\
0 & \cos\left(\frac{\pi}{3}\right) & \sin\left(\frac{\pi}{3}\right) & 0 & 0 & 0 \\
0 & -\sin\left(\frac{\pi}{3}\right) & \cos\left(\frac{\pi}{3}\right) & 0 & 0 & 0 \\
0 & 0 & 0 & 1 & 0 & 0 \\
0 & 0 & 0 & 0 & \cos\left(\frac{\pi}{3}\right) & \sin\left(\frac{\pi}{3}\right) \\
0 & 0 & 0 & 0 & -\sin\left(\frac{\pi}{3}\right) & \cos\left(\frac{\pi}{3}\right)
\end{bmatrix}.
\tag{13.34}
$$

The three chains are connected parallel to the platform. The summation of external forces F_{c1}^p, F_{c2}^p, and F_{c3}^p is zero:

$$
\boldsymbol{f}_{c1}\boldsymbol{F}_{c1}^p + \boldsymbol{f}_{c2}\boldsymbol{F}_{c2}^p + \boldsymbol{f}_{c3}\boldsymbol{F}_{c3}^p = 0,
\tag{13.35}
$$

where $\boldsymbol{f}_{c1}, \boldsymbol{f}_{c2}$, and $\boldsymbol{f}_{c3}$ are the force equilibrium matrices, which can be determined by Equation (13.12) as follows:

$$
\boldsymbol{f}_{c1} =
\begin{bmatrix}
1 & 0 & 0 & 0 & 0 & 0 \\
0 & 1 & 0 & 0 & 0 & 0 \\
0 & 0 & 1 & 0 & 0 & 0 \\
0 & 0 & R & 1 & 0 & 0 \\
0 & 0 & 0 & 0 & 1 & 0 \\
-R & 0 & 0 & 0 & 0 & 1
\end{bmatrix}
$$

$$
\boldsymbol{f}_{c2} =
\begin{bmatrix}
1 & 0 & 0 & 0 & 0 & 0 \\
0 & 1 & 0 & 0 & 0 & 0 \\
0 & 0 & 1 & 0 & 0 & 0 \\
0 & \frac{\sqrt{3}}{2}R & \frac{1}{2}R & 1 & 0 & 0 \\
-\frac{\sqrt{3}}{2}R & 0 & 0 & 0 & 1 & 0 \\
-\frac{1}{2}R & 0 & 0 & 0 & 0 & 1
\end{bmatrix}
$$

$$
\boldsymbol{f}_{c3} =
\begin{bmatrix}
1 & 0 & 0 & 0 & 0 & 0 \\
0 & 1 & 0 & 0 & 0 & 0 \\
0 & 0 & 1 & 0 & 0 & 0 \\
0 & -\frac{\sqrt{3}}{2}R & \frac{1}{2}R & 1 & 0 & 0 \\
\frac{\sqrt{3}}{2}R & 0 & 0 & 0 & 1 & 0 \\
-\frac{1}{2}R & 0 & 0 & 0 & 0 & 1
\end{bmatrix}.
$$

The relationship between the displacements of the three chains and displacement of the platform can be expressed as

$$
\boldsymbol{u}_{c1}^p = \lambda_{c1}\boldsymbol{u} \qquad \boldsymbol{u}_{c2}^p = \lambda_{c2}\boldsymbol{u} \qquad \boldsymbol{u}_{c3}^p = \lambda_{c3}\boldsymbol{u},
\tag{13.36}
$$

where $\boldsymbol{u}$ is the displacement of the platform and λ_{c1}, λ_{c2}, and λ_{c3} are displacement equilibrium matrices.

Besides, we can construct the relationship between the external forces of the chains and the total external forces as follows:

$$
\boldsymbol{F}_{c1}^p = \boldsymbol{a}_1\boldsymbol{F} \qquad \boldsymbol{F}_{c2}^p = \boldsymbol{a}_2\boldsymbol{F} \qquad \boldsymbol{F}_{c3}^p = \boldsymbol{a}_3\boldsymbol{F},
\tag{13.37}
$$

where F is the total external force and a_1, a_2, and a_3 are force transformation matrices.

Substituting Equations (13.28), (13.31), (13.32), (13.36), and (13.37) into Equation (13.35), we can get

$$F = Ku, \tag{13.38}$$

where

$$K = P^{-1}Q. \tag{13.39}$$

$$P = f_{c1}n_1^{-1}n_2a_1 + f_{c2}(n_1T_{c2})^{-1}n_2T_{c2}a_2 + f_{c3}(n_1T_{c3})^{-1}n_2T_{c3}a_3$$

$$Q = f_{c1}n_1^{-1}m_1\lambda_{c1} + f_{c2}(n_1T_{c2})^{-1}m_1T_{c2}\lambda_{c2} + f_{c3}(n_1T_{c3})^{-1}m_1T_{c3}\lambda_{c3}.$$

Equation (13.38) is the stiffness model of the proposed micromanipulator. K is the stiffness matrix. On the basis of Equation (13.38), on one hand, we can figure out how many Newtons of forces are needed to achieve a required displacement. On the other hand, we can calculate the corresponding displacement of the platform when certain external forces act on the three P modules.

13.3.6
Model Validation Based on FEA

In this section, the derived stiffness models of the compliant P module and the whole mechanism will be verified by using FEA software package ANSYS. Alloy Al-7075 is adopted as the material of the micromanipulator. The material parameters and mechanical structural parameters are listed in Tables 13.1 and 13.2, respectively.

Substituting the values of the material and structural parameters into Eq.(1.14), we have

$$k_p = \begin{bmatrix} 0.1815 & 0 & 0 & 0 & 0 & 0 \\ 0 & 72.5962 & 0 & 0 & 0 & 0 \\ 0 & 0 & 129.0600 & 0 & 0 & 0 \\ 0 & 0 & 0 & 0.0199 & 0 & 0 \\ 0 & 0 & 0 & 0 & 0.0166 & 0 \\ 0 & 0 & 0 & 0 & 0 & 0.0022 \end{bmatrix} \times 10^6,$$

where the units of $k_p(1, 1)$, $k_p(2, 2)$ and $k_p(3, 3)$ are N m^{-1}, and units of $k_p(4, 4)$, $k_p(5, 5)$ and $k_p(6, 6)$ are (N·m) rad^{-1}, among which $k_p(1, 1)$ is the stiffness along the

Table 13.1 Material parameters.

Material	Young's modulus	Yield strength	Poisson's ratio
	E(GPa)	Σ(MPa)	μ
Al-7075	71.7	503	0.33

Table 13.2 Mechanical parameters.

Parameter	Nomenclature	Value	Unit
Thickness of the beam flexures	h	0.6	mm
Length of the beam flexures	l_1	16	mm
Width of the beam flexures	b	12	mm
Central distance of the beam flexures	m	9.4	mm
Length of the platform of the P joint	n	26	mm
Diameter of the cylinder flexures	D	1	mm
Central distance of the cylinder flexures	d	16	mm
Length of the cylinder flexures	l_2	46	mm
Tilt angle of the cylinder flexures	α	30	°
Radius of the platform	R	40	mm

dominant motion direction. It can be observed that there are no parasitic motions due to the symmetrical structure.

According to Equation (13.15), we can also obtain the compliance matrix of the P module. That is

$$
\mathbf{c}_p = \begin{bmatrix}
5.5099 & 0 & 0 & 0 & 0 & 0 \\
0 & 0.0138 & 0 & 0 & 0 & 0 \\
0 & 0 & 0.0077 & 0 & 0 & 0 \\
0 & 0 & 0 & 50.3699 & 0 & 0 \\
0 & 0 & 0 & 0 & 60.0768 & 0 \\
0 & 0 & 0 & 0 & 0 & 457.1774
\end{bmatrix} \times 10^{-6}.
$$

It is shown that a displacement of 5.5099 μm will be achieved when a unit force is applied along the working direction. On the basis of Hooke's law, the displacement is proportional to the applied force within the linear elastic range. Thus, the stroke of the compliant P joint can be designed according to the driving capacity of the actuator.

FEA simulation of the deformation along the working direction is carried out, which is shown in Figure 13.6. Compared with the analytical results obtained by Equations (13.14) and (13.15), the error is less than 1%, which indicates the accuracy and reliability of the analytical model.
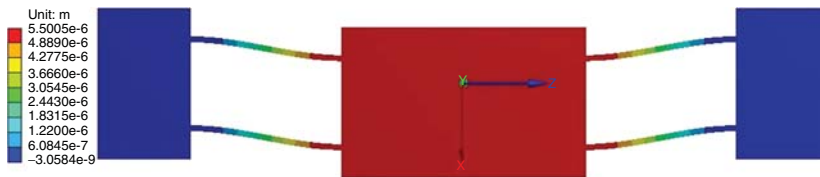
Figure 13.6 Deformation of the compliant P joint.

According to Equation (13.39), the compliance of the complete mechanism can be obtained as follows:

$$C = Q^{-1}P. \tag{13.40}$$

Substituting the parameters into Equation (13.40) yields

$$C = \begin{bmatrix} -3.8955 & 4.7027 & 4.7027 & 0 & 0 & 0.9480 \\ -13.5224 & 6.7612 & 6.7612 & 0 & 0 & -0.9324 \\ 0 & 3.6357 & -3.6357 & -0.1217 & -0.4530 & 0 \\ 0 & 25.0515 & -25.0515 & 48.3705 & 68.2835 & 0 \\ 0 & -25.0903 & 25.0903 & -0.9238 & -2.8611 & 0 \\ -19.8672 & 9.9336 & 9.9336 & 0 & 0 & 48.9329 \end{bmatrix} \times 10^{-6}.$$

Assume F_1, F_2, and F_3 are actual forces acting on chains 1, 2, and 3, respectively; u_x, u_y, and u_z are the corresponding translational displacements of the platform along x, y, and z axes, respectively; and θ_x, θ_y, and θ_z are rotational displacements around x, y, and z axes, respectively. That is

$$F = \begin{bmatrix} F_1 & F_2 & F_3 & 0 & 0 & 0 \end{bmatrix}^T \tag{13.41}$$

$$u = \begin{bmatrix} u_x & u_y & u_z & \theta_x & \theta_y & \theta_z \end{bmatrix}^T. \tag{13.42}$$

According to $u = CF$, we can obtain the following equations:

$$\begin{cases} u_x = -3.8955 \times 10^{-6}F_1 + 4.7027 \times 10^{-6}\left(F_2 + F_3\right) \\ u_y = -6.7612 \times 10^{-6}\left(2F_1 - F_2 - F_3\right) \\ u_z = 3.6357 \times 10^{-6}\left(F_2 - F_3\right) \\ \theta_x = 25.0515 \times 10^{-6}\left(F_2 - F_3\right) \\ \theta_y = -25.0903 \times 10^{-6}\left(F_2 - F_3\right) \\ \theta_z = -9.9336 \times 10^{-6}\left(2F_1 - F_2 - F_3\right) \end{cases} \tag{13.43}$$

The units for the translational and rotational displacements are m and rad, respectively. On the basis of Eq.(13.43), the following conclusions can be made:

1) When $F_1 = F_2 = F_3$, the displacement of the platform can be written as

   $$u_x = 5.5099 \times 10^{-6}F_1, \tag{13.44}$$

   which means when $F_1 = F_2 = F_3 = 1N$, the platform will move along the x-axis with 5.5099 µm.

2) When $F_1 = 2.4144F_2 = 2.4144F_3$, the displacements of the platform can be obtained as

   $$u_y = -7.9217 \times 10^{-6}F_1 \tag{13.45}$$

   $$\theta_z = -11.6387 \times 10^{-6}F_1. \tag{13.46}$$

   Under this condition, both translational displacement along the y-axis and rotational displacement around z-axis will be generated.

3) When $F_1 = 0$ and $F_2 = -F_3$, the displacements of the platform can be written as

$$u_z = 7.2714 \times 10^{-6} F_2 \tag{13.47}$$

$$\theta_x = 50.1029 \times 10^{-6} F_2 \tag{13.48}$$

$$\theta_y = -50.1805 \times 10^{-6} F_2. \tag{13.49}$$

Assuming that u_x, u_y, and u_z are the dominant motions, then θ_x, θ_y, and θ_z are parasitic motions. Figures 13.7–13.9 are FEA simulations of the three load conditions, where directional deformations of the manipulator along the x, y, and z axes are illustrated.

When the three compliant P modules are applied with a unit of force simultaneously (Figure 13.7), it is observed that the displacement of the platform is 5.5001 μm, which agrees with that obtained by Equation (13.44), and the error is only 0.18%.

When $F_1 = 2.4144$ N, $F_2 = 1$ N, and $F_3 = 1$ N, the platform will move along the y-axis and rotate around the z-axis (Figure 13.8). It is noticeable that since there exists parasitic motion, the translational displacement of the platform is not equal to the maximum deformation. In this situation, deformation probes are adopted to detect the displacements of the platform. The translational displacement along the y-axis is -18.949 μm and the rotational displacement around the z-axis is -2.865×10^{-5} rad. The errors between the static analysis and theoretical calculation can be derived as 0.93% and 1%, respectively.

When $F_1 = 0$ N, $F_2 = -1$ N, and $F_3 = 1$ N (Figure 13.9), the translational displacement of the platform along the dominant direction(z-axis) is -6.868 μm

Unit: m
5.5001e-6
4.8886e-6
4.2772e-6
3.6657e-6
3.0543e-6
2.4428e-6
1.8313e-6
1.2199e-6
6.0843e-7
−3.0238e-9
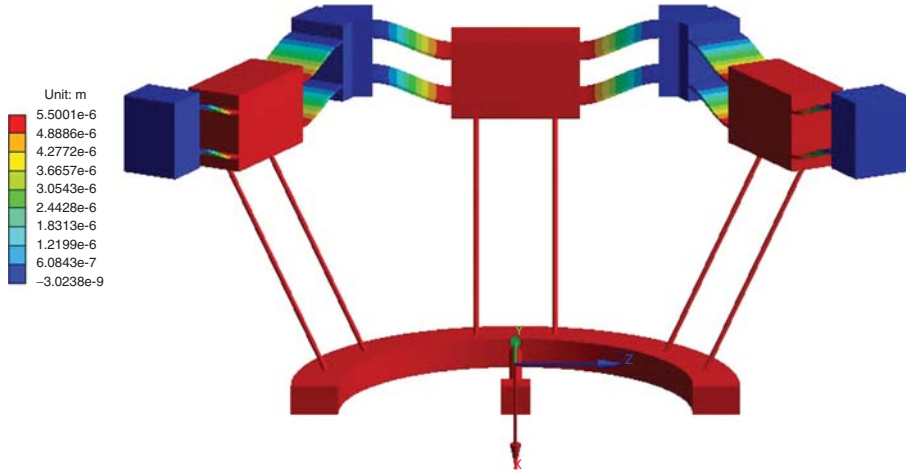
Figure 13.7 x-axis directional deformation when $\boldsymbol{F} = \begin{bmatrix} 1 & 1 & 1 & 0 & 0 & 0 \end{bmatrix}^T$.
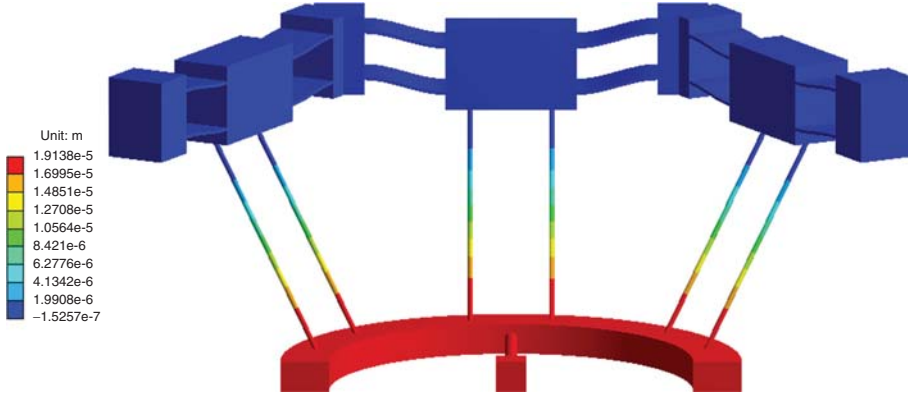
Figure 13.8 *y*-axis directional deformation when $F = \begin{bmatrix} 2.4144 & 1 & 1 & 0 & 0 & 0 \end{bmatrix}^T$.
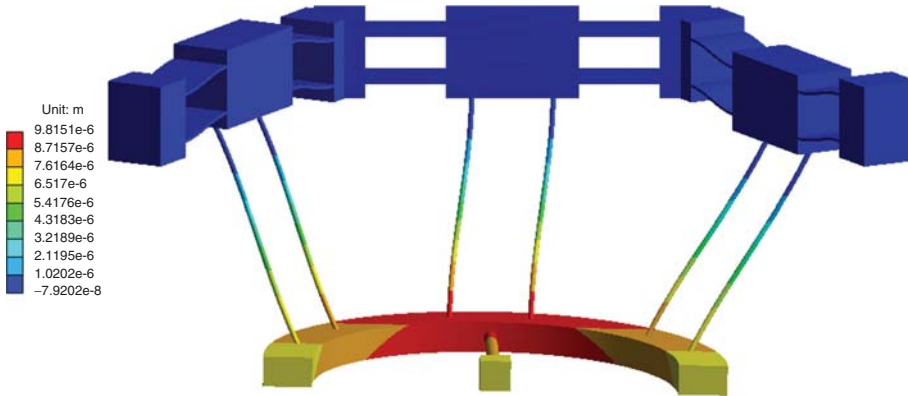
Figure 13.9 *z*-axis directional deformation when $F = \begin{bmatrix} 0 & -1 & 1 & 0 & 0 & 0 \end{bmatrix}^T$.

without considering the rotational displacements, and the error is 5.9% compared with that obtained by Equation (13.47).

The FEA simulation results reveal that the deviation is below 6%, which is acceptable in the early design stage. The errors result from various reasons, such as inaccuracy of the theoretical modeling and element meshing during the FEA simulations.

13.4
Kinematics Modeling of the Micromanipulator

An accurate kinematics model is beneficial for the performance evaluation. Moreover, it can be used for control purpose for the micromanipulator. On the basis of the stiffness modeling method, the kinematics model of the proposed micromanipulator is derived in this section.

Combining Equations (13.23), (13.26), and (13.27), we have

$$u_{c1}^{p} = -m_1^{-1}f_9 F_{c1} + m_1^{-1}(f_9 k_p - m_2)u_{c1}^{e}. \tag{13.50}$$

Making the following substitutions:

$$B_1 = -m_1^{-1}f_9 \tag{13.51}$$

$$B_2 = m_1^{-1}(f_9 k_p - m_2), \tag{13.52}$$

Equation (13.50) can be rewritten as

$$u_{c1}^{p} = B_1 F_{c1} + B_2 u_{c1}^{e}. \tag{13.53}$$

Equation (13.53) is the input and output displacement relationship of chain 1. Similarly, input and output displacement relationships of chains 2 and 3 can be derived as

$$T_{c2}u_{c2}^{p} = B_1 T_{c2}F_{c2} + B_2 T_{c2}u_{c2}^{e} \tag{13.54}$$

$$T_{c3}u_{c3}^{p} = B_1 T_{c3}F_{c3} + B_2 T_{c3}u_{c3}^{e}. \tag{13.55}$$

Combining Equations (13.53)–(13.55), we can get

$$u_{c1}^{p} + u_{c2}^{p} + u_{c3}^{p} = B_1 F_{c1} + T_{c2}^{-1}B_1 T_{c2}F_{c2} + T_{c3}^{-1}B_1 T_{c3}F_{c3} +$$
$$B_2 u_{c1}^{e} + T_{c2}^{-1}B_2 T_{c2}u_{c2}^{e} + T_{c3}^{-1}B_2 T_{c3}u_{c3}^{e}. \tag{13.56}$$

Again, we can construct the relationship between the input displacement of the chains and the total input displacement as

$$u_{c1}^{e} = a_1 u_{in} \quad u_{c2}^{e} = a_2 u_{in} \quad u_{c3}^{e} = a_3 u_{in}, \tag{13.57}$$

where u_{in} is the total input displacement of the micromanipulator.

Substituting Equations (13.36), (13.37), and (13.57) into Equation (13.56), we have

$$(\lambda_{c1} + \lambda_{c2} + \lambda_{c3})u = (B_1 a_1 + T_{c2}^{-1}B_1 T_{c2}a_2 + T_{c3}^{-1}B_1 T_{c3}a_3)F$$

$$+ (B_2 a_1 + T_{c2}^{-1}B_2 T_{c2}a_2 + T_{c3}^{-1}B_2 T_{c3}a_3)u_{in}. \tag{13.58}$$

Since $F = Ku$, we can get

$$u = Ju_{in}, \tag{13.59}$$

where J is the relationship matrix of the input and output displacements, and

$$J = ((\lambda_{c1} + \lambda_{c2} + \lambda_{c3}) - (B_1 a_1 + T_{c2}^{-1}B_1 T_{c2}a_2 +$$

$$T_{c3}^{-1}B_1 T_{c3}a_3)K)^{-1}(B_2 a_1 + T_{c2}^{-1}B_2 T_{c2}a_2 + T_{c3}^{-1}B_2 T_{c3}a_3). \tag{13.60}$$

Equation (13.59) is the forward kinematics of the micromanipulator, based on which the output displacements of the platform can be calculated when the input displacements are given.

Substituting the parameters listed in Tables 13.1 and 13.2 into Equation (13.60), we can get

$$
J = \begin{bmatrix}
-0.6216 & 0.8018 & 0.8018 & 0 & 0 & -1.9022 \\
-2.4548 & 1.2274 & 1.2274 & 0 & 0 & 9.7243 \\
0 & 0.6795 & -0.6795 & -0.0014 & -0.6370 & 0 \\
0 & 4.6850 & -4.6850 & 0.9676 & -4.5706 & 0 \\
0 & -4.6892 & 4.6892 & -0.0254 & 4.3979 & 0 \\
-3.5967 & 1.7984 & 1.7984 & 0 & 0 & 13.7608
\end{bmatrix}.
$$

Let u_1, u_2, and u_3 be the input displacements of chains 1, 2, and 3, respectively. That is

$$
\boldsymbol{u}_{\text{in}} = \begin{bmatrix} u_1 & u_2 & u_3 & 0 & 0 & 0 \end{bmatrix}^T. \tag{13.61}
$$

According to Equation (13.59), we can obtain

$$
\begin{cases}
u_x = -0.6216u_1 + 0.8108\left(u_2 + u_3\right) \\
u_y = -1.2274\left(2u_1 - u_2 - u_3\right) \\
u_z = 0.6795\left(u_2 - u_3\right) \\
\theta_x = 4.6850\left(u_2 - u_3\right) \\
\theta_y = -4.6892\left(u_2 - u_3\right) \\
\theta_z = -1.7984\left(2u_1 - u_2 - u_3\right)
\end{cases} \tag{13.62}
$$

Further, we have

$$
\begin{bmatrix} u_x \\ u_y \\ u_z \end{bmatrix} = \begin{bmatrix}
-0.6216 & 0.8108 & 0.8108 \\
-2.4548 & 1.2274 & 1.2274 \\
0 & 0.6795 & -0.6795
\end{bmatrix} \begin{bmatrix} u_1 \\ u_2 \\ u_3 \end{bmatrix}. \tag{13.63}
$$

By inverting the coefficient matrix of Equation (13.63), we can obtain

$$
\begin{bmatrix} u_1 \\ u_2 \\ u_3 \end{bmatrix} = \begin{bmatrix}
1.0000 & -0.6606 & 0 \\
1.0000 & -0.2532 & 0.7359 \\
1.0000 & -0.2532 & -0.7359
\end{bmatrix} \begin{bmatrix} u_x \\ u_y \\ u_z \end{bmatrix}. \tag{13.64}
$$

Equations (13.63) and (13.64) give the input-output displacement relationship of the micromanipulator without considering the rotational motion. It is observed that when giving an expected position of the platform, we can figure out the needed input displacements. Equation (13.64) can be served as a reference for the controller design when piezoelectric actuators are adopted.

FEA static analyses are carried out to evaluate the derived kinematics models. The output displacements are compared between the mathematical model and the FEA method in Tables 13.3–13.5. Among them, the theoretical output displacements in Tables 13.3 and 13.4 are calculated by Equation (13.63) when input displacements are preassigned.

Table 13.3 Result comparison when $u_1 = 1, u_2 = 1,$ and $u_3 = 1\,(\mu m)$.

	u_x (μm)	u_y (μm)	u_z (μm)
Mathematical model	1	0	0
FEA	0.9999	-2.2897×10^{-5}	-1.2654×10^{-5}
Error	0.01%	N/A	N/A

Table 13.4 Result comparison when $u_1 = 0, u_2 = -1,$ and $u_3 = 1\,(\mu m)$.

	u_x (μm)	u_y (μm)	u_z (μm)
Mathematical model	0	0	-1.3592
FEA	3.7142×10^{-5}	1.2658×10^{-4}	-1.2752
Error	N/A	N/A	6.59%

Table 13.5 Result comparison when $u_1 = 0.3394, u_2 = 1.4827,$ and $u_3 = 0.0109\,(\mu m)$.

	u_x (μm)	u_y (μm)	u_z (μm)
Mathematical model	1	0	1
FEA	0.9999	-3.9274×10^{-5}	0.9478
Error	0.01%	N/A	5.50%

While in Table 13.5, the output displacements are prespecified and the input displacements are calculated by Equation (13.64), FEA results are obtained by setting different input displacements.

It is noticeable that the errors between the theoretical models and the FEA analyses are small, which indicate that the method is feasible. The error is caused by either the analytical model or the FEA model.

On the basis of the consideration that the parasitic rotational motions can enlarge the workspace of the micromanipulator, they are not investigated in this section. However, the parasitic motions will cause difficulties on control. Therefore, they should be decreased or eliminated, which may be realized by structure optimization.

13.5
Conclusion

This chapter presents the stiffness and kinematic analysis of a novel compliant parallel micromanipulator. First, configuration and mechanical design of the manipulator are illustrated, in which beam flexures and cylinder flexures are adopted to construct the compliant P module and 4S module of the P(4S) chain.

Then, the stiffness and kinematics models of the manipulator are derived based on the matrix displacement method. The derivation process sequentially starts from the elements to the chains and finally to the whole mechanism. Finally, in order to validate the derived stiffness and kinematics models, evaluations with software such as MATLAB and ANSYS are carried out. The mathematical and FEA results agree with each other within a small error, which indicates the correctness of the stiffness and kinematics models.

The manipulator is compact in size and large in stroke, which makes it suitable for biomedical manipulations in a limited space. The stiffness and kinematic analysis method is implemented on the proposed manipulator as an example. It is widely suitable and can be used in many compliant mechanisms in terms of planar and spatial mechanism configurations.

References

1. Bi, S. and Hua, G. (2000) Some issues on bio-micromanipulator system. *Chin. J. Sci. Instrum.*, **21** (6), 560–573.
2. Li, Y., Tang, H., Xu, Q., and Yun, Y. (2011) Development status of micromanipulator technology for biomedical applications. *Chin. J. Mech. Eng.*, **47** (23), 1–13.
3. Yong, Y.K., Aphale, S.S., and Moheimani, S.O.R. (2009) Design, identification, and control of a flexure-based XY stage for fast nanoscale positioning. *IEEE Trans. Nanotechnol.*, **8** (1), 46–54.
4. Zhao, J., Wang, H., Gao, R., Hu, P., and Yang, Y. (2012) A novel alignment mechanism employing orthogonal connected multi-layered flexible hinges for both leveling and centering. *Rev. Sci. Instrum.*, **83** (6), 065102.
5. Zhang, Y., Tan, K., and Huang, S. (2009) Vision-servo system for automated cell injection. *IEEE Trans. Ind. Electron.*, **56** (1), 231–238.
6. Li, Y. and Xu, Q. (2011) A novel piezoactuated XY stage with parallel, decoupled, and stacked flexure structure for micro-/nanopositioning. *IEEE Trans. Ind. Electron.*, **58** (8), 3601–3615.
7. Awtar, S. (2003) Synthesis and analysis of parallel kinematic XY flexure mechanisms. PhD dissertation. Massachusetts Institute of Technology, Cambridge.
8. Tanikawa, T. and Arai, T. (1999) Development of a micro-manipulation system having a two-fingered micro-hand. *IEEE Trans. Rob. Autom.*, **15** (1), 152–162.
9. Dong, W., Sun, L., and Du, Z. (2008) Stiffness research on a high-precision, large-workspace parallel mechanism with compliant joints. *Precis. Eng.*, **32** (3), 222–231.
10. Xiao, S. and Li, Y. (2014) Model based sliding mode control for a 3-DOF translational micro parallel positioning stage. IEEE International Conference on Robotics and Automation, Hongkong, China, May 31- June 5, 2333–2338.
11. Pashkevich, A., Chablat, D., and Wenger, P. (2009) Stiffness analysis of overconstrained parallel manipulators. *Mech. Mach. Theory*, **44** (5), 966–982.
12. Gosselin, C. (1985) Kinematic analysis, optimization and programming of parallel robotic manipulators. PhD dissertation. McGill University, Montreal.
13. Li, Y. and Xu, Q. (2008) Stiffness analysis for a 3-PUU parallel kinematic machine. *Mech. Mach. Theory*, **43** (2), 186–200.
14. Yi, B.J., Chung, G.B., Na, H.Y., Kim, W.K., and Suh, I.H. (2003) Design and experiment of a 3-DOF parallel micromechanism utilizing flexure hinges. *IEEE Trans. Rob. Autom.*, **19** (4), 604–612.
15. Yang, G., Teo, T.J., Chen, I.M., and Lin, W. (2011) Analysis and design of a 3-DOF flexure-based zero-torsion parallel manipulator for nano-alignment

applications. IEEE International Conference on Robotics and Automation, Shanghai, China, May 9-11, 2751–2756.

16. Kaveh, A. (1992) *Structural Mechanics: Graph and Matrix Methods*, Research Studies Press, Ltd, Taunton, Somerset, England.

17. Tang, H. and Li, Y. (2013) Design, analysis and test of a novel 2-DOF nanopositioning system driven by dual-mode. *IEEE Trans. Rob.*, **29** (3), 650–662.

18. Li, Y., Xiao, X., and Tang, H. (2013) Design and analysis of a novel 3-DOF large stroke micro-positioning platform. *Chin. J. Mech. Eng.*, **49** (19), 48–54.

19. Xiao, S. and Li, Y. (2013) Modeling and high dynamic compensating the rate-dependent hysteresis of piezoelectric actuators via a novel modidfied inverse Preisach model. *IEEE Trans. Control Syst. Technol.*, **21** (5), 1549–1557.

20. Hao, G. and Wen, X. (2012) Design and modeling of a large-range modular XYZ compliant parallel manipulator using identical spatial modules. *ASME J. Mech. Rob.*, **4** (2), 021009.

21. Gong, J.L., Zhang, Y.F., and Hu, G.X. (2013) Deformation rules of the contact surface between flexible units. *Chin. J. Mech. Eng.*, **49** (9), 17–23.

22. Pham, H.H. and Chen, I.M. (2005) Stiffness modeling of flexure parallel mechanism. *Precis. Eng.*, **29** (4), 467–478.

14
Robotic Micromanipulation of Cells and Small Organisms

Xianke Dong, Wes Johnson, Yu Sun, and Xinyu Liu

14.1
Introduction

As a critical experimental approach for physical interactions with biological cells and small organisms, robotic micromanipulation has brought unprecedented capabilities to biological and biomedical research, and found important applications in a variety of fields, such as genetics, development, pathology, and pharmaceutics, to name a few. Leveraging techniques in robotics, automation, and micro-electro-mechanical systems (MEMS), robotic micromanipulation systems have been increasingly accurate, efficient, intelligent, and capable of performing manipulation tasks on biological samples ranging from small organisms to single cells and subcellular organelles. In the past two decades, a number of novel and effective robotic systems have been developed to target various micromanipulation tasks, with motivations to automate the micromanipulation processes and provide much enhanced manipulation accuracy, efficiency, and consistency. This chapter reviews the systems, techniques, and methodologies for robotic manipulation of cells and small organisms.

Of the topics to be discussed, cell injection is well established in both the engineering and medicine communities owing to its important applications such as intracytoplasmic sperm injection (ICSI), which greatly improves *in vitro* fertilization results. Even though it is one of the oldest forms of cell manipulation, the use of robotic techniques in cell injection has allowed for many recent technical innovations and performance improvements, as discussed in Section 14.2.

This chapter then moves on to discuss robotic biosample transfer, which includes the transportation of cells or small organisms to a desirable target location. Examples of biosample transfer include the relocation of a nucleus or other organelles inside a cell or the relocation of cells within the culture medium. Conventionally, this type of experiment is conducted by a highly skilled operator through a manually controlled micropipette. New advancements in robotic micromanipulation have opened up many new options for biosample transfer, as discussed in Section 14.3.

The final section of this chapter introduces robotic techniques for mechanical characterization of biosamples, which has attracted significant research interests from the fields of both engineering and biological/medical sciences. Mechanical characterization of single cells is of great importance from an engineering point of view as it provides useful information for a robotic system on how to interact with delicate cells. In biology and medicine, the mechanical property of certain types of cells can be used as an additional clue for identifying pathological conditions because some diseases (e.g., cancer and leukemia) are known to alter cellular physical characteristics.

14.2
Robotic Microinjection of Cells and Small Organisms

Microinjection is a biomanipulation technique for delivering a controlled tiny amount of foreign materials (compounds or biomolecules) into biosamples using a sharp pipette/needle with a micrometer-sized tip. Among other cell material delivery technologies, microinjection is particularly effective in delivering soluble and insoluble macromolecules into differently sized biosamples (e.g., mammalian cells, animal embryos, tissues, and small organisms). Another important characteristic of microinjection is that, with accurate position control, a pipette can be used to deposit the compound/biomolecule into a specific internal site of the biosample (e.g., the nucleus of a cell), which cannot be easily realized by other approaches. Because of these advantageous features, microinjection has become an irreplaceable experimental method for performing a number of biological studies and medical practices, including animal transgenics (e.g., microinjection of zebrafish/mouse embryos and *Caenorhabditis elegans*), assisted reproduction (e.g., ICSI), and cell-based compound/molecule testing (e.g., microinjection of adherent cells). This section introduces the technical details of existing robotic microinjection systems for two types of biosamples – single cells (mammalian cells and oocytes/embryos) and small organisms (*C. elegans*).

14.2.1
Robotic Cell Injection

Several experimental methods have been developed to introduce foreign materials into single cells, including virus vectors [1, 2], lipofection [3], electroporation [4–6], and microinjection [7]. Among these methods, virus vectors and lipofection rely on engineered molecules (modified viruses and liposomes) to introduce foreign molecules into cells, and are performed in batches of cells. Electroporation and microinjection both belong to the same category of physical methods, which use electrical and mechanical forces, respectively to make the foreign material cross over the cell membrane [4]. Cell injection is performed by puncturing the cell membrane with a glass needle and subsequently delivering the material by applying a well-controlled pressure pulse to the pipette capillary. Even though

electroporation could cause less cell damage than microinjection, microinjection has the advantage that the quantity of the delivered material can be well controlled by adjusting the duration and amplitude of the applied pressure pulse. In addition to this, microinjection allows for the selection of the intracellular target location (e.g., cytoplasm or nucleus) to which the material is deposited. Compared with other methods mentioned earlier, microinjection is a more universal approach since it is applicable to many types of cells and materials. Meanwhile, the whole injection process is controllable and feasible to be standardized. With all these advantages, microinjection is widely used in transgenic animal production [8], *in vitro* fertilization [9–11], stem cell study [12], and developmental biology [13].

In biological laboratories, cell injection is conventionally performed by well-trained human operators. According to the cell types, cell injection can be divided into two types: suspended cell injection (e.g., zebrafish and mouse oocytes/embryos) [13, 14] and adhesive cell injection (e.g., HeLa cells, fibroblasts, and endothelial) [15, 16]. Conventional suspended cell injection employs a holding pipette for immobilizing a cell and an injection pipette for penetrating the cell and delivering a foreign material. The manipulation tasks of controlling the holding pipette, searching, immobilizing, and injecting a cell are highly skill dependent, tedious, and time consuming. For instance, several months are needed for training an operator for microinjection of mouse oocytes/embryos, and the risk of operation inconsistency and sample contamination due to human involvement could reduce the success and survival rates of cell injection.

Teleoperated robotic cell injection systems have been developed to provide solutions to these technical obstacles and improve the injection process [17–21]. These systems typically employ bilateral master/slave architecture with multimodality feedback (position, vision, and force), which allows an operator to control the position of a micromanipulator and feel/regulate the interaction forces during cell injection. Compared with traditional cell injection systems, the teleoprated robotic systems improve operation accuracy, consistency, and reliability by providing the operator with visual and tactile feedback.

Even though teleoperated robotic systems provide useful assistance for manual cell injection, fully automated cell injection systems are desired to further improve operation accuracy and efficiency, and eliminate possible inconsistency due to human involvement. Multidisciplinary expertise from robotics, automation, and MEMS has been utilized to realize fully automated injection of both suspended and adherent cells. Since the early work of Sun and Nelson [8] (Figure 14.1a), a number of automated robotic injection systems have been developed in the past decade for injecting different types of cells [11, 13–16, 22–28]. For suspended cell injection, the automated cell injection system reported in [13] immobilizes a large number of zebrafish embryos into a regular pattern using a cell holding device, and coordinately controls multiple robotic devices for high-speed cell injection. The tasks of system calibration, cellular structure recognition, multirobot coordinate position control, and cell injection have all been automated, and high success and survival rates (both close to 100%) have been achieved thanks to the highly consistent robotic operation [13].

Coarse manipulator · Inverted microscope · 3-DOF microrobot

(a)

(b)
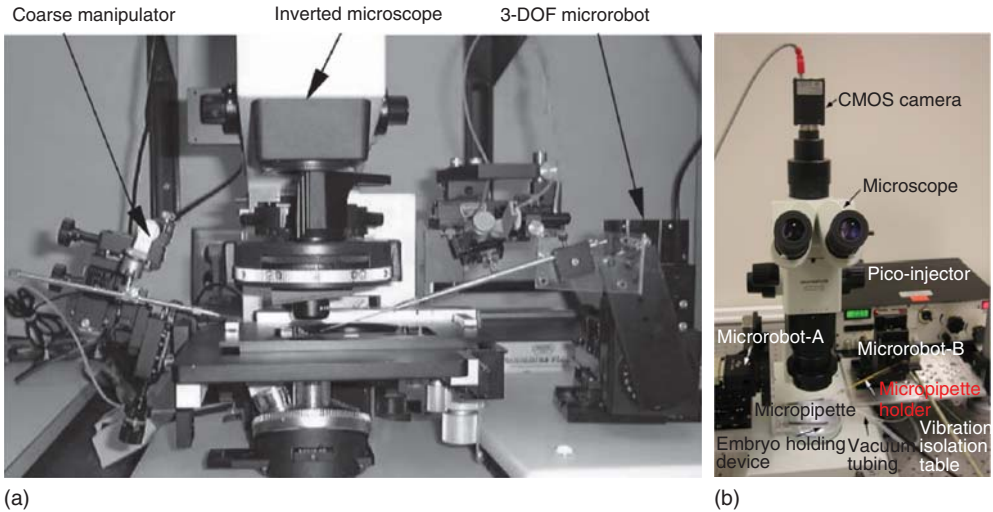
Figure 14.1 Typical system setups of automated cell injection systems. (Reproduced from [8, 13].)

Figure 14.1b shows the automated robotic system for zebrafish embryo injection [13]. The system includes a vacuum-based cell holding device for immobilizing an array of cells, an optical microscope with a digital camera for supervising the operation process and providing visual feedback, a 3-degree-of-freedom (3-DOF) micromanipulator (microrobot-A) for positioning the cells immobilized on the cell holding device, a 3-DOF micromanipulator (microrobot-B) for control motions of the injection needle, a pressure-driven microinjector for regulating the amount of deposited material, and a host computer for running image processing and motion control algorithms. The cell holding device immobilizes 25 zebrafish embryos within 12 s. An image processing algorithm identifies the structure of the target cell and the position of the pipette tip in the field of view of the microscope, and the visual feedback information is used by the robotic system for coordinate motion control of the two micromanipulators.

For adherent cell injection, the cells are directly injected on their culture petri dishes, and no cell immobilization process is needed. The tasks of system calibration and position control can be realized using similar techniques to the ones used in suspended cell injection; however, there are *two unique challenges* for injecting adhesion cells. First, the irregular shapes of adherent cells make visual recognition of the cellular structures more difficult [29]. Ghanbari *et al*. [30] proposed a pattern recognition algorithm to identify the nucleus boundary of adherent cells and thus the centroid of the nucleus as the injection target. Becattini *et al*. [27] developed a diffusion-tensor-based algorithm for anisotropic cell contour completion and identification of injection target points on adherent cells. There are also other advanced image processing and computer algorithms that have been developed for adherent cell recognitions but have not yet been applied to robotic

cell injection [31, 32]. Second, the height of an adherent cell attaching to the culture substrate typically ranges from 3 to 6 μm, with large variations from cell to cell. The vertical position control of the injection pipette tip during cell injection requires accurate knowledge of the relative position of the pipette tip and the cell. Lukkari *et al.* [33] proposed the use of electrical impedance between the pipette tip and the target cell for contact detection. Wang *et al.* [15] developed a vision-based technique for detecting the contact between the pipette tip and the culture substrate (accuracy: 0.2 μm), and an average distance of 3 μm was used as the height of the cell nuclei relative to the culture substrate. In addition, another image-based contact detection algorithm for needle tip and cell membrane is proposed by Liu *et al.*, which is based on visual recognition of the movement of the cell surface upon touching by a pipette, and can detect the contact of the pipette tip and any surface.

In the following subsections, the major techniques that have been utilized for robotic cell injection are reviewed in detail, including suspended cell immobilization methods, image processing and computer vision techniques, control system design, force sensing and control, and parallel cell injection.

14.2.1.1 Cell Immobilization Methods

Cell immobilization is an important procedure of automated suspended cell injection, which can greatly simplify the cell search/positioning tasks and improve operation efficiency. Four types of cell immobilization methods have been reported. As shown in Figure 14.2a, the conventional method, which is most widely used in manual injection, is to immobilize a cell using a holding pipette. The holding pipette, made from a glass capillary, has an inner diameter at a fraction of the target cell diameter and an outer diameter much larger than the inner one, forming a flat side wall at the tip for supporting the cell when it is injected laterally by an injection pipette (Figure 14.2a). The holding pipette is connected with a negative pressure source and immobilizes the cell [8]. The second method, illustrated in Figure 14.2b, is to immobilize multiple cells into a regular pattern via vacuum suction [11, 13, 14]. An advantage of this method is that, upon suction, the cells are automatically positioned and immobilized at locations of through-holes underneath, and the remaining un-immobilized cells are flushed away for next injection batches. Cell holding devices with an array of through-holes connected to a vacuum source have been demonstrated to immobilize zebrafish, mouse, and human embryos/oocytes. To immobilize cells of different sizes, the size of the through-holes ranges from tens of micrometers to over 1 mm. Either conventional machining or microfabrication was used to construct the cell holding devices. A similar suction-based method has also been used to immobilize and inject *Xenopus laevis* and zebrafish oocytes [35, 36]. The third method utilized half-circular grooves combined with cavities in the grooves for immobilizing a number of zebrafish embryos, and the device was fabricated via micromolding of agarose gel [26]. The inner walls of the groove/cavity provide mechanical support for cells during injection. The last method, illustrated by Figure 14.2d, is to attach single cells on a substrate surface by gluing [22, 34, 37].

(a)

(b)

(c)

(d)
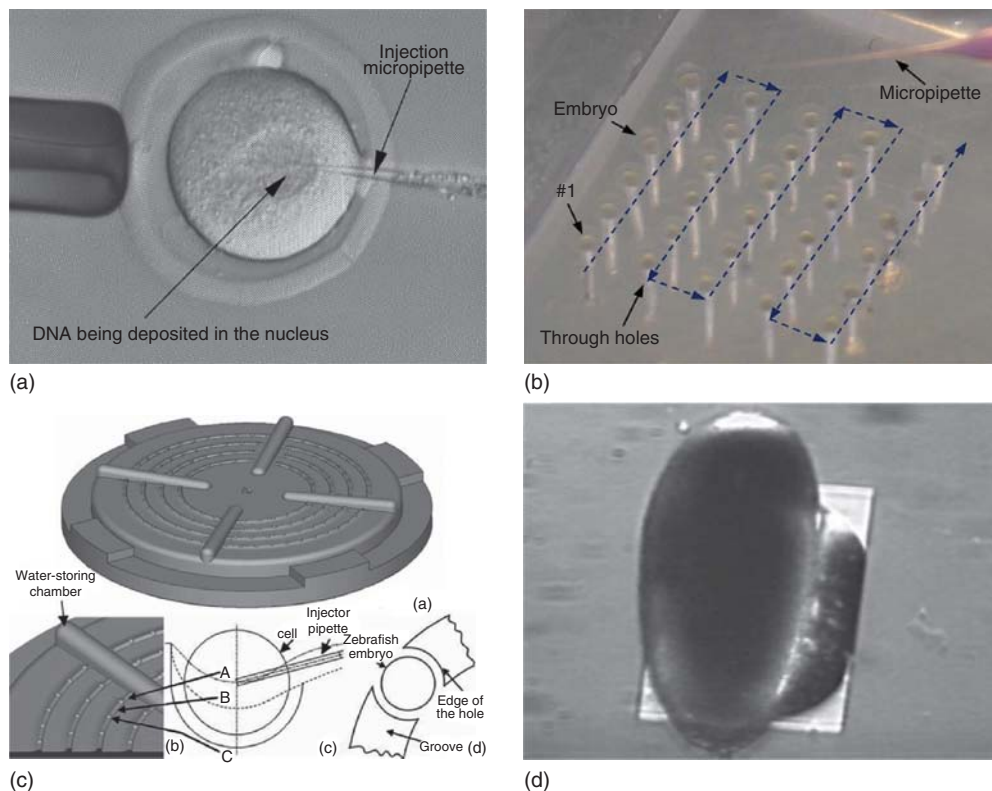
Figure 14.2 Example cell immobilization methods. (Reproduced from [8, 13, 26, 34].)

Note that, for all the four methods, the immobilization process always requires certain level of manual operation (e.g., depositing cells onto the cell holding device and positioning cells to the locations of grooves/cavities or glue points).

14.2.1.2 Image Processing and Computer Vision Techniques

In robotic cell injection, image processing and computer vision algorithms have been widely used for recognizing the structure of the target cell and the position of the injection needle tip [38], providing visual feedback for robotic control [9, 10] and analyzing cellular forces from cell contour deformations [39–41]. To achieve real-time performance, the efficiency of involved algorithms should be optimized. Edge detection algorithms are usually employed as the first step for obtaining edge and corner information of the cellular structure. The *Canny edge detector*, also known as the *optimal edge detector*, is the most commonly used edge detection algorithm, which minimizes the distance between the detected and real-edge pixels. The output of Canny edge detection is a binary image containing the position of the detected edges. For the tracking of low-contrast objects, the *Canny*

edge detector may be less feasible since the edges in low-contrast images are often blurry or even lost. On the basis of the Mumford-Shah functional for segmentation and level sets, Chan *et al.* [42] developed an active contour-based algorithm that is capable of detecting objects whose boundaries are not necessarily defined by a gradient. *Kalman filters* are also an option for detecting low-contrast objects that exhibit linear and Gaussian temporal dynamics [43].

The detected edges containing geometry and position information of the target cell are further analyzed by feature extraction/recognition algorithms. The *Hough transform* algorithm is effective for detecting regular shapes that can be characterized by a line, rectangle, or ellipse. For example, in many cell injection experiments, Hough line transform can be used to detect the needle tip, and Hough circle transform is capable of identifying circular membranes of cells and intracellular organelles (e.g., nucleus). However, the *Hough transform* is ineffective for recognizing samples with complex geometric features. In this regard, mathematical morphology-based imagine processing algorithms are used to recognize the complex shapes of cell contours and find target locations for injection. For instance, an imaging processing algorithm utilized convex hulls formed on cytoplasmic contours of zebrafish embryos to identify the orientation of embryo's yolk and cells [13].

For visual servo control of the target cell or the injection needle tip, computer vision tracking algorithms are needed. *Template matching* is often adopted to track objects with distinct features in the field of view [13, 44]. This algorithm extracts a local region from the initial image frame as a template, and seeks to search for a region in subsequent frames that maximizes the similarity measure (for which the sum of squared difference – SSD – of the pixel intensities is usually used) with the template. Support vector machines (SVMs) are also effective tools to track complex objects [45]. SVMs are one type of discriminative classifiers defined by a separation hyperplane that gives the largest minimum distance to the labeled training data. Algorithms developed from the shearlet multiscale directional transform [46] and Kalman filter [43] are also employed for visual tracking. On the basis of a motion history image and an active contour model, Liu *et al.* [38] proposed a technique that can search for out-of-focus, low-contrast end-effectors with complex contours and applied it to robotic micromanipulation including cell injection.

14.2.1.3 Control System Design

As an important component of a robotic micromanipulation system, control system design has also attracted considerable attentions in the development of robotic cell injection systems. Since microscopic vision is the major feedback modality available in cell injection systems, visual servo control is one of the most often adopted control schemes. Since the entire cell injection process is performed in the field of view of the microscope, motion path planning of the target cell and the injection pipette tip is typically conducted in the image frame. Therefore, image-based visual servo control is employed more often. Robotic micropositioning devices are driven by direct-current (DC) or stepper

motors, which can be treated as linear components in large motion ranges. Thus, conventional proportional-integral-derivative (PID) controllers can be effective as the visual servo control law. Figure 14.3 shows typical image-based visual servo control architecture of a robotic cell injection system. Compared to regular visual servo systems [47, 48], the visual servo controller used in robotic cell injection is simplified due to two factors: (i) The camera is fixed on the microscope, and the system operation is observed from a top-down view, yielding a simple two-dimensional (2D) visual servo problem. (ii) The cell injection process usually requires only translational motions of the cell samples and the injection needle tip. Thus, robots involved in cell injection (e.g., microrobot-A and microrobot-B in Figure 14.1b) are typically three-axis Cartesian ($x-y-z$) micropositioning devices, and their coordinate frames can be prealigned to avoid rotational coordinate transformations [25].

However, there is one exception in robotic injection of mouse/human oocytes, where the target cell may need to be oriented to avoid the penetration of the polar body of the oocytes. For this purpose, a visual servo system with both translational and rotational micropositioning devices has been developed to rotate a cell before injection, and online calibration of coordinate transformations was performed during visual servoing [44]. Another strategy for automated mouse oocyte orientation utilized a holding pipette to generate laminar flows to hydrodynamically orient a target cell both in plane and out of plane [49]. Image processing and computer vision algorithms were developed to recognize and track the polar body of the target cell in real time, and a visual servo controller was used to regulate the generated laminar flow and control the motions of multiple micropositioning devices during automated cell orientation.

In some cell injection systems, only closed-loop position control of the micropositioning devices was employed, and no closed-loop visual servo control was involved to avoid potential visual tracking failure [13, 14]. In these systems, either image processing algorithms or human input (through a click on the computer screen) was used to identify a target cell and the injection pipette tip and feed the information into the position controller, forming a "looking-then-moving" architecture [47]. Closed-loop force control can be also integrated into the robotic cell injection system for regulating interaction forces between the target
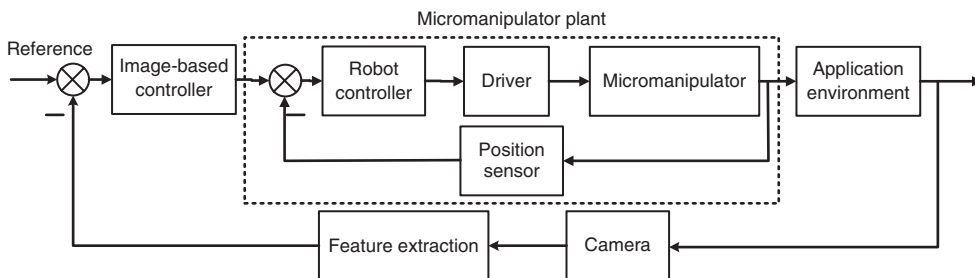
Figure 14.3 Image-based visual servo control architecture for robotic micromanipulation.

cell and the injection pipette tip. This forms hybrid position/vision/force control architecture, which is discussed in the next subsection.

14.2.1.4 Force Sensing and Control

From the robotics perspective, it is a straightforward option to integrate force sensing and control capabilities into the cell injection system, which could potentially improve manipulation dexterity and reliability. It has been demonstrated that measurement and control of interaction forces between the target cell and the injection pipette tip provide three useful functionalities: (i) Monitoring the axial injection force could accurately predict the penetration of the cell membrane during injection, which is a useful indicator for the injection system to deposit the foreign material after penetration [50–52]. As shown in Figure 14.4, the cell injection force of a zebrafish embryo gradually increases when the pipette tip comes in contact with the cell membrane and drops to zero when the membrane is penetrated [51]. The time point of cell penetration can be accurately detected from the injection force data. (ii) Measuring the injection force and corresponding cell deformation data could allow the injection system to perform *in situ* cell mechanical characterization during injection, and the measured mechanical property of the target cell could provide useful information about the quality of the cell [52]. (iii) Measuring the lateral contact force (along the tangential direction of the injection pipette motion) between the pipette tip and the target cell could assist the alignment of the tip and the center of the target cell once the tip is in contact with the cell, because the lateral contact force becomes minimal once the tip and
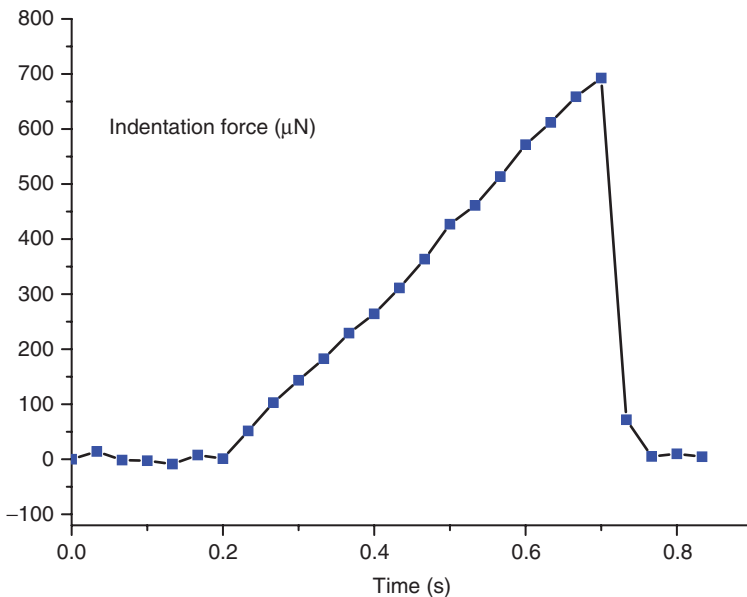
Figure 14.4 Injection force profile during microinjection of a zebrafish embryo.

the cell center are well aligned [53]. Another possible benefit of controlling the injection force to follow a desired profile is the potential reduction of injection-induced damage to the cell and the resultant enhancement of the postinjection survival rate [26, 54].

The injection forces for different cell types are in the range of (sub)nanonewtons to micronewtons [28, 52], the measurement of which requires microforce sensors with high resolutions. Even though silicon-based MEMS piezoresistive and capacitive force sensors have been used to measure injection forces of zebrafish and mouse embryos [50, 53], it is relatively difficult to efficiently integrate these fragile silicon-based force sensors into a practical robotic cell injection system, especially considering the fact that the injection pipette, attached to the force sensor, needs to be replaced frequently. Piezoelectric polyvinylidene fluoride (PVDF), as a flexible fluoropolymer material, has also been used to fabricate microforce sensors for measuring injection forces [17, 28], which are more robust mechanically for integration with robotic cell injection systems.

Another force sensing strategy is visual-based force measurement [39–41, 51, 55], which maps the injection force from deformations of a cell membrane or low-stiffness elastomeric structures (which supports the cell being injected). The relationship between the injection force and the induced cell deformation is a nonlinear mapping determined by a proper cell mechanical model. With major parameters of the cell mechanical model (i.e., cell mechanical property) estimated through off-line calibration, injection forces can be calculated from the cell deformation data [39, 40, 54, 55]. Uncertainties of this technique can be attributed to mechanical property variations across cells, and off-line calibrated data may become significantly off from the real mechanical property of the target cell being injected.

Instead of using cell deformation for injection force calculation, Liu *et al.* [51] developed a polydimethylsiloxane (PDMS) cell holding device on which flexible microposts were used to support the target cell during injection (Figure 14.5a). The injection force was then transmitted to the supporting microposts. Deflections of the microposts (Figure 14.5b) were fed into a linear mechanical model to calculate

(a)　　　　　　　　　　　　(b)
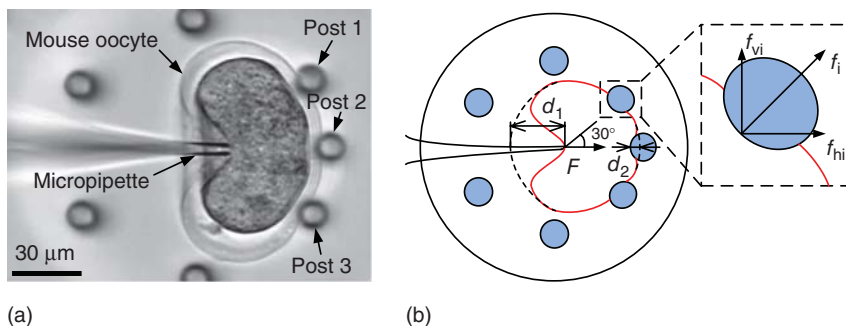
Figure 14.5 PDMS-based mechanical characterization of cells.

the injection force. As PDMS is a highly elastic material with consistent mechanical property, the calculation of the injection force from the micropost deflections can be highly accurate with properly characterized mechanical properties of the PDMS microposts. Note that, even though vision-based force measurement does not add to the hardware complexity of the cell injection system, its sampling rate is limited to the frame rate of microscopic vision (e.g., $\leq 100\,\text{Hz}$).

For force-controlled cell injection, a hybrid position/vision/force control scheme is needed to coordinate the three feedback loops and complete different steps of the injection task via different control loops and control laws. Figure 14.6 illustrates the block diagram of a hybrid position/vision/force control system. Huang *et al*. [26] proposed a hybrid control scheme with decoupled force and position control loops, where an impedance force control loop was applied along the z-axis of the injection pipette to regulate the injection force, and a position control loop along the x and y axes of the pipette for controlling in-plane motions of the pipette tip.

14.2.1.5 Experimental Validation of Injection Success and Survival Rates

A successful injection should deposit the desired amount of foreign material to the target location inside the cell, and meanwhile minimize negative effect on the survival, proliferation, and development of the injected cell. The first indicator of a successful injection is no lysis of the target cell after retracting the injection pipette out of the cell. The operation parameters that affect the lysis rate of injected cells include injection pressure (for depositing the material), injection speed, and retraction speed of the pipette. These parameters must be optimized to minimize the lysis rate after injection. In addition, it must be confirmed that the foreign material has been deposited to the desired intracellular location. Usually, injection induces little observable morphological changes to target location inside the cells, making it difficult to determine whether the operation has been successful achieved via microscopic observation. In order to validate successful material deposition, fluorescence buffers are often chosen as a model material to be injected, and the deposited material is observed right after injection via fluorescence microscopy [14, 36]. After microinjection, the injected cells are usually cultivated under their normal culture conditions to examine their survival rate
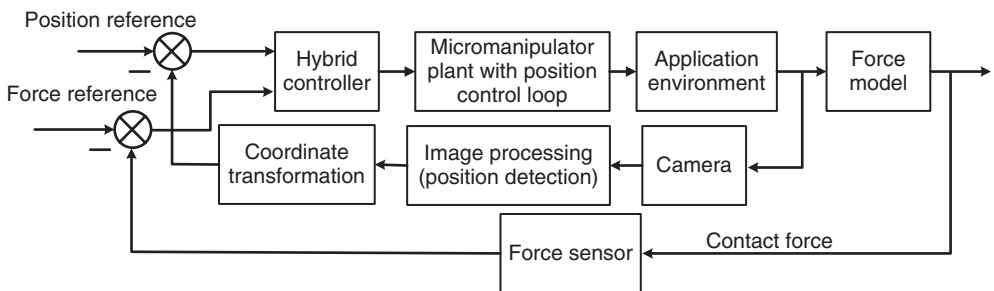
Figure 14.6 Block diagram of a hybrid position/vision/force feedback control architecture.

and even possibly induced biological pathways or phenotypes if biomolecules or drug compounds are injected [13, 16].

14.2.1.6 Parallel Cell Injection

Robotic cell injection can also be classified into serial cell injection and batch cell injection. In parallel/batch cell injection, cells are immobilized into a pattern and then injected all at once using a microfabricated microneedle array [56–58]. Theoretically, batch cell injection can be more efficient than serial cell injection; however, patterning and immobilizing cells on a substrate device were still realized manually. In addition, in existing batch injection systems, the injection microneedle array vertically penetrates the patterned cells, and a standard microscope cannot provide visual feedback on the injection process because the view is blocked by the microneedle array, which is typically made from nontransparent silicon. The lack of visual feedback makes the vertical alignment between individual needle tips and cells problematic, and may also induce cell-to-cell operation inconsistency in the same batch due to the variation in cell size and stiffness. Consequently, serial cell injection is still the dominant injection method, which robotic systems target to realize.

14.2.2
Robotic Injection of *Caenorhabditis elegans*

Mechanical injection is also adopted in the research of small model organisms, such as the nematode worm *C. elegans* and *Drosophila* [59–62]. Most of the techniques discussed in Section 14.2.1 are applicable to worm injection. Here, we discuss existing techniques for worm immobilization, which is a challenge that needs to be solved in the development of robotic worm injection systems. Existing robotic worm injection systems reported in the literature are also briefly discussed.

The immobilization of *C. elegans* is challenging because the worm is a live organism and is highly locomotive. The worm immobilization mechanism should be able to capture, immobilize, and release individual worms rapidly. In conventional manual injection, the worms are attached to the substrate of a petri dish via gluing or anesthetics [63], which is a low-throughput, labor-intensive process. Researchers from the microfluidics community have developed a series of microfluidic techniques for immobilizing *C. elegans* for applications such as high-resolution imaging and laser microsurgery [64–66]. However, these techniques immobilize worms in enclosed microfluidic channels, and therefore do not allow the injection pipette to reach the worms for injection. To solve this issue, Zhao *et al*. [67] developed an open-channel microfluidic device to load and inject single worms sequentially. The microfluidic device was designed to immobilize the worm by sucking the head and tail in an open microfluidic channel. Using the device, manually controlled worm injection was demonstrated. Other work focused on the development of worm injection systems and still used the conventional gluing method for worm immobilization. For instance, Hirano *et al*.

[59] developed an injection method for *C. elegans* based on a hybrid system combining optical microscopy and environmental scanning electron microscopy (E-SEM). Even though E-SEM provides a low-vacuum environment for the worms to survive, the exposure to electron beam radiation and negative pressure may still pose adverse effect on the injected worms.

14.3
Robotic Transfer of Biosamples

Biosample transfer is another important application of robotic micromanipulation. By transferring cells or small organisms from one location to another, numerous tasks can be performed, such as cell sorting and isolation [68], cell interaction [69], cell fusion [70], and other potential applications in biomedical engineering and the drug industry. The most commonly used transfer tools are transfer pipettes, mechanical microgrippers, untethered microrobots, and optical tweezers, which are reviewed in this section.

14.3.1
Pipette-Based Cell Transfer

Pipette-based transfer is a traditional approach widely used in biological experiments for single-cell manipulation [71–73]. This technique employs a glass micropipette, connected with a pressure unit, to aspirate and dispense cells. When the pipette tip approaches a target suspended cell, a negative pressure is applied in the capillary to aspirate the cell into the pipette or at the tip. After the cell is moved to the desired location, a positive pressure is applied to release the cell. For system setup, the micropipette is attached to a micromanipulator, which controls the position of the pipette. Several pipette-based manual manipulation systems are commercially available, such as the Quixell® Cell Transfer and Selection System (Stoelting, Wood Dale, USA) and the Eppendorf TransferMan® NK 2 micromanipulator (Eppendorf, Hamburg, Germany). Both commercial systems allow a user to use a joystick or a computer mouse/keyboard for controlling a pipette and transferring biosamples; however, the user still needs to be heavily involved to perform the tasks.

Pipette-based transfer can be divided into two categories: whole cell aspiration [72] and partial cell aspiration [74], as shown in Figure 14.7a. For whole cell aspiration, the inner diameter of the pipette tip should be slightly larger than the size of the target cell so that the whole cell can be aspirated into the pipette. The whole cell aspiration technique has been used in robotic ICSI [9, 11], in which an injection pipette aspires a single sperm cell and injects it into a human oocyte (Figure 14.7b). Before injection, the aspirated sperm needs to be brought to the pipette tip and an image-based visual servo controller was developed to automatically move the sperm to the desired location inside the pipette by regulating the sucking pressure generated by a syringe pump connected to the pipette [9]. The whole
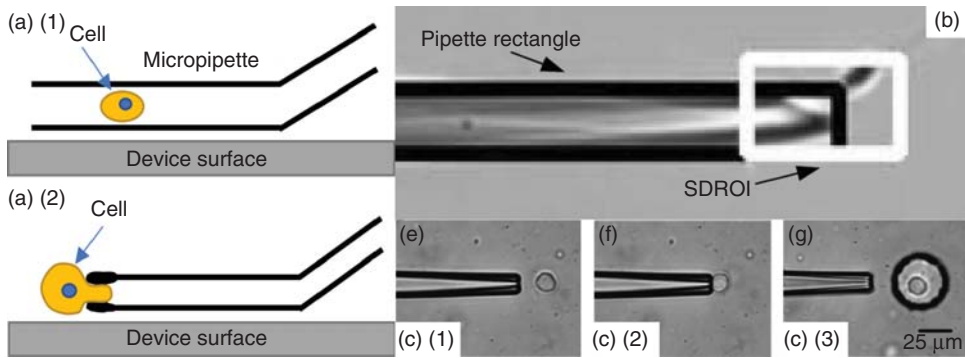
Figure 14.7 Whole and partial cell aspiration. ((b) Reproduced from [9], (c) reproduced from [72].)

robotic ICSI process includes the following steps [11]. A motile sperm is first detected and tracked using computer vision. The sperm is then immobilized by using the pipette tip to "tap" the sperm tail, and then aspirated into the injection pipette. The location of the sperm inside the pipette is accurately controlled to be at the pipette tip by the visual servo controller. Finally, the pipette penetrates the human oocyte and delivers the sperm into the oocyte's cytoplasm.

For partial cell aspiration, the inner diameter of the glass pipette must be smaller than the size of the target cell so that the target cell can be immobilized at the tip of the pipette for transfer, as shown in Figure 14.7c [72]. A small portion of the cell is aspirated into the pipette by a low negative pressure. According to Ref. [72], a negative pressure of 180 Pa caused a cell elongation of 1 µm into the pipette for fibroblasts and endothelial cells. Besides cell transfer, partial aspiration can also be used as the immobilization technique for cell injection, as discussed in Section 14.2.1.

14.3.2
Microgripper/Microhand-Based Cell Transfer

Besides micropipettes, microgrippers and microhands have also been developed to manipulate cells. These end-effectors are able to conduct manipulation tasks such as grasping, transferring, releasing, and even cell microsurgery [21, 75–78]. In addition, force-controlled microgrippers can also be used to characterize the mechanical property of single cells, which is discussed in Section 14.4.1.

To securely manipulate cells, the two grasping arms of a microgripper must have a size matching that of a single cell. In addition, displacements of the grasping arms should be controlled in suitable ranges with high resolutions. MEMS devices can meet these requirements, and some of these devices have evolved into commercial products (e.g., FemtoTools® FT-G100). For details of design and fabrication of MEMS devices, one can refer to [79]. For biomanipulation, MEMS

microgrippers are usually required to partially operate in liquid media, and that operation should not alter the properties (e.g., chemical composition, temperature, and electrical property) of the media. Meanwhile, the actuation mechanism that converts certain type of energy (typically electrical energy) into mechanical motions should be selected by taking the aqueous environment into account.

Most MEMS actuation mechanisms are not suitable for operation in liquid media [75]. For example, electrostatic actuators can cause electrolysis in electrolytic media [76]. Electrothermal microgrippers are activated based on the deformation of a beam at high temperatures, which is not typically compatible with liquid environment. A widely adopted solution is to design long gripping arms of the microgripper, which can be immerged into liquid media and keep the actuator part of the device out of the liquid during operation [76, 77, 80]. In order to avoid interference between the on-chip actuator and the aqueous environment, the gripping arm must be electrically insulated. Chronis *et al.* [75] proposed an SU-8-based microgripper that can operate in both air and liquid environments. The design leverages the large coefficient of thermal expansion of SU-8, which allows for electrothermal actuation in ionic physiological solutions at low voltage and temperature changes.

Accurate measurement and control of the grasping force during microgripper-based cell transfer is necessary for avoiding cell damage. Several MEMS microgrippers have integrated multiaxis force sensors [76, 77], and closed-loop grasping force control has been performed [77]. Kim *et al.* [77] developed a MEMS microgripper (Figure 14.8) with electrothermal actuator and two-axis capacitive force sensor for measuring the gripping force and the contact force (between the
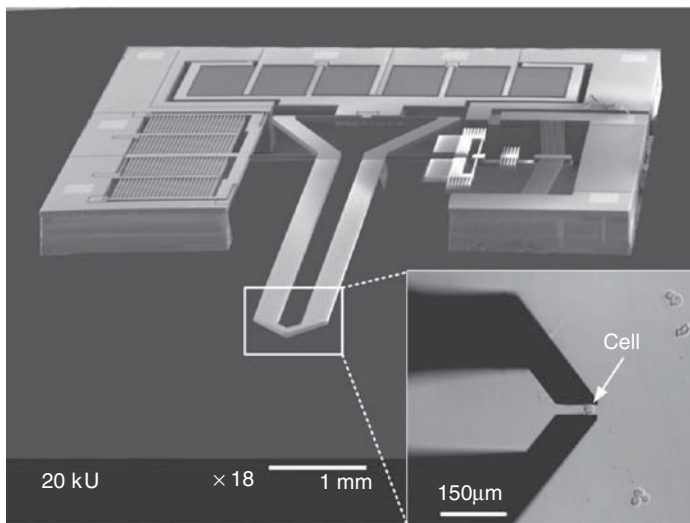
Figure 14.8   MEMS microgripper with an electrothermal actuator and a two-axis capacitive force sensor for force-controlled cell manipulation.   (Reproduced from [77].)

gripping arm tips and the biosample/substrate along the axis of gripping arms). Closed-loop control of the grasping force was performed during pick-transport-place of single cells, and nanonewton-level force control resolution was achieved. Another method of performing force measurement on MEMS microgrippers is vision-based force measurement, where deformations of flexure beams on the MEMS device are measured through real-time visual tracking [81, 82].

Besides MEMS microgrippers, a two-finger microhand has also been developed for manipulating single cells. The microhand consists of two sticks with sharp micrometer-sized tips [83–86], which are actuated by two 3-DOF parallel mechanisms and mimic the operation strategy of chopsticks for cell manipulation. The user interface for controlling the microhand includes custom-made software [83] and a haptic device [85]. With cooperative control implemented, the two fingers of the microhand work like the thumb and forefinger of a hand, with high dexterity and flexibility. In addition to common cell manipulation tasks, such as pick-transport-place and injection, the two-fingered microhand is also capable of rotating and tearing cells and extracting intracellular species (Figure 14.9) [86].

14.3.3
Microrobot-Based Cell Transfer

Magnetically actuated microrobots have also been used in cell manipulation [87, 88]. These microrobots are made from ferromagnetic materials and can act as a mobile manipulator in aqueous solutions. With the surrounding magnetic field regulated by currents in coils of external circuitry, forces acting on a magnetic microrobot can be accurately controlled. Since most cells and small organisms
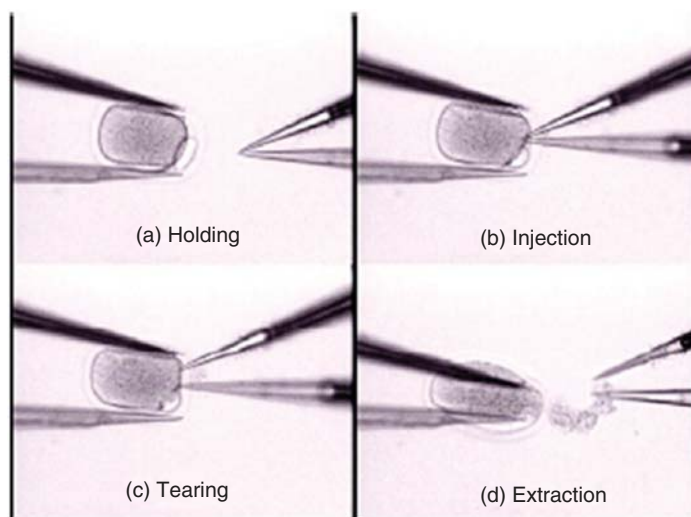
Figure 14.9 Operations of a two-fingered microhand. (Reproduced from [86].)

are not sensitive to magnetic fields, these biosamples can be manipulated by the microrobot without being displaced by the magnetic field. Magnetic microrobots are effective in pushing the biosample in plane. Furthermore, viscous forces dominate inertial forces on the microscale, and the motion of the microrobot causes little mixing or agitation of the surrounding aqueous environment. Thus, microrobot-based transfer is a less-invasive manipulation method. Figure 14.10 illustrates the process of transferring multiple cells by a three-dimensional (3D) porous magnetic microrobot reported in [89]. The 3D transporter was fabricated from a photocurable polymer and coated with nickel (Ni) and titanium (Ti), where a number of human embryonic kidney 293 cells were cultured. The microrobot was capable of translational and rotational motions, and accurate following of a predefined route for cell transfer.

14.3.4
Laser Trapping-Based Cell Transfer

Laser trapping is able to apply controlled manipulative forces on micro- or nanoparticles for manipulation. When illuminated by a focused low-power laser beam (also called *laser traps*) on one side (Figure 14.11a), a particle can overcome the viscous force and move to the center of the laser beam due to the optical trapping force [91]. This technique can manipulate cells and particles with sizes ranging from tens of micrometers down to submicrometers, and function as robotic end-effectors [91–94]. For cells that are larger than the laser beam focal volume, the optical trap acts like laser tweezers exerting strong forces
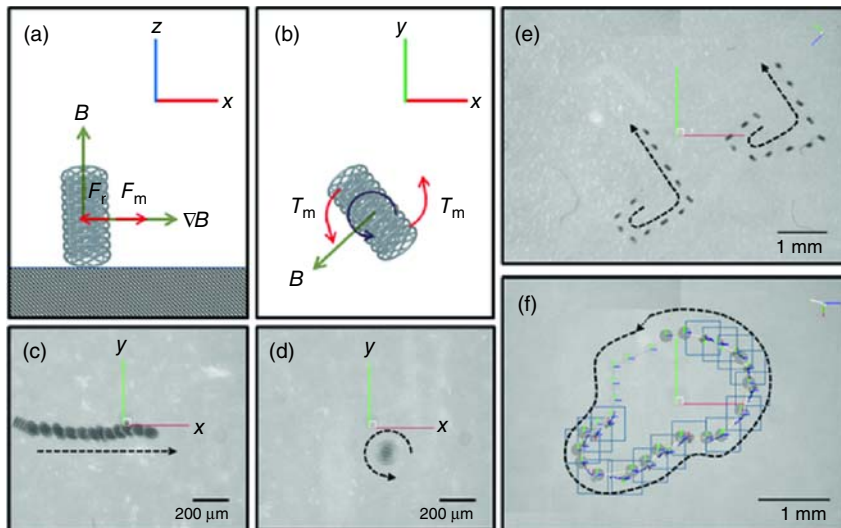
Figure 14.10 Untethered magnetic microrobot for cell manipulation. (Reproduced from [89].)
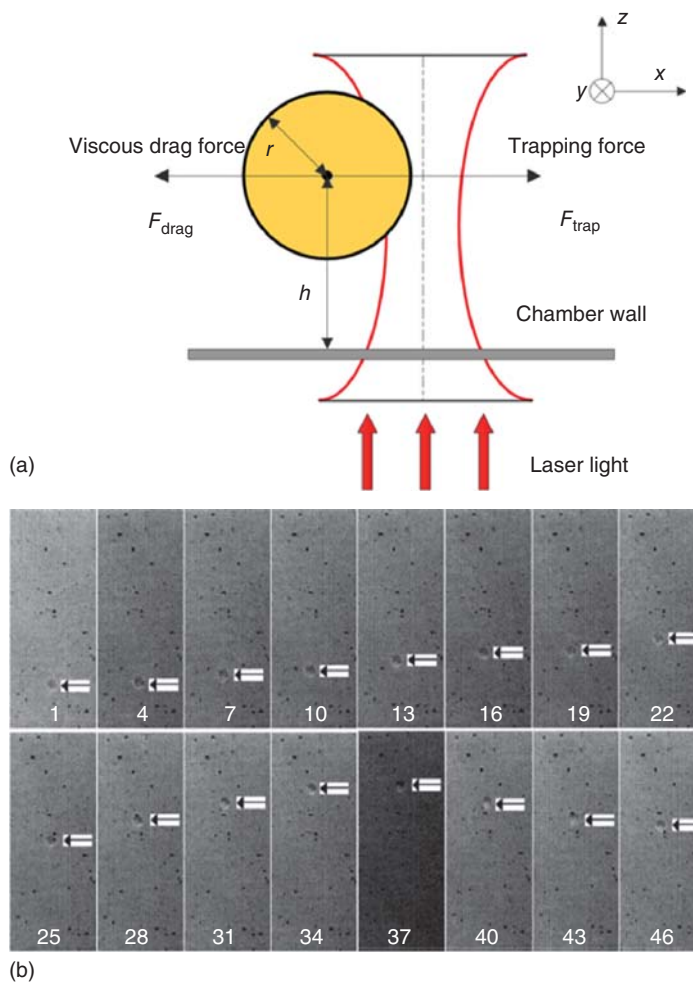
Figure 14.11 Laser trapping-based cell transfer. (a) Schematic diagram of a cell in a laser trap. (b) Cell transfer by laser trapping. (Reproduced from [90].)

near the boundaries of the cell. For small cells or organisms, it exerts maximum force at the point of maximum intensity gradient within the beam focal region [95].

Despite the concern of potential laser-induced damage to cells, laser trapping is capable of precise, flexible, and parallel manipulation of cells. Figure 14.11b shows an example of transporting a bovine red blood cell using a laser trapping manipulation system [90]. On the basis of the dynamic model of cells in laser traps, Hu *et al.* proposed a trajectory planning and path tracking/control algorithm [91]. Because of its high resolution, laser trapping has also been applied to manipulating intracellular organelles. Ashkin *et al.* [95] developed a laser

trapping system that applies well-controlled forces inside a cell while keeping the cell membrane intact. Using infrared laser traps, intracellular microsurgeries were demonstrated for manipulating large organelles such as chloroplasts and nuclei and studying biological problems such as cytoplasmic streaming, intra-cellular membranes, and organelle attachments. In addition, laser trapping has also been applied to mechanical characterization of cells, which is discussed in Section 14.4.

14.4
Robot-Assisted Mechanical Characterization of Cells

Cell mechanics reflects developmental and physiological states of cells, such as locomotion, differentiation, electromotility, and cell pathology [96]. The onset and progression of certain diseases are known to be associated with changes in cellular mechanical property. In addition, cell mechanical characterization techniques are also used for experimental validation of cell mechanical models, which could facilitate biomanipulation tasks such as cell injection and grasping. Consequently, much effort has been made on developing micromanipulation systems for cell mechanical characterization [40, 52, 53, 97–107]. This section discusses four major strategies of cell mechanical characterization, including MEMS-based characterization, micropipette aspiration, laser trapping-based characterization, and atomic force microscopy (AFM)-based characterization.

14.4.1
MEMS-Based Cell Characterization

A number of MEMS-based micromanipulation systems have been developed for mechanical characterization of biosamples [52, 53, 93, 97, 101, 107]. Sun *et al.* [53] developed a two-axis capacitive MEMS force sensor for characterizing the mechanical property of mouse embryo membranes (zona pellucida), and established a point-load mechanical model of the membrane for extracting the mechanical property from force deformation data. Using force feedback from a MEMS microgripper, Kim *et al.* [92] quantified elastic and viscoelastic parameters of alginate microcapsules. The developed technique can be readily extended to characterizing single cells.

Unlike silicon-based MEMS devices with dedicated force sensors, polymer-based MEMS devices often make use of vision-based force measurement to measure forces applied to a cell. The PDMS cell holding device developed by Liu *et al.* [51] was used for characterizing the elastic and viscoelastic properties of mouse oocytes [107]. The characterization process was conducted during cell injection, and the injection force was measured in real time by tracking micropost deflections and inputting the deflection data into a force-analysis

model. A two-step, large-deformation mechanical model was used to quantify mouse oocytes' elastic and viscoelastic properties.

14.4.2
Laser Trapping-Based Cell Characterization

As discussed in Section 14.3.4, laser trapping is an effective biomanipulation method for performing cell transfer tasks. It has also been applied to cell mechanical characterization [108, 109]. Laser traps are used to apply a known force to a cell and induce a measurable deformation, and the force deformation information is used to calculate the mechanical properties of the cell. To deform a cell, microbeads are typically attached to the cell membrane, and laser traps are applied to the microbeads to stretch the cell (Figure 14.12). The applied trapping force is a function of a few experimental parameters, including (i) the intensity of laser power, (ii) the shape of laser focus, (iii) the size and shape of the trapped microbeads, and (iv) the refraction index of the microbeads relative to the surrounding medium. Overall, the trapping force can be expressed as $F = -kx$, where k is the trap stiffness and x is the displacement of the microbead away from the center of laser trap. Details for the calibration of the trap stiffness can be found in [110]. For calibrating cells in culture medium, hydrodynamic drag forces on the microbeads also need to be considered, which are usually in the laminar flow regime [109]. This method has been used to characterize the mechanical properties of a variety of cell types, such as red blood cells [108] and human embryonic stem cells [109].
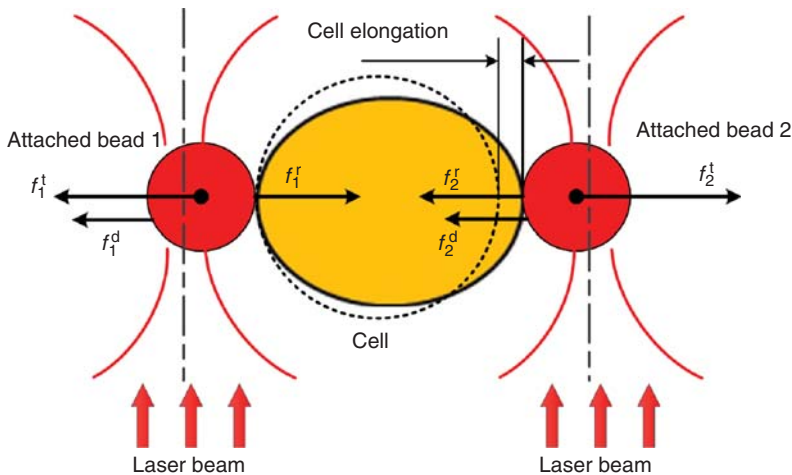
Figure 14.12 Schematic of a cell stretched by two microbeads driven by laser traps, where f^t is the laser trapping force, f^r is the cell restoration force caused by elongation, and f^d is the viscous drag force exerted on the bead by the fluid.

14.4.3
Atomic Force Microscopy (AFM)-Based Cell Characterization

AFM uses microcantilevers with micro- to nanometer-sized tips to interact with cell surfaces, and the cantilever deflection is converted to the contact force (between the cantilever tip and the cell) and cell surface topography [111]. Cell mechanical characterization is conducted by indenting a cell using an AFM cantilever to obtain experimental data of indentation force vs. cell deformation (indentation depth). The Young's modulus of the cell in the contact area is calculated by fitting an appropriate contact mechanics model to the force displacement data. In [112], a haptics-enabled AFM system was developed to mechanically manipulate and characterize embryonic stem cells. On the basis of force and vision feedback control, contact mechanics of human cervix epithelial HeLa cells was investigated in [113]. The research works on the dynamics and mechanical properties of intact cells associated with different cell events, such as locomotion, differentiation, aging, physiological activation, electromotility, and pathology, are reviewed in [114]. Many other AFM characterization systems have also been reported for cell mechanical characterization [114–120].

AFM nanoindentation has also been integrated into a scanning electron microscope (SEM) for cell mechanical characterization. Ahmad *et al*. [93] developed an E-SEM-based system that uses a customized AFM cantilever with a nanoneedle for indentation of single yeast cells. With the calibrated buckling characteristics of the nanoneedle, local Young's moduli of the yeast cells were measured via visual tracking of the nanoneedle deformations.

14.4.4
Micropipette Aspiration

Micropipette aspiration is a conventional technique developed for cell mechanics studies [121], and its principle is to aspirate a portion of a cell into a glass micropipette using a precisely applied negative pressure. Cell mechanical properties are calculated from the applied pressure and the measured cell deformation using well-established elastic and viscoelastic models [121]. Figure 14.13 shows a sequence of microscopic images showing a cell being characterized via micropipette aspiration. Robotics and automation techniques have been developed to improve the accuracy and efficiency of micropipette aspiration. Liu *et al*. [24] proposed an automatic cell contour measurement technique and a data synchronization mechanism for real-time, high-accuracy micropipette aspiration of mammalian cells, such as interstitial cells and white blood cells. Shojaei-Baghini *et al*. [122] developed a robotic micromanipulation system for automating the entire process of micropipette aspiration. Using the automated system, malignant urothelial cells were characterized to have significantly lower Young's modulus values compared to benign urothelial cells in voided urine [123].
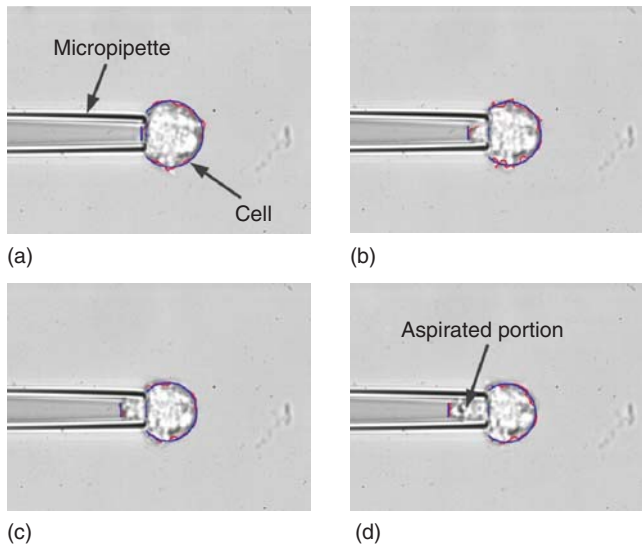
Figure 14.13 Micropipette aspiration of single cells.

14.5
Conclusion

Leveraging emerging techniques in robotics, automation, and MEMS, robotic micromanipulation has found important applications in biological and medical research. Foreign materials can be effectively delivered into single cells and small organisms. Single cells can be transferred to a desired environment. Cellular mechanical properties can be efficiently measured. Even the internal elements of a cell or organism can be manipulated by these micromanipulation systems. This chapter provided an introduction to existing robotic micromanipulation techniques and systems and their applications to three classical biomanipulation tasks – microinjection, transfer, and mechanical characterization – for handling single cells and small organisms. Significant innovations have been made to create new robotic tools for: (i) assisting in the conventional manual operations; (ii) automating the manipulation processes with unparalleled accuracy, consistency, and throughput; and (iii) enabling new types of manipulation tasks that cannot be achieved with conventional techniques. With new advancements in biology and medicine, the demand for enabling powerful biomanipulation tools becomes stronger. It is believed that the field of robotic biomanipulation will grow more and more rapidly with focuses on: (i) further technological innovations to meet requirements of newly emerging biomanipulation tasks and (ii) continuous engineering development of existing prototype systems and platforms to make them more practical and reliable for real use by biological and medical end users.

References

1. White, J., Thesier, D., Swain, J., Katz, M., Tomasulo, C., Henderson, A. *et al* (2011) Myocardial gene delivery using molecular cardiac surgery with recombinant adeno-associated virus vectors in vivo. *Gene Ther.*, **18** (6), 546–552.

2. Nonnenmacher, M. and Weber, T. (2012) Intracellular transport of recombinant adeno-associated virus vectors. *Gene Ther.*, **19** (6), 649–658.

3. Enlund, E., Fischer, S., Handrick, R., Otte, K., Debatin, K.-M., Wabitsch, M. *et al* (2014) Establishment of lipofection for studying miRNA function in human adipocytes. *PLoS One*, **9** (5), e98023.

4. Weaver, J.C. and Chizmadzhev, Y.A. (1996) Theory of electroporation: a review. *Bioelectrochem. Bioenerg.*, **41** (2), 135–160.

5. Weaver, J.C. (2000) Electroporation of cells and tissues. *IEEE Trans. Plasma Sci.*, **28** (1), 24–33.

6. Sakaki, K., Dechev, N., Burke, R.D., and Park, E.J. (2009) Development of an autonomous biological cell manipulator with single-cell electroporation and visual servoing capabilities. *IEEE Trans. Biomed. Eng.*, **56** (8), 2064–2074.

7. Zhang, Y. and Yu, L.-C. (2008) Microinjection as a tool of mechanical delivery. *Curr. Opin. Biotechnol.*, **19** (5), 506–510.

8. Sun, Y. and Nelson, B.J. (2002) Biological cell injection using an autonomous microrobotic system. *Int. J. Rob. Res.*, **21** (10–11), 861–868.

9. Zhang, X., Leung, C., Lu, Z., Esfandiari, N., Casper, R.F., and Sun, Y. (2012) Controlled aspiration and positioning of biological cells in a micropipette. *IEEE Trans. Biomed. Eng.*, **59** (4), 1032–1040.

10. Leung, C., Lu, Z., Esfandiari, N., Casper, R.F., and Sun, Y. (2011) Automated sperm immobilization for intracytoplasmic sperm injection. *IEEE Trans. Biomed. Eng.*, **58** (4), 935–942.

11. Lu, Z., Zhang, X., Leung, C., Esfandiari, N., Casper, R.F., and Sun, Y. (2011) Robotic ICSI (intracytoplasmic sperm injection). *IEEE Trans. Biomed. Eng.*, **58** (7), 2102–2108.

12. Matsuoka, H., Shimoda, S., Miwa, Y., and Saito, M. (2006) Automatic positioning of a microinjector in mouse ES cells and rice protoplasts. *Bioelectrochemistry*, **69** (2), 187–192.

13. Wang, W., Liu, X., Gelinas, D., Ciruna, B., and Sun, Y. (2007) A fully automated robotic system for microinjection of zebrafish embryos. *PLoS One*, **2** (9), e862.

14. Liu, X., Fernandes, R., Gertsenstein, M., Perumalsamy, A., Lai, I., Chi, M. *et al.* (2011) Automated microinjection of recombinant BCL-X into mouse zygotes enhances embryo development. *PLoS One*, **6** (7), e21687.

15. Wang, W., Sun, Y., Zhang, M., Anderson, R., Langille, L., and Chan, W. (2008) A system for high-speed microinjection of adherent cells. *Rev. Sci. Instrum.*, **79** (10), 1–6.

16. Liu, J., Siragam, V., Gong, Z., Chen, J., Fridman, M., Leung, C. *et al.* (2014) Robotic Adherent Cell Injection (RACI) for characterizing cell-cell communication. *IEEE Trans. Biomed. Eng.*, **62** (99), 119–125.

17. Pillarisetti, A., Pekarev, M., Brooks, A.D., and Desai, J.P. (2007) Evaluating the effect of force feedback in cell injection. *IEEE Trans. Autom. Sci. Eng.*, **4** (3), 322–331.

18. Kim, J., Ladjal, H., Folio, D., Ferreira, A., and Kim, J. (2012) Evaluation of telerobotic shared control strategy for efficient single-cell manipulation. *IEEE Trans. Autom. Sci. Eng.*, **9** (2), 402–406.

19. Mattos, L. and Caldwell, D. (2009) Interface design for microbiomanipulation and teleoperation. Proceedings of the 2nd International Conferences on Advances in Computer-Human Interactions (ACHI), 2009, pp. 342–347.

20. Gaponov, I., Ryu, J-H., Choi, S-J., Cho, H-C., and Poduraev, Y. (2008) Telerobotic system for cell manipulation. Proceedings of IEEE/ASME International Conference on Advanced Intelligent Mechatronics (AIM), 2008, IEEE, pp. 165–169.

21. Vijayasai, A.P., Sivakumar, G., Mulsow, M., Lacouture, S., Holness, A., and Dallas, T.E. (2010) Haptic controlled three-axis MEMS gripper system. *Rev. Sci. Instrum.*, **81** (10), 105114.

22. Zappe, S., Fish, M., Scott, M.P., and Solgaard, O. (2006) Automated MEMS-based Drosophila embryo injection system for high-throughput RNAi screens. *Lab Chip*, **6** (8), 1012–1019.

23. Cornell, E., Fisher, W., Nordmeyer, R., Yegian, D., Dong, M., Biggin, M. *et al.* (2008) Automating fruit fly Drosophila embryo injection for high throughput transgenic studies. *Rev. Sci. Instrum.*, **79** (1), 013705.

24. Liu, X., Wang, Y., and Sun, Y. (2009) Cell contour tracking and data synchronization for real-time, high-accuracy micropipette aspiration. *IEEE Trans. Autom. Sci. Eng.*, **6** (3), 536–543.

25. Wang, W.H., Liu, X.Y., and Sun, Y. (2009) High-throughput automated injection of individual biological cells. *IEEE Trans. Autom. Sci. Eng.*, **6** (2), 209–219.

26. Huang, H.B., Sun, D., Mills, J.K., and Cheng, S.H. (2009) Robotic cell injection system with position and force control: toward automatic batch biomanipulation. *IEEE Trans. Rob.*, **25** (3), 727–737.

27. Becattini, G., Mattos, L.S., and Caldwell, D.G. (2014) A fully automated system for adherent cells microinjection. *IEEE J. Biomed. Health Inf.*, **18** (1), 83–93.

28. Huang, H., Sun, D., Mills, J.K., Li, W.J., and Cheng, S.H. (2009) Visual-based impedance control of out-of-plane cell injection systems. *IEEE Trans. Autom. Sci. Eng.*, **6** (3), 565–571.

29. Kallio, P. and Kuncová, J. (2003) Manipulation of living biological cells: challenges in automation. Proceedings of IEEE/RSJ International Conference on Intelligent Robots and Systems (IROS), Citeseer.

30. Ghanbari, A., Wang, W., Hann, C.E., Chase, J.G., and Chen, X. (2009) Cell image recognition and visual servo control for automated cell injection.

Proceedings of 4th International Conference on Autonomous Robots and Agents (ICARA), IEEE, pp. 92–96.

31. Long, X., Cleveland, W.L., and Yao, Y.L. (2005) A new preprocessing approach for cell recognition. *IEEE Trans. Inf. Technol. Biomed.*, **9** (3), 407–412.

32. Carpenter, A.E., Jones, T.R., Lamprecht, M.R., Clarke, C., Kang, I.H., Friman, O. *et al.* (2006) CellProfiler: image analysis software for identifying and quantifying cell phenotypes. *Genome Biol.*, **7** (10), R100.

33. Lukkari, M., Karjalainen, M., Sarkanen, R., Linne, M., Jalonen, T., and Kallio, P. (2004) Electrical detection of the contact between a microinjection pipette and cells. Proceedings of 26th Annual International Conference of the IEEE Engineering in Medicine and Biology Society (EMBS), 2004.

34. Bernstein, R.W., Zhang, X., Zappe, S., Fish, M., Scott, M., and Solgaard, O. (2002) *Proceedings of the International Conference on Miniaturized Systems for Chemistry and Life Sciences (MicroTAS)*, Springer, pp. 793–795.

35. Graf, S.F., Madigou, T., Li, R., Chesné, C., Stemmer, A., and Knapp, H.F. (2011) Fully automated microinjection system for Xenopus laevis oocytes with integrated sorting and collection. *J. Assoc. Lab. Autom.*, **16** (3), 186–196.

36. Hogg, R.C., Bandelier, F., Benoit, A., Dosch, R., and Bertrand, D. (2008) An automated system for intracellular and intranuclear injection. *J. Neurosci. Methods*, **169** (1), 65–75.

37. Bernstein, R.W., Scott, M., and Solgaard, O. (2004) BioMEMS for high-throughput handling and microinjection of embryos. Proceedings of Photonics Asia, International Society for Optics and Photonics, 2004, pp. 67–73.

38. Liu, J., Gong, Z., Tang, K., Lu, Z., Ru, C., Luo, J. *et al.* (2014) Locating end-effector tips in robotic micromanipulation. *IEEE Trans. Rob.*, **30** (1), 125–130.

39. Han, M.L., Zhang, Y.L., Yu, M.Y., Shee, C.Y., and Ang, W.T. (2011) Non-contact force sensing for real-time stressing of

biological cells. *Micro Nano Lett.*, **6** (5), 306–310.

40. Zhang, Y., Han, M., Vidyalakshmi, J., Shee, C., and Ang, W. (2009) Automatic control of mechanical forces acting on cell biomembranes using a vision-guided microrobotic system in computer microscopy. *J. Microsc.*, **236** (1), 70–78.

41. Greminger, M.A. and Nelson, B.J. (2004) Vision-based force measurement. *IEEE Trans. Pattern Anal. Mach. Intell.*, **26** (3), 290–298.

42. Chan, T.F. and Vese, L.A. (2001) Active contours without edges. *IEEE Trans. Image Process.*, **10** (2), 266–277.

43. Liu, J., Leung, C., Lu, Z., and Sun, Y. (2013) Quantitative analysis of locomotive behavior of human sperm head and tail. *IEEE Trans. Biomed. Eng.*, **60** (2), 390–396.

44. Liu, X., Lu, Z., and Sun, Y. (2011) Orientation control of biological cells under inverted microscopy. *IEEE/ASME Trans. Mechatron.*, **16** (5), 918–924.

45. Kuba, H., Hotta, K., and Takahashi, H. (2009) *Advances in Neuro-Information Processing*, Springer, pp. 361–368.

46. Yi, S., Labate, D., Easley, G.R., and Krim, H. (2009) A shearlet approach to edge analysis and detection. *IEEE Trans. Image Process.*, **18** (5), 929–941.

47. Hutchinson, S., Hager, G.D., and Corke, P.I. (1996) A tutorial on visual servo control. *IEEE Trans. Rob. Autom.*, **12** (5), 651–670.

48. Chaumette, F. and Hutchinson, S. (2006) Visual servo control. I. Basic approaches. *IEEE Rob. Autom. Mag.*, **13** (4), 82–90.

49. Leung, C., Zhe, L., Zhang, X.P., and Yu, S. (2012) Three-dimensional rotation of mouse embryos. *IEEE Trans. Biomed. Eng.*, **59** (4), 1049–1056.

50. Zhe, L., Peter, C.Y.C., Joohoo, N., Ruowen, G., and Wei, L. (2007) A micromanipulation system with dynamic force-feedback for automatic batch microinjection. *J. Micromech. Microeng.*, **17** (2), 314.

51. Liu, X., Sun, Y., Wang, W., and Lansdorp, B.M. (2007) Vision-based cellular force measurement using

52. Liu, X., Fernandes, R., Jurisicova, A., Casper, R.F., and Sun, Y. (2010) In situ mechanical characterization of mouse oocytes using a cell holding device. *Lab Chip*, **10** (16), 2154–2161.

53. Sun, Y., Wan, K.-T., Roberts, K.P., Bischof, J.C., and Nelson, B.J. (2003) Mechanical property characterization of mouse zona pellucida. *IEEE Trans. NanoBiosci.*, **2** (4), 279–286.

54. Xie, Y., Sun, D., Liu, C., Tse, H.Y., and Cheng, S.H. (2010) A force control approach to a robot-assisted cell microinjection system. *Int. J. Rob. Res.*, **29** (9), 1222–1232.

55. Greminger, M.A. and Nelson, B.J. (2008) A deformable object tracking algorithm based on the boundary element method that is robust to occlusions and spurious edges. *Int. J. Comput. Vision*, **78** (1), 29–45.

56. Chun, K., Hashiguchi, G., and Hiroyuki Fujita, H.T. (1999) Fabrication of array of hollow microcapillaries used for injection of genetic materials into animal/plant cells. *Jpn. J. Appl. Phys.*, **38** (3A), L279.

57. Paik, S.-J., Park, S., Zarnitsyn, V., Choi, S., Guo, X.D., Prausnitz, M.R. *et al.* (2012) A highly dense nanoneedle array for intracellular gene delivery. Proceedings of Hilton Head Workshop, South Carolina, pp. 149–152.

58. Wang, Y., Yang, Y., Yan, L., Kwok, S.Y., Li, W., Wang, Z. *et al.* (2014) Poking cells for efficient vector-free intracellular delivery. *Nat. Commun.*, **5** (4466), 1–9.

59. Hirano, T., Nakajima, M., Kojima, M., Hisamoto, N., Homma, M., and Fukuda, T. (2011) Selective nano-injection using nano-probe based on nanomanipulation under hybrid microscope. Proceedings of 2011 International Symposium on Micro-Nano Mechatronics and Human Science (MHS), 2011, IEEE, pp. 216–221.

60. Nakajima, M., Hirano, T., Kojima, M., Hisamoto, N., Nakanishi, N., Tajima, H. *et al.* (2012) Local nano-injection of fluorescent nano-beads inside C. elegans based on nanomanipulation.

Proceedings of 2012 IEEE/RSJ International Conference on Intelligent Robots and Systems (IROS), 2012, IEEE, pp. 3241–3246.

61. Nakajima, M., Nakanishi, N., Hisamoto, N., Tajima, H., Homma, M., and Fukuda, T. (2012) Local injection probe of functional micro-nano gel tools into Caenorhabditis elegans. Proceedings of 2012 International Symposium on Micro-Nano Mechatronics and Human Science (MHS), 2012, IEEE, pp. 59–63.

62. Nakanishi, N., Nakajima, M., Hisamoto, N., Takeuchi, M., Homma, M., and Fukuda, T. (2013) Local drug micro-injection to Caenorhabditis elegans with micro-gel beads. Proceedings of 2013 International Symposium on Micro-NanoMechatronics and Human Science (MHS, 2013, IEEE), pp. 1–4.

63. Chronis, N. (2010) Worm chips: microtools for C. elegans biology. *Lab Chip*, **10** (4), 432–437.

64. Gilleland, C.L., Rohde, C.B., Zeng, F., and Yanik, M.F. (2010) Microfluidic immobilization of physiologically active Caenorhabditis elegans. *Nat. Protoc.*, **5** (12), 1888–1902.

65. Chokshi, T.V., Ben-Yakar, A., and Chronis, N. (2009) CO 2 and compressive immobilization of C. elegans on-chip. *Lab Chip*, **9** (1), 151–157.

66. Hulme, S.E., Shevkoplyas, S.S., Apfeld, J., Fontana, W., and Whitesides, G.M. (2007) A microfabricated array of clamps for immobilizing and imaging C. elegans. *Lab Chip*, **7** (11), 1515–1523.

67. Zhao, X., Xu, F., Tang, L., Du, W., Feng, X., and Liu, B.-F. (2013) Microfluidic chip-based C. elegans microinjection system for investigating cell–cell communication in vivo. *Biosens. Bioelectron.*, **50**, 28–34.

68. Wang, X., Chen, S., Kong, M., Wang, Z., Costa, K.D., Li, R.A. *et al.* (2011) Enhanced cell sorting and manipulation with combined optical tweezer and microfluidic chip technologies. *Lab Chip*, **11** (21), 3656–3662.

69. Lee, P.J., Hung, P.J., Shaw, R., Jan, L., and Lee, L.P. (2005) Microfluidic application-specific integrated device for monitoring direct cell-cell communication via gap junctions between individual cell pairs. *Appl. Phys. Lett.*, **86** (22), 223902.

70. Steubing, R.W., Cheng, S., Wright, W.H., Numajiri, Y., and Berns, M.W. (1991) Laser induced cell fusion in combination with optical tweezers: the laser cell fusion trap. *Cytometry*, **12** (6), 505–510.

71. Takeuchi, M., Nakajima, M., Kojima, M., and Fukuda, T. (2011) Probe device for soft handling of single cells using thermoresponsive polymer. Proceedings of 2011 IEEE International Conference on Robotics and Automation (ICRA), IEEE, pp. 3163–3168.

72. Lu, Z., Moraes, C., Ye, G., Simmons, C.A., and Sun, Y. (2010) Single cell deposition and patterning with a robotic system. *PLoS One*, **5** (10), e13542.

73. Zhang, K., Han, X., Li, Y., Li, S.Y., Zu, Y., Wang, Z. *et al.* (2014) Hand-held and integrated single-cell pipettes. *J. Am. Chem. Soc.*, **136** (31), 10858–10861.

74. Anis, Y.H., Holl, M.R., and Meldrum, D.R. (2010) Automated selection and placement of single cells using vision-based feedback control. *IEEE Trans. Autom. Sci. Eng.*, **7** (3), 598–606.

75. Chronis, N. and Lee, L.P. (2005) Electrothermally activated SU-8 microgripper for single cell manipulation in solution. *J. Microelectromech. Syst.*, **14** (4), 857–863.

76. Beyeler, F., Neild, A., Oberti, S., Bell, D.J., Sun, Y., Dual, J. *et al.* (2007) Monolithically fabricated microgripper with integrated force sensor for manipulating microobjects and biological cells aligned in an ultrasonic field. *J. Microelectromech. Syst.*, **16** (1), 7–15.

77. Kim, K., Liu, X., Zhang, Y., and Sun, Y. (2008) Nanonewton force-controlled manipulation of biological cells using a monolithic MEMS microgripper with two-axis force feedback. *J. Micromech. Microeng.*, **18** (5), 055013.

78. Leong, T.G., Randall, C.L., Benson, B.R., Bassik, N., Stern, G.M., and Gracias, D.H. (2009) Tetherless thermo-biochemically actuated microgrippers.

Proc. Natl. Acad. Sci. U.S.A., **106**, 703–708.

79. Liu, C. (ed) (2006) *Foundations of MEMS*, Prentice Hall, Upper Saddle River, NJ, USA.

80. Wester, B.A., Rajaraman, S., Ross, J.D., LaPlaca, M.C., and Allen, M.G. (2011) Development and characterization of a packaged mechanically actuated microtweezer system. *Sens. Actuators, A*, **167** (2), 502–511.

81. Ni, Z., Bolopion, A., Agnus, J., Benosman, R., and Régnier, S. (2012) Asynchronous event-based visual shape tracking for stable haptic feedback in microrobotics. *IEEE Trans. Rob.*, **28** (5), 1081–1089.

82. Greminger, M.A., Sezen, A.S., and Nelson, B.J. (2005) A four degree of freedom MEMS microgripper with novel bi-directional thermal actuators. Proceedings of IEEE/RSJ International Conference on Intelligent Robots and Systems (IROS), 2005, pp. 2814–2819.

83. Nguyen, C.-N., Ohara, K., Avci, E., Takubo, T., Mae, Y., and Arai, T. (2011) Automated micromanipulation for a microhand with All-In-Focus imaging system. Proceedings of 2011 IEEE/RSJ International Conference on Intelligent Robots and Systems (IROS), 2011, IEEE, pp. 427–432.

84. Kawakami, D., Ohara, K., Takubo, T., Mae, Y., Ichikawa, A., Tanikawa, T. *et al.* (2011) Cell hardness measurement by using two-fingered microhand with micro force sensor. Proceedings of 2011 IEEE/RSJ International Conference on Intelligent Robots and Systems (IROS), 2011, IEEE, pp. 25–30.

85. Tanikawa, T. and Arai, T. (1999) Development of a micro-manipulation system having a two-fingered microhand. *IEEE Trans. Rob. Autom.*, **15** (1), 152–162.

86. Inoue, K., Tanikawa, T., and Arai, T. (2008) Micro-manipulation system with a two-fingered micro-hand and its potential application in bioscience. *J. Biotechnol.*, **133** (2), 219–224.

87. Steager, E.B., Selman Sakar, M., Magee, C., Kennedy, M., Cowley, A., and Kumar, V. (2013) Automated biomanipulation of single cells using magnetic microrobots. *Int. J. Rob. Res.*, **32** (3), 346–359.

88. Ye, Z. and Sitti, M. (2014) Dynamic trapping and two-dimensional transport of swimming microorganisms using a rotating magnetic microrobot. *Lab Chip*, **14** (13), 2177–2182.

89. Kim, S., Qiu, F., Kim, S., Ghanbari, A., Moon, C., Zhang, L. *et al.* (2013) Fabrication and characterization of magnetic microrobots for three-dimensional cell culture and targeted transportation. *Adv. Mater.*, **25** (41), 5863–5868.

90. Applegate, R. Jr., Squier, J., Vestad, T., Oakey, J., and Marr, D. (2004) Optical trapping, manipulation, and sorting of cells and colloids in microfluidic systems with diode laser bars. *Opt. Express*, **12** (19), 4390–4398.

91. Hu, S. and Sun, D. (2011) Automated transportation of single cells using robot-tweezer manipulation system. *J. Lab. Autom.*, **16** (4), 263–270.

92. Kim, K.Y., Liu, X.Y., Zhang, Y., Cheng, J., Wu, S. and Sun, Y. (2009) Elastic and viscoelastic characterization of microcapsules for drug delivery using a force-feedback MEMS microgripper. *Biomedical Microdevices*, **11** (2), 421–427.

93. Ahmad, M.R., Nakajima, M., Kojima, S., Homma, M., and Fukuda, T. (2008) In situ single cell mechanics characterization of yeast cells using nanoneedles inside environmental SEM. *IEEE Trans. Nanotechnol.*, **7** (5), 607–616.

94. Arai, F., Maruyama, H., Sakami, T., Ichikawa, A., and Fukuda, T. (2003) Pinpoint injection of microtools for minimally invasive micromanipulation of microbe by laser trap. *IEEE/ASME Trans. Mechatron.*, **8** (1), 3–9.

95. Ashkin, A. and Dziedzic, J. (1989) Internal cell manipulation using infrared laser traps. *Proc. Natl. Acad. Sci. U.S.A.*, **86**, 7914–7918.

96. Tan, Y., Sun, D., Cheng, S.H., and Li, R.A. (2011) Robotic cell manipulation with optical tweezers for biomechanical characterization. Proceedings of IEEE International Conference on Robotics and Automation (ICRA), 2011, IEEE, pp. 4104–4109.

97. Serrell, D.B., Law, J., Slifka, A.J., Mahajan, R.L., and Finch, D.S. (2008) A uniaxial bioMEMS device for imaging single cell response during quantitative force-displacement measurements. *Biomed. Microdevices*, **10** (6), 883–889.

98. Kim, D.-H., Hwang, C.N., Sun, Y., Lee, S.H., Kim, B., and Nelson, B.J. (2006) Mechanical analysis of chorion softening in prehatching stages of zebrafish embryos. *IEEE Trans. NanoBiosci.*, **5** (2), 89–94.

99. Tan, Y., Sun, D., Huang, W., and Cheng, S.H. (2008) Mechanical modeling of biological cells in microinjection. *IEEE Trans. NanoBiosci.*, **7** (4), 257–266.

100. Ladjal, H., Hanus, J.-L., and Ferreira, A. (2013) Micro-to-nano biomechanical modeling for assisted biological cell injection. *IEEE Trans. Biomed. Eng.*, **60** (9), 2461–2471.

101. Yang, S. and Saif, T. (2005) Reversible and repeatable linear local cell force response under large stretches. *Exp. Cell Res.*, **305** (1), 42–50.

102. Tan, J.L., Tien, J., Pirone, D.M., Gray, D.S., Bhadriraju, K., and Chen, C.S. (2003) Cells lying on a bed of microneedles: an approach to isolate mechanical force. *Proc. Natl. Acad. Sci. U.S.A.*, **100**, 1484–1489.

103. Li, B., Xie, L., Starr, Z.C., Yang, Z., Lin, J.S., and Wang, J.H.C. (2007) Development of micropost force sensor array with culture experiments for determination of cell traction forces. *Cell Motil. Cytoskeleton*, **64** (7), 509–518.

104. Du Roure, O., Saez, A., Buguin, A., Austin, R.H., Chavrier, P., Siberzan, P. et al. (2005) Force mapping in epithelial cell migration. *Proc. Natl. Acad. Sci. U.S.A.*, **102**, 2390–2395.

105. Yang, M.T., Sniadecki, N.J., and Chen, C.S. (2007) Geometric considerations of micro-to-nanoscale elastomeric post arrays to study cellular traction forces. *Adv. Mater.*, **19** (20), 3119–3123.

106. Dembo, M. and Wang, Y.-L. (1999) Stresses at the cell-to-substrate interface during locomotion of fibroblasts. *Biophys. J.*, **76** (4), 2307–2316.

107. Liu, X., Shi, J., Zong, Z., Wan, K.-T., and Sun, Y. (2012) Elastic and viscoelastic characterization of mouse oocytes using micropipette indentation. *Ann. Biomed. Eng.*, **40** (10), 2122–2130.

108. Lim, C.T., Dao, M., Suresh, S., Sow, C.H., and Chew, K.T. (2004) Large deformation of living cells using laser traps. *Acta Mater.*, **52** (7), 1837–1845.

109. Tan, Y., Kong, C.-W., Chen, S., Cheng, S.H., Li, R.A., and Sun, D. (2012) Probing the mechanobiological properties of human embryonic stem cells in cardiac differentiation by optical tweezers. *J. Biomech.*, **45** (1), 123–128.

110. Zhang, H. and Liu, K.-K. (2008) Optical tweezers for single cells. *J. R. Soc. Interface*, **5** (24), 671–690.

111. Morris, V.J., Kirby, A.R., and Gunning, A.P. (eds) (1999) *Atomic Force Microscopy for Biologists*, World Scientific.

112. Pillarisetti, A., Keefer, C., and Desai, J.P. (2009) *Proceedings of International Symposium on Experimental Robotics*, Springer, pp. 261–269.

113. Girot, M., Boukallel, M., and Régnier, S. (2006) Modeling soft contact mechanism of biological cells using an atomic force bio-microscope. Proceedings of IEEE/RSJ International Conference on Intelligent Robots and Systems, 2006, IEEE, pp. 1831–1836.

114. Kuznetsova, T.G., Starodubtseva, M.N., Yegorenkov, N.I., Chizhik, S.A., and Zhdanov, R.I. (2007) Atomic force microscopy probing of cell elasticity. *Micron*, **38** (8), 824–833.

115. Meister, A., Gabi, M., Behr, P., Studer, P., Vörös, J.n., Niedermann, P. *et al.* (2009) FluidFM: combining atomic force microscopy and nanofluidics in a universal liquid delivery system for single cell applications and beyond. *Nano Lett.*, **9** (6), 2501–2507.

116. Obataya, I., Nakamura, C., Han, S., Nakamura, N., and Miyake, J. (2005) Nanoscale operation of a living cell using an atomic force microscope with a nanoneedle. *Nano Lett.*, **5** (1), 27–30.

117. Takai, E., Costa, K.D., Shaheen, A., Hung, C.T., and Guo, X.E. (2005)

Osteoblast elastic modulus measured by atomic force microscopy is substrate dependent. *Ann. Biomed. Eng.*, **33** (7), 963−971.

118. Tian, X., Liu, L., Jiao, N., Wang, Y., Dong, Z., and Xi, N. (2004) 3D nano forces sensing for an AFM based nanomanipulator. Proceedings of International Conference on Information Acquisition, 2004, IEEE, pp. 208−212.

119. Fung, C.K.M., Seiffert-Sinha, K., Lai, K.W.C., Yang, R., Panyard, D., Zhang, J. *et al.* (2010) Investigation of human keratinocyte cell adhesion using atomic force microscopy. *Nanomed. Nanotechnol. Biol. Med.*, **6** (1), 191−200.

120. Li, M., Zhang, C., Wang, L., Liu, L., Xi, N., Wang, Y. *et al.* (2013) Investigating the morphology and mechanical

properties of blastomeres with atomic force microscopy. *Surf. Interface Anal.*, **45** (8), 1193−1196.

121. Hochmuth, R.M. (2000) Micropipette aspiration of living cells. *J. Biomech.*, **33** (1), 15−22.

122. Shojaei-Baghini, E., Zheng, Y., and Sun, Y. (2013) Automated micropipette aspiration of single cells. *Ann. Biomed. Eng.*, **41** (6), 1208−1216.

123. Shojaei-Baghini, E., Zheng, Y., Jewett, M.A.S., Geddie, W.B., and Sun, Y. (2013) Mechanical characterization of benign and malignant urothelial cells from voided urine. *Appl. Phys. Lett.*, **102** (12), 123704.

15
Industrial Tools for Micromanipulation

Michaël Gauthier, Cédric Clévy, David Hériban, and Pasi Kallio

15.1
Introduction

The market of miniaturized and highly integrated products is growing every year. Historically, fabrication processes in microscale were limited to high-volume market, and innovative assembly robots have been recently placed on the market to enable the fabrication of low or medium volume of miniaturized and highly integrated products. This development of a new market for robotics is a worldwide trend and is mentioned in the US Robotics 2013 roadmap "robotics is applied to applications in novel domains such the manipulation of parts on the nano- and micro-scales" [1] as well as in the European Robotics roadmap: "The use of robot manipulation in the industrial production of complex miniature devices is also an emerging area of application, with particular application in micro-optical systems and the volume assembly of microscale components" [2].

Companies involved in the market of industrial miniaturized robot are SMEs, which have shown an impressive two digits growth or even three digits growth. This market sector represents a significant growth potential for robot industries and opens the way to the reduction of costs and improvement of end user performances of microproducts.

Microsystem manufacturing is a growing field that deals with fabrication and packaging of fragile microcomponents (size from 1 μm to 5 mm) to be used in a variety of domains: instrumentation, mini-invasive surgery, automotive industry, IT peripherals and telecommunications [3], biomedicine, and so on. Production of existing microsystems such as MEMS is a huge market where several million pieces are batch-produced annually. Dedicated packaging systems are already available (Figure 15.1). However, in packaging design, assembly is most simplified to guarantee the throughput, with techniques such as flip-chip bonding.

The wide spectrum of applications for microsystems industry and the great variety of systems designs in one domain push the need for more flexible production means. The possibility to deal with smaller batches and more dedicated products would give SMEs a considerable advantage.

Figure 15.1   SET SAS flip-chip bonding machine [4]. (SET SAS website.)

The first step to improve manufacturing flexibility is often the robotization of processes. Robots bring flexibility because they are designed for multiple purposes and can be used in different ways for numerous processes. Even though current industrial robots are dedicated for humankind manipulation abilities, with quite good accuracy and repeatability at our scale (0.1 mm), they are far from the requirements in micromanufacturing (0.005 mm and even less). Specific miniaturized robots emerge especially in Europe, carried by several young and innovative companies such as SmarAct [5], FemtoTools [6], Imina Technologies [7], and Percipio Robotics [8]. Their innovative efforts tackle the accuracy issue in micromanufacturing process in a robotic approach, in competition to high-accuracy automated machines already supplied by worldwide players such as Palomar Technologies [9], Finetech [10], Essemtec [11], and SET SAS [4].

However, robotics and especially microrobotics require specific technical skills (precision, …) to perform usual tasks performed in manufacturing. Because of this technology barrier, big players in micromanufacturing delay the transition to smaller/more complex products batches and the robotization effort of those products remains low. Typical examples of robotization of current processes deal with the market of scientific microinstrumentation, where many high-value and competitive products are developed and produced. In this field, the production is usually started on prototypes and very small series, mainly assembled on demand by hand under microscopes and requiring outstanding human manipulation abilities. This situation is a perfect playground for innovation in the robotic domain to bring plug-and-produce miniaturized robots dedicated for assembly of high-value microsystems.

This chapter synthesizes the state of the art of the industrial tools for micromanipulation in two major fields of application: (i) the scientific instrumentation and (ii) the manufacturing. Some perspectives will be drawn in a last section.

15.2
Microrobotics for Scientific Instrumentation

The first major market for microrobotics is to enable operations on microsamples with a better precision than the human hand. Microrobotic tools notably enable the accurate manipulation of very small samples useful to study local properties of innovative materials. Then, mechanical tests or measurements can be achieved as well as electrical or optical characterization. Several tests can also be advantageously combined together or being achieved simultaneously to study, for example, optical properties of a strained sample. The scientific instrumentation segment includes different market challenges detailed in the following.

15.2.1
MEMS Mechanical Testing

Micro-electro-mechanical systems (MEMS) have become a key enabling technology for many of today's high-technology products. It has been recognized for some time that the "back end" of MEMS production has been hindering the ability of the "front end" to realize the innovative potential of MEMS. In short, a lack of testing standards is increasing the time and costs of MEMS innovation with percentage of testing being between 20% and 50% of the cost of the device, often with the most complex and promising devices having the highest test costs [12]. Testing MEMS is quite different from testing Integrated Circuits (ICs). When testing MEMS sensors, one big problem arises: instead of testing electrical signals, the electrical response to mechanical inputs needs to be examined. Furthermore, in case of MEMS actuators, the mechanical response to electrical inputs is evaluated.

Research and development in mechanical MEMS testing is currently performed by (i) optical methods (laser Doppler vibrometer) or (ii) probe-based methods (atomic force microscopes and nanoindentors).

Optical testing (Polytec Inc.) is the most frequently used method nowadays. The advantage of this technology is the fast, noncontact deflection measurement over a large frequency range. The disadvantage is that only deflections of the MEMS structures can be measured. Direct measurement of stiffness, force, linearity, hysteresis, yield strength, and so on is not possible and are usually calculated based on mathematical models. Another limitation is that curved, reflective surfaces cause problems when the light is not reflected back to the photosensor resulting in measurement errors. Atomic force microscopes and nanoindenters are systems that are provided by several companies (Bruker, Agilent, CSM, Hysitron, etc.). Their hardware and software have been optimized for other applications than MEMS testing (e.g., surface profile measurement and indentation). In addition, the systems are normally limited to vertical measurements only and cannot be used for in-plane deflection/force measurement. A third group of probe-based testing instruments are the surface profilers (Bruker, KLA-Tencor). These systems are frequently used for topography measurements on wafers, but cannot extract the mechanical properties of the sample to be tested.
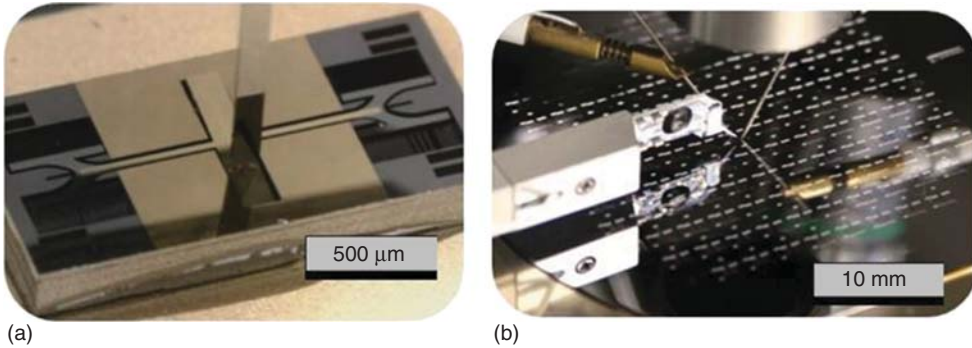
Figure 15.2 (a) Robotic measurement of torsional stiffness of a MEMS mirror; (b) Combined micromechanical and electrical MEMS testing of structures on a wafer using microrobots (FemtoTools, Switzerland [6]). (Courtesy of FemtoTools GmbH.)

Some innovative machines have been developed recently to perform complete and advanced tests including both electrical and mechanical control. FemtoTools is one of the industry leader in ultrahigh-precision instruments for mechanical testing and robotic handling in the micro- and nanodomains (Figure 15.2). This company has, for example, developed the "FemtoTools FT-FS1000 Mechanical Probe," which is one of the most versatile micromechanical testing instrument. The system is designed for the direct and accurate probe-based mechanical testing for applications in MEMS testing, nanoscience, material science, and biology, and builds on over 10 years of experience in the field of micromechanical testing. Equipped with one of the FemtoTools FT-S Microforce Sensing Probes, this system can perform a wide range of micromechanical testing principles such as compression testing, tensile testing, bending testing, creep testing, and cyclic testing. Because of the modular buildup of the FT-FS1000 Mechanical Probe, the instrument can be adapted to the requirements of a specific application and integrated into the most suitable microscope. It can perform the following operations:

- Vertical (out-of-plane) compression testing of a MEMS-based micromirror on a probe station (top view) for the measurement of stiffness, deformation range, and actuation force (Figures 15.3).
- Horizontal (in-plane) cyclic stretching of a protein fiber submerged in liquid on an inverted (biological) microscope for the measurement of elastic/plastic deformations under cyclic loads.

15.2.2
Mechanical Testing of Fibrous Micro- and NanoScale Materials

Testing mechanical properties of micro- and nanoscale materials has experienced a significant increase in importance with the development and industrialization of micro- and nanodevices. This is evident in a recent survey on this field, where as many as 600 articles published from 1920 to 2014 were investigated [13].

Figure 15.3 FemtoTools Modular Sensing systems [6]. (Courtesy of FemtoTools GmbH.)

According to the survey, more than 70% of the articles have been published in the last decade (2004-2014). It is known that the bulk properties of material are different from the properties in small scale [14]. A special class of micro- and nanoscale materials is fibrous materials, such as natural fibrous materials, including textile fibers and paper fibers, whose tests are linked with large-scale industries, such as textile- and papermakers. The use of microrobotic tools in these fields is emerging at the same time with the development of microrobotic sensing capabilities and a progress in automation.

The material properties of fiber-based products are largely determined by the properties of the underlying fiber network and its two main components: the fibers and the bonds between the fibers. In papermaking, the dimensions of fibers vary from 0.8 to 4.5 mm in length and the diameters are in the range of $10-70$ μm. Two main approaches exist to estimate the mechanical properties of individual fibers (tensile and bending properties) and interfiber bonds (bond strength): (i) indirect measurements based on force measured from bulk and (ii) direct measurement requiring micrograsping of a fiber. Many methods to estimate the properties indirectly from bulk, that is, from paper sheets, have been proposed and are currently commonly used. The most common methods include peel testing [15], Clark's cohesiveness test [16], Scott bond testing, and modified zero span test [17]. Similar to other bulk material tests, these methods provide only inaccurate estimates on the average values and the obtained results are not coupled with undesired information. Therefore, they have limitations in modeling and predicting strength properties of paper and board products. For example, when studying the effects of various strength additives – critical components for the manufacture of paper and board – bulk methods fail to provide accurate information on the influences of the additives on the bonding capability of fibers as the number of bonds in the bulk is not known.

Therefore, direct methods to study mechanical properties of fibers have been proposed, for example, in Refs [18] and [19] and recently in Refs [20 – 22]. The main

limitations of these methods are their (i) slowness (a single measurement requires time-consuming preparations enabling only few measurements per day) and (ii) unreliability (e.g., the glue that is typically used to fix the fibers during measurements can affect their observed mechanical properties). Therefore, these methods are not suitable for performing a sufficient number of tests to provide statistically reliable data on the distribution of mechanical properties of these extremely heterogeneous materials.

There are several challenges in mechanical characterization of fibrous materials that dictate the use and further development of microrobotic tools in this application domain. The typical sample diameter (10−70 μm) makes manual characterization in large quantities impossible. The dimensions together with the scale of the strength properties set requirements for positioning accuracy and sensors that are out reach of traditional robotics. The second challenge in the handling and characterization of natural fibers is their true three-dimensional (3D) morphology. Therefore, precise estimation of the location of the samples in three dimensions using microscopic stereo vision, for example, is needed. The third challenge is the large variation in the mechanical properties of the samples. For example, the bending stiffness of kraft pulp fibers can vary from 2 to 100 10^9 Nm. Furthermore, the distribution is not necessarily Gaussian but can be skewed. Therefore, a large number of measurements should be performed to obtain statistically reliable results on the distribution of the property. In order to obtain the results in industrially feasible time, a high throughput is needed, which necessitates automation in the measurement process. Because of the aforementioned challenges, the use of microrobotic tools especially in industrial scale applications is urged.

Recently, Tampere University of Technology (TUT) has proposed the use of microrobotic tools for performing fiber measurements [23−25]. Currently, microrobotic fiber characterization is provided in a lab-scale platform, where dozens of measurements have been performed in a teleoperation mode and some parts of the operation sequence have been performed automatically (Figure 15.4). The measured properties include flexibility of individual fibers, bond strength of individual fiber−fiber bonds both in shear and z-directional modes, and dry friction between fibers.
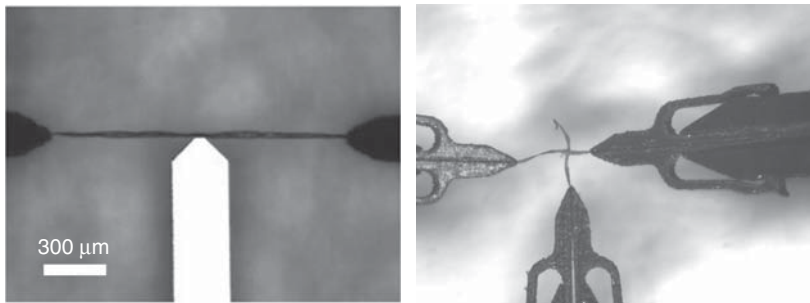
Figure 15.4 Measurement of bending strength and interbond strength using microrobotics (Tampere University of Technology, Finland). (Courtesy of Tampere University of Technology.)

New nanomaterials require advancements in their electrical and mechanical characterizations. Micro- and nanorobotic tools can be used in testing such samples as silicon nanowires (SiNWs) or carbon nanotubes (CNTs). Such mechanical tests are of great interest in several fields and scientific communities as well as from an industrial point of view.

15.2.3
Mobile Microrobots for Testing

One of the other promising approaches to perform test is to use several mobile robots working around the sample. The miBot™ developed by Imina Technologies is an extremely versatile piezo-based manipulator that can be used in combination with various third-party instruments to position probe tips on electronic devices and MEMS, or to handle and characterize nanoparticles and biological samples (Figure 15.5).

miBots™ have ultrasmall size with platforms specifically designed to minimize their footprint on cluttered experimental setups and environmental chambers. The compact stages are available in various shapes and dimensions that accommodate 1, 2, or 4 miBots™. The design allows to easily reconfigure setups for new experiments. Not directly attached to the sample, these stages are ideal for use at low optical working distance. They are also well adapted to contact large substrates mounted on sample holders that are moved by a positioning stage (e.g., wafer chucks and Petri dishes).

The miBase makes installation and use of miBots™ extremely convenient. The platform accommodates samples up to 5 cm (2 in.) diameter. It offers several mounting interfaces that fit most optical and electron microscopes, and moving from one to another is a matter of minutes. It embeds a MultiBot controller which allows you to run up to 4 miBots™ with a single piezo driver (syDrive), and
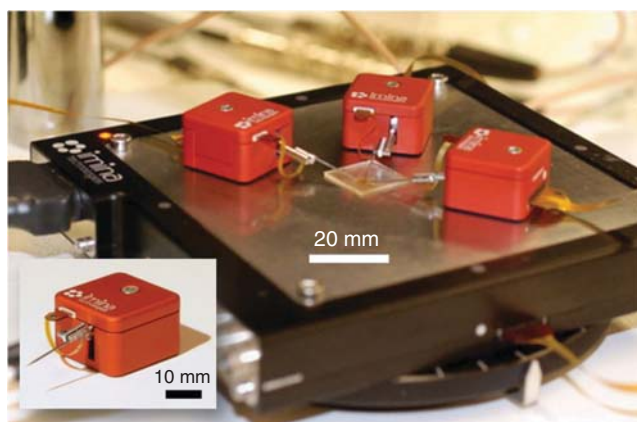
Figure 15.5 Electromechanical characterization of organic MEMS cantilevers using mobile robots miBot™ (Imina Technologies, Switzerland) [7]. (Courtesy of Imina Technologies SA.)
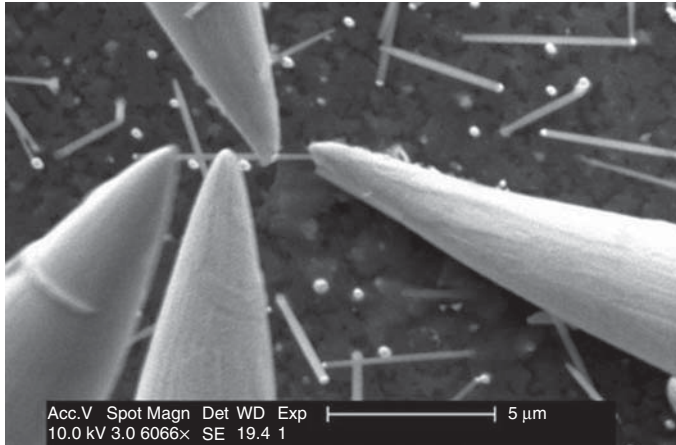
Figure 15.6 Four-point probe measurements (Imina Technologies, Switzerland) [7]. (Courtesy of Imina Technologies SA.)

cabling is reduced to the minimum. Electrical signals can be measured or injected at the miBot™ probe tips by third-party instruments by connecting them to the coaxial connectors on the front panel.

miBots™ is also available to perform tasks in vacuum. The nanoprobing platform is a unique solution that turns the miBot™ nanomanipulators into powerful nanoprobers for in situ electrical characterization of semiconductor devices and advanced materials in SEM and FIB. Carefully designed to minimize interferences with measuring signals, leakage currents can be as low as 100 fA V^{-1}. Separate shielded cables connect each probe from the stage to industry standard feedthrough connectors. This platform allows to position independently up to four probes over a workspace of several millimeters with a resolution up to the nanometer. Figure 15.6 presents an example of four-point probe measurement of nanowires. Manipulation and characterization of individual nanowires with a noninvasive approach are crucial for the perfect understanding of their properties. In this application, a semiconductor silicon nanowire (200 nm in diameter and 6 μm in length) grown by vapor–liquid–solid method (VLS) is probed by four miBots™.

15.3
Microrobotics for Microassembly

The second market or microrobotics consists in providing robots that are able to assemble microcomponents to produce complex microsystems. Extreme assembly process requires accurate handling capabilities of components, and the miniaturization of components changes both the way to assemble and handle them. Micromanipulation is a major issue in high-accuracy assembly

of miniaturized products. First, industrial robots are designed to copy human gestures whose accuracy is limited to a few tenths of micrometers. For a 200-μm object, mechanical fixtures' size is close to $10-20$ μm and the accuracy needed to perform the assembly is below 1 μm. Secondly, classical handling systems (vacuum gripper on robots for automated handling) are not enough accurate regarding to the objects' size. Beyond accuracy, the size itself brings numerous disturbing effects. Capillary, electrostatic, and van der Waals forces are much more important than objects' weight: they stay in contact with grippers, even if they are released. In the air at normal conditions, objects stick on the vacuum gripper's needle and it needs to be blown for release. But low mass means low inertia and blow-off could throw the micro-object far from its target. Despite the strong interest (multiaxis measurement, quite good range and resolution) and extended use, the vision of microscopic objects brings its own drawbacks. Highest magnification on photonic microscopes is limited by its resolution (0.2 μm min.), and trade-off between measurement range and resolution has to be done. Micrometer accuracy needs microscope instead of classical camera macro-objectives, with high illumination, short work distance, and small depth of field (sometimes objects are seen in focus only on 2 μm depth).

The first challenge in improving accuracy is to break with industrial robotics and build a robot with much more accurate components. Already present in research laboratories in microtechnology, compact robotic system are used for accurate positioning. They are made from single, compact, and accurate linear and rotation stages, assembled together in multi-degrees of freedom (DOF) robotic systems [26–28]. It is also possible to use nanopositioning systems that are based on compliant (then backlash-free) structures.

The second challenge in improving accuracy during a microassembly task is to improve the behavior of object handling and release. Tens of microgripping devices have been developed, and microtweezers present the largest flexibility. On the basis of finger grasping, and high-resolution actuation, several devices based on monolithic approach are available [29, 30] and few ones on piezoelectric actuation [26] (Figure 15.7). Grasping MEMS by tweezers principle is mostly successful on simple and complex shapes, from few micrometers to few millimeters in size, and various materials such as silicon, glass, metal, and polymers.

15.3.1
Microassembly of Micromechanisms

In the micromechanism industry, most assembly tasks to build miniaturized products are performed by hand by highly qualified operators. Using standard machines to handle and accurately assemble microcomponents is difficult, and human expertise and flexibility are still required. However, miniaturization and production growth require more and more accuracy and productivity, and operators can no more realize the task without robotic assistance. A new robotic system, based on the concept of cobotics, combines the accuracy and productivity of the robot with the flexibility and smartness of the operator operating it.
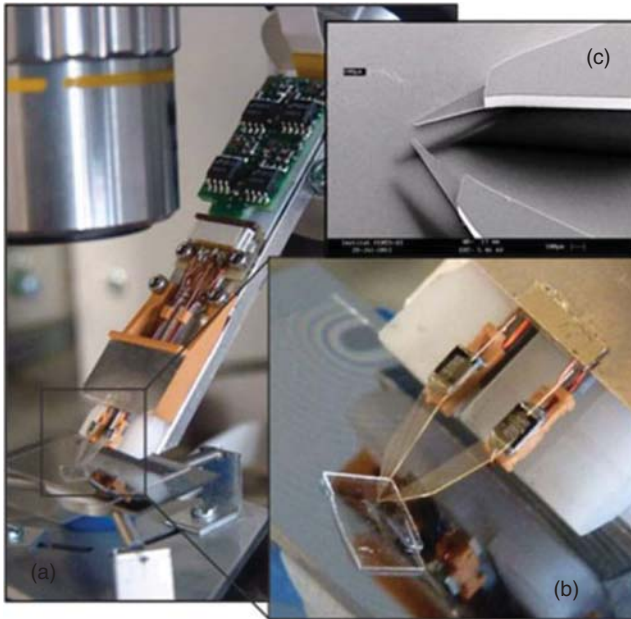
Figure 15.7 Serial 6-DOF robotic system placed above an inverted microscope (Percipio Robotics, France) [8]. (Courtesy of Percipio Robotics SA.)

The typical example of this market is the watch industries in which complex assembly operations of tiny components are carried out manually. In some extreme cases, the precision of the human hand is not sufficient and the reliability of the assembly becomes too low (typ. 10% successful assembly). Microrobot enables to move more precisely the tweezers and the microcomponents to their final target. The better precision of the trajectory enables to avoid unexpected contact and thus enables also to use smaller end-effectors, which in turn enable to reach some currently inaccessible parts of the watch during the assembly. A second example deals with the manipulation and the positioning of microsamples in front of testing machines for physical characterization and experiments. As an example, the analysis of proteins is currently done using micrometric protein crystals. Microrobots enable to position protein crystal in front of X-ray detectors to analyze their structure.

In industrial microassembly tasks, two major issues need to be resolved to increase industrial interest in robotic systems. The first one is the lack of accuracy of common industrial robots and grippers: handling 100 μm parts with a robot is still a difficult task. Robots, grippers, and sensors have to be improved or adapted to be able to reach the high level of performance required. The second issue is the difference in flexibility between human and robot operation. Thanks to our brain, the human hand is the most flexible tool we know. For a robot's control system to be used more easily, it has to be improved. Without decent artificial intelligence,

one of the best ways to improve flexibility is to combine human operators and robots to perform microassembly tasks.

A micromanipulation and microassembly machine consist in a microgripper and vision tools integrated in a high-precision robotic structure. These three key elements are detailed in the next sections.

15.3.1.1 Microgrippers

Two kinds of grippers are used for microassembly: manual tweezers for small or medium series of products for complex objects (e.g., the watch industry) and vacuum grippers for simple shapes (e.g., planar surfaces and spheres) mostly for large series (e.g., microelectronics). Even if the vacuum gripper is carried by an accurate robot, the accurate assembly of submillimeter parts is difficult and is mainly limited to planar components to be manipulated along two directions (3D assembly remains particularly complex with this technique). Moreover, this tool is disturbed by the object's behavior at the microscale, especially by capillarity and low mass. In the air at normal conditions, objects stick to the vacuum gripper's needle, which means they then need to be blown off to be released. But, low mass means low inertia and being blown off could displace the micro-object far from its target. In that case, using tweezers is an interesting way to grasp objects; here, a very small contact surface is used to avoid surface force disturbance. To place tweezers on accurate robots, the French research institute FEMTO-ST has developed a specific technology based on piezoelectric actuation (Figure 15.8), which has then be transferred to Percipio Robotics. Percipio improved it to use robotic microtweezers in industrial assemblies.

In the piezogripper provided by Percipio Robotics (Figure 15.8), two piezoelectric beams are used as the fingers of a pair of tweezers, and a specific voltage over the electrodes of the beams causes them to bend with high resolution (about 0.1 μm) and large stroke (more than 200 μm opening).

Force sensors have recently been tested at the lab scale offering a very good manipulation ability (they notably enable to take into account previously

Figure 15.8 4-DOF piezoelectric microgripper (FEMTO-ST & Percipio Robotics, France) [8]. (Courtesy of Percipio Robotics SA & FEMTO-ST institute.)
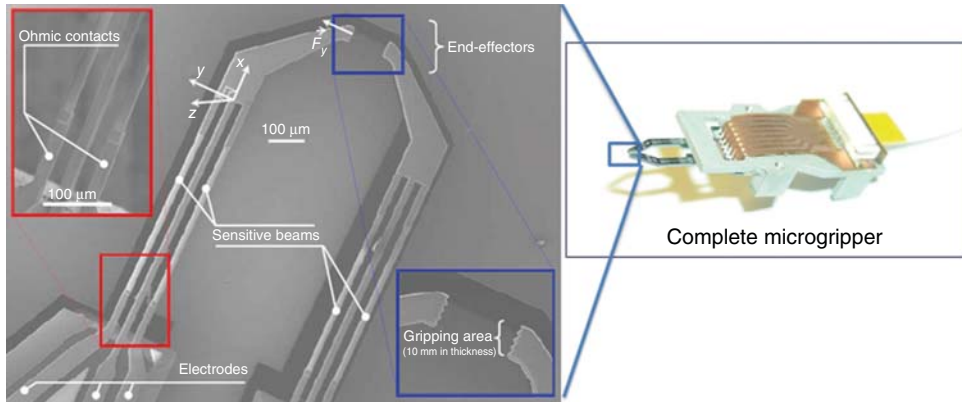
Figure 15.9 Piezoresistive force sensors integrated in microgripper's Silicon fingertips. (FEMTO-ST, France) (Courtesy of FEMTO-ST institute.)

mentioned surfaces forces during manipulation). These force sensors are integrated within the fingertips of the microgripper, which are made of silicon (Figure 15.9). They use the piezoresistive effect of this material, which possesses high gauge factors allowing a very good sensitivity. Sensors are very small ($700 \times 100 \times 12$ μm) and have 2 mN sensing range and very high signal-to-noise ratio, typically 50 dB [31].

15.3.1.2 High-Resolution Vision System

To be efficient, flexible robots for high-accuracy assembly need computer vision with high-resolution optics. These measuring tools are extremely used because they enable multi-DOF measurement quite good range/resolution ratio. In addition, these technologies recently have made impressive progresses integrating higher quality optics and higher resolution optical sensors. Nevertheless, microscope optics are often difficult to integrate into machines, even more for compact ones. Moreover, the high magnification required by assembly implies a small field of vision, a few hundreds of micrometers wide. To open up the field and make integration easy, Percipio Robotics built a new kind of vision system with high-resolution compact optics, high-resolution cameras (>10 megapixels), and specific software.

With this system, cameras observe a "large" field of view (6 mm wide) while optical resolution on the full image is about 1.5 μm per pixel. In order to avoid low image refresh on full-scale images, the software downgrades the resolution to the screen resolution. When the assembly task needs to observe a small area, only the field of interest is captured by the camera, in high resolution, at the speed of 25 frames per second. It is then possible to zoom in up to six times on the screen, without touching the camera's objectives, and even move the field of interest at full resolution anywhere in the field.

15.3.1.3 **Integrated Assembly Platform**

Once all these pieces of technology are available, the final path to microassembly is to build a compact, accurate, and flexible robotic system to perform microassembly tasks. Percipio Robotics has already completed this step with Chronogrip, a fully integrated robotic platform with modular robotics, piezogrippers, and a high-resolution visual system (see Figure 15.10). This device is compact (it can be placed on a table), can be easily transported in a protective case, is easy to mount and start (<5 min), and is available in different configurations depending on the application. In the standard version, the table moves and rotates in the horizontal plane relative to the gripper and the cameras. The gripper is positioned by two linear axes. The robot has a motion resolution of 0.1 μm and an accuracy of ± 2 μm with closed loop (visual servoing). Axis speed can be set from 1 μm s^{-1} (precise task) to 10 mm s^{-1}.

The Chronogrip robotic platform is now being used for microassembly tasks. Even if technological improvements were made to allow flexible and accurate operation, operating the robot is still a complex task. In industrial robotics, numerous robots are programmed offline and execute the same task again and again in open-loop processes. Task analysis is increasingly needed during the operation to close the loop, with computer vision used to operate the robot (e.g., pick-and-place). At a microscale, computer vision is very difficult to use (small depth of field, heterogeneous light, diffraction), and achieving a fully automated microassembly task can be too time consuming. Percipio Robotics took a step forward by using the principle of cobotics ("collaborative robotics") on microassembly tasks. Cobotics is the collaboration of a human being and a robot to perform a task. The robot is operated by the operator, but not in a master/slave mode. The robot uses its sensors to send a full set of information to the operator (e.g., vision, haptics, and augmented reality) and can correct operator's commands to improve motion behavior (e.g., compensating for a

Figure 15.10 Chronogrip robotic platform for microassembly (Percipio Robotics, France) [8]. (Courtesy of Percipio Robotics SA.)

shaky hand). This interaction between the robot and the operator is the most flexible way of creating accurate and fast microassembly tasks. The robot needs the smartness and flexibility of the operator to achieve its task, while the operator needs the accuracy and stability of the robot to move the microgripper.

The Chronogrip is in fact operated by an operator who is using a joystick and a tablet PC with touch screen. The joystick is used to move the robot, and the tablet PC is used to view the video stream from the camera and operate the zoom and image position. Moreover, this new technology appears as particularly intuitive making it usable by many people even having poor robotic or computer engineering background.

15.3.2
Microassembly in MEMS and MOEMS Industries

Robotic microassembly has also a strong market potential in MEMS and MOEMS industries. Indeed, in electronic industry and more recently in MEMS/MOEMS industry, packaging of systems (flip-chip, bonding, and sealing) is a well-known mass manufacturing process, where accuracy of $5-10$ µm and no flexibility are needed. For example, automatic flip-chip machines and die bonders aided by machine vision can achieve a high throughput (e.g., 10,000 units per hour at 12 µm accuracy (8800 FC QUANTUM, Datacon, Austria)).

The trend of miniaturization requires smaller components, smaller interconnections, and consequently higher accuracy. However, the throughput is dramatically decreased if a higher accuracy has to be achieved. For example, some machines can only package 240 units/h at 0.5 µm accuracy (FC 300R, SET-SAS, France [4]). Moreover, flexibility is important for smaller production batches in the case of more specialized and high-value products. Some machines use robot-like systems to increase their capabilities in manipulation and reconfiguration such as the products of Percipio Robotics, which can handle objects from few microns to few millimeters with 1 µm accuracy [8].

New principles emerged from packaging of silicon dies in electronic industry. Packaging is now much more capable than assembly of single dies in individual ICs. 2.5D packaging started first by enabling packaging of several dies on interposers to connect them inside the same package. 3D packaging went further by enabling stacking of functional dies to create 3D ICs function and save space in the package. Most of the research in the field tackles the challenge of interconnecting dies, with ultraminiature through-silicon via (TSV), microball grid arrays, and so on [32].

Miniaturized robots presented earlier are able to handle very small parts with high accuracy (better than 1 µm [33]) and 6-DOF positioning capabilities. Miniaturized robots integrated in industrial packaging machines could dramatically increase production capabilities in the field of complex MEMS and MOEMS. In up-to-date machines, including industrial robots such as the Hydra machine from ESSEMTEC, throughput is $1000-2500$ assemblies per hour for 3D positioning with 45 µm accuracy [11]. This machine is able to dispense adhesive,

grasp component, position and release it with right orientation within 1.5–5 s. Research level miniaturized robots for microassembly perform similar tasks with ten times higher accuracy within 5 s. Accuracy-increased performances bring the technology to actual requirement in MEMS/MOEMS high-precision packaging, especially for small TSV arrays alignment from dies to interposers [34].

But grasping, positioning and assembly capabilities of miniaturized robots could even open new possibilities for extreme 3D assemblies of MEMS / MOEMS device at the wafer level. Out-of-plane assemblies of silicon dies, coupling of optical components and silicon photonics, and micro- and nanofiber assemblies on silicon MEMS for high-performance sensors are among the current applications of such systems. Two of them are actually demonstrated and could raise interest in the packaging field. First one is the stacking of ultrathin dies for high-density memories applications. The second one is a demonstrator for flexible MOEMS assembly bench, with reconfigurable setup for high-performance prototyping.

15.3.2.1 Thin Die Packaging

Ultrathin dies are the thinned semiconductor chips having thickness below 50 μm. The primary need for ultrathin die fabrication and assembly techniques is in the so-called 3D integration, where different active dies are vertically connected in stacks using through-silicon via (TSV). Ultrathin dies offer several benefits for such die stacks. They enable lower package height for thin IC applications, enhanced heat flow for high-power components, shorter interconnections for faster operation, and easier TSV formation due to reduced thickness.

The major challenge in ultrathin die stacking is to fulfill the requirement of high-accuracy and high-throughput simultaneously, while avoiding damage to the dies. For 3D die stacks, the alignment accuracy of TSVs between the dies is crucial to ensure working electrical connections. According to the ITRS roadmap for 3D die stacks, the required alignment accuracies are approaching the submicron level while the number of aligned layers is increasing beyond two [35]. To tackle the throughput and accuracy dilemma, Liimatainen *et al.* [36] uses an assembly method for ultrathin dies based on capillary self-alignment-assisted robotic pick-and-place. This hybrid method exploiting both robotic manipulation and local self-alignment using capillary forces has been tested during the European projects Hydromel and FAB2ASM [37]. The method is built upon the recent efforts on combining robotic microhandling and self-assembly into a hybrid microassembly strategy, where high-speed robotic pick-and-place is used for coarse positioning, and high accuracy is reached by capillary self-alignment of a droplet, driven by the capillary force between the die and the receptor site [38, 39]. Despite the previous studies carried out on hybrid microassembly, the ultrathin die stacking brought many new challenges to be tackled, including the handling of fragile die, the potential effect of such die on self-alignment, and if the required accuracy can be achieved.

In order to avoid damaging the fragile ultrathin dies during processing (thinning and singulation) and handling, the ultrathin dies are prepared in an SOI wafer within a thin device layer. These dies are tethered to the wafer's frame with

a breakable part, designed on purpose [40]. The breakable tethers are useful to keep dies on the wafer after the fabrication process allowing as easy handling as UV tape.

In Reference [36], vacuum gripper was used to untether silicon dies from the wafer, helped with an accurate robotic system for positioning. Because of a lack of accuracy of the vacuum gripper, an original solution was proposed with capillarity positioning. Water droplets are dispensed on the assembly site, then handled die is released above the droplet. Capillary force helps release of the die from the vacuum gripper's nozzle and positions the die according to the edge geometry with high accuracy (2 μm).

Experimental assemblies have been performed to validate the process, and up to 12 dies of 10 μm thickness were assembled with micrometer accuracy (Figure 15.11).

To avoid use of vacuum grippers and water droplets, experiments have been conducted in Ref. [41] with piezoelectric microtweezers. Grasping and release of thin silicon dies (5 μm) were achieved (Figure 15.12).

15.3.2.2 Flexible MOEMS Extreme Assembly

The 3D integration of hybrid chips is a viable approach for the micro-optical technologies to reduce the costs of assembly and packaging. The fabrication of complex MOEMS products through assembling has recently been experienced demonstrating the large potential of the approach. Weber *et al.* notably succeeded in miniaturizing a complex optical bench based on the combination of several basic generic silicon components [42]. Numerous optical arrangements are possible in very small volumes making it particularly interesting for endoscopic optical-based systems (Figure 15.13). Zyvex (USA) also succeeded in assembling a complex miniaturized scanning electron microscope (Figure 15.14). In Reference [33], a technology platform for the hybrid integration of MOEMS components on a reconfigurable silicon free-space micro-optical bench (FS-MOB) is presented. Their concept relies on the robotic assembly of holder components onto a
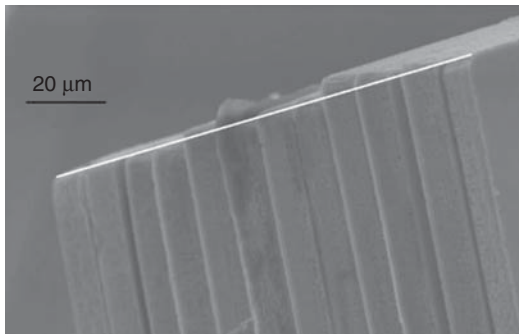
Figure 15.11 12 ultrathin dies (10 μm) stacked (FEMTO-ST, France). (Courtesy of FEMTO-ST institute.)
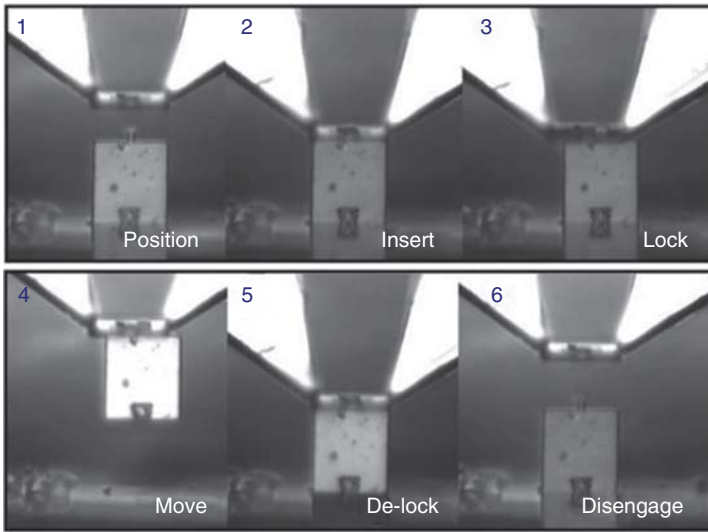
Figure 15.12   3D assembly of two $40 \times 40 \times 5$ µm silicon dies (perpendicular) (FEMTO-ST, France). (Courtesy of FEMTO-ST institute.)
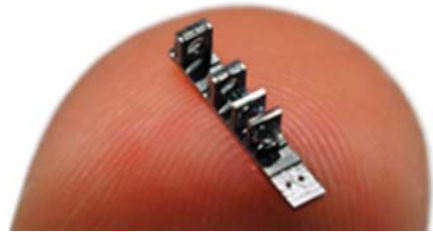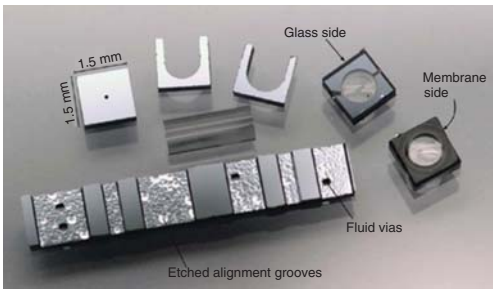
Figure 15.13   Several basic silicon and optical components and picture of an assembled micro-optical bench based on such components (IMTEK, Germany, 13). (Courtesy of Gisela and Erwin Sick Chair of Micro-optics, IMTEK, Germany.)

Figure 15.14   Microassembled electron lens to form a miniaturized scanning electron microscope (Zyvex labs, USA, [43]). (Zyvex website.)

substrate. Different kinds of holders exist or could be manufactured, such as mirror, ball lens holder, beam splitter, holders with various apertures, sensors, and laser sources. These holders can be assembled onto the substrate at different locations along one or several optical axes. Many holder combinations can be achieved to build various kinds of basic optical functionalities up to more advanced ones or even complex devices, such as microinterferometers, for instance.

This 3D integration based on assembling is of great industrial potential, but relies on efficient and accurate microassembly systems. The coupling of two monomode fibers done with a positioning error of 1 µm typically induces 50% optical intensity loss. To succeed in such precision, several teams used novel technologies and control algorithms. For example, FEMTO-ST institute developed a 6-DOF robotic system with piezoelectric tweezers to handle holders and assemble basic optical components to the substrate. Silicon holders are grasped horizontally and rotated to be vertically inserted in the substrate. Fine positioning and force feedback are required to guide the holder inside V-grooves and release the part with high accuracy (Figure 15.15). Also specific assembly strategies have been proposed to succeed in achieving complex automated tasks, such as guiding or insertion [44].

Robotized microassembly enables assembly of hybrid components (glass spheres, VCSEL, etc.) on silicon holders and silicon holders themselves on a silicon substrate (Figure 15.15). Such technology could be used on different kinds of MEMS to allow 3D integration of parts having incompatible fabrication processes. Popa *et al.* also developed flexible and highly accurate robotized assembly system. They notably succeed in assembling a microspectrometer composed of several basic optical blocks (laser source, ball lens, beam splitter, mirrors all assembled along a Michelson interferometer configuration). The interferometer also integrates a scanning MEMS mirror based on an electrothermal actuator [45] (Figure 15.16).
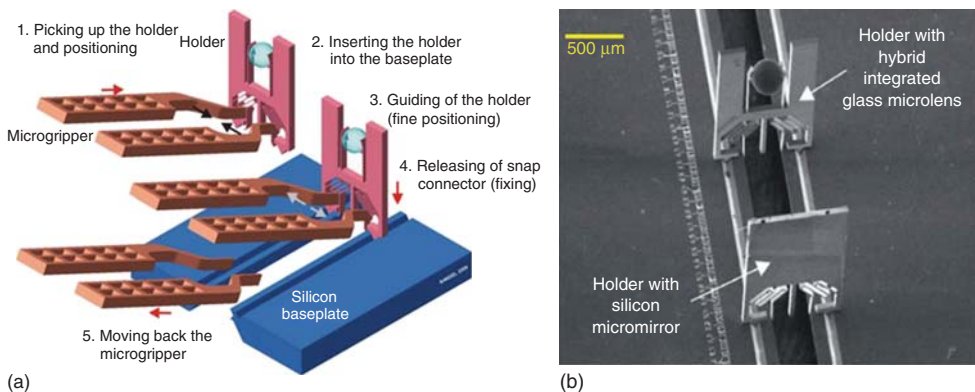
Figure 15.15 (a) Principle and (b) example of out-of-plane MOEMS assembly (FEMTO-ST Institute, France). (Courtesy of FEMTO-ST institute.)
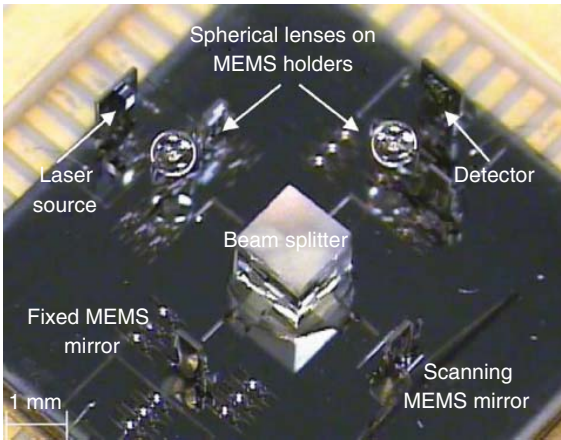
Figure 15.16   Microspectrometer assembled with robots and gripping tools (ARRI Institute, USA). (Courtesy of ARRI institute.)

15.4
Future Challenges

Despite many progresses recently achieved based on really innovative proof of concepts and the fast industrial development of microrobotic tools, many challenges still have to be addressed to enable a higher industrial maturity. Among them, the recent development of integrated sensors (force and position) will undeniably enable to increase the accuracy, then the reproducibility and reliability of motions to be generated. In the same way, commercially available microrobotic systems are mostly working in teleoperated mode. Integration of sensors and development of machine learning methods will enable automation. Important gains in terms of yields, throughputs, product quality, and productivity are expected. Important progresses are also expected in terms of manipulability and dexterity based on more complex and smarter microgripper designs. This opportunity also relies on recent innovative materials used as actuators. Dexterity will induce very light gripping systems than having ultrafast and accurate motion capabilities. This will notably enable to reach very high manipulation speeds within large workspaces.

15.4.1
Current Opportunities

The current market opportunities in industrial applications of miniaturized robotics deal with:

- the request of teleoperated robotic production and testing replacing the manual microassembly production lines and
- the request of automatic microassembly lines and testing systems.

The development of this market will enable to improve the reliability and performance of the complex microassembly fabrication processes mostly done by hand. The end user markets are the biomedical devices, watch industries and micromechanics, and scientific instrumentation. This market has been also targeted in US Robotics 2013 roadmap: "Dramatic advances in robotics and automation technologies are even more critical with the next generation of high-value products that rely on embedded computers, advanced sensors and microelectronics requiring micro- and nanoscale assembly, for which labor-intensive manufacturing with human workers is no longer a viable option."

15.4.2
Future Opportunity

Behind the current opportunities, the market of miniaturized robot for microassembly will open the wider and promising future opportunities in two major end user markets: telecommunication and environmental supervision. Until 2020, microassembly robots will enable the production of complex micro-optical systems requiring high-precision and high-throughput assemblies. This capability will enable the production of more precise and cheaper optical components in the framework of the fiber-to-the-Home (FTTH) markets. The second future opportunity deals with the production of nanosensors for environmental supervision. Nanosensors market growth is currently limited by the lack of powerful manufacturing aims. The advent of miniaturized robots will enable the assembly of micro- and nanocomponents in nanosensors with better performances and lower cost.

The barriers to reach this market are mostly technical barriers requiring new robotic tools, architecture, and approaches to reach both high precision and industrial throughput in micro- and nanoscales.

15.4.3
Barriers to Market

In industrial miniaturized robotics, market barriers consist of technological limitations on robot components, process limitations, and automation and autonomy of the robot.

Regarding current opportunities in the field of teleoperated and automatic assembly, the current technology maturity of robotic components (grippers, sensors, etc.) is around TRL[1]4-5 and future developments are required to improve the reliability of the systems in order to push technologies on the market TRL8-9. The maturity of automation and autonomy of these systems are still very

---

1) TRL: Technology Readiness Levels. TRL1: Basic Principles Observed; TRL2: Technology Concept Formulated; TRL3: Experimental Proof of concept; TRL4: Technology Validated in Laboratory; TRL5: Technology Validated in Relevant Environment; TRL6 Technology Demonstrated in Relevant Environment; TRL7: System Prototype Demonstration in Operational Environment; TRL8: System Complete and Qualified, TRL9: Actual System Proven in Operational Environment.

low TRL2-3 and research activities in this field are highly required in the next years. Regarding future opportunities in the fields of optic component assembly and nanosensors assembly, the current maturity is around TRL2-3 and some research activities are also highly needed to push innovative robot on the market.

15.4.4
Key Market Data

The major characteristic of the market of industrial miniaturized robot is the impressive growth of this market. Indeed, the turnover of SME in miniaturized robotic production has a typical start-up successful business with a two digits or three digits growth. This growth will be maintained as an impressive level in the next years until 2020. Indeed the miniaturized robot for microassembly has been recently reached the technology level to be launched on the market. The manual microassembly is no more a viable option and the request of robot will grow significantly for the next years.

The market of robotics in a field can be estimated as a part of the final market (e.g., 2–4% of the global market). The current market in watch industry[2] and micromechanics which may take benefit of microassembly is around 6.4 billion Euros per year. The total addressable market (TAM) of miniaturized robotic assembly in Horizon 2020 may reach 250 million Euros per year (4% of the application market).

Regarding nanosensors, the global environmental sensor and monitoring market were valued at US$11.1 billion in 2010 [47]. This market is expected to reach US$15.3 billion in 2016, a compound annual growth rate (CAGR) of 6.5% between 2011 and 2016. The TAM for "innovative micro-nano-robot for nanosensors" may reach 306 million Euros in Horizon 2020 (2% of the application market).

Regarding future opportunities, the current total accessible market for miniaturized robot for optical microcomponents manufacturing is still low around 1 million Euros per year. The prevision of the growth of this market is still complex to establish. Indeed, the advent of new robotic manufacturing and testing methods will enable to open the market in the next years. The market is consequently highly linked with the development of the robotic capabilities in this field. The challenge consists in improving the R&D effort in this field to open the market.

References

1. Robotics vo (2013) A Roadmap for U.S. Robotics, from Internet to Robotics, Available on line on *https://robotics-vo.us* (accessed 8 May 2015).
2. eu Robotics AISBL (2014) Robotics 2020: strategic research agenda for robotics in Europe, euRobotics, Available on line on *www.eu-robotics.net* (accessed 8 May 2015).
3. Wechsung, R. (ed) (2005) *Market Analysis for MEMS and Microsystems 2005–2009*, A Report from the NEXUS Task Force, MST.
4. *www.set-sas.fr* (accessed 8 May 2015).

2) As an example, the Swiss watch industry represents a total market of 18 billion Euros [46].

5. *www.smaract.de* (accessed 8 May 2015).

6. *www.femtotools.com* (accessed 8 May 2015).

7. *www.imina.ch* (accessed 8 May 2015).

8. *www.percipio-robotics.com* (accessed 8 May 2015).

9. *www.palomartechnologies.com* (accessed 8 May 2015).

10. *www.finetech.de* (accessed 8 May 2015).

11. *www.essemtec.fr* (accessed 8 May 2015).

12. (2011) Report on MEMS testing workshop.

13. Pantano, M.F., Espinosa, H.D., and Pagnotta, L. (2012) Mechanical characterization of materials at small length scales. *J. Mech. Sci. Technol.*, **26** (2), 545–561.

14. Doerner, M.F., Gardner, D.S., and Nix, W.D. (1986) Plastic properties of thin films on substrates as measured by submicron indentation hardness and substrate curvature techniques. *J. Mater. Res.*, **1** (6), 845–851.

15. Skowronski, J. (1991) Fibre-to-fibre bonds in paper. Part II: measurment of the breaking energy of fibre-to-fibre bonds. *J. Pulp Paper Sci.*, **17**, 217–222.

16. Clark, J. (1978) *Pulp Technology and Treatment for Paper*, Miller Freeman Publications.

17. Joshi, K., Batchelor, W., and Rasid, K.A. (2011) Investigation of the effect of drying and refining on the fiber-fiber shear bond strength measured using tensile fracture line analysis of sheets weakened by acid gas exposure. *Cellulose*, **18**, 1407–1421.

18. Stratton, R.A. and Colson, N.L. (1990) Dependence of Fiber/Fiber Bonding on Some Papermaking Variables. Technical Report, IPST Technical Paper Series, Institute of Paper Science and Technology.

19. W. Batchelor, J. He, R.E.J. (2003) An analytical model for number of fibre-fibre contacts in paper and expressions for relative bonded area. Proceedings of the International Paper Physics Conference, pp. 77–83.

20. Fischer, W.J., Hirn, U., Bauer, W., and Schennach, R. (2012) Testing of individual fiber-fiber joints under biaxial load and simultaneous analysis of deformation. *Nord. Pulp Paper Res. J.*, **27** (2), 237–244.

21. Magnusson, M.S., Zhang, X., and Ostlund, S. (2013) Experimental evaluation of the interfibre joint strength of papermaking fibres in terms of manufacturing parameters and in two different loading directions. *Exp. Mech.*, **53** (9), 1621–1634.

22. Schmied, F.J., Teichert, C., Kappel, L., Hirn, U., Bauer, W., and Schennach, R. (2013) What holds paper together: nanometre scale exploration of bonding between paper fibres. *Sci. Rep.*, **3**, 2432.

23. Saketi, P., Treimanis, A., Fardim, P., Ronkanen, P., and Kallio, P. (2010) Microrobotic platform for manipulation and flexibility measurement of individual paper fibers. *Proceedings of the IEEE/RSJ International Conference on Intelligent Robots and Systems*, pp. 5762–5767.

24. Saketi, P. and Kallio, P. (2011) Microrobotic platform for making, manipulating and breaking individual paper fiber bonds. *Proceedings of the 5th International Symposium on Assembly and Manufacturing*, pp. 1–6.

25. von Essen, M., Hirvonen, J., Kuikka, S., and Kallio, P. (2014) Robotic software frameworks and software component models in the development of automated handling of individual natural fibers. *J. Micro-Bio Rob.*, **9** (1–2), 29–45, doi: 0.1007/s12213-014-0078-8.

26. Agnus, J., Chaillet, N., Clévy, C., Dembélé, S., Gauthier, M., Haddab, Y., Laurent, G., Lutz, P., Piat, N., Rabenorosoa, K., Rakotondrabe, M., and Tamadazte, B. (2013) Robotic microassembly and micromanipulation at FEMTO-ST. *J. Mol. Biol. Res.*, **8** (2), 91–106.

27. Das, A.N., Murthy, R., Popa, D.O., and Stephanou, H.E. (2012) A multiscale assembly and packaging system for manufacturing of complex micro-nano devices. *IEEE Trans. Autom. Sci. Eng.*, **9** (1), 160–170.

28. Saketi, P., Essen, M.V., Mikczinski, M., Heinemann, S., Fatikow, S., and Kallio, P. (2012) A flexible microrobotic platform for handling microscale specimens of

fibrous materials for microscopic studies. *J. Microsc.*, **248** (2), 163–171.

29. Chen, B.K., Zhang, Y., Perovic, D.D., and Sun, Y. (2011) MEMS microgrippers with thin gripping tips. J. Micromech. Microeng., 21 (10), 105 004.

30. Diederichs, C. and Fatikow, S. (2013) FPGA-based object detection and motion tracking in micro-and nanorobotics. *Int. J. Intell. Mechatron. Rob.*, **3** (1), 27–37.

31. Komati, B., Agnus, J., Clévy, C., and Lutz, P. (2014) Prototyping of a high performant and integrated piezoresistive force sensor for microscale applications. *J. Micromech. Microeng.*, **24**, 035018.

32. Mourier, T., Ribiere, C., Romera, G., Gottardi, M., Allouti, N., Eleouet, R., and Sillon, N. (2013) 3d integration challenges today from technological toolbox to industrial prototypes. *IEEE International Interconnect Technology Conference*, pp. 1–3.

33. Clévy, C., Lungu, I., Rabenorosoa, K., and Lutz, P. (2014) Positioning accuracy characterization of assembled microscale components for micro-optical benches. *Assembly Autom.*, **34** (1), 69–77.

34. Beyne, E., Ribot, H., Wolf, J., and von Trapp, F. (2014) 3d TSV without limits webinar. *European 3D TSV Summit*.

35. International Technology Roadmap for Semiconductor - ITRS, *www.itrs.net* (accessed 8 May 2015).

36. Liimatainen, V., Kharboutly, M., Rostoucher, D., Gauthier, M., and Zhou, Q. (2013) Capillary self-alignment assisted hybrid robotic handling for ultra-thin die stacking. *IEEE International Conference on Robotics and Automation*, pp. 1403–1408.

37. fab2asm European Project fab2asm: Efficient and Precise 3d Integration of Heterogeneous Microsystems from Fabrication to Assembly, *www.fab2asm.eu* (accessed 8 May 2015).

38. Shah, A., Chang, B., Suihkonen, S., Zhou, Q., and Lipsanen, H. (2013) Surface-tension-driven self-alignment of microchips on black-silicon-based hybrid template in ambient air. *J. Microelectromech. Syst.*, **22** (3), 739–746.

39. Chang, B., Shah, A., Routa, L., Lipsanen, H., and Zhou, Q. (2014) Low-height sharp edged patterns for capillary self-alignment assisted hybrid microassembly. *J. Micro-Bio Rob.*, **9**, 1–10.

40. Hériban, D., Agnus, J., Pétrini, V., and Gauthier, M. (2009) A mechanical de-tethering technique for silicon MEMS etched with a drie process. *J. Micromech. Microeng.*, **19**, 055011.

41. Hériban, D. and Gauthier, M. (2008) Robotic micro-assembly of microparts using a piezogripper. *IEEE/RSJ International Conference on Intelligent Robots and Systems*, pp. 4042–4047.

42. Weber, N., Zappe, H., and Seifert, A. (2012) A tunable optofluidic silicon optical bench. *J. Microelectromech. Syst.*, **21**, 1357–1364.

43. *http://www.zyvex.com/* (accessed 8 May 2015).

44. Komati, B., Rabenorosoa, K., Clévy, C., and Lutz, P. (2013) Automated guiding task of a flexible micropart using a two-sensing-fingers microgripper. *IEEE Trans. Autom. Sci. Eng.*, **A10** (3), 515–524.

45. Das, A., Murthy, R., Popa, D., and Stephanou, H. (2012) A multiscale assembly and packaging system for manufacturing of complex micro-nano devices. *IEEE Trans. Autom. Sci. Eng.*, **9** (1), 160–170.

46. (2013) Swiss Watch Industry, Prospects and Challenges, Credit Suisse.

47. Nanosensors: A Market Opportunity Analysis, A New Report from Nanomarkets, LC.

16
Robot-Aided Micromanipulation of Biological Cells with Integrated Optical Tweezers and Microfluidic Chip

Xiaolin Wang, Shuxun Chen, and Dong Sun

16.1
Introduction

Sorting of specific target cells from the heterogeneous mixtures is an important manipulation process in biological research and clinical medicine. Even though conventional cell sorting methods, such as gradient centrifugation, magnetic activated cell sorting, and fluorescence activated cell sorting, have been widely used for their advantages of mature engineering development and high throughput, these methods require large sample volumes. In many applications, cells of interest, such as stem cells or primary cells, are rare and very difficult to be obtained.

In recent years, cell sorting and manipulation using microfluidics have been widely investigated because of the many excellent features of microfluidics, such as laminar flow and low-cost fabrication [1]. Using microfluidic cell sorters, a small amount of samples can be handled, and the reagent used is reduced dramatically in such a microenvironment. In addition, the microfluidic cell sorter has provided a way for applying a large variety of force filed, which can be combined with the hydrodynamic force within the microchannel to achieve the sophisticated cell manipulation difficult to realize by conventional macroscale cell sorters. Examples include the use of electric mechanism [2], optical mechanism [3], magnetic mechanism [4], acoustic mechanism [5], and optoelectronic mechanism [6].

Optical tweezers are photonic devices that exploit a tightly focused laser beam to manipulate the dielectric particles in three dimensions in a noninvasive manner. Forces imposed on particles and the corresponding deformations are in the order of piconewtons (pN, 10^{-12} N) and nanometers (nm, 10^{-9} m), respectively [7]. Owing to these advantages, optical tweezers have become attractive and powerful tools for cell manipulation and have been used in a variety of biological applications, such as characterizing the mechanical force in manipulating live cells [8], cell separation [9], assembling and organizing cells [10], analyzing the single-cell dynamics upon environmental change [11], and probing mechanical properties of microbiological cells [12], to name a few.

The cell sorter with combined optical tweezer and microfluidic chip technologies exhibits the advantages of noninvasive cell contact and minimal contamination in the sorting process. The sorter can be designed as either a passive sorter or an active sorter, depending on whether real-time recognition with information feedback is used. The optical microfluidic sorter in a passive sorting pattern utilizes intrinsic parameters, such as cell size and/or refractive index difference, which have not yet been verified for a large variety of cells [13, 14]. The active sorting pattern utilizes intrinsic or extrinsic features of cells, and it is versatile in the microfluidic environment. Lin *et al.* [15] developed an image processing method to identify the target particles based on their size differences and displaced them from the main sample stream to the neighboring sheath flow using a focused laser beam. Wang *et al.* [16] applied a fluorescence-activated microfluidic cell sorter to move the unstressed living mammalian cells laterally by using all-optical switching. Perroud *et al.* [17] developed a microfluidic cell sorter using an infrared laser to isolate a subpopulation of macrophages highly infected with the fluorescently labeled *Francisella tularensis*. In all these approaches, the laser position is fixed, and thus the separation range of gradient or scattering force of the laser beam is limited. Subsequently, the sample flow is hydrodynamically focused into a single-cell flow to prevent the reduction of the recovery rate, which adds more complexity in the fluid control. Moreover, these approaches suffer from a relatively lower recognition capability because only one specific cell feature (e.g., fluorescence) was used. Therefore, an enhanced cell sorting strategy based on the optical tweezer and microfluidics technologies should be proposed.

In micro total analysis systems (μTAS), multiple functions, such as cell transportation, cell culture, cell separation, and cell analysis, can be realized on a single microfluidic chip [18]. Similarly, the cell sorter should not be a stand-alone thing, and could be an integrated component in a more complicated microfluidic system [19]. One limitation of the microfluidic flow cytometry is the snapshot of the instant cellular information during inspection, which makes it unsuitable for measuring dynamic cellular responses over time. In addition, the restriction of most microfluidic flow cytometry is the random distribution of the isolated cells in the collection reservoir, which makes it difficult to do further manipulation on these cells with high accuracy. Thus, these cells have to be removed from the collection reservoir by pipette or through an output fluidics interface, which may induce cell damage or cell losses.

In order to circumvent these problems, array-based platforms, such as the microwell array or obstacle array, incorporated with programmable time-resolved live-cell imaging, can be used to monitor the cellular information of the hydrodynamically confined cells with high spatiotemporal resolution [20, 21]. Combined with the array-based platforms, precise and dynamic manipulation of individual cells is a prerequisite for developing such an advanced manipulation tool. The laser capture microdissection (LCM) [22] and micromanipulators, such as the glass capillary micropipette [23], are commonly used for single-cell manipulation. This kind of mechanical contact operation suffers from some drawbacks, such as easily causing damage to cells and unable to manipulate the cells in sealed

environment. As a result, nonphysical contact techniques for cell manipulation are highly desired. For optical positioning methods, Kovac *et al.* [24] utilized the scattering force from an infrared laser to levitate the cell of interest along the light propagation from the microfluidic microwell array into the flow field for collection. In this work, only one laser beam with the spatial resolution roughly equal to the cell diameter (∼9 μm) was used to manipulate the cell of interest manually. Furthermore, the levitated cells were collected by the fluid flow, which could not achieve the precise cell deposition. Luo *et al.* [25] set up a microfluidic device with combined optical tweezers for cell manipulation and localization between microwells; however, it lacked the abilities of cell recognition and isolation. Therefore, it is highly necessary to develop an advanced manipulation tool with the ability to isolate interesting cells from rare cell populations and deposit these isolated cells to the predefined location accurately.

In the following, after a brief introduction of the cell micromanipulation system combined with optical tweezer and microfluidics technologies, details of the enhanced cell sorting strategy and novel cell manipulation tool will be given, respectively.

16.2
Cell Micromanipulation System with Optical Tweezers and Microfluidic Chip

The cell micromanipulation system mainly consisted of four modules: optical tweezers module, motorized stage module, computer vision module, and microfluidic chip module, as illustrated in Figure 16.1a [26]. A continuous-wave (CW) laser beam (V-106C-3000 OEM J-series, Spectra Physics), with a wavelength of 1064 nm, is sculpted using the holographic optical trapping (HOT) device, creating multiple optical traps simultaneously. The laser beam, after being
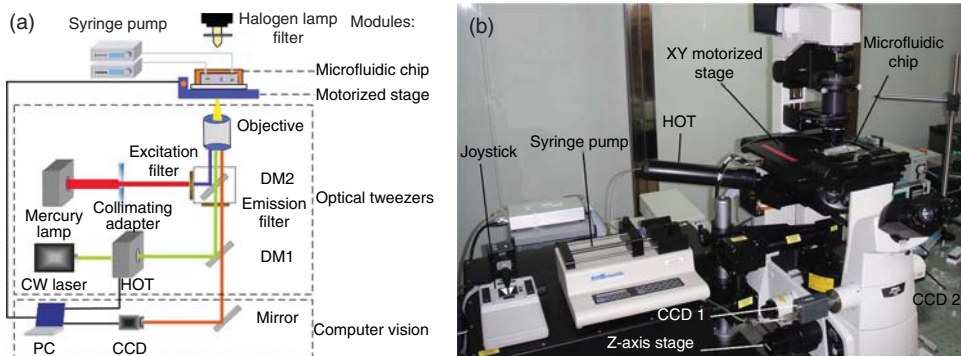
Figure 16.1 The setup of cell micromanipulation system with combined holographic optical tweezers and microfluidic chip. (a) Schematic illustration. (Reproduced by permission of IOP Publishing.) (b) Experimental setup.

reflected by the dichroic mirror (DM1), enters into the microscopic objective (Nikon 60X, numerical aperture = 1.2, water) to generate a three-dimensional (3D) optical trap. A microfluidic chip with biological samples, which is linked to the syringe pump (KDS 200P, KD Scientific) by tubing, is placed on the 2D X–Y motorized stage (ProScan, Prior Scientific) with a positioning accuracy of 15 nm. When the halogen lamp is on, a bright field of the microfluidic channel can be seen by the CCD camera. The fluorescence images also can be captured by turning on the mercury lamp. The excitation beam from the mercury lamp is filtered by the excitation filter (450–490 nm), reflected by the DM2 (500 nm), and then focused on the microfluidic channel by the objective. The fluorescence signals are collected through the objective with the emission filter (515 nm). The CCD camera with high sensitivity is used to capture the fluorescence image. The positions of the target cells can be determined by digital image processing, and they serve as feedback to guide the sorting process. All the mechanical components are supported by an antivibration table. Figure 16.1b shows the experimental setup in our laboratory.

A homemade control software consisting of the laser control, optical trap control, CCD camera control, image processing, and motorized stage control modules is developed. The system can be operated in full-automatic mode, such that all these modules will be coordinated by the software to achieve both the open- and closed-loop controls for accurate cell micromanipulation. Meanwhile, the software enables specific functions through the specifically defined user interface.

16.3
Enhanced Cell Sorting Strategy

16.3.1
Operation Principle

The schematic of the enhanced cell sorting strategy with the developed cell micro-manipulation system is shown in Figure 16.2 [26]. The sample flow and buffer flow are driven into the microfluidic chip from the upper and lower inlets separately with a syringe pump. A CCD camera is used to capture images of cells as they pass through the region of interest (ROI) located at the upper section of the branching junction channel. The digital image processing technique is utilized to detect and recognize the target cells. Furthermore, if multiple target cells appear in the ROI simultaneously, the multiparticle tracking algorithm is utilized to distinguish and track them. After identification and tracking, control signals are generated to position the dynamic optical traps on the target cells, which can be moved away from the upper sample flow to the lower buffer flow. After these target cells arrive at the desired destination, the optical traps release the cells, which will flow into the outlet for collection with the buffer flow. The other nontarget particles will flow into the outlet as waste with the sample flow. On the basis of this dynamic fluid and
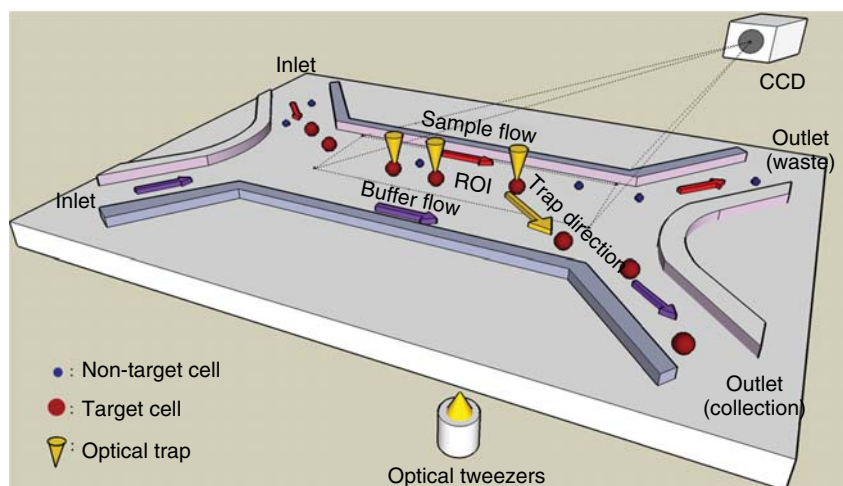
Figure 16.2 Schematic of the enhanced cell sorting strategy. (Reproduced by permission of The Royal Society of Chemistry.)

dynamic light pattern, fewer particle-to-particle interactions, such as clustering or incomplete separation, may be induced, which can achieve high efficiency in the sorting process.

16.3.2
Microfluidic Chip Design

Figure 16.3a illustrates the overall structure and dimension of the designed microfluidic chip [26]. The microfluidic cell sorter consists of four branches with two inlet channels and two outlet channels. Sample flow and buffer flow come from inlet reservoirs A and B, respectively. The waste and target particles are collected in outlet reservoirs C and D, respectively. The two inlet channels and two outlet channels are all 25-μm wide and 1000-μm long, and the branching junction channel is 50-μm wide and 70-μm long. The diameters of the four reservoirs are 1 mm. The height of the microchannel is 50 μm. Figure 16.3b shows the photograph of the designed prototype with PDMS and cover slip using soft lithography technology [27].

In order to understand better the microenvironment inside the microfluidic chip, the flow behavior of fluid within the microchannel is simulated by the Comsol Multiphysics finite element program using the MEMS module with the "incompressible Navier–Stokes" and "convection and diffusion" application modes [28]. Figure 16.3c shows the simulation result. The slice plot represents the concentration distribution of the flow. The sample flow from the upper inlet channel does not diffuse into the buffer flow from the lower inlet channel. The arrow plot represents the velocity profile of the laminar flow within the microchannel.
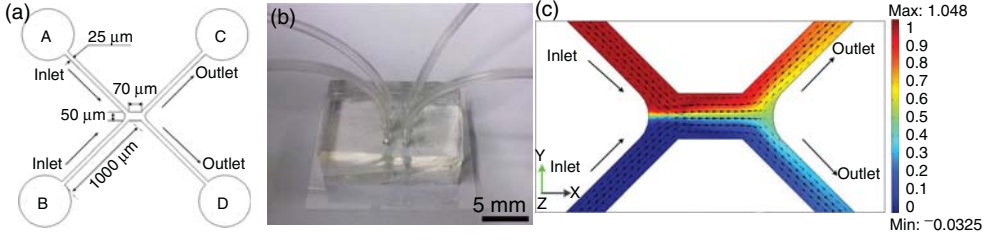
Figure 16.3 Microfluidic chip design. (a) Structure and dimension of the microfluidic chip. The arrows represent the flow direction within the microchannel. (b) Photograph of the microfluidic chip prototype. (c) Simulation result of flow behavior in the designed microfluidic chip. (Reproduced by permission of The Royal Society of Chemistry.)

16.3.3
Cell Transportation by Optical Tweezers

An adaptive image processing method is developed to recognize the target cells with different cell features, either intrinsic like the different size of cells or extrinsic like the fluorescence label, such as green fluorescence protein (GFP). After identification of the target cells, optical tweezers are used to transport the distinguished cells to the desired destination. The motion control of the optical trap in the cell transportation process is optimized by analyzing the cell motion dynamics.

When the target cell is trapped and moved in the fluid flow by the optical trap, both the fluid drag force (F_d) and the optical trapping force (F_t) act on the cell simultaneously [29]. The dynamics of the cell movement is

$$m\frac{d^2r}{dt^2} = F_t(r) + F_d(r), \tag{16.1}$$

where m denotes the mass of the cell, $r = [r_x, r_y]^T$ is the central position of the cell, and t is the time interval determined by the frame rate of the camera. Given the flow velocity V_s, according to Stokes' law, the F_d of the moving particles in the fluid flow can be expressed as

$$F_d(r) = 6\pi\eta R\left(V_s - \frac{dr}{dt}\right), \tag{16.2}$$

where η is the fluid viscosity coefficient and R is the radius of the cell. When the cell reaches the maximum velocity, its acceleration is zero, implying that the fluid drag force and the optical trapping force are in equilibrium. Therefore, Eq. (16.1) can be simplified as follows:

$$\frac{dr}{dt} - V_s = \frac{F_t(r)}{6\pi\eta R}. \tag{16.3}$$

Assuming horizontal direction to be the same as the flow direction, the velocity of the optical trap in the horizontal direction is designed to be the same as the flow speed. As a result, no trapping force is required on the target cell in the flow direction, which means the energy of the optical trap is not dissipated. Given the

laminar nature of microfluidic flows, the fluid velocity perpendicular to the flow direction is zero. As a result, Eq. (16.3) is simplified as

$$\frac{dr_y}{dt} = \frac{F_t(r_y)}{6\pi\eta R}. \tag{16.4}$$

The optical trap should move the target cell as fast as possible perpendicular to the flow direction. Increasing cell movement speed can improve operation efficiency. To trap the cell effectively with low laser power, the relationship between the cell maximum moving velocity and the laser power is calibrated. The trapping force of the optical tweezers can be determined using the viscous drag force technique [30]. The maximum moving velocity is determined by gradually increasing the moving velocity of the cell until the cell escapes from the optical trap. Figure 16.4 [26, 31] illustrates the maximum moving velocity and the trapping force under different laser powers obtained from our tests on yeast cells and human embryonic stem cells (hESCs), respectively. From the figure, the trapping force of the optical trap is approximately proportional to the laser power. Notably, that laser power is the laser emission power, and the actual laser power at the beam focus is much less than the emission power.

In applications where a quick movement of the optical trap is required, moving the cell with a step of the cell radius is beneficial [32]. Equation (16.4) can then be modified as

$$\frac{R}{dt} = \frac{F_t(r_y)}{6\pi\eta R}. \tag{16.5}$$

Figure 16.5 [26] shows the motion trajectory of the optically trapped particle in the flowing fluid based on the designed motion control of the optical trap. Before the optical trapping, the target particle is transported by the fluid flow horizontally along the branching junction channel. When isolating cells, the optical trap is generated on the target particle at position P_1. With the resultant velocity combining the dragging velocity of the fluid and the trapping velocity of the optical trap,
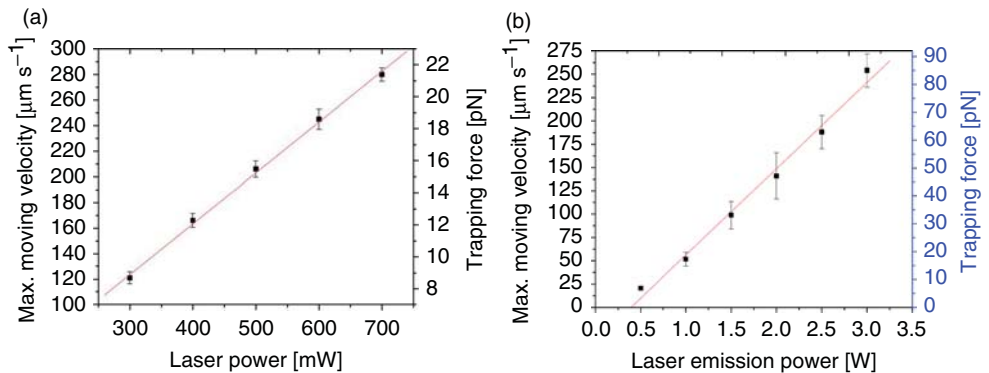
Figure 16.4 The calibration result of the maximum moving velocity and the trapping force under different laser powers. (a) Yeast cells. (Reproduced by permission of The Royal Society of Chemistry.) (b) hESCs. (Reproduced by permission of IOP Publishing.)
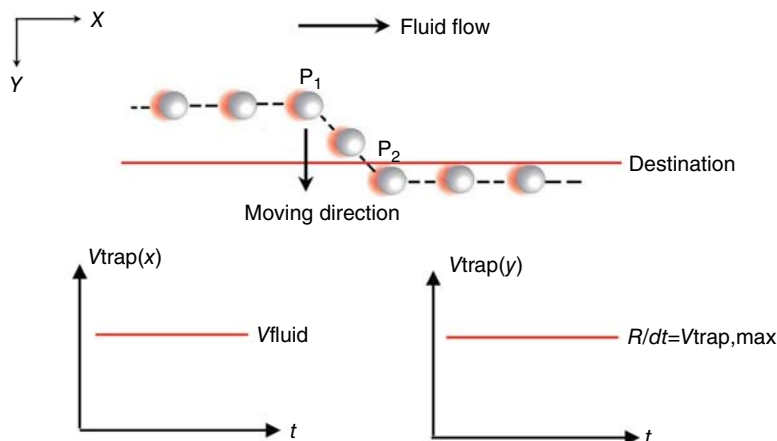
Figure 16.5 Motion trajectory of the optically trapped particle in the flowing fluid based on the designed motion control of the optical trap. (Reproduced by permission of The Royal Society of Chemistry.)

the target cell is moved to the destination quickly. After reaching the destination position P_2, the optical trap is destroyed, and the cell is released from the laser trap and then moves with the fluid flow to the target outlet for collection.

16.3.4
Experimental Results and Discussion

16.3.4.1 Isolation of Yeast Cells

First, yeast cells are isolated from the microbead mixture to evaluate the sorting performance of the proposed enhanced cell sorter. Both sample flow and buffer flow (deionized water) enter the microfluidic channel from two separate inlets. *Yeast cells* are defined as the target particles and collected in the collection reservoir. When the microbeads move with the sample flow and pass through the ROI, they are recognized as nontargeted particles and flow into the waste channel with the sample flow, as shown in Figure 16.6a,b. When the yeast cells pass through the ROI, they are detected as target cells and are moved away from the sample flow by the optical tweezers. Finally, the yeast cells flow into the collection channel via the buffer flow, as shown in Figure 16.6c–f [26].

In the experiment, the output laser power is set to 350 mW, and the yeast cells move at a velocity of 120 μm s^{-1} in a direction perpendicular to the flow. Considering the fluid flow (67 μm s^{-1}), the yeast cell can be quickly moved away from the sample flow to the buffer flow at a speed of 137 μm s^{-1}.

The throughput can be increased without the penalty of purity and recovery rate by employing the multitrap parallel sorting strategy based on the multiparticle tracking algorithm and the motion control of the optical trap. The enhanced cell sorter prototype can use up to five optical traps for sorting yeast cells and two
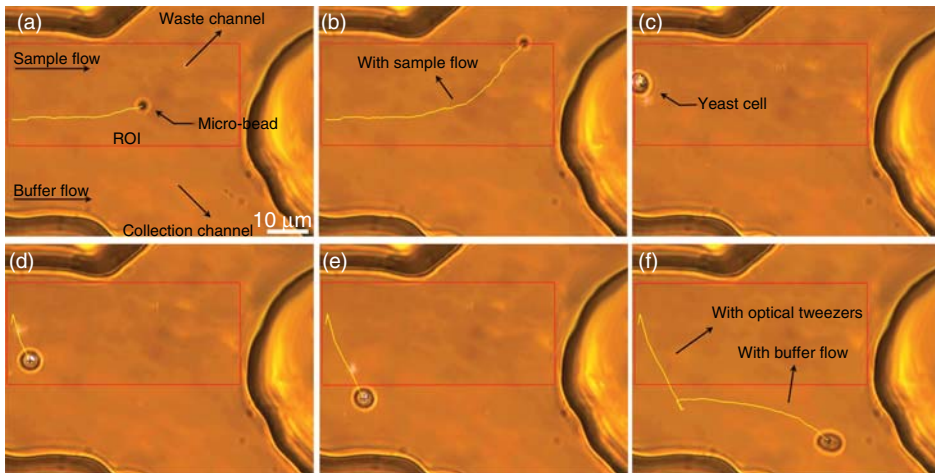
Figure 16.6 Isolation of yeast cells from microbeads. (a,b) Trajectory of the microbead without optical trap on it. The microbead finally flows into the waste channel with the sample flow. (c–f) Trajectory of the yeast cell with a moving optical trap on it. The yeast cell is separated from the sample flow using optical tweezers and finally flows into the collection channel with the buffer flow (the light spot on the yeast cell is the optical trap). (Reproduced by permission of The Royal Society of Chemistry.)

optical traps for sorting GFP-tagged hESC. The maximum number of optical traps simultaneously available for use is determined based on the type of sorted cells, cell concentration, and limitation of the laser power. The actual number of optical traps used depends on the number of target cells appearing in the ROI. Figure 16.7 [26] shows the experimental process of sorting multiple yeast cells by utilizing the multitrap parallel sorting strategy. In this test, three optical traps are generated simultaneously to drive three yeast cells when they are recognized in the ROI. After these yeast cells arrive at the desired destinations, the corresponding optical
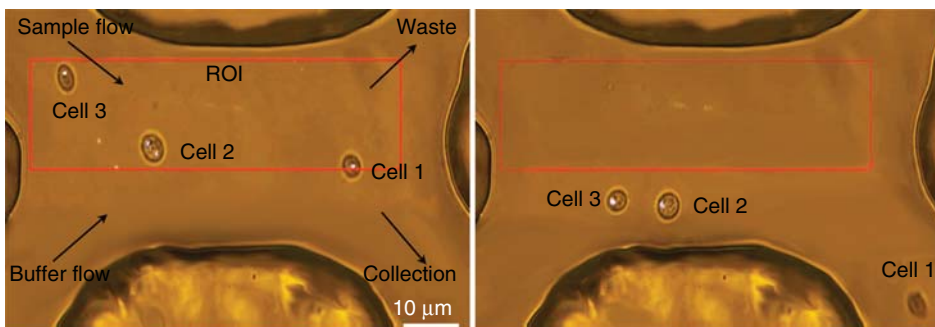
Figure 16.7 Multitrap parallel sorting strategy on yeast cells (the light spot on the yeast cell is the optical trap). (Reproduced by permission of The Royal Society of Chemistry.)

Table 16.1 Sorting results.

Sample	Strategy	Concentration (particles/ml)	Total sorted particles	Recovery rate (%)	Purity (%)
Yeast cells plus microbeads	Single-trap serial sorting	1.2×10^7	438	97	98
	Multitrap parallel sorting	5×10^7	1062	94	96
GFP-tagged hESC plus nontagged cells	Multitrap parallel sorting	1×10^7	210	90	90

Reproduced by permission of The Royal Society of Chemistry.

trap is destroyed. Finally, the yeast cells flow with the buffer flow into the collection channel.

Table 16.1 [26] shows the experimental results of the recovery rate and purity when sorting yeast cells using single-trap serial sorting and multitrap parallel sorting strategies. With the single-trap serial sorting strategy, 438 particles, including 205 yeast cells, passed through the sorter at a throughput of 1 particle per second. With the single optical trap, 199 out of 205 yeast cells were isolated successfully with a recovery rate of 97%. In the collection reservoir, we received 199 yeast cells and 4 microbeads after sorting, indicating a purity of 98% for yeast cells. With the multitrap parallel sorting strategy, 1062 particles were sorted at a throughput of 5 particles per second, with 94% recovery rate and 96% purity. Even though the multitrap parallel sorting strategy exhibited relatively poorer performance in terms of recovery rate and purity than the single-trap serial sorting strategy, it met the requirements for a relatively higher throughput.

16.3.4.2 Isolation of hESCs

We further isolated hESCs from a mixture of different cells. As shown in Figure 16.8a [26], the size of hESCs is quite similar to that of others in the mixture. Therefore, the size-dependent image processing method could not be used for this sorting application. Figure 16.8b illustrates that the target hESC is labeled with GFP, whereas the other nontarget cells are without any fluorescence label. The fluorescence-dependent image processing method was utilized in the experiment to recognize the target cells. hESCs have a much larger size (i.e., $10-15\,\mu m$) than yeast cells, higher laser power (1.5 W) was utilized to supply sufficient trapping force to move hESCs. The manipulation process was the same as that in the isolation of yeast cells. As shown in Figure 16.8c,d, hESCs with GFP were driven to the collection channel by the optical trap and then flowed into the collection channel with the medium flow. The other nontarget cells without GFP flowed into the waste channel with the sample flow. Two optical traps can be generated simultaneously during the parallel sorting process. After sorting, 26 hESCs with GFP and 3 other cells without GFP were observed in the collection
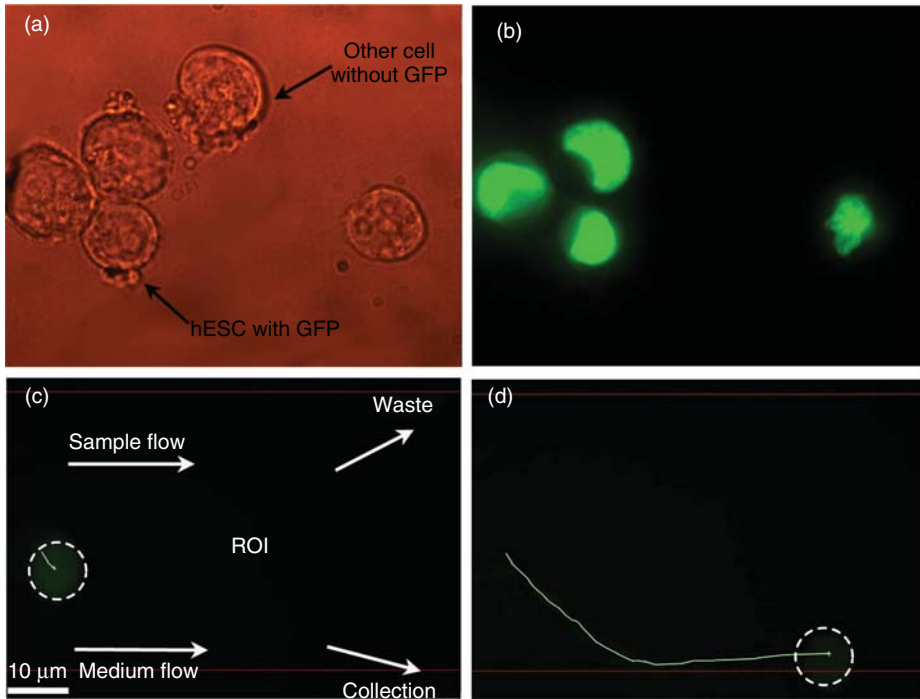
Figure 16.8 Isolation of hESC. (a) Bright-field image of hESCs and other cells. (b) Fluorescence image of hESCs with GFP over a long exposure time (700 ms). (c) Recognition of hESC with GFP based on the fluorescence image processing method. (d) Trajectory of hESC driven by optical trap toward the collection channel. Other cells flow into the waste channel. (Reproduced by permission of The Royal Society of Chemistry.)

reservoir, and 178 cells without GFP and 3 hESCs with GFP were observed in the waste reservoir. As shown in Table 16.1, 90% recovery rate and 90% purity were achieved.

16.3.4.3 Discussion

Compared with the existing cell sorter, our enhanced cell sorting strategy based on the established cell micromanipulation system with integrated optical tweezers and microfluidic chip has three unique characteristics. First, it exhibits high purity and high recovery rate in handling small sample population sorting and is ideally suited for rare cell isolation and enrichment. Second, the cell sorter is designed based on the analysis of the dynamic fluid and dynamic light pattern, which offers greater degrees of freedom to improve cell sorting performance. Multiple optical traps can be generated simultaneously to achieve multiparticle parallel sorting in the same ROI. Third, the sorter has a unique capability for recognizing multiple cell features and distinguishing multiple target cells in the same ROI based on image processing techniques.

16.4
Novel Cell Manipulation Tool

16.4.1
Operation Principle

Figure 16.9 illustrates the schematic of a series of cell micromanipulation processes with this novel cell manipulation tool [31]. The operation procedures include passive hydrodynamic docking of cells within the microwell array, image processing for the target cell detection in the microwell, active trapping and assembling of target cells using optical traps, and automatic cell transportation and deposition to the specific target locations with the motorized stage. First, the prepared suspended single cells were injected into the channel through the sample inlet and settled into the microwell arrays for cell docking, as shown in Figure 16.9a. After loading, the cells outside the microwells were cleared away by flowing the culture medium gently (Figure 16.9b). After cell docking, image processing was performed for target cell detection, and optical traps were positioned on these recognized cells for cell trapping, as shown in Figure 16.9c. Then, these optically trapped cells were levitated from the cell docking microwell by moving up the objective Z stage and assembled into specific structure according to different further applications by dynamically moving multiple optical traps, as shown in Figure 16.9d. Figure 16.9e shows that the assembled cells were transported above the microwell array layer to the predefined target microwell by the programmed microscope X−Y stage. Finally, the levitated cells with specific structure were deposited into the target microwell by moving down the objective Z stage and releasing the optical traps, as shown in Figure 16.9f.
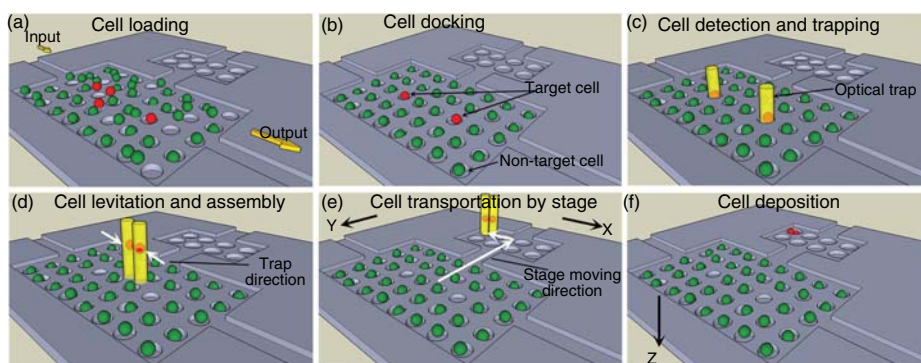
Figure 16.9 Schematic of a series of cell manipulation processes from cell loading to cell deposition. (Reproduced by permission of IOP Publishing.)

16.4.2
Microwell Array-Based Microfluidic Chip Design

The microfluidic chip consisted of two parts: the bottom microwell array layer and the top PDMS fluidic channel, as shown in Figure 16.10a [31]. The microwell arrays were fabricated on the cover glass (0.13–0.16 μm thick) using negative photoresist SU-8 (35-μm thick, 4000 rpm, SU-3050, MicroChem). Each microwell array had 80 microwells, which were arranged in a 8×10 array. The separation distance between two microwell arrays was 700 μm. The microwell was designed to have a diameter of 100 μm at intervals of 100 μm or 30 μm at intervals of 40 μm. The master of the PDMS fluidic channel was fabricated on the silicon wafer using the same SU-8 (100-μm thick, 1500 rpm). The separate microwell arrays for cell docking and cell deposition were connected by a narrow passage on the PDMS fluidic
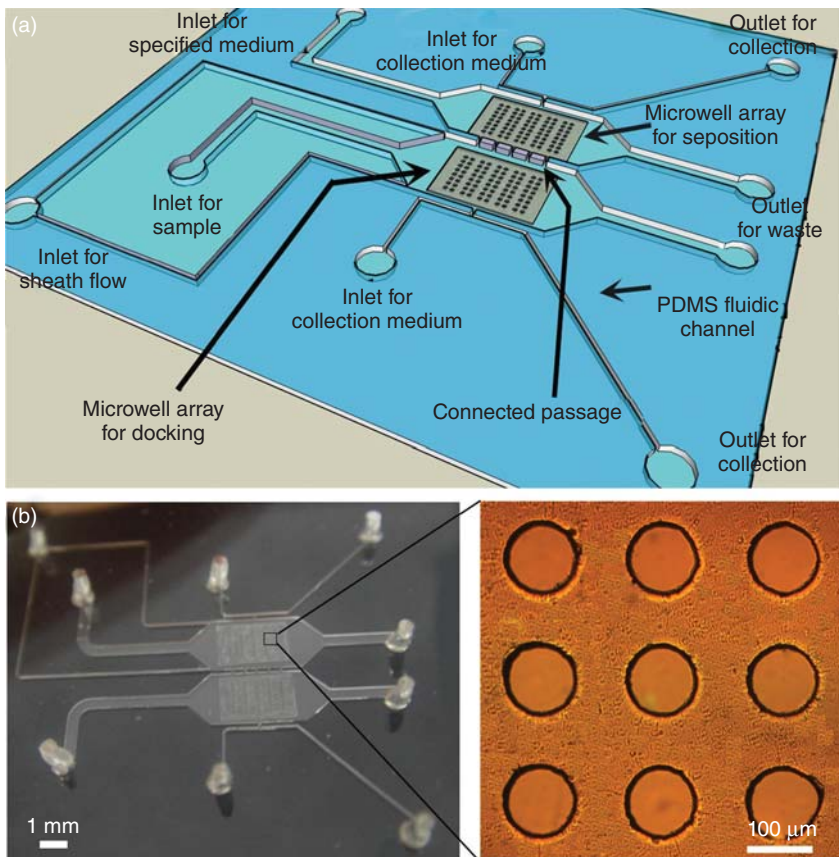
Figure 16.10 Microfluidic chip design. (a) The schematic design of the microwell array-based microfluidic chip. (b) The prototype of the designed microfluidic chip with microwell array. (Reproduced by permission of IOP Publishing.)

channel. There existed five connected passages, and the length of each connected passage was designed to be 200 μm. The widths of two inlet channels for the sample flow and the specified medium were designed to be 500 μm, and the widths of the other channels and the connected passage were all designed to be 100 μm. PDMS molding was carried out to obtain the reverse structure of the master. After punching holes at the inlets and outlets, the surface of PDMS with fluidic channel and the cleaned cover glass with the microwell array were activated in an oxygen plasma, and then aligned accurately and bonded together immediately to form an irreversible seal. The prototype of the microfluidic chip is shown in Figure 16.10b.

To visualize the flow characteristics and cell's trace in the microwell with different dimensions, we utilized the MEMS module with the "incompressible Navier–Stokes" application mode in the Comsol Multiphysics finite element program (COMSOL 3.5, Comsol AB, Burlington) [33]. Figure 16.11 illustrates the simulation results on the two microwells with diameters of 30 and 100 μm at the height of 35 μm, respectively. Figure 16.11a shows the velocity contours, and Figure 16.11b shows the streamlines with the cell's trace at the inlet velocity of $2 \times 10^{-4}\,m\,s^{-1}$ [31]. As expected, for a given microwell depth, the increase in the microwell diameter led to a decrease of the recirculation area. The cells moved along the flow direction but were still confined within the 100-μm microwell at the low flow velocity. In the 30-μm microwell, the cells could not be removed even at high velocity, and moved back and forth at the opposite direction of the flow in the microwell.

16.4.3
Chip Preparation and Fluid Operation

Before the experiments, the channels of the microfluidic chip were filled with 70% ethanol for sterilization. Then, we flushed the channels with phosphate-buffered
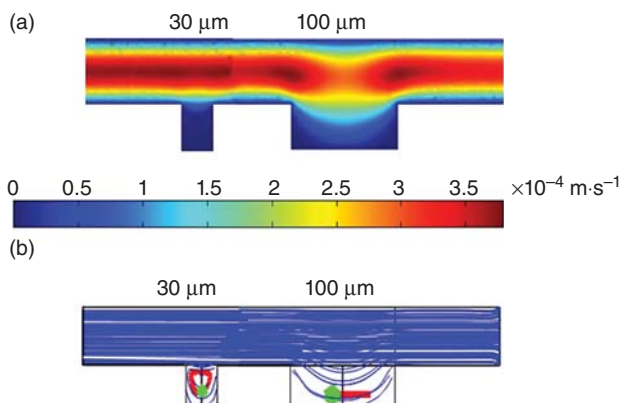
Figure 16.11 Simulation results of fluid flow in microwells with different diameters of 30 and 100 μm at the same height of 35 μm. (a) Velocity contours. (b) Streamlines of flow and the cell's trace. (Reproduced by permission of IOP Publishing.)

saline (PBS), followed by filling with PBS containing $10\,\text{mg}\,\text{ml}^{-1}$ bovine serum albumin (BSA). The chip was dried at room temperature and kept at $4\,°\text{C}$ for 2 days until the plasma effect was gone, which could prevent cell adhesion to the channels. For the experiment, the channels were washed two times with the cell culture medium, and the air bubbles were removed from the microwells by placing the chip in a vacuum chamber. Then, the microfluidic chip was orientated and fixed on the motorized stage to make sure the upper side of the microwell array was orthogonal to the left side of the image, which could facilitate the accurate position of each microwell and precise control of the motorized stage.

The suspended cells were pumped into the microfluidic chip through the sample inlet with the syringe pump (KDS 200P, KD Scientific) at the flow rate of $1\,\mu\text{l}\,\text{min}^{-1}$. The culture medium flowed through the sheath flow inlet at the flow rate of $0.3\,\mu\text{l}\,\text{min}^{-1}$, which could focus the cells at the region of microwell array for cell docking. Meanwhile, the fresh media flowed through the microwell array for cell deposition through the specified medium inlet at the flow rate of $1\,\mu\text{l}\,\text{min}^{-1}$. After the cells spread all over the cell docking microwell array, we stopped the flow from all the inlets for about 5 min, which could allow the cells to deposit into the cell docking microwells. Then, we pumped the fresh cell media from all inlets at the flow rate of $0.4\,\mu\text{l}\,\text{min}^{-1}$, which could remove the cells outside the cell docking microwells while still confining the deposited cells in the microwell. After cell docking, we stopped all the flows from the inlets in order to perform the entire experiment in the flow-free environment.

16.4.4
Experimental Results and Discussion

16.4.4.1 Cell Levitation from Microwell
Even though the holographic optical tweezers can perform 3D cell manipulation, the levitated cell will be out of image focus with only the optical trap along the Z direction. As an alternative way, we here combined with the objective Z stage to levitate the optically trapped cells while keeping them at the focus plane of the image for constant inspection. The operation process had two steps. First, the optical traps were positioned on the interesting cells, and the gradient force quickly dragged the cells toward the focus of the optical traps. Second, the objective Z stage moved up, which resulted in the levitation of the optically trapped cells out of the microwell. In the experiment, the levitation distance was set at $50\,\mu\text{m}$, which was slightly larger than the height of the microwell ($35\,\mu\text{m}$). The schematic of the levitation process of the optically trapped cell from the microwell by moving up the objective Z stage is shown in Figure 16.12a. As shown in Figure 16.12b, two hESCs were levitated from the microwell utilizing two optical traps simultaneously [31]. On the average, the time needed to levitate the cell out of the microwell was about 3 s, as determined by the levitation distance and the moving speed of the objective Z stage.
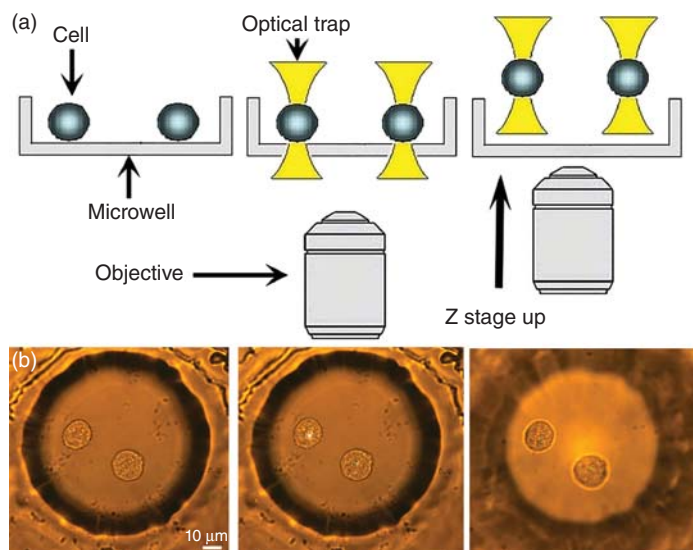
Figure 16.12 Cell levitation from the microwell. (a) Schematic of the cell levitation process from the microwell. (b) Levitation of two hESC cells from the microwell with two optical traps simultaneously. The levitated cells were always in the focus of the image plane for inspection, whereas the microwell became blurred after levitation. (Reproduced by permission of IOP Publishing.)

16.4.4.2 Cell Assembly by Multiple Optical Traps

Upon successful cell levitation from the microwell, multiple optical traps can be controlled dynamically to move these optically trapped cells into a certain structure prepared for further analysis or manipulation. During the assembly process, the moving velocity of the trapped cells should not exceed the cell maximum moving velocity. The calibration results of the maximum moving velocity and the trapping force under different laser powers is as shown in Figure 16.4.

As shown in Figure 16.13 [31], two levitated hESCs were assembled toward the assembly point at a moving velocity of $30\,\mu m\,s^{-1}$, and stuck each other tightly in pairs, which could make preparation for further study like cell fusion or cell-to-cell interaction. Under the restriction of maximal 3 W laser emission power from the laser source, we can generate total four optical traps simultaneously in order to perform multitrap parallel manipulation, and the laser emission power of each optical trap is 0.75 W. It was known through calibration study that the moving velocity of $30\,\mu m\,s$ could be reached in the experiment at the 0.75 W laser emission power of each optical trap. Note that all the given laser emission power here is the laser output power from the laser source.

16.4.4.3 Automated Cell Transportation and Deposition

After successful cell assembly, the next procedure is to precisely transfer these assembled cells to the specified microenvironment. The optical tweezers normally need high numeral aperture, so the moving distance purely based on the optical
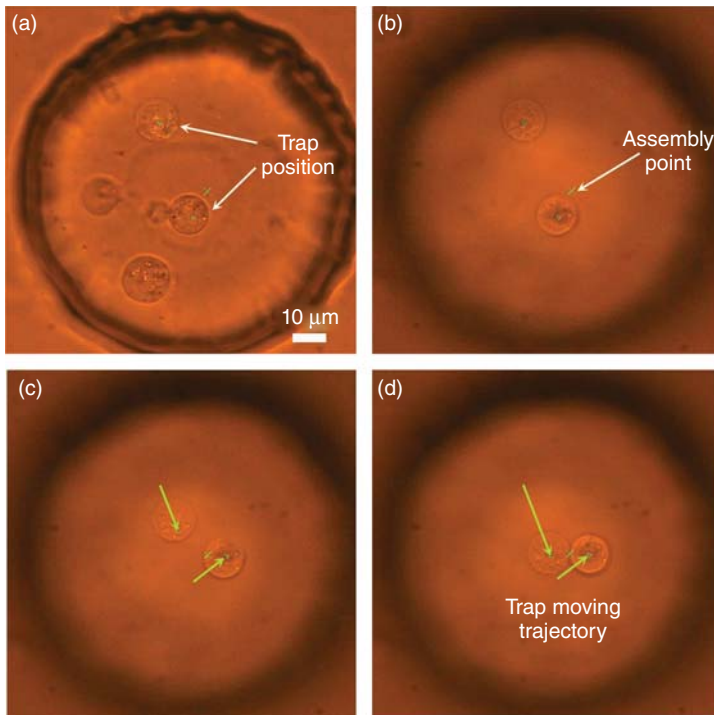
Figure 16.13 Assembly process of two hESCs into pairs after successful levitation. (a) Two hESCs trapped in the microwell. (b) Cells levitation from the microwell. (c) Assembly process. (d) Cells stuck each other tightly in pairs after assembly. (Reproduced by permission of IOP Publishing.)

trap is limited by the field of view. In order to solve this problem, we used the microscope X–Y stage for moving these optically trapped cells in the flow-free environment while keeping them in the field of view. After recording the position of the first microwell, the coordinates of the other microwells and the transfer pathway could be calculated automatically based on the known chip geometry. Taking advantage of the cell levitation from the microwell, we could transport the assembled cells to the desired location without the need for specific path planning to avoid collisions with the other cells. However, inclination might happen when the microfluidic chip was mounted on the motorized stage, which might cause the collision between the trapped cells and the microwell array. Therefore, calibrating the bottom plane of the microwell array is necessary, which can be determined by using three microwells that are not in the straight line [34].

The schematic of the transfer pathway is shown in Figure 16.14a [31]. Figure 16.14b–d show a sequence of the photographs taken from the microscope, where the cells were levitated and moved out of the microwell in the cell docking area, transported along the transfer pathway, and moved to the target microwell in the deposition area. During the whole transportation, the paired cells were
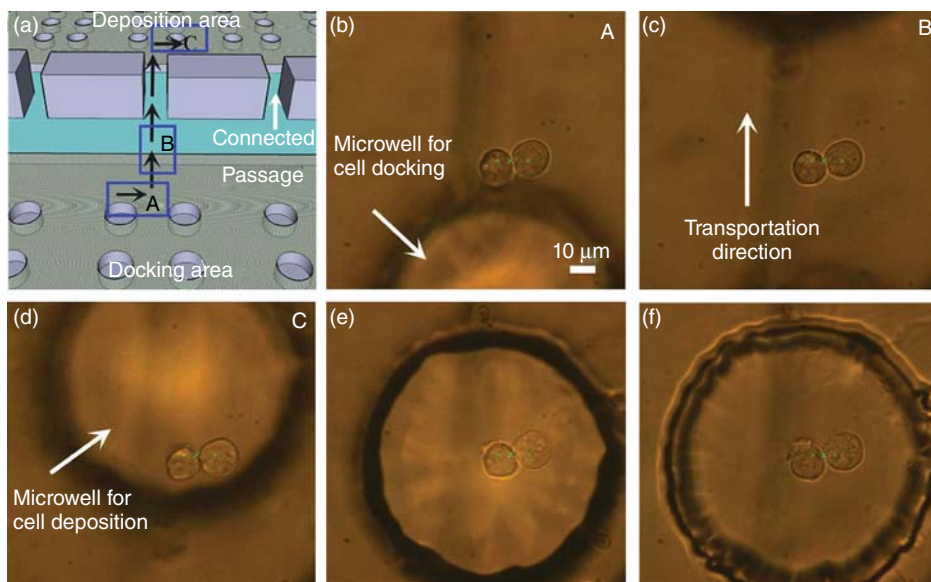
Figure 16.14 Automated cell transportation and deposition after successful assembly. (a) Schematic of the cell transportation from the microwell in cell docking area to the microwell in cell deposition area along the computed transfer pathway. Black-lettered rectangles correspond to the photographs taken from the microscope presented in (b–d). (b) Cell levitation out from the microwell in the docking area. (c) Cell transportation. (d) Reaching the target microwell in the deposition area. (e) Deposition process. (f) Successful deposition of assembled cells in the target microwell. (Reproduced by permission of IOP Publishing.)

always kept in close contact manner. Moreover, the objective Z stage was always adjusting to maintain the relative distance between the bottom plane of the microwell array and the optical trap plane to be the constant (50 μm). After reaching the top of the target microwell, the objective Z stage moved down and the deposition distance was also set at 50 μm. Figure 16.14e shows the deposition process, and Figure 16.14f shows that the assembled cells were deposited in the target microwell successfully with the paired pattern.

16.4.4.4 Isolation and Deposition on hESCs and Yeast Cells

We first performed the test on hESCs isolation and deposition from a mixture of different cells based on the fluorescence label. After loading the hESC lines transfected with LV-Oct4 promoter-driven GFP, both the hESCs with GFP and/or the other cells without GFP could be confined in the microwell, as shown in Figure 16.15a [31]. Both the bright-field and fluorescence images could be inspected with high spatial and temporal resolution over time. Fluorescence-based image processing method was utilized to distinguish the GFP-tagged hESCs from the other nontagged cells in the marked microwell, as shown in Figure 16.15b. Then, two optical traps were generated on the two detected
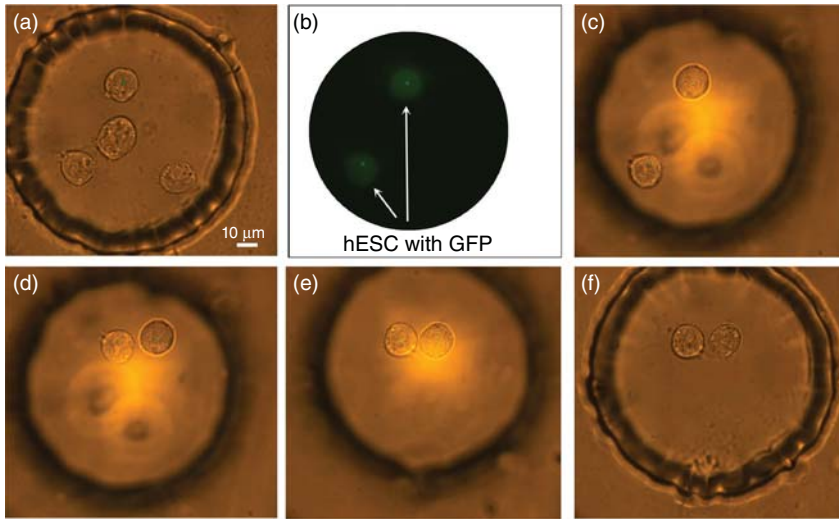
Figure 16.15 Fluorescence-based cell isolation and deposition on hESC. (a) Bright-field image of four cells confined in the microwell. (b) The corresponding fluorescence image of two target hESCs with GFP in the marked microwell (exposure time: 500 ms). (c) Levitation of hESCs from the microwell while leaving the other cells in the microwell. (d) Assembly of the optically trapped two hESCs into pairs. (e) Reaching the destination at the top of the desired microwell for deposition. (f) Cell deposition. (Reproduced by permission of IOP Publishing.)

hESCs to levitate them from the microwell, and the other cells without GFP were still confined in the microwell, as shown in Figure 16.15c. In Figure 16.15d, the levitated hESCs were assembled into pairs. Then, the program-controlled motorized stage transferred the paired cells to the desired location for deposition, as shown in Figure 16.15e. Figure 16.15f shows that the hESCs were deposited in the desired microwell with the paired pattern.

The image processing algorithm can be adjusted for detection and recognition of different target cells with different features. The developed image-based cell manipulation tool can isolate the cells based on the extrinsic features such as the fluorescence proteins as well as intrinsic features such as the morphology difference. It does not restrict to any specific cell types. Figure 16.16 shows the experimental results of isolation and deposition of yeast cells from the microbeads based on the feature of size [31]. The manipulation process is the same as that of GFP-tagged hESCs as described early.

16.4.4.5 Quantification of the Experimental Results

The statistical results of isolation and deposition on hESCs and yeast cells with the developed tool are given in Table 16.2 [31], where the successful levitation rate refers to the percentage of successfully levitated cells to the total number of target cells that we attempt to levitate, *successful transfer rate* is defined as the ratio of the nonescaped cells from the optical traps during the transfer process to
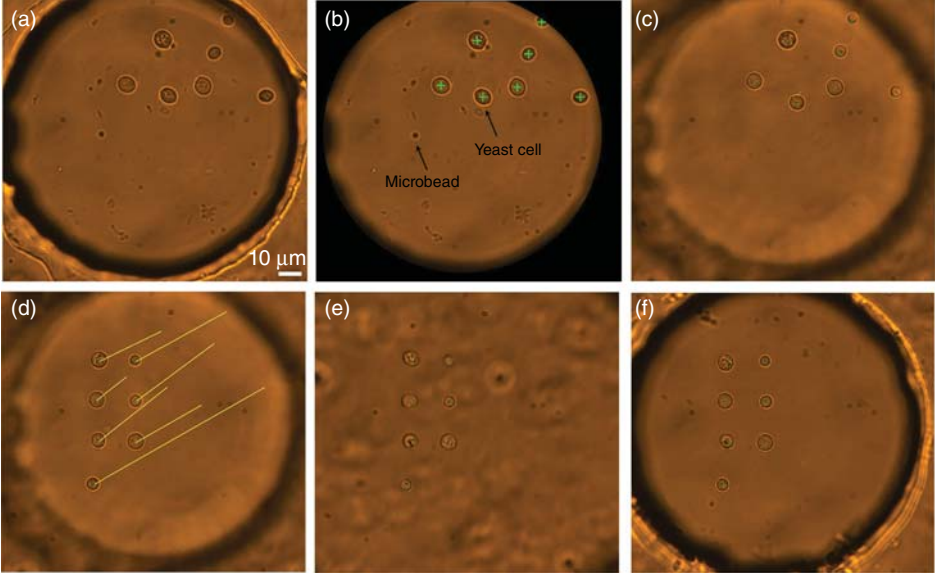
Figure 16.16 Size-based cell isolation and deposition of yeast cells from microbeads. (a) Bright-field image of cells and microbeads confined in the microwell. (b) Size-based image processing technique for yeast cell identification and position in the marked microwell. (c) Levitation of seven yeast cells from the microwell while leaving the microbeads in the microwell. (d) Assembly the optically levitated yeast cells. (e) Transportation process. (f) Cell deposition in the target microwell. (Reproduced by permission of IOP Publishing.)

Table 16.2 Statistical results of isolation and deposition on hESC and yeast cell, given as means ± standard deviations.

Cell type	Total cells ($n = 4$)	Initial purity before isolation (%)	Successful levitation rate (%)	Successful transfer rate (%)	Final purity after isolation (%)
hESC	2912	12.75 ± 0.96	78.5 ± 5.4	97 ± 1.41	96.75 ± 1.5
Yeast cell	1290	52.25 ± 10.27	86.37 ± 4.75	99.25 ± 0.95	95.25 ± 1.89

all the levitated cells, and the final target cell purity after isolation is the percentage of the target cells to all the cells in the cell deposition microwells.

In the experiment, we collected data from four groups of total 2912 hESCs and four groups of total 1290 yeast cells, respectively. The successful levitation rates from the microwell were influenced by nonspecific surface adhesion. The successful transfer rates for both cell types were high, which were due to the optimized precise control of cell trace during the transportation process. The impurity of the target cells in the deposition microwell was mainly induced

by the random trapping of the nontarget particles when the target cells and the nontarget particles were close or adherent to each other.

The average time needed in the cell manipulation process was about 27–37 s, where cell levitation was about 3 s, cell assembly 1 s, cell transportation 20–30 s, and cell deposition 3 s. The most time-consuming process was the cell transportation process. This time cost can be highly reduced by shortening the transportation distance between the cell docking area and the cell deposition area. Furthermore, packing the microwells more densely by reducing the well-to-well distance can increase the throughput to a certain extent.

Maintaining cell health and viability is another great concern. Laser-induced photo damage and thermal damage are the two main effects on the biological cells, which are highly dependent on the laser wavelength, as well as the applied laser power. When the wavelength was above 800 nm, the heating effect was the major factor resulting in cell damage [35]. In our system, the near-infrared laser with wavelength of 1064 nm was chosen as the laser source. In order to avoid or reduce thermal damage to the cell, the laser power that is as low as possible should be adopted according to the calibration result of the optical trap. In addition, in most common experimental circumstances, adsorption of laser light by the surrounded medium, and not by the particle itself, is the most important contribution to heating [36]. In our experiment, the trapped particles are transported in the medium, so the heat transfer can be made more efficient by the moving fluid.

Moreover, we utilized two methods to test the viability of the hESC affected by the optical trap: (i) the use of the SYTOX Orange dead cell stain and (ii) the use of the trypan blue, as shown in Figure 16.17 [31]. We exposed the cells under the optical trap with 3 W laser emission power (the maximum laser emission power of the laser source) for up to 15 min. When using the SYTOX Orange nucleic acid stain, no red fluorescence was detected in the healthy cells trapped by the optical trap for 15 min. For the controlled cells, it was found that the dye could penetrate the dead cell membrane, which exhibited the red fluorescence when excited with the 488-nm lasers. Similarly, utilizing the trypan blue exclusion assay, no stain was observed in the healthy cells when applying the 3 W laser emission power for 15 min. However, for the controlled cells, the whole cell was stained with dye as an indicator of cell death.

16.4.4.6   Discussion

The developed novel cell micromanipulation tool with combined robotics and optical tweezer technologies has three characteristics. First, the tool can realize a set of cell manipulation processes, including cell docking, cell recognition and levitation, cell assembly, and cell transportation and deposition. Second, the tool exhibits high manipulation accuracy and flexibility. It enables cell inspection with high spatiotemporal resolution with the recognition capability of different cell phenotypes. Multiple independent optical traps combined with the motorized stage can realize dynamic and parallel cell manipulation in three dimensions while always keeping the cells at the image focus plane for constant inspection. Third, the isolated target cells can be transported and deposited to the specified
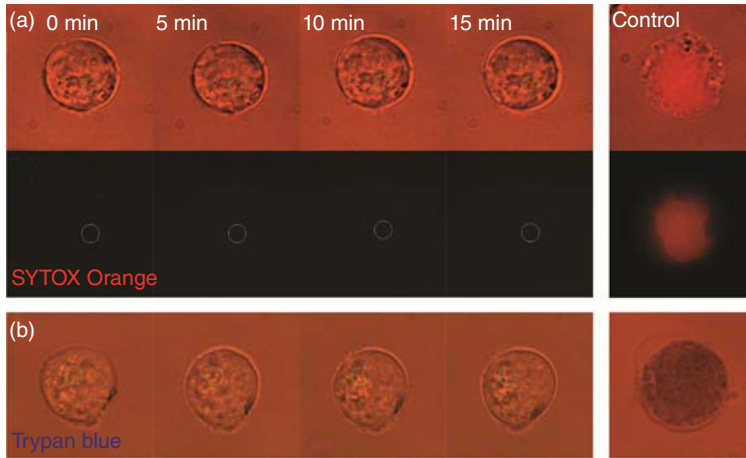
Figure 16.17 Viability test of the hESC affected by the optical trap. (a) Viability test using SYTOX Orange dead cell stain. For healthy cells, no red fluorescence was detected with 3 W laser emission power for up to 15 min. For controlled cell, red fluorescence was detected in the fluorescence image. (b) Viability test using trypan blue. No stain was observed in the healthy cells when applying the 3 W laser emission power for up to 15 min. For controlled cell, the whole cell was stained with dye as indicator of cell death. (Reproduced by permission of IOP Publishing.)

target location precisely, which exhibits a great potential for integration with other on-chip functionalities without removing these cells from the chip, such as cell fusion [37].

16.5
Conclusion

In this chapter, a cell micromanipulation system combining optical tweezers and microfluidic chip is established, which exhibits the advantages of noninvasive cell contact and minimal contamination during the cell manipulation process. With this platform, an enhanced cell sorting strategy based on dynamic fluid and dynamic light pattern is proposed to realize small cell population sorting with high recovery rate and purity. In addition, multitrap parallel sorting can be realized to improve the throughput without losing the purity and recovery rate. Furthermore, a novel cell manipulation tool with optical tweezers is proposed for automated parallel cell isolation, transportation, and deposition based on a uniquely designed microfluidic chip with microwell array. Therefore, the tool exhibits a great potential for integration with other on-chip functionalities without removing the cells from the chip. The effectiveness of the proposed cell micromanipulation system with the enhanced cell sorting strategy as well as the novel cell manipulation tool is demonstrated by performing the experiments on yeast cells and hESCs.

References

1. Dittrich, P.S., Tachikawa, K., and Manz, A. (2006) Micro total analysis systems. Latest advancements and trends. *Anal. Chem.*, **78** (12), 3887–3907.

2. Yao, B., Luo, G.A., Feng, X., Wang, W., Chen, L.X., and Wang, Y.M. (2004) A microfluidic device based on gravity and electric force driving for flow cytometry and fluorescence activated cell sorting. *Lab Chip*, **4** (6), 603–607.

3. Macdonald, M.P., Spalding, G., Dholakia, K., and Spalding, G. (2003) Microfluidic sorting in an optical lattice. *Nature*, **426** (6965), 421–424.

4. Ramadan, Q., Samper, V., Poenar, D.P., and Yu, C. (2006) An integrated microfluidic platform for magnetic microbeads separation and confinement. *Biosens. Bioelectron.*, **21** (9), 1693–1702.

5. Petersson, F., Nilsson, A., Holm, C., Jönsson, H., and Laurell, T. (2005) Continuous separation of lipid particles from erythrocytes by means of laminar flow and acoustic standing wave forces. *Lab Chip*, **5** (1), 20–22.

6. Shah, G.J., Ohta, A.T., Chiou, E.P., Wu, M.C., and Kim, C.J. (2009) EWOD-driven droplet microfluidic device integrated with optoelectronic tweezers as an automated platform for cellular isolation and analysis. *Lab Chip*, **9** (12), 1732–1739.

7. Ashkin, A. (1992) Forces of a single-beam gradient laser trap on a dielectric sphere in the ray optics regime. *Biophys. J.*, **61** (2), 569–582.

8. Wu, Y., Sun, D., and Huang, W. (2011) Mechanical force characterization in manipulating live cells with optical tweezers. *J. Biomech.*, **44** (4), 741–746.

9. Enger, J., Goksör, M., Ramser, K., Hagberg, P., and Hanstorp, D. (2004) Optical tweezers applied to a microfluidic system. *Lab Chip*, **4** (3), 196–200.

10. Tanaka, Y., Kawada, H., Tsutsui, S., Ishikawa, M., and Kitajima, H. (2009) Dynamic micro-bead arrays using optical tweezers combined with intelligent control techniques. *Opt. Express*, **17** (26), 24102–24111.

11. Eriksson, E., Enger, J., Nordlander, B., Erjavec, N., Ramser, K., Goksör, M., Hohmann, S., Nyström, T., and Hanstorp, D. (2007) A microfluidic system in combination with optical tweezers for analyzing rapid and reversible cytological alterations in single cells upon environmental changes. *Lab Chip*, **7** (1), 71–76.

12. Tan, Y., Sun, D., Wang, J., and Huang, W. (2010) Mechanical characterization of human red blood cells under different osmotic conditions by robotic manipulation with optical tweezers. *IEEE Trans. Biomed. Eng.*, **57** (7), 1816–1825.

13. Milne, G., Rhodes, D., MacDonald, M., and Dholakia, K. (2007) Fractionation of polydisperse colloid with acousto-optically generated potential energy landscapes. *Opt. Lett.*, **32** (9), 1144–1146.

14. Hart, S.J., Terray, A.V., and Arnold, J. (2007) Particle separation and collection using an optical chromatographic filter. *Appl. Phys. Lett.*, **91** (17), 171121.

15. Lin, C.C., Chen, A., and Lin, C.H. (2008) Microfluidic cell counter/sorter utilizing multiple particle tracing technique and optically switching approach. *Biomed. Microdevices*, **10** (1), 55–63.

16. Wang, M.M., Tu, E., Raymond, D.E., Yang, J.M., Zhang, H., Norbert, H., Dees, B., Mercer, E.M., Forster, A.H., Kariv, I., Marchand, P.J., and Butler, W.F. (2005) Microfluidic sorting of mammalian cells by optical force switching. *Nat. Biotechnol.*, **23** (1), 83–87.

17. Perroud, T.D., Kaiser, J.N., Sy, J.C., Lane, T.W., Branda, C.S., Singh, A.K., and Patel, K.D. (2008) Microfluidic-based cell sorting of Francisella tularensis infected macrophages using optical forces. *Anal. Chem.*, **80** (16), 6365–6372.

18. El-Ali, J., Sorger, P.K., and Jensen, K.F. (2006) Cells on chips. *Nature*, **442** (7101), 403–411.

19. Eisenstein, M. (2006) Cell sorting: divide and conquer. *Nature*, **441** (7097), 1179–1185.

20. Park, M.C., Hur, J.Y., Cho, H.S., Park, S.H., and Suh, K.Y. (2011) High-throughput single-cell quantification

using simple microwell-based cell dock-ing and programmable time-course live-cell imaging. *Lab Chip*, **11** (1), 79–86.

21. Skelley, A.M., Kirak, O., Suh, H., Jaenisch, R., and Voldman, J. (2009) Microfluidic control of cell pairing and fusion. *Nat. Methods*, **6** (2), 147–152.

22. Revzin, A., Sekine, K., Sin, A., Tompkins, R.G., and Toner, M. (2005) Development of a microfabricated cytometry plat-form for characterization and sorting of individual leukocytes. *Lab Chip*, **5** (1), 30–37.

23. Lu, Z., Moraes, C., Ye, G., Simmons, C.A., and Sun, Y. (2010) Single cell deposition and patterning with a robotic system. *PLoS One*, **5** (10), e13542.

24. Kovac, J.R. and Voldman, J. (2007) Intuitive, image-based cell sorting using optofluidic cell sorting. *Anal. Chem.*, **79** (24), 9321–9330.

25. Luo, C.X., Li, H., Xiong, C.Y., Peng, X.L., Kou, Q.L., Chen, Y., Ji, H., and Ouyang, Q. (2007) The combination of optical tweezers and microwell array for cells physical manipulation and local-ization in microfluidic device. *Biomed. Microdevices*, **9** (4), 573–578.

26. Wang, X., Chen, S., Kong, M., Wang, Z., Costa, K.D., Li, R.A., and Sun, D. (2011) Enhanced cell sorting and manipula-tion with combined optical tweezer and microfluidic chip technologies. *Lab Chip*, **11** (21), 3656–3662.

27. Xia, Y. and Whitesides, G.M. (1998) Soft lithography. *Annu. Rev. Mater. Sci.*, **28** (1), 153–184.

28. Olofsson, J., Pihl, J., Sinclair, J., Sahlin, E., Karlsson, M., and Orwar, O. (2004) A microfluidics approach to the problem of creating separate solution environments accessible from macroscopic volumes. *Anal. Chem.*, **76** (17), 4968–4976.

29. Lin, H.C. and Hsu, L. (2009) Study of the line optical tweezers characteristics using a novel method and establishing a model for cell sorting. *Jpn. J. Appl. Phys.*, **48** (7), 072502.

30. Wright, W.H., Sonek, G.J., and Berns, M.W. (1994) Parametric study of the forces on microspheres held by optical tweezers. *Appl. Opt.*, **33** (9), 1735–1748.

31. Wang, X., Gou, X., Chen, S., Yan, X., and Sun, D. (2013) Cell manipulation tool with combined microwell array and optical tweezers for cell isolation and deposition. *J. Micromech. Microeng.*, **23** (7), 075006.

32. Eriksson, E., Keen, S., Leach, J., Goksör, M., and Padgett, M.J. (2007) The effect of external forces on discrete motion within holographic optical tweezers. *Opt. Express*, **15** (26), 18268–18274.

33. Cioffi, M., Moretti, M., Manbachi, A., Chung, B.G., Khademhosseini, A., and Dubinim, G. (2010) A computational and experimental study inside microfluidic systems: the role of shear stress and flow recirculation in cell docking. *Biomed. Microdevices*, **12** (4), 619–626.

34. Anis, Y.H., Holl, M.P., and Meldrum, D.R. (2010) Automated selection and placement of single cell using vision-based feedback control. *IEEE Trans. Autom. Sci. Eng.*, **7** (3), 598–606.

35. Zhang, H. and Liu, K.K. (2008) Opti-cal tweezers for single cells. *J. R. Soc. Interface*, **5** (24), 671–690.

36. Peterman, E.J.G., Gittes, F., and Schmidt, C.F. (2003) Laser-induced heating in optical traps. *Biophys. J.*, **84** (2), 1308–1316.

37. Wang, X., Chen, S., Chow, Y., Kong, C., Li, R., and Sun, D. (2013) A micro-engineered cell fusion approach with combined optical tweezers and microw-ell array technologies. *RSC Adv.*, **3**, 23589–23595.

17
Investigating the Molecular Specific Interactions on Cell Surface Using Atomic Force Microscopy

Mi Li, Lianqing Liu, Ning Xi, and Yuechao Wang

17.1
Background

Cancer is the leading cause of death in economically developed countries and the second leading cause of death in developing countries [1]. The new cancer cases will increase from 12.7 million in 2008 to 22.2 million by 2030, while the cancer-related deaths will increase from 7.6 million in 2008 to 13.2 million by 2030 [2]. Carcinogenesis and tumor progression are complex and progressive processes that are associated with numerous genetic and epigenetic alterations [3]. Our growing understanding of tumor biology and genomics paves the way to the development of new therapy approaches, and marked progress has been achieved in overcoming treatment resistance through precision medicine and immunotherapy [4]. However, because of the fact that the exact reason why a cell becomes cancerous is unknown (the only one cancer whose cause is clear is cervical cancer), the current cancer treatments cannot prevent the recurrence of cancers and the age-adjusted mortality rate for cancer is about the same in the twenty-first century as it was 50 years ago [5].

Lymphomas, solid tumors of the immune system [6], account for 4%−5% of all cancers [7]. Hodgkin's lymphoma accounts for about 10% of all lymphomas and the remaining 90% are referred to as *non-Hodgkin lymphoma* (*NHL*) [6]. NHL can be divided into many subtypes according to the combination of morphology, immunophenotype, genetic, molecular, and clinical features of the tumors [8]. Approximately, 85% of NHL in adults arises from B cells [9], and the rest are T-cell origin [10]. Follicular lymphoma and diffuse large B-cell lymphoma are the two most common B-cell NHLs, comprising 60% of new B-cell NHL diagnoses each year in North America [11]. In 1997, US Food and Drug Administration (FDA) approved rituximab (an anti-CD20 monoclonal antibody (mAb)) for treating B-cell NHLs. CD20 is 297 amino acids long with a molecule weight of about 33 kDa [12]. The exact biological function of CD20 is currently unknown [13], partly because it has no known natural ligand and CD20 knockout mice display an almost normal phenotype [14]. Many of the functions of CD20 have been determined using artificial ligands (antibody) [15]. *In vitro* experiments proposed that CD20

itself functioned as a calcium ion channel, although direct evidence was lacking [16]. CD20 is an ideal target for mAbs, as it is expressed at high levels on most tumor B cells, but does not become internalized or shed from the plasma membrane after being bound by mAb [17]. Besides, CD20 is absent from hematopoietic stem cells, thus normal B cells are able to regenerate after the rituximab treatment and return to pretreatment levels within several months or even years [18].

In vitro research works have proved that the binding of rituximab to CD20 causes the death of B cells through three mechanisms, including antibody-dependent cellular cytotoxicity (ADCC), complement-dependent cytotoxicity (CDC), and direct induction of programmed cell death (PCD) [19]. While it is widely accepted that ADCC is critical in the killing effect of rituximab, the role of CDC and PCD is still disputed [20]. The schematic diagram of ADCC mechanism is shown in Figure 17.1. During the ADCC, the Fab portion of rituximab binds to CD20 on the surface of tumor cells, and then the Fc portion of rituximab binds to the Fc receptor (FcR) on the surface of immune cells (e.g., macrophage and Natural killer [NK] cell), which triggers the effector functions of immune cells. The macrophage kills the tumor cell via phagocytosis, while the NK cell releases perforin and granzymes that can lyse the tumor cell [21]. The exact contribution of macrophage and NK cell *in vivo* is so far still unclear [17]. Current research about rituximab's killing effects were virtually performed *in vitro*, thus the *in vivo* mechanisms are yet to be elucidated [19]. Even though its *in vivo* mechanism is unclear, rituximab has proven to be very effective in clinical practice either by itself or when combined with chemotherapy (such as Cyclophosphamide-Hydroxydaunorubicin- Oncovin- Prednisone [CHOP]), significantly improving the response rates and survival outcomes of B-cell NHL patients [22]. Rituximab with the standard dose of 375 mg m^{-2} [23] has been widely accepted in the clinical treatment of B-cell NHLs.
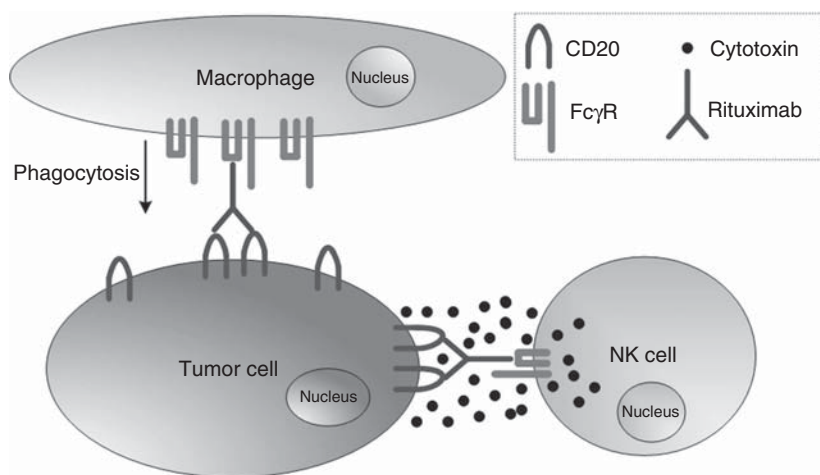
Figure 17.1 The ADCC mechanism of rituximab.

Despite the fact that rituximab achieved unprecedented success in clinical treatments, there are still about 40%−50% of patients who have no responses or develop resistance to the rituximab therapy [24]. Several new antibodies with enhanced effector functions demonstrated that *in vitro* tests have been developed (e.g., Ofatumumab, Ocrelizumab, Veltuzumab, AME-133V, PRO131921 and GA101) [23], but to date their clinical performances are disappointed in direct comparison with rituximab [25], and whether such new antibodies will be clinically superior to rituximab therapy remains to be seen [26]. In recent years, requirements for developing new antibodies to provide effective therapies for those patients who are insensitive or develop resistance to rituximab are increasingly urgent [23]. Addressing the problem of rituximab's variable efficacies among different patients will greatly promote the development of new antibody drugs and thus will improve the quality of life patients.

To further enhance the potency of anti-CD20 mAbs beyond that achieved with rituximab, it is becoming increasingly important for us to develop closer links between the laboratory and the clinic [23]. To obtain closer links, two aspects of current biochemical experiments need improvement. The first aspect is that traditional biochemical experiments are based on bulk averaging experiments that hide the behavior of single cells and single molecules [27]. For a better understanding of the underlying mechanisms of cellular physiological activities, single-cell and single-molecule experiments are required to obtain complementary information to that from bulk experiments. The second aspect needing improvement is that most current experiments were carried out on cells cultured *in vitro*. We know that the growth environment of cells cultured *in vitro* was quite different from the environment of cells *in vivo* [28]. For cells cultured *in vitro*, they lose the neurohumoral regulation and cell−cell influence, and this huge difference of growth environment may cause the changes of the cell structures and functions. Hence, the experimental results obtained from cells cultured *in vitro* may not completely reflect the real situation *in vivo*. So far the knowledge of rituximab's *in vivo* mechanisms is very scarce, greatly hindering the development of anti-CD20 mAbs. In order to develop new anti-CD20 mAbs with enhanced efficacy, we should have a thorough understanding of the physiological activities involved in rituximab's killing mechanisms, particularly the activities *in vivo*. Viewed from this aspect, directly investigating the behavior of tumor cells from B-cell NHL patients will be of significant clinical impact.

The advent of atomic force microscopy (AFM) [29] provides a powerful platform for investigating the cellular behavior at single-cell and single-molecule levels. Compared with other biochemical methods, AFM has several unique advantages. First, it has nanometer spatial resolution and can work in liquids that enable it to observe the activities of single molecules on the surface of living cells. We know that optical microscopy cannot reveal the activities of single molecules due to the 200-nm resolution limitation, and electron microscopy can only observe the behavior of chemically fixed and dried samples. Second, while chemical (fluorescence) labeling of proteins might change their surface characteristics so that their

natural activity is impaired [30], AFM is label-free and noninvasive. Third, AFM can obtain multiple complementary parameters of the biological systems (from single molecules to cells and tissues), for example, topography, adhesion, elasticity, and dissipation [31]. These parameters are of great significance for us to understand the underlying mechanisms of biological systems. These advantages have made AFM widely used in the life sciences in the past decades.

In this chapter, we describe the application of AFM in investigating the molecular specific interactions involved in rituximab targeted therapy of lymphoma on cell surface. The structure of this chapter is as follows. We begin by providing an introduction about the principle and method of AFM single-molecule force spectroscopy (SMFS), a technique that can probe the molecular interactions at single-molecule levels. In the next section, we discuss how to measure the drug–target interactions directly on tumor cells from lymphoma patients. Next, investigations about mapping the nanoscale distribution of target proteins on the surface of tumor cells are presented and the relationship between the distribution of target protein and the clinical rituximab efficacy is analyzed. The last section is the summary.

17.2
Single-Molecule Force Spectroscopy

SMFS specifically probes the membrane proteins by linking their cognate ligands to the AFM tip, as depicted in Figure 17.2a. With the ligands on the AFM tip that can bind to the specific membrane proteins, one can localize, detect, and manipulate the membrane proteins on the living cell [27]. An AFM cantilever has one end fixed to a piezoelectric ceramic driver, and the free end has a sharp tip. The vertical movement of the probe is driven by a piezoelectric ceramic, and any deformation of the cantilever due to repulsive or attractive forces is monitored by a four-quadrant photodetector that senses laser light reflected from the back of the cantilever. According to Hooke's law ($F = kx$), if the spring constant k and the deformation x of the cantilever are known, then the force F applied to the cantilever can be computed. The vertical displacement of the probe is obtained from the piezoelectric ceramic driver. In the force curve mode, the tip gradually approaches and contacts the cell such that the ligands bind to the membrane proteins. Then, the tip is retracted from the cell surface. After recording the displacement of the driver and the force on the cantilever during the approach–retract cycle, a force versus distance curve (also called *force curve*) is obtained, as shown in Figure 17.2b. The arrows indicate the process of obtaining the force curve. When the tip does not contact the cell, the cantilever remains unchanged and the force curve is flat (Figure 17.2b(I)). After contacting the cell, the cantilever is deformed (bent) and the force curve becomes bent (Figure 17.2b(II)). If the ligands on the AFM tip bind to the membrane proteins during the contact between AFM tip and cell surface, then the protein–ligand pair is stretched when the tip is retracted (Figure 17.2b(III)). When the pulling
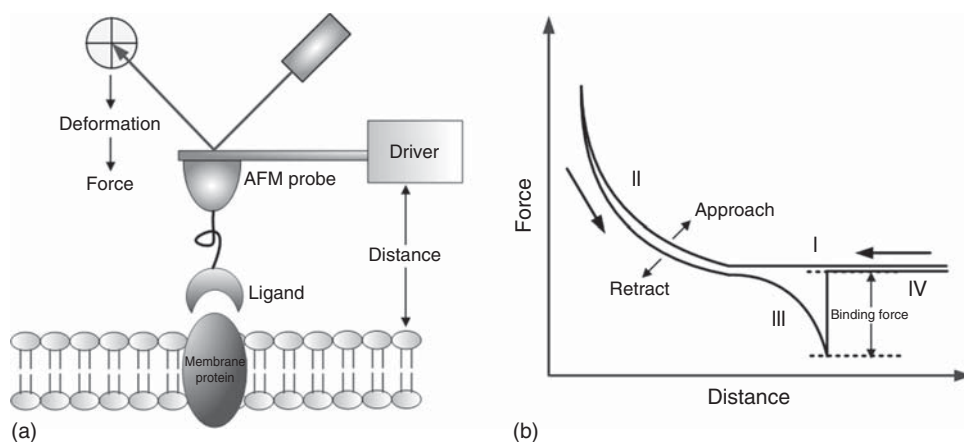
Figure 17.2 Principle of SMFS. (a) Ligands attached to an AFM tip probe a membrane protein. (b) Example of a force curve. When the cantilever/tip is far away from the cell, no deformation occurs, creating a flat force curve (I). After the tip contacts the cell, cantilever deformation occurs and the force curve becomes curved (II). When the tip retracts, the protein–ligand bond is stretched until it ruptures (III). The tip finally retracts to the original position (IV). (Reprinted with permission from Ref. [32]. Copyright 2014 Science China Press.)

force exerted by the cantilever becomes larger than the binding force of the protein–ligand pair, then the protein–ligand bond ruptures and a specific unbinding jump appears in the retraction curve. The magnitude of the jump (denoted by the double-head arrow in Figure 17.2b) corresponds to the binding force between membrane protein and ligand. Then the tip retracts to its original position, as shown in Figure 17.2b(IV).

The prerequisite for using SMFS to measure molecular binding forces is the linking of ligands onto the AFM tip, which is called *tip functionalization*. There are three main methods for tip functionalization, including protein physisorption, chemisorption of alkanethiols on gold, and covalent coupling of silanes on silicon oxide [33]. The major drawback of protein physisorption is that it often exhibits many molecular binding events during the measurement and it is therefore difficult to accurately measure the binding force of a single molecular pair [34]. The disadvantage of alkanethiol chemisorption is that it requires the tip to be coated with a 5-nm-thick chromium layer, followed by a 30-nm-thick gold layer [35]. This causes a significant increase in the tip radius that decreases the spatial resolution during scanning [36]. The covalent coupling method can be performed directly on a silicon tip, and the binding strength of a covalent bond is much stronger than that of physisorption or chemisorption [37, 38]. Therefore, this method is very well suited for molecular force measurement. During covalent coupling, a silicon tip is first coated with NH_2, and then the ligands are linked onto the tip via hetero-bifunctional polyethylene glycol (PEG) molecules (e.g., NHS–PEG–PDP [33]). The NHS end of the PEG linker covalently binds to the

NH_2 on the tip surface, and the PDP end forms covalent disulfide bonds to SH groups on the ligands. Most extracellular proteins (such as antibodies) do not have SH groups; however, they can be formed with N-succinimidyl 3-(acetylthio) propionate (SATP) [39]. The insertion of a PEG spacer between the ligand and the tip has many advantages. It allows the ligand to freely reorient with respect to the membrane proteins, it avoids the danger of ligands being compressed during contact between the tip and the cell surface, and it allows a clear distinction between specific and unspecific binding because of the soft and nonlinear elasticity of the PEG linker [34, 36]. Furthermore, because the PEG is covalently bound to both the tip and the ligand, its binding strength is much stronger than the protein−ligand bond. Thus, the membrane protein−ligand bond ruptures first during retraction and therefore ensures that the measured force is associated only with the protein−ligand binding. To perform single-molecule measurements, the density of ligands linked to the tip must be low enough (fluorescence labeling can be used to estimate the number of ligands in the contact area of a tip of known radius [40]) to ensure that only one protein−ligand bond forms [41].

In order to link rituximab to the surface of AFM tip, NHS−PEG−MAL linker (JenKem Technology, Beijing, China) was used here. Commercial rituximab stock solution ($10\,mg\,ml^{-1}$) was obtained from Chinese Affiliated Hospital of Military Medical Academy of Sciences. The silicon nitride probe (Bruker, Santa Barbara, CA, USA) was used for functionalization. The process of tip functionalization was according to the Ref. [42, 43]. Aminopropyltriethoxysilan (APTES) ($30\,\mu l$) and N,N-diisopropylethylamine ($10\,\mu l$) were used to coat the AFM stylus with the NH_2 groups under argon gas in a glass desiccator for $0.5-2\,h$. The PEG linker and triethylamine were mixed in chloroform and then incubated with the NH_2-modified probes for $2-3\,h$, which allowed the NHS end of the PEG linker to covalently bind to the NH_2 groups on the surface of AFM tip. Rituximab was treated with SATP to form thiol functional groups. Finally, the probes were placed in the SATP−rituximab mixture containing hydroxylamine and buffer solution (pH 7.5) for $1\,h$, which allowed the MAL end of the PEG linker to bind to the thiols on the rituximab. The functionalized probes were stored in phosphate buffered saline (PBS) at $4\,°C$. In order to demonstrate the activity of the rituximab-functionalized probe, force curves were obtained on the surface of lymphoma Raji cells, as shown in Figure 17.3a. Raji cell is a Burkitt's lymphoma cell line and expresses CD20 on the cell surface. We can see that there was an unbinding peak in the retract curve, as denoted by the arrow in Figure 17.3a. The unbinding peak was determined by the change in the slope during the retract process, which reflected the stretching of the flexible linker molecules [44]. A key feature in molecular recognition studies by SMFS is to demonstrate the specificity of the measured unbinding forces, which can be achieved by block experiments [33]. Here, force curves were obtained on Raji cells again after adding free rituximabs, and a typical force curve is shown in Figure 17.3b. We can see that the unbinding peak vanished, which demonstrated that the unbinding peak in Figure 17.3a corresponded to the CD20−rituximab interactions. The experimental results in Figure 17.3 indicated the activity of the rituximab-functionalized probe.
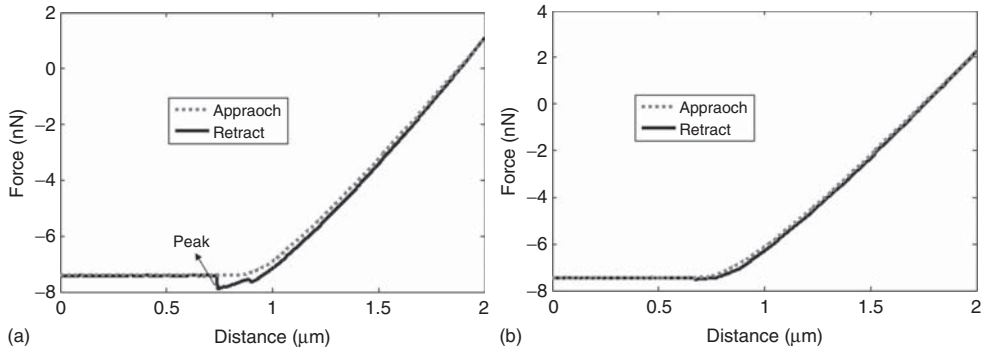
Figure 17.3 The use of rituximab-conjugated probe to obtain force curves on lymphoma Raji cells. (a) A typical force curve (with unbinding peak) obtained on Raji cells. (b) A typical force curve obtained on rituximab-blocked Raji cells. (Reprinted with permission from Ref. [43]. Copyright 2011 Science China Press.)

17.3
Force Spectroscopy of Molecular Interactions on Tumor Cells from Patients

B cells are a type of lymphocyte that expresses clonally diverse cell surface immunoglobulin (Ig) receptors recognizing specific antigenic epitopes [45]. B cells can produce antibodies, which make them perform as positive regulators of immune responses and central contributors to the pathogenesis of immune-related diseases [46]. B-cell NHL results from the process of canceration by which healthy B cells transformed into cancer B cells. B-cell NHL commonly involves the bone marrow invasion. The bone marrow samples (obtained from B-cell NHL patients with bone marrow invasion) contain cancer B cells, healthy B cells, and other healthy cells. Both cancer B cells and healthy B cells express CD20. Rituximab can bind to CD20s on the surface of both cancer B cells and healthy B cells, and this binding then leads to the cell lysis via several mechanisms [23]. We are interested in the binding of rituximab to the CD20s on the surface of cancer B cells, because this binding has direct impact on the rituximab's treatment efficacies. In order to investigate the CD20 on cancer B cells, we need to recognize cancer B cells first. Recent research work indicate that receptor tyrosine kinase-like orphan receptor 1 (ROR1) is a specific cell surface marker expressed on some B-cell lymphomas (such as mantle cell lymphoma, marginal zone lymphoma, diffuse B-cell lymphoma, and follicular lymphoma) but not on virtually all normal adult tissues [47, 48]. Hence, ROR1 is a suitable marker for distinguishing tumor B cells from healthy cells.

We first tested the ROR1 fluorescence labeling on Raji cells. Figure 17.4a−d shows the ROR1 fluorescence labeling experimental results of Raji cells. Raji cells were cultured in RPMI-1640 medium containing 10% fetal bovine serum at 37 °C (5% CO_2) for 24 h before experiments. Cells were harvested at 1000 rpm for 5 min. After removing the supernatant, the cells were resuspended by PBS. Then, a drop of cell suspension was placed on a poly-L-lysine-coated glass slide
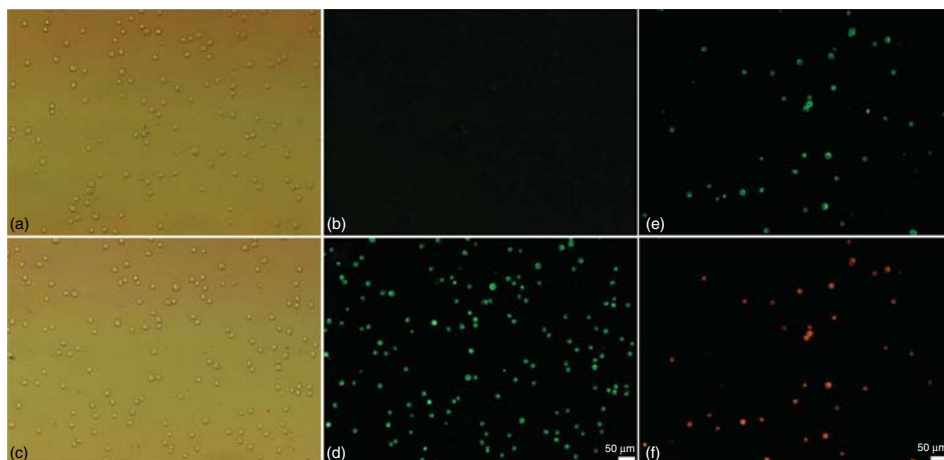
Figure 17.4 ROR1 fluorescence labeling of Raji cells. (a) Optical image of the control group. (b) Fluorescence image of the control group. (c) Optical image of the ROR1 group. (d) Fluorescence image of the ROR1 group. (e,f) ROR1 and CD20 labeling of Raji cells. (e) ROR1 fluorescence image of Raji cells. (f) CD20 fluorescence image of Raji cells. (Reprinted with permission from Ref. [49]. Copyright 2013 John Wiley & Sons, Ltd.)

and subsequently fixed for 30 min with 4% paraformaldehyde. The procedure of fluorescence labeling experiments was the following: (i) After washing the prepared sample three times (each time 10 min) with PBS, add donkey blocking serum and then incubate for 30 min at room temperature. (ii) Add 40 μl goat-antihuman-ROR1 antibody solution (R&D company, USA), incubate for 3 h at room temperature. For control experiment, ROR1 antibody was not added. (iii) Wash the sample three times with PBS, and then add 20 μl FITC-conjugated donkey-antigoat IgG (Kangchen company, Shanghai, China), and incubate for 30 min. (iv) Wash the sample three times with PBS, and place it onto the stage of the fluorescence microscope (Ti, Nikon company, Japan). Goat-antihuman-ROR1 antibody can bind to the ROR1 on the cell surface and FITC-conjugated donkey-antigoat IgG can bind to the goat-antihuman ROR1 antibody. If there was ROR1 on the cell surface, then the cell displayed green light after the excitation of blue light. Figure 17.4a was the optical image of control group and Figure 17.4b was the corresponding fluorescence image. Figure 17.4c was the optical image of ROR1 group and Figure 17.4d was the corresponding fluorescence image. We can see that Raji cells did not exhibit fluorescence without ROR1 antibody (Figure 17.4b). While cells exhibit bright green fluorescence with ROR1 antibody (Figure 17.4d), these experiments indicate that Raji cells express ROR1. ROR1 is the receptor tyrosine kinase-like orphan receptor 1 and functional data suggest that ROR1 may act in Wnt-signaling and promote the survival of malignant cells [49, 50]. Raji cell line is from a Burkitt's lymphoma patient, which is a subtype of B-cell NHL. Previous research works have shown that several B-cell lymphomas express ROR1 [47] and here we can see that Burkitt's lymphoma also express

ROR1. Our goal is to measure the CD20–rituximab binding force based on the ROR1 fluorescence recognition, and in order to examine whether the ROR1 fluorescence labeling influence the CD20s on the cell surface, we perform CD20 fluorescence labeling experiments on ROR1-labeled cells (Figure 17.4e,f). The color of fluorescent dye of ROR1 labeling experiments was green (FITC) and in order to discriminate the color, we chose a red fluorescent dye (RBITC) for CD20 labeling experiments. Figure 17.4e was the ROR1 fluorescence image and Figure 17.4f was the corresponding CD20 fluorescence image. The optical image was not shown. We can see that after ROR1 labeling, the cells still exhibit red fluorescence indicating that there are CD20s on the cell surface.

The results of Figure 17.4 indicated that there were CD20s on the ROR1-labeled cells and we then examined whether the CD20–rituximab binding force can be measured on ROR1-labeled cells. Rituximab was linked onto the AFM tip surface and SMFS technique was applied to measure the CD20–rituximab binding force on the cell surface. Raji cells were chemically fixed by 4% paraformaldehyde. The experiments were performed in PBS. Dimension 3100 AFM (Veeco, Santa Barbara, CA, USA) was used. First, the AFM tip was moved onto the surface of Raji cells under the guidance of optical microscopy and the cell morphology was acquired by AFM imaging at contact mode. Figure 17.5a was the AFM height image and Figure 17.5b was the AFM deflection image of a Raji cell. Then the AFM tip was localized to the small area of the cell surface and force curves were obtained by converting the imaging mode into force measurement mode. Figure 17.5c was a typical force curve obtained on the ROR1-labeled Raji cells. Each force curve contains two curves, approach curve and retract curve. The approach curve corresponded to the approach process during which the tip carrying rituximab approached and touched the cells. When the tip did not touch the cell surface, the curve was flat. After touching the cell surface, the curve bent. The retract curve corresponded to the retract process during which the tip moved back from the cell surface. The rituximab density on the tip surface was controlled to be low to ensure that only one CD20–rituximab complex formed
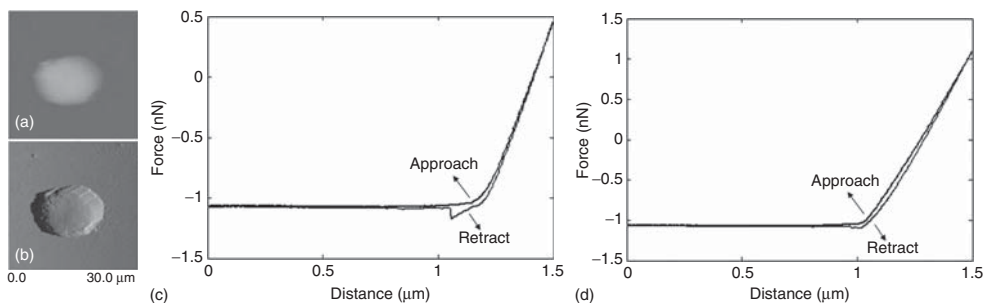
Figure 17.5 Obtaining force curves on ROR1-labeled Raji cells. (a) AFM height image and (b) deflection image of a Raji cell. (c) A typical force curve with CD20–rituximab-specific binding occurred. (d) A typical force curve after blocking. (Reprinted with permission from Ref. [49]. Copyright 2013 John Wiley & Sons, Ltd.)

during each approach–retract cycle. If CD20–rituximab complex formed during the approach–retract cycle, then there would be a specific peak in the retract curve, which indicated the rupture of CD20–rituximab complex. We can see that there was a peak in the retract curve. The shape of the peak indicated that specific molecular binding occurred during the approach–retract process. In order to validate that the binding was from CD20–rituximab, we added free rituximab into the solution to block the CD20s on the cell surface and then obtained force curves again. A typical force curve after blocking was shown in Figure 17.5d. We can see that there was only a tiny peak in the retract curve and the peak shape indicated that it was nonspecific binding. This demonstrated that the unbinding peak in the retract curve corresponded to the CD20–rituximab interactions on the surface of Raji cells.

The above results indicated that CD20–rituximab binding force can be measured on ROR1-labeled Raji cells. Then, we applied the established procedures on pathological cells prepared from the bone marrow of a follicular lymphoma patient whose bone marrow had been invaded by cancer cells. Because fluorescence was required to recognize the cancer cells, BioScope Catalyst AFM (Bruker, Santa Barbara, CA, USA) was used. Follicular lymphoma is a subtype of B-cell NHL, and previous research works have indicated that follicular lymphoma cells express ROR1 [47]. The pathological cell samples contained normal cells and cancer cells. Since only cancer cells express ROR1 (normal cells do not express ROR1), they can be recognized by ROR1 fluorescence labeling. Figure 17.6 shows the AFM imaging of cancer cells assisted by the ROR1 fluorescence recognition. Figure 17.6a was the optical image, Figure 17.6b was the fluorescence image, and Figure 17.6c was the merge of optical and fluorescence images. From the fluorescence image (Figure 17.6b), there was a clear cancer cell that exhibited bright fluorescence (denoted by the white circle). From the inset of the merge image (Figure 17.6c), we can see many normal cells around the shining cancer cell. Under the guidance of fluorescence, the AFM probe was moved onto the cancer cell to image the cellular morphology. The imaging mode was contact mode and both height image and deflection error image were obtained. Figure 17.6d was the height image and Figure 17.6e was the deflection error image. The range of AFM image (50 μm) corresponded to the area denoted by the red dotted square in Figure 17.6c. The color range of the height image was 15 μm and the color range of the deflection error image was 1.5 μm. The cancer cell can be clearly discerned in AFM images (denoted by the square in Figure 17.6d). The section curve (Figure 17.6f) indicated that the height of the cell was about 3 μm and the diameter was about 13 μm. Most current AFM imaging experiments were performed on cells cultured *in vitro* [51]. Here we imaged the cellular morphology of cancer cells from patients under the assistance of fluorescence recognition. We know that cells grown *in vitro* can be quite different from those grown *in vivo*, thus directly investigating the behavior of primary cells from clinical patients is of great significance for us to understand the underlying mechanisms that regulate the cellular activities. However, it should be noted that the patient cancer cells here for AFM imaging were chemically fixed and thus lost
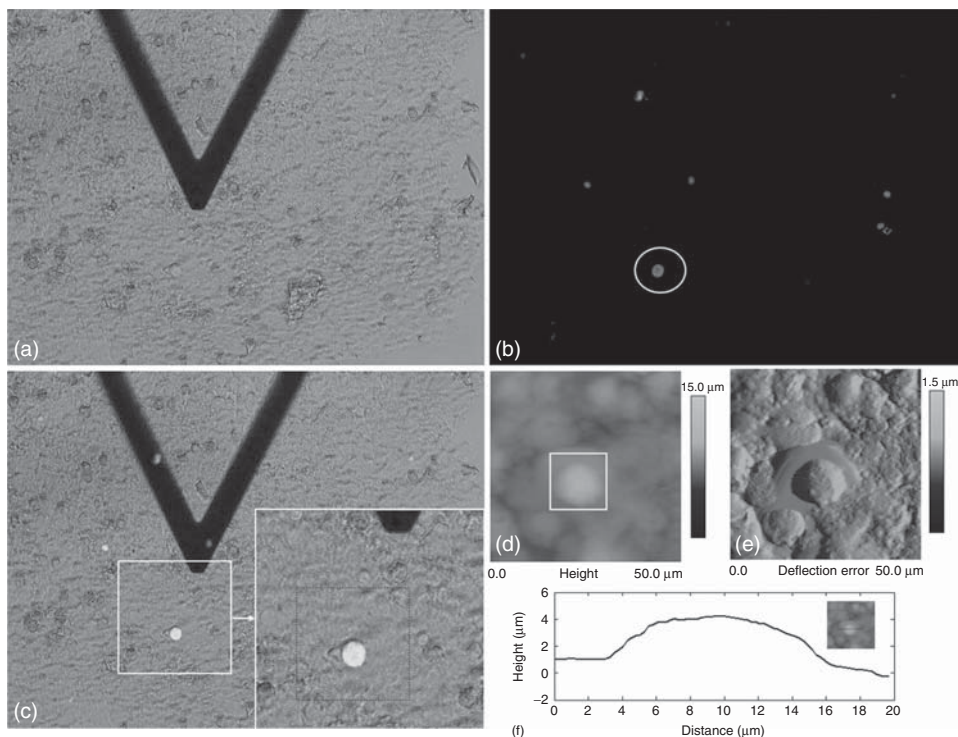
Figure 17.6 Under the guidance of ROR1 fluorescence, AFM probe was moved to the cancer cell to image the cellular morphology. (a) Optical image and (b) fluorescence image of the pathological cell sample. (c) Merge image of optical and fluorescence images. (d) AFM height image of the cancer cell (denoted by the red square in (c)). (e) AFM deflection error image of the cancer cell. (f) Section curve. (Reprinted with permission from Ref. [49]. Copyright 2013 John Wiley & Sons, Ltd.) (For color version, the reader is referred to the Web version of the Ref. [49].)

living activity. In the future, we want to obtain the topography images of living cancer cells from clinical patients. In this situation, we should isolate and collect tumor cells, for example, by flow cytometry [52]. Besides, due to the suspended trait of the lymphoma cell, we should develop adequate methods to immobilize them for living-cell AFM imaging, for example, micro well array chip [53] and thin film having small pores [54]. Investigating the behavior of living tumor cells from patients will enable us to detect and monitor the physiological properties of living tumor cells (e.g., the cellular changes after the stimulation of drugs), bringing novel information that is closer to the real cellular activities.

Then the AFM imaging mode was converted into force measurement mode and force curves were obtained on the ROR1-labeled cancer cells. Figure 17.7a was a typical force curve obtained on the cancer cell. We can see that in the retract curve there was a specific peak which indicated the CD20−rituximab binding. Because there is a change in the slope during the retraction process which is a result of a
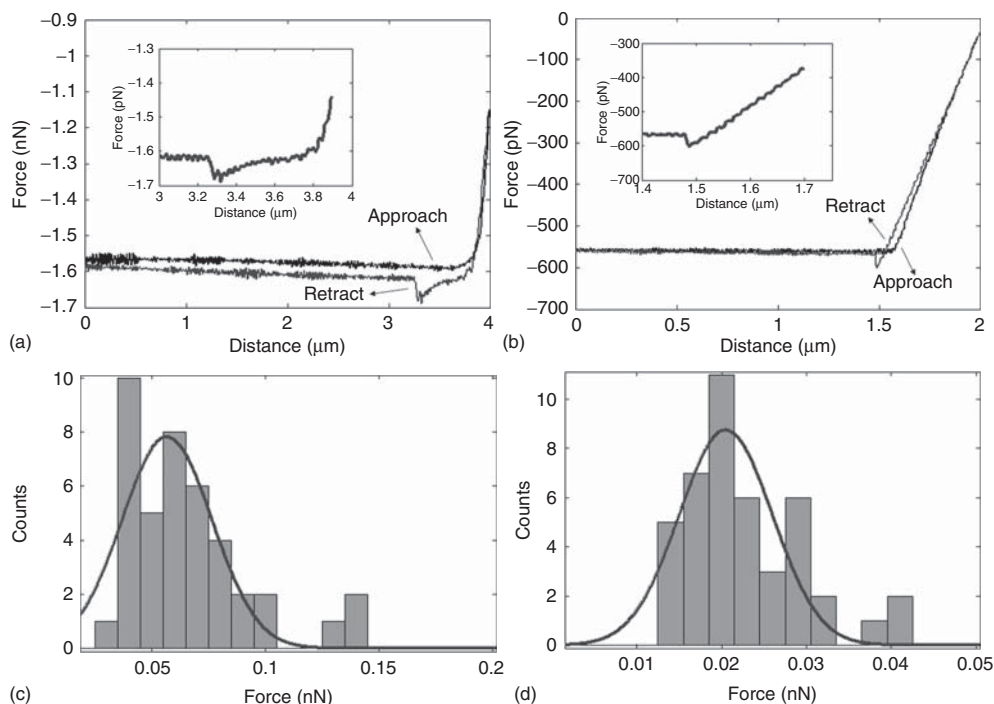
Figure 17.7 Measuring the CD20–rituximab binding force on patient cancer cells. (a) A typical force curve obtained on cancer cells. The inset was the amplifying plot of the retract curve. (b) A typical force curve obtained on normal cells. The inset was the amplifying plot of the retract curve. (c) Histogram of CD20–rituximab binding forces on cancer cells. (d) Histogram of non-specific binding forces on normal cells. (Reprinted with permission from Ref. [49]. Copyright 2013 John Wiley & Sons, Ltd.)

decreased effective spring constant [44], the specific peak can be clearly discerned when zooming in the retract curve. Follicular lymphoma patient cancer cells had CD20s on the cell surface and the CD20–rituximab complex formed during the approach–retract cycle with rituximab-conjugated tip. Also, force curves on normal cells, which did not exhibit fluorescence, were obtained and a typical force curve was shown in Figure 17.7b. We can see that the force curve on normal cells had only a tiny non specific peak in the retract curve where there is not a change in the slope. The non specific peak indicated the non specific molecular binding. Healthy cells in the pathological sample prepared from patient's bone marrow contain normal B cells and other cells, such as T cells and NK cells. If the force curves were obtained on normal B cells, then there should be specific peak in the force curve, but there was not specific peak in the force curve in Figure 17.7b. Hence, the force curve in Figure 17.7b was not obtained on normal B cells but on other normal cells. From the retraction curve with specific peak obtained on cancer cells, the CD20–rituximab binding force was computed: the binding force was equal to the magnitude of the peak. Because of the random spatial orientation of the binding

partners at the tip and cell surface, it is usually necessary to collect many force curves to determine the distribution of the binding force [44]. The histogram of the CD20−rituximab binding forces was shown in Figure 17.7c. Gaussian fit of the histogram indicated that the binding force was 57 ± 28 pN. The histogram of the non specific binding forces on normal cells was shown in Figure 17.7d and Gaussian fit of the histogram indicated that the non specific binding force was 21 ± 7 pN. We can see that non specific binding force was significantly lower than the specific binding force. The CD20−rituximab binding forces were measured at four different loading rates and the relationship between binding force and loading rate was shown in Figure 17.8. We can see that the binding force is linearly related to the logarithm of the loading rate. This phenomenon can be explained by Bell−Evans model [55], which characterizes the behavior of molecular unbinding pulled by an external force. SMFS is a mature single-molecule technique and many researchers have used SMFS to measure the molecular binding force on cells grown *in vitro*, such as receptor−drug [41], receptor−ligand [56], fibrinogen−erythrocyte [57], and aptamer−protein [58], showing that the binding force of receptor−ligand was in the range of 20−200 pN [59]. Here, we measured the CD20−rituximab binding force on patient cancer cells based on the fluorescence recognition of the specific cancer cell surface marker and the binding force was in the range of molecular binding force. Directly investigating the molecular interactions on cancer cells from clinical patients is of special significance. We know that the prerequisite for personalized medicine is having accurate diagnostic tests that identify patients who can benefit from the therapy [60]. This requires an accurate characterization of the pathology. However, current biochemical research is usually performed on
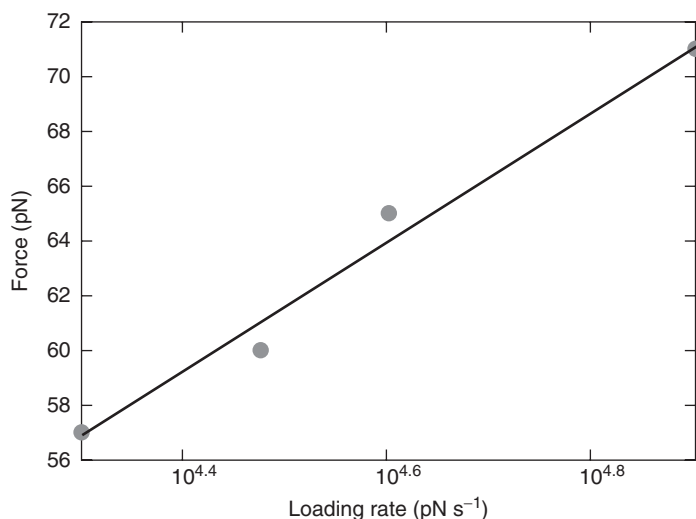
Figure 17.8 The CD20−rituximab binding force is linearly related to the logarithm of loading rates. (Reprinted with permission from Ref. [49]. Copyright 2013 John Wiley & Sons, Ltd.)

cells grown *in vitro*, leaving a large gap between laboratory results and clinical requirements. If we can directly investigate the behavior of tumor cells in the biopsy samples from patients, then we can get more valuable information. Combining such information with clinical data will likely lead to the development of novel, meaningful biomarkers. AFM single-cell and single-molecule techniques were used here to directly investigate the affinity of target proteins (CD20) on tumor cells from clinical patients with the assistance of the specific tumor cell surface biomarker ROR1. This work provided novel insights concerning biophysical properties of target proteins in near *in vivo* conditions, and provided a new way to explore potentially meaningful biomarkers for clinical practice.

17.4
Mapping the Distribution of Membrane Proteins on Tumor Cells

By using SMFS at force volume mode, we can also detect the distribution of membrane proteins on the cell surface [61]. At this mode, AFM tips carrying specific molecules (e.g., antibodies and ligands) were controlled to obtain arrays of force curves at the local areas on the cell surface. To map the distribution of CD20 on the surface of cancer cells, arrays of force curves (16×16) were obtained in the local areas ($500\,nm \times 500\,nm$) of the cancer cell. Each force curve corresponds to an adhesion force. After converting these forces into the gray colors ($0-255$), then a force map was constructed. The map reflects the distribution of CD20 on the cell surface. Figure 17.9 shows the results of mapping the nanoscale distribution of CD20 on the surface of tumor cells. First, under the guidance of ROR1 fluorescence, cancer cells were recognized. Figure 17.9a was the overlay image of bright field image and fluorescence image. We can see one cancer cell in the overlay image, as denoted by the red square. Then, AFM tip carrying rituximabs was moved to the cancer cell to obtain the cellular topography images. Figure 17.9b was the AFM height image of the cancer cell and Figure 17.9c was the corresponding deflection image. Figure 17.9d,e shows AFM images of three healthy cells denoted by the blue square in Figure 17.9a. From the AFM images of the three cells, we can see that cell 1 was a red blood cell due to the special shape of oval biconcave disk. Because red blood cell does not express CD20 on the cell surface, it can be used for negative control experiments.

Then, imaging mode was converted into force curve mode and 16×16 force curves were obtained at the $500\,nm \times 500\,nm$ areas on the surface of cancer cells and healthy cells. By analyzing the force curves, adhesion force gray maps were constructed using image processing software. In order to statistically characterize the nanoscale distribution of CD20 on the surface of cancer cells, we obtained force curves on eight cancer cells with five functionalized tips. For each cell, we obtained several distribution maps on different areas on the cell surface. The representative maps were shown in Figure 17.9f. From the force maps of cancer cells, there were many bright pixels, whereas only few gray pixels in the maps of red blood cells and these pixels were dim. From the distribution maps, we can
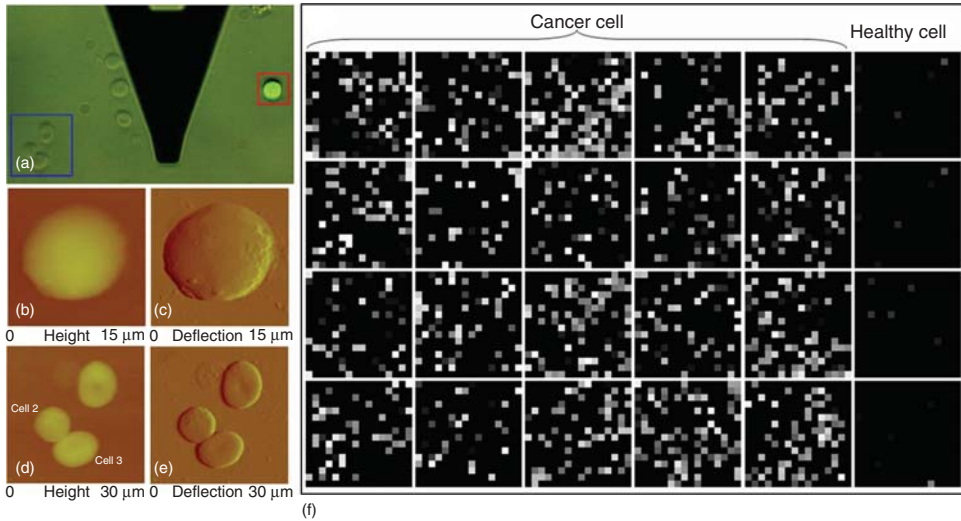
Figure 17.9 Mapping the nanoscale distribution of CD20 on tumor cells. (a) Overlay of optical bright field and fluorescence images. (b) AFM height and (c) deflection image of the tumor cell indicated by the red square in (a). (d) AFM height and (e) deflection image of the three healthy cells indicated by the blue square in (a). (f) CD20 distribution maps on cancer cells and healthy cells. The gray scale bar was 0–100 pN. (Reprinted with permission from Ref. [61]. Copyright 2013 Elsevier Inc.

see that the CD20 distribution on the cell surface was non uniform. The number of CD20 molecules was variable in different local $500 \times 500 \, nm^2$ area on the cell surface. In some other areas on the cell surface, there were more CD20 molecules, whereas in some areas, there were less CD20 molecules. We know that cell membranes are heterogeneous in composition, and the structures responsible for this heterogeneity are lipid rafts [62]. Lipid rafts are fluctuating nanoscale assemblies of sphingolipid, cholesterol, and proteins that can be stabilized to coalesce, forming platforms that function in membrane signaling and trafficking [63]. Besides, cell membrane are dynamic (proteins are free to move with the lipid bilayer), and this means that the distribution of membrane proteins on the cell surface changes dynamically. Recently, researchers have directly observed the motion of single-membrane proteins by using high-speed AFM [64]. In addition, cell membranes have variable membrane curvatures in different positions on the cell surface and these curvatures are dynamically remodeled during physiological processes [65]. All these features of cell membranes may cause the results that the distributions of CD20s on the cancer cell surface are non uniform. On the force maps of red blood cells, there were few gray pixels, which were dim. Red blood cells do not express CD20 and hence their maps were dim.

In order to demonstrate that the maps reflect the CD20 distribution on the cell surface, verification experiments were performed, as shown in Figure 17.10. Figure 17.10a shows the merged image of optical and fluorescence images of the clinical bone marrow cell sample and we can see two cancer cells in the image.
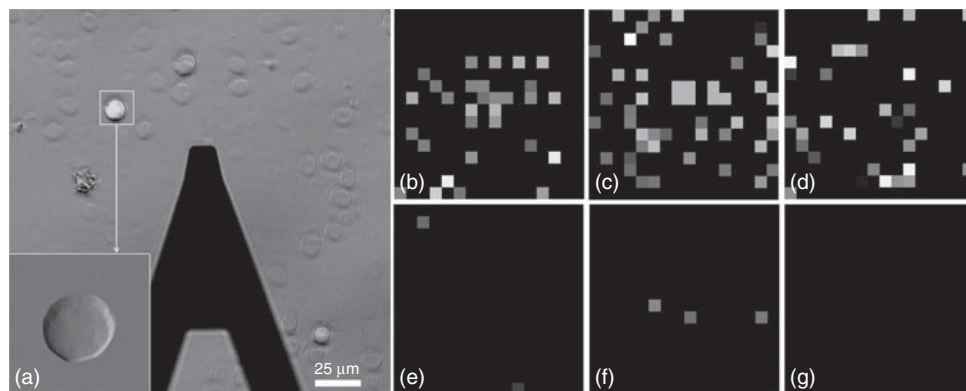
Figure 17.10 Verification of specific CD20–rituximab interactions on cancer cells. (a) Merged image of optical image and fluorescence image of the clinical bone marrow cell sample. The inset is the AFM image of the cancer cell. (b–d) CD20 distribution maps on the cancer cells. (e–g) CD20 distribution maps on the cancer cells after blocking. The gray scale bar was 0–100 pN. (Reprinted with permission from Ref. [61]. Copyright 2013 Elsevier Inc.) (For color version, the reader is referred to the web version of the Ref. [61].)

Under the guidance of fluorescence, AFM-functionalized tips were moved to the cancer cells to image the cell morphology and obtain force curves on the cell surface. From the distribution maps (Figure 17.10b–d), we can see that there are many gray pixels which is consistent with the results in Figure 17.9. After blocking, arrays of force curves were obtained again on the cancer cells, and the distribution maps are shown in Figure 17.10e–g. We can see that after blocking, the gray pixels dramatically decreased, which is because that the CD20s on the cancer cells had been blocked. The results in Figure 17.10 demonstrate the specific CD20–rituximab recognition on the cell surface and therefore the force maps reflect the distribution of CD20s on the cancer cells.

By applying the established method described earlier on the bone marrow cells from three clinical B-cell NHL patients, we obtained the binding affinity and nanoscale distribution of CD20 on the tumor cells for the three patients [66], as shown in Figure 17.11. To investigate the CD20 affinity and nanoscale distribution of different lymphoma patients, we selected three B-cell NHL patients for the study. All of the three patients were with bone marrow infiltration. ROR1 fluorescence labeling experiments were performed to confirm that there were ROR1s on the tumor cell surface of the three patients. The clinical data of the three patients was shown in Table 17.1. For each patient, their bone marrow cells were dropped onto the glass slides and subsequent chemical fixation and ROR1-fluorescence labeling were performed. And then under the guidance of ROR1 fluorescence, about 10 tumor cells were selected and arrays of force curves were obtained on five different local areas on the surface of each cell using functionalized AFM tips. Figure 17.11a–c were the CD20 binding affinities of tumor cells from patient 1, patient 2, and patient 3, respectively. The CD20
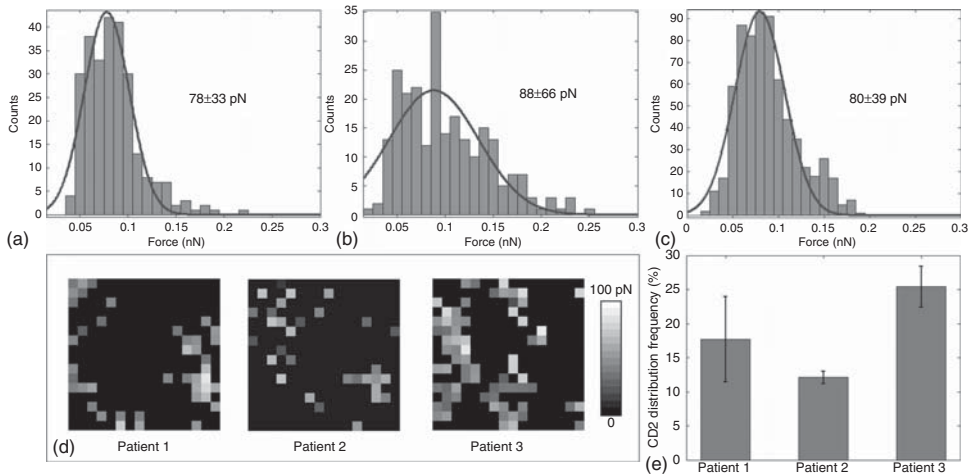
Figure 17.11 Comparison of CD20 binding affinity and nanoscale distribution of tumor cells from three different B-cell NHL patients. The CD20 binding affinity of tumor cells of patient 1 (a), patient 2 (b), and patient 3 (c). (D) Typical adhesion force maps of the three patients. (e) The CD20 distribution frequencies of the three patients. (Reprinted with permission from Ref. [66]. Copyright 2014 Royal Microscopical Society.)

Table 17.1 Clinical information of three clinical lymphoma patients.

Case no.	Sex	Age	Tumor subtype	Clinical therapy	Therapy outcome
1	Female	64	Splenic marginal zone B-cell lymphoma	Rituximab + Fludarabine + Cyclophosphamide	Complete remission
2	Male	56	Small B-cell lymphoma	Rituximab + CHOP	Lesion stability
3	Female	51	Diffuse large B-cell lymphoma	Rituximab + CHOP	Partial remission

Reprinted with permission from Ref. [66]. Copyright 2014 Royal Microscopical Society.

binding affinities to rituximab were computed from the force curves which had specific molecular unbinding peaks. From the histogram, the Gaussian fitting indicated that the CD20 binding affinities of the three patients were 78 ± 33, 88 ± 66, 80 ± 39 pN, respectively. We can see that the binding affinities were not a remarkable variable between the three patients. Figure 17.11d shows the typical adhesion force maps of the three patients. To quantitatively characterize the nanoscale distribution of CD20s, we calculate the CD20 distribution frequency for each adhesion force map to characterize the CD20 density of the cells. For each adhesion force map, we can compute the number of gray and bright pixels (n), and the number of overall pixels of the adhesion force map was known ($16 \times 16 = 256$). The CD20 distribution frequency of this adhesion force map was equal to the

ratio (n/256). Figure 17.11e shows the CD20 distribution frequencies of the three patients. Analyzing the relationship between CD20 density and clinical therapy outcomes, we can find some interesting phenomenon. The combined therapy (rituximab + chemotherapy) was effective for patient 1 and patient 3, but was ineffective for patient 2, while the histogram of distribution frequencies indicated that the CD20 density of patient 2 was the smallest. This indicated that if there were more CD20s on the surface of tumor cells, the clinical efficacy was better. However, the efficacy of patient 3 was worse than that of patient 1, while the CD20 density of patient 3 was larger than that of patient 1. This indicated that the therapy effects were not linearly proportional to the CD20 density of the tumor cells. The experimental results showed that the clinical efficacy of rituximab was to some extent related to the CD20 density, and the relationship was not linear but may be complicated.

We know that the main theory in pharmacology to characterize the efficacies of drugs is receptor theory [67]. Drugs produce therapeutic effects by binding to the receptors on the cell surface. Hence it is reasonable that when more drug molecules bind to the receptors on the cell surface, the effects become stronger. But the drug effects are not linearly proportional to the number of receptors occupied and the maximum effect can be produced by a drug when occupying just only a small proportion of the receptors [68]. The experimental results here indicated that the variance of CD20 binding affinities was not prominent among the three lymphoma patients in the study here, while the CD20 density of tumor cells was related to the efficacy of the clinical treatment. When rituximabs bind to the CD20s on the tumor cell, the Fc domains of rituximab can bind to the FcRs on the effector cells, which can then kill the tumor cells. The Fc domains of rituximab can also activate the classical complement pathway, which eventually causes the lysis of the tumor cells [17]. Compared to the binding affinity between CD20 and rituximab, the CD20 density on the cell surface may play a more important role in the rituximab's therapy effects. If there are more CD20s on the tumor cell surface, then possibly more rituximabs can bind to the cell surface and more effector cells can be recruited, which causes that the therapy effects become stronger. But there may exist a threshold of the number of CD20 on the surface of tumor cells. If the number of CD20s exceeds this threshold, the efficacies of rituximab do not increase, as the observed phenomenon of patient 1 and patient 3. Researchers [69] have investigated the relationship between CD20 expression level and rituximab-mediated cell kill and the results indicated that rituximab-induced CDC clearly depends on the CD20 expression level. While in the rituximab's killing mechanisms, rituximab displays a remarkable ability to activate complement and elicit CDC [16]. These evidence indicated that CD20 expression is closely related to the therapeutic effects of rituximab. However, exactly elucidating the mechanisms that determine the clinical efficacies of rituximab is a challenge. First, even though the rituximab's three mechanisms have been demonstrated *in vitro*, the situations *in vivo* is not unknown. Limited by the technique, we now cannot investigate the drug actions in the human body, meaning that we can only obtain conclusions by indirect methods (e.g., *in vitro* test and

animal model), which cannot reflect the real behavior in the human [70]. Second, the rituximab is typically combined with chemotherapy in the practice, and thus the contribution of rituximab to the efficacy is difficult to evaluate [71]. Third, the problem of rituximab's variable efficacies among different patients is complicated, and various aspects need to be taken into consideration, such as tumor profiling, analysis of the microenvironment, assessment of host immune effector function, and genetic polymorphisms of FcR [23]. Here, we investigated the relationship between CD20 density of tumor cells and the clinical therapy effects, and the results indicated that the therapy effects are related to the CD20 density in a certain range. However, we only investigated three clinical lymphoma cases, and more cases are needed to be investigated in the future to obtain a robust result.

In the future, we want to collect more lymphoma cases to investigate the biophysical properties of tumor cells. Besides the binding affinity and distribution of CD20 on the tumor cells, we would like to measure the binding affinity and distribution of FcRs on the effector cells (e.g., NK cell and macrophage) from the patients. We know that the efficacies of rituximab are related not only to the tumor but also to the host immune systems. In the ADCC action of rituximab, rituximab binds to the CD20 on the tumor cells, and then the Fc domain of rituximab binds to the FcR on the effectors. We can see that two types of molecular interactions occur in ADCC, including CD20–rituximab and FcR–rituximab. Many experiments have demonstrated that FcR plays a central role in the killing mechanism of rituximab [17], and several new anti-CD20 antibodies (e.g., Ofatumumab, Ocrelizumab, Veltuzumab, AME-133V, PRO131921, GA101) with enhanced FcR-mediated effector functions have been developed for clinical trials [23]. Clinical trials of these new antibodies will help us to know which mechanism of rituximab is indispensable in the therapy [26]. Consequently, simultaneously measuring the molecular interactions of CD20–rituximab and FcR–rituximab will significantly improve our understanding of rituximab action and may bring meaningful information.

17.5
Summary

Developing personalized drugs for the subpopulations of patients has become the trend of treating major diseases such as cancer, which will bring far-reaching impact on biomedical and pharmaceutical industry. The success of personalized medicine depends on having accurate diagnostic tests that indent patients who can benefit from targeted therapies [60]. However, current biochemical techniques have several serious deficiencies, such as low resolution, difficult to quantify, offline testing, and cannot reveal the heterogeneity between cells. The invention of AFM provides a powerful tool for investigating the cellular behavior at single-cell and single-molecule levels. The wide use of AFM-based SMFS technique has provided a wealth of novel knowledge about the physiological activities of single molecules on the cell surface, improving our understanding of

the underlying mechanisms that guide cellular functions. AFM has been proven to be an exciting tool for analyzing the heterogeneity between cells and will play an important role in the era of personalized medicine.

Acknowledgments

References

1. Jemal, A., Bray, F., Center, M.M., Ferlay, J., Ward, E., and Forman, D. (2011) Global cancer statistics. *CA Cancer J. Clin.*, **61**, 69–90.

2. Bray, F., Jemal, A., Grey, N., Frelay, J., and Forman, D. (2012) Global cancer transitions according to the human development index (2008-2030): a population-based study. *Lancet Oncol.*, **13**, 790–801.

3. Schwarzenbach, H., Hoon, D.S.B., and Pantel, K. (2011) Cell-free nucleic acids as biomarkers in cancer patients. *Nat. Rev. Cancer*, **11**, 426–437.

4. Patel, J.D. *et al* (2014) Clinical cancer advances 2013: annual report on progress against cancer from the American society of clinical oncology. *J. Clin. Oncol.*, **32**, 129–160.

5. Varmus, H. (2006) The new era in cancer research. *Science*, **312**, 1162–1165.

6. Shankland, K.R., Armitage, J.O., and Hancock, B.W. (2012) Non-hodgkin lymphoma. *Lancet*, **380**, 848–857.

7. Siegel, R., Naishadham, D., and Jemal, A. (2013) Cancer statistics, 2013. *CA Cancer J. Clin.*, **63**, 11–30.

8. Campo, E., Swerdlow, S.H., Harris, N.L., Pileri, S., Stein, H., and Jaffe, E.S. (2011) The 2008 WHO classification of lymphoid neoplasms and beyond: evolving concepts and practical applications. *Blood*, **117**, 5019–5032.

9. Cheson, B.D. and Leonard, J.P. (2008) Monoclonal antibody therapy for B-cell non-Hodgkin's lymphoma. *N. Engl. J. Med.*, **359**, 613–626.

10. Kuppers, R. (2005) Mechanisms of B-cell lymphoma pathogenesis. *Nat. Rev. Cancer*, **5**, 251–262.

11. Morin, R.D. *et al* (2011) Frequent mutation of histone-modifying genes in non-Hodgkin lymphoma. *Nature*, **476**, 298–303.

12. Deans, J.P., Li, H., and Polyak, M.J. (2002) CD20-mediated apoptosis: signaling through lipid rafts. *Immunology*, **107**, 176–182.

13. Boross, P. and Leusen, J.H.W. (2012) Mechanisms of action of CD20 antibodies. *Am. J. Cancer Res.*, **2**, 676–690.

14. Cragg, M.S., Walshe, C.A., Ivanov, A.O., and Glennie, M.J. (2005) The biology of CD20 and its potential as a target for mAb therapy. *Curr. Dir. Autoimmun.*, **8**, 140–174.

15. Perosa, F., Prete, M., Racanelli, V., and Dammacco, F. (2010) CD20-depleting therapy in autoimmune diseases: from basic research to the clinic. *J. Int. Med.*, **267**, 260–277.

16. Beers, S.A., Chan, C.H.T., French, R.R., Cragg, M.S., and Glennie, M.J. (2010) CD20 as a target for therapeutic type I and II monoclonal antibodies. *Semin. Hematol.*, **47**, 107–114.

17. Glennie, M.J., French, R.R., Cragg, M.S., and Taylor, R.P. (2007) Mechanisms of killing by anti-CD20 monoclonal antibodies. *Mol. Immunol.*, **44**, 3823–3837.

18. Leandro, M.J. (2013) B-cell subpopulations in humans and their differential susceptibility to depletion with anti-CD20 monoclonal antibodies. *Arthritis Res. Ther.*, **15**, S3.

19. Cartron, G., Watier, H., Golay, J., and Solal-Celigny, P. (2004) From the bench to the bedside: ways to improve rituximab efficacy. *Blood*, **104**, 2635–2642.

20. Lim, S.H., Beers, S.A., French, R.R., Johnson, P.W.M., Glennie, M.J., and Cragg, M.S. (2010) Anti-CD20 monoclonal antibodies: historical and future perspectives. *Haematologica*, **95**, 135–143.

21. Adams, G.P. and Weiner, L.M. (2005) Monoclonal antibody therapy of cancer. *Nat. Biotechnol.*, **23**, 1147–1157.

22. Molina, A. (2008) A decade of rituximab: improving survival outcomes in non-Hodgkin's lymphoma. *Ann. Rev. Med.*, **59**, 237–250.

23. Alduaij, W. and Illidge, T.M. (2011) The future of anti-CD20 monoclonal antibodies: are we making progress. *Blood*, **117**, 2993–3001.

24. Zwick, C., Murawski, N., and Pfreundschuh, M. (2010) Rituximab in high-grade lymphoma. *Semin. Hematol.*, **47**, 148–155.

25. Maloney, D.G. (2012) Anti-CD20 antibody therapy for B-cell lymphomas. *N. Engl. J. Med.*, **366**, 2008–2016.

26. Weiner, G.J. (2010) Rituximab: mechanism of action. *Semin. Hematol.*, **47**, 115–123.

27. Dupres, V., Alsteens, D., Andre, G., Verbelen, C., and Dufrene, Y.F. (2009) Fishing single molecules on live cells. *Nano Today*, **4**, 262–268.

28. Yamada, K.M. and Cukierman, E. (2007) Modeling tissue morphogenesis and cancer in 3D. *Cell*, **130**, 601–610.

29. Binning, G., Quate, C.F., and Gerber, C. (1986) Atomic force microscope. *Phys. Rev. Lett.*, **56**, 930–933.

30. Yu, X., Xu, D., and Cheng, Q. (2006) Label-free detection methods for protein microarrays. *Proteomics*, **6**, 5493–5503.

31. Dufrene, Y.F., Martinez-Martin, D., Medalsy, I., Alsteens, D., and Muller, D.J. (2013) Multiparametric imaging of biological systems by force-distance curve-based AFM. *Nat. Methods*, **10**, 847–854.

32. Li, M., Liu, L., Xi, N., and Wang, Y. (2014) Progress in measuring biophysical properties of membrane proteins with AFM single-molecule force spectroscopy. *Chin. Sci. Bull.*, **59**, 2717–2725.

33. Hinterdorfer, P. and Dufrene, Y.F. (2006) Detection and localization of single molecular recognition events using atomic force microscopy. *Nat. Methods*, **3**, 347–355.

34. Barattin, R. and Voyer, N. (2008) Chemical modifications of AFM tips for the study of molecular recognition events. *Chem. Commun.*, 1513–1532.

35. Dupres, V., Menozzi, F.D., Locht, C. et al (2005) Nanoscale mapping and functional analysis of individual adhesions on living bacteria. *Nat. Methods*, **2**, 515–520.

36. Carvalho, F.A. and Santos, N.C. (2012) Atomic force microscopy-based force spectroscopy- biological and biomedical applications. *IUBMB Life*, **64**, 465–472.

37. Grandbois, M., Beyer, M., Rief, M., Clausen-Schaumann, H., and Gaub, H.E. (1999) How strong is a covalent bond. *Science*, **283**, 1727–1730.

38. Merkel, R., Nassoy, P., Leung, A., Ritchie, K., and Evans, E. (1999) Energy landscapes of receptor-ligand bonds explored with dynamic force spectroscopy. *Nature*, **397**, 50–53.

39. Ebner, A., Wildling, L., Kamruzzahan, A.S.M., Rankl, C., Wruss, J., Hahn, C.D., Holzl, M., Zhu, R., Kienberger, F., Blaas, D., Hinterdorfer, P., and Gruber, H.J. (2007) A new, simple method for linking of antibodies to atomic force microscopy tips. *Bioconjugate Chem.*, **18**, 1176–1184.

40. Hinterdorfer, P., Baumgartner, W., Gruber, H.J., Schilcher, K., and Schindler, H. (1996) Detection and localization of individual antibody-antigen recognition events by atomic force microscopy. *Proc. Natl. Acad. Sci. U.S.A.*, **93**, 3477–3481.

41. Shi, X., Xu, L., Yu, J., and Fang, X. (2009) Study of inhibition effect of Herceptin on interaction between Heregulin and ErbB receptors HER3/HER2 by single-molecule force spectroscopy. *Exp. Cell. Res.*, **315**, 2847–2855.

42. Stroh, C., Wang, H., Bash, R., Ashcroft, B., Nelson, J., Gruber, H., Lohr, D., Lindsay, S.M., and Hinterdorfer, P.

(2004) Single-molecule recognition imaging microscopy. *Proc. Natl. Acad. Sci. U.S.A.*, **101**, 12503–12507.

43. Li, M., Liu, L., Xi, N., Wang, Y., Dong, Z., Li, G., Xiao, X., and Zhang, W. (2011) Detecting CD20-rituximab interaction forces using AFM single-molecule force spectroscopy. *Chin. Sci. Bull.*, **56**, 3829–3835.

44. Lee, C.K., Wang, Y.M., Huang, L.S., and Lin, S. (2007) Atomic force microscopy: determining of unbinding force, off rate and energy barrier for protein-ligand interaction. *Micron*, **38**, 446–461.

45. Lebien, T.W. and Tedder, T.F. (2008) B lymphocyte: how they develop and function. *Blood*, **112**, 1570–1579.

46. Mauri, C. and Bosma, A. (2012) Immune regulatory function of B cells. *Ann. Rev. Immunol.*, **30**, 221–241.

47. Barna, G., Mihalik, R., Timar, B., Tombol, J., Csende, Z., Sebestyen, A., Bodor, C., Csernus, B., Reiniger, L., Petak, I., and Matolcsy, A. (2011) ROR1 expression is not a unique marker of CLL. *Hematol. Oncol.*, **29**, 17–21.

48. Zhang, S., Chen, L., Wang-Rodriguez, J., Zhang, L., Cui, B., Frankel, W., Wu, R., and Kipps, T.J. (2012) The onco-embryonic antigen ROR1 is expressed by a variety of human cancers. *Am. J. Pathol.*, **181**, 1903–1910.

49. Li, M., Xiao, X., Liu, L., Xi, N., Wang, Y., Dong, Z., and Zhang, W. (2013) Atomic force microscopy study of the antigen-antibody binding force on patient cancer cells based on ROR1 fluorescence recognition. *J. Mol. Recognit.*, **26**, 432–438.

50. Hudecek, M., Schmitt, T.M., Baskar, S., Lupo-Stanghellini, M.T., Nishida, T., Yamamoto, T.N., Bleakley, M., Turtle, C.J., Chang, W.C., Greisman, H.A., Wood, B., Maloney, D.G., Jensen, M.C., Rader, C., and Riddell, S.R. (2010) The B-cell tumor-associated antigen ROR1 can be targeted with T cells modified to express a ROR1-specific chimeric antigen receptor. *Blood*, **116**, 4532–4541.

51. Casuso, I., Rico, F., and Scheuring, S. (2011) Biological AFM: where we come from – where we are – where we may go. *J. Mol. Recognit.*, **24**, 406–413.

52. Suzuki, A., Sekiya, S., Onishi, M., Oshima, N., Kiyonari, H., Nakauchi, H.,

and Taniquchi, H. (2008) Flow cytometric isolation and clonal identification of self-renewing bipotent hepatic progenitor cells in adult mouse liver. *Hepatology*, **48**, 1964–1978.

53. Li, M., Liu, L.Q., Xi, N., Wang, Y., Dong, Z., Xiao, X., and Zhang, W. (2013) Atomic force microscopy imaging of live mammalian cells. *Sci. China Life Sci.*, **56**, 811–817.

54. Ando, T. (2012) High-speed atomic force microscopy coming of age. *Nanotechnology*, **23**, 062001.

55. Zhang, J., Wu, G., Song, C., Li, Y., Qiao, H., Zhu, P., Hinterdorfer, P., Zhang, B., and Tang, J. (2012) Single molecular recognition force spectroscopy study of a luteinizing hormone-releasing hormone analogue as a carcinoma target drug. *J. Phys. Chem. B*, **116**, 13331–13337.

56. Puntheeranurak, T., Wildling, L., Gruber, H.J., Kinne, R.K.H., and Hinterdorfer, P. (2006) Ligands on the string: single-molecule AFM studies on the interaction of antibodies and substrates with the Na+-glucose co-transporter SGLT1 in living cells. *J. Cell Sci.*, **119**, 2960–2967.

57. Carvalho, F.A., Connell, S., Miltenberger-Miltenyi, G., Pereira, S.V., Tavares, A., Ariens, R.A.S., and Santos, N.C. (2010) Atomic force microscopy-based molecular recognition of a fibrinogen receptor on human erythrocytes. *ACS Nano*, **4**, 4609–4620.

58. Li, Y., Qiao, H., Yan, W., Zhang, J., Xing, C., Wang, H., Zhang, B., and Tang, J. (2013) Molecular recognition force spectroscopy study of the dynamic interaction between aptamer GBI-10 and extracellular matrix protein tenascin-C on human glioblastoma cell. *J. Mol. Recognit.*, **26**, 46–50.

59. Muller, D.J., Helenius, J., Alsteens, D., and Dufrene, Y.F. (2009) Force probing surfaces of living cells to molecular resolution. *Nat. Chem. Biol.*, **5**, 383–390.

60. Humburg, M.A. and Collins, F.S. (2010) The path to personalized medicine. *N. Engl. J. Med.*, **363**, 301–304.

61. Li, M., Xiao, X., Liu, L., Xi, N., Wang, Y., Dong, Z., and Zhang, W. (2013) Nanoscale mapping and organization analysis of target proteins on cancer cells

from B-cell lymphoma patients. *Exp. Cell. Res.*, **319**, 2812–2821.

62. Sanchez, S.A., Tricerri, M.A., and Gratton, E. (2012) Laurdan generalized polarization fluctuations measures membrane packing micro-heterogeneity in vivo. *Proc. Natl. Acad. Sci. U.S.A.*, **109**, 7314–7319.

63. Lingwood, D. and Simons, K. (2010) Lipid rafts as a membrane-organizing principle. *Science*, **327**, 46–50.

64. Casuso, I., Khao, J., Chami, M., Paul-Gilloteaux, P., Husain, M., Duneau, J.P., Stahlberg, H., Sturgis, J.N., and Scheuring, S. (2012) Characterization of the motion of membrane proteins using high-speed atomic force microscopy. *Nat. Nanotechnol.*, **7**, 525–529.

65. McMahon, H.T. and Gallop, J.L. (2005) Membrane curvature and mechanisms of dynamic cell membrane remodeling. *Nature*, **438**, 590–596.

66. Li, M., Xiao, X., Zhang, W., Liu, L., Xi, N., and Wang, Y. (2014) Nanoscale distribution of CD20 on B-cell lymphoma tumour cells and its potential role in the clinical efficacy of rituximab. *J. Microsc.*, **254**, 19–30.

67. Kenakin, T. (2004) Principles: receptor theory in pharmacology. *Trends Pharmacol. Sci.*, **25**, 186–192.

68. Stephenson, R.P. (1956) A modification of receptor theory. *Br. J. Pharmacol.*, **11**, 379–393.

69. van Meerten, T., van Rijn, R.S., Hol, S., Hagenbeek, A., and Ebeling, S.B. (2006) Complement-induced cell death by rituximab depends on CD20 expression level and acts complementary to antibody-dependent cellular cytotoxicity. *Clin. Cancer Res.*, **12**, 4027–4035.

70. Junttila, M.R. and Sauvage, F.J.D. (2013) Influence of tumour micro-environment heterogeneity on therapeutic response. *Nature*, **501**, 346–354.

71. Rezvani, A.R. and Manoney, D.G. (2011) Rituximab resistance. *Best Pract. Res. Clin. Haematol.*, **24**, 203–216.

18

Flexible Robotic AFM-Based System for Manipulation and Characterization of Micro- and Nano-Objects

Hui Xie and Stéphane Régnier

It is well known that pick-and-place is very important for three-dimensional (3D) microstructure fabrication since it is an indispensable step in the bottom-up building process [1–3]. The main difficulty in sufficiently completing such pick-and-place manipulation at this scale lies in fabricating a very sharp end-effector that is capable of smoothly releasing micro-objects deposited on the substrate. Moreover, this end-effector has to provide enough grasping force to overcome strong adhesion forces [4–6] from the substrate as well as being capable of sensing and controlling interactions with the micro-objects. Furthermore, compared with the manipulation of larger micro-objects under an optical microscope, visual feedback at several microns more suffers from shorter depth of focus and narrower field of view of lenses with high magnifications, although different schemes or algorithms have been introduced on techniques of autofocusing [7, 8] and extending focus depth [9]. Compared with vision-based automated two-dimensional (2D) micromanipulation, automated 3D micromanipulation at the scale of several microns to submicrons is more challenging because of optical microscope's resolution limit (typically 200 nm). Moreover, additional manipulation feedback is needed that is beyond the capability of optical vision, such as in the cases of vertical contact detection along the optical axis or manipulation obstructed by opaque components. Therefore, multifeedback is of vital importance to achieve such accurate and stable 3D micromanipulation at the scale of several microns to submicrons.

Pick-and-place nanomanipulation is also a promising technique in 3D nanostructure fabrication, since it is an indispensable step in the bottom-up building process. It can overcome limitations of bottom-up and top-down methods of nanomanufacturing and further combine advantages of these two methods to build complex 3D nanostructures. In literature, nanostructures have been manipulated, assembled, and characterized by integrating nanomanipulators or nanogrippers into scanning electron microscopes (SEMs) and transmission electron microscopes (TEMs) [10–14]. Both SEMs and TEMs provide a vacuum environment where the van der Waals force is the main force to be overcome during the manipulation. 3D nanomanipulation could be also achieved with optical tweezers in liquid, where the adhesion forces are greatly

reduced [15−17]. However, the pick-and-place nanomanipulation in air is still a great challenge due to the presence of strong adhesion forces, including van der Waals, electrostatic, and capillary forces [18]. In this case, the main difficulties in achieving the 3D nanomanipulation are fabricating sharp end-effectors with enough grasping force, as well as capabilities of force sensing while controlling interactions between the nano-object and the tool or the substrate.

Peeling force measurement at the nanoscale is also clearly of interest and crucial for measuring adhesive strength of micro- and nanoscopic bonding of nanostructures [19], for example, interfacial energy measurement for reinforcement of composite materials [20−23], bionanotechnology characterization [23−25], and fabrication of nanostructures and nanodevices [26−33]. The peeling test of nanostructures is thus a necessity to understand the interfacial phenomena at the nanoscale contact.

Unfortunately, it is generally hard to perform a nanoscale mechanical peeling test, which requires facilities with capabilities to locate, manipulate, and displace nanostructures with nanoscale precision ($\sim$ nm) while sensing extremely small peeling forces ($\sim$ nN). As a uniquely suitable facility capable of nanoscale surface imaging and ultrasmall force sensing, the conventional atomic force microscope (AFM) in the past two decades has succeeded in manipulating nanoparticles [34−36], single molecules [37], nanorods [38], and nanotubes [39] by typical used in-plane pushing or pulling manipulation. However, the nanoscale peeling force measurement, which typically requires out-of-plane manipulation, is still a challenge. Up to now, a few nanoscale peeling research have been carried out. For instance, nanoscale peeling methods were developed to successfully peel multiwalled carbon nanotubes (MWCNTs) attached to the end of a tipless microcantilever [19] in an AFM or the tip of a self-detective microcantilever [40] integrated in a SEM that enables a so-called visualized nanoscale peeling process. The current methods might require strenuous labors of sample preparations by sorting straight MWCNTs out and then attaching them on the microcantilevers. An effective peeling tool is thus necessarily to be developed to facilitate the nanoscale peeling tests.

In addition, cell adhesion is mainly responsible for tissue cohesion and dynamic regulation of adhesion and de-adhesion processes, which enable tissue remodeling and cell migration. These interactions are fundamental to physiological and physiopathological processes. Numerous methods have been developed to qualitatively and quantitatively analyze cell adhesion. Microscopy-based methods have been utilized to qualitatively analyze cell adhesion. For instance, fluorescence resonance energy transfer has been used to determine the composition for dynamic protein−protein interactions [41]. Semiqualitative methods have been used to determine cell adhesion in biomaterial research. Washing is a commonly used method [42, 43], in which nonattached or weakly attached cells on the substrate are washed away by flow, and the percentage of cells still attached on the substrate can be determined. To elaborately control the detaching process, better-controlled hydrodynamic shear forces [44, 45], or centrifugal force [46] has been

used to analyze cell adhesion. The cells are laterally sheared off by forces parallel to the substrate. One major drawback of these techniques is the dependence of shear forces on cell geometry, size, and cell−substrate attachment. Thus, shear forces are not uniformly distributed along the cell surface or vary from different cells.

In order to analyze cell adhesion quantitatively and in detail, methods have been developed to directly measure cell−cell and cell−substrate adhesion forces by single-cell force spectroscopy (SCFS) [47]. Quantitative data have been obtained using magnetic tweezers [48, 49], optical tweezers [50, 51], and femtosecond laser impulses [52]. The maximum vertical force of hundreds of piconewtons that can be performed with magnetic and optical tweezers restricts measurement of cell−substrate adhesion from hundreds of nanonewtons to micronewtons. Alternatively, micropipettes [53, 54] and nanoforks [55] have been used to detach cells, but their applications are limited because of the difficulty to analyze the adhesion process in detail. By contrast, AFM has been proven to be important in characterizing living biological samples because of its high spatial resolution and ability to work in different conditions (e.g., in aqueous environments). AFM-based SCFS uses a single cell attached to an AFM cantilever and probed on the substrate [56−59] or another single cell [60−63] for cell−cell and cell−substrate adhesion force measurement, respectively. Detaching forces of cell adhesion ranging from 10 pN to 10^6pN can be recorded by this method [47]. Functionalized AFM probes have been used to alternatively probe a single cell immobilized on the substrate [64−66]. The mechanism by which surface chemistry or topography affects cell adhesion can be elucidated.

AFM-based SCFS still has some limitations despite its versatility and strength. One of them is the poor outcome because the current protocols for attaching a living cell or biomaterials to an AFM cantilever are labor intensive and require specific expertise [58], thus limiting the measurements to a few cells per day [66]. These procedures must be repeated to detach the cell from the cantilever with specific chemicals for new testing, or replace the functionalized cantilever because the surface becomes restructured and contaminated with debris from the cell [67]. When the contact time exceeds 20 min, the cell−substrate adhesion force measurement becomes difficult because the existing thermal drifts among the cell, cantilever, and substrate are hardly determined; cell−substrate adhesion may become stronger than the adhesion of the cell to the AFM cantilever [58]. Therefore, faster, more accurate, and more skillful approaches and manipulation systems for cell adhesion measurement are necessary.

In this chapter, we present a novel flexible robotic AFM-based system for micro- or nanomanipulation, in situ nanoscale peeling of one-dimensional (1D) nanostructures using a dual-probe nanotweezer, and in situ quantification of cell−cell and cell−substrate adhesion forces.

18.1
AFM-Based Flexible Robotic System for Micro- or Nanomanipulation

18.1.1
The AFM-Based Flexible Robotic System

18.1.1.1 The Flexible Robotic Setup

Figure 18.1a shows the system setup, which is in the configuration for nanoscale pick-and-place. The system is equipped with an optical microscope and two sets of modules commonly used in a conventional AFM, mainly including two AFM cantilevers (namely, tip I and tip II, ATEC−FM Nanosensors, see Figure 18.1b), two sets of nanopositioning devices and optical levers. The motion modules include an open-loop X-Y-Z piezoscanner (PI P-153.10H), an X-Y-Z closed-loop nanostage (MCL Nano-Bio2M on the X- and Y-axes, PI P−732.ZC on the Z-axis), an X-Y-Z motorized stage, and an X-Y-Z manual stage. Detailed specifications of the motion modules are summarized in Table 18.1. A data acquisition (NI 6289) card is used for high-speed ($500 \sim 800$Hz of sampling frequency for force and 600 kHz for amplitude) capture of the photodiode voltage output to estimate deflections on both tips induced by force loading or resonant oscillation. A multithread planning and control system based on the C + + is developed for AFM image scan and two-tip coordination control during manipulation. This control system enables programming of complex tasks on the highly distributed reconfigurable system.

18.1.1.2 Force Sensing during Pick-and-Place

Figure 18.2 shows a schematic diagram of the nanotip gripper for the micro- or nanoscale pick-and-place operation that has a clamping angle $\theta \approx 44°$ micro- or
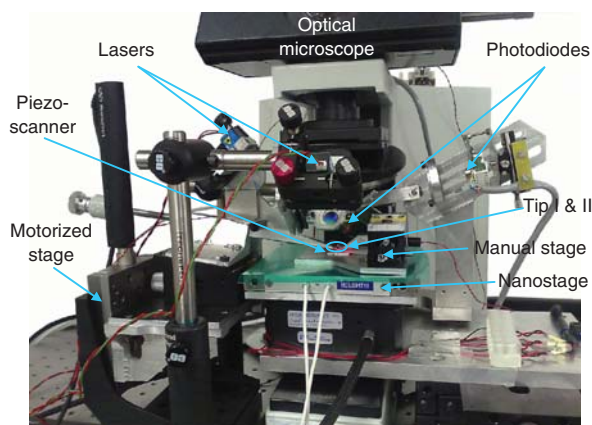
(a)
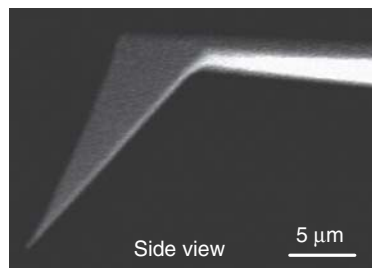
(b)

Figure 18.1 (a) A photo of the flexible robotic system on the configuration for nanoscale pick-and-place manipulation. (b) A SEM image of the cantilever fabricated with a protruding tip.

Table 18.1 Specifications of each motion module.

Actuator	Travel range	Resolution
X-Y-Z piezoscanner	$10 \times 10 \times 10$ (μm)	sub-nm
X-Y-Z nanostage	$50 \times 50 \times 10$ (μm)	0.1 nm
X-Y-Z motorized stage	$25 \times 25 \times 25$ (mm)	50 nm
X-Y-Z manual stage	$5 \times 5 \times 5$ (mm)	0.5 μm

Figure 18.2 Schematic diagram of the nanotip gripper and force simulation during the pickup manipulation.

nanoscale pickup manipulation, for instance, interactive forces applied on tip I include repulsive forces F_{r1}, friction forces F_{f1}, and adhesive forces F_{a1}.

The forces applied on tip I can be resolved into two components on the *X*-axis and *Z*-axis in the defined frame, namely, F_{x1} and F_{z1}, respectively. F_{x1} is the clamping force that holds the micro- or nano-object. F_{z1} is the pickup force that balances adhesion forces from the substrate. In order to sense the pickup force, it is necessary to know the normal deflection on both cantilevers. The normal deflection ζ_{n1} associated with the normal voltage output of the optical lever on tip I is given by

$$\zeta_{n1} = \frac{F_{z1}\cos\gamma + F_{x1}\sin\gamma}{k_n} + \frac{F_{z1}\sin\gamma + F_{x1}\cos\gamma}{k_{xz}}, \qquad (18.1)$$

where γ is the mounting angle of the cantilever and $k_{xz} = 2lk_n/3h$ is the bending stiffness due to the moment applied on the tip end, where h is the tip height. Assuming the magnitudes of F_{z1} and F_{x1} are of the same order, contributions from the F_{x1} to the normal deflection of tip I are relatively very small since $k_{xz} \gg k_n$ and $\gamma = 5°$. Therefore, the normal deflection induced from F_{z1} is only considered in the following calculations of the adhesion force F_a applied on the micro- or

nano-object. Thus, F_{z1} can be simplified by estimating the normal voltage output ΔV_{n1} from the tip I:

$$F_{z1} = \beta_1 \times \Delta V_{n1}, \tag{18.2}$$

where β_1 is the normal force sensitivity of the optical lever. A similar pickup force F_{z2} can be also obtained on tip II. Before the gripper pulls off the substrate, the adhesion force F_a can be estimated as

$$F_a = F_{z1} + F_{z2} = \beta_1 \Delta V_{n1} + \beta_2 \Delta V_{n2} - (F_{a1} + F_{a2}), \tag{18.3}$$

where β_2, ΔV_{n2}, and F_{a2} are respectively the normal force sensitivity, normal voltage output, and adhesive force on tip II. Once the gripper pulls off the substrate, for example, in the case of nanowire/tube pick-and-place, the adhesion force F_a is estimated as

$$F_a = F_{z1} + F_{z2} = \beta_1 \Delta V_{n1} + \beta_2 \Delta V_{n2} \tag{18.4}$$

18.1.2
Experimental Results

18.1.2.1 **3D Micromanipulation Robotic System**
 As the size of micro-objects is reduced to several microns or submicrons, problems will arise with these conventional grippers: (i) Sticking phenomena become more severe due to the relatively larger contact area between the gripper and the micro-object. (ii) The tip diameters of the microfabricated clamping jaws are comparable in size to the micro-objects to be grasped. Conventional grippers are not geometrically sharp enough to pick up micro-objects of several micrometers deposited on the substrate. Fortunately, the AFM tip has a very tiny apex (typically ~ 10 nm in radius) with respect to the size of the micro-object to be manipulated. Thus, the nanotip gripper can be used to achieve pick-and-place at the scale of several microns since the contact area of the gripper micro-object is much smaller than the micro-object–substrate contact. Moreover, real-time force sensing makes the manipulation more controllable.

As shown in Figure 18.3a, the system configuration for 3D micromanipulation is reconfigured as follows:

1) For a large manipulation travel range, the nanostage here is used to support the sample platform and transport the micro-object during the manipulation.
2) Tip I, immovable during the pick-and-place micromanipulation, is fixed on the motorized stage for coarse positioning.
3) Tip II is actuated by the piezoscanner for gripper opening and closing operations. The piezoscanner is supported by the manual stage for coarse positioning.

Benefiting from AFM-based accurate and stable amplitude feedback of a dithering cantilever, the grasping state can be successfully achieved by the amplitude feedback, with very weak interaction at the nanonewton scale,
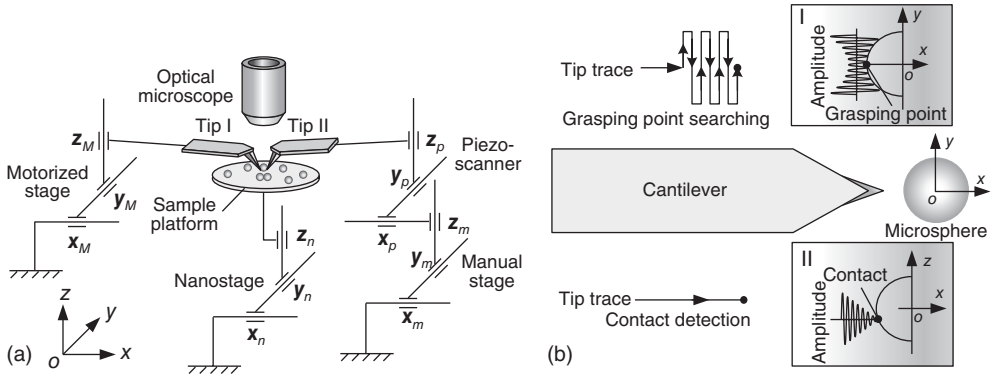
Figure 18.3 (a) A kinematic configuration and (b) schematic diagrams for 3D micromanipulation at scales of several micrometers or grasping point searching (inset I) and contact detection (inset II) with amplitude feedback of the dithering cantilever.

protecting the fragile tips and the micro-objects from damage during manipulation. As shown in inset I of Figure 18.3b-(I), the dithering cantilever with its first resonant mode is used to locate grasping points and detect contact. When approaching the microsphere with a separation between the tip and the substrate (typically 500 nm), the tip laterally sweeps the microsphere over the lower part of the microsphere. By this means, the grasping point can be accurately found by locating the minimum amplitude response of each single scan.

From the scheme depicted in inset II of Figure 18.3b-(II), the amplitude feedback is also used for contact detection. Tip–microsphere contact is detected as the amplitude reduces to a steady value close to zero. As shown in Figure 18.4a, a protocol for pick-and-place microspheres mainly consists of four steps:

- *System initialization and task planning:* Each axis of the nanostage and the piezoscanner are set in a proper position, supplying the manipulation with enough travel range on each axis. Then the task is planned in Figure 18.4a-(I) with a global view of the manipulation area that provides coarse positions of the microspheres and tips.
- *Making tip I-microsphere in contact:* In Figure 18.4a-(II), tip I is started to approach the microsphere by moving the nanostage with amplitude feedback to search for the grasping point and detect contact.
- *Forming the gripper:* Similarly, tip II approaches the microsphere by moving the piezoscanner. Once tip II and the microsphere are in contact, a nanotip gripper is configured in Figure 18.4a-(III) for a manipulation.
- *Pick-and-place micromanipulation:* In Figure 18.4a-(IV), the microsphere is picked up, transported, and released by moving the nanostage with a proper displacement on each axis that depends on the diameter of the microsphere and its destination. The whole process of 3D micromanipulation is monitored by real-time force sensing.
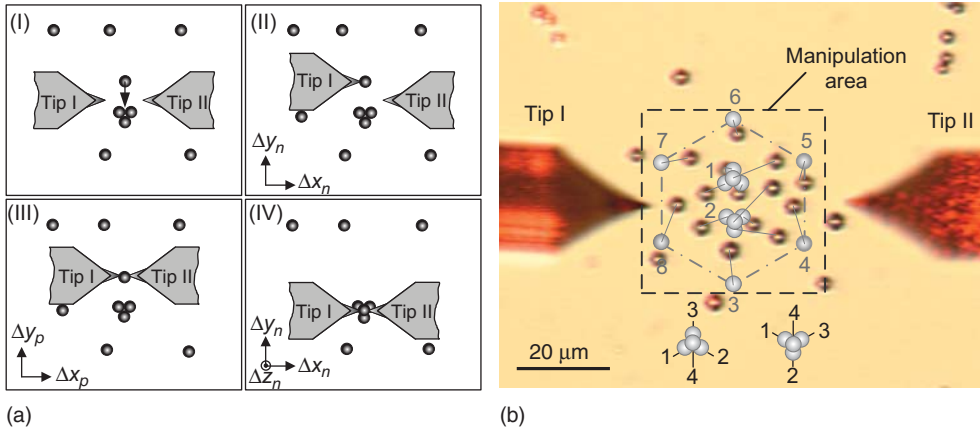
Figure 18.4 Microsphere manipulation protocol. (a) (I)Task planning; (II) Tip I and the microsphere are in contact; (III) The nanotip gripper is formed; (IV) Pick up and release the microsphere to its target position. (b) Task descriptions of the microsphere assembly.

Nylon microspheres with diameter of about 3∼4 µm were manipulated to build 3D microstructures in experiments. The microspheres were deposited on a freshly cleaned glass slide and then an area of interest was selected under the optical microscope. Figure 18.4b shows a plan view of the selected area, in which 14 microspheres separated in a 50-µm square frame are going to be manipulated to build two 3D micropyramids and a regular 2D hexagon labeled by assembly sequences from 1 to 8. Each pyramid is constructed from four microspheres with two layers, and the assembly sequences are shown in the bottom insets for two different arrangements of the pyramids.

Figure 18.5a shows a result of grasping point searching, in which the dithering tip II laterally sweeps the microsphere within a range of 1.75 µm on the y-axis and with a free oscillating amplitude of about 285 nm. Ten different distances to the microsphere were tested from 100 to 10 nm with an interval of 10 nm and, consequently, the grasping point is well located with an accuracy of ±10 nm. Figure 18.5b shows a full force spectroscopy curve during the pick-and-place of a microsphere deposited on a glass slide with an ambient temperature of 20 °C and relative humidity of 40%. In this curve, point A represents the start of the pick-and-place; point B, the pull-off location of the microsphere−substrate contact; point C, nonlinear force restitution due to the tip-microsphere frictions; and point D, the snap-in point between the microsphere and the substrate. The force spectroscopy curve is synthesized from force responses on tip I and tip II.

Figure 18.6 shows an automated microassembly result consisting of two 3D micropyramids and a 2D pattern of a regular hexagon. The whole manipulation process was completed in 11 min, so the average manipulation time for each microsphere is about 47 s, which mainly breaks down in about 20 s for
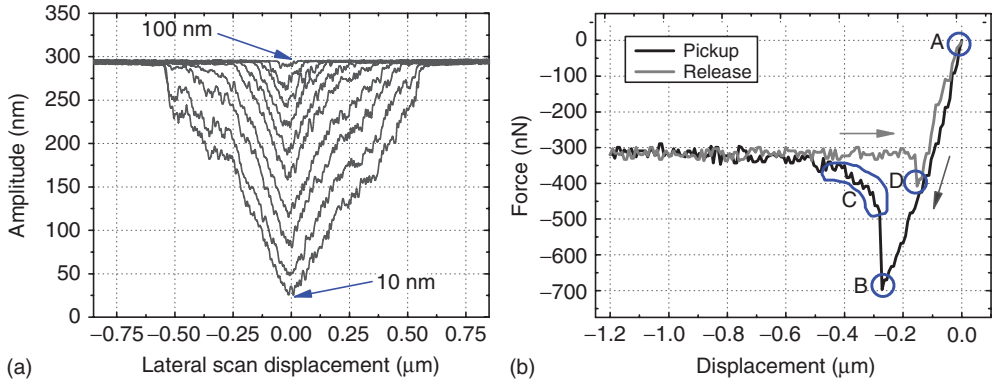
Figure 18.5 Experimental results. (a) Amplitude responses on tip II when searching the grasping points. (b) Synthesized normal force responses from both the tips in the pick-and-place micromanipulation.
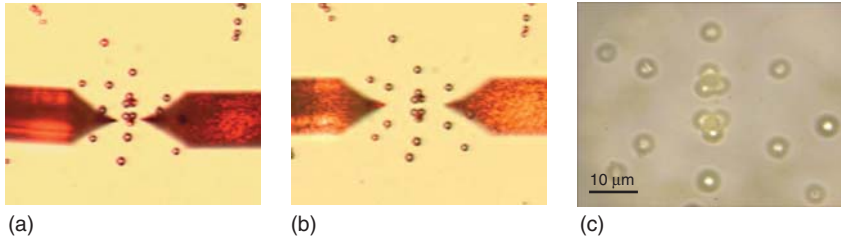
Figure 18.6 A microassembly result. (a) Before the microassembly. (b) Micropyramids were built. (c) Enlarged image of the microassembly result under a magnification of 100×.

microsphere grasping, including the grasping point search and contact detection processes using amplitude feedback, 10~35 s for microsphere release, and the remaining time for transport.

Assembly of the fourth is the key to success in building a micropyramid. During pick-and-place of the fourth microsphere, microscopic vision was firstly used for coarse positioning of the target, then the normal force feedback of the gripper was used to detect the vertical contact between the fourth microsphere and other three microspheres on the base. When the contact is established, a small vertical force was applied on the fourth microsphere by moving the nanostage upward and it will adjust to contact with all the base microspheres.

18.1.2.2 3D Nanomanipulation Robotic System

Compared with the 3D micromanipulation, tip alignment precision is the key factor in succeeding the nanoscale pick-and-place. Therefore, the closed-loop nanostage is considered in this configuration for accurate tip alignment. As shown in
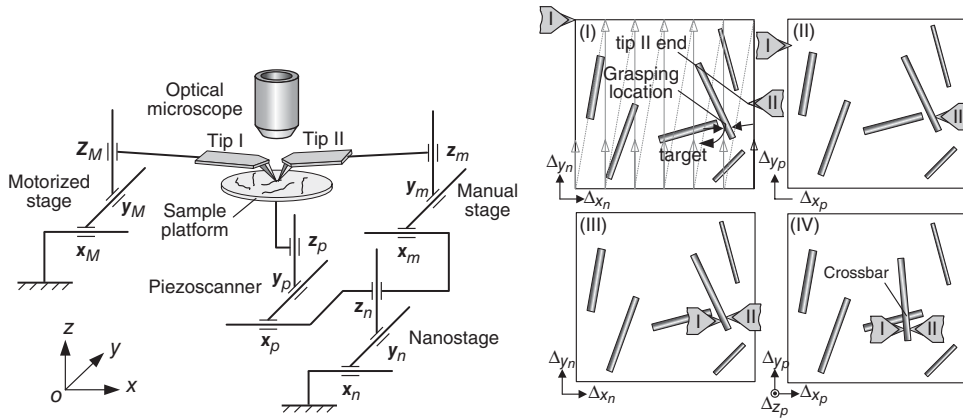
Figure 18.7 (a) A kinematic configuration of the AFM-RFS for nanoscale pick-and-place. (b) Protocol for nanowire pick-and-place: (I) Image scan for task planning; (II) Tip II is in contact with the nanowire; (III) Tip I is in contact with the nanowire, forming a nanotip gripper; and (IV) Pick up and release a nanowire to its target position.

Figure 18.7a, the system configuration for 3D nanomanipulation is reconfigured as follows:

1) The nanostage is used for image scan with tip I.
2) Nano-objects are supported and transported by the piezoscanner.
3) Tip I, fixed on the motorized stage for coarse positioning, is immovable during the pick-and-place micromanipulation. Before manipulation, cantilever I acts as an image sensor for nano-object positioning.
4) For accurate gripper alignment between tip I and tip II, tip II is fixed on the nanostage rather than the piezoscanner. Tip II is supported by the manual stage for coarse positioning.

Nanowires and nanotubes are being intensively investigated. Thus, a protocol is developed here for nanowire or nanotube pick-and-place. However, applications can easily be extended to, for example, pick-and-place of nanorods or nanoparticles dispersed on a substrate.

Once the manipulation area is selected under the optical microscope, both the tips are aligned as a quasi-gripper above the center of the manipulation area. Each axis of the nanostage and the piezoscanner is initialized at an appropriate position to allow for enough manipulation motion travel.

In this step, tip I is used to fully scan the relevant area obtaining a topographic image that contains nano-objects to be manipulated and the end of tip II. Figure 18.7b-(I) shows a simulated image that contains the topography of two nanowires and the end of tip II. The image provides the following pick-and-place with relative positions between tip I, tip II, and the nano-objects to be manipulated. However, after a long-period image scan, relocating tip II is recommened to eliminate the system's thermal drift.

As shown in Figure 18.7b-(II), tip II approaches the nanowire to make contact by moving the X-axis of the piezoscanner. A gap (typically ∼20 nm above the snap-in boundary) between tip II and the substrate should be maintained during the approach to enable a negative deflection response in the form of a tiny force applied on tip II, and hence, sensitive detection of the tip−nanowire contact.

Similarly, in Figure 18.7b-(III), once tip I is in contact with the nanowire, a nanotip gripper is configured for pick-and-place manipulation of the nanowire.

The nanotip gripper in this step is used to pick up, transport, and release the nanowire to its target position by moving the piezoscanner on the X-, Y-, or Z-axis. The displacement on each axis depends on the dimensions of the nanowire and the location of the destination. Figure 18.7b-(VI) shows a simulated postmanipulation image, in which a nanowire crossbar is built. The complete pick-and-place procedure is monitored by force sensing.

In experiments, silicon nanowires (SiNWs) were deposited on a freshly cleaned silicon wafer coated with 300-nm silicon dioxide. AFM images show that the SiNWs have a taper shape and have diameters of 25 nm (top) ∼200 nm (root) and lengths of about 4∼7 μm.

Figure 18.8a shows an example of the contact detection with tip II: Point A and point C are where the tip contacts with the SiNW and the Si substrate, respectively; Point B and point D are where the tip breaks the contact with the Si substrate and the SiNW, respectively. Figure 18.8b shows a curve of the peeling force spectroscopy on tip II for the pick-and-place manipulation of the SiNW: Point A and point B are where the tip snaps in and pulls off the Si substrate, respectively. The shape of curve of the force responses on tip I are similar except for the force magnitude due to different force sensitivities on each tip and uneven grasping due to asymmetric alignment of the SiNW relative to the grasping direction. This force spectroscopy during the pickup operation shows stable grasping for further SiNW transport.

Figure 18.9 shows an experimental result of 3D SiNW manipulation. A prescanned image (9 μm × 9 μm) is shown in Figure 18.9a, which includes the topographic image of SiNWs and the local image of tip II. A grasping location of the nanowire to be manipulated is marked with a−a, where the SiNW has a height of 160 nm. Figure 18.9b is a postmanipulation image. It can be seen that the SiNW has been successfully transported and piled onto another SiNW. The manipulation procedure is described as follows. Once the SiNW was reliably grasped, the piezoscanner moved down 560 nm at a velocity of 80 nm s^{-1}. In this step, the SiNW was transported a distance of 4.4 μm along the X-axis at a velocity of 120 nm s^{-1} and 0.12 μm along the Y-axis at a lower velocity of 3.3 nm s^{-1}. In the releasing step, the piezoscanner moved up at a velocity of 100 nm s^{-1}. As tip II was slightly bent upward leading to a positive response of 0.015 V, tip I and tip II were separated by moving both the nanostage and the piezoscanner on the X-axis to release the SiNW from the nanotip gripper.

(a)

(b)
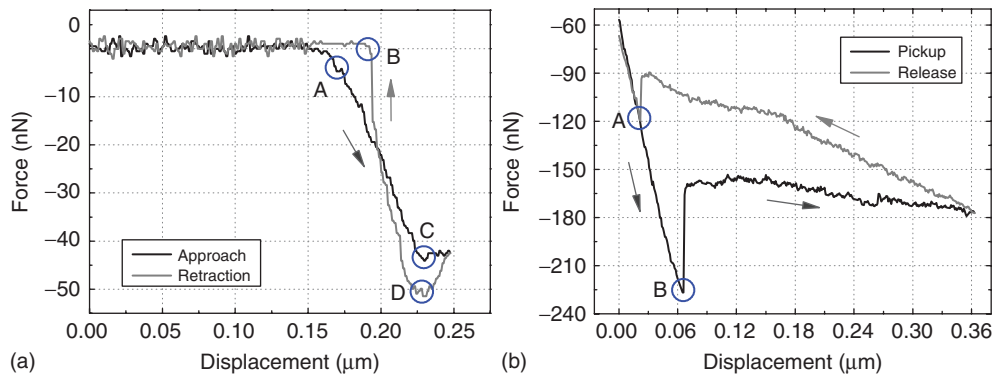
Figure 18.8 Contact and force detection. (a) Contact detection on the SiNW with tip II. (b) Force detection on tip II during the pick-and-place nanomanipulation of the SiNW.

(a)

(b)
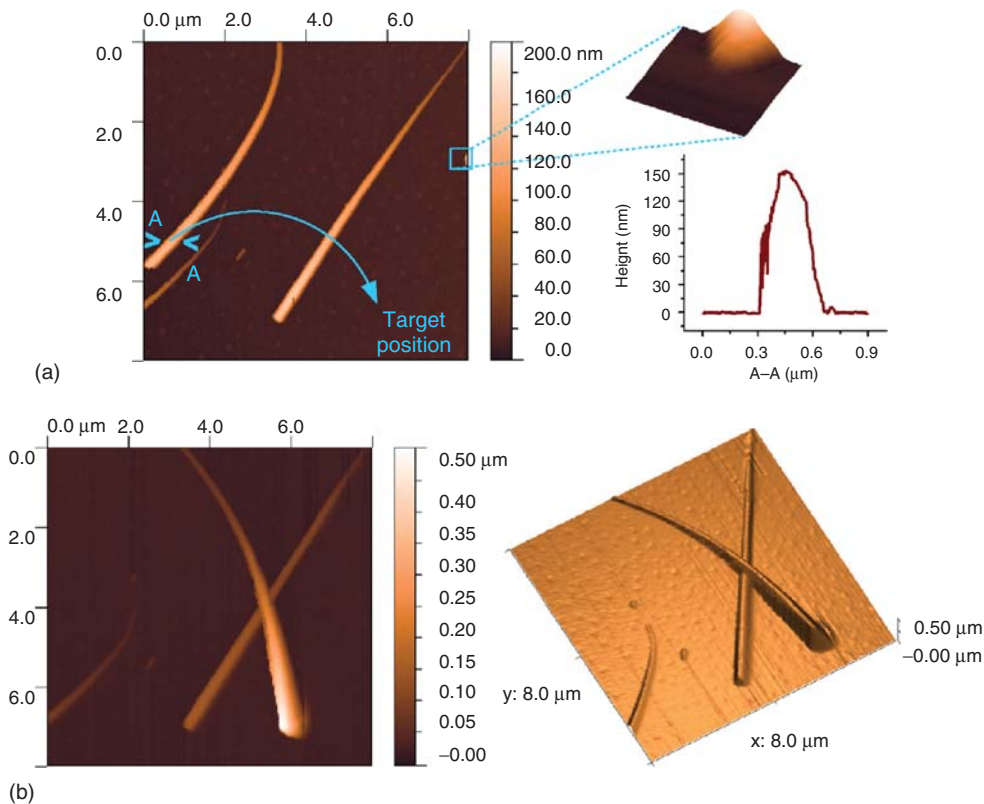
Figure 18.9 Pick-and-place results of the SiNWs. (a) A prescanned image, in which a–a and G are the grasping location and the target position, respectively. Inset: AFM image of tip II end and nanowire profile extracted from the grasping location. (b) A postmanipulation image verifies that the manipulated SiNW is piled upon another nanowire deposited on the Si substrate.

18.1.3
Conclusion

We have developed an AFM-based robotic system for multiscale micro- or nanomanipulation and assembly applications. Using AFM-based accurate force sensing and the tiny apex of the AFM tip, a nanotip gripper able to pick and place very tiny samples was constructed. Using this nanotip gripper, 3D manipulation from the nanoscale to the scale of several microns was achieved.

18.2
In situ Peeling of 1D Nanostructures Using a Dual-Probe Nanotweezer

18.2.1
Methods

The nanotweezer is formed by two force modulation microcantilevers (NANOSENSORS ATEC-FM, with a nominal stiffness of 2.8 N m^{-1}). Forces on each cantilever are independently detected by its own optical lever, which is typically composed of a laser and a quartered photodiode. The calibrated [68] open-loop X-Y-Z piezotube (PI P-153.10H) in this configuration is removed from the system base and then fixed on the closed-loop X-Y-Z nanostage (MCL Nano-Bio2M on X- and Y-axes, PI P-732.ZC on Z-axis) to form a dual-driven nanopositioning stage. This stage can be used for image scanning, nanotweezer aligning, and nano samples handling with a specially developed control system. The left microcantilever (probe I) is fixed to the base, while the right microcantilever (probe II) is actuated by the nanostage. The proposed dual-probe nanotweezer is capable of the nanoscale peeling thanks to the following:

1) In comparison with the normal diameter of 1D nanostructures to be peeled, the tip apex of the probe is very tiny (typically with an apex radius of 10 nm or less), which leads to a geometrical condition for grasping at the nanoscale as well as smaller adhesive forces between the nanotweezer and the 1D nanostructures that favor the release process.

2) More importantly, the nanotweezer can be used as a normal AFM to image the 1D nanostructures, as well as to locate the probes for tweezer alignment. This function makes it possible to perform nanoscale grasping without visual feedback (normally in scanning and transmission electron microscopes) in ambient conditions.

Figure 18.10 shows a schematic diagram of the peeling test of 1D nanostructures with the proposed nanotweezer. Figure 18.10a and b respectively shows the peeling occurring at the end and the middle of a 1D nanostructure. For stiff 1D nanostructures, peeling locations can be at either the end or the middle, whereas for soft 1D nanostructures, notably with a small diameter or a long length, or made up of soft materials, the peeling location is recommended at the middle to avoid
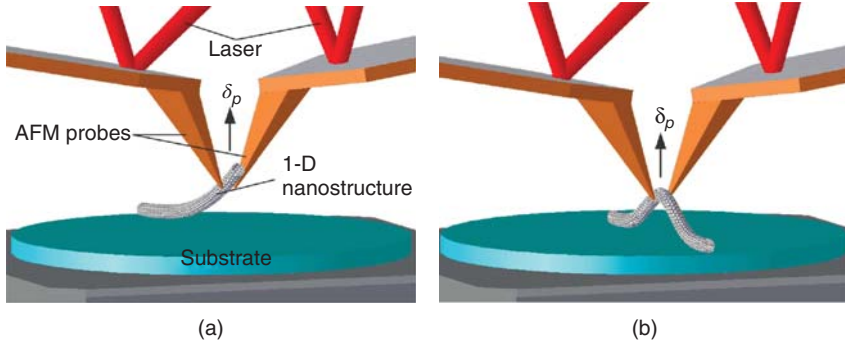
Figure 18.10 A schematic diagram of a 1D nanostructure peeling force measurement using the dual-probe nanotweezer. (a) Peeling occurs at the end of the 1D nanostructure. (b) Peeling occurs at the middle of the 1D nanostructure. δ_p is the gap between the substrate and the peeling location on the 1D nanostructure. The peeling process is performed by moving the piezotube on the Z-axis while the nanotweezer is fixed. The peeling force is synthesized from bending forces on both cantilevers that are individually detected by their own optical levers.

sliding off from the nanotweezer during the peeling process. A peeling protocol using the dual-probe nanotweezer can be summarized as follows: [i)]

1) First, testing 1D nanostructures and the end of probe II are accurately located by image scan with probe I by moving the nanostage.
2) Once the target 1D nanostructure and peeling locations are determined from the scanned image, the nanotweezer is formed and then approaches to the target peeling location by moving the piezotube and the nanostage alternately.
3) Peeling test is started by moving the piezotube on the Z-axis when a reliable grasping on the nanostructure is detected with force monitoring. For peeling energy computation, peeling forces are recorded during the whole procedure of the test.

Figure 18.11a and b respectively shows elastic deformations of a 1D nanostructure when the peeling occurs at the end and the middle. The gap between the peeling location and the substrate is defined as δ_p, while F_p is the peeling force applied by the nanotweezer at the peeling location. The parameter $z(x)$ describes the gap along the 1D nanostructure from the substrate. As a peeling force computation model shown in Figure 18.11c, F_p can be calculated from the microcantilever's stiffness k_n and deflection δ_n by $F_p = 2k_n\delta_n$. In the models, δ_t is the peeling distance on the nanotweezer that can be described as a sum of δ_p and microcantilever's deflection δ_n. In the actual use, δ_p cannot be directly measured. Instead, $F_p - \delta_t$ curve during the whole peeling procedure with pickup and release processes is used to estimate the peeling energies.

Figure 18.12 shows a mechanical analysis of a nanotweezer probe during a peeling operation. Forces applied on the probe tip can be resolved into two components on the X-axis and the Z-axis in the defined frame, that is, F_x and F_z, respectively. F_x is the clamping force that holds the 1D nanostructure and F_z is
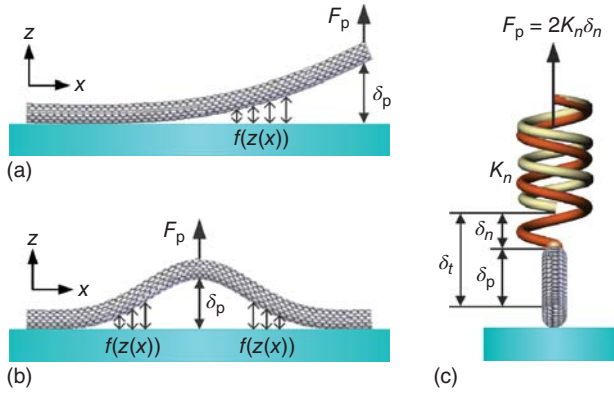
Figure 18.11 Deflection simulations for peeling locations at (a) the end and (b) the middle. (c) Peeling force computation model of the peeling test. F_p is the peeling force applied on the peeling location, $f(z(x))$ is the separating gap along the 1D nanostructure, k_n is the stiffness of the cantilever, δ_n, δ_p, and δ_t are respectively the cantilever's normal deflection, the gap on the peeling location, and the displacement on the nanotweezer.
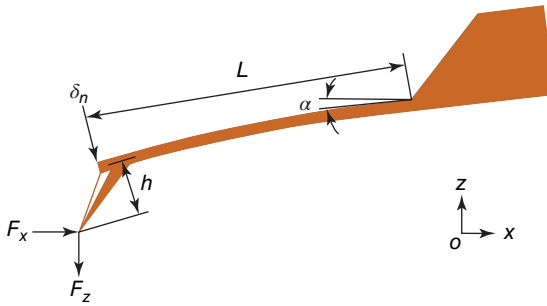
Figure 18.12 Analysis of mechanics of the nanotweezer probe (a cantilever with beam length L, mounting angle α, and tip height h) during a peeling test. A normal deflection δ_n on a microcantilever is caused by both the clamping force F_x and the peeling force F_z applied on the end of the tip.

the peeling force that balances adhesion forces from the substrate. To sense the peeling force, it is necessary to detect the normal deflection δ_n on each cantilever. δ_n can be calculated by

$$\delta_n = \frac{F_z \cos \alpha + F_x \sin \alpha}{k_n} + \frac{F_z \sin \alpha + F_x \cos \alpha}{k_{xz}}, \tag{18.5}$$

where $\alpha = 5°$ is the mounting angle of the cantilever and $k_{xz} = 2lk_n/3h$ is the bending stiffness due to the moment applied on the tip end, where h is the tip height and l is the beam length of the cantilever. Assuming magnitudes of F_z and F_x are of the same order, contributions from F_x to δ_n can be ignored since it is very small compared with that of F_z due to $k_{xz} \gg k_n$ with $L = 250$ μm and $h = 15$ μm. Thus, only F_z is considered for the normal deflection δ_n calculation, which can be estimated
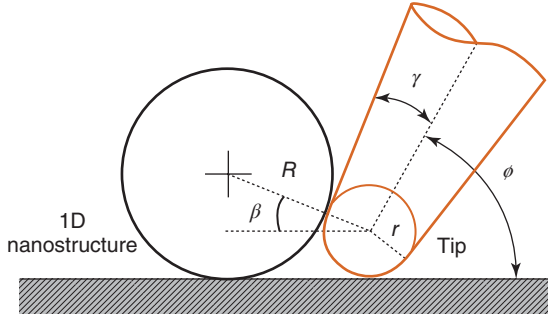
Figure 18.13 A schematic diagram of a geometry simulation of grasping limit on the size of the 1D nanostructure. ϕ and γ are respectively the tip's tilted angle relative to the substrate and half-cone angle, R and r are respectively the radii of 1D nanostructure and the tip apex, and β is defined as the contact angle between the tip apex and the 1D nanostructure.

from the normal voltage output ΔV_n of the optical levers by

$$F_z = C_n \Delta V_n, \tag{18.6}$$

where C_n is the normal force convention factor of the optical lever. The peeling force F_p can be synthesized from bending forces F_{z1} and F_{z2} that are estimated from the voltage outputs ΔV_{n1} and ΔV_{n2}, respectively on probe I and probe II:

$$F_p = F_{z1} + F_{z2} = C_{n1}\Delta V_{n1} + C_{n2}\Delta V_{n2}. \tag{18.7}$$

However, like other manipulation tools, the dual-probe nanotweezer has its own grasping limit on the diameter of 1D nanostructures. The minimum diameter that can be peeled is generally determined by the size of the tip apex and tip's deformations during peeling. Effects from the deformations can be counteracted by preloading a clamping force F_x. Thus, the size of the tip apex is the determinative factor. A geometric simulation of the grasping limit is seen in the bottom inset of Figure 18.13, in which $\phi = 60°$ is the tip's tilted angle through its rotation axis relative to the substrate; $\gamma = 8°$ is the half-cone angle of the tip; $r = 8$ nm and R are respectively the radii of the tip apex and the 1D nanostructure. The grasping limit R_{min} can be theoretically equal to r with a proper clamping force. However, grasping will lose when R decreases below the point where the contact is between the tip apex and the 1D nanostructure (sphere–sphere contact with a smaller contact angle β). Thus, from the relation

$$R = \frac{1 + \sin\beta}{1 - \sin\beta} \times r, \tag{18.8}$$

where $\beta_{max} = 90° - \phi - \gamma = 22°$, a grasping limit $D_{min} = 2R_{min} = 35.2$ nm can be calculated. It can be found that a wide range of peeling sizes from the nanoscale to the scale of several micrometers can be expected [69].

18.2.2
Results and Discussion

Peeling tests of a silicon nanowire (SiNW) have been processed with the proposed nanotweezer in an ambient temperature of 20 °C and a relative humidity of 40%. As seen in Figure 18.14a, the cone-shaped SiNWs, with a diameter of 25 nm (top)~200 nm (root) and a length of about 7 μm, were deposited on a silicon substrate (with 300-nm silicon dioxide) for peeling tests. Once the SiNW was clamped, the peeling was started by moving the piezotube down while the nanotweezer was kept immovable, followed by a retraction for releasing as the SiNW was completely peeled from the substrate. The tests were repeated dozens of times. Figure 18.14b shows a postpeeling image after 25 tests at the end. Then, 20 tests were performed at the middle of the SiNW. As seen in the postpeeling image (Figure 18.14c), the peeled SiNW was displaced due to complicated interactions among the SiNW, nanotweezer, and the substrate. Figure 18.14d shows heights at peeling locations: 196 nm at the end and 145 nm at the middle of the SiNW.

Figure 18.15a shows a full peeling force spectroscopy curve for the peeling point at the end of the SiNW. When the peeling begins (yellow line), the peeling force F_{p} decreases rapidly. At $\delta_t = -115$ nm, the nanotweezer pulls off the substrate. Further peeling leads to four local increases of the force magnitude that are followed respectively by discontinuous jumps $J_1 - J_4$ respectively with distances $d_1 - d_4$. At $\delta_t = -755$ nm, the peeling force jumped to zero. Upon still further moving the substrate down, the peeling force remains zero, indicating that the SiNW has been fully peeled from the surface. As seen in the green part of Figure 18.15a, during the retraction, neither the nanotweezer nor the SiNW interacts with the approaching surface and the force on the nanotweezer remains around zero. Eventually, the nanotweezer snaps into the substrate at the location close to the starting point. Figure 18.15b shows a full peeling force spectroscopy curve when the peeling location is at the middle of the SiNW. A shorter peeling distance and only two distinct jumps are observed, which is attributed to double peeling interfaces in this case, and reasonably, larger peeling force is obtained. From records of the 25 peeling tests at the end, an average value of the adhesion energies of 1185 keV is calculated. An adhesion energy of 906 keV at the middle is averaged from the 20 peeling tests, which is slightly smaller than the peeling energy at the end. The results are reasonable since the peeling at the middle needs stronger clamping force before peeling that might already break a small part of adhesion at the peeling location.

18.2.3
Conclusion

In summary, we have presented a method for in situ peeling test of 1D nanostructures. This method uses a dual-probe nanotweezer that has capabilities to pick-and-place the 1D structures as well as accurate force sensing during
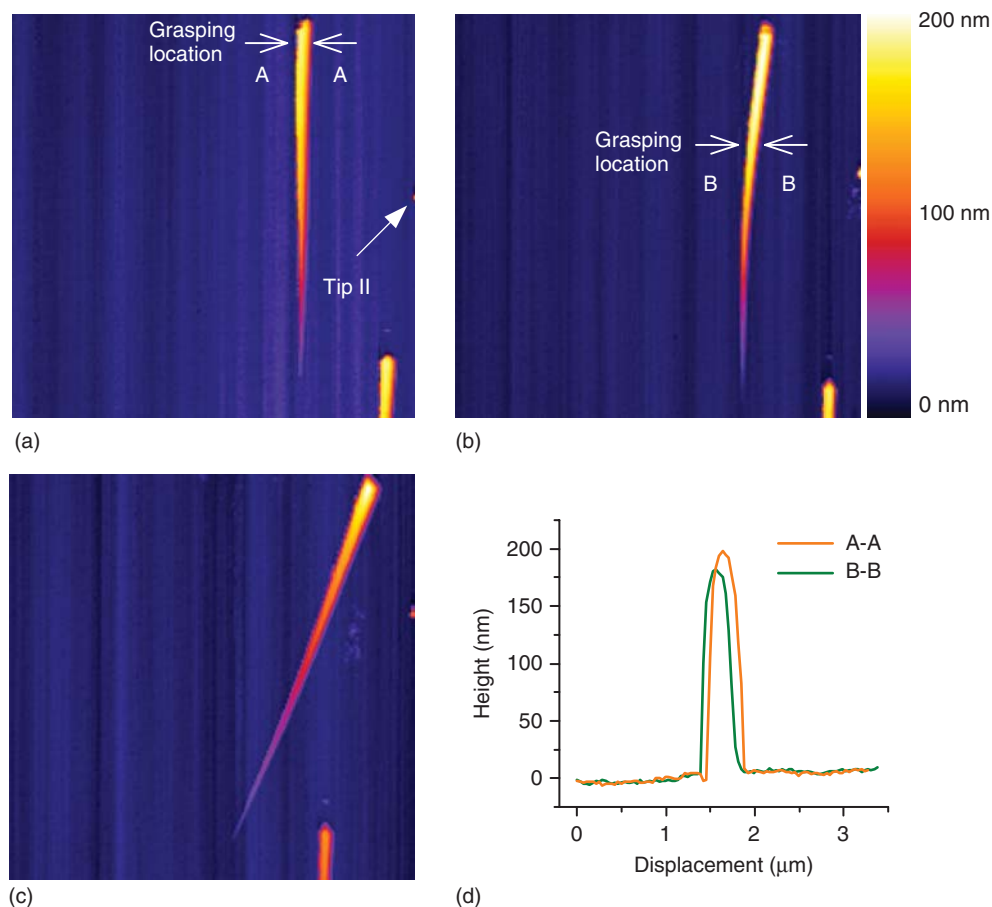
Figure 18.14 (a) Prescanned image of SiNWs and the end of probe II. A peeling location is firstly defined at the end (root) of a selected SiNW. (b) A postpeeling image after 25 peeling tests at the end. Another peeling location is then defined at the middle of the SiNW. (c) A postpeeling image after 20 peeling tests at the middle, in which the peeled SiNW was displaced due to complicated interactions among the nanotweezer, the SiNW, and the substrate. (d) Line scans show heights of the peeling locations at the end (196 nm) and the middle of the SiNW (145 nm).

the manipulation. With this method, a 1D nanostructure can be easily peeled from the surface by grasping it at various locations without complicated sample preparation. Experimental results of SiNW peeling tests on a silicon surface validate the proposed method. Moreover, peeling applications of the dual-probe nanotweezer could be used to peel other types of nanostructures, for example, zero-dimensional (0D) nanoparticles and 3D nanostructures. In addition, peeling applications of the dual-probe nanotweezer can be extended from the nanoscale to the scale of several micrometers.
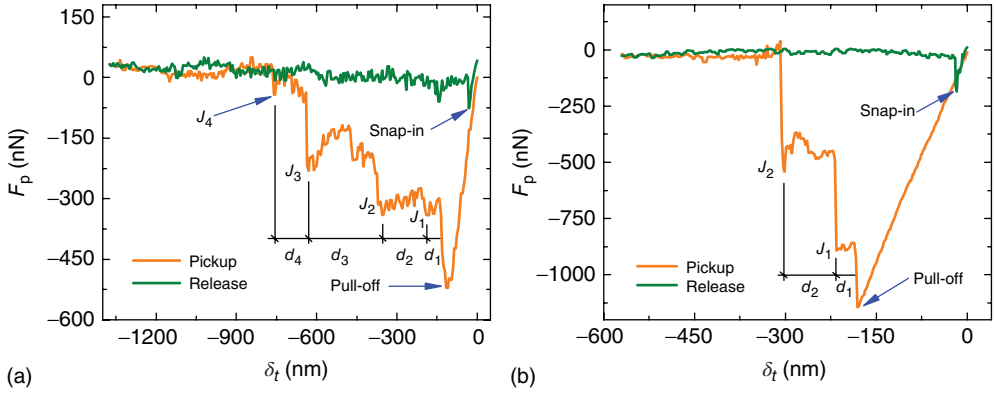
Figure 18.15 (a) A full peeling force spectroscopy curve recorded by peeling the end of the SiNW. (b) A full peeling force spectroscopy curve recorded by peeling the middle of the SiNW.

18.3

In situ Quantification of Living Cell Adhesion Forces: Single-Cell Force Spectroscopy with a Nanotweezer

18.3.1
Materials and Methods

18.3.1.1 Nanotweezer Setup

Figure 18.16a shows the configuration of the AFM-based nanorobotic system for cell adhesion force measurement, which is equipped with a nanotweezer constructed from two opposed probes (probes I and II) with protruding tips. Each probe is independently actuated and sensed. Probe I is supported by micropositioning stage I (MP I), and the applied forces are detected by optical lever I comprising laser I and position-sensitive detector I (PSD I, a four-quadrant photodiode). Probe II, which is sensed by optical lever II comprising laser II and PSD II, is mounted on nanopositioning stage II (NP II, travel range: 10 μm × 10 μm × 10 μm) that is supported by MP II. The sample platform is placed on NP I (travel range: 75 μm × 75 μm × 50 μm) that is supported by MP III. An optical microscope (equipped with a 20× lens) is used to position the laser spots on the probes and coarsely locate probes above target cells for adhesion force measurements. A multithread planning and control system is developed for AFM image scanning and dual-probe coordination control during manipulation. This system enables programming of complex tasks of cell–substrate and cell–cell adhesion quantifications, which is placed in a sealed mini-environment, wherein the CO_2 concentration and temperature (37 °C) of the system are controllable. The nanorobotic system was originally developed for 3D nanomanipulation and nanoassembly. More detailed specifications can be obtained from our previous article [70].

(a)

(b)

(c)
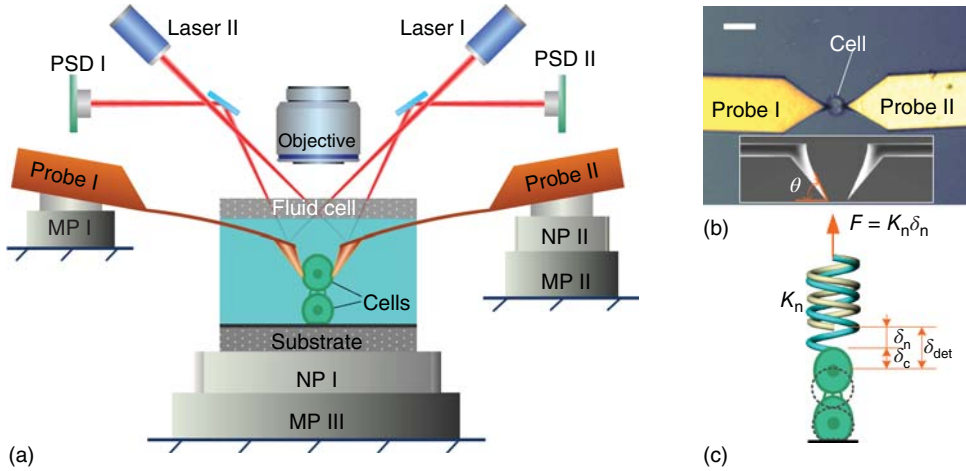
Figure 18.16 Schematic image of cell adhesion force quantification using the dual-probe nanotweezer. (a) System configuration of the dual-probe nanotweezer. When the cell is grasped by the nanotweezer, the adhesion force measurement begins by moving the NP I downward and upward on the Z-axis while the nanotweezer is immobilized. The detaching force is synthesized from bending forces on both probes individually detected by their own optical levers. This scheme is also suitable for cell–substrate adhesion force measurement. (b) Optical microscope image of the nanotweezer while grasping a cell. SEM image (inset) shows the configuration of the nanotweezer constructed from two AFM probes with protruding tips. The scale bar is 20 μm. (c) Adhesion force computation model, where F is the detaching force and k_n is the normal spring constant stiffness of the nanotweezer. δ_n, δ_c, and δ_{det} denote the normal deflection, cell deformation, and detaching distance of the nanotweezer, respectively.

Figure 18.16b shows an optical microscope image (top view) of the nanotweezer while grasping a cell. An inset of a SEM image (side view) shows the "V" configuration of the nanotweezer formed by two AFM probe tips tilted from the probe beam with an angle $\theta \approx 63°$. This angle enables a stronger hold resulting from the combined effect of the clamping, friction forces, and tip-cell adhesion forces during cell detachment [71].

Figure 18.16c shows the computation model of adhesion force measurement. The detaching force $F = k_n \delta_n$ loaded on the nanotweezer is synthesized from bending forces on each probe individually detected by the optical lever. k_n is the sum of the stiffness of both probes, δ_n is the deflection of the nanotweezer, and δ_{det} is the detaching distance, which is the sum of cell deformation δ_c and nanotweezer deflection δ_n.

The adhesion force of the cell grasped by the nanotweezer is given by the bending forces applied on the probes during cell detachment, that is, the pickup force applied on the cell that balances the adhesion forces from the substrate or another target cell. To detect the pickup force, determining the normal sensitivities and

voltage outputs of the PSDs of both probes is necessary. The bending force F_{n-I} on probe I can be estimated by the voltage output ΔV_{n-I} from PSD I as follows:

$$F_{n-I} = \beta_I \times \Delta V_{n-I} \tag{18.9}$$

where β_I is the normal force sensitivity of PSD I. The same treatment applies to the pickup force F_{n-II} on probe II. Thus, the pickup force applied on the cell, which is the cell adhesion force F_{det}, can be synthesized from the bending forces on both probes via

$$F_{det} = F_{n-I} + F_{n-II} = \beta_I \Delta V_{n-I} + \beta_{II} \Delta V_{n-II}, \tag{18.10}$$

where β_{II} and ΔV_{n-II} are the normal force sensitivity and voltage output of PSD II.

18.3.1.2 Cell Cultivation and Sample Preparation

C2C12 cells (mouse myoblast adherent) were cultured in Dulbecco's modified Eagle's medium (DMEM, pH 7.5) supplemented with 1.0 g l^{-1} glucose, l-glutamine, sodium pyruvate, 5958 mg l^{-1} HEPES, 100 U ml^{-1} penicillin, and 100 U ml^{-1} streptomycin. The cell line was maintained in 5% CO_2 atmosphere at $37 \pm 0.1°C$. Before the experiments, an appropriate number of cells was transferred into a Ø 35 mm Petri dish (Corning, #3294) containing normal DMEM/F12 medium and 10% fetal bovine serum. The Petri dish was immediately mounted in a fluid cell (with a temperature control unit at $37 \pm 0.2°C$) that was further mounted on the sample platform of the nanorobotic system placed in a mini-environment control (5% CO_2).

18.3.1.3 Nanotweezer Preparation

The cantilevers (ATEC-CONTAu, Nanosensors) were cleansed in pure alcohol for 1 h and thoroughly rinsed with Milli-Q water. The cantilevers were then placed on a glass slide and inserted into a high-temperature vacuum sterilizer. The cantilever holders were cleansed in pure alcohol for 1 h and thoroughly rinsed with Milli-Q water. The cantilevers were placed on the holders, which were put into a high-temperature vacuum sterilizer.

Before the experiment, the spring constants of both cantilevers were calibrated using the method proposed by Sader *et al.* [72], with values of 0.19 and 0.18 N/m. The respective normal sensitivities of the two probes in cell-culture medium were calibrated as 4.51 and 4.53 V/µm which yielded force conversional factors of 42.1 and 39.7 nN V^{-1} on probes I and II, respectively. Considering the voltage noise of about 0.94 mV_{p-p}, force accuracies were 39.6 and 37.3 pN on probes I and II, respectively, which were both better than 10 pN measured using an electrical system with higher signal-to-noise ratio and soft probes.

To reduce the thermal drift of the system, starting the nanorobotic system, the mini-environment controller, and the temperature controller of the fluid at least 1 h before the sample preparation was necessary. Upon stabilizing the thermal drift, a Petri dish containing prepared cells was fixed on the sample platform of the nanorobotic system. The two AFM headers were immediately mounted on this system. By driving MP I and MP II, probes I and II were located at the center of the

optical microscope view. The apexes of both tips were precisely aligned to form a nanotweezer with an opening distance of $2-4\,\mu m$ wider than the cell diameter. The laser spots were focused on the rearward of the corresponding probe beams, and the positions of PSDs were adjusted to set the signals around zero where PSDs held the most sensitive responses. For the entire experiment, the CO_2 concentration within the mini-environment and the temperature of the fluid cell were stabilized at 5% and 37 °C, respectively.

18.3.2
Protocol of the Adhesion Force Measurement

Figure 18.17 shows a schematic of the protocol for single-cell adhesion force measurement using the proposed nanotweezer. Cell–substrate adhesion force measurement was performed (Figure 18.17a). When the cell was completely picked up from the substrate, the detached cell was released from the nanotweezer to serially detach the next cell or used as a testing cell for cell–cell adhesion experiments (Figure 18.17b). Figure 18.17c shows six optical microscope images (under a 20× objective) obtained during the experiment. The following processes describe the cell adhesion measurement performed with the nanotweezer.

1) *System initialization.* Each axis of the nano- and micropositioning stages was set in appropriate positions that provide pick-and-place manipulation with sufficient motion range on each axis. MP III was driven to move a favorable cell into the center of the optical microscope view.

2) *Nanotweezer location at the testing cell.* Figure 18.17a-(I) shows that by driving MP III, the nanotweezer was placed over the favorable cell under the optical microscope, aligning tips I and II on the left- and right-hand sides of the cell, respectively. MP I and MP II were moved on the z-axis until both tips were close to the substrate with a distance less than 10 μm. The force servo control was started to move NP I and NP II alternately to make both tips in contact with the substrate. To avoid grasping the cell–substrate interactive interface, the substrate was moved down to create a gap of $2-3\,\mu m$ ($1/4-1/3$ of the cell diameter) from the nanotweezer by driving the NP I on the z-axis.

3) *Grasping the cell with the nanotweezer.* Figure 18.17a-(II) shows that tip I initially approached the cell by moving NP I on the x-axis. Similarly, tip II approached the cell by moving NP II on the x-axis. Once both tips were in contact with the cell, a nanotweezer was configured to grasp the cell with a clamping force for cell–substrate adhesion force measurement. The clamping force should be well controlled to achieve successful grasping and protect the cell from damage during this process.

4) *Detachment of the cell from the substrate.* Following the detection of reliable grasping on the cell with force monitoring, the cell–substrate adhesion force measuring process was started by moving the NP I downward on the z-axis (Figures 18.17a-(III) and 18.17a-(IV)). For the computation of the

cell−substrate adhesion force, force−distance (F−D) data on both probes were recorded during the approach and retraction processes.

Critical step: The cell release operation (retraction process) is presented in detail in the next section. Once the cell is released from the nanotweezer, the cell−substrate adhesion force measurement can be restarted from step (1) for serial adhesion measurement of different cells. The measurement is restarted from step (3) if multiple tests on the same cell are required. In this case, the release operation will be different from the required contact time. To ensure that the time needed for release (from step II to IV in Figure 18.4) and grasping is less than the contact time, cell release operation being processed to step II in Figure 4 for contact times less than several minutes is recommended. Otherwise, the cell can be completely released at step IV in Figure 4 for longer contact times.

5) *Holding the cell for cell−cell adhesion force measurement.* Figure 18.17a-(V) shows that the cell completely detached from the substrate was still held by the nanotweezer for cell−cell adhesion force measurement, and was located above a target cell by moving MP III on the $x−y$ plane (Figure 18.17b-(I)).

6) *Attachment of the grasped cell to the target cell.* Figure 18.17b-(II) shows that after at least 10 min of cell recovery, the grasped cell vertically approached the target cell attached on the substrate with real-time force monitoring by driving NP-I. The contact force should be between 0.5 and 1.5 nN, and the approach rate should be less than 0.5 µm s^{-1}.

   Note: If the contact time is longer than 30 s, opening the nanotweezer to revert the cell to an original form of phantom lines (Figure 18.17b-(II)) is necessary to effectively reduce the effects on the building of the cell−cell adhesion from the clamping force or the thermal drift of the system.

7) Detachment of the grasped cell from the target cell (Figure 18.17b-(III) and (IV)). The grasped cell is vertically retraced from the target cell after a suitable contact time while driving NP I, in which the retraction rate is less than 0.5 µm s^{-1}. F−D data on both probes are recorded for cell−cell adhesion force computation. Adjusting the contact time, multiple cell−cell adhesion force measurements from step (6) for the same target cell can be restarted, from step (5) for different target cells, or from step (1) for different grasped cells.

Figure 18.17c shows images captured during the adhesion force measurement. Figure 18.17c-(I) shows that the nanotweezer is located at the testing cell that is brought in contact with probe I in Figure 18.17c-(II), and clamped by the nanotweezer in Figure 18.2c-(III) when probe II is in contact with the cell. Once the cell is completely detached from the substrate (Figure 18.17c-(IV)), the former is transferred to the target cell for cell−cell adhesion measurement, (Figure 18.17c-(V)). The grasped cell is brought in contact with the target cell (Figure 18.17c-(VI)).

Compared with time-consuming cell immobilization performed using traditional SCFS, cell grasping can be efficiently completed with the nanotweezer within 1.2 min with from steps (1) to (3), thereby significantly reducing the cycle time for each cell adhesion measurement. Serial quantification of cell−substrate

(a)

(b)

(c)
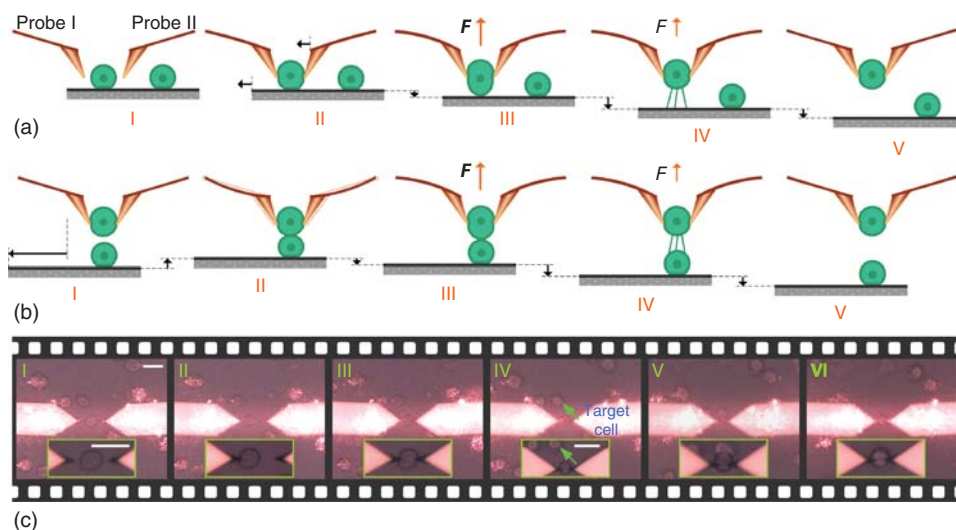
Figure 18.17 Schematic of the protocol for single-cell adhesion force measurement and the optical images taken during measurement with the nanotweezer. (a) The procedure for the cell–substrate adhesion force measurement. (I) Both tips are aligned to the left- and right-hand sides of the cell. (II) Probe I is in contact with the cell and then does probe II. (III and IV) The cell is grasped and picked up by moving NP I on the Z-axis with a rate of 0.5 μm s^{-1} and (V) detached from the substrate. (b) The procedure for the cell–cell adhesion force measurement. (I) The detached cell (in step V of Figure 18.17a) is transferred over the target cell and is (II) brought in contact with the target cell with a contact force and a setting value between 0.5 and 1.5 nN. Both probes can retrace a suitable distance to reduce the clamping force for long contact times. (III and IV) The cell is picked up from the target cell and is completely detached in step (V). (c) Optical images captured during the adhesion force measurement. (I) Before grasping. (II) Probe I is in contact with the cell and (II) then does the probe II. (III) The cell is detached from the substrate and (IV) transferred to the target cell. (VI) Both cells are brought in contact for cell–cell adhesion force measurement. Scale bars represent 20 μm.

adhesion could also be reduced to less than 3−4 min, which is mainly determined by the detaching speed and distance. Thus, more than 100 serial quantifications of cell–substrate adhesion could be obtained in a workday. Even though cell–cell adhesion measurement was less efficient because the nanotweezer should be held up during the contact time, the nanotweezer can simply and efficiently perform the cell–cell adhesion measurement of different cells.

18.3.3
Clamping Detection during Cell Grasping

Clamping detection and control yield successful cell grasping and protect the cell from damage. To detect the interaction between the cell and the tip during cell grasping, bending force control on the probe begins when the probes approach and further clamp the cell. Figure 18.18 shows an example of the contact detection
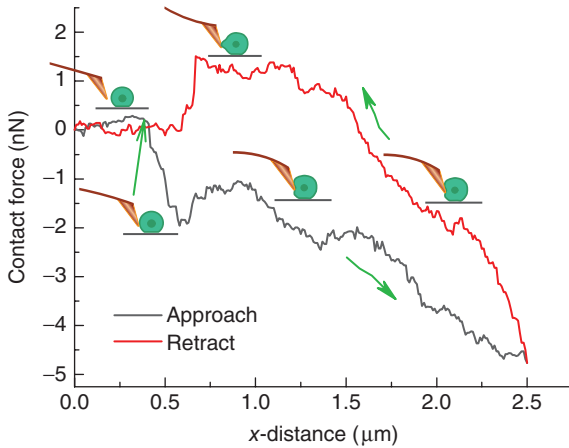
Figure 18.18 Clamping detection by normal force sensing on probe I. The force curve shows the bending behavior of the cantilever during approach, contact, and retraction.

on the cell with probe I. The force curve starts from a noncontact state between the probe and the cell, and the probe tip is in contact with the cell at 0.4 μm. As the probe tip further moves toward the cell, this tip is bent downward to about 10.5 nm, leading to negative forces. In this part, the bending force decreases gradually to −2 nN with a displacement of about 200 nm. Further movement leads to cell deformation that causes a slow decrease of the bending force to the minimum value of −4.8 nN at a total distance of 2.5 μm, wherein the cell is trapped with a clamping force of about 43 nN through mechanical analysis [71]. During retraction, the tip slowly reverts to the original shape. Before the tip pulls off from the cell, the adhesion force between the tip and the cell induces an increase of the bending force to 1.5 nN. After the probe-cell adhesion breakage, the cell no sooner recovers when the bending force sharply reaches zero at 0.6 μm, with a deformation of 0.2 μm.

The force response described (Figure 18.18) is sufficient to detect not only the contact between the tip and the cell, but also the clamping state. Building a computation model for contact between the soft cell and the nanotweezer to estimate an exact clamping force that is sufficient to overcome cell adhesion is complicated compared with solid−solid contact between the nanotweezer and micro- or nano-objects. Compared with the maximum grasping force of several micronewtons occurring at the solid−solid contact interface [71], the deformed soft cell can be more reliably held and picked up by the nanotweezer. This assumption has been validated by experiments that indicate successful cell detachment when the cell is trapped by the nanotweezer with an empirical normal bending force of subnanonewtons to several nanonewtons on each probe for cell−cell adhesion, and dozens of nanonewtons for the case of the cell−substrate adhesion.

18.3.3.1 Cell Release

To analyze the adhesion force of different cells with the traditional SCFS, an operation was performed to bind a single cell to a clean and freshly mounted cantilever. However, along with the release of the tested cell, this process is time consuming. The cell attached on the cantilever is removed with chemicals or is directly changed to a clean cantilever for new testing. In this study, cell sticking often occurs in the nanotweezer after adhesion force measurement. Fortunately, the cell is not strongly stuck to the nanotweezer because of the small contact area between the cell and the unfunctionalized probe tip, thereby successfully releasing the cell on the substrate by a simple scheme (Figure 18.4).

1) Figure 18.19a-(I) shows the retraction process by moving up NP I on the z-axis to place the cell in contact with the substrate, with a contact force of several nanonewtons. $F-D$ data on both probes were recorded during the retraction process.

2) In figure 18.19-(II), to reduce the effects of the cell–substrate adhesion on the setup, the clamping force is immediately reduced by opening the nanotweezer until the cell recovers its original circular shape. A contact time ranging from 10 to 30 s is normally set to obtain sufficient cell–substrate adhesion force for cell release in the succeeding steps.

3) By simultaneously moving NP I and NP II on the x-axis, both probes retrace from the cell with a low rate of 0.1 μm s^{-1}. Figure 18.19a-(III) shows the gradual detachment of the probes from the cell and the successful detachment of the probes from the cell (Figure 18.19a-(IV)). Figure 18.19b-(I)–(IV) shows the optical images related to the release scheme.

In the experiments, almost all cells can be successfully released with a contact time of 10–30 s if the cell is active and the probes are not severely contaminated with cell debris. However, the probes should be changed after about 20 testing procedures for the next batch of adhesion force measurements to reduce effects from the contaminated probes on the cell activities and increase the force accuracy of testing.

18.3.4
Experimental Results

18.3.4.1 Cell–Substrate Adhesion Force Measurement

When the setup is ready for adhesion force measurement, the nanotweezer is initially used to quantify the cell–substrate adhesion forces in the first set of experiments. Using the optical microscope and force feedback, the favorable cell is clamped by the nanotweezer. The sample platform is moved downward to detach the cell from the substrate by moving the NP I on the z-axis while recording the nanotweezer bending force required to detach the cell. Once the cell is completely detached from the substrate, the cell is transferred to another target cell attached to the substrate for cell–cell adhesion force measurement (Figure 18.2b), or the cell is released from the nanotweezer to the substrate
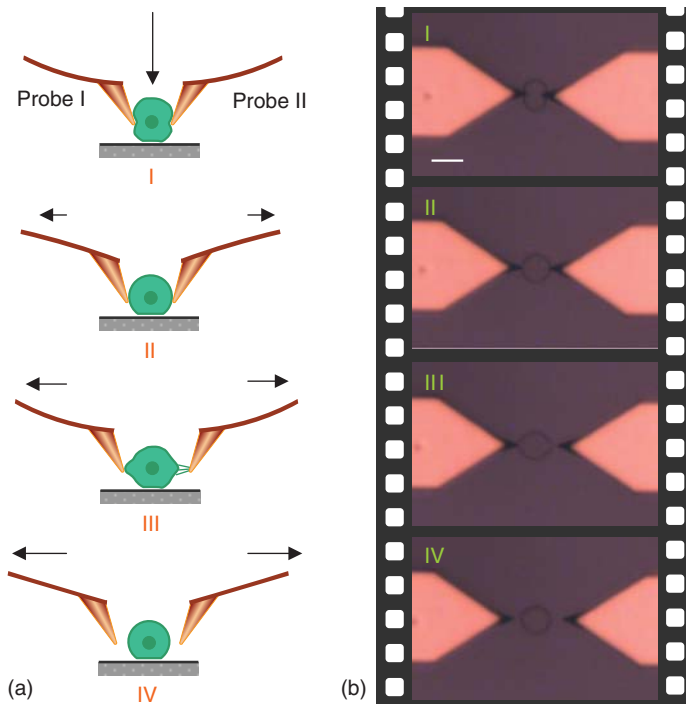
Figure 18.19 A schematic of cell release to the substrate. (a) Protocol of the cell release. Step I: The nanotweezer is constantly holding the cell and NP I is moved upward on the z-axis to place the cell in contact with the substrate. Step II: To reduce the effects of cell–substrate adhesion on the setup, the clamping force is immediately reduced by separating both probes until the cell recovers its original circular shape. Step III: Following a contact time of 10–30 s, both probes are simultaneously separated from the cell until the cell is thoroughly released in step IV. (b) Optical microscope images (20×) I–IV capture using the steps performed in (a).

(Figure 18.4), such that next cell can be tested. Instead of chemically immobilizing the cells to the AFM cantilever as in conventional SCFS, we used robotic grasping to immobilize the cell to the nanotweezer. The cell is not attached on the nanotweezer during the cell–substrate adhesion setup. This method can be used to quantify time-dependent cell adhesion forces with contact times of several hours, which is impractical with conventional SCFS. The latter is prone to failure at these times because the cell–substrate adhesion forces often surpass those used for the fixation of the cells to the cantilever and the thermal drift of the system imposes difficulty in holding the cantilever at the correct position. The nanotweezer is demonstrated to successfully detach dozens of cells from the glass substrate (bottom of the Petri dish), with contact times ranging from 5 to 125 min.

(a)

(b)
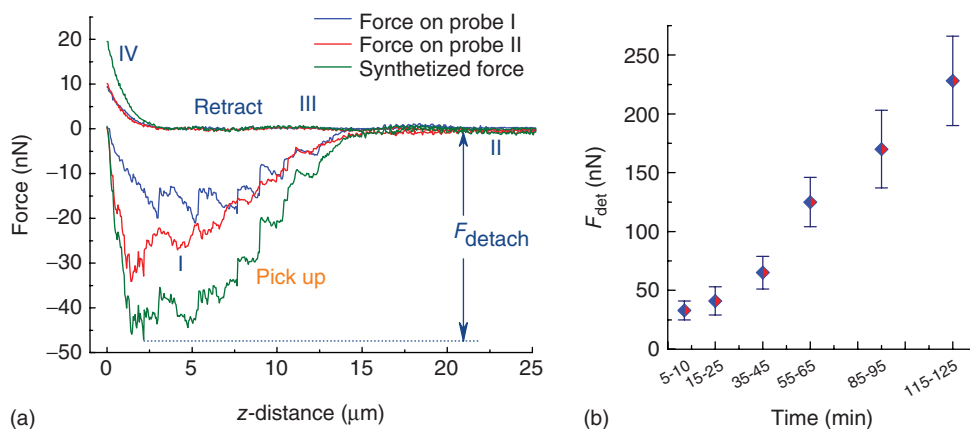
Figure 18.20 Cell–substrate adhesion of C2C12 cells to the bottom of the Petri dish. (a) Representative example of F–D curves obtained with a contact time of 20 min. Data show a maximum adhesion force of 47.5 nN that is synthesized (green curve) from forces measured on probes I (blue curve) and II (red curve). (b) Time-dependent maximum adhesion forces with contact times ranging from 5 to 125 min. The analysis in (b) involved the recording of at least 10 F–D curves per time frame. The data are represented as mean and standard error ($\pm$).

Figure 18.20 shows a representative example of the F–D curves obtained with a contact time of 20 min between the cell and the substrate. The green curve represents the force response during cell–substrate adhesion force measurement, that is, the synthesized forces measured on probes I (blue curve) and II (red curve). Response differences on the probes are mainly due to the cell's large asymmetrical deformation deduced by strong adhesion that might be nonuniformly distributed at the cell–substrate interface (the adhesion force is not through the center of the nanotweezer), which causes nonsymmetrical force loading on both probes during the detaching process.

The curve starts from the contact state between the nanotweezer and the cell. When a load is applied to the cell–substrate adhesion by moving NP I downward to pick up the cell at a constant rate of 500 nm s^{-1}, both cantilevers are bent from the strength of the cell–substrate adhesion, so that the nanotweezer exerts a detaching force on this adhesion.

The receptor remains anchored in the cell cortex and unbinds as the force increases when the position reaches 2.26 µm during pickup, and the cell jumps from the substrate with a maximum adhesion force of 47.5 nN. As NP I is further moved down, the force magnitude constantly and slightly decreases with the discontinuous jumps (part I). In this part, receptor anchoring is lost and membrane tethers are pulled out of the cell at a detachment distance of 17 µm, denoted as the long-distance tethers. Once the cell is completely detached from the substrate (part II), the nanotweezer retracts to the starting position and the cell is released using a previously discussed strategy (part III). Following the retraction at 2.2 µm, further retraction leads to a continuous increase until the nanotweezer is back
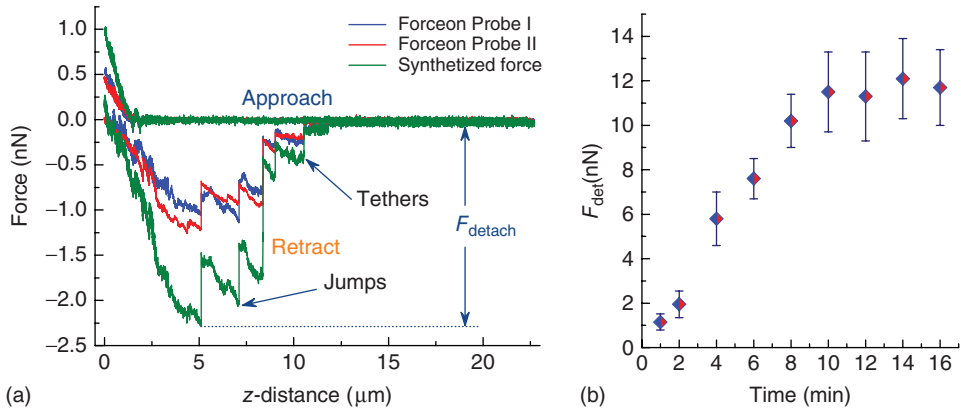
Figure 18.21 Cell–cell adhesion of C2C12 cells. (a) Representative example of the F–D curves obtained with a contact time of 2 min. Data show a maximum adhesion force of 2.23 nN synthesized (green curve) from forces measured on probes I (blue curve) and II (red curve). (b) Time-dependent maximum adhesion forces with contact times ranging from 1 to 16 min. The analysis in (b) involved the recording of at least five F–D curves per time frame. Data are represented as mean and standard error (±).

at the starting point (part IV). The force on the nanotweezer increases because of the extending cell deformation during the pickup manipulation, which places the cell in contact with the substrate before retraction of the nanotweezer to the starting point. The maximum downward force exerted on the nanotweezer is defined as the detachment force ($F_{det} = 47.5$ nN).

Detachment tasks are repeated with the protocol described above for different incubation times. A total of 64 cells were measured serially using the same probes, obtaining reliable force data. Incubation time of the tested cells ranged from 5 to 125 min, indicating that long incubation time on the substrate results in higher adhesion force (Figure 18.20b). The maximum average adhesion force is 228 ± 38 nN with an incubation time of around 2 h. The adhesion will increase with longer incubation time; the cell simultaneously spreads more widely on the substrate and will be eventually stabilized after several hours of contact, which was demonstrated by previous works [73]. We tested adhesion of cells incubated within 125 min because the nanotweezers formed by the selected contact mode cantilevers are stiff enough to pick up the cells, and the corresponding force response is in the linear range. Thus, stiffer cantilevers (e.g., ATEC-FMAu, Nanosensors; stiffness: 2.8 N m^{-1}) should be used to build the nanotweezer for cells incubated with longer contact time. The adhesion will reach from hundreds of nanonewtons to several micronewtons.

18.3.4.2 Cell–Cell Adhesion Force Measurement

Cell–cell adhesion force measurement was also performed with our developed nanotweezer. Figure 18.21a shows a representative example of the F–D curves of the cell–cell adhesion measurement obtained with a contact time of 2 min.

Once the grasped cell is optically located over the target cell with a vertical distance sufficient to cover the detaching distance, this cell approaches the target cell by moving NP I upward at a constant rate of 500 nm s^{-1}. When the position reaches 1.8 μm, two cells are brought into contact with a snap-in response followed by slight fluctuations before the cells are compressed with a preload of 1 nN. Following the given contact time of 2 min, a load to the cell–cell adhesion is applied by moving NP I downward to pick up the cell at a constant rate of 500 nm s^{-1}. Both cantilevers are bent from the strength of cell–cell adhesion, so that the nanotweezer exerts a detaching force on the grasped cell. During retraction, the grasping force on the nanotweezer continuously increases before the position reaches 5 μm. The grasped cell jumps from the target cell with a maximum adhesion force of 2.23 nN. As NP I is further moved down, the force magnitude constantly decreases initially with discontinuous jumps, followed by the unbinding of membrane tethers before the grasped cell is thoroughly detached from the target cell at about 12 μm. The maximum force exerted on the nanotweezer is defined as the detachment force (F_{det} = 2.23 nN).

As the nanotweezer retracts to the start position, pick-and-place tasks were repeated with a setting time ranging from 1 to 16 min. A total of 10 cells were measured, thereby obtaining reliable data. Mean F_{det} increases from 1.12 ± 0.36 nN to about 12.14 ± 2.08 nN with the increase of time interval. Figure 18.21b shows that the required cell separation force increased rapidly within 8 min. The detaching force became gradually stabilized around 12 nN after 10 min of contact. A similar phenomenon was observed in cell adhesion quantification of two S180 cells, such that the adhesion forces stabilized after 1 h contact [53]. However, the magnitude of the maximal adhesion force and the stable period measured by each group are different because of the different cells and culture media, validating the capability of the proposed nanotweezer in measuring cell–cell adhesion force demonstrated at the nanonewton scale.

18.3.5
Discussion

Efficiency is the main concern for the application of SCFS. Chemical fixation of a single cell on the cantilever in traditional SCFS is time consuming [58, 65]. Contact times ranging from several seconds to hours are needed for each testing to build adhesion between the cell and target surface, limiting the adhesion measurement to a few cells per workday and inducing a labor-intensive acquisition of statistically significant amount of data. Compared with the traditional SCFS, cell fixation is not needed using the proposed nanotweezer, by which adhesion testing can be performed rapidly and serially cell by cell, instead of holding up during the contact time. Probes forming the nanotweezer can be used to grasp and release more than 20 cells with a mount of testing before contamination. Newly cleaned probes can be changed rapidly for the next batch of adhesion force measurements. These measurements can be more than 100 cells daily, which substantially improves the

efficiency of SCFS testing compared with the traditional AFM-SCFS. Neverthe-less, current adhesion measurement and data analysis are not ideally rapid because of manual and semiautomatic operations. To further improve the efficiency of SCFS testing with the proposed nanotweezer, methodologies and software will be developed for future studies to complete an automated and high-throughput measurement of cell adhesion and batch analysis of the F−D data recorded by the nanotweezer-SCFS system.

18.3.6
Conclusion

A nanorobotic system equipped with a dual-probe nanotweezer is developed for SCFS experiments. The nanotweezer has a high positioning accuracy and it easily manipulates biological cells and biomolecules. Protocols for in situ quantification of cell−substrate and cell−cell adhesion forces are given. Experiments on time-dependent cell−substrate (Petri dish substrate) and cell−cell adhesion forces of C2C12 cells have been successfully performed using the nanotweezer. Cell immo-bilization with chemical binding is not required initially, so this method is practical to significantly improve the efficiency of SCFS experiments. Long-term adhesion force measurement is also logical because the proposed nanotweezer is capable of detecting forces ranging from piconewtons to micronewtons. This method is con-siderably suitable for studying cell adhesion with different biomaterials [74−76], analyzing cell adhesion with different contact areas [77], and examining temper-ature dependence of single-cell adhesion [78]. This study elucidates single-cell interaction with external matrices, and would be beneficial in medical and bio-logical fields.

18.4
Conclusion and Future Directions

A flexible robotic system developed for multiscale manipulation and character-ization from nanoscale to microscale is presented. This system is based on the principle of AFM and comprises two independently actuated probes that form a dual-probe nanotweezer. After reconfiguration, the robotic system could be used for pick-and-place manipulation from nanoscale to the scale of several micrometers. Flexibilities and capabilities of the developed system are validated by 3D manipulation of micro- and nano-objects. Moreover, a 1D nanostructure can be also easily peeled by the proposed nanotweezer from the surface by grasping it at various locations without complicated sample preparation. Exper-imental results of SiNW peeling tests on a silicon surface validate the proposed method. Peeling applications of the nanotweezer could be used to peel other types of nanostructures, for example, 0D nanoparticles and 3D nanostructures. In addition, the nanotweezer is capable of pick-and-place manipulation of a single living cell for cell−cell and cell−substrate adhesion measurements. Compared

with SCFS based on traditional AFM, cell immobilization via chemical trapping is unnecessary and the test cell can be efficiently released using the nanotweezer to significantly enhance production of the SCFS.

Complicated micro- or nanomanipulation, assembly, and characterization can be reliably and efficiently performed using the proposed flexible robotic system. 3D nanomanipulation methods are indispensable for heterogeneous integration of complex nanodevices. Serial nanomanipulation systems could only enable low-volume prototyping applications. However, high-volume and high-speed nanomanipulation systems are indispensable for future nanotechnology products. Therefore, autonomous and massively parallel AFM systems are required.

References

1. Carlson, K., Andersen, K.N., Eichhorn, V., Petersen, D.H., M, K., Bu, I.Y.Y., Teo, K.B.K., Milne, W.I., Fatikow, S., and B, P. (2007) A carbon nanofibre scanning probe assembled using an electrothermal microgripper. *Nanotechnology*, **18** (34), 345501.

2. Xie, H., Haliyo, D.S., and Régnier, S. (2009) A versatile atomic force microscope for three-dimensional nanomanipulation and nanoassembly. *Appl. Phys. Lett.*, **94**, 153106.

3. Xie, H., Rong, W.B., Sun, L.N., and Chen, W. (2006) *Image fusion and 3-D surface reconstruction of microparts using complex valued wavelet transforms*. IEEE International Conference on Image Process, Atlanta, GA, pp. 2137–2140.

4. Menciassi, A., Eisinberg, A., Izzo, I., and Dario, P. (2004) From "Macro" to Micro" manipulation: models and experiments. IEEE-ASME Trans. *Mechatron.*, **9** (2), 311–320.

5. Lambert, P. and Régnier, S. (2006) Surface and contact forces models within the framework of microassembly. *J. Micromechatron.*, **3** (2), 123–157.

6. Sitti, M. (2007) Microscale and nanoscale robotics systems characteristics, state of the art, and grand challenges. *IEEE Rob. Autom. Mag.*, **14** (1), 53–60.

7. Xie, H., Rong, W.B., and Sun, L.N. (2007) Construction and evaluation of a wavelet-based Focus measure for microscopy imaging. *Microsc. Res. Tech.*, **70**, 987–995.

8. Liu, X.Y., Wang, W.H., and Sun, Y. (2007) Dynamic evaluation of autofocusing for automated microscopic analysis of blood smear and pap smear. *J. Microsc.*, **227**, 15–223.

9. Xie, H., Vitard, J., Haliyo, S., and Régnier, S. (2008) Optical lever calibration in atomic force microscope with a mechanical lever. *Rev. Sci. Instrum.*, **79**, 096101.

10. Fukuda, T., Arai, F., and Dong, L.X. (2003) Assembly of nanodevices with carbon nanotubes through nanorobotic manipulations. *Proc. IEEE*, **91**, 1803–1818.

11. Dong, L.X., Arai, F., and Fukuda, T. (2002) Electron-beam-induced deposition with carbon nanotube emitters. *Appl. Phys. Lett.*, **81**, 1919–1921.

12. Dong, L.X., Arai, F., and Fukuda, T. (2004) Destructive constructions of nanostructures with carbon nanotubes through nanorobotic manipulation. *IEEE/ASME Trans. Mechatron.*, **9**, 350–357.

13. Molhave, K., Wich, T., Kortschack, A., and Boggild, P. (2006) Pick-and-place nanomanipulation using microfabricated grippers. *Nanotechnology*, **17**, 2434–2441.

14. Dong, L.X., Tao, X.Y., Zhang, L., Nelson, B.J., and Zhang, X.B. (2007) Nanorobotic spot welding: controlled metal deposition with attogram precision from copper-filled carbon nanotubes. *Nano Lett.*, **7**, 58–63.

15. Leach, J., Sinclair, G., Jordan, P., Courtial, J., Padgett, M.J., Cooper, J., and Laczik,

Z.J. (2004) 3D manipulation of particles into crystal structures using holographic optical tweezers. *Opt. Express*, **12**, 220–226.

16. Yu, T., Cheong, F.C., and Sow, C.H. (2004) The manipulation and assembly of CuO nanorods with line optical tweezers. *Nanotechnology*, **15**, 1732–1736.

17. Bosanac, L., Aabo, T., Bendix, P.M., and Oddershede, L.B. (2008) Efficient optical trapping and visualization of silver nanoparticles. *Nano Lett.*, **8**, 1486–1491.

18. Rollot, Y., Régnier, S., and Guinot, J.C. (1999) Simulation of micromanipulations: Adhesion forces and specific dynamic models. *Int. J. Adhes. Adhes.*, **19**, 35–48.

19. Barber, A.H., Cohen, S.R., and Wagner, H.D. (2003) Measurement of carbon-nanotubepolymer interfacial strength. *Appl. Phys. Lett.*, **82** (23), 4140–4142.

20. Breuer, O. and Sungararaj, U. (2004) Big returns from small fibers: a review of polymer/carbon nanotube composites. *Polym. Compos.*, **25**, 630–645.

21. Strus, M.C., Cano, C.I., Pipes, R.B., Nguyen, C.V., and Raman, A. (2009) Interfacial energy between carbon nanotubes and polymers measured from nanoscale peel tests in the atomic force microscope. *Compos. Sci. Technol.*, **69**, 1580–1586.

22. Sever, M.J., Weisser, J.T., Monahan, J., Srinivasan, S., and Wilker, J.J. (2004) Metal-mediated cross-linking in the generation of a marine-mussel adhesive. *Angew. Chem. Int. Ed.*, **43**, 448–450.

23. Shi, X., Kong, Y., Zhao, Y., and Gao, H. (2005) Molecular dynamics simulation of peeling a DNA molecule on substrate. *Acta Mech. Sin.*, **21**, 249–256.

24. Ge, L., Sethi, S., Ci, L., Ajayan, P.M., and Dhinojwala, A. (2007) Carbon nanotube-based synthetic gecko tapes. *Proc. Natl. Acad. Sci. U.S.A.*, **104** (26), 10792–10795.

25. Jang, J.E., Cha, S.N., Choi, Y., Amaratunga, G.A.J., Kang, D.J., Hasko, D.G., Jung, J.E., and Kim, J.M. (2005) Nanoelectromechanical switches with vertically aligned carbon nanotubes. *Appl. Phys. Lett.*, **87**, 163114–1631203.

26. Dujardin, E., Derycke, V., Goffman, M.F., Lefèvre, R., and Bour-Goin, J.P. (2005) Self-assembled switches based on electroactuated multiwalled nanotubes. *Appl. Phys. Lett.*, **87**, 193107–193113.

27. Cha, S.N., Jang, J.E., Choi, Y., Amaratungab, G.A.J., Kang, D.J., Hasko, D.G., Jung, J.E., and Kim, J.M. (2005) Fabrication of nanoelectromechanical switch using a suspended carbon nanotube. *Appl. Phys. Lett.*, **86**, 083105.

28. Ekinci, K.L. and Roukes, M.L. (2005) Nanoelectromechanical systems. *Rev. Sci. Instrum.*, **76**, 061101.

29. Mahar, B., Laslau, C., Yip, R., and Sun, Y. (2007) Development of carbon nanotube-based sensors – a review. *IEEE Sens. J.*, **7**, 266–284.

30. Dragoman, M., Takacs, A., Muller, A.A., Hartnagel, H., Plana, R., Grenier, K., and Dubuc, D. (2007) Nanoelectromechanical switches based on carbon nanotubes for microwave and millimeter waves. *Appl. Phys. Lett.*, **90**, 113102.

31. Li, Q., Koo, S.M., Richter, C.A., Edelstein, M.D., Bonevich, J.E., Kopanski, J.J., Suehle, J.S., and Vogel, E.M. (2007) Precise alignment of single nanowires and fabrication of nanoel ectromechanical switch and other test structures. *IEEE Trans. Nanotechnol.*, **6**, 256–263.

32. Popov, I., Gemming, S., Okano, S., Ranjan, N., and Seifert, Gotthard. (2008) Electromechanical switch based on Mo6S6 nanowires. *Nano Lett.*, **8**, 4093–4097.

33. Metin, S. and Hideki, H. (2000) Controlled pushing of nanoparticles: modeling and experiments. *IEEE/ASME Trans. Mechatron.*, **5**, 199–211.

34. Tong, L., Zhu, T., and Liu, Z. (2008) Atomic force microscope manipulation of gold nanoparticles for controlled Raman enhancement. *Appl. Phys. Lett.*, **92**, 023109.

35. Shin, C.H., Jeon, I.S., Jeon, S.H., and Khim, Z.G. (2009) Single nanoparticle alignment by atomic force microscopy indentation. *Appl. Phys. Lett.*, **94**, 163107.

36. Yoshiharu, I., Akihiko, I., and Toshio, Y. (2001) Single molecule nanomanipulation of biomolecules. *Trends Biotechnol.*, **19**, 211–216.

37. Falvo, M.R., Taylor, R.M.I., Helser, A., Chi, V., Brooks, F.P.J., Washburn, S., and Superfine, R. (1999) Nanometre-scale

rolling and sliding of carbon nanotubes. *Nature*, **397**, 236–239.

38. Tranvouez, E., Boer-Duchemin, E., Comtet, G., and Dujardin, G. (2007) Active drift compensation applied to nanorod manipulation with an atomic force microscope. *Rev. Sci. Instrum.*, **78** (11), 115103.

39. Strus, M.C., Zalamea, L., Raman, A., Pipes, R.B., Nguyen, C.V., and Stach, E.A. (2008) Peeling force spectroscopy: exposing the adhesive nanomechanics of one-dimensional nanostructures. *Nano Lett.*, **8** (2), 544–550.

40. Ishikawa, M., Harada, R., Sasaki, N., and Miura, K. (2008) Visualization of nanoscale peeling of carbon nanotube on graphite. *Appl. Phys. Lett.*, **93**, 083122.

41. Kam, Z., Volberg, T., and Geiger, B. (1995) Mapping of adherens junction components using microscopic resonance energy transfer imaging. *J. Cell Sci.*, **108** (3), 1051–1062.

42. Humphries, M.J. (2001) Cell-substrate adhesion assays. *Curr. Protoc. Cell Biol.*, **9** (1), 1–11.

43. Connors, W.L. and Heino, J. (2005) A duplexed microsphere-based cellular adhesion assay. *Anal. Biochem.*, **337**, 246–255.

44. Alon, R., Hammer, D.A., and Springer, T.A. (1995) Lifetime of the P-selectin-carbohydrate bond and its response to tensile force in hydrodynamic flow. *Nature*, **374**, 539–542.

45. Garcíab, A.J., Ducheyneb, P., and Boettiger, D. (1997) Quantification of cell adhesion using a spinning disc device and application to surface-reactive materials. *Biomaterials*, **18** (16), 1091–1098.

46. Lotz, M.M., Burdsal, C.A., Erickson, H.P., and McClay, D.R. (1989) Cell adhesion to fibronectin and tenascin: quantitative measurements of initial binding and subsequent strengthening response. *J. Cell Biol.*, **109**, 1795–1805.

47. Helenius, J., Heisenberg, C.P., Gaub, H.E., and Muller, D.J. (2008) Single-cell force spectroscopy. *J. Cell Sci.*, **121**, 1785–1791.

48. Walter, N., Selhuber, C., Kessler, H., and Spatz, J.P. (2006) Cellular unbinding forces of initial adhesion processes on nanopatterned surfaces probed with magnetic tweezers. *Nano Lett.*, **6** (3), 398–402.

49. Neuman, K.C. and Nagy, A. (2008) Single-molecule force spectroscopy: optical tweezers, magnetic tweezers and atomic force microscopy. *Nat. Methods*, **5**, 491–505.

50. Sako, Y., Nagafuchi, A., Tsukita, S., Takeichi, M., and Kusumi, A. (1998) Cytoplasmic regulation of the movement of E-Cadherin on the free cell surface as studied by optical tweezers and single particle tracking: corralling and tethering by the membrane skeleton. *J. Cell Biol.*, 140z (5), 1227–1240.

51. Andersson, M., Madgavkar, A., Stjerndahl, M., Wu, Y., Tan, W., Duran, R., Niehren, S., Mustafa, K., Arvidson, K., and Wennerberg, A. (2007) Using optical tweezers for measuring the interaction forces between human bone cells and implant surfaces: system design and force calibration. *Rev. Sci. Instrum.*, **78** (7), 074302–074302.

52. Hosokawa, Y., Hagiyama, M., Iino, T., Murakami, Y., and Ito, A. (2011) Noncontact estimation of intercellular breaking force using a femtosecond laser impulse quantified by atomic force microscopy. *Proc. Natl. Acad. Sci. U.S.A.*, **108** (5), 1777–1782.

53. Chu, Y.S., Thomas, W.A., Eder, O., Pincet, F., Perez, E., Thiery, J.P., and Dufour, S. (2004) Force measurements in E-cadherin-mediated cell doublets reveal rapid adhesion strengthened by actin cytoskeleton remodeling through Rac and Cdc42. *J. Cell Biol.*, **167** (6), 1183–1194.

54. Jégou, A., Pincet, F., Perez, E., Wolf, J.P., Ziyyat, A., and Gourier, C. (2008) Mapping mouse gamete interaction forces reveal several oocyte membrane regions with different mechanical and adhesive properties. *Langmuir*, **24**, 1451–1458.

55. Ahmad, M.R., Nakajima, M., Kojima, M., Kojima, S., Homma, M., and Fukuda, T. (2012) Nanofork for single cells adhesion measurement via ESEM-nanomanipulator system. *IEEE Trans. Nanobiosci.*, **11** (1), 70–78.

56. Kang, S. and Elimelech, M. (2009) Bioinspired single bacterial cell force spectroscopy. *Langmuir*, **25** (17), 9656–9659.

57. Puech, P.H., Taubenberger, A., Ulrich, F., Krieg, M., Muller, D.J., and Heisenberg, C.P. (2005) Measuring cell adhesion forces of primary gastrulating cells from zebrafish using atomic force microscopy. *J. Cell Sci.*, **118** (18), 4199–4206.

58. Friedrichs, J., Helenius, J., and Muller, D.J. (2010) Quantifying cellular adhesion to extracellular matrix components by single-cell force spectroscopy. *Nat. Protoc.*, **5** (7), 1353–1361.

59. Yermolenko, I.S., Fuhrmann, A., Magonov, S.N., Lishko, V.K., Oshkadyerov, S.P., Ros, R., and Ugarova, T.P. (2010) Origin of the nonadhesive properties of fibrinogen matrices probed by force spectroscopy. *Langmuir*, **26** (22), 17269–17277.

60. Benoit, M., Gabriel, D., Gerisch, G., and Gaub, H.E. (2000) Discrete interactions in cell adhesion measured by single-molecule force spectroscopy. *Nat. Cell Biol.*, **2**, 313–317.

61. Müller, D.J., Helenius, J., Alsteens, D., and Dufrene, Y.F. (2009) Force probing surfaces of living cells to molecular resolution. *Nat. Chem. Biol.*, **5**, 383–390.

62. Chaudhuri, O., Parekh, S.H., Lam, W.A., and Fletcher, D.A. (2009) Combined atomic force microscopy and side-view optical imaging for mechanical studies of cells. *Nat. Methods*, **6** (5), 383–387.

63. Shen, Y., Nakajima, M., Kojima, S., Homma, M., and Fukuda, T. (2011) Study of the time effect on the strength of cell-cell adhesion force by a novel nano-picker. *Biochem. Biophys. Res. Commun.*, **409**, 160–165.

64. Lehenkari, P.P. and Horton, M.A. (1999) Single integrin molecule adhesion forces in intact cells measured by atomic force microscopy. *Biochem. Biophys. Res. Commun.*, **259**, 645–650.

65. McNamee, C.E., Armini, S., Yamamoto, S., and Higashitani, K. (2009) Determination of the binding of non-cross-linked and cross-linked gels to living cells by atomic force microscopy. *Langmuir*, **25** (12), 6977–6984.

66. Weder, G., Blondiaux, N., Giazzon, M., Matthey, N., Klein, M., Pugin, R., Heinzelmann, H., and Liley, M. (2010) Use of force spectroscopy to investigate the adhesion of living adherent cells. *Langmuir*, **26** (11), 8180–8186.

67. Friedrichs, J., Torkko, J.M., Helenius, J., Teravainen, T.P., Fullekrug, J., Muller, D.J., Simons, K., and Manninen, A. (2007) Contributions of galectin-3 and -9 to epithelial cell adhesion analyzed by single cell force spectroscopy. *J. Biol. Chem.*, **282** (40), 29375–29383.

68. Xie, H., Rakotondrabe, M., and Régnier, S. (2009) Characterizing piezoscanner hysteresis and creep using optical levers and a reference nanopositioning stage. *Rev. Sci. Instrum.*, **80** (4), 046102.

69. Xie, H. and Régnier, S. (2009) Three-dimensional automated micromanipulation using a nanotip gripper with multi-feedback. *J. Micromech. Microeng.*, **19**, 075009.

70. Xie, H. and Régnier, S. (2011) Development of a flexible robotic system for multiscale applications of micro/nanoscale manipulation and assembly. IEEE/ASME Trans. *Mech.*, **16** (2), 266–276.

71. Xie, H., Lambert, P., and Régnier, S. (2011) Analysis of nanoscale mechanical grasping under ambient conditions. *J. Micromech. Microeng.*, **21** (4), 045009.

72. Sader, J.E., Chon, J.W., and Mulvaney, P. (1999) Calibration of rectangular atomic force microscope cantilevers. *Rev. Sci. Instrum.*, **70**, 3967–3969.

73. Sagvolden, G., Giaever, I., Pettersen, E.O., and Feder, J. (1999) Cell adhesion force microscopy. *Proc. Natl. Acad. Sci. U.S.A.*, **96**, 471–476.

74. Stevens, M.M. and George, J.H. (2005) Exploring and engineering the cell surface interface. *Science*, **310** (5751), 1135–1138.

75. Yu, Q., Zhang, Y., Chen, H., Zhou, F., Wu, Z., Huang, H., and Brash, J.L. (2010) Protein adsorption and cell adhesion/detachment behavior on dual-responsive silicon surfaces modified with poly (N-isopropylacrylamide)-block-polystyrene copolymer. *Langmuir*, **26** (11), 8582–8588.

76. Wohlrab, S., Müller, S., Schmidt, A., Neubauer, S., Kessler, H., Leal-Egaña, A., and Scheibel, T. (2012) Cell adhesion and

proliferation on RGD-modified recombinant spider silk proteins. *Biomaterials*, **33** (28), 6650–6659.

77. Ranella, A., Barberoglou, M., Bakogianni, S., Fotakis, C., and Stratakis, E. (2010) Tuning cell adhesion by controlling the roughness and wettability of 3D micro/nano silicon structures. *Acta Biomater.*, **6** (7), 2711–2720.

78. Zhao, J., Wu, J., and Veatch, S.L. (2013) Adhesion stabilizes robust lipid heterogeneity in supercritical membranes at physiological temperature. *Biophys. J.*, **104** (4), 825–834.

19
Nanorobotic Manipulation of Helical Nanostructures

Lixin Dong, Li Zhang, Miao Yu, and Bradley J. Nelson

19.1
Introduction

Three-dimensional (3D) helical structures with nanofeatures, such as carbon nanocoils, helical carbon nanotubes (CNTs) [1], and zinc oxide nanobelts [2], have attracted research interest because of their potential applications in nano-electro-mechanical systems (NEMSs) and other nanosystems. A new method of creating 3D helical structures with nanometer-scale dimensions has recently been presented [3] and can be fabricated in a controllable way [4] (Figure 19.1). The structures are created through a top-down fabrication process in which a strained nanometer-thick heteroepitaxial bilayer curls up (Figure 19.1a) by a pair of opposing forces (F_1 and F_2) to form 3D structures with nanoscale features, such as SiGe/Si tubes (Figure 19.1b, diameters between 10 nm and 10 μm), Si/Cr rings (Figure 19.1c, [5], see Ref. [9] for InGaAs/metal structures), SiGe/Si coils [4] (Figure 19.1d), InGaAs/GaAs coils [6] (Figure 19.1e), small-pitch InGaAs/GaAs coils (Figure 19.1f), Si/Cr claws (Figure 19.1g), Si/Cr spirals [8] (Figure 19.1h), and small-pitch SiGe/Si/Cr coils [7] (Figure 19.1i). Because of their interesting morphology, mechanical, electrical, and electromagnetic properties, applications and potential ones of these nanostructures in NEMS and other nanosystems include nanosprings, electromechanical sensors, magnetic field detectors, chemical or biological sensors, generators of magnetic beams, inductors, actuators, high-performance electromagnetic wave absorbers, and optical antennas.

Nanorobotic manipulation enables a hybrid approach by combining top-down and bottom-up processes for creating NEMS and other nanosystems (Figure 19.2) that can attain a higher functionality because they possess more complex structures. Because the as-fabricated nanostructures are not free-standing from their substrate, nanorobotic assembly is virtually the only way to incorporate them into devices at present. Moreover, for these structures,
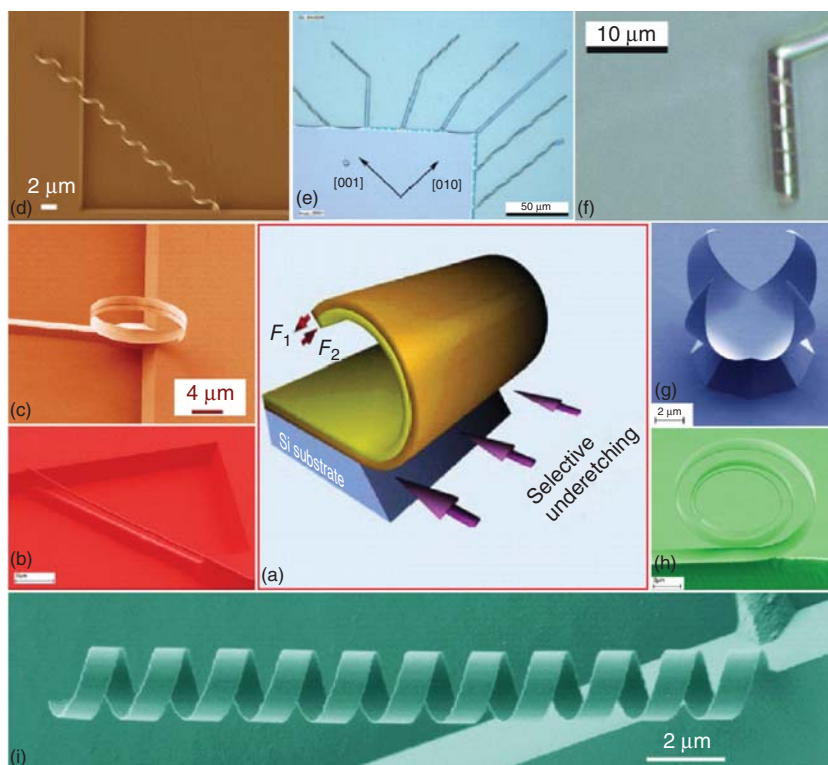
Figure 19.1 3D helical nanostructures. (a) Schematic diagram of rolled-up helical structures. (b) A SiGe/Si tube [4]. (c) A Si/Cr ring [5]. (d) A SiGe/Si coil [4]. (e) InGaAs/GaAs coils [6]. (f) A small-pitch InGaAs/GaAs coil [7]. (g) A Si/Cr claw. (h) A Si/Cr spiral [8]. (i) A small-pitch SiGe/Si/Cr coil [7].

nanorobotic manipulation is still the only technique capable of *in situ* structuring and characterization. Moreover, property characterization can be performed after intermediate processes, and *in situ* active characterization can be performed using manipulation rather than conventional static observations. Nanorobotics expands the lower limit of robotic exploration further into the nanometer scale, and it will provide nanoscale sensors and actuators, structuring and assembly technology for building nanorobots. Nanorobotic manipulation is featured by multidegrees of freedom and 3D processes, differentiating it from scanning probe techniques. Nanomaterial science, bionanotechnology, and nanoelectronics will also benefit from advances in this new nanomanufacturing technique from the perspectives of property characterization, fabrication, and assembly.
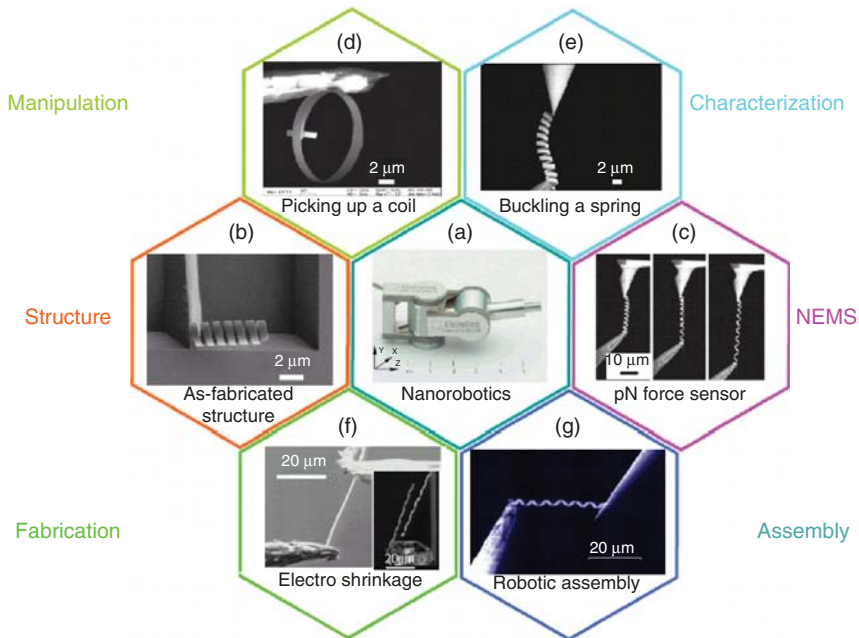
Figure 19.2 A nanorobotic manipulation approach to NEMS. Nanorobotics (a) is a unique approach for functionalizing the as-fabricated helical nanostructures (b) into NEMS (c) by changing their position/orientation (manipulation (d)), deforming their shapes (characterization (e)), modifying their structures (fabrication (f)), and increasing their numbers (assembly (g)).

19.2
Nanorobotic Manipulation Tools and Processes

19.2.1
Nanomanipulators and Tools

Nanomanipulators (MM3A^{TM} from Kleindiek) installed inside a scanning electron microscope (SEM) or under an optical microscope are used for the experiments. The manipulator (as shown in Figure 19.2a) has three degrees of freedom, and 5, 3.5, and 0.25 nm resolution in X, Y, and Z directions at the tip, respectively. Each joint has a piezoactuator with open-loop control. Kinematic analysis shows that when scanning in the X/Y directions using rotary joints, the additional linear motion in Z direction is very small. For example, when the arm length is 50 mm, the additional motion in the Z direction is only $0.25-1$ nm when moving in the X direction for $5-10\,\mu m$; these errors can be ignored or compensated with the last prismatic joint, which has a 0.25-nm resolution.
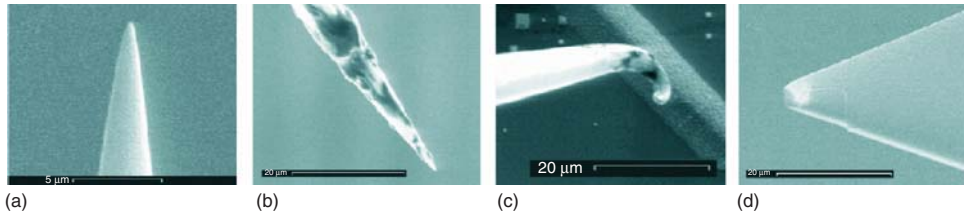
Figure 19.3 Tools for nanomanipulation. (a) Sharp tip. (b) Sticky probe. (c) Hook. (d) AFM cantilever.

The standard tool of the manipulator is a commercially available tungsten sharp probe (Picoprobe T-1-10-1 mm (Figure 19.3a) and T-1-10). In order to facilitate different processes, special tools have been fabricated, including a nanohook (Figure 19.3b) prepared by controlled "tip-crashing" of a sharp probe onto a substrate, and a "sticky" probe (Figure 19.3c) prepared by tip dipping into a double-sided SEM silver conductive tape (Ted Pella, Inc.). Atomic force microscope (AFM) cantilevers (nanoprobe, NP-S, Figure 19.3d) are used for measuring forces or as electrodes.

19.2.2
Nanorobotic Manipulation Processes

The construction of NEMS and other systems using 3D helical nanostructures typically involves the assembly of as-fabricated building blocks, which is a significant challenge from a fabrication standpoint. Focusing on the unique aspects of manipulating 3D helical nanostructures due to their helical geometry, high elasticity, single-end fixation on a chip, and strong adhesion of the coils to the substrate due to wet etching, a series of new processes has been developed using the manipulator installed in a SEM or under an optical microscope. As shown in Figure 19.4, experiments demonstrate that the as-fabricated nanostructures can be released from a chip by picking up with a "sticky" probe from their free ends (Figure 19.4a, tubes), fixed ends (Figure 19.4d,e, coils), external surfaces (Figure 19.4g, rings), or internal surfaces (Figure 19.4j, spirals), and bridged between the probe and another probe (Figure 19.4k) or an AFM cantilever (Figure 19.4b,f1,h), showing a promising approach for robotic assembly of these structures into other sites (Figure 19.4f2) to form complex systems. Axial pulling (Figure 19.5)/pushing, radial compressing (Figure 19.4i1–i5)/releasing, bending/buckling (Figure 19.4c1–c4), and unrolling (Figure 19.4l1–l5, spirals; and Figure 19.4n1–n8, claws) have also been demonstrated for property characterization.

Electrical properties can be characterized by placing a coil between two probes or electrodes [10]. An interesting phenomenon found in the measurements is that the SiGe/Si nanocoils with Cr layers can shrink further by passing current through them or by placing a charged probe on them. A 5-turn as-fabricated coil
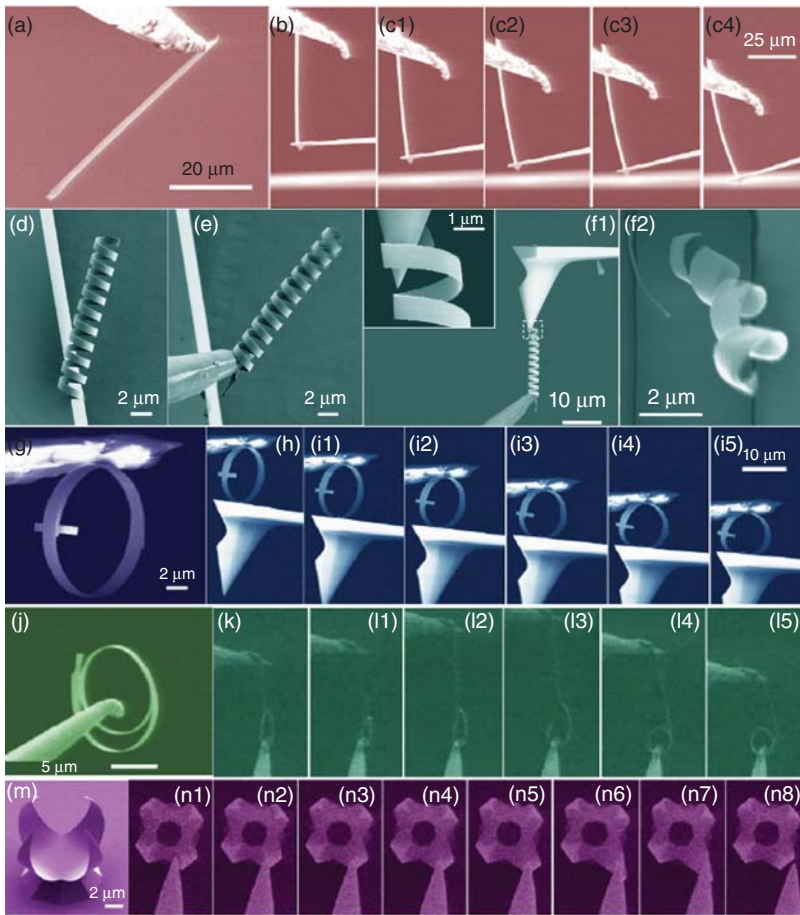
Figure 19.4 Nanorobotic manipulation of 3D helical structures. Pick up a tube (a), bridge it between a probe and an AFM cantilever (b), and buckle it (c1–c4) for electromechanical property characterization for force measuring. Pick up a small-pitch coil (d,e), bridge it between a probe and an AFM cantilever (f1), or assemble it on another site (f2). Pick up a ring (external diameter: 12.56 μm; stripe width: 1.2 μm; number of turns: 2.5; thickness: Si/Cr 35/10 nm) (g), bridge it between a probe and an AFM cantilever (h), and compress it for mechanical property characterization for understanding its stiffness (i1–i5). Pick up a spiral (Si/Cr layer thickness: 35/10 nm) (j), bridge it between a probe and another probe (k), and unroll it for mechanical property characterization for understanding its interlayer interaction (taken from a video clip) (l1–l5). Unroll a leaf of claws (m) for mechanical property characterization for understanding its "shape memory" (taken from a video clip) (n1–n8).
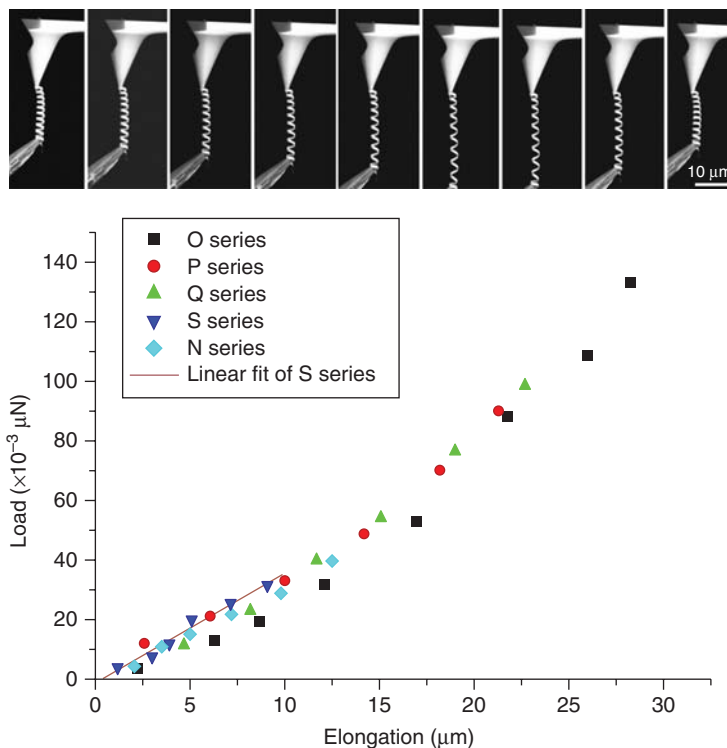
Figure 19.5 Characterization of the stiffness of a nanocoil using axial pulling.

was observed to become an 11-turn coil, showing the possibility of structuring them (Figure 19.2f).

These processes demonstrate the effectiveness of manipulation for the characterization of the 3D helical nanostructures and their assembly for NEMS, which have otherwise been unavailable.

19.3
Characterization of Helical Nanobelts

In situ characterization of as-fabricated helical nanobelts is one of the main applications of the basic nanorobotic manipulation processes demonstrated in the previous section. Mechanical properties of individual rolled-up SiGe/Si tubes and Si/Cr rings are investigated experimentally by axial extending, lateral bending, axial buckling, tangential unrolling, and radial stretching using nanorobotic manipulation. The objectives are to understand their elasticity, fracture resistance, mechanical stability, interlayer bonding, radial stiffness, and so on.

19.3.1
Axial Pulling of Rolled-Up Helical Nanostructures

The stiffness of the tube, the coil, and the ring has been measured from the SEM images (Figures 19.4 and 19.5) by extracting the AFM tip displacement and the deformation of the structures. The stiffness of the tube, the ring, and the coil springs was estimated to be ~10, 0.137, and 0.003 N m^{-1} (calibrated AFM cantilever stiffness: 0.038 N m^{-1}), showing a large range for selection. The linear elastic region of the small-pitch coils reaches up to 90% (Figure 19.5). Unrolling experiments show that these structures have excellent ability on memorizing their original shapes.

The excellent elasticity of nanocoils suggests that they can be used to sense ultrasmall forces by monitoring the deformation of the spring as a "spring balance" (Figure 19.5). If working in a SEM, suppose an imaging resolution of 1 nm can be obtained (the best commercially available field emission scanning electron microscope (FESEM) can provide such a resolution in an ideal environment), a "spring balance" constructed with the calibrated coil (10 turns, 0.003 N m^{-1}) can provide a 3 pN nm^{-1} resolution for force measurement. With smaller stripe widths or more turns, nanocoils can potentially provide fN resolution. In the SEM used in these experiments, the available imaging resolution is 10 nm, which provides a 30 pN/10-nm resolution.

19.3.2
Lateral Bending and Local Buckling of a Rolled-Up SiGe/Si Microtube

Tightly wound tubes [11, 12] with a variety of materials including semiconductors, metals, and insulators indicate a variety of potential applications in micro-electro-mechanical systems (MEMS) or NEMS [12], optoelectronics [13], and microfluidic devices [14]. For these applications, it is obviously important to understand their mechanical properties. Nanorobotic manipulation has been applied to investigate the mechanical properties of individual SiGe/Si microtubes [15].

To investigate the instability of microtubes, a probe (hook-shaped) is used to bend a tube with deflection angles between 0° and 180° to the substrate plane (Figure 19.6). The prepatterned SiGe/Si bilayer was scrolled into freestanding tubes with a diameter d of approximately 1.25 μm. The as-fabricated SiGe/Si microtubes are straight and have a uniform size from their free end to the fixed end. Microtubes with freestanding length greater than 50 μm were employed for bending tests. The results from a 1.6-turn tube show that various deformation modes were observed depending upon the bending angle. Under small deflection, that is, not more than 10°, the horizontal diameter (d_h) of the whole freestanding part of the tube decreases as the cross section of tube becomes oval, demonstrating the Brazier effect [16], in which the horizontal diameter reduces approximately 15% with a 10° bending angle. By increasing the bending angle to 27.6°, the horizontal diameter decreased significantly in a local regime (see inset of Figure 19.6a) due to local buckling of the tube [16].
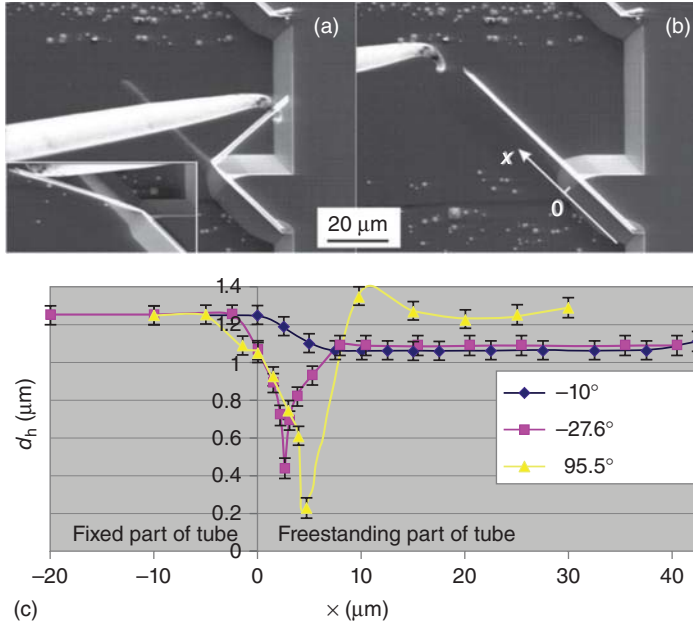
Figure 19.6 Bending tests of freestanding SiGe/Si microtubes. (a) A SiGe/Si microtube is buckled locally with a bending angle of 95.5° and −27.6° by manipulator probe. (b) The tube recovers to its original shape after the probe is removed. (c) The curves show that the local diameter of tube (d_h) from a top-view SEM image depends on tube axis x.

The dependence of the horizontal diameter (d_h) on the tube axis (x) indicates that both local buckling and Brazier effects exist [17], as shown in Figure 19.6c. If the microtube undergoes a larger bending angle, for example, 95.5° as shown in Figure 19.6a, local buckling dominates the deformation of the tube, whereas the uniform Brazier effect disappears. In Figure 19.6c, the value of d_h is larger than that of d, and is mainly attributed to the twisting of the tube in the buckled regime. If we release the bending force, the microtube recovers to its original shape and diameter as shown in Figure 19.6b. Interestingly, both 1.2- and 1.6-turn microtubes recover to their original shape even bent 180° or more. No catastrophic damage or permanent distortion of their shape was observed in the SEM, indicating that these freestanding microtubes are extremely flexible even under a large deflection. Unlike kinked CNTs [18, 19], no plastic deformation was found in our tests. The excellent elasticity of these microtubes also implies that the as-grown SiGe/Si heterostructure has a good quality, that is, nearly free from dislocations. However, with a very large deflection, stress will concentrate quickly at the buckled position of the tube. Eventually, the tube will fracture due to the severe deformation at the buckled position after repeating this bending test. With large deflection angles, that is, larger than 120°, the tube has a fatigue failure within less than 10 bending test cycles. We have never observed the

failure of microtubes by repeated bending tests when the bending angle is smaller than 10°.

19.3.3
Axial Buckling of Rolled-Up SiGe/Si Microtubes

To investigate the mechanical instability of microtubes under axial compressive loads, the individual SiGe/Si tube is manipulated using a "sticky" probe. Manipulation processes are demonstrated in Figure 19.7. To pick up a SiGe/Si microtube from the substrate, a shear force is applied at the fixed end of the tube by lateral pushing of the "sticky" probe (see inset of Figure 19.7a). Then the free end of microtube is mounted on the back of an AFM cantilever and rotated such that its axis is perpendicular to the AFM cantilever. The manipulation demonstrates that the boundary condition of the "sticky" probe and the microtube is "hinged," that is, resembling a ball joint. At the other end of the microtube, the boundary condition between an AFM cantilever and a microtube depends on the back of the AFM cantilever. When an AFM cantilever has a smooth back, the boundary condition can be considered free on the plane. Whereas for an AFM cantilever with a pyramid hole at the back (see inset of Figure 19.7b), the boundary condition becomes fixed. The fixed boundary condition is preferable. This makes it possible to adjust the angle between a tube and the manipulator probe to 90°, and the microtube will not readily slide during loading. By pushing the "sticky" probe along the tube axis, the microtube is subjected to an axial compressive stress and deflects the AFM cantilever. This deflection gives the compressive force applied to the longitudinal axes of the tube, from which the load and the stress on the microtube can be obtained.

According to axial compressive load tests, the dependence of deformation on applied force for SiGe/Si tubes with 1.2 and 1.6 turns is shown in Figure 19.8a. The deformation of the tube is measured as the shortened length of the tube between its fixed end on the manipulator probe and its free end on the AFM cantilever. Distance is measured from the SEM image. For the tube "a," three deformation regimes can be identified in the buckling test. Initially, the load increases linearly
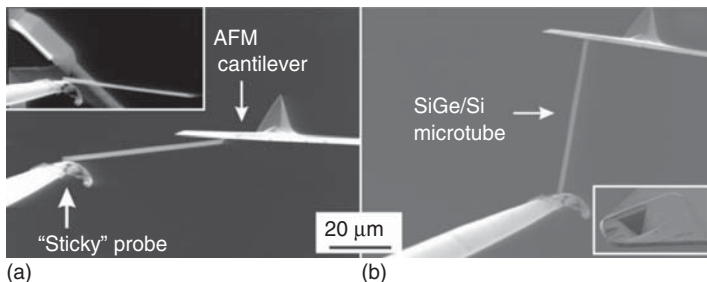
Figure 19.7 Nanorobotic manipulation of a freestanding SiGe/Si microtube. (a) Placing a microtube on the back of an AFM cantilever. Inset: Cutting of a microtube from Si substrate. (b) Rotating a microtube on an AFM cantilever. Inset: AFM cantilever with a hole on its back.
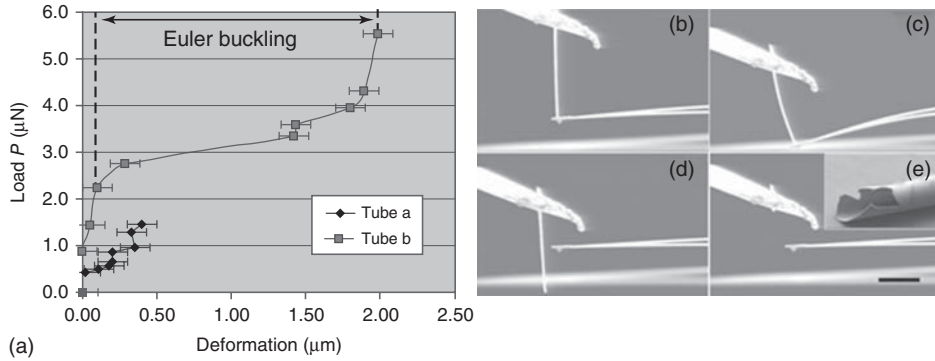
Figure 19.8 (a) Experimental curve of force versus displacement resulting from buckling tests for 61.6- and 43.5-µm-long SiGe/Si microtubes with 1.6 and 1.2 turns, respectively. The Euler buckling regions of the 61.6-µm-long tube are marked in the diagram. (b) A tube is stable under axial compressive load. (c) Euler buckling of a 61.6-µm-long SiGe/Si tube. (d) The tube recovered from its postbuckling state. (e) The tube was fractured when load is larger than 5.5 µN. Inset: The fractured region of the SiGe/Si tube.

with very small displacement; the tube is in a stable equilibrium state and remains straight (see Figure 19.8b). In the second regime, the curve becomes flat. The sudden drop of the slope indicates that the tube begins to buckle. Finally, in the third regime, the slope again becomes steep while the wall of the tube severely bends, which is shown in Figure 19.8c. Figure 19.8d shows that the tube can recover from its post-buckling state. A further increase of the load leads to severe local deformation of the tube and, finally, to mechanical fracture of the microtube.

The kink in the curve between the first and the second regimes represents a neutral equilibrium of the microtube. The *corresponding load* is defined as the critical load (P_{cr}). As shown in Figure 19.8a, the value of the critical load of approximately 2.2 µN is determined for a 61.6-µm long, 1.6-turn SiGe/Si microtube (i.e., tube "a"). The critical stress (δ_{cr}) can be expressed as $\delta_{cr} = P_{cr}/A$, where A is the cross-sectional area of the tube. The critical stress in this tube is 18.4 MPa. In contrast to 1.6-turn microtubes, 1.2-turn tube (tube "b") shows less critical load, that is, 1.5 µN. It should be noted that bilayers scrolled into unclosed tubes, for example, 3/4 of a turn, showed a critical stress approximately 1 order of magnitude smaller than that of the films scrolled by 1.6 turns.

According to Euler's formula [20], the critical load can be expressed as $P_{cr} = \pi^2 EI/(L_{eff})^2$ in which EI is the flexural rigidity and L_{eff} is the effective length of the tube ($L_{eff} = 2L$, for hinged-fixed condition [21]). Using this formula, the calculated critical load for an ideal seamless Si microtube with 61.6-µm length under hinged-fixed condition is approximately 1.23 µN. Here, the Young's modulus of Si from bulk material [22] and the Si tube with a diameter of 1.25 µm and a wall width of 19 nm have been assumed. The 1.6-turn rolled-up tube is approximated as a combination of an ideal tube and a 0.6-turn tube, so the cross-sectional area is the sum of a thin circular ring and a thin circular arc. For this 1.6-turned ideal tube, the critical load is calculated to be 2.0 µN, close to the

experimental value (2.2 μN). This result indicates that the mechanical stability of a scrolled microtube, with 1.6 turns, is very similar to a seamless tube, whereas the calculated critical load of the 1.2-turn microtube is 3.0 μN, which is double of the experimental value. On the basis of the above results, it is presumed that the seamless model for calculation of the critical load and the flexural rigidity (EI) of the scrolled microtube would be even more accurate for a tightly scrolled tube with the number of turns greater than 1.6, since the shape of rolled-up tube will be even more similar to a ring shape of that of an ideal seamless tube.

The deviation of the real flexural rigidity of a scrolled microtube and the calculated value from the ideal tube model may result from the difference in the moment of inertia of cross-sectional area I. For an ideal seamless tube, I is calculated as $\pi d^3 t/8$ when $t \ll d$ [21], where d and t are the diameter and the wall thickness of the tube. However, the 1.6-turn rolled-up microtube actually has a seam along the tube axis.

In the rolled-up bilayer, the two edges of the rolled sheet do not bond to form a seamless tube. However, when these edges overlap sufficiently, the tube becomes very stable. Surprisingly, the microtubes do not open along the seam when the axial compressive force is larger than the critical load. In addition, the microtubes exhibit an excellent ability to recover from the postbuckling stage to their initial straight shape, as shown in Figure 19.8c. Moreover, in cycling the experiment, the critical load remained unchanged after the microtube recovered from the buckled state. This implies that the microtube is elastically deformed and no permanent damage occurs in the SiGe/Si crystalline structure, even after it experiences an unstable state. An interesting observation is that in the third regime, the microtube becomes stiffer again (see Figure 19.8a). This may be attributed to the increase of the moment of inertia of the cross-sectional area of the microtube. When the microtube is heavily buckled, the neighboring walls of the spiral-like cross section of the tube may interact with each other, leading to a reinforcement of the stiffness of the tube. In addition, glue on the "stick" probe may start absorbing strain energy with a large compressive load, so the load of tube may be overestimated. When the microtube is strongly buckled, the internal (compression) sidewall of the tube is open locally, which leads to highly localized stress. In our experiments, this indicated the forthcoming failure of the tube. Inset of Figure 19.8e shows such a fractured microtube resulted from axial compression test, in which the curvature of the tube at the local region did not change.FESEM inspections also show that cracked edges prefer to propagate along the cleavage direction, that is, <110>. Thus, the tubes are destroyed in a brittle failure mode, which implies that the SiGe/Si microtubes may have much lower resistance fracture under tension or shear [21].

Both local buckling and Euler buckling phenomena have been experimentally observed in SiGe/Si microtubes when they are subjected to bending and axial compressive load, respectively. The flexural rigidity of the scrolled SiGe/Si microtube is close to the ideal seamless tube. The self-scrolled SiGe/Si microtubes show no plastic deformation and excellent elastic recovery from a postbuckling state.

19.3.4
Tangential Unrolling of a Rolled-Up Si/Cr Ring

Ring-like micro- or nanostructures synthesized or self-assembled from various materials have stimulated extensive investigation [23, 24]. Ring-closed rolled-up nanobelts can also be fabricated from a nanoribbon. From a geometrical point of view, a multiwalled nanobelt can be regarded as a spiral nanoribbon with no gap between adjacent turns. In developing these types of structures, it is important to probe the interaction between the rolled-up layers and the radial stiffness. The mechanical properties of individual as-fabricated Si/Cr multiwalled nanobelts are characterized using nanorobotic manipulation [5]. To characterize the flexibility and the interaction of the neighboring layers of as-fabricated Si/Cr nanobelts, a tungsten probe mounted on a manipulator is inserted into the nanobelt, as shown in Figure 19.9a. Then, the probe is translated along the longitudinal axis of the nanoribbon to unroll the structure (Figure 19.9b–f). It can be seen that the multi-walled (2.5-turn) Si/Cr nanobelt is highly deformed during the unrolling process. The maximum relative elongation of the nanobelt along this direction is approximately 75% as shown in Figure 19.9d. When the nanobelt is extended to less than one circumference, its curvature elastically recovers to its original shape, as can be seen in Figure 19.9e. The unrolling tests reveal that the adjacent bilayers of the Si/Cr multiwalled nanobelt are bonded together forming a closed-ring structure. The adhesion force is relatively strong, particularly for nanobelts with ribbon widths in the micrometer range. For example, a Si/Cr nanobelt with a ribbon width of 1.1 μm, as indicated by a white arrow in Figure 19.9a, was fractured at its fixed end before it could be unrolled. The result implies that van der Waals force is not the sole contribution to the adhesion of adjacent bilayers, because both the van der Waals force and the tensile rigidity of the nanoribbon increase linearly with the increasing ribbon width. We attribute another possible interaction between the bilayers to hydrogen bonding, because the rolled-up objects were formed after a wet etching and drying process. It is presumed that water molecules remain and link to one another to form a bridge between the adjacent bilayers [25] due to the
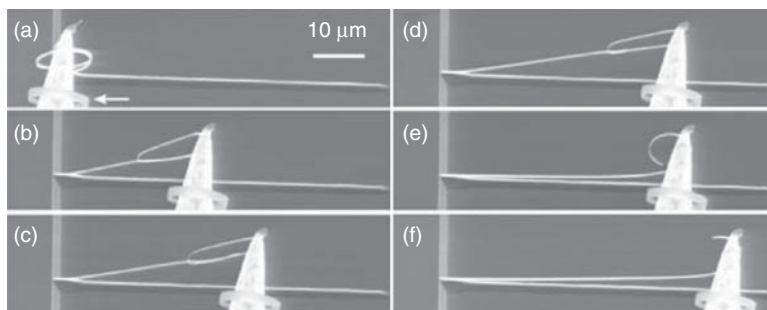
Figure 19.9 (a–f) SEM images showing the manipulator probe translating from left to right to unroll the Si/Cr nanobelt ($w = 500$ nm). The white arrow in (a) points to another nanobelt with a ribbon width of 1.1 μm.

imperfect surface roughness of the thermally evaporated Cr layer. The condensed liquid increases the contact area significantly, resulting in a large increase in adhesion [25]. When the width of the Si/Cr nanoribbon is larger than a critical value, the interaction bonding force will overwhelm the fracture force of the nanoribbon under tension. Thus, it is reasonable to assume that for multiple-turn Si/Cr or SiGe/Si/Cr micro- or nanotubes, the bonding force between the neighboring turns is sufficient to maintain closure before fracture, although the bonding force will be much smaller than covalent bonding in adjacent bilayers of the semiconductor micro- or nanotubes [26]. Moreover, it is expected that the bonding energy at the interface of adjacent Si/Cr bilayer can be improved by thermal annealing, a process often used for wafer bonding [25]. The aforementioned manipulation results indicate that it is possible to use these micro- or nanotubes as pipelines [14] for microfluidic devices or as needles for microinjection.

19.3.5
Radial Stretching of a Si/Cr Nanoring

To characterize the radial stiffness of a Si/Cr nanobelt under tensile load, an upright Si/Cr nanobelt with an indicating bar at the free end of the nanoribbon was prepared using a "T"-shaped patterned bilayer. The nanoribbon is aligned 2.5° from <110>. The mask design is shown in the inset of Figure 19.10a. This nanobelt has a diameter of 12.5 μm with a ribbon width of 1.2 μm. This design allows sliding between adjacent bilayers to be monitored by the movement of the crossbar when the structure is under tensile load. To perform the stretching test of the nanobelt, it is cut and picked up with a "sticky" probe prepared by dipping the tip of the probe into a double-sided SEM silver conductive tape. The sticky probe is carefully attached to the outer sidewall of the nanobelt, and the probe is then moved along the scrolling direction of the nanoribbon to break the nanobelt from the substrate, as shown in Figure 19.11a. Unlike the unrolling test, the nanobelt is cut at its fixed end by applying a shear force with the nanomanipulator. Afterward, the manipulator is used to bring the nanobelt to the back of an AFM cantilever so that the manipulator probe is on top of the nanobelt, and the AFM cantilever is at the bottom of the nanobelt (see Figure 19.10b). The other contact point of the nanobelt to the AFM cantilever is soldered by electron beam-induced deposition (EBID) [18]. Then, the stretching test for the nanobelt is performed by moving the probe upward away from the AFM cantilever. The tensile load can be measured by the deflection of the AFM cantilever and its calibrated spring constant ($0.038 \, \mathrm{N \, m^{-1}}$). The elongation of the nanobelt is measured along the loading direction.

   A series of FESEM micrographs in the inset of Figure 19.10c shows the evolution of the process of subjecting a 2.5-turn Si/Cr nanobelt to an increasing tensile force. According to the manipulation tests, neither permanent deformation of the nanobelt nor clear sliding between the adjacent bilayers is observed, indicating that the multiwalled nanobelt remains closed during deformation under the applied load. It is expected that more energy is required to open a multiwalled
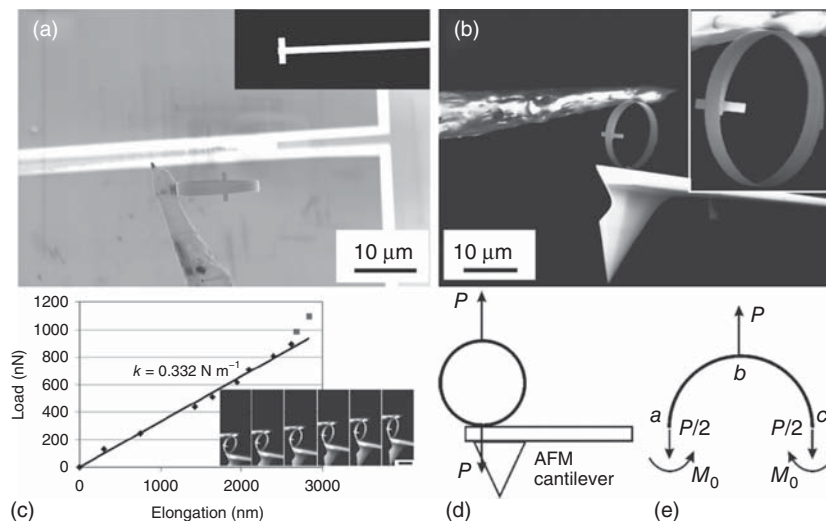
Figure 19.10 (a) A Si/Cr nanobelt is cut from the substrate by a sticky probe. Inset: The initial pattern design used to fabricate a Si/Cr nanobelt with a crossbar. (b) A Si/Cr ring is manipulated to the back of an AFM cantilever with a manipulator probe. Inset: Magnified image of the nanobelt with crossbar. (c) Radial stiffness test of an individual Si/Cr nanobelt (35/10 nm). Inset: A series of

FESEM images with increasing tensile load on the Si/Cr nanobelt. The scale bar is 10 μm for all images. (d) Schematic drawing of a ring undergoing a stretching test. (e) The upper-half of the ring structure is deformed due to the bending moment induced by the tensile load. The bending moments at points *a* and *c* of the ring are the same, that is, M_0.
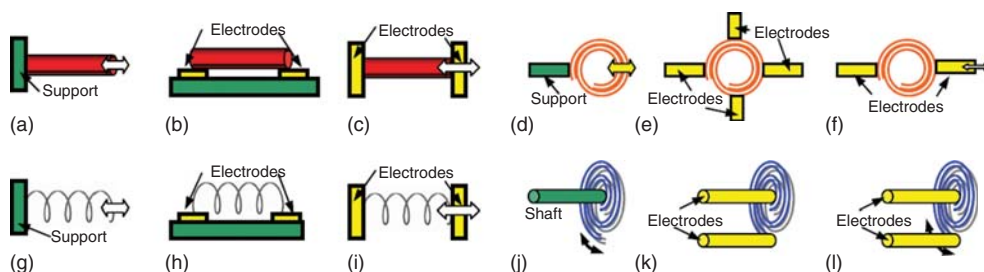
Figure 19.11 Configuration of 3D helical nanostructures-based NEMS. (a–c) Tubes. (d–f) Rings. (g–i) Coils. (j–l) Spirals. (a, d, g, j) Cantilevered. (b, e, h, k) Bridged (fixed). (c, f, i, l) Bridged (moveable).

nanobelt by a stretching test than an unrolling test, because the bonding energy must be simultaneously overcome between the adjacent bilayers. The radial stiffness of the 2.5-turn Si/Cr nanobelt is obtained by measuring the slope of the tensile load versus the corresponding elongation along the load direction, as shown in Figure 19.10c, revealing a linear relation when the relative elongation of the nanobelt is smaller than 23%. Thus, a corresponding radial stiffness of 0.332 N m^{-1} is determined using Hooke's law. However, the radial stiffness increases rapidly for

deformations beyond 23%. The load versus elongation curve demonstrates that a Si/Cr nanobelt can perform as a mechanical spring when subjected to an external tensile load. When compared with a helical nanospring [6], the nanobelt offers tunable stiffness by varying the number of the turns, wall thickness, and the ribbon width with only a small change in overall size. The increasing radial stiffness results mainly from the change of the force component from bending to tension in the region near points *a* and *c* (see Figure 19.10d). When the nanobelt experiences large deformations, the bending force gradually becomes tensile, and the curvature changes significantly, for example, at points *a* and *c* in Figure 19.10e. Timoshenko analyzed an ideal seamless ring structure under small deformation from a compressive load *P*, where the radial stiffness k_r along the compression direction can be expressed as [27]

$$k_r = (4EI)/[R^3(1 - v^2)(\pi - 8/\pi)], \tag{19.1}$$

where *E* is the Young's modulus, *I* is the moment of inertia of the cross-sectional area of the ring, *R* is the radius of the ring, and *v* is the Poisson ratio. If the ring has a rectangular cross-sectional area with ribbon width *w* and wall thickness *h*, *I* is $wh^3/12$. For an ideal ring, the radial stiffness should be the same when applying compression or tension. Thus, this equation is also valid as the nanobelt undergoes tensile deformation (see Figure 19.10d–e). The tensile stiffness of two straight belts connected in parallel with length (*L*) equal to πR (half-circumference of the ring) is given by $k_t = 2EA/L = 2Ewh/\pi R$. The ratio of tensile stiffness to radial stiffness for this configuration is expressed as

$$\frac{k_t}{k_r} = \frac{2Ewh/\pi R}{Ewh^3/3R^3(1 - v^2)(\pi - 8/\pi)} \approx 1.14(1 - v^2)\left(\frac{R}{h}\right)^2. \tag{19.2}$$

For experimental analysis, the radius of the nanobelt and wall thickness are 6.25 μm and 45 nm/turn (35 nm Si and 10 nm Cr), respectively. It is known that the Poisson ratios of Si and Cr are less than 0.4, thus the ratio of k_t to k_r is much larger than 1, that is, $k_t \gg k_r$, indicating increasing radial stiffness for large deformations of the nanobelt. Considering the as-fabricated Si/Cr nanobelt as an ideal closed system, Eq. (19.1) is used to compare experimental results. For a Si/Cr bilayer nanoribbon, the Young's modulus of the Si layer along 2.5° from the <110> orientation is 168 GPa [22], and a thermally evaporated Cr thin film has Young's modulus of 140 GPa. The Poisson ratios of the Si and the Cr layers are 0.06 (along <110>) and 0.21, respectively. In order to simplify the calculation, we assumed that the Cr thin film has the same Young's modulus and Poisson ratio as the Si thin film, and the cross-sectional area of the rolled-up nanobelt is considered to be a rectangle. Since the Si/Cr bilayer has a total thickness of 45 nm, two- and three-turn nanobelts have 90 and 135 nm total wall thicknesses, respectively. Calculations show that the radial stiffnesses of two- and three-turn Si/Cr nanobelts are 0.34 and 1.15 N m⁻¹, respectively. For the 2.5-turn rolled-up nanobelt, its radial stiffness in its linear region is very similar to a two-turn ideal ring. Since the bottom-half of the nanobelt has one turn less than the upper-half, the bottom-half of the nanobelt is more compliant and undergoes the most

deformation. Nevertheless, the upper-half of the ring with larger wall thickness still deforms and increases the radial stiffness of the ring. Thus, the as-fabricated Si/Cr nanobelt as a whole is less stiff than the estimate. The overestimation of the radial stiffness is mainly attributed to the following factors: (i) In the calculation, the Young's modulus of the Cr thin film increased from 140 to 168 GPa. (ii) The flexural rigidity (*EI*) is proportional to the cubic power of the wall thickness of the nanobelt, and the real wall thickness may be slightly thinner than the calculated one due to surface roughness of the Cr layer or imperfect wet etching selectivity of the Si layer [8]. For example, for a wall thickness of 44 nm that is 1 nm thinner than the assumed value, the radial stiffness will be 6% less than the calculated result. In addition, a thin 1–2 nm native amorphous chromium oxidation layer [28] may be formed on the Si/Cr nanoribbon, which can deviate the estimated value from the experimental result slightly.

19.4
Applications

19.4.1
Typical Configurations of NEMS

Typical configurations of NEMS based on 3D helical nanostructures are shown in Figure 19.11. The cantilevered structures shown in Figure 19.11 (a, tubes; d, rings; g, coils; and j, spirals) can serve as nanosprings using their elasticity in axial (tubes and coils), radial (rings), and tangential/rotary (spirals) directions. Nanoelectromagnets, chemical sensors nanoinductors, and capacitors involve building blocks bridged between two electrodes (two or four for rings) as shown in Figure 19.11 (b, tubes; e, rings; h, coils; and k, spirals). Electromechanical sensors can use a similar configuration but with one end connected to a moveable electrode as shown in Figure 19.11 (c, tubes; f, rings; i, coils; and l, spirals). Mechanical stiffness and electrical conductivity are fundamental properties for these devices that must be further investigated. Electron microscopy imaging or their intrinsic electromechanical coupling property can serve as readout mechanisms. Taking a so-called motion converter as an example, the design, fabrication, characterization, and application of helical nanostructure-based nanodevices are described in the following section.

19.4.2
Motion Converters

Mechanical motion, particularly resonance, is at the core of many NEMS [29–34] that are envisioned, and conversion between various forms of motions will play an important role in future nanosystem applications. Motion converters have been widely used for millennia to transmit actuator motion at different speeds, torques, or in different directions. Typical examples include such pairs

as pinion-gear, pinion-rack, pinion-worm, wheel-belt, wheel-chain, cable-pulley, and linkage mechanisms. The most commonly used mechanisms for converting linear motion to rotary motion use a piston moving in a cylinder to rotate a crank shaft by means of a link. It is interesting to note that at molecular scales in nature, similar converters also play an important role in motion conversion [35].

One application area of motion conversion is for 3D microscopy, in which samples are rotated (Figure 19.12a) so that different views are exposed to light, electron beams, or focused ion beams (FIBs). Conventional rotary/tilt stages usually consist of gear trains, bearings, and other elements actuated by motors. Because of the clearance of the motion pairs and the deviation between the optical axis and the rotary axis, it is commonly required to readjust the imaging field, focal plane, and other parameters. Furthermore, due to mechanical constraints, a 360° rotation is extremely difficult to achieve, leaving some aspects inaccessible. Goniometry has been an important technique in transmission electron microscopes (TEMs) for obtaining electron diffraction patterns, high-resolution images, and tomography, but conventional goniometers do not generate more than 60° rotations. Tilt stages of SEMs and tilt holders of TEMs suffer with similar limitations.

Nanoscale rotary motion can also be applied to other forms of microscopy. Scanning tunneling microscopes (STMs) [36], AFMs [37], and other scanning probe microscopes (SPMs) allow us to perform tasks such as characterization [38], manipulation [39], and fabrication [40, 41], in addition to imaging, on single molecules, atoms, and bonds, thereby providing a tool that operates at the ultimate limits of manufacturing. While tremendous progress [42, 43] has been made in enhancing their spatial resolution, sensing mechanisms, and probe tips [44−46], less attention has been paid to their conventional $X-Y$ planar scanning stages [47], which are best suited for features on a planar surface. Investigation of freestanding individual nanostructures is becoming increasingly important due
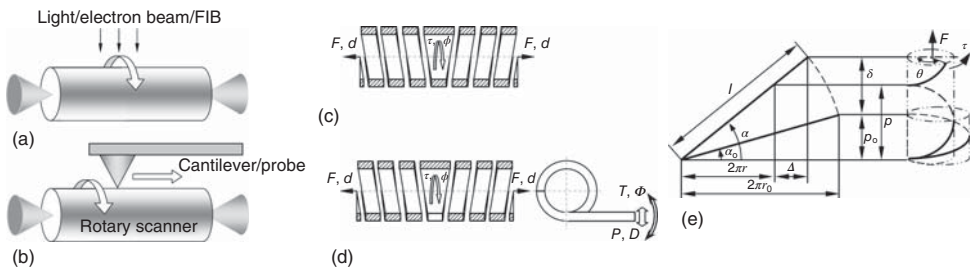
Figure 19.12 Motion converters using DCHNBs. (a) A linear-to-rotary motion converter for 3D microscopy using an irradiation source (light, electron beam, or FIB). (b) A linear-to-rotary motion converter for 3D scanning probe microscopy. (c) A linear motion to rotary motion converter using a DCHNB. (d) A transmission converting linear motion to extended linear (small displacement)/rotary (large displacement) motion. (e) One-pitch helix under an axial extension force. 3D and plan view show how the geometry changes from the initial position (radius r_0, pitch angle α_0) to the deflected position (radius r, pitch angle α) with a deflection δ and an induced rotational angle θ.

to the possibility of avoiding side effects from the substrate on the specimen. A single-walled carbon nanotube (SWNT) freely suspended over a trench has been investigated with atomic resolution using an STM [48] and correlated to electrical transport measurement [49]. A rotary scanning stage will enable the exposure of different aspects of an individual nanostructure to the probe tip, essentially creating a 3D SPM (Figure 19.12b), for fully correlating atomic structures and physical properties.

Because of the difficulty in generating precise rotation without clearance issues or backlash, linear-to-rotary motion converters would be an effective way to realize rotation from a linear actuator, which is generally easier to achieve at nanometer resolutions using solid-state actuators such as piezoelectrics. Among various nano-building blocks, dual-chirality helical nanobelts (DCHNBs) was demonstrated experimentally as a compact and unique transmission device for converting between linear and rotary motion [50].

19.4.2.1 Design of Motion Converters

As schematically shown in Figure 19.12c, the motion converter consists of a DCHNB with a left-handed and a right-handed part. By linearly extending the two ends of the DCHNB, the central part outputs rotary motion; providing a unique and fundamental mechanical mechanism for realizing linear-to-rotary motion conversion, a property not previously demonstrated in other nanostructures. With an extended arm (Figure 19.12d), the output can be linear (small displacement) or rotary (large displacement) motion.

As illustrated in Figure 19.12d, we define the ratio between the output torque τ and input force F as the load conversion ratio: $R_F = \tau / F$, and between the output angular displacement ϕ to the input extension d as the displacement conversion ratio: $R_d = \phi / d$. The extended arm (Figure 19.12e) amplifies the output further into linear (small displacement) motion with a force P and displacement D, or rotary (large displacement) motion with a torque T and a rotation Φ. We define r_0, p_0, and α_0 as the radius, pitch, and pitch angle, respectively, of the initial DCHNB. When a tensile force F is applied to the DCHNB, it elongates and rotates about the unwinding direction. At this deflected state, r, p, and α indicate the radius, pitch, and pitch angle, respectively. According to the plane view of a one-pitch DCHNB as illustrated in Figure 19.12e, the unwinding angle ϕ of a DCHNB is given by [51]

$$\phi = n\theta = 2\pi n \left(\frac{r_0}{r} \frac{\cos \alpha}{\cos \alpha_0} - 1 \right), \tag{19.3}$$

where n is the number of turns of a half-DCHNB (right-handed part in Figure 19.12e). Considering the mirror symmetry, the other half with opposite chirality has the same unwinding angle.

Once the DCHNB is elongated $2d$, each half of the DCHNB will deflect d. For each turn, the deflection will be $\delta = d/n$. According to the geometry, if one assumes that the length of the nanobelt L of a half-DCHNB (the length per turn: $l = L/n$) is constant (which is reasonable for springs with a large index [31]), the number of

turns of the deformed DCHNB m will be

$$m = \frac{r}{r_0} \sqrt{1 - \frac{d}{n\pi r_0} \tan \alpha_0 - \frac{d^2}{4n^2\pi^2 r_0{}^2}} \ n. \tag{19.4}$$

Noting that $\phi = 2\pi(m - n)$ and $p_0 = 2\pi r_0 \tan \alpha_0$, the unwinding angle ϕ can be expressed as a function of d

$$\phi = 2\pi n \left(\frac{r}{r_0} \sqrt{1 - \left(2 + \frac{d}{np_0} \right) \frac{d}{np_0} \tan^2 \alpha_0 - 1} \right) \tag{19.5}$$

with a geometric constraint of

$$\left(-1 - \sqrt{1 + \cot^2 \alpha_0} \right) np_0 \ \le d \ \le \left(-1 + \sqrt{1 + \cot^2 \alpha_0} \right) np_0. \tag{19.6}$$

For small deflection, the change of the radius of a DCHNB can be ignored ($\Delta \approx 0$ in Figure 19.12e), that is, $r \approx r_0$.

As an example, for a DCHNB with $\alpha_0 = 58°$, $p_0 = 5.4\,\mu m$, and $n = 7$, we can depict ϕ versus d (Figure 19.13a). It can be seen that the linear range is quite large before the DCHNB straightens (see inset of Figure 19.13a for long-range ϕ vs d curve). An accurate displacement conversion ratio can be obtained from Eq. (19.5): $R_d = \phi/d = 179.4°/\mu m$ or 3.75 turns/pitch.

19.4.2.2 Displacement Conversion

The fabrication process for helical nanobelts by the scrolling of strained SiGe/Si or InGaAs/GaAs bilayer has been reported elsewhere [27, 28]. On the basis of V-shaped mesa designs (see inset of Figure 19.13b), freestanding DCHNBs can be achieved [25]. Figure 19.13a shows an as-fabricated SiGe/Si DCHNB with a diameter of about 1 μm. The helix is formed by an 8-nm thick $Si_{0.6}Ge_{0.4}$ and a 10-nm thick Si layer.
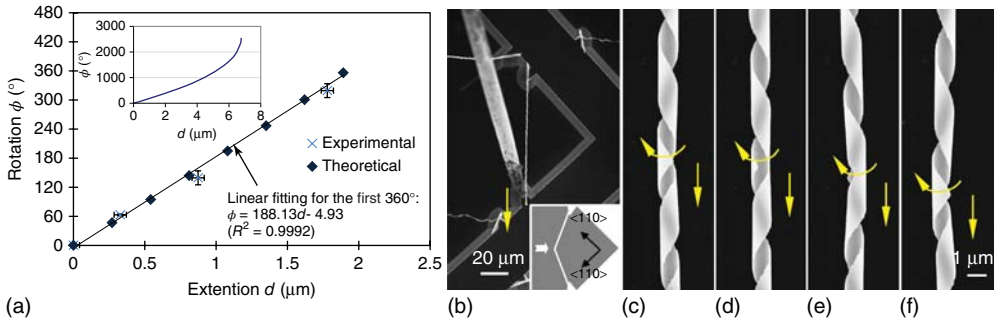
Figure 19.13 Linear-to-rotary motion conversion ratio. (a) Linear-to-rotary motion (d to ϕ) conversion curve of a DCHNB ($\alpha_0 = 58°$, $p_0 = 5.4\,\mu m$, and $n = 7$) for the first turn. (Inset: Long-range ϕ vs d curve). (b–f) *In situ* characterization of motion conversion using nanorobotic manipulation. (b) One end of an as-fabricated DCHNB (Inset: A V-shaped mesa) is cut and attached to a "sticky" probe. (c–f) Rotation of the central part while moving the probe downward.

To implement and characterize motion converters, such as the one shown in Figure 19.13b, experimental investigations have been performed in an FESEM (Zeiss ULTRA 55) using a nanomanipulator (MM3A, Kleindiek) equipped with a tungsten probe (Picoprobe, T-4-10-1 mm, Figure 19.2b) and an AFM cantilever (Mikromasch, CSC38/Ti−Pt, calibrated [32] stiffness: $0.1400\,N\,m^{-1}$). Manipulation of an as-fabricated DCHNB was performed by cutting the lower end of the DCHNB with the probe shown in Figure 19.14b. A "sticky" probe [33] is then prepared by dipping a Picoprobe into a silver tape and attached on the lower end of the DCHNB. Rotation is then generated in the central part (Figures 19.13c−f) by moving the probe downward. We then measured the extension and rotation from Figure 19.13b−e and plotted them in Figure 19.13a. (The DCHNB has the same parameters as that used in Figure 19.13a.) It can be seen that the experimental and theoretical values are in excellent agreement.
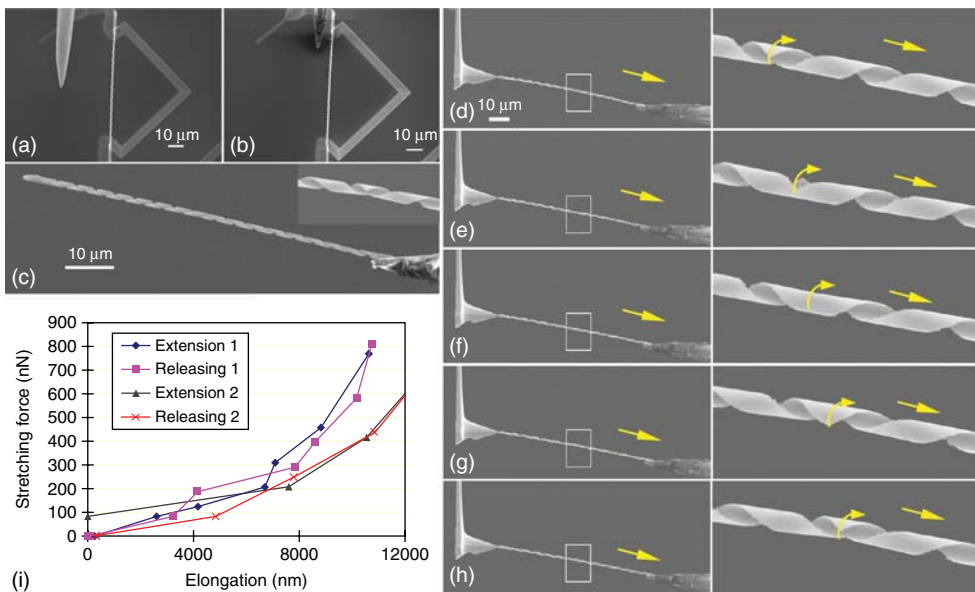
Figure 19.14 Force-to-elongation characterization. (a–c) Manipulation of a DCHNB. (a) An as-fabricated DCHNB with a tungsten probe for manipulation being visible. (b) The lower end of the DCHNB was broken with the probe shown in (a). A "sticky" probe is also visible. (c) A DCHNB was picked up with a "sticky" probe. The inset shows the middle part. (d–i) Mechanical property characterization of a linear-to-rotary motion converter. (d–h) Sequential SEM images show the generation of rotary motion by pulling a tungsten probe attached to one end of a DCHNB against an AFM cantilever using a nanomanipulator in a FESEM. The ratio of linear-to-rotary motion conversion is $\sim$171.3°/µm. (i) Elongation versus tension curves show that the stiffness in the first linear range is about $0.033\,N\,m^{-1}$.

19.4.2.3 Load Conversion

In order to fully understand the load conversion, the mechanical properties of a DCHNB are characterized by cutting it and picking it up with a "sticky" probe as shown in Figure 19.14a–c. The free end of the DCHNB is then attached on an AFM cantilever and fixed with EBID [34] as shown in Figure 19.14d. Then, the tungsten probe attached to one end of a DCHNB is moved to the right to extend the DCHNB against an AFM cantilever using the nanomanipulator. Images in Figure 19.14d–h are sequential SEM images showing the linear-to-rotary motion conversion. The generated rotary motion can be seen from the magnified frames. If both ends are equally displaced, the center of rotation will not translate in the axial direction. According to the apparent distance, the rotary angle ϕ can be determined. The ratio of linear-to-rotary motion conversion R_d is observed to be 171.3°/μm according to Figure 19.14d–h. In the experiment, the radius of the tested DCHNB decreased approximately 4%, confirming that the radius change can be ignored. According to Eq. (19.5), the unwinding angle is calculated as 170.1°/μm (2.47 turns/pitch), in good agreement with experiment results.

Elongation versus tension curves (Figure 19.14i) show that the stiffness in the first linear range is approximately $0.033\,\mathrm{N\,m^{-1}}$. This is surprisingly small when compared to bottom-up synthesized carbon coils ($0.12\,\mathrm{N\,m^{-1}}$) [35] and ZnO nanosprings ($4.2\,\mathrm{N\,m^{-1}}$) [23], and comparable to the most compliant commercially available AFM cantilevers ($\sim 10^{-2}\,\mathrm{N\,m^{-1}}$). Using this device as a vision-based force sensor, the nanospring can provide a resolution of $11\,\mathrm{pN\,nm^{-1}}$ assuming an imaging resolution of 1 nm. A low stiffness will facilitate the actuation of the motion converters. With large extension ($>7\,\mu m$), the stiffness becomes larger. The reasons for the nonlinearity of the stiffness are however not well understood yet. Several mechanisms are under investigation: (i) the helical nanobelts have a prestressed two-layer structure (one layer preextended, whereas the other layer precompressed), so extension will make the internal stress redistributed, (ii) the helical nanobelts have stress competition between the longitudinal direction and the transverse direction [36], so extension stiffness is a resultant result due to this competition, and (iii) the electron beam has side effects on the nanobelts, including electron beam-induced deposition [34] and hardening. These points may also be the reason of why the stretching force did not return to zero at zero elongation for the second round of extension (Figure 19.14i) besides SEM image drifting. It should be noted that, without the use of gears, bearings, or other types of pairs, such a "solid-state" motion converter will also be able to generate higher precision motion and will provide the possibility for measuring torque with a force sensor. This allows both higher precision positioning and more precise force application.

It is interesting to note that, due to the opposite chirality, the extension-induced torques at both ends can be self-compensated. This feature can be very useful for such applications as force measurement to avoid the side effect of end rotation as compressing or extending the other end.
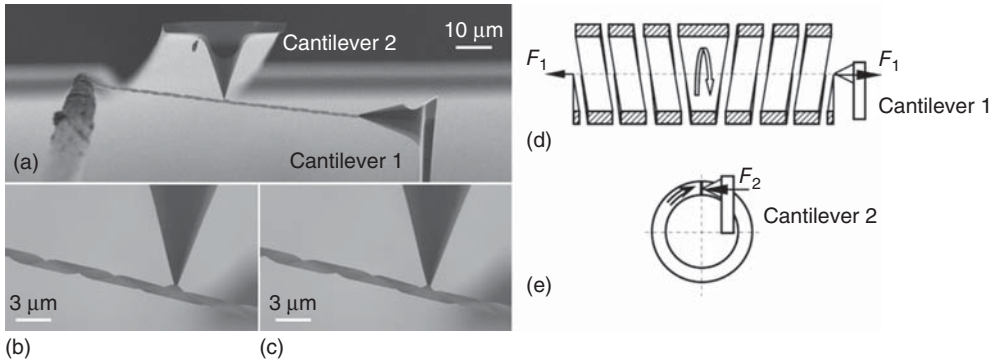
Figure 19.15 Force-to-torque conversion ratio. (a–c) The ratio of force-to-torque conversion is characterized using a probe and two AFM cantilevers. The ratio between the input force (d) to the output torque (e) is found to be 2.110×10^{-6} N m N^{-1}. (coil diameter: 947 nm; extension force F_1: 1.280 nN; rotary force F_2: 5.707 nN; torque: 2.702×10^{-15} Nm; rotary angle: 0.258 rad; torsional stiffness: 1.047×10^{14} Nm rad^{-1}.)

Figure 19.15a–c shows the characterization of the ratio of force-to-torque conversion using a probe and two AFM cantilevers (Mikromasch, CSC38/Ti–Pt, calibrated stiffness of cantilevers 1 and 2: 0.1400 and 0.0492 N m^{-1}). The ratio of the input force (Figure 19.15d) to the output torque R_F (Figure 19.15e) is found to be 2.110×10^{-6} N m N^{-1}. This process resembles the application of the motion converter as a rotary stage for 3D AFM. The investigation on the same nanospecimen from both axial and radial directions using two AFM cantilever is the first demonstration of this type of device.

19.4.2.4 Application in 3D Microscopy

A fundamental application of this type of motion converter is for 3D microscopy. Figure 19.16 shows 3D imaging of a pollen grain. An Au-coated grain is first picked up by a Picoprobe (probe 1) and actuated with a manipulator (Figure 19.16a). Then, the probe is moved to a SiGe/Si/Cr DCHNB motion converter (Figure 19.16b). A DCHNB with narrow width and relatively big space between the adjacent turns has been selected for exposing the sample surface to the maximum. One end of the DCHNB has been cut and attached to a sticky Picoprobe (probe 2). The pollen grain is then released from probe 1 by pushing the probe till the pollen attaches to the chip surface, and then pushed toward the DCHNB to attach to it. By incorporating a gripper, sample loading can be further simplified. Probe 2 is then moved downward to make the contact (Figure 19.16c) and upward so that the motion converter with the attached pollen sample moves away from the substrate. A different imaging angle shows that the pollen only attached to the center of the DCHNB (Figure 19.16d). The motion converter has been characterized before loading the sample (Figure 19.16e–h).

Figure 19.17 shows that the sample rotates for 360° when stretching the DCHNB. Basically, for micro- and nanometer-scale samples, the deformation of the DCHNB due to the sample weight can be ignored. It can be seen that the
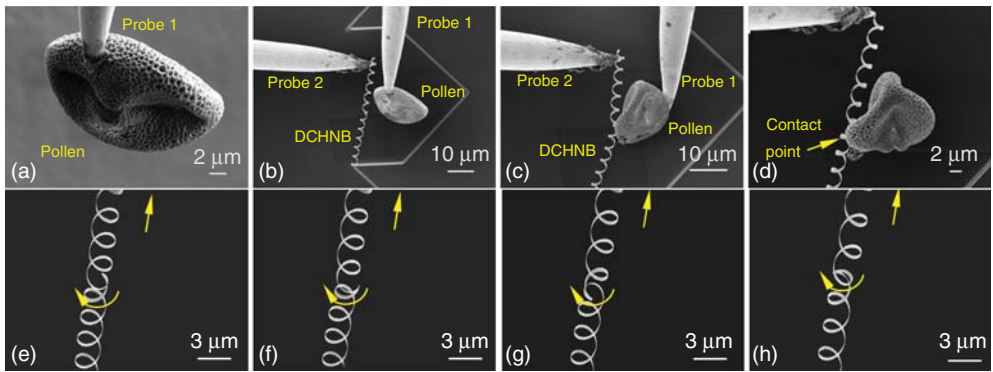
Figure 19.16 3D microscopy of a pollen grain. (a) A Au-coated pollen grain is picked up by a Picoprobe (probe 1). (b) The probe is then moved to a DCHNB motion converter. One end of the DCHNB has been cut and attached to a sticky Picoprobe (probe 2). (c) The grain is then released from probe 1 by pushing the probe till the grain attaches to the chip surface, and then the chip is pushed toward the DCHNB to attach. Probe 2 moves downward to make contact. (d) Then probe 2 moves upward so that the motion converter with the attached pollen grain sample can detach from the substrate. A different imaging angle demonstrates that the pollen grain only attaches to the center of the DCHNB. (e–h) The motion converter was been characterized before loading the sample.
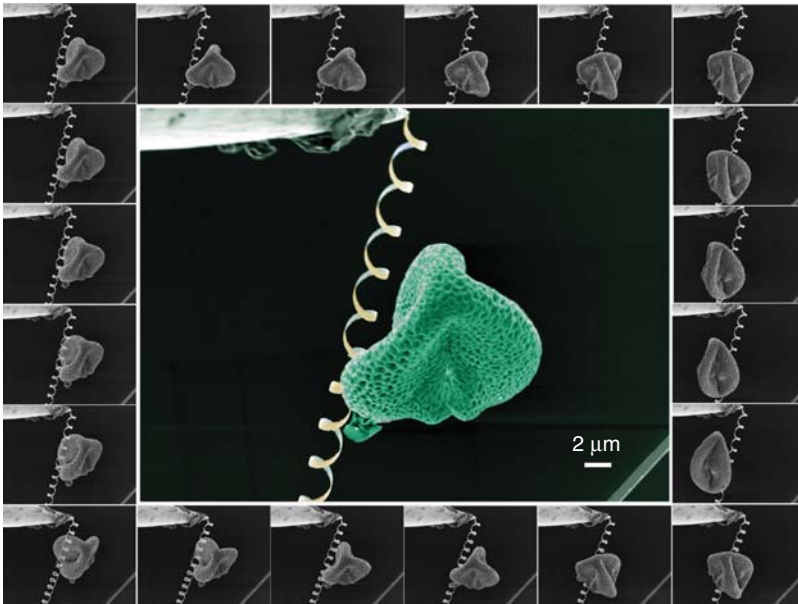
Figure 19.17 When stretching the DCHNB, the sample (a pollen grain) rotates for 360° (top view).
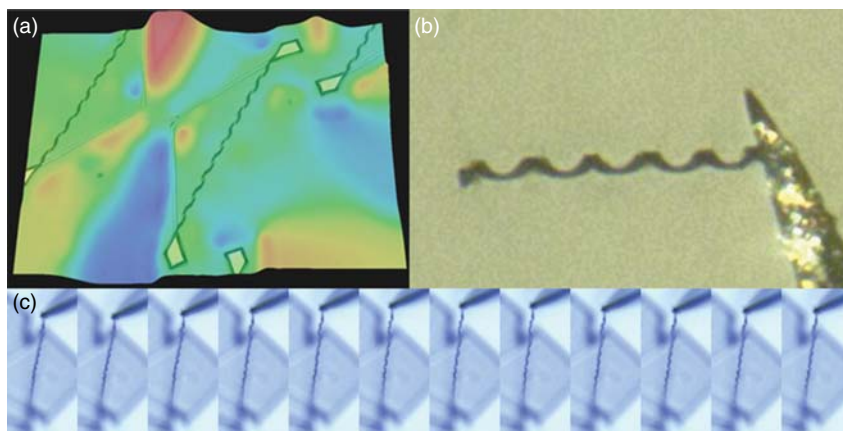
Figure 19.18 Imaging and manipulation of helical nanostructures under an optical microscope. (a) A 3D optical image of a DCHNB. (b) A coil picked up onto a probe. (c) Video frames (1 frame/2 s) showing the stretching (first six) frames and releasing (last six) frames of a DCHNB.

different aspects of the sample can be exposed to the electron beam simply by extending or releasing the DCHNB with a small displacement. In the experiment, we have rotated the samples unidirectionally (clockwise from the top view) for four turns, leaving the DCHNB with no obvious residual change in its shape. Further possibilities for this converter include goniometry for TEM, tomography for SEM or TEM, and 3D SPM. Nanorobotic manipulation has been shown effective for sample attachment. For fixation, besides van der Waals forces, electron beam-induced deposition and focused ion beam-induced deposition are optional approaches. By integrating in the fabrication processes of DCHNB, rolled-up spirals can serve as claws for holding relatively large samples. Similar experiments have been done under a digital optical microscope (Figure 19.18). It can be noted that the resolution of both imaging and manipulation is reasonable. This will further extend the applications of the manipulation of helical nanostructures in the air or liquid environments, which are of particular interest in the fields of biology and optics.

19.5
Summary

Robotic manipulation at the nanometer scale is a promising technology for structuring, characterizing, and assembling nano building blocks into NEMS and other nanosystems. On the basis of recently developed rolled-up nanofabrication processes, 3D helical nanostructures, such as tubes, rings, coils, and spirals, have been created in a highly controllable manner. Nanorobotic manipulation tools and processes for these structures are overviewed in this chapter. "Sticky" probes and

nanohooks have been specially created for the manipulation of these structures. Basic processes including picking and placing, pulling and pushing, bending and buckling, and rolling and unrolling have been experimentally demonstrated. Their applications in property characterization of stiffness, elasticity, stability, interlayer bonding, and displacement and load conversion have been demonstrated. Design configurations of NEMS and device prototyping using nanorobotic manipulation have been investigated by taking a motion converter as an example.

References

1. Zhang, X.B., Zhang, X.F, Bernaerts, D., Vantendeloo, G.T., Amelinckx, S., Vanlanduyt, J., Ivanov, V., Nagy, J.B., Lambin, P., and Lucas, A.A. (1994) The texture of catalytically grown coil-shaped carbon nanotubules. *Europhys. Lett.*, **27**, 141–146.

2. Kong, X.Y. and Wang, Z.L. (2003) Spontaneous polarization-induced nanohelixes, nanosprings, and nanorings of piezoelectric nanobelts. *Nano Lett.*, **3**, 1625–1631.

3. Prinz, V.Y., Seleznev, V.A., Gutakovsky, A.K., Chehovskiy, A.V., Preobrazhenskii, V.V., Putyato, M.A., and Gavrilova, T.A. (2000) Free-standing and overgrown InGaAs/GaAs nanotubes, nanohelices and their arrays. *Physica E*, **6**, 828–831.

4. Zhang, L., Deckhardt, E., Weber, A., Schonenberger, C., and Grutzmacher, D. (2005) Controllable fabrication of SiGe/Si and SiGe/Si/Cr helical nanobelts. *Nanotechnology*, **16**, 655–663.

5. Zhang, L., Dong, L.X., and Nelson, B.J. (2008) Ring closure of rolled-up Si/Cr nanoribbons. *Appl. Phys. Lett.*, **92**, 1–3.

6. Bell, D.J., Dong, L.X., Nelson, B.J., Golling, M., Zhang, L., and Grutzmacher, D. (2006) Fabrication and characterization of three-dimensional InGaAs/GaAs nanosprings. *Nano Lett.*, **6**, 725–729.

7. Zhang, L., Ruh, E., Grutzmacher, D., Dong, L.X., Bell, D.J., Nelson, B.J., and Schonenberger, C. (2006) Anomalous coiling of SiGe/Si and SiGe/Si/Cr helical nanobelts. *Nano Lett.*, **6**, 1311–1317.

8. Zhang, L., Dong, L.X., Bell, D.J., Nelson, B.J., Schönenberger, C., and Grützmacher, D. (2006) Fabrication and characterization of freestanding Si/Cr

micro- and nanospirals. *Microelectron. Eng.*, **83**, 1237–1240.

9. Schumacher, O., Mendach, S., Welsch, H., Schramm, A., Heyn, C., and Hansen, W. (2005) Lithographically defined metal-semiconductor-hybrid nanoscrolls. *Appl. Phys. Lett.*, **86**, 1–3.

10. Bell, D.J., Sun, Y., Zhang, L., Dong, L.X., Nelson, B.J., and Grützmacher, D. (2006) Three-dimensional nanosprings for electromechanical sensors. *Sens. Actuators, A*, **130-131**, 54–61.

11. Songmuang, R., Deneke, C., and Schmidt, O.G. (2006) Rolled-up micro- and nanotubes from single-material thin films. *Appl. Phys. Lett.*, **89**, 1–3.

12. Schmidt, O.G. and Eberl, K. (2001) Nanotechnology – thin solid films roll up into nanotubes. *Nature*, **410**, 168.

13. Songmuang, R., Rastelli, A., Mendach, S., and Schmidt, O.G. (2007) SiOx/Si radial superlattices and microtube optical ring resonators. *Appl. Phys. Lett.*, **90**, 1–3.

14. Schmidt, O.G. and Jin-Phillipp, N.Y. (2001) Free-standing SiGe-based nanopipelines on Si (001) substrates. *Appl. Phys. Lett.*, **78**, 3310–3312.

15. Zhang, L., Dong, L.X., and Nelson, B.J. (2008) Bending and buckling of rolled-up SiGe/Si microtubes using nanorobotic manipulation. *Appl. Phys. Lett.*, **92**, 1–3.

16. Calladine, C.R. (1983) *Theory of Shell Structures*, 1st edn, Cambridge University Press, Cambridge, MA.

17. Ju, G.T. and Kyriakides, S. (1992) Bifurcation and localization instabilities in cylindrical-shells under bending. 2. Predictions. *Int. J. Solids Struct.*, **29**, 1143.

18. Dong, L.X., Arai, F., and Fukuda, T. (2004) Destructive constructions of

nanostructures with carbon nanotubes through nanorobotic manipulation. *IEEE/ASME Trans. Mechatron.*, **9**, 350–357.

19. Falvo, M.R., Clary, G.J., Taylor, R.M., Chi, V., Brooks, F.P., Washburn, S., and Superfine, R. (1997) Bending and buckling of carbon nanotubes under large strain. *Nature*, **389**, 582–584.

20. Timoshenko, S.P. and Gere, J.M. (1985) *Theory of Elastic Stability*, Mcgraw-Hill, New York.

21. Gere, J.M. (2004) *Mechanics of Materials*, 6th edn, Brook/Cole-Thomson Learning, Belmont, CA.

22. Wortman, J.J. and Evans, R.A. (1965) Young's modulus, shear modulus, and poisson's ratio in silicon and germanium. *J. Appl. Phys.*, **36**, 153–156.

23. Sano, M., Kamino, A., Okamura, J., and Shinkai, S. (2001) Ring closure of carbon nanotubes. *Science*, **293**, 1299–1301.

24. Kong, X.Y., Ding, Y., Yang, R., and Wang, Z.L. (2004) Single-crystal nanorings formed by epitaxial self-coiling of polar nanobelts. *Science*, **303**, 1348–1351.

25. Tong, Q.Y. and Goesele, U. (1999) *Semiconductor Wafer Bonding*, John Wiley & Sons, Inc., New York.

26. Jin-Phillipp, N.Y., Thomas, J., Kelsch, M., Deneke, C., Songmuang, R., and Schmidt, O.G. (2006) Electron microscopy study on structure of rolled-up semiconductor nanotubes. *Appl. Phys. Lett.*, **88**, 033113.

27. Timoshenko, S.P. (1961) *Theory of Elastic Stability*, 2nd edn, McGraw-Hill Kogakusha, Tokyo.

28. Deneke, C., Sigle, W., Eigenthaler, U., van Aken, P.A., Schutz, G., and Schmidt, O.G. (2007) Interfaces in semiconductor/metal radial superlattices. *Appl. Phys. Lett.*, **90**, 263107, art. no. 10.1063/1.2742323|issn 0003-6951.

29. Dong, L.X. and Nelson, B.J. (2007) Robotics in the small, part II: nanorobotics. *IEEE Rob. Autom Mag.*, **14**, 111–121.

30. Yang, Y.T., Callegari, C., Feng, X.L., Ekinci, K.L., and Roukes, M.L. (2006) Zeptogram-scale nanomechanical mass sensing. *Nano Lett.*, **6**, 583–586.

31. Rief, M., Oesterhelt, F., Heymann, B., and Gaub, H.E. (1997) Single molecule force spectroscopy on polysaccharides by atomic force microscopy. *Science*, **275**, 1295–1297.

32. Dong, L.X., Tao, X.Y., Zhang, L., Zhang, X.B., and Nelson, B.J. (2007) Nanorobotic spot welding: controlled metal deposition with attogram precision from copper-filled carbon nanotubes. *Nano Lett.*, **7**, 58–63.

33. Cumings, J. and Zettl, A. (2000) Low-friction nanoscale linear bearing realized from multiwall carbon nanotubes. *Science*, **289**, 602–604.

34. Dong, L.X., Nelson, B.J., Fukuda, T., and Arai, F. (2006) Towards nanotube linear servomotors. *IEEE Trans. Autom. Sci. Eng.*, **3**, 228–235.

35. Ohki, T., Mikhailenko, S.V., Morales, M.F., Onishi, H., and Mochizuki, N. (2004) Transmission of force and displacement within the myosin molecule. *Biochemistry*, **43**, 13707–13714.

36. Binnig, G., Rohrer, H., Gerber, C., and Weibel, E. (1982) Surface studies by scanning tunneling microscopy. *Phys. Rev. Lett.*, **49**, 57–61.

37. Binnig, G., Quate, C.F., and Gerber, C. (1986) Atomic force microscope. *Phys. Rev. Lett.*, **56**, 930–933.

38. Wong, E.W., Sheehan, P.E., and Lieber, C.M. (1997) Nanobeam mechanics: elasticity, strength, and toughness of nanorods and nanotubes. *Science*, **277**, 1971–1975.

39. Eigler, D.M. and Schweizer, E.K. (1990) Positioning single atoms with a scanning tunneling microscope. *Nature*, **344**, 524–526.

40. Piner, R.D., Zhu, J., Xu, F., Hong, S.H., and Mirkin, C.A. (1999) "Dip-pen" nanolithography. *Science*, **283**, 661–663.

41. Lee, H.J. and Ho, W. (1999) Single-bond formation and characterization with a scanning tunneling microscope. *Science*, **286**, 1719–1722.

42. Binnig, G. and Rohrer, H. (1987) Scanning tunneling microscopy – from birth to adolescence. *Rev. Mod. Phys.*, **59**, 615–625.

43. Gerber, C. and Lang, H.P. (2006) How the doors to the nanoworld were opened. *Nat. Nanotechnol.*, **1**, 3–5.

44. Erlandsson, R., McClelland, G.M., Mate, C.M., and Chiang, S. (1988) Atomic

force microscopy using optical interferometry. *J. Vac. Sci. Technol., A-Vac. Surf. Films*, **6**, 266–270.

45. Meyer, G. and Amer, N.M. (1988) Novel optical approach to atomic force microscopy. *Appl. Phys. Lett.*, **53**, 1045–1047.

46. Dai, H.J., Hafner, J.H., Rinzler, A.G., Colbert, D.T., and Smalley, R.E. (1996) Nanotubes as nanoprobes in scanning probe microscopy. *Nature*, **384**, 147–150.

47. Binnig, G. and Smith, D.P.E. (1986) Single-tube 3-dimensional scanner for scanning tunneling microscopy. *Rev. Sci. Instrum.*, **57**, 1688–1689.

48. LeRoy, B.J., Lemay, S.G., Kong, J., and Dekker, C. (2004) Scanning tunneling

spectroscopy of suspended single-wall carbon nanotubes. *Appl. Phys. Lett.*, **84**, 4280–4282.

49. LeRoy, B.J., Heller, I., Pahilwani, V.K., Dekker, C., and Lemay, S.G. (2007) Simultaneous electrical transport and scanning tunneling spectroscopy of carbon nanotubes. *Nano Lett.*, **7**, 2937–2941.

50. Dong, L.X., Zhang, L., Kratochvil, B.E., Shou, K.Y., and Nelson, B.J. (2009) Dual-chirality helical nanobelts: linear-to-rotary motion converters for three-dimensional microscopy. *J. Microelectromech. Syst.*, **18**, 1047–1053.

51. Wahl, A.W. (1944) *Mechanical Springs*, 1st edn, Penton Publishing Company, Cleveland, QLD.

20
Automated Micro- and Nanohandling Inside the Scanning Electron Microscope

Malte Bartenwerfer, Sören Zimmermann, Tobias Tiemerding, Manuel Mikczinski, and Sergej Fatikow

20.1
Introduction and Motivation

Since the early establishment of mechanical systems in a preindustrial society, the size of objects is a crucial figure of merit for almost all tools and devices used by mankind. Objects and devices, which seem to be inconsiderable, are important parts of our daily lives and would be inexisting without the miniaturization process during our history. For centuries, this miniaturization applied only to mechanical systems and one of the most intuitive examples is clocks: immobile clocks first became pocket watches and finally wrist watches. For electronics, this miniaturization is even more impressive, since they evolved on a much smaller timescale: the first commercial transistor – the Raytheon CK703 released in 1949[1] – had the size of roughly $2\,cm \times 6\,mm$. Nowadays, an average transistor as individual electronic component has the size of about $1.4\,mm \times 1.1\,mm$. For transistors embedded in an *integrated circuit*, the today's minimum feature size is in the range of few tens of nanometers [1]. In electromechanical systems – the combination of mechanics and electronics – miniaturization led to a whole bunch of novel sensors; first of all, the most successful example is the acceleration sensor, which can be found 1000-fold in all fields of devices. Those and many other kinds of sensors are based on the miniaturization and contribute in an important but much unseen way to our daily lives. Last but not least, the miniaturization of energy storage systems contributed to the development of portable devices with high computing capacity and sensing abilities. The most widespread example of a device, which benefits from this technological development, is the smart phone. But beside this consumer device, particularly medical devices such as pacemakers and hearing aids improved tremendously by the miniaturization.

In contrast to the developments occurred in the past, the upcoming developments of miniaturization have to be different. The conventional downscaling of

---

1) Some publications claim 1948.

building blocks reaches inherent technological limits and especially in semiconductor industry, the physical limits will be reached soon.

Indeed, the challenge is huge, but on the other side of the coin are the large potentials that are accompanied to this next step of downscaling: the appearance and behavior of almost any material change compared to its bulk properties, if the size of the element is in the nanometer scale. Hence, nanoscale objects in general possess unique physical properties that are caused by either their special atomic configuration or solely their nanoscopic size. The first takes benefit from quantum mechanical effects, the latter results in an enormous surface-to-volume ratio, which alone is already an important advantage for sensing applications.

Materials with a size of less than 100 nm in at least one of the three dimensions – generally called *nanomaterials* – are still very promising candidates for new sensors, actuators, computing units, and energy converters. Furthermore, nanomaterials are dealt as fundamental base for absolutely novel devices such as light traps and hydrogen stores.

Nano-objects – using a similar definition as nanomaterials – do not necessarily use quantum behavior or exploit fundamental physical effects. Mostly they rather act as components with nanometer dimensions in order to work as tiny electrodes or ultrasharp probes. In this way, they can be treated as micro- or nanoscale building blocks, which have to be integrated into complete systems.

A common requirement for many applications and concepts of nanomaterials and microcomponents is essentially the feasibility to build up a real device. In today's applications of nanomaterials, they are very often rather a kind of mass-additive to other components and cannot contribute their full potential. The unique properties can be exploited only if these objects are integrated as individual and functional objects into devices. This integration requirement is a major challenge for the handling abilities of these objects.

There are several considerable approaches to handle and manipulate nano-objects toward a seamless integration. However, general approaches from macroscopic handling and robotics, using different kinds of grippers and visual feedback, cannot be applied directly to the micro- and nanoscales. Instead, micro- and nanohandling approaches take advantage of certain effects on the nanoscale and most of them are introduced in this textbook. Most approaches in micro- and nanohandling are well suited for one particular handling operation, since they are developed with focus on this specific problem and take benefit from the specific environment. A general understanding of the forces ruling on the nanoscale is existing, but direct transfer to the development of handling strategies is lacking, since these forces are hardly controllable and measurable – despite the fact that they are deterministic.

20.1.1
SEM-Based Manipulation

The apparent need of micro- and nanomanipulation can be particularly addressed by the scanning electron microscope (SEM). This device is a well-known tool for

microsystems technology and can be found worldwide in almost all laboratories and companies working in this field. The SEM offers some clear advantages in comparison to other imaging and analyzing tools:

– **Resolution:** The SEM offers resolutions down to few nanometers. At the same time, the field of view is continuously scalable from some centimeters down to the resolution's limit of about a nanometer.
– **Speed:** The image acquisition rate of the SEM is in the range of some Hertz, using regions of interest even higher. This is sufficient for handling, even for automated handling processes. However, the acquisition speed is inversely proportional to the noise level of the images. Fast image acquisition in the region of a Hertz involves already images with significant noise.
– **Space:** The working chamber of the SEM is spacious enough – at least some hundreds of cubic centimeters – for the integration of multiple robotic stages, actuators, and end-effectors.

However, the usage of the SEM is also accompanied with some disadvantages:

– **Complexity:** Overall, the usage of SEM requires a large instrumental effort. The SEM itself requires many surrounding devices and additional properties of the evolved instruments.
– **Compatibility:** Because of its working principle, the SEM is not suitable for all kinds of samples. All samples must be vacuum-compatible and at least slightly conductive, in order to allow for an undisturbed image acquisition. Hence, sample preparation is often necessary.
– **Invasiveness:** The interaction of sample and electron beam of the SEM can lead to changes of the sample. Very sensitive samples (e.g., graphene) can change their atomic configuration and hence their properties. All samples exposed to the electron beam can suffer amorphous carbon contamination of their surface caused by the residual gas in the vacuum chamber.
– **Image distortions:** The same interaction of sample and electron beam can lead to little image distortions such as shifting or deformation. Therefore, the SEM cannot be used as an absolute position sensor by all means.

In conclusion, the SEM has to be seen as one possibility for micro- and nanohandling amongst others. Especially possible contaminations have to be considered carefully if one has to deal with nano-objects. But even some of the unwanted side effects can be turned into powerful tools for the SEM-based nanohandling, as described in this chapter. This conversion of side effects into useful auxiliaries, as well as the usage of the evident advantages of the SEM, is described for exemplary use cases in Chapter 1.4. But first of all, if one works with objects having nanometer size in two or even three dimensions, the SEM is the best compromise device. Especially, the need of automation of handling processes relies on fast and accurate position information.

20.2
State of the Art

20.2.1
The Scanning Electron Microscope as Fundamental Tool

The SEM is originally a powerful tool for the acquisition of high-magnification images. Precise manipulations on the other hand need some kind of feedback to ensure that a manipulation task has completed successfully. In combination of these two facts, nanomanipulation in SEM conditions seems to be theoretically an apparent approach.

The general working principle of the SEM is to rasterize a sample with a well-focused electron beam. At each point, where the beam hits the sample, an electron interaction with the surface results in new emitted electrons. Hence, a detector can observe a grayscale value for each point. A general requirement for the generation and propagation of the beam is a vacuum atmosphere.

In practice, there were several obstacles to be solved before working in SEM conditions to make it a possible environment for micro- and nanomanipulation:

– **Environment:** The vacuum environment of the SEM is already a restriction to all kinds of materials that are involved. In general, all materials need to be compatible with high vacuum, which excludes especially living materials. However, special SEM approaches allow working in fine vacuum conditions.
– **Insulation:** The most important restriction is the vacuum chamber of the SEM itself. A direct mechanical access to the observation area of the microscope is not possible, which makes a huge difference to all handling strategies used in optical microscopy conditions. Therefore, fine manipulations can be performed by using simple but efficient mechanical linkage as reduction.

However, these limitations do not always apply and they also can be tackled in different ways. Generally, most materials and objects can be visualized with the SEM in high-vacuum mode (10^{-6} mbar) without any problems. Hence, every handling strategy, using only compatible component, can be realized without any limitations inside the SEM. Using other components or working on other materials leads to a higher instrumental effort. Outgassing materials, especially in forms of living cells or cellulose fibers, cannot withstand the low pressure in high vacuum or are nonconductive, or even both. In order to overcome this drawback, some SEMs allow visualization at higher pressures ($0.1 - 30$ mbar).

The insulation of the working areas, caused by the vacuum chamber, became less severe in recent years, since robotic platforms are smaller, cheaper and more flexible. Today, the integration of robotic platforms with several degrees of freedom is a task, which can be solved easily with commercial or commercially customized setups (please refer to Section 20.3.1 for examples). The existence of control electronics, digital communication, and programming interfaces for control PCs is part of this development. Hence, not only the mechanical integration but also steering and controlling are feasible, which are crucial for automation desires.

The interaction of the SEM electron beam and the inspected and manipulated samples is very important for handling and automation. On the one hand, the electron beam can cause unintended damage and contamination, as mentioned in Section 20.1. This is a major obstacle which always has to be considered. On the other hand, the beam−sample interaction and its consequences can be used as measure or interactive probe. Local charge, emitted secondary electrons, and their amount can be used to derive more information as just the plain overview image of the scenery.

20.2.2
Conditions for Automation on the Micro- and Nanoscales

As described in Ref. [2], automation on the micro- and nanoscales requires special approaches that differ from the established ones used in macrorobotics. In general, the approaches differ especially in regards to the used actuation principles (direct driving instead of kinematic chains [3]) as well the extensive use of sensors. The sensors available on the micro- and nanoscales are mainly:

- Optical systems (depending on the application and the size of the objects involved)
    1. optical microscopes and cameras (mainly for microworld applications) [4, 5]
    2. scanning electron microscopes (nanoscale) [6]
    3. other imaging techniques with sufficient resolution
- Atomic force microscopes, used both for imaging and measurement tasks
- Internal position sensors for linear or rotary positioning systems, for example, integrated inside robots from SmarAct GmbH,[2] Physik Instrumente,[3] or attocube[4]
- Microforce sensors such as the FT-S Microforce Sensing Probe from Femto-Tools[5]
- Microscopic electrode probes, such as those from Capres,[6] which can be used for conductivity mapping of samples.

One of the main tasks of automation is to position robots, tools, and objects precise to each other. This is the only way how complex operations on micro- and nanoscales, like pick-and-place, can be conducted reliably. In addition, it is required to bring multiple robots and tools in the same working volume to allow for cooperative handling. For positioning tasks, the available internal position sensor of robots is not sufficient for two major reasons: At first, a distance of several millimeters or even centimeters between the actuator base to the tool center point (TCP) is not unusual and is a large influence for mechanical changes. This is, for example, shown in Figure 20.2, where the used AFM probes are several

---

2) *http://www.smaract.de/index.php/products/options/positioningsensors.*
3) *http://www.physikinstrumente.com/en/products/nanopositioning.*
4) *http://www.attocube.com/.*
5) *http://www.femtotools.com/index.php?id=products-s.*
6) *http://www.capres.com/Default.aspx?ID=49.*

centimeters away from both the fine and the coarse positioning stages. On the other hand, due to the ever-present effects on the small, for example, thermal drift and electrostatic charge, the sensor information is not reliable enough on positioning of robots and tools [7, 8]. Therefore, the main sensor used on the small scale is an optical system (assigned to applications as listed above).

A typical control loop architecture based on automation is shown in Figure 20.1. Because optical systems are the main sensor, automation processes highly focus on object tracking and perception based on visual information. The gained insights from these sensors are used to perform actuation of the used robotic setups, which of course impacts the values measured by these sensors.
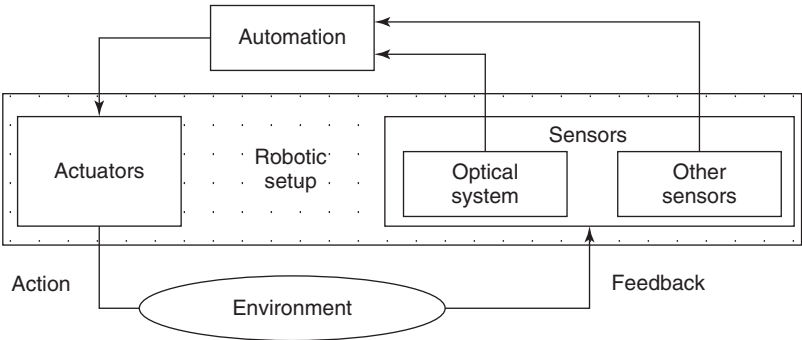
Figure 20.1 A control loop architecture for automation on the micro- and nanoscales.
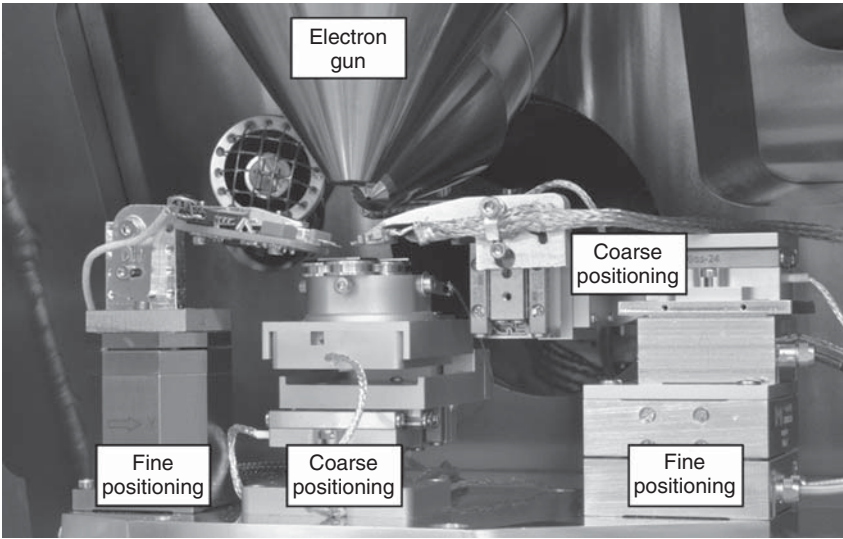
Figure 20.2 Dual-probe nanorobotic setup integrated within a scanning electron microscope environment.

The extent of automation varies at this point ranging from not automated via semi to fully automated setups. Manual handling on the small scale is not discussed further in the following. Semiautomation is most common, for example, used for setup preparation, preprocessing, and/or user support. Thus, typical tasks include bringing robots and/or tools into a common volume of work, sample exchange using robotic stages, or point-and-click movements. Full automation, representing a rarity in the sector of microrobotics, performs normally well-understood processes (mainly in assembly). The preceding process is normally: (i) Manual assembly (using telecontrol); (ii) Optimizing the process for automation; (iii) Semiautomation through all process steps; and (iv) Merge all semiautomated steps into a comprehensive sequence. In the following paragraph, we highlight some current works done in this field to give a sense demonstrating what is possible. More sound case studies can be found in Section 20.4.

20.3
Automation Environment

20.3.1
Robotic Setup

In general, nanorobotic setups need to fulfill several preconditions concerning their choice of materials when they are integrated within a scanning electron microscope. In particular, vacuum compatibility and electrical conductivity of the end-effectors are additional requirements. Furthermore, the space within the vacuum chamber is often strictly limited and therefore, compact constructions are advantageous.

20.3.1.1 Dedicated Setups
So far, most of the integrated nanorobotic setups are dedicated to one particular task. The most prominent examples for these setups are scanning probe microscopes [9, 10]. Because of their high resolution down to the atomic scale and their ability to provide topographical information of the sample, the scanning probe setups enhance and complement the abilities of the scanning electron microscope significantly. Beyond surface analysis, nanomanipulation is one of the most important fields of application of these setups. The main advantage is the direct visual feedback of the scanning electron microscope as it facilitates the manipulation sequences. However, most of the commercially available setups are restricted to working ranges of few micrometers and therefore, the nanomanipulation capabilities of these setups are constrained. Moreover and in contrast to the macroworld, nanomanipulation with only one end-effector remains challenging as releasing of nanosized objects is often not reproducible due to the dominant adhesive forces on the nanoscale. As an example, one dedicated setup, tailored for cooperate interaction between two end-effectors and designed to overcome the

limitations of the restricted working ranges, is described in more detail within the following.

The overall setup that is integrated within the vacuum chamber of a scanning electron microscope is shown in Figure 20.2.

The setup consists of an arrangement of four individual nanorobotic stages, each of them offering three orthogonally aligned linear axes. All four stages are placed onto a common baseplate and are mounted onto the standard stage of the electron microscope. The operational workspace of the end-effectors is on the uppermost part of the setup. In this way, the whole nanorobotic setup can be tilted, enabling the observation of the interaction between the end-effectors and the used surfaces and objects from different angles. The stages itself can be divided into fine and coarse positioning types. As all stages are actuated applying the piezoelectric effect, the main difference between these two stage types is solely their actuation principle. For all tasks requiring highly precise movements of the end-effectors, continuous piezo-driven stages are applied. For closed-loop control, these fine positioning stages are equipped with capacitive positioning sensors, allowing an absolute positioning accuracy of 1.6 nm. However, as mentioned earlier, their range is limited to several micrometers. To overcome this restriction, the fine positioning stages are complemented through coarse positioning stages that are actuated using the slip-stick driving principle enabling travel ranges of up to few centimeters in tandem with a positioning accuracy below 100 nm. One of these coarse positioning stages is applied as the sample holder. In this way, samples can be exchanged during handling sequences without any movements of the end-effectors. The second coarse positioning stage is used for the alignment of the two end-effectors or to exchange the end-effector. For this purpose, it has been mounted onto one of the fine positioning stages. Overall, this nanorobotic setup allows for cooperate nanomanipulation applying two end-effectors. In addition, it enables to incorporate macroscopic workspaces.

The performance of this setup with respect to nanomanipulation of colloidal nanoparticles will be further highlighted in Section 20.4.2.1.

20.3.1.2 Modular Setups

A dedicated setup is the best choice if one type of manipulation or characterization is planned. However, in research and development, often different tasks need to be tested or miscellaneous materials and objects require different accuracies or end-effectors. It is undoubtedly inefficient to spend expensive systems, materials, and working time on a setup for one-time use.

Modular setups offer a useful option in this respect. However, combining actuators and end-effectors from different suppliers requires a suitable mechanical interface as well as an easy way to control these systems on demand. Section 20.3.2 presents such a flexible control software.

Mechanical interfacing is necessary on (i) the SEM−setup, (ii) setup−actuator, and (iii) actuator−end-effector interfaces to obtain best possible interchangeability. This means a carrier is necessary that can be mounted inside the SEM,

Different base plates, e.g.:

Base
+ Modules
= System

Various modules, e.g.:
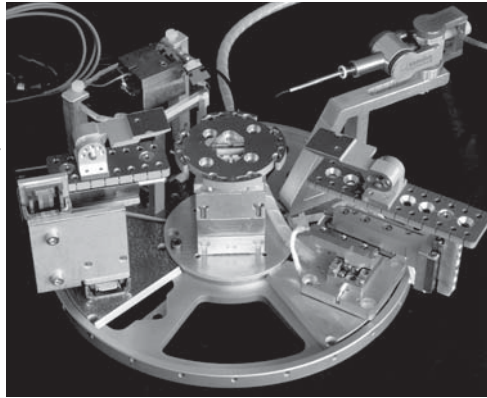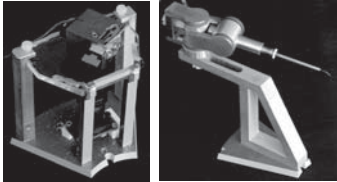
Figure 20.3 PS-AMiR: Combining different modules quickly to versatile setups. The exemplary setup comprises 15 DOF plus maintaining the SEM's DOF.

consisting of the base for the different positioning units. These units together with a small baseplate are the main modules that offer either coarse or fine positioning. Every module can be equipped with different end-effectors or samples. The interfaces between these parts need to be as stiff as possible to avoid vibrations, but easy to open. A classical approach in mechanical engineering for this problem is the dovetail joint. Two complementary formed parts are combined like a jigsaw puzzle. By pressing the two parts together, for example, by fastening a screw, they can be considered as one unit as the joint withstands high forces. This is a good choice for the positioning modules, whereas the end-effectors possibly require a higher flexibility in positioning. Therefore, a hole grid, which allows for fastening the end-effector in different positions, can be used.

For the work with wood and paper fibers, see Section 20.4.4, such a modular system was developed, see also [11]. On a circular base frame, or a segment of it, different modules can be placed and fastened, like in Figure 20.3. This allows for the angle-independent placement of different perimeter modules around a center module and center-oriented working, as common in SEMs. The base can be integrated into three different SEMs from different manufacturers and therefore also the subsequent setup can be transferred from one to the other. In the center position, one half of a dovetail is realized by a conical disc. The other half is realized by setscrews, which also fasten the modules. The positioning systems are placed on small ring segments, the module plates, which are beveled. On top of every positioning module a grid plate is fixed. On this plate, all kinds of end-effectors can be fixed.

This flexible, modular system allows for the quick development of countless combinations of experimental setups. As it focuses primarily on the positioning capabilities, it was called AMiR Positioning Station (PS-AMiR).

20.3.2
Control Environment

As pointed out in Section 20.2, automation on the micro- and nanoscales heavily relies on image processing. Furthermore, automation processes on this scale are mostly prototypic in nature. A control environment should therefore allow for rapid prototyping of automation sequences based on image processing. This should include telecontrol of the used robotic setups. Experience has shown that telecontrol is very useful in order to gain a deep process understanding, which is required in order to automate processes later on [12].

Because of the technological advances in micro- and nanorobotic technologies, there is a shift of focus from hardware development toward system- and software-level aspects. In a typical case, the robotic setups are controlled with a custom-designed monolithic software offered by the hardware manufacturer. However, a few general-purpose robotic software frameworks (RSFs) have been developed in the recent years, targeting micro- and nanorobotics. These include, for example, the software developed in the PRONOMIA research project by Gauthier *et al.* [13, 14], the nanomanipulation control framework developed at the USC by Arbuckle *et al.* [15], or the OFFIS automation framework developed at the University of Oldenburg [16, 17]. In addition, macrorobotic software frameworks are adapted and used as proposed in Ref. [18]. Even though microrobotic applications are distinct from industrial and service robotics, these RSFs are also applicable, especially because they offer a solid code base and often a lot of libraries, thus enabling rapid prototyping. The most widely known RSFs are ROS (Robot Operating System) [19], ORCA [20], OROCOS [21], OpenRAVE [22], OpenRTM-aist [23], OpenRDK [24], and YARP [25].

20.3.2.1 OFFIS Automation Framework
As described by Abbott *et al.* [2] and Gendreau *et al.* [14], the technical and physical constraints must be taken into account in order to design reliable micro- and nanorobotic software systems. The OFFIS automation framework is an RSF that facilitates this approach. It has been developed during several European and national projects and was made freely available and open-source for the operating systems such as Windows, UNIX, and Mac OS X platforms.[7),8)] Several goals have been pursued driven by the following needs [16]:

- Provide an easy-to-use image processing system with drag-and-drop.
- Provide a basis for vision-based automation tasks based on simple scripts.
- Provide high-level access to tools, robots, or sensors.
- Allow for telecontrol of all robotic units using intuitive gamepads or haptic interfaces.
- Provide easy extensibility in order to include new units as well as problem-tailored image processing solutions.

7) *http://automation.offis.de.*
8) *https://github.com/OFFIS-Automation/Framework.*
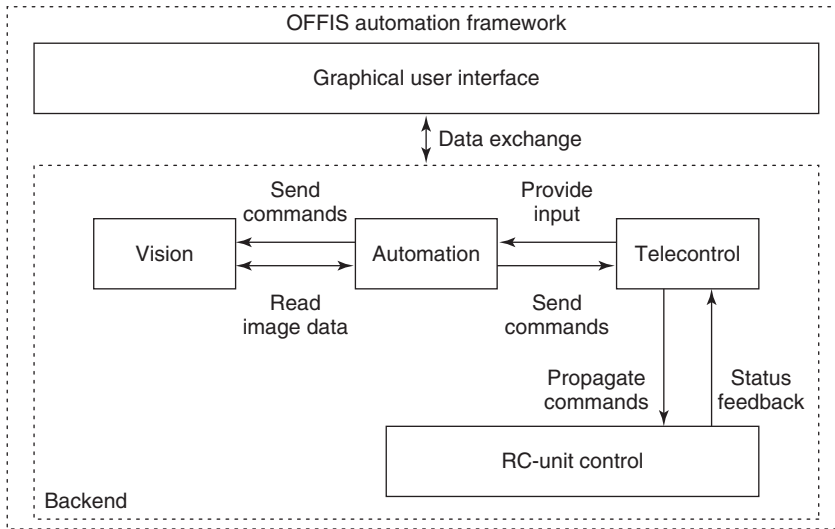
Figure 20.4 The high-level architecture of the framework. It consists mainly of two parts: (i) the front end with a graphical user interface and (ii) the back end [16, 27]. The latter consists of different subsystems, namely (1) RC-unit control, (2) telecontrol, (3) automation, and (4) vision. The subsystems can interact with each other, for example, vision can be used from the automation. The framework can be extended with custom RC-units and vision plug-ins.

As shown in Figure 20.4, the OFFIS automation framework consists of multiple subsystems, each one with a specific purpose:

– **Vision:** The vision subsystem provides multiple image filters, partly based on the comprehensive computer vision library, OpenCV [26] and partly on own development. The functions of these filters range from simple image preprocessing (e.g., thresholding, color correction, and binary morphology) to more complex operations such as object detection and feature extraction (based on *contour* and *moments detection*[9]). The filters can be connected to image processing pipelines using a drag-and-drop interface (see left-hand side of Figure 20.5). Thus, the software allows for simply extracting relevant data from any kind of optical sensor system.
– **RC-Unit control and Telecontrol:** A remote-controllable unit (RC-unit) is the interface between the framework and the actual hardware component. At first, it is a hardware abstraction layer (HAL). Such an abstraction layer is required because most systems in microrobotics use components from different vendors (compare Section 20.3.1). These normally offer a software-based interface, which, however, is not uniform and needs to be adapted to a common interface. In addition, an RC-unit encapsulates the low-level functionality of tools,

9) *http://docs.opencv.org/modules/imgproc/doc/structural_analysis_and_shape_descriptors.html.*
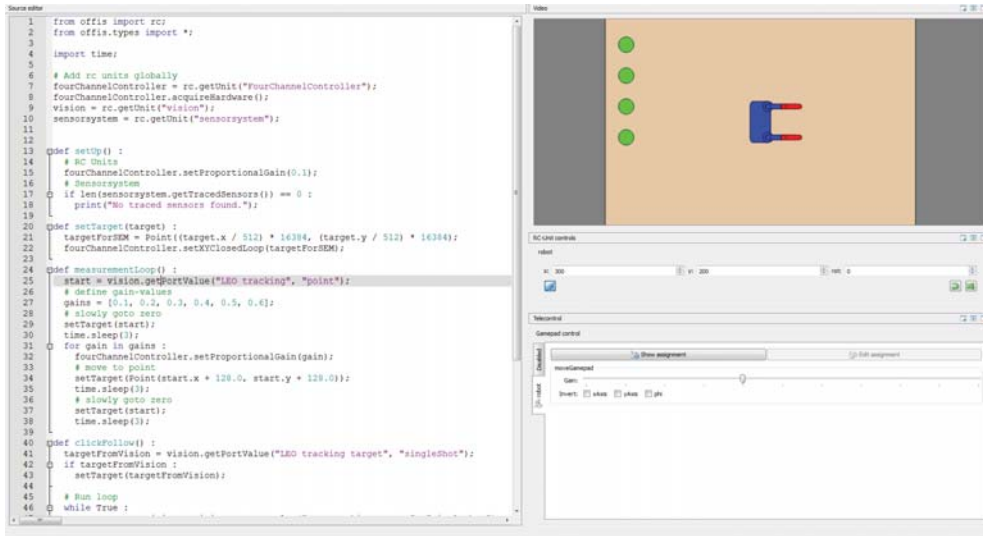
Figure 20.5 Screenshots of the OFFIS automation framework's GUI. The screenshot on the left-hand side shows the vision subsystem with a created image processing pipeline. The right hand side shows the GUI's of the other subsystems: RC-unit control, Telecontrol and Automation.

robots, and sensors and offers high-level commands to the framework (e.g., "Rotate robot 180°"). RC-units are created by extending a supplied C++ template. In this way, RC-units can also be controlled by either writing automation sequences or using haptic devices and gamepads.

– **Automation:** Using the widespread and open-source Python programming language,[10] a user can create simple as well as highly complex automation sequences (see Figure 20.5 right-hand side). By including supplied program libraries, each script can interact with RC-units and the vision subsystem.

As can be seen from the description of the different subsystems, the OFFIS automation framework enables the complete development cycle (and the associated steps) required for micro- and nanorobotics. Thus, for example, telecontrol can be used for manual assembly and process exploration, while the Python-based automation allows for automation in various forms. The vision subsystem may be used at any time for both process observation and visual servoing.

The OFFIS automation framework enables all case studies described Section 20.4. Further information on this framework can be found in Refs [16, 27]. Apart from that, it is used in several other use cases:

– **AFM sidewall scans [28]:** By using special tips for AFM measurements, so-called NanoBits, it is possible to operate in new modes, allowing for

10) *http://www.python.org.*

sidewall scanning. The framework is used to realize this high-resolution sidewall scanning as part of the NanoBits project (for more information, see Section 20.4.2).

– **Mechanical characterization of graphene samples [29]:** A graphene sample is put on a perforated silicon wafer. The framework is used to visually detect holes beneath graphene sample and perform visual servoing of a self-sensing AFM cantilever toward their coordinates. On each coordinate, an indentation measurement is performed. The process is fully automated.

– **Handling of graphene flakes [30]:** Using the framework, a user is able to perform teleoperated nanorobotic handling of graphene flakes. The goal of the handling is to assemble the graphene flakes to prototypic nanoelectronic devices.

– **Control of Desktop-factory [31]:** The framework is used as control software of a desktop-factory. The framework enables the fabrication of products from a few up to several hundred parts per year. This is especially because multiple areas of control are covered by default (starting with simple telecontrol and then via semi to full automation).

– **High-speed servoing [32]:** Servoing and control of a commercial nanostage (Physik Instrumente Hera) using the SEM-based high-speed visual servoing based on dedicated line scans, as described in Section 20.4.1.

20.4
Case Studies

20.4.1
Manipulation and Automation Overview

• **TEM Lamella Handling:** The first relevant and complex application of SEM-based handling was the transfer of lamellas for transmission electron microscope (TEM) inspection from a sample substrate of a TEM-grid. This process has been performed also ex situ, in environmental conditions, but the availability of robotic systems inside the SEM chamber improved that approach tremendously. Most works with this target are published during the first years of this century, and all of them affirm the huge benefit of the robotic handling [33, 34]. The in situ TEM lamella handling uses a simple wire of fiber, which is glued to the lamella to be handled. This technique has been improved over several years, but did not change very much. Gripper-based approaches were successfully investigated as well (cf. Figure 20.6b). The general handling strategy and precision demands are in the range of several micrometers. Today, many SEM manufacturers offer already built-in automation tasks for the TEM lamella preparation [35]-[37], but in many cases this is limited to an automated coating, cutting, and thinning of samples. The actual transfer of the prepared TEM lamella remains as a challenge, which is either excluded from a fully automated process or needs additional expansive investments and development [38].

- **Biological Samples** A long history of micromanipulation of biological objects inside the SEM is presented by the Japanese research group of Toshio Fukuda. They developed several approaches to handle and especially characterize micro- and nanoscale objects using robotic tools. The major focus lays in the mechanical characterization of objects. Because of the limitations of force sensors, suitable for this regime, a major contribution is the development of force feedback by visual observation of deformations by the SEM. This has been done using standard cantilevers, silicon nanoneedles, and special structured cantilevers with "fingers," called *nanoforks*. The fundamental working principle of this optical detection method is image processing and an accurate calibration: the end-effector (cantilever tip, nanoneedle, nanofork) is pressed against a device under test, while the movement of the end-effector's base is monitored by the positioning stage. The relative movement and relative orientation of the end-effector are monitored by the SEM and reveal additional information, which can be used to calculate the overall deflection. Taking the mechanical properties into account, the applied force can be calculated. These principles are used to measure viscoelastic deformation and adhesive forces of biological cells.

  Not only living cells, but also other organic cells, such as wood and paper fibers are handled inside the SEM. In the beginning of SEM use, the ultrastructure of paper fibers was in the focus (e.g., [39]). With technological evolution, also smallest structures, such as nanofibrils – the ultrastructure of paper fibers – with diameters below 20 nm, became visible [40]. However, measuring mechanical properties with a high-magnification observation is today's goal. The SEM is used to visualize the deformation and cracking behavior. For example, the tensile testing of wood or paper fibers with observation of their failure behavior was performed [41]. Furthermore, the focused ion beam (FIB) technique is used to prepare fibers for tests. In Reference [42], a pole with a diameter of less than 5 µm was FIB-cut from the cell wall and compressed. Environmental FE-SEMs with in-lens detectors and working distances below 2 mm are the best choice to obtain insights into the material composition and structure of natural materials. However, the degree of automation is very low in these examples and most steps are still performed manually by an operator except for the measurement sequence.

  Using a nanohandling robot station, image processing with object recognition and tracking, Krohs *et al.* [43] could perform highly automated characterization of biological cells (cf. Figure 20.6a). A light microscope was used as a position sensor for the self-sensing, piezoresistive AFM-cantilever (end-effector) as well as for detection of single cells and ideal indentation points. The AFM-tip then was moved to each point to perform an indention measurement.

- **Nanowire Handling:** The Canadian research group of Yu Sun contributed significant research on the handling of nano-objects inside the SEM. They worked on nanowire field-effect transistors, which can be used as ultrasensitive and miniaturized sensors for detection of different chemical and biological molecules as used in medical and environmental applications. These devices

(a)   (b)
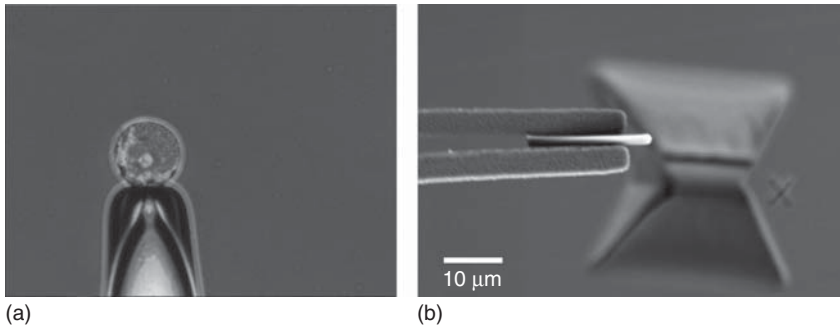
Figure 20.6 Examples of robotic handling scenarios. (a) Handling of a cell in liquid conditions using a robot-driven capillary. (b) Lift-out of a TEM lamella inside the SEM using a robot-driven gripper.

are fabricated in a batch microfabrication process. However, the number of nanowires on these devices varies and hence, nanomanipulation can be used as a postprocessing step [44]. By automating nanowire detection and selection, contact detection, and nanowire severing, it was possible to remove unwanted wires with a success rate of 95%. Furthermore, this group used handling strategies for the transfer of single nanowires applying sharp tungsten probes as end-effectors. The probe is brought into contact with the nanowire to be transferred. An extensive exposure to the electron beam is sufficient to glue the nanowire to the probe. In the same way, the nanowire is placed onto a receiving substrate. In particular, they developed strategies for a fully automated pick-and-place process of this task [45]. In order to achieve this, image processing of the SEM image has been engaged: nanowire and probe are detected and tracked by template matching. The target of the manipulation – a gap in a substrate – is detected by a Hough transformation of the image.

The German group of Sergej Fatikow works in particular on handling processes of nano-objects inside the SEM. Eichhorn *et al.* used a microfactory inside the SEM for systematic characterization as well as handling of carbon nanotubes (CNTs) [46]. Using SEM-based visual servoing and a depth-from-shadow approach, it was possible to grip a CNT and place it reliable on a target substrate. For automated detection of the CNTs, algorithms developed by Wortman and Fatikow [47] were used.

20.4.1.1 High-Speed Object Tracking Inside the SEM

As described in Section 20.2, image processing is a key for all automation tasks on the small scale. Nowadays, there exist several specialized image processing algorithms, adapted to noisy SEM image data. Most known are template matching based on cross correlation [48] or snakes (also known as active contours) [49, 50]. Unfortunately, even with optimizations toward noisy image data and for (very) small regions of interest, only update rates of 20 Hz are possible [51]. Even though this is sufficient for some application, as described in Section 20.4, for visual servoing of microrobots demands much higher update rates [52].
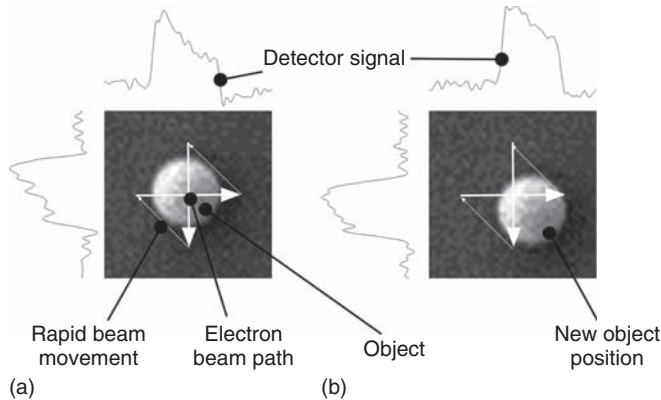
Figure 20.7 Object tracking using decisive control of the SEM beam demonstrated using 1 μm-sized spheres: (a) Sphere stays stationary and (b) sphere is moving. As one can see a movement results in a deviation of the detector signal.

Jasper [53] proposed to use the SEM directly as a position sensor without the process of image acquisition and subsequent processing. Instead, the method uses decisive control of the SEM beam. The only requirement is that the object, which should be tracked, stands out from the background. For objects like nanospheres, this is naturally given, as shown in Figure 20.7. For any other object, it might be possible to apply a pattern to be tracked, for example, using focused ion beam (FIB) milling.

As a first step, algorithms described earlier can be used, to find the initial position of the object or pattern in the SEM image. Subsequently, the method only performs two consecutive orthogonal line scans exactly located over the last known position of the object or pattern. For a square-shaped pattern, the detector generates a square wave signal. A distinction is made between two cases (see Figure 20.7):

a) The object/pattern is stationary and thus the line scan is centered over the middle of this object/pattern.
b) For a moving object/pattern, the two line scans are no longer performed over the center of that object/pattern. This leads to a deviation of the detector signal, which can be used to retrieve the movement in Δx and Δy and the associated new position. Thus, the line scan can be conducted over the new center and a object/pattern can be tracked continuously over long distances.

A single line scan, adjustable in directions, length and number of measurement values, can be performed significantly faster than a whole image acquisition. Therefore, update rates of 1 kHz and measurable movement speeds of up to 400 μm s^{-1} for a 1 μm × 1 μm-sized pattern can be achieved [53, 54]. As can be seen, the update rate is way higher than for the traditional approaches. In addition, these approaches are getting unreliable for speeds higher than 100 μm/s [54].

The approach has been successfully implemented using FPGA-based hardware for high-speed visual servoing of mobile microrobots [52, 54] and a commercial nanostage [32]. An FPGA-based hardware approach was chosen, because software interfaces for current SEMs are infeasible. On the one hand, they introduce a significant latency of at least 10 ms [55] and on the other hand they cannot be adapted for flexible beam control.

20.4.2
Assembly of Building Blocks: NanoBits

One of the major challenges of micro- and nanotechnologies is the integration of nanoscale building blocks. This concerns multiphysically functional components (transducers) as well as mechanical or electrical components.

The assembly of mechanical components is tackled within the NanoBits-Project. There, the so-called *NanoBits* have to be inserted into microcartridges. NanoBits are small silicon flakes, $2 \times 5 \,\mu m^2$ in size and about 200 nm in thickness [56]. On this scale, this task is very challenging, since it requires picking up, turning, tearing off, transportation, and assembly of those objects.

The goal on the other hand is apparent: Today's devices in micro- and nanotechnologies are expected to guarantee a high performance. They are required to be in well-defined, reproducible, and traceable properties. In order to ensure this, precise controlling, metrology steps, and especially measurements are necessary. Many of them at the critical dimension – the threshold where the measurement system reaches its resolution limit – and today's systems are already pushed to that limit. NanoBits in a cartridge, which are fed to a standard AFM, provide a tremendous extension of possibilities for this machine. They can be produced with a large variety of shapes: NanoBits with ultralarge aspect ratio; sidewise-oriented tips; dual tips for tip-enhanced Raman spectroscopy; and many more are possible.

20.4.2.1 **Assembly Environment and Tools**
The robotic setup is identical to the setup introduced in Section 20.3.1: It consists of a coarse and a fine positioning unit, carrying the samples and a thermo-electrical gripper, respectively. Long-traveling actions such as sample exchange are performed by the coarse positioning stage and accurate movements such as the pickup process and the insertion are performed by the fine positioning stage. At least two samples are mounted on the coarse positioning unit for the automated assembly sequence: (i) production substrate as NanoBits source, shown in Figure 20.8a and (ii) a microcartridge sample as target of the transfer, shown in Figure 20.8b. The fine positioning unit carries the microgripper, which is in the center of the setup and the SEM's image.

As prerequisite of the automation, two positions are stored, where the gripper is in a 50 μm proximity to the NanoBits and the reservoir, respectively. All tasks of the automation are done using the same magnification of about 7000. In addition, templates at the same magnification are needed of gripper, NanoBits and

(a)

(b)
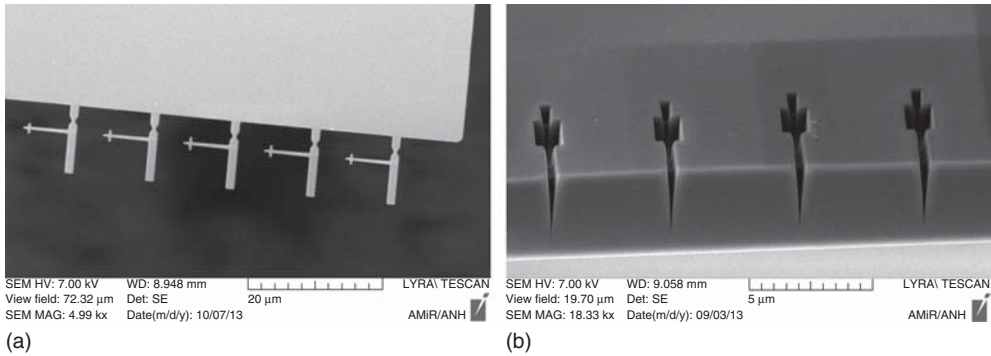
Figure 20.8 SEM image of the NanoBit's production substrate, where NanoBits are suspended (a). Mircocartridge, where the NanoBits have to be inserted (b).

reservoir. These templates are used for regular template matching algorithms for the determination of the positions. Furthermore, an initial calibration of the fine positioning system has to be done. The gripper moves to five different positions in x, y, and z, where its position is detected in the image. In combination with the internal sensors of the fine positioning system, an image-robotic coordinate plane transformation matrix is calculated.

The actual handling tasks of the entire assembly sequence are consistently structured.

– **Coarse xy-alignment:** The first step is a coarse alignment in xy-plane. This starts with the acquisition of an overview image with a viewfield of 50 μm. The positions of the gripper and the target (NanoBit or cartridge's slit) are detected in this image by template matching. Since surface charges of all components cause small image distortions, the position information extracted from the image and the calculated distances does not correspond with the actual physical situation. Hence, the gripper is first moved to the target, but keeping an margin of about 8 μm to the right-hand side.

– **Fine xy-alignment:** A region of interest (ROI) is set around the gripper and the target, which reduces the image acquisition time by 2 orders of magnitude. The new position of all objects, as well as the ROI itself causes new image distortions. From here, all positioning steps are performed relatively to the current position and according to the estimated distance measured in the image.

  – **Gripping:** The relative alignment of gripper and NanoBits is realized using binary large objects. The image is separated only in black and white parts, where the white parts are treated as single objects. In this case, two objects (the gripper jaws) are vertically aligned to the third object (the NanoBit's handle) (cf. Figure 20.9a).

  – **Insertion:** For the insertion, the tip in the NanoBit has to be detected first. This is done by scanning the region in front of the gripper line by line. The line with the largest white part and the end of that white part represent the position of the NanoBit's tip. This position is subtracted from the detected

(a)   (b)
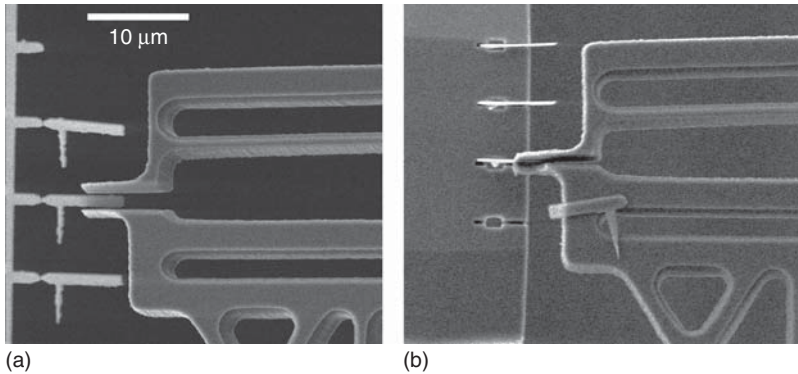
Figure 20.9 SEM images of the NanoBit's assembly process during (a) the grasping sequence and (b) the insertion of the grasped NanoBit.

position of the gripper. Afterward, iterative look-and-move steps using template matching are performed, until the NanoBit masks the cartridge's slit completely.

– ***z*-alignment:** After this xy-approach, the z-approach is performed. This movement is straight parallel to the optical axis, due to the calibration. Two different approaches are used to detect the correct height, depending on the task:

  – **Gripping:** A shadowing effect of the NanoBit's handle can be detected, when handle and gripper are in the same height. The accuracy is at least than 200 nm, which is more than sufficient to guarantee a proper grasping.

  – **Insertion:** The gripper moves downward until the NanoBit's handle touches the reservoir. This leads to a significant change of the surface charge resulting in a reduction of the image distortion. This causes a shift in the image, which can be easily detected. The achieved uncertainty is about 200 nm.

The entire handling sequence takes about 60 s, in which the most time-consuming operation is the z-approach. This could be easily optimized for the assembly from the second NanoBit, since the z-position of the previous NanoBit can be used as prior knowledge.

The current success rate of the entire handling sequence is 80%. The gripping sequence is nearly perfect as long as the conditions of the NanoBits do not vary. The success rate of the insertion process is about 80%. The limiting factor is the release of the NanoBit in the cartridge. In this case, the retracting gripper drags the NanoBit along.

For further developments, of the automated assembly, the uncertainties should be tackled. This can be done by two different approaches: (i) The physical conditions have to be very specific without any variation or (ii) the automation sequence has to involve validation and verification steps between all tasks. In a long-term view, microgrippers with more degrees of freedom would be very useful, since they could compensate a lack of robotic freedom on this scale.

20.4.3
Handling of Colloidal Nanoparticles

Homogeneous spherical nanoparticles can be made from different kinds of materials, covering the whole spectrum of electronic properties. If these nanoparticles are arranged in periodic patterns, they can interact collectively with light, enabling several novel applications in photonics or optronics.

Commonly, the nanoparticles are available in colloidal suspensions. Depending on speed and colloid concentration, drying of these suspensions results in either self-assembled colloidal crystal nanostructures or randomly aligned individual nanoparticles. The individual nanoparticles are ideal candidates for robotic manipulation. So far, several approaches have been presented to pick and place these particles into well-defined spatial orders. The simplest approach to do so is the direct application of atomic force microscopes to visualize and manipulate the particles [57, 58]. However, due to the comparably low image acquisition rate and the limited range, the application perspective of this approach is constrained. The application of light microscopes in combination with robotic setups allows for much faster handling sequences, as the particles can be identified using the visual feedback [59]. Anyhow, due to the resolution limit of light microscopes, this technique is restricted to particle classes with microscopic rather than nanoscopic dimensions. The most promising way to pick and place spherical nanoparticles with sufficient precision and within a reasonable amount of time is to apply the combination of a nanorobotic setup and a scanning electron microscope due to all advantages mentioned Section 20.3.1.

In general, pick-and-place handling on the micro- and nanoscales is challenging as the overall process is dominated through the strong adhesive forces. Therefore, the contact area of end-effector and nanoparticle is the key parameter that needs to be considered. Picking of nanoparticles can only be realized if the contact area of nanoparticle and end-effector is larger than the contact area of the nanoparticle and the initial substrate. For placing, it is just the other way around.

To address this challenge, different solutions have been proposed so far. The application of microgrippers with integrated plunging mechanism has been proposed [60]. In this way, sufficient momenta to overcome the adhesion forces could be realized reliably when using particles around $10\,\mu m$ diameters. Another approach focused on utilizing interferometric force sensors and a complex tilting routine of one end-effector during placement of the nanoparticle, in order to minimize the contact area of particle and end-effector [61, 62]. However, this approach required very complex handling routines. A comparably simple approach is to apply two end-effectors [63, 64] instead of one. In this way, each end-effector can be tailored for either the picking or the placing process, respectively. A setup for dual-probe processing inside scanning electron microscopes has already been introduced in 20.3.1. A suitable pick-and-place handling strategy for nanoparticles based on this dual-probe approach is illustrated in Figure 20.10.
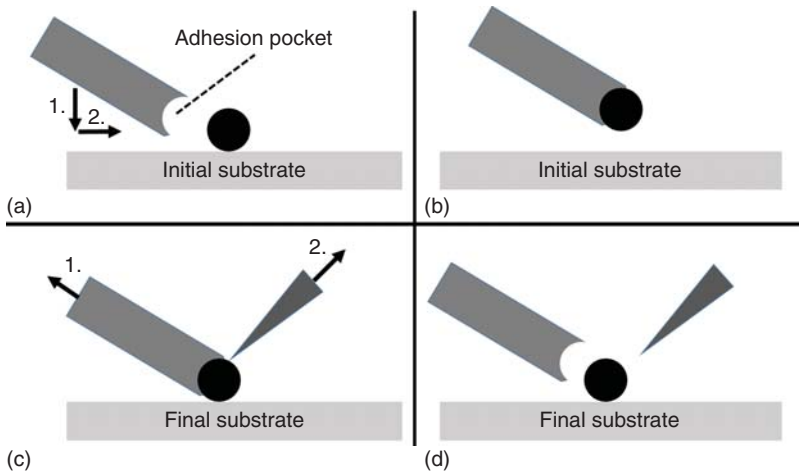
Figure 20.10 Illustration of a handling strategy for micro- and nanoparticles using two tailored end-effectors.

The two end-effectors are optimized for offering a maximized or minimized contact area of the particle, respectively. The end-effector with the maximized contact area is equipped with an *adhesion pocket* that is adapted to a certain particle diameter and that creates a form closure connection to the particle. Conversely, the end-effector with the minimized contact area is simply a high-aspect ratio tip and, therefore, only point or line contact is possible between tip and particle.

On the basis of the setup described in 20.3.1, the overall handling process can be divided into three steps:

– **Picking:** The end-effector with the adhesion pocket touches down to the initial substrate near a single nanoparticle and subsequently moves laterally to the particle. Because of the strong adhesion, the particle aligns itself within the adhesion pocket. Afterward, the end-effector can be removed from the initial substrate together with the particle.
– **Substrate Exchange:** The samples can be exchanged using the slip-stick-driven sample stage. Because of the large overall range of the stage, the distance between initial and final substrates can reach up to several millimeters.
– **Placing:** The placing process starts with the attachment of the end-effector with the adhesion pocket to the final substrate. To release the sphere from the adhesion pocket, the second end-effector fixates the particle on the final substrate. Subsequently, the end-effector with the adhesion pocket can be retracted. As the adhesive forces of substrate and particle exceed those between particle and tip, the tip can also be retracted from the particle, leaving it at the intended position.

This overall handling strategy has been proven to be reliable for packaging of two- and three-dimensional patterns of micro- and nanoparticles when applying

(a)

(b)

(c)

(d)
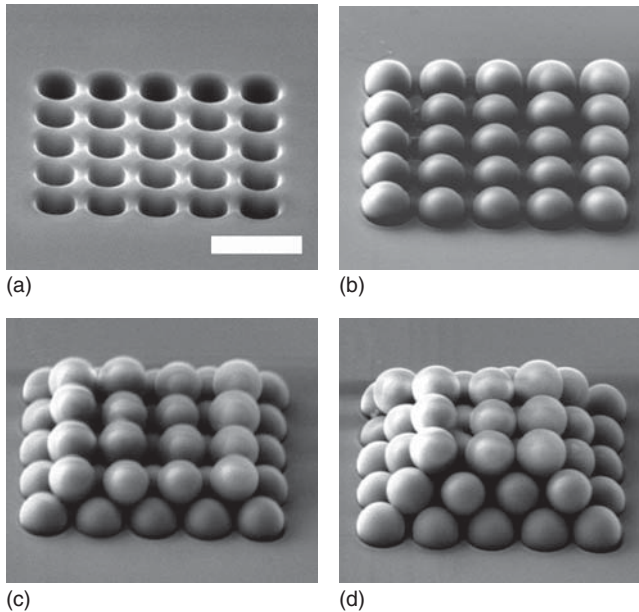
Figure 20.11 Scanning electron micrographs of the layer-by-layer assembly of a pyramidal structure consisting of silica spheres with 1.1 μm diameter. Scale Bar: 2 μm.

force control and using haptic devices [64]. As an example of potential target structures, the layer-by-layer assembly of a three-dimensional structure is shown in Figure 20.11

So far, the application perspectives of the robotic assembly approach of individual particles into an overall periodic structure are limited as most of them are time consuming and require manual input. The only way forward is to push these techniques to fully automated sequences. Even though significant progress has been made within the last decade, supplementary efforts must be made to push these techniques to application maturity.

20.4.4
Measuring the Transverse Fiber Compression

The printed edition of this textbook uses natural resources: cellulose fibers. Cellulose is the most abundant natural polymer on earth, and it is used for centuries in many different forms. One of these appearances is paper: Single cellulose fibers with sizes from 15 to 80 μm diameter and up to several millimeters length are processed in sheet form.[11] How single cellulose fibers bond to each other and how their mechanical properties are altered in detail in the paper production are still

---

11) Typical production speeds range from 800 to 1800 m/s at paper widths of up to 10 m.

not fully understood. PowerBonds, a recent European project, focused on some of the open questions.

Enhancement of fiber and bond strength properties for creating added value in paper products is the main goal of PowerBonds. Reducing the grammage of paper and board products offers a considerable potential to reduce material and energy consumption in the production. However, a lower grammage (mass of fibers per unit area) means that the product is weaker due to lower number of fibers and interfiber bonds. Another factor on the strength is the processing of the fibers. Thermal, chemical, and mechanical treatments are used, for example, bleaching. Starting from the initial separation of the fibers from the wood chips up to the refining before the pulp[12] is led into the paper machine. Mechanical refining has a large impact on the fiber structure and mechanical properties. The fibers are randomly compressed and crumpled, which reduces their stiffness. For example, more limp fibers provide a smoother surface because the fibers come to lay smoother on one another. However, the mechanisms are not fully understood. Therefore, current models are based on ad hoc assumptions and statistical data of huge amounts of fibers. PowerBonds aims at gathering additional knowledge throughout the scales to improve the current simulation models. More information on single fiber level is necessary, which requires new characterization techniques. Different aspects, such as fiber and bond strengths at dry and wet states or flexibility and compressibility of fibers and bonds, are addressed. Even though characterization techniques using micro- and nanorobotic systems exist, they are often performed under light microscope [65, 66].

One of the newly developed measurements is the transverse compression of single fibers with high-resolution cross-sectional imaging. This measurement is performed inside the SEM in low-vacuum mode for two reasons. First, the visualization of the fiber cross section requires high-resolution imaging and the SEM provides this necessary resolution. Second, the nonconducting sample fibers cannot be coated in order to avoid influences on the mechanical properties. Therefore, the fibers are tested in a water atmosphere at a pressure of 0.8 mbar. With an acceleration voltage of 10 kV or less, the image quality is good enough to monitor the compression and see possible cracking of the fiber.

Single fiber compression has already been addressed occasionally since the 1970s. At that time, axial testing of single fibers has been performed for a decade by Jayne [67] and others. Jan Nyrén has developed the first test bench to compress whole fibers in the transverse direction [68]. He developed a system, which was placed under a light microscope with a view on the fiber top. He observed that in the beginning, the fiber collapsed and after that the fiber wall itself is compressed. More than three decades later, Peter Wild and his coworkers developed a system, which was capable of testing a fiber segment of ca. 300 μm [69]. Their system consisted of a hammer-anvil approach, but details in the force regime directly after the initial contact could not be properly recorded. As a bottom-up approach,

---

12) Aqueous mixture of (cellulose) fibers and additives, which eventually form the paper.

fibers were tested by means of AFM. Christian Ganser indented a fiber wall with a silicon tip [70]. However, the state of the art still leaves a gap between AFM and larger forces. Therefore, a stiffness measurement system is needed, which tests very locally on the fiber with a maximum resolution.

Nanorobotics allow for the measurement of this stiffness value in a rather small force regime ($0-1$ mN) and it becomes possible to evaluate the compressive effect. To achieve this, two modules of the PS-AMiR (cf. section 20.3.1) are used: (i) Fine positioning module in the center position and (ii) coarse positioning module in the perimeter position. The coarse positioning module carries the FemtoTools FT-S270 capacitive force sensor. It has a nominal force limit of 2 mN and a theoretical resolution of $0.4\,\mu$N. Its tip is a square of $50\,\mu$m $\times$ $50\,\mu$m. For the coarse positioning SmarAct's SLC, axes with a travel of ca. 12 mm are used. These piezo-driven actuators are fast (13 mm/s) and accurate (50 nm minimum step width). For the fine positioning unit, Hera Nanopositioning Stages from Physik Instrumente are used. These compact drives are piezo-based and are extremely accurate at a stroke of $50\,\mu$m in closed loop. The setup can be seen in Figure 20.12a). All these different tools are connected to one central control computer with the automation software installed (see Section 20.3.2). It is used to control the movement as well as read the sensor data.

Cellulose fibers are taken from a suspension or in dry state and placed on a specially prepared SEM stub. A standard 12.5 mm circular stub is flattened and equipped with silicon tiles and standard carbon sticky pad. The fiber is placed with one end on the sticky pad and the other protrudes over the silicon tile. Finally, the protruding fiber end is cut with a razor blade to obtain a clear cross section. In this way, the fiber can be tested against a very flat and stiff surface. The stubs with the fibers are placed at an angle of 90° inside the SEM. The cross section is therewith directly accessible by the electron beam. Subsequently, the sensor
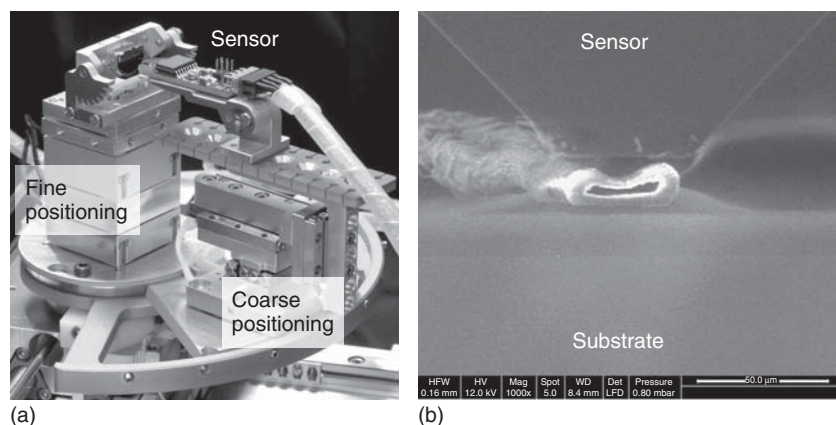
Figure 20.12 (a) Setup for and (b) SEM view of the transverse compression of single fibers. The sensor is pointing toward the fiber and presses it against a rigid silicon surface.

tip is brought into close proximity of the next fiber to be tested and vacuum is applied.

With SEM observation, the sensor tip is moved by telecontrol to bend the fiber toward the silicon tile. In the automation software, two phases are scripted. In the first phase, a calibration step, the maximum travel is determined. On detection, the current distance value is stored and the force sensor is retracted at once to the parking position. The second phase is the characterization. The fiber is loaded to the maximum distance and unloaded at a user-defined speed. This cycle is done as often as specified by the user. The measurement curve is a voltage representation of the force and distance. With the sensor sensitivity and the distance – voltage conversion factor, the force – distance curves can be plotted.

The results show different behaviors. It is dependent on the initial state of the fiber (collapsed or with open lumen) and its material composition (lignin content). Different states can also be distinguished. In Figure 20.13), an exemplary force – distance curve is shown. In the beginning, a slow rise in force can be related to the final bending of fiber toward the silicon substrate. The second regime shows the fiber compression until the fiber totally collapses. Eventually, the force rises quickly to a maximum when the fiber wall itself is compressed. The loading (upper curve) and unloading (lower curve) can be clearly distinguished. Both curves encircle the dissipation energy, which decreases with a rising number of compression cycles. The slope of the unloading curve from its peak can be seen as the transverse compression stiffness. In addition, the dissipation energy and different fiber loading states can be characterized.

In summary, nanorobotics in the SEM make it possible to characterize even unstructured materials and objects, such as wood and paper fibers from cellulose, with high resolution, both in visual and mechanical sense. The stiffness values resulting from the force – distance curves are implemented into single fiber models and enhance our understanding of this natural fiber material.
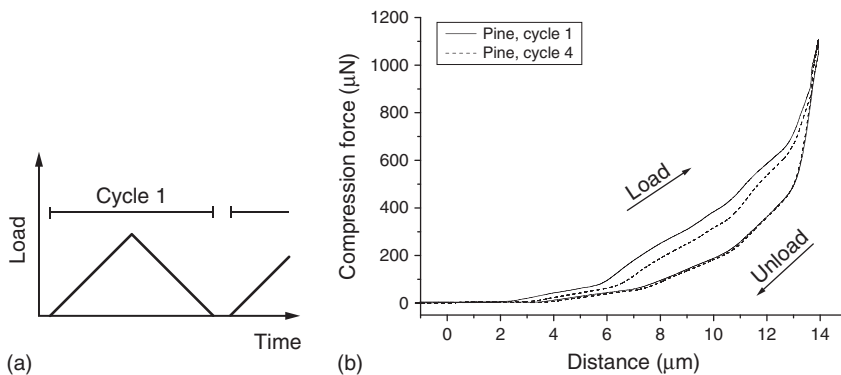
Figure 20.13 (a) Loading profile and (b) result of a single fiber compression. The result is exemplary for a Pine fiber with a nearly collapsed lumen. Cycles 1 and 4 show the drop in dissipation energy.

20.5
Outlook

20.5.1
Future Developments

In conclusion of the current state of the art and the presented works, it has been shown that SEM-based micro- and nanomanipulation offer a large contribution to existing challenges in micro- and nanotechnologies. The ability to handle individual tiny objects with a very high precision has been demonstrated. Furthermore, it revealed that the most important key technology for this approach is automation: very challenging tasks can be performed on this scale in a reasonable time and success rate, if it can be done automatically.

A tremendous improvement in micro- or nanohandling can be contributed by further developments of smart and functional end-effectors: today, the degrees of freedom for robotic manipulation is very limited and consist a bottleneck for handling tasks. Especially, rotational degrees of freedom could improve the abilities of nanohandling setups significantly. In addition, in most cases, each end-effector can fulfill only one specific task. In combination, this means that space is quite limited in proximity to the sample, if one wants to perform more complex tasks.

In the near future, nanorobotics will remain a very important tool for researchers and industrial feasibility studies. But further developments will help to turn nanorobotics into a powerful tool for a directed micro- or nanointegration, helping industry to build novel devices exploiting nanomaterials. To achieve this, solutions for hardware interfacing and sample exchange are necessary.

20.5.2
Software and Automation

In terms of future software developments, the focus has to be put on a unification. Even though there are a few robotic software frameworks targeting micro- and nanorobotics, as described in Section 20.3.2, monolithic individual software solutions, provided by the manufacturer or specially tailored, still dominate. This is due to several reasons: The lack of open implementation guidelines and (industrial) standards, software interfacing in-house hardware solutions, and the prototypic implementation of many micro- and nanorobotic applications [18, 27].

As described above, a few approaches have been developed in recent years to overcome the aforementioned problems, including the development of new RSFs (e.g., the OFFIS automation framework described in Section 20.3.2) or the adaption of an established macrorobotic RSF [18], such as the robot operating system (ROS) [19].

One of the future challenges is to join these approaches, thus combining their benefits. This is mainly due to avoidance of constant reinvention: Micro- and nanorobotics are a still niche market, and the research community is not very large. It is necessary to provide the research community with means that enable

easy integration of software produced by different partners. Reimplementation of existing functionality leads to a huge waste of resources and furthermore hinders the development of robust source code [18]. Software development for micro- and nanoscale applications should aim toward modular, component-based design, where functional components could be exchanged without the need for writing large quantities of additional source code.

Acknowledgments

References

1. ITRS (2013) International Technology Roadmap for Semiconductors (ITRS 2013), *http://www.itrs.net* (accessed 11 May 2015).

2. Abbott, J.J., Nagy, Z., Beyeler, F., and Nelson, B.J. (2007) Robotics in the small, Part I: microbotics. *IEEE Rob. Autom. Mag.*, **14** (2), 92–103, *http://dblp.uni-trier.de/db/journals/ram/ram14.html#AbbottNBN07*.

3. Kortschack, A. and Fatikow, S. (2004) Development of a mobile nanohandling robot. *J. Micromechatron.*, **2** (3-4), 249–269.

4. Sievers, T., Jähnisch, M., Schrader, C., and Fatikow, S. (2006) Vision feedback in an automatic nanohandling station inside an SEM. *Optomechatron. Micro/Nano Devices Compon. II*, **6376** (1), 63 760B.

5. Sievers, T. and Fatikow, S. (2006) Real-time object tracking for the robot-based nanohandling in a scanning electron microscope. *J. Micromechatron.*, **3** (3-4), 267–284(18).

6. Wich, T., Edeler, C., Stolle, C., and Fatikow, S. (2009) Micro-nano-integration based on automated serial assembly. Proceedings of the 5th Annual IEEE International Conference on Automation Science and Engineering (CASE'09), IEEE Press, Piscataway, NJ, pp. 573–578, doi: 10.1109/COASE.2009.5234150.

7. Wich, T., Stolle, C., Edeler, C., and Fatikow, S. (2009) Parasitic effects on nanoassembly processes. Proceedings of the 2009 IEEE/RSJ International Conference on Intelligent Robots and Systems (IROS'09), IEEE Press, Piscataway, NJ, pp. 1389–1394, doi: 10.1109/IROS.2009.5354016.

8. Diederichs, C., Dahmen, C., Bartenwerfer, M., and Fatikow, S. (2012) Tracking algorithms for closed-loop positioning of mobile microrobots. Proceedings of IEEE/ASME International Conference on Advanced Intelligent Mechatronics, AIM2012, pp. 568–573.

9. Fukushima, K., Saya, D., and Kawakatsu, H. (2000) Development of a versatile atomic force microscope within a scanning electron microscope. *Jpn. J. Appl. Phys.*, **39** (6S), 3747, *http://stacks.iop.org/1347-4065/39/i=6S/a=3747*.

10. Joachimsthaler, I., Heiderhoff, R., and Balk, L.J. (2003) A universal scanning-probe-microscope-based hybrid system. *Meas. Sci. Technol.*, **14** (1), 87, *http://stacks.iop.org/0957-0233/14/i=1/a=313*.

11. Mikczinski, M., Bartenwerfer, M., Saketi, P., Heinemann, S., Passas, R., Kallio,

P., and Fatikow, S. (2011) Towards automated manipulation and characterisation of paper-making fibres and its components, in *Fine Structure of Papermaking Fibres* (eds P. Ander, W. Bauer, S. Heinemann, P. Kallio, R. Passas, and A. Treimanis), Swedish University of Agricultural Sciences, pp. 163–178.

12. Bartenwerfer, M., Fatikow, S., Tunnell, R., Mick, U., Stolle, C., Diederichs, C., Jasper, D., and Eichhorn, V. (2011) Towards automated AFM-based nanomanipulation in a combined nanorobotic AFM/HRSEM/FIB system. Proceedings of International Conference on Mechatronics and Automation (ICMA), pp. 183–188, doi: 10.1109/ICMA.2011.5985653.

13. Gauthier, M., Hériban, D., Gendreau, D., Regnier, S., Chaillet, N., and Lutz, P. (2006) Micro-factory for submerged assembly: interests and architectures. Proceedings of the 5th International Workshop on MicroFactories, IWMF'06, vol. 1, Besançon, France.

14. Gendreau, D., Gauthier, M., Hériban, D., and Lutz, P. (2010) Modular architecture of the microfactories for automatic micro-assembly. *Rob. Comput. Integr. Manuf.*, **26** (4), 354–360, doi: 10.1016/j.rcim.2009.11.013.

15. Arbuckle, D.J., Kelly, J., and Requicha, A.A.G. (2006) A high-level nanomanipulation control framework. Proceedings of International Advanced Robotics Programme (IARP) Workshop on Micro and Nano Robotics, Paris, France.

16. Diederichs, C., Bartenwerfer, M., Mikczinski, M., Zimmermann, S., Tiemerding, T., Geldmann, C., Nguyen, H., Dahmen, C., and Fatikow, S. (2013) A rapid automation framework for applications on the micro- and nanoscale. Proceedings of the Australasian Conference on Robotics and Automation 2013, p. 8.

17. Dahmen, C., Wortman, T., and Fatikow, S. (2008) OLVIS: a modular image processing software architecture and applications for micro- NAMD nanohandling. Proceedings of IASTED International Conference on Visualization, Imaging and Image Processing (VIIP).

18. von Essen, M., Hirvonen, J., Kuikka, S., and Kallio, P. (2013) Towards fully automated pick and place operations of individual natural fibers. Proceedings of International Conference on Manipulation, Manufacturing and Measurement on the Nanoscale (3M-NANO).

19. Quigley, M., Conley, K., Gerkey, B.P., Faust, J., Foote, T., Leibs, J., Wheeler, R., and Ng, A.Y. (2009) ROS: an open-source robot operating system. ICRA Workshop on Open Source Software.

20. Makarenko, A., Brooks, A., and Kaupp, T. (2006) Orca: components for robotics. 2006 IEEE/RSJ International Conference on Intelligent Robots and Systems (IROS), Beijing, China.

21. Bruyninckx, H. (2001) Open robot control software: the OROCOS project. Proceedings of 2001 IEEE International Conference on Robotics and Automation (ICRA), vol. 3, IEEE, pp. 2523–2528, doi: 10.1109/robot.2001.933002.

22. Diankov, R. and Kuffner, J. (2008) OpenRAVE: A Planning Architecture for Autonomous Robotics. Technical Report CMU-RI-TR-08-34, Robotics Institute, Pittsburgh, PA.

23. Ando, N., Suehiro, T., and Kotoku, T. (2008) A software platform for component based RT-system development: OpenRTM-Aist, in *Simulation, Modeling, and Programming for Autonomous Robots*, Lecture Notes in Computer Science, vol. 5325 (eds S. Carpin, I. Noda, E. Pagello, M. Reggiani, and O. Stryk), Springer-Verlag, Berlin and Heidelberg, pp. 87–98.

24. Calisi, D., Censi, A., Iocchi, L., and Nardi, D. (2008) OpenRDK: a modular framework for robotic software development. Proceedings of International Conference on Intelligent Robots and Systems (IROS), pp. 1872–1877, doi: 10.1109/IROS.2008.4651213.

25. Metta, G., Fitzpatrick, P., and Natale, P. (2006) YARP: yet another robot platform. *Int. J. Adv. Rob. Syst.*, **3** (1), 43–48.

26. Bradski, G. (2000) The OpenCV library. *Dr. Dobb's J. Softw. Tools*, **25** (11), 120, 122–125, *http://www.ddj.com/ftp/2000/2000_11/opencv.txt*.

27. Tiemerding, T., von Essen, M., Diederichs, C., Kallio, P., and Fatikow, S. (2014) Integrating robotic software frameworks for convenient software component exchange in micro- and nanoscale applications. Proceedings of IEEE/ASME International Conference on Advanced Intelligent Mechatronics, accepted.

28. Krohs, F. and Fatikow, S. (2013) Novel high-resolution sidewall imaging using standard atomic force microscopy equipment. International Conference on Sensing Technology (ICST), 2013.

29. Zimmermann, S., Tiemerding, T., Li, T., Wang, W., Wang, Y., and Fatikow, S. (2013) Automated mechanical characterization of 2D materials using SEM based visual servoing. *Int. J. Optomechatron.*, **7** (4), 283–295.

30. Sören Zimmermann, S.A.G. and Fatikow, S. (2014) Nanorobotic processing of graphene for rapid device prototyping. IEEE International Conference on Nano/Micro Engineered and Molecular Systems, 2014. Proceedings 2014 IEEE-NEMS.

31. Diederichs, C., Mikczinski, M., and Tiemerding, T. (2014) A flexible and compact high precision micro-factory for low volume production and lab-automation. Proceedings of the 45th International Symposium on Robotics (ISR), Munich, Germany.

32. Tiemerding, T., Diederichs, C., and Fatikow, S. (2013) High speed visual servoing and control of a commercial nanostage inside the SEM. Proceedings of International Conference on Manipulation, Manufacturing and Measurement on the Nanoscale (3M-NANO), Suzhou, China, pp. 35–39.

33. Mucha, H., Kato, T., Arai, S., Saka, H., Kuroda, K., and Wielage, B. (2005) Focused ion beam preparation techniques dedicated for the fabrication of TEM lamellae of fibre-reinforced composites. *J. Electron. Microsc. (Tokyo)*, **54** (1), 43–49, doi: 10.1093/jmicro/dfh102.

34. Graff, A., Grosse, C., Simon, M., and Altmann, F. (2007) New tool for in-situ lift out of TEM samples. *Microsc. Microanal.*, **13**, 88–89, doi: 10.1017/S1431927607080440.

35. ZEISS (2014) Tem Lift-Out Tools for FIB Prepared Lamellas, Product Advertisement, *http://www.zeiss.co. kr/C1256E4600307C70/EmbedTitelIntern/ EN_40_011_030_tem_lift-out_tools.pdf/ $File/EN_40_011_030_tem_lift-out_tools.pdf* (accessed 11 May 2015).

36. TESCAN (2014) AutoSlicer - Sample Preparation Tool, Product Advertisement, *http://www.tescan.com/en/other-products/software/autoslicer-sample-preparation-tool* (accessed 11 May 2015).

37. Mayer, J., Giannuzzi, L.A., Kamino, T., and Michael, J. (2007) TEM sample preparation and FIB-induced damage. *MRS Bull.*, **32**, 400–407, doi: 10.1557/mrs2007.63.

38. Klocke Nanotechnik (2014) Preparation of TEM-Samples, Product Advertisement, *http://www.nanomotor.de/aa_tem.htm*.

39. Fengel, D. (1969) The ultrastructure of cellulose from wood. *Wood Sci. Technol.*, **3** (3), 203–217.

40. Syverud, K., Xhanari, K., Chinga-Carrasco, G., Yu, Y., and Stenius, P. (2011) Films made of cellulose nanofibrils: surface modification by adsorption of a cationic surfactant and characterization by computer-assisted electron microscopy. *J. Nanopart. Res.*, **13** (2), 773–782.

41. Mott, L., Shaler, S.M., Groom, L.H., and Liang, B.H. (1995) The tensile testing of individual wood fibers using environmental scanning electron microscopy and video analysis. *Tappi J.*, **78** (5), 143–148.

42. Adusumalli, R.B., Raghavan, R., Ghisleni, R., Zimmermann, T., and Michler, J. (2010) Deformation and failure mechanism of secondary cell wall in spruce late wood. *Appl. Phys. A*, **100** (2), 447–452.

43. Krohs, F., Hagemann, S., and Fatikow, S. (2007) Automated cell characterization by a nanohandling robot station. Proceedings of the Mediterranean Conference on Control and Automation (MED'07), Athens, Greece, pp. ThA−5.

44. Zhang, Y.L., Li, J., To, S., Zhang, Y., Ye, X., You, L., and Sun, Y. (2012) Automated nanomanipulation for nanodevice

construction. *Nanotechnology*, **23** (6), 065 304, *http://stacks.iop.org/0957-4484/23/i=6/a=065304*.

45. Ye, X., Zhang, Y., Ru, C., Luo, J., Xie, S., and Sun, Y. (2013) Automated pick-place of silicon nanowires. *IEEE Trans. Autom. Sci. Eng.*, **10** (3), 554–561, doi: 10.1109/TASE.2013.2244082.

46. Eichhorn, V., Fatikow, S., Wich, T., Dahmen, C., Sievers, T., Andersen, K.N., Carlson, K., and Bøggild, P. (2008) Depth-detection methods for micro-gripper based CNT manipulation in a scanning electron microscope. *J. Micro - Nano Mechatron.*, **4** (1-2), 27–36.

47. Wortman, T. and Fatikow, S. (2009) Carbon nanotube detection by scanning electron microscopy. Proceedings of the 11th IAPR Conference on Machine Vision Applications (MVA).

48. Goudail, F. and Refregier, P. (2004) *Statistical Image Processing Techniques for Noisy Images*, Plenum Publishers.

49. Kass, M., Witkin, A., and Terzopolous, D. (1988) Snakes: active contour models. *Int. J. Comput. Vision*, **1**, 321–331.

50. Sievers, T. and Fatikow, S. (2006) Real-time object tracking for the robot-based nanohandling in a scanning electron microscope. *J. Micromechatron.*, **3**, 268–284.

51. Kratochvil, B., Dong, L., and Nelson, B. (2009) Real-time rigid-body visual tracking in a scanning electron microscope. *Int. J. Rob. Res.*, **28**, 498–511.

52. Jasper, D. (2011) SEM-based motion control for automated robotic nanohandling. PhD thesis. Oldenburg University.

53. Jasper, D. (2009) High-speed position tracking for nanohandling inside scanning electron microscopes. Proceedings of IEEE International Conference on Robotics and Automation (ICRA), pp. 508–513.

54. Jasper, D., Edeler, C., Diederichs, C., and Fatikow, S. (2010) High-speed nanorobot position control inside a scanning electron microscope. Proceedings of Electrical Engineering/Electronics, Computer, Telecommunications and Information Technology Conference, Chiang Mai, Thailand, pp. 542–546, Best Paper Award.

55. Jasper, D. and Fatikow, S. (2010) Line scan-based high-speed position tracking inside the SEM. *Int. J. Optomechatron.*, **4** (2), 115–135.

56. Rajendra Kumar, R.T., Hassan, S.U., Sardan, O., Eichhorn, V., Krohs, F., Fatikow, S., and Bøggild, P. (2009) Nanobits: customisable scanning probe tips. *Nanotechnology*, **20** (39), 395 703–(6pp−), doi: 10.1088/0957-4484/20/39/395703.

57. Ding, W. (2008) Micro/nano-particle manipulation and adhesion studies. *J. Adhes. Sci. Technol.*, **22** (5-6), 457–480, doi: 10.1163/156856108X295563.

58. Mokaberi, B., Yun, J., Wang, M., and Requicha, A.A.G. (2007) Automated nanomanipulation with atomic force microscopes. 2007 IEEE International Conference on Robotics and Automation, pp. 1406–1412.

59. Xie, H., Haliyo, D.S., and Régnier, S. (2009) Parallel imaging/manipulation force microscopy. *Appl. Phys. Lett.*, **94** (15), 153106, doi: http://dx.doi.org/10.1063/1.3119686.

60. Chen, B., Zhang, Y., and Sun, Y. (2009) Active release of microobjects using a MEMS microgripper to overcome adhesion forces. *J. Microelectromech. Syst.*, **18** (3), 652–659.

61. Kasaya, T., Miyazaki, H.T., Saito, S., Koyano, K., Yamaura, T., and Sato, T. (2004) Image-based autonomous micromanipulation system for arrangement of spheres in a scanning electron microscope. *Rev. Sci. Instrum.*, **75** (6), 2033–2042, doi: http://dx.doi.org/10.1063/1.1753106.

62. Miyazaki, H.T., Tomizawa, Y., Koyano, K., Sato, T., and Shinya, N. (2000) Adhesion force measurement system for micro-objects in a scanning electron microscope. *Rev. Sci. Instrum.*, **71** (8), 3123–3131, doi: http://dx.doi.org/10.1063/1.1305812.

63. Xie, H., Haliyo, D.S., and Régnier, S. (2009) A versatile atomic force microscope for three-dimensional nanomanipulation and nanoassembly. *Nanotechnology*, **20** (21), 215 301.

64. Tiemerding, T., Zimmermann, S., and Fatikow, S. (2014) Robotic dual probe

setup for reliable pick and place processing on the nanoscale using haptic devices. Proceedings of IEEE/RSJ International Conference on Intelligent Robots and Systems, accepted.

65. Saketi, P., Treimanis, A., Fardim, P., Ronkanen, P., and Kallio, P. (2010) Microrobotic platform for manipulation and flexibility measurement of individual paper fibers. International Conference on Intelligent Robots and Systems (IROS) 2010 (eds IEEE and RSJ).

66. Saketi, P., von Essen, M., Mikczinski, M., Heinemann, S., Fatikow, S., and Kallio, P. (2012) A flexible microrobotic platform for handling microscale specimens of fibrous materials for microscopic studies. *J. Microsc.*, **248** (2), 163–171.

67. Jayne, B.A. (1959) Mechanical properties of wood fibers. *Tappi J.*, **42** (6), 461–467.

68. Nyrén, J. (1971) The transverse compressibility of pulp fibres. *Pulp Paper Mag. Can.*, **72** (10), 81–83.

69. Wild, P.M., Omholt, I., Steinke, D., and Schuetze, A. (2005) Experimental characterization of the behaviour of wet single wood-pulp fibres under transverse compression. *J. Pulp Pap. Sci.*, **31** (3), 116–120.

70. Ganser, C., Hirn, U., Rohm, S., Schennach, R., and Teichert, C. (2014) AFM nanoindentation of pulp fibers and thin cellulose films at varying relative humidity. *Holzforschung*, **68** (1), 53–60.

21
Manipulation of Biological Cells under ESEM and Microfluidic Systems

Toshio Fukuda, Masahiro Nakajima, Masaru Takeuchi, and Mohd Ridzuan Ahmad

21.1
Introduction

Cell manipulation is defined as an ability to reorient and reposition cells in three-dimensional (3D) space. The size of the biological cells ranges from $1-10\,\mu m$ (Prokaryotes) to $10-30\,\mu m$ (Eukaryotic animal cells) to $10-100$ (Eukaryotic plant cells and Human eggs) to $800\,\mu m$ (large Amoeba). As the size of the cells is relatively small to be captured by human naked eyes, observation magnification tools, for example, optical or electron microscope, are needed to observe such small samples. The microscope was invented by Anton van Leeuwenhoek in the late seventeenth century [1]. He managed to develop lens tube that had a magnification power of 270× and could view objects one millionth of a meter. With his microscope, samples such as bacteria and yeasts could be observed. Theoretically, the modern optical microscopes can have resolution up to 200 nm (up to 2000× magnification). Later in 1931, Ernst Ruska started to build the first electron microscope [2]. The electron microscopes can have a magnification of 500 000× (transmission electron microscope, TEM) and 100 000× (scanning electron microscope, SEM). Electron microscopes are used to investigate the *ultrastructure* of a wide range of biological and inorganic specimens including microorganisms, cells, large molecules, biopsy samples, metals, and crystals.

Cell manipulation requires not only the ability to observe the cells but also the ability to probe the cells. Available experimental techniques to probe single cells include micropipette aspiration [3], optical tweezers [4], magnetic tweezers [5], atomic/molecular force probes [6], nanoindenters [7], microplate manipulators [8], and optical stretchers [9]. These probing techniques have one significant limitation, which is low throughput due to the active probing method and large searching area. Active probing means that the probe is moved to make contact with the sample. Since the searching area is large (depend on the size of the sample's substrate), the searching for samples can be a daunting task and time consuming. Microfluidics, the manipulation of fluids in channels with dimensions of tens of micrometers, on the other hand, uses passive probing technique, in

which, the sample is moved to make a contact with a probe [10]. The path for the sample to navigate is a narrow-guided channel, for example, $1-10\,\mu m$ width. With these methods, that is, passive and narrow-guided sample path, high-throughput measurement could be realized.

This chapter focuses on the manipulation of biological samples inside two different platforms, that is, environmental scanning electron microscope (ESEM) and microfluidic device. One example of cell manipulation inside ESEM platform will be presented, that is, the manipulation of cells using dual nanoprobe, and one example of cell manipulation inside microfluidic device will be highlighted, that is, the manipulation of cells using thermoresponsive polymer actuated (TPA) probe.

21.2
ESEM-Nanomanipulation System

We have developed an integrated ESEM-nanomanipulator system. Unlike the conventional SEM, ESEM enables soft, moist, and/or electrically insulating materials to be imaged without prior specimen preparation. Figure 21.1a shows the image of the ESEM instrument. A low-pressure (up to around 1333 Pa) gas can be accommodated around the sample. When this gas is water, hydrated samples
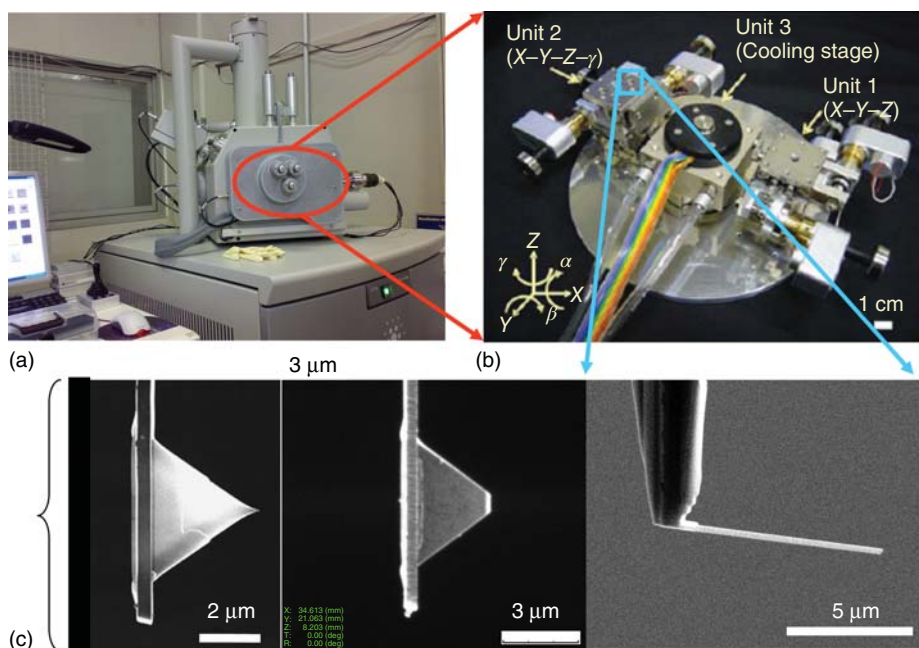
Figure 21.1 Overview of the (a,b) ESEM-nanomanipulator system incorporated with (c) various kind of nanoprobes.

can be maintained in their native state. Sample temperature can be controlled ($0-40\,°$C) by using the cooling stage assembled inside the ESEM chamber. By controlling the chamber pressure ($10-2600$ Pa) and sample temperature, single-cell property characterizations and analyses can be conducted by using a nanomanipulator and image analysis.

There are two main advantages of the ESEM system compared to the Atomic Force Microscope (AFM) system. The first advantage is that AFM system is difficult to provide a real-time sample observation and the image is mainly constructed after the scanning of the AFM tip on the sample surface is finished. Therefore, it is difficult, if not impossible, to directly observe the response of the object during the sample manipulation. On the other hand, ESEM system provides real-time sample observation, which can be obtained before, during, and after the manipulation. This real-time observation capability of the ESEM system has many advantages such as in analyzing the dynamic response of the sample and sample selection/sorting for certain properties like cell size, become much easier.

The second advantage is related to the manipulation aspect. The AFM system can only provide two-dimensional (2D) manipulation, due to the difficulty of the real-time observation. Even though 2D manipulation can measure the stiffness property of the sample, it lacks the flexibility of manipulation, thus limiting the area of sample which can be analyzed. Unlike AFM system, ESEM-nanomanipulation system can provide both 2D and 3D manipulations on the sample, thus increasing the flexibility of the measurement. ESEM system can provide environmental conditions for the cells in their native state without any effect of the osmotic pressure. Cells can be sustained by releasing low-pressure H_2O molecule gas inside the ESEM chamber to provide high relative humidity (up to 100%).

Nanomanipulation is an effective strategy for the characterization of basic properties of individual nanoscale objects and construction nanoscale devices quickly and effectively. Previously, we have constructed a hybrid nanorobotic manipulation system integrated with a TEM – nanorobotic manipulator (TEM manipulator) and a SEM – nanorobotic manipulator (SEM manipulator). This system allows effective sample preparation inside SEM with wide working area and many degrees of freedom (DOFs) of manipulation. It has high-resolution measurement and evaluation of samples inside a TEM capability. The sample chambers of these electron microscopes are set under high-vacuum (HV) condition to reduce the disturbance of electron beam for observation. However, to observe the water-containing samples, for example, biocells, dry treatment processes are additionally needed. Hence, direct observations of water-containing samples are normally quite difficult in these electron microscopes. This limitation was overcome by using ESEM.

In the present study, we used the nanorobotic manipulators inside ESEM. It has been constructed with 3 units and 7 DOFs in total (Figure 21.1b). The ESEM-nanomanipulator system can be easily incorporated with various kinds of nanoprobes for single-cell analysis as shown in Figure 21.1c.

21.3
ESEM Observation of Single Cells

Wild-type yeast cells (*W303*) were used for observation and measurements by ESEM-nanomanipulation system. The *W303* cells were cultured on yeast peptone dextrose (YPD) plates (1% yeast extract, 2% peptone, 2% glucose, 2% agar) in a 37 °C incubator for 24 h and dispersed in pure water. Several microliters of dispersed cells were placed on aluminum block on the cooling stage. The HV mode is operated at a temperature of 16.7 °C and 3.03×10^{-3} Pa pressure. All yeast cells appeared concave and broken under HV mode. The ESEM mode is operated at 0.0 °C and ~600 Pa pressure and acceleration voltage is set at 15 kV. Under the ESEM mode, on decreasing the pressure from ~700 Pa, water gradually evaporates and the samples can be seen underneath. Their images are shown with HV and ESEM modes as shown in Figure 21.2a,b. The remaining water can be seen at the intercellular spaces of yeast cells as black contrast (Figure 21.2b). Almost all yeast cells appear sphere shaped by water-contained condition under the ESEM operation.

In order to reveal the influence of an electron beam observation under HV and ESEM modes, yeast cells were cultured once again after observation. Yeast cells were observed under the ESEM mode, and after the observation, we collected the cells from the observation stage (aluminum block) by a sterilized toothpick and inoculated onto the fresh YPD plate, and grew them overnight. To compare the cell viability with untreated cell, water-dispersed yeast cells were inoculated on the same plate for the control. The cultured plate is shown in Figure 21.3. The plate was divided into three regions: cultured after water dispersion; SEM observation; and ESEM observation. The numbers of yeast cell colonies on the ESEM mode were higher than on the HV mode. From this experiment, the living cell rate on the ESEM mode is almost the same order with initial condition of the water dispersion method.

(a)   (b)
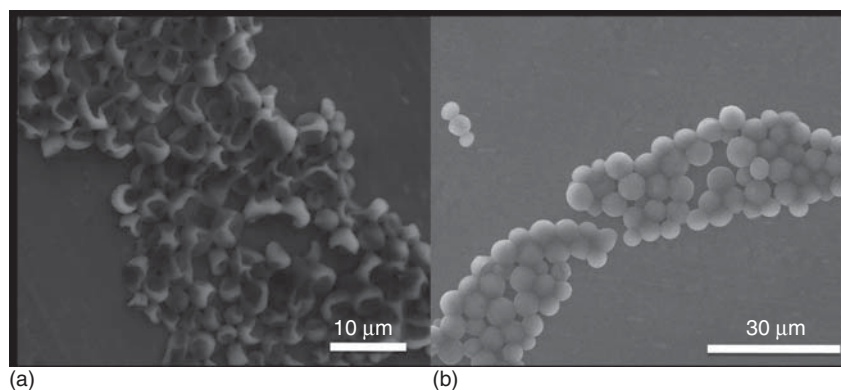
Figure 21.2 Images of *W303* yeast cells under (a) HV mode and (b) ESEM mode.
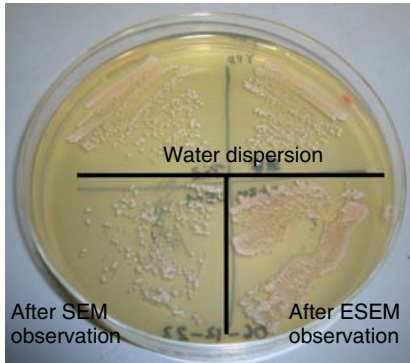
Figure 21.3 Cell culture plate of *W303* yeast cells after observations under SEM condition (bottom left of the plate area) and ESEM condition (bottom right of the plate area) as compared to the control cell culture by a standard water dispersion method (upper area of the plate).

21.4
Manipulation of Biological Cells under ESEM

21.4.1
Cell Viability Detection Using Dual Nanoprobe

Figure 21.4 shows a schematic of a single-cell electrical measurement using dual nanoprobe inside ESEM. The electrical measurement is performed under ESEM mode (600 Pa and 0 °C), which provides 98–100% humidity level of an environment around the cells. High-humidity condition is needed in order to sustain the physiological condition of the cells.

The electrical measurement is performed by applying 2V 220-ms excitation single pulses on a single cell and measuring single pulses current across that cell. Single pulses voltage sourcing and current measuring technique has twofold purposes. First, single pulses voltage sourcing is expected to greatly minimize the thermal noise, which may influence the accuracy of the measurement data.
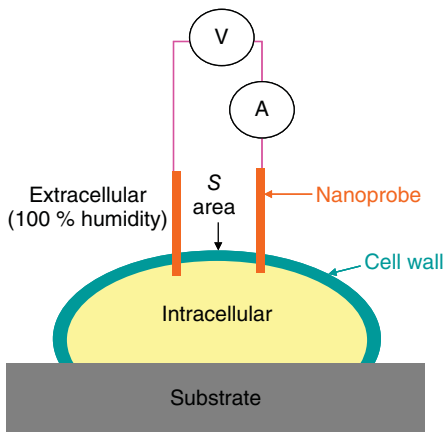
Figure 21.4 Schematic of the single cell electrical measurement using dual nanoprobe.
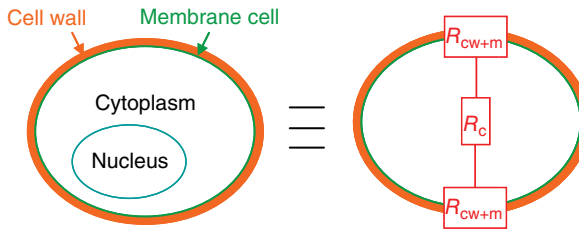
Figure 21.5 Schematic of the electrical model of a single biological cell.

Second, damage to the cells due to the Joule heating from the tip of the nanoprobe, which normally happen under continuous voltage sourcing technique, can be greatly minimized, if not eliminated.

A potential of 2 V was used so as to improve the reliability of the measured data. By using a lower potential input, it is difficult to differentiate the true measured data from the noise data as both are mixed together. The investigations of the thermal, nanomanipulator, and acceleration beam noises have been discussed elsewhere [11].

In order to obtain useful single pulses current data from cells that have strong cell wall, such as *W303* cells, several considerations are required. Figure 21.5 showed the schematics of the electrical model of a *W303* cell. It is expected that the resistance of the cell wall and cellular membrane of the *W303* cells are very high as compared to the resistance of the cytoplasm [12]. Therefore, in order to obtain more reliable single pulses current data from *W303* cells, the cytoplasm is chosen as a medium of measurement.

Because of this, in order to obtain a significant electrical characterization on single cells, the electrical measurement must be done at the intracellular area of the cell, that is, cytoplasm, by penetrating a dual nanoprobe inside the cell. This can be done with the help of the nanomanipulator unit which can provide a high resolution of linear motion (30 nm) for the dual nanoprobe to slightly penetrate a cell. Deeper penetration by a dual nanoprobe will burst the cells as the *S* area that covers the region on the cell surface between first and second nanoprobes, as shown in Figure 21.4, will have high stress level during penetration. Previously, we have reported single-cell surgery using nanoneedle [13]. The issue, that is, cell bursting due to weak *S* area during penetration, is solved by performing short penetration. In this configuration, only the tip of the dual nanoprobe is in contact with the intracellular area of the cell. By using this strategy, the electrical property of the single cells could be obtained.

Several studies reported that biological cells have a tendency to recover from small wounds [14]. Therefore, it is expected that the measured cells are still alive after being slightly penetrated by the dual nanoprobe. Furthermore, in order to prevent excessive damages to the cells during the penetration, small diameter of the tip of the dual nanoprobe in the range of 246 nm is used.

Sample's cell sizes used in this experiment are from 4 to 6 μm. It is expected, however, that the cell size of the sample does not influence the measurement of

the electrical property of the cytoplasm. The cytoplasm can be analogous to an electrolyte solution which contains ions. Ions act as corpuscles that carry electricity. The conductivity of the cytoplasm depends on the type and concentration of ions present [15], the temperature of the electrolyte solutions [16], the cross-sectional area of the electrode, and the distance between the electrodes [17]. In our experiments, the cross-sectional area of the electrode and the distance between the electrodes are constant, that is, 1.46 μm and 0.06 pm^2, respectively. The temperatures of the environment during the measurements are kept constant, that is, approximately 17 °C/0% humidity (for HV mode) and 1 °C/98 – 100% humidity (for ESEM mode). It is suspected that when the integrity of the cellular membrane is deteriorated, the ionic concentration of the cytoplasm cannot be maintained as a result of the ions or cytoplasm lost.

21.4.2
Preparation of Dead Cell Colonies of W303 Cells

The viability of the "dead cells" was confirmed qualitatively from two methods, that is, the uptake of the methylene blue dye inside the cells and the morphology change of the cells. The former method showed that the color of the cells turned to blue when died while the living cells remained nonblue (see Figure 21.6). The latter approach indicated that the dead cells have shrinkage morphology as opposed to round shape for living cells when observed under ESEM. By having these two levels of verifications, we strongly believe that the tested dead cells were in fact dead during the electrical measurement. The preparation of the dead cell colonies was done by following the protocol proposed by Kucsera *et al.* [18]. The methylene blue dye was added to the 25-ml YPD agar at 10 μmol l^{-1}. Plates were inoculated by streaking a yeast strain prepared from about 2-day-old agar culture and incubated for about 48 h at 30 °C. In a model experiment, cells were killed within colonies growing on plates by applying an 80 μl drop of amphotericin B (1 mg ml^{-1}) on the surface and allowing it to spread. Dye uptake from the medium was examined after
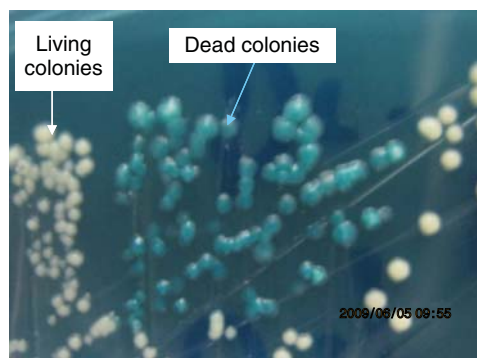
Figure 21.6 Image of the *W303* colonies at two conditions, that is, dead (blue) and live (white).

48 h of incubation at 30 °C. Figure 21.6 showed the images of dead cell colonies and live cell colonies on the same agar plate culture. The dead cell colonies are light-blue as the cellular membrane is not functioning and, therefore, unable to prevent the die from coming inside the cells. The live cell colonies are white.

21.4.3
Fabrication of the Dual Nanoprobe

The dual nanoprobe was fabricated by using focused ion beam (FIB) etching and deposition processes on a commercially available piezoresistive cantilever (Keyence) (see Figure 21.7a). First, the FIB etching (30 kV at 8221.5×1015 ion dose) was performed to remove the insulator layer (SiO_2) of the piezoresistive cantilever (see Figure 21.7b). Then, the FIB deposition (30 kV at 15268.6×1015 ion dose) was executed to deposit tungsten (W) material on the conductive layer (doped Si) of the cantilever (see Figure 21.7c).

Next, the FIB etching was performed to etch the cantilever plate into two separate plates where each plate contains the W deposition (see Figure 21.7d). Finally, the FIB etching was used to trim the W deposition into nanoneedle shape (see Figure 21.6e,f). In order to apply the nanoprobe under high-humidity environment (~100% humidity level), the conductive layers located on the printed circuit
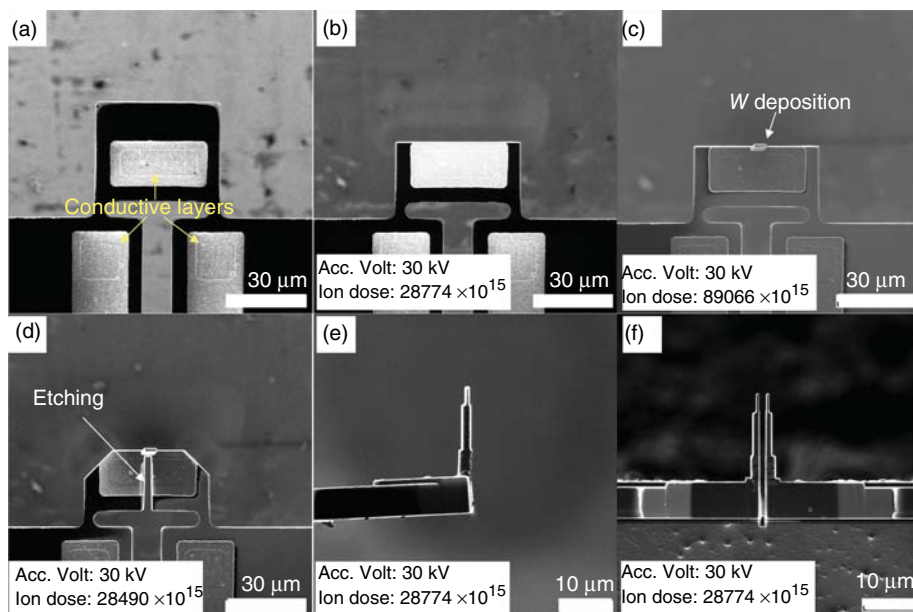
Figure 21.7 SEM images during the fabrication of the dual nanoprobe. (a) Standard piezoresistive cantilever, (b) removal of an insulator layer, (c) deposition of tungsten (W) material, (d) separation of a cantilever, (e) trimming of a side W deposition, and (f) trimming of a top W deposition.
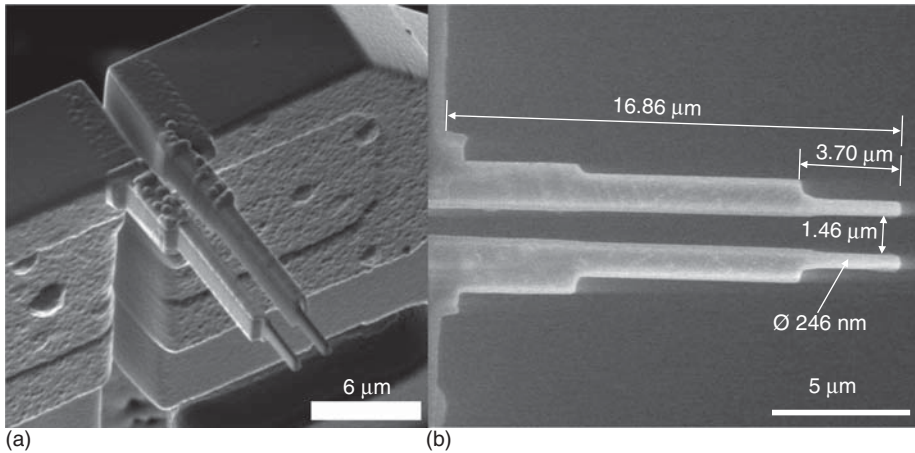
Figure 21.8 SEM images of the dual nanoprobe at (a) perspective view and (b) top view.

board of the nanoprobe as shown in Figure 21.7a were coated with the parylene material between steps in Figure 21.7d,e. The thickness of the parylene coating was around 200–300 nm. Because of the trimming steps (see Figure 21.6e,f), the parylene coating was removed at the nanoprobe area. The parylene coating is not only functioned as an insulator that protects the conductive layers from the interaction with water molecules under high-humidity environment but can also provide a support to the base area of the nanoprobe, which enhance the rigidity and strength of the nanoprobe during the contact with single cells. Figure 21.8 shows the SEM images of the fabricated dual nanoprobe. The typical diameter and length of the nanoprobe are about 200–300 nm and 10–17 μm, respectively. The gap between the probes is about 1.5 μm. The physical dimensions of the dual nanoprobe were designed for measuring electrical property of single cells, which have minimal size of at least 2 μm and above. For the electrical measurement on single cells, the fabricated nanoprobe is placed on the nanomanipulator unit inside the ESEM chamber.

21.4.4
Electrical Measurement Setup

Figure 21.9 shows the measurement setup for the single-cell electrical measurement system. The nanoprobe was attached to the nanomanipulator unit inside the ESEM chamber. The nanoprobe provides a connection with the sub-femtoamp sourcemeter, which was located outside the ESEM chamber. The sourcemeter was further connected with the data acquisition card inside the computer. The home-made graphical user interface (GUI) on the PC was developed using LabView source code (National Instrument Corporation, Austin, TX). The measurement
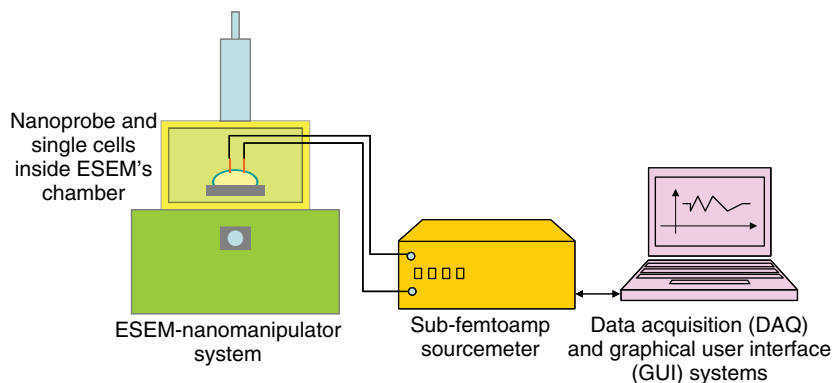
Figure 21.9 Measurement setup for the single cells electrical characterization.

protocol is based on the single-pulse source voltage (2 V) and single-pulse measured current. The pulse width (PW*)* of the source voltage is 0.22 s, which was obtained from the following equation, pw $= (c/f) + s$, where c, f, and s are the number of power line cycles, power line frequency, and source delay. The values for c and s were programmed to be 1 and 0.2, respectively, while the value for f was 60 Hz.

21.4.5
Experimental Results and Discussions

The electrical measurement on single cells using the dual nanoprobe was done by first approaching the dual nanoprobe to a single cell with a coarse speed (2 kHz) of the nanomanipulator. Once the dual nanoprobe was quite near (about 5 μm) to the cell, the speed of the nanomanipulator was reduced to 20 Hz. The speed reduction of the nanomanipulator will ensure a smooth contact between the dual nanoprobe and the single cell as well to minimize noise during electrical measurement. The ESEM observation was done at 20V acceleration voltage and 3.0 spot size. Once the contact between the dual nanoprobe and the single cell was achieved, the ESEM observation was disabled to eliminate the noise from the electron beam during electrical measurements. Then, the electrical measurement was started by sourcing 2V single pulses voltage and recording single pulses current with a measurement bandwidth of 18.84 Hz. While recording the single pulses current, the dual nanoprobe was further slowly indenting (speed of 20 Hz) the single-cell until penetration of about 300–350 nm was achieved as verified using an image analysis. The penetration depth of 300–350 nm was adequate to enable the dual nanoprobe to reach inside the cytoplasm area as the thickness of the cell wall and the cellular membrane are in the range of 100–200 and 5–10 nm, respectively [19]. The measurement results are suspected to highly depend on the ionic level of the cytoplasm of the cells which can indicate cell conditions, that is, cell

death or cell being affected by the influence of the chemical dye as discussed in the following sections.

21.4.5.1 Single-Cell Viability Assessment by Electrical Measurement under HV Mode

Figure 21.10 shows ESEM images of a typical electrical probing on single cells by using a dual nanoprobe. The measurement was recorded when the dual nanoprobe penetrated slightly the cell wall of the single cells as shown in Figure 21.10b. Once the contact was established, the electron beam was turned OFF and the single pulses of 2 V with 0.22-s PW were applied. The electron beam was turned OFF to eliminate the influence of noise from the electron beam source. The single pulses current were then recorded. The single-pulse voltage was selected, and not the continuous source voltage, as it can reduce the effect of the noise interferences and also minimize the effect of an excessive electrical potential to the physiology of the cells. The single-pulse current source and measurement was based on a homemade source code based on LabView programming syntax [20]. The contact marks on the cell can be seen as shown in Figure 21.10c. In order to simulate the dead cells condition, the cells were placed under HV mode. HV mode provides critical condition for the cells where most of the cells will be shrunk, that is, dead. The living cells were obtained by placing the cells under ESEM mode. Under ESEM mode, the cell condition is much better. Figure 21.11 shows a typical result of the electrical probing on single cells using nanoprobe under HV mode and ESEM mode. It is interesting to note that under HV mode, there was hardly
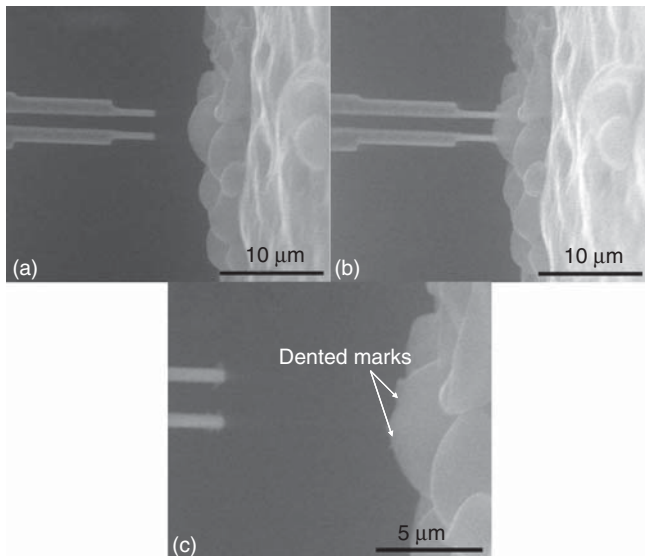
Figure 21.10 Typical ESEM images during the electrical probing on single cells using nanoprobe, (a) before contact and (b) during contact. Successful contact can be confirmed from the dented marks on a cell surface as shown in (c).
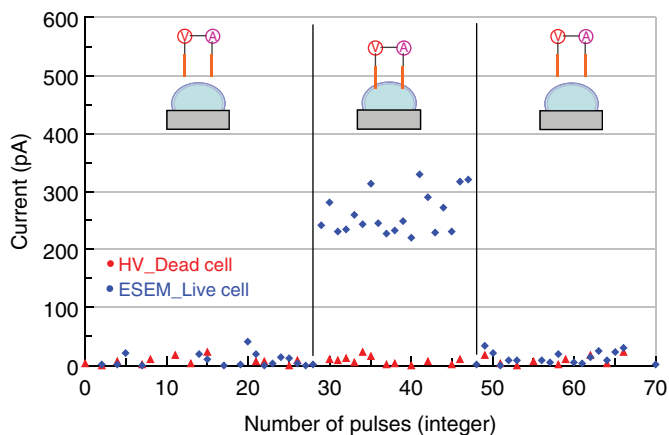
Figure 21.11 Results of the electrical probing on single cells at two environmental conditions, that is, HV condition for dead cells (red points) and (b) ESEM condition for live cells (blue points).

any current flow through the cells. Interestingly, when the cells were placed under ESEM mode, the conducted electrical measurement found electrical current flow through the single cell, that is, 262 ± 18 pA (19 pulses). The statistical analysis was based on the Student's t test. A confident level of 95% was used. The Student's t test is normally used when the mean population of the sample was unknown and the number of tested sample was small. Here, the single pulses current measurements for dead cells were obtained by placing the cells under HV condition. Under HV condition ($\sim 1 \times 10^{-3}$ Pa), the survivability of the cells is very low due to the dramatic change in the pressure level. This can be comprehended from the result shown in Figure 21.11. On the other hand, when the cells are placed under ESEM mode (98% humidity level), the survivability of the cells is improved due to the high humidity level, which preserved the condition of the cells.

In addition to the result shown in Figure 21.11, which compares the electrical measurements of the cells under two different conditions, that is, HV and ESEM modes, it would be interesting and convincing if the electrical measurement for the dead cells and living cells could be performed under the same environmental setting, that is, ESEM mode. The following section discusses such comparison.

21.4.5.2 Single-Cell Viability Assessment by Electrical Measurement under ESEM Mode

In order to compare the electrical property of dead and live cells under ESEM mode, the $W303$ yeast cells were grown under YPD + methylene blue plate culture. Then, some cell colonies were killed by spreading 1 mg ml^{-1} of amphotericin B solution on some regions of the cell colonies. The dead cell colonies are light-blue as compared to the white appearance of the living cell colonies as shown in Figure 21.6. The addition of the amphotericin B solution on the cell colonies will affect the integrity of the cellular membrane. It is expected that the cellular membrane of the $W303$ cells lost its integrity when mixed with the amphotericin B

Table 21.1 Results of the electrical measurements at various single cells' conditions under ESEM mode.

Cell condition	Sensing current (pA)
Live cells growth without methylene blue ($n = 5$)	262 ± 18
Live cells growth with methylene blue ($n = 5$)	140 ± 2
Dead cells ($n = 10$)	2 ± 5

solution. Because of this, the cellular membrane could not prevent the methylene blue dye from going inside the cell. The intrusion of the dye inside the cell colonies can be confirmed from Figure 21.6. The loss of the integrity of the cellular membrane is one of the indicators for dead cell [21]. Table 21.1 shows the result of the electrical measurement of dead and live cells under ESEM mode. The dead cells were obtained from the YPD + methylene blue plate culture. The living cells, on the other hand, were obtained from the normal YPD plate culture. For the dead cells, as expected, there was no current flow through the cell, that is, 2 ± 5 pA. It is suspected that the cytoplasm could not provide an electrical path between the electrical probes. The inability of the cytoplasm to provide an electrical path may be due to the depreciation of the ionic level of the cytoplasm or due to the cytoplasm lost from the cells [22]. On the other hand, when the cells were not mixed with the amphotericin B, the cytoplasm could provide an electrical path for the electrical probes. The average single pulses current measurement recorded by the electrical probes on live cells was 262 ± 18 pA as shown in Table 21.1. Further investigation showed that the methylene blue dye could reduce the conductivity of the cells. The average value of the recorded single pulses current measurement on the living cells that were growing on the YPD + methylene blue dye was lower than that on the living cells that were growing on the YPD plate culture only, that is, 140 ± 2 pA. It is suspected that the methylene blue dye may change the chemical composition of the cytoplasmic materials of the cells. The change of the chemical composition of the cells may reduce the ionic level of the cytoplasmic materials, which resulted in the reduction of the single pulses current measurement [22, 23].

21.5
Manipulation of Biological Cells under Microfluidics

21.5.1
Nanoliters Discharge/Suction by Thermoresponsive Polymer Actuated Probe

The TPA probe which uses thermoresponsive polymer poly(N-isopropylacrylamide) (PNIPAAm) volume change as an actuator was developed. The developed probe is applicable to single-cell analysis, especially single-cell manipulation. The

TPA probe can discharge and suck solution in several nanoliters (nl) using the volume change of thermoresponsive polymer solution. Normally, it is difficult to realize solution discharge and suction less than several dozens of nanoliters by the conventional air- or oil-pressure-actuated probes. We designed the TPA probe for low-cost fabrication and disposable use. The probe also takes in and ejects on a nanoliter order by simply switching a heater on and off. PNIPAAm solution volume change was evaluated in this work. The manipulation of single microbead and the suction of target cell were also demonstrated by the TPA probe in microfluidic device. It is considered that the TPA probe can contribute to the manipulation of single cell.

21.5.2
Fabrication of TPA Probe

We propose the novel probe device for discharge and suction of solution to use in the semiclosed microchip, which we proposed [24] for single-cell manipulation. The semiclosed microchip can achieve probe manipulation inside the microfluidic device. The probe device uses the volume change of thermoresponsive solution 10 wt% PNIPAAm. The volume change is caused during the soluble–insoluble transition of the PNIPAAm solution.

It is needed to discharge and suck solution on a nanoliter scale for single-cell manipulation because target cells have to be manipulated alone without affecting surrounding cells. Discharge and suction also be easy to control. We therefore focused on thermoresponsive solution 10 wt% PNIPAAm volume change to be used as an actuator.

The 10 wt% PNIPAAm solution clouds and a white solid is formed over 32 °C [25–27]. This soluble–insoluble transition temperature is near room temperature and not as high as used for other thermosensitive solution, such as methylcellulose, which is clouded over 50 °C [28]. PNIPAAm solution saves energy when generating the soluble–insoluble transition.

Figure 21.12 shows the TPA probe design. The glass micropipette was made from a borosilicate glass tube with an outer diameter of 1 mm and an inner diameter of 0.6 mm (GD-1, Narishige). A vertical pipette puller (PC-10, Narishige) was used to obtain the micropipette. Figure 21.13 shows how the microheater for the TPA probe is fabricated. A filament used in a miniature bulb is placed in a silicon tube (1 mm inner diameter) and sealed using polydimethylsiloxane (PDMS) (SILPOT 184 W/C, Dow Corning Toray). Figure 21.14 shows the
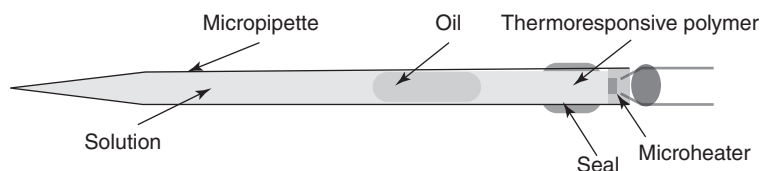
Figure 21.12 TPA probe design.
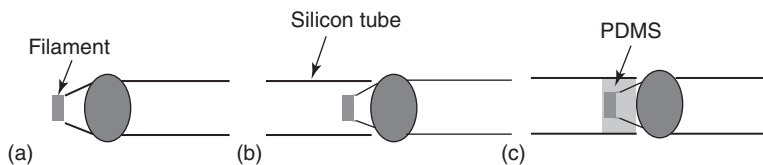
Figure 21.13 Microheater fabrication for the TPA probe. (a) A filament is prepared as a heater. (b) The filament is inserted into a silicon tube. (c) PDMS is placed in the silicon tube and cured.
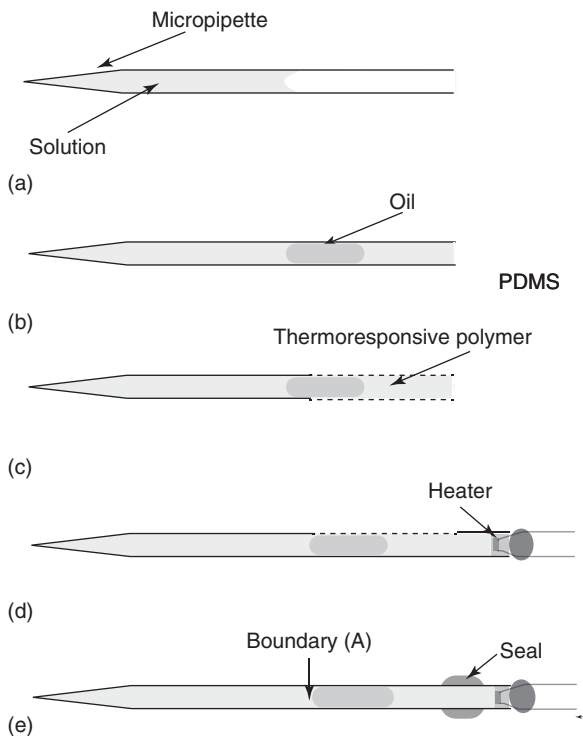
Figure 21.14 TPA probe fabrication. (a) Solution is placed in a micropipette, (b) oil is placed in the micropipette, (c) PNIPAAm solution is placed in the micropipette, (d) the micropipette is inserted into the heater, and (e) the heater and the micropipette are sealed together.

fabrication procedure of the TPA probe. Solution is placed in the micropipette (Figure 21.14a), then, oil (liquid paraffin, Wako Pure Chemical Industries, Ltd) and 10 wt% PNIPAAm solution are placed in the micropipette in this order (Figure 21.14b,c). The 10 wt% PNIPAAm solution was prepared by dissolving PNIPAAm (molecular weight: 20 000 – 25 000, ALDRICH) in pure water. The soluble – insoluble transition temperature was confirmed by a thermostatic chamber. When the temperature of the thermostatic chamber increases over 32 °C, the 10 wt% PNIPAAm solution becomes clouded and a white solid is formed.
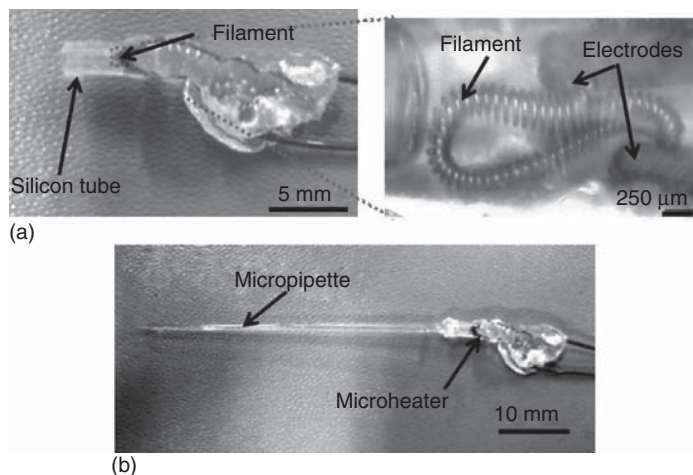
Figure 21.15 Fabricated microheater of the TPA probe. (a) Fabricated heater and (b) a micropipette is inserted to the heater.

The oil is used to divide PNIPAAm from the solution to keep the PNIPAAm concentration at 10 wt%. Then, these solutions were placed in the micropipette and the micropipette was inserted into the silicon tube of the fabricated microheater (Figure 21.14d). Finally, the microheater and micropipette were sealed together (Figure 21.14e). Figure 21.15a shows the fabricated microheater. Figure 21.15b shows the situation after the micropipette is inserted into the microheater and micropipette and microheater are sealed together. The soluble–insoluble transition can be caused only to turn the heater on and off. After using the TPA probe, the microheater can be detached from the micropipette and the microheater can be used repeatedly. Only the conventional micropipette needs to be replaced and disposable use can be realized at a low cost by the TPA probe.

21.5.3
Solution Discharge by TPA Probe

To demonstrate solution discharge using the TPA probe, pure water, which was stained red using Congo red (Wako Pure Chemical Industries, Ltd.), was placed into the probe, whose tip was 3 µm in inner diameter, to check solution discharge. In this experiment, the volumes of the red solution, oil, and 10 wt% PNIPAAm solution were 9, 0.8, and 2 µl, respectively. After the TPA probe was inserted into the bath, 0.25 A was applied to the heater and 10 wt% PNIPAAm solution clouded by the generated Joule heat.

Figure 21.16 shows experimental results. Discharge of red solution was observed when the heater was turned on. And this discharge was stopped when the current was turned off. From the results, it can be concluded that PNIPAAm solution volume increased when PNIPAAm was clouded, and this volume change
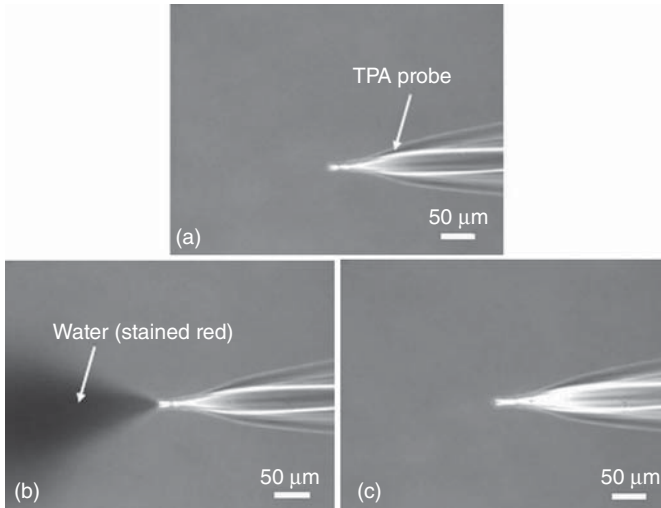
Figure 21.16 Experimental results with solution discharge by the TPA probe. (a) Before and (b) during heating of the PNIPAAm, and (c) after turning off the microheater.

is used to actuate solution discharge. PNIPAAm solution volume also decreased when the PNIPAAm becomes transparent again, and this volume change is used for solution suction.

21.5.4
Suction and Discharge of Micro-Object by TPA Probe Inside Semiclosed Microchip

21.5.4.1 Semiclosed Microchip
We proposed a semiclosed microchip [24] as shown in Figure 21.17. The microchannel was fabricated in the microchip to achieve exchange of solution in the bath. To realize the probe manipulation, the semiclosed microchip has the bath in the middle of microchannel. The probe devices can be inserted into the microchip through the bath. The bath is sealed by a thin oil film to prevent evaporation of the solution in the bath. The probe devices can be inserted and taken out with keeping the seal of the bath.

Indium tin oxide (ITO) electrodes are fabricated as heaters at the center of the bath [24]. The 10 wt% PNIPAAm solution is made into a white solid by applying voltage to these electrodes. Cells in the semiclosed microchip are then fixed by the generated white solid. This cell fixation realizes the stable observation under a microscope during cell culture and analysis in the semiclosed microchip [24].

Yeast cells were cultured in the semiclosed microchip after fixing cells using the PNIPAAm. Cell division was observed during cell culture and cultured yeast cell survivability was checked using 5-(and-6)-Carboxyfluorescein diacetate (CFDA) (AnaSpec, Inc.), a fluorescent probe for staining living cells.
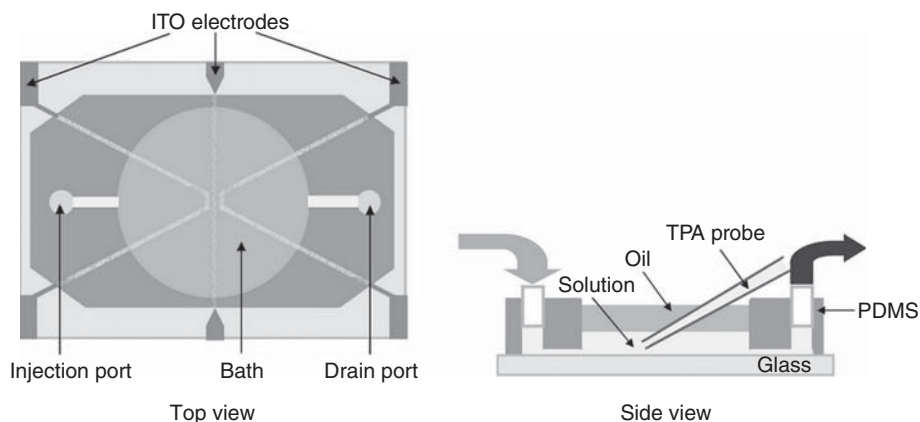
Figure 21.17 Semiclosed microchip design.
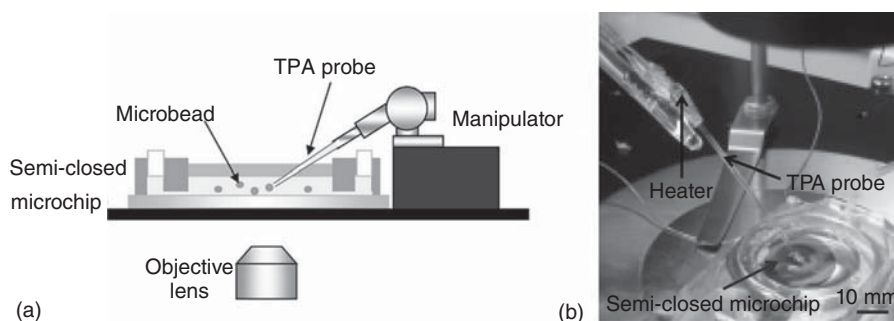
Figure 21.18 Experimental setup of microbead manipulation by the TPA probe. (a) Setup and (b) photograph of the setup.

21.5.4.2 Suction and Discharge of Microbead by TPA Probe Inside Semiclosed Microchip

Microbeads were discharged and sucked by the TPA probe as shown in Figure 21.18. In the experiments, two different microbeads, 10 and 1.3 μm in diameter (Duke Scientific Corp.), were used. Microbeads were first dispersed in the bath, and then the TPA probe was inserted into the semiclosed microchip and manipulated under a microscope. The inner diameter of the probe was 23 μm for 10-μm microbeads and 4 μm for 1.3-μm microbeads.

The microheater of the TPA probe was turned on before the microbead was sucked, and turned off to suck the microbead after the TPA probe was positioned. Currents of 0.25 A to manipulate 10-μm microbeads and 0.12 A for 1.3-μm microbeads were applied. After suction of the target microbead, the probe was moved to prepare for discharge. The microbead in the probe was discharged by turning the microheater on again.
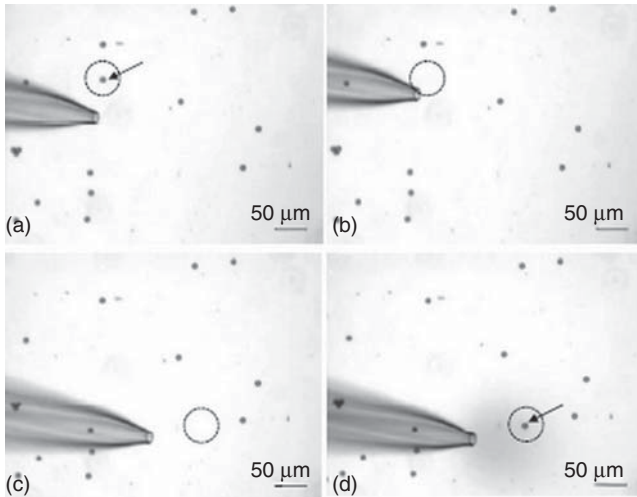
Figure 21.19 Experimental results for manipulating the 10-μm microbead by the TPA probe. (a) Positioning of the probe for suction, (b) after the target microbead is sucked, (c) positioning of the probe for discharge, and (d) after the microbead is discharged.
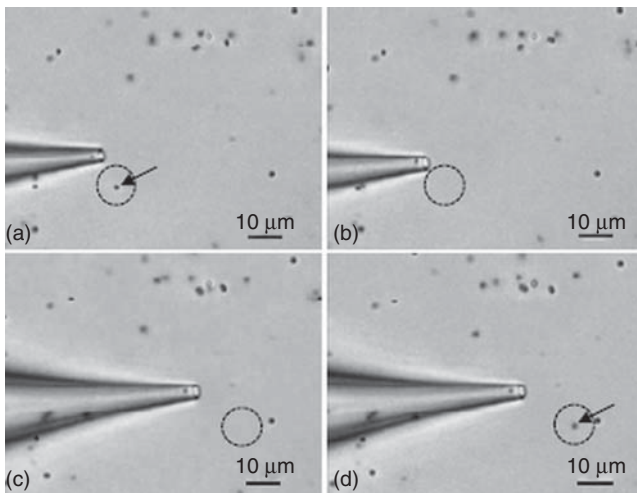
Figure 21.20 Experimental results for manipulating the 1.3-μm microbead by the TPA probe. (a) positioning of the probe for suction, (b) after the target microbead is sucked, (c) positioning of the probe for discharge, and (d) after the microbead is discharged.

Figures 21.19 and 21.20 showed experimental results for manipulating microbeads, both of which successfully sucked, manipulated, and discharged by changing the current applied to the TPA probe. Cells were manipulated by simply switching the heater on and off when the TPA probe was used.
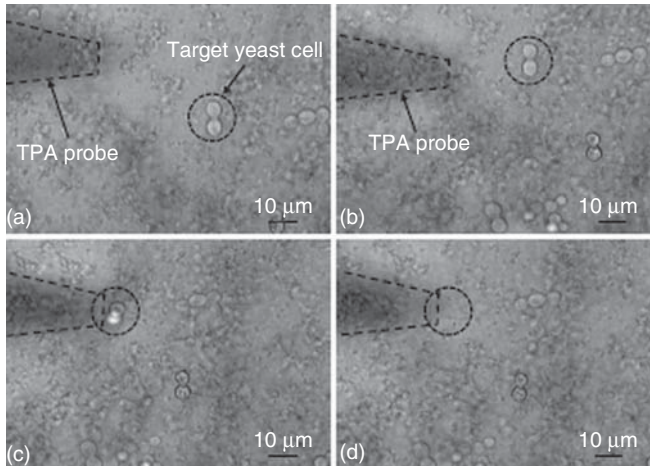
Figure 21.21 Experimental results for yeast cells suction by the TPA probe. (a) Before probe positioning, (b) after probe positioning to the target yeast cells, (c) during suction, and (d) after suction.

21.5.4.3 Cell Suction by TPA Probe Inside Semiclosed Microchip

To apply the TPA probe to manipulate biological cells in the semiclosed microchip, cell suction was demonstrated in experiments under a microscope. Voltage was applied to the ITO electrodes in the semiclosed microchip, where yeast cells were fixed with the PNIPAAm. The TPA probe, whose tip was 20 μm in inner diameter, was used to suck the target yeast cells fixed by the PNIPAAm. The TPA probe was set on the micromanipulator. Solution was sucked and discharged, as stated, by turning the microheater on and off using an applied current of 0.25 A.

Figure 21.21 shows experimental results. After current was applied to the microheater of the probe, the probe was moved to yeast cells (Figure 21.21a) and positioned (Figure 21.21b). The current applied to the microheater is turned off to start suction of target cells. As shown in Figure 21.21c,d, targeted yeast cells, which were fixed by the PNIPAAm, were sucked into the TPA probe. Cells fixed in PNIPAAm were maintained as is in the semiclosed microchip. The TPA probe is therefore applicable to the single-cell manipulation. The TPA probe also sucks cells fixed in the PNIPAAm in the semiclosed microchip.

21.6
Conclusion

In this chapter, we presented two techniques for manipulating biological cells. The former technique was based on ESEM-nanomanipulation approach, while the latter was based on microfluidic system. To explain both techniques in more detail,

one example was highlighted for each technique. Example for the former technique was based on a quantitative method for single-cell viability detection by employing single cells electrical characterization using dual nanoprobe. On the other hand, the manipulation of cell using TPA probe was presented as an example for the latter technique.

References

1. Kriss, T.C. and Kriss, V.M. (1998) History of the operating microscope: from magnifying glass to microneurosurgery. *Neurosurgery*, **42**, 899–907.

2. Oatley, C.W. (1982) The early history of the scanning electron microscope. *J. Appl. Phys. Lett.*, **53**, R1–R13.

3. Chu, Y.S., Dufour, S., Thiery, J.P., Perez, E., and Pincet, F. (2005) Johnson-Kendall-Roberts theory applied to living cells. *Phys. Rev. Lett.*, **94**, 028102.

4. Suresh, S., Spatz, J., Mills, J.P., Micoulet, A., Dao, M., Lim, C.T., Beil, M., and Seufferlein, T. (2005) Connections between single-cell biomechanics and human disease states: gastrointestinal cancer and malaria. *J. Acta Biomater.*, **1**, 15–30.

5. Wang, N., Butler, J.P., and Ingber, D.E. (1993) Mechanotransduction across the cell surface and through the cytoskeleton. *Science*, **260**, 1124–1127.

6. Vliet, K.J.V., Bao, G., and Suresh, S. (2003) The biomechanics toolbox: experimental approaches to living cells and biomolecules. *Acta Mater.*, **51**, 5881–5905.

7. Fischer-Cripps, A.C. (2002) *Nanoindentation*, 1st edn, Springer.

8. Thoumine, O. and Ott, A. (1997) Time scale dependent viscoelastic and contractile regimes in fibroblasts probed by microplate manipulation. *J. Cell Sci.*, **110**, 2109–2116.

9. Guck, J., Ananthakrishnan, R., Mahmood, H., Moon, T.J., Cunningham, C.C., and Kas, J. (2001) The optical stretcher: a novel laser tool to micromanipulate cells. *Biophys. J.*, **81**, 767–784.

10. Whitesides, G.M. (2006) The origins and the future of microfluidics. *Nature*, **442**, 368–373.

11. Ahmad, M.R., Nakajima, M., Kojima, S., Homma, M., and Fukuda, T. (2012) Instantaneous and quantitative single cells viability determination using dual nanoprobe inside ESEM. *IEEE Trans. Nanotechnol.*, **11** (2), 298–306.

12. Raicu, V., Raicu, G., and Turcu, G. (1996) Dielectric properties of yeast cells as simulated by the two-shell model. *Biochim. Biophys. Acta*, **1274**, 143–148.

13. Ahmad, M.R., Nakajima, M., Kojima, S., Homma, M., and Fukuda, T. (2008) In situ single cell mechanics characterization of yeast cells using nanoneedles inside environmental sem. *IEEE Trans. Nanotechnol.*, **7**, 607–616.

14. Martin, P. and Lewis, J. (1992) Actin cables and epidermal movement in embryonic wound healing. *Nature*, **360**, 179–183.

15. Bianchi, H. and Fernandez-Prini, R. (1993) The conductivity of dilute electrolyte solutions: expanded Lee and Wheaton equation for symmetrical, unsymmetrical and mixed electrolytes. *J. Solution Chem.*, **22**, 557–570.

16. Kuyucak, S. and Chung, S.-H. (1994) Temperature dependence of conductivity in electrolyte solutions and ionic channels of biological membranes. *Biophys. Chem.*, **52**, 15–24.

17. Bester-Rogac, M. and Habe, D. (2006) Modern advances in electrical conductivity measurements of solutions. *Acta Chim. Slov.*, **53**, 391–395.

18. Kucsera, J., Yarita, K., and Takeo, K. (2000) Simple detection method for distinguishing dead and living yeast colonies. *J. Microbiol. Methods*, **41**, 19–21.

19. Walker, G.M. (1998) *Yeast Physiology and Biotechnology*, John Wiley & Sons, Ltd., Chichester.

20. 2007) *Labview: Getting Started with Labview*, National Instruments Corp..

21. Darzynkiewicz, Z., Li, X., and Gong, J.P. (1994) Assays of cell viability: discrimination of cells dying by apotosis. *Methods Cell Biol.*, **41**, 15–38.

22. Krupa, J. and Terlecki, J. (1976) A nondestructive method for measuring electrical conductivity of intracellular matter of tissue in situ. *Rad. Environ. Biophys.*, **13**, 79–88.

23. Hamill, O.P., Marty, A., Neher, E., Sakmann, B., and Sigworth, F.J. (1981) Improved patch-clamp techniques for high-resolution current recording from cells and cell-free membrane patches. *Eur. J. Physiol.*, **391**, 85–100.

24. Takeuchi, M., Nakajima, M., and Fukuda, T. (2009) Semi-closed microchip for probe manipulation and the target cell harvesting. Proceedings International Conference on Robotics and Automation, pp. 1838-1843.

25. Ichikawa, A., Arai, F., Yoshikawa, K., Uchida, T., and Fukuda, T. (2005) In situ formation of a gel microbead for indirect laser micromanipulation of microorganisms. *Appl. Phys. Lett.*, **87**, 191108.

26. Yamanishi, Y., Teramoto, J., Magariyama, Y., Ishihama, A., Fukuda, T., and Arai, F. (2009) On-chip cell immobilization and monitoring system using thermosensitive gel controlled by suspended polymeric microbridge. *IEEE Trans. Nanobiosci.*, **8**, 312–317.

27. Walsh, D., Hall, S.R., Moir, A., Wimbush, S.C., and Palazzo, B. (2007) Carbonated water mediated preparation of poly(*N*-isopropylacrylamide) thermoresponsive gels and liquids. *Biomacromol.*, **8**, 3800–3805.

28. Arai, F., Ichikawa, A., Fukuda, T., and Katsuragi, T. (2003) Isolation and extraction of target microbes using thermal sol-gel transformation. *Analyst*, **128**, 547–551.

Index

WILEY END USER LICENSE AGREEMENT

Go to www.wiley.com/go/eula to access Wiley's ebook EULA.